TECHNISCHE UNIVERSITÄT MÜNCHEN
Physik Department
Arbeitsgebiet stark korrelierte Elektronensysteme

Investigation of itinerant antiferromagnets and cubic chiral helimagnets

Dipl.-Phys. Univ. Andreas Bauer

Vollständiger Abdruck der von der
Fakultät für Physik der Technischen Universität München
zur Erlangung des akademischen Grades eines

Doktors der Naturwissenschaften (Dr. rer. nat.)

genehmigten Dissertation.

Vorsitzender:		Univ.-Prof. Dr. Wilhelm Zwerger
Prüfer der Dissertation:	1.	Univ.-Prof. Christian Pfleiderer, Ph.D.
	2.	Univ.-Prof. Dr. Rudolf Gross
	3.	Univ.-Prof. Wolf Assmus, Goethe-Universität Frankfurt a. M. (nur schriftliche Beurteilung)

Die Dissertation wurde am 03.09.2014 an der Technischen Universität München eingereicht
und durch die Fakultät für Physik am 10.12.2014 angenommen.

Contents

Complex forms of electronic and magnetic order

Materials that exhibit complex forms of electronic or magnetic order, often in combination with strong electronic correlations, are of growing interest for both basic and applied solid state research. The complexity of these systems, in general, may be both a curse and a blessing. While the disentanglement of the underlying mechanisms usually proves to be demanding, their unraveling promises fresh insights to fundamental condensed matter physics and the design of new materials with enhanced or novel functionalities. A long standing puzzle, for instance, comprises the origin of the high-T_c superconductivity in cuprates [1, 2] which still remains enigmatic and is debated controversially after nearly three decades of research. In parallel to the ceramic cuprates, metallic heavy fermion compounds [3, 4], further layered oxides [5, 6], and, since a few years, iron pnictides [7, 8] are investigated for unconventional superconductivity.

These types of superconductivity, as well as other forms of complex behavior, often emerge near quantum phase transitions, where conventional long-range magnetic order is suppressed by a non-thermal tuning parameter. In metals this suppression is often accompanied by a breakdown of the standard model for their description—the Fermi liquid theory [9, 10]. Most of the resulting non-Fermi liquid properties are not yet fully understood. In this context, a fascinating example is the formation of a topological non-Fermi liquid in MnSi under hydrostatic pressure [11]. Here, the concept of topology is associated with complex real-space spin textures that may not be continuously transformed to topologically trivial states such as paramagnets, ferromagnets, or helimagnets [12]. In addition, in recent years topology also has become an important keyword when accounting for phenomena in reciprocal space. One of the most prominent examples concerns the band inversion in a topological insulator that gives rise to a Dirac cone and a metallic state at its surface [13, 14]. The topology of the bulk Fermi surface may change as a pocket or a neck appears or disappears at a Lifshitz transition, also referred to as electronic topological transition [15, 16]. Further sources for complex behavior comprise, for instance, the effects of strong geometric frustration [17] and the coupled degrees of freedom in multiferroic compounds [18, 19].

Whereas the brief account above is essentially restricted to three-dimensional systems, in fact also low-dimensional structures exhibit complex forms of order and strong electronic correlations. Examples include highly mobile or even superconducting electron gases at the interface between insulating oxides [20, 21], topologically insulating heterostructures [22, 23], monolayers with complex magnetic textures [24, 25], and multiferroic thin films [26, 27].

The work reported below was embedded into two research frameworks, namely 'Single Crystal Growth of Metals with Complex Order' in the Transregional Collaborative Research Center 'From Electronic Correlations to Functionality' and 'Topological Spin Solitons for Information Technology'. These titles nicely reflect central topics of this thesis, which is organized as follows.

Chapter 1 starts with a short introduction to the single crystal growth of intermetallic compounds. The resulting high-quality samples are essential for the determination of the intrinsic properties of three-dimensional solid state systems, in particular if probing phenomena sensitive to disorder, defects, or the crystalline orientation. As part of this thesis the single crystal preparation chain for intermetallic compounds under ultra-high vacuum compatible conditions of our group was extended, amongst others by the integration of electrotransport into optical float-zoning. The corresponding technical developments are described in detail. Subsequently, we present the experimental methods for the metallurgical characterization and the study of the low-temperature properties of the samples grown. Three classes of compounds were addressed in detail; (i) hexagonal diborides, (ii) cubic Heusler compounds, and (iii) cubic chiral helimagnets. The diborides and the Heuslers both allow for a remarkable variety of electronic and magnetic properties in the same comparably simple crystallographic environment. To a certain degree, this aspect also holds true for the cubic chiral helimagnets as they include metals, semiconductors, and insulators with essentially identical magnetic behavior.

Chapter 2 is concerned with the (itinerant) antiferromagnets CrB_2, MnB_2, and CuMnSb. CrB_2 displays an incommensurate spin structure and turns out to be the perhaps closest weak analog to the itinerant antiferromagnet chromium. Speculations about the properties of nonmagnetic CrB_2, i.e., if tuned through a quantum phase transition, suggest that it may provide a missing link between heavy fermion superconductivity in rare earth based compounds and the high-T_c superconductivity in the cuprates. In contrast, the isostructural sibling MnB_2 reveals a commensurate antiferromagnetic structure of local-moments at high temperatures that cants at low temperatures. The second antiferromagnet investigated in detail, the half-Heusler compound CuMnSb, oddishly shares magnetic properties believed to be hallmarks of either itinerant or local-moment magnetism. In phase-pure specimens we additionally observe a canting of the commensurate magnetic structure at low temperatures. Decoding the behavior of CuMnSb will help to fully understand magnetism in Heusler compounds, where antiferromagnets are very rare among transition metal based compounds, and may ultimately permit the design of materials for so-called all-Heusler-devices.

Chapter 3 finally accounts for the cubic chiral helimagnets MnSi, $Mn_{1-x}Fe_xSi$, $Fe_{1-x}Co_xSi$, and Cu_2OSeO_3. Perhaps most interestingly, these compounds give rise to a regular arrangement of topologically non-trivial spin whirls—the Skyrmion lattice. After a comprehensive general introduction and material specific descriptions of the state of the art, we account for the optimization of the single crystal growth of MnSi. Moreover, we present detailed studies of the magnetic phase diagrams of the cubic chiral helimagnets by means of magnetization, ac susceptibility, and specific heat measurements. Universally, we find a single pocket of Skyrmion lattice phase surrounded by first-order phase boundaries that are accompanied by regimes of slow dynamics. The existence of a field-induced tricritical point in MnSi and $Mn_{1-x}Fe_xSi$ is revealed corroborating a Brazovskii-type fluctuation-induced first-order transition in zero field. An account for the compositional tuning of $Fe_{1-x}Co_xSi$ allows to adjust key parameters of the magnetic order over a wide range and the hysteresis of its phase diagram enables us to prepare different states as a function of the temperature and field history. Our studies thereby establish a solid basis for future projects that eventually promise new concepts for magnonics or ultra-dense storage devices.

CHAPTER 1

Single crystal growth under ultra-high vacuum compatible conditions

A crucial part of this thesis concerned the development of a single crystal preparation chain for intermetallic compounds under ultra-high vacuum compatible conditions and under high-purity inert atmosphere, respectively. On the one hand, this task included the upgrade of the existing rod casting furnace and the ultra-high vacuum compatible image furnace. On the other hand, an argon glove box in combination with a horizontal cold boat furnace, an arc melting furnace, and a bespoke sample loading system were designed. A solid state electrotransport setup and an annealing furnace complete the preparation chain. Finally, an electrotransport option was integrated into the optical floating zone furnace.

After a brief introduction to the crystal growth of intermetallic compounds in Sec. 1.1, we will present the single crystal preparation chain available in the crystal growth laboratory of the chair for the Topology of Correlated Systems in Sec. 1.2. The technical details of the apparatus built or improved in this thesis will be discussed in Secs. 1.3 through 1.7. Subsequently, Sec. 1.8 describes the experimental methods used for the metallurgical characterization of the samples and for the determination of their low-temperature properties. The single crystals of various transition metal and rare earth compounds grown during this thesis are presented in Sec. 1.9 before we finally summarize the central aspects of this chapter and give an outlook in Sec. 1.10.

1.1 Introduction to single crystal growth

Single crystals of high quality are a valuable resource for technical devices and an important prerequisites for basic research. Commercially large single crystals of semiconductors possess by far the highest relevance. Other applications range from neodymium-doped yttrium aluminum garnet, Nd:$Y_3Al_5O_{12}$, as solid state laser medium [28] to sapphire, Al_2O_3, as high-resistant window material. Moreover, single crystals are utilized as detector material, where a recent example comprises the search for so-called weakly interacting massive particles (WIMPs) using high-purity $CaWO_4$ [29]. In contrast, basic solid state research is concerned with the properties of the single crystal itself. Fascinating phenomena in materials with strong electronic correlations, that have been extensively studied in recent years, include various forms of superconductivity [4, 7, 8, 30–33], magnetic monopoles in spin ice [34–38], spin liquids in frustrated magnets [39], complex spin textures in chiral magnets [12, 40–42] and other materials [43], topological insulators [13, 14, 44–47], as well as the breakdown of Fermi liquid description at magnetic quantum phase transitions [9, 10]. Impurities, defects, or grain boundaries may cause the perturbation or even destruction of such delicate phenomena.

However, in view of simple entropic considerations structural defects can never be avoided completely. Starting from a molten state at high temperatures, T, the material solidifies if the Gibbs free energy of the solid, $G_\mathrm{s} = H_\mathrm{s} - TS_\mathrm{s}$, falls below the Gibbs free energy of the liquid, $G_\mathrm{s} < G_\mathrm{l}$. Here, S is the entropy, i.e., a measure for the disorder, and H is the enthalpy, i.e., a measure for the total energy, and we neglect effects like supercooling that occur in real systems. As the crystallization takes place at finite temperatures, a growing crystal will always be subject to a certain amount of disorder in order to increase its entropy and minimize its Gibbs free energy.

Defects may be classified by their dimensionality. Zero-dimensional defects are referred to as point defects and arise at a single lattice site. In metallic compounds typical examples are vacancies (missing atoms), anti-site defects (constituent atoms on sites that are regularly occupied by other constituents), as well as impurities, i.e., atoms from non-matrix elements that either replace matrix atoms, so-called substitutional impurities, or occupy sites where no atom is expected, so-called interstitial impurities. The latter usually only happens if the impurity atom has a much smaller diameter than the matrix constituents. Dislocations are one-dimensional line defects that may be imagined as the end of an atomic plane in the bulk of the crystal. Grain and twin boundaries as well as stacking faults are viewed as two-dimensional planar defects. Three-dimensional defects finally include voids (clusters of vacancies) and pockets of impurity phases that are also denoted as precipitates.

In this section, we give a short overview of the most common techniques for the preparation of intermetallic samples, namely arc melting as well as single crystal growth by means of the Czochralsky, the Bridgman, and the chemical vapor transport technique. Float-zoning, as our method of choice, will be explain in more detail. Finally, we briefly describe the read-out of binary metallurgical phase diagrams.

1.1.1 Single crystal growth of intermetallic compounds

The necessary size of a single-crystalline sample is largely determined by the measurement method to be used. While experiments in pressure cells are often carried out on samples with volumes of the order of $0.1\,\mathrm{mm}^3$, (inelastic) neutron scattering experiments usually require or at least benefit from volumes exceeding $1\,\mathrm{cm}^3$. In general, single crystal growth may take place from the melt, through a solid state reaction, from the gas phase, or from a solution. High-quality samples of intermetallic compounds are mostly prepared from the melt.

Besides the impurities left in commercially available starting elements, the main sources of contaminations are the atmosphere and the crucible in which the crystal growth takes place. Here, the high affinity of the starting elements to oxygen, nitrogen, and carbon is a major constraint for the purity of intermetallic samples. As a result, an atmosphere as free of oxygen, nitrogen, water, and hydrocarbons as possible is indispensable for a high-quality crystal growth of intermetallic compounds, cf. Sec. 1.3 for more details. Contamination introduced through contact between the hot sample and a crucible can be reduced by choosing a suitable material combination as well as by cooling the crucible. Crucible-free methods like levitation melting or float-zoning completely avoid any contact and therefore any risk of contamination. Another possibility is that the crucible is formed by the material to be grown like it is done in the skull melting growth of zirconia, ZrO_2.

A very common sample preparation technique for intermetallic compounds is arc melting, often combined with a subsequent annealing of the sample. This method is a fast and comparable cost-efficient method, but only yields polycrystalline material or small single crystal grains. Large single crystals of intermetallic compounds are mostly prepared via the Czochralsky or the Bridgman technique. These techniques, as well as chemical vapor transport, will be briefly explained in the following, whereas the float-zoning method is addressed separately, cf. Sec. 1.1.2.

- For Czochralsky growth the raw material is melted via tetra-arc, induction, or resistive heating. A seed crystal, ideally an oriented single crystal, is brought in contact with the melt. The crystal grows while the seed is rotated and slowly pulled away from the melt. Czochralsky growth is usually performed from a crucible, though the raw material may also be contained via inductive levitation. Moreover, since the whole raw material is molten during the growth high vapor pressures can lead to serious difficulties and incongruent forming compounds can hardly be dealt with.

- For Bridgman growth the educts are sealed inside a crucible made of ceramics, glass, high-melting metals, or combinations thereof. After heating the sample above its melting temperature the crucible is slowly withdrawn from the heat source. While the usage of hot crucibles is inevitable for the Bridgman technique and related slow cooling methods, the small sealed volume inside the crucible is beneficial for treating materials with a high vapor pressure such as the itinerant ferromagnet $ZrZn_2$ [48–50] or topological insulators such as Bi_2Se_3 [46, 47, 51]. A variant, the so-called flux Bridgman growth, renders it possible to address complicated metallurgical phase diagrams. Here, in addition to the stoichiometric educts the crucible is filled with a flux material. The volume of the flux is a few times larger than the volume of the sample and it usually consists of either the lowest melting educt or another low melting element like tin, lead, or antimony. After the growth, the remaining flux is removed from the sample, e.g., by centrifuging or etching. In general, very slow cooling rates are applied. The resulting single crystals are often thin platelets oriented along certain crystallographic directions and flux inclusions are a problem frequently observed.

- Chemical vapor transport finally is a method that is used to grow intermetallic compounds from a gaseous phase. Here, small amounts of the educts are placed in one side of an sealed ampule that is filled with a gaseous transport agent, mostly a halogen. The educts are heated until they react with the transport agent, i.e., not above their melting temperature. At the other end of the ampule, which is kept at a slightly lower temperature, tiny single crystals of the desired compound may form spontaneously and grow in size. Since chemical vapor transport provides rather small crystals growing at very slow rates, it is usually only used for materials that may not be grown from the melt. An example with relevance for this thesis is FeGe [52], an isostructural sibling of the helimagnet MnSi. Moreover, the samples of the insulating helimagnet Cu_2OSeO_3 investigated in this thesis were grown via chemical vapor transport by Helmuth Berger at the École polytechnique fédérale de Lausanne (EPFL) [53].

1.1.2 Float-zoning

Float-zoning is a crucible-free method for single crystal growth in which a narrow molten zone is created from and traversed through a polycrystalline feed rod. The ideal growth rate is material

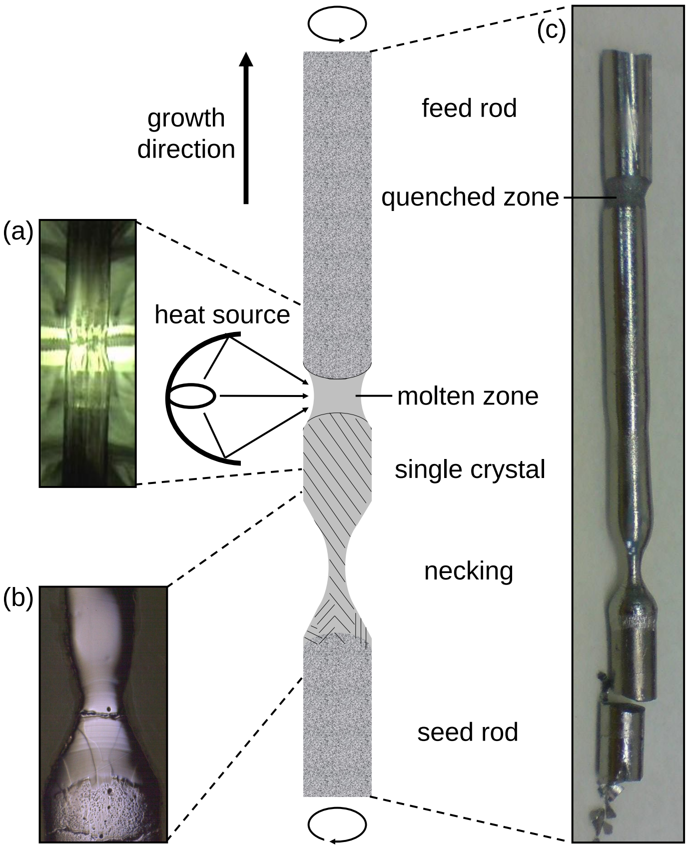

Figure 1.1: Schematic diagram of the vertical float-zoning process used in this thesis. A molten zone is created through a heat source between the lower seed and the upper feed rod. This zone is passed through the polycrystalline material from bottom to top while the seed rod and the feed rod are counter-rotating. (a) Picture of the molten zone during optical float-zoning. (b) Polished cut of the beginning of a single crystal growth of $Mn_{0.96}Co_{0.04}Si$. Beneath the lower boundary of the first molten zone the seed is polycrystalline. After a grain selection, promoted by a necking, we observe single crystallinity over the entire rod diameter. (c) Float-zoned sample of $Mn_{0.78}Fe_{0.22}Si$ that is a single crystal between the necking and the last quenched zone.

specific and usually ranges between a few 0.1 mm/h and a few 10 mm/h. The molten zone is supported only by the polycrystalline feed rods and, for diameters relevant for this thesis, is held in place by its surface tension. A schematic picture is shown in Fig. 1.1.

The heating of the zone may be carried out by various sources including radio-frequency induction, light, or an electron beam. For intermetallic compounds inductive heating is the most common technique while optical heating has been widely used for the growth of oxides during the last decades. In recent years, however, a growing number of groups is applying optical heating also to intermetallics. The temperature profile resulting from optical heating combined with the absence of electromagnetic stirring leads to a very stable molten zone with a convex interface between the zone and the growing crystal. Since single crystal grains tend to grow perpendicular to the crystallization front such an interface shape is highly desirable. The average length required to reach single crystallinity over the whole rod cross-section is inversely proportional to the rod diameter. Hence, grain selection may be promoted by necking, as shown in Fig. 1.1(b). The usage of single-crystal seeds renders grain selection as well as necking redundant and allows for the growth of large oriented samples. In most cases, feed and seed rod are counter-rotated at a few rounds per minute in order to stabilize the molten zone and to enhance its intermixture.

The so-called traveling solvent float-zoning method allows to access metallurgically complex phase diagrams. In this technique the molten zone is created from a small pill that is placed between the seed and the feed rod. While the latter usually possess the composition of the target compound, the composition of the pill and hence the molten zone differs. Commonly, a pill that corresponds to the liquid endpoint of a peritectic reaction is used, but, similar to flux Bridgman growth, it may also consist of a completely different material. During the float-zoning, the amount of material fed into the molten zone from the feed matches the amount that is deposited on the seed and all concentrations stay in dynamic equilibrium. This process generally requires small growth rates. For slightly peritectic formations a self-flux approach may be used. Here, starting from stoichiometric feed rods without a pill, the composition of the molten zone adjusts itself by precipitating the compound at the solid endpoint of the peritectic reaction at the beginning of the growth. The introduction of a necking, in general, is counterproductive for traveling solvent float-zoning as the volume of the molten zone should be kept constant.

Besides being crucible-free, float-zoning has two decisive advantages when it comes to the crystalline quality. First, only a small portion of the raw material is in the molten state. Thus, when handling compounds with a high vapor pressure, evaporation losses are drastically reduced, e.g., compared to the Czochralsky technique. Second, most impurities possess a higher solubility in the liquid than in the solid state. As a result, they gather in the molten zone and solidify as the last zone is quenched at the end of the growth. For purification purposes float-zoning may be repeated several times, which is also referred to as zone refining.

One of the disadvantages of float-zoning is the need for mechanically stable and reasonably shaped feed rods with the correct composition. When growing oxides, such as the cuprate superconductors, the feed rods are commonly produced by pressing and/or sintering powder into an appropriate shape. This method may also be applied for some intermetallics, however, most feed rods are produced by casting material molten by either arc melting or inductive heating. The advancement of a preparation chain for high-quality intermetallic feed rods, in particular suitable for elements that are sensitive to air, was one of the tasks of this thesis and is explained in detail in Secs. 1.2 through 1.5.

For intermetallics high-purity conditions are inevitable as they not only ensure a high crystalline quality but also stable growth conditions. Metal oxides in general possess higher melting temperatures and smaller densities when compared to the corresponding elements. As a result, oxide contaminations tend to float on top of the molten zone. These contaminants, however, result in an inhomogeneous temperature distribution in the zone and, if large amounts of oxides form a closed layer, may ultimately lead to a breaking or a dripping-off of the molten zone and hence to the interruption of the crystal growth. Moreover, it has been demonstrated, e.g., for Er_2PdSi_3, that oxides may even prevent grain selection as the individual intermetallic grains are covered by oxidic precipitates (Er_2O_3) [54].

1.1.3 Binary phase diagrams

Binary phase diagrams provide valuable information on how a binary compound may be grown. These phase diagrams are the result of the minimization of the Gibbs free energy of the different

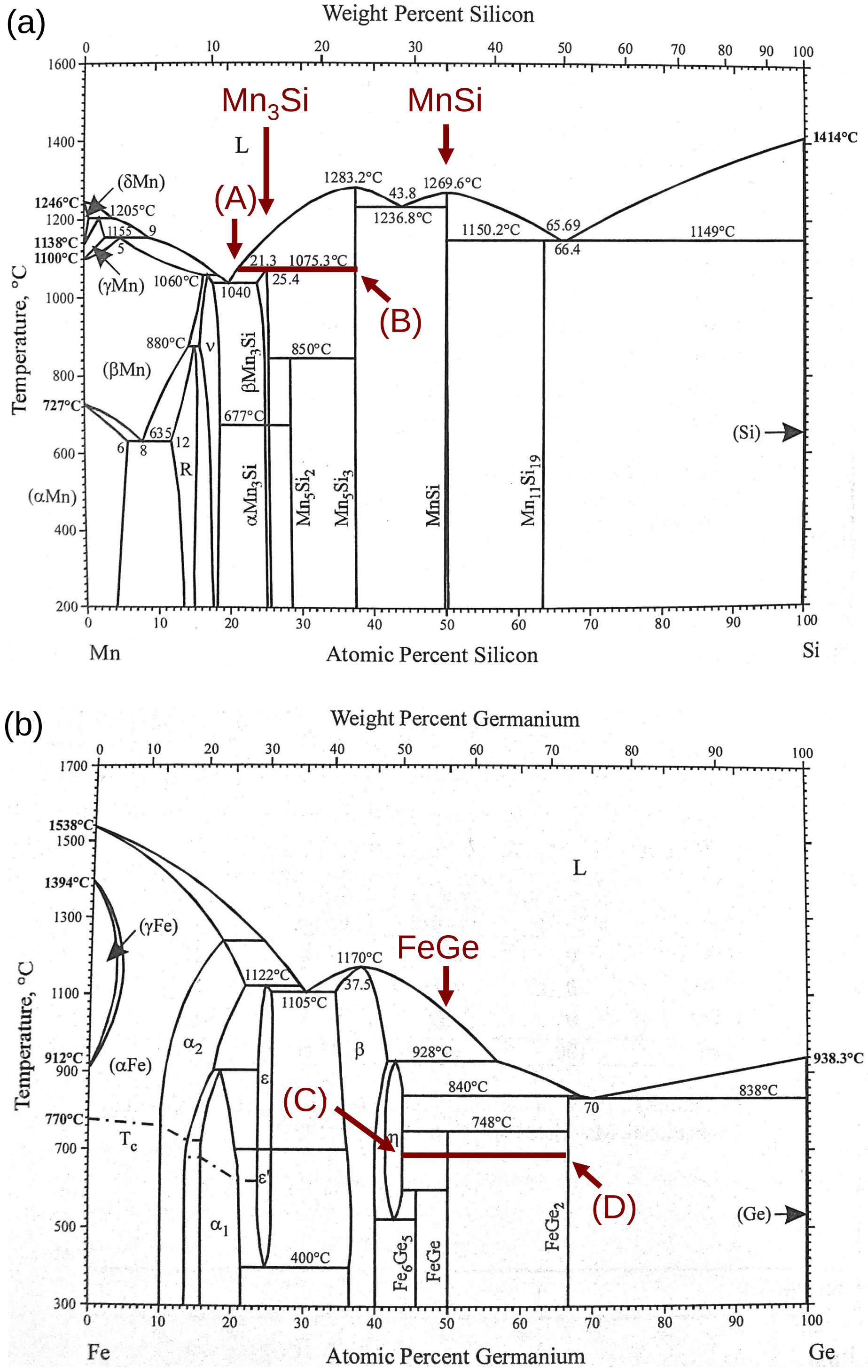

Figure 1.2: Binary metallurgical phase diagrams. (a) The manganese-silicon system. At high temperatures the whole system is liquid (L). MnSi is a congruently melting compound, while Mn3Si forms in a peritectic reaction [55]. (b) The iron-germanium system. FeGe is synthesized in a peritectoid reaction [56], i.e., it may not be grown from the melt. See text for details. Pictures taken from Ref. [57].

phases and as a consequence of the whole system. In real systems, however, this minimization is often a complex problem and theoretical modeling is mostly used to support experimental studies utilizing methods of chemical analysis, differential thermal analysis, x-ray diffraction, and the measurement of various physical properties. A detailed introduction to compositional phase diagrams is given in Ref. [57]. In the following, three typical scenarios for intermetallic compounds are described. As examples we use the manganese-silicon system, cf. Fig. 1.2(a), with the helimagnet MnSi and the itinerant antiferromagnet Mn_3Si as well as the iron-germanium system, cf. Fig. 1.2(b), with the helimagnet FeGe.

MnSi is a congruently melting compound, i.e., it crystallizes directly from a melt with the same composition as the solid. This situation is desirable as it implies that large single crystals may be grown directly from the melt at high rates exceeding 1 cm/h with various techniques such as Bridgman, Czochralsky, or float-zoning. In contrast, Mn_3Si forms in a peritectic reaction, i.e., from a liquid (comprising some 21 % Mn and 79 % Si, A) and a solid (Mn_5Si_3, B) educt. Thus, Mn_3Si can only be grown using advanced techniques like flux Bridgman growth or traveling solvent float-zoning with moderate growth rates barely reaching 1 mm/h. Since the compositional distance from the liquid phase is relatively small for Mn_3Si, traveling solvent float-zoning may be achieved from a self-flux approach.

FeGe, albeit being isostructural to MnSi and exhibiting similar physical properties, behaves distinctively different from a metallurgical point of view. FeGe is buried beneath other phases and forms in a peritectoid reaction, i.e., only solids are involved (the η-phase comprising 40.8 % to 43.5 % Ge, C, and $FeGe_2$, D). For this reason, FeGe may not be grown from the melt and is only accessible through techniques like chemical vapor transport. Using iodine as transport agent, the growth of small single crystals of less than 1 mm^3 within a few weeks has been reported [52, 58].

Adding a third element to a phase diagram drastically increases its complexity. A possible visualization of such ternary phase diagram consists of isothermal cuts shown as regular triangles with the pure elements in the corners. Given the mere number of possible combinations of three elements and the experimental effort to determine just one ternary phase diagram, it is obvious why less than one percent of these systems have been investigated in detail [59]. As a consequence, when growing ternary or even quaternary compounds, in most cases one has to decide based on the results of a first try whether and how to proceed.

1.2 Crystal growth laboratory

Nearly all crystal growth reported in this thesis took place in the crystal growth laboratory of the chair for the Topology of Correlated Systems shown in Fig. 1.3. Here, the focus is placed on the preparation of large single crystals of intermetallic compounds at the highest purity achievable. All furnaces are all-metal sealed and bakeable allowing to reach ultra-high vacuum, often as prerequisite for an ultra-pure inert atmosphere. The resulting ultra-clean crystal growth environment is often referred to as ultra-high vacuum compatible conditions. In addition, water-cooled crucibles and crucible-free techniques are used almost exclusively. The equipment available in our laboratory was extended significantly during the course of this thesis, following on the work performed as part of the Ph.D. thesis of Andreas Neubauer [60], as well as in the diploma theses of Wolgang Münzer [61] and myself [62]. Georg Benka contributed with the design of an arc melting furnace and an annealing furnace during an internship and his master's thesis [63].

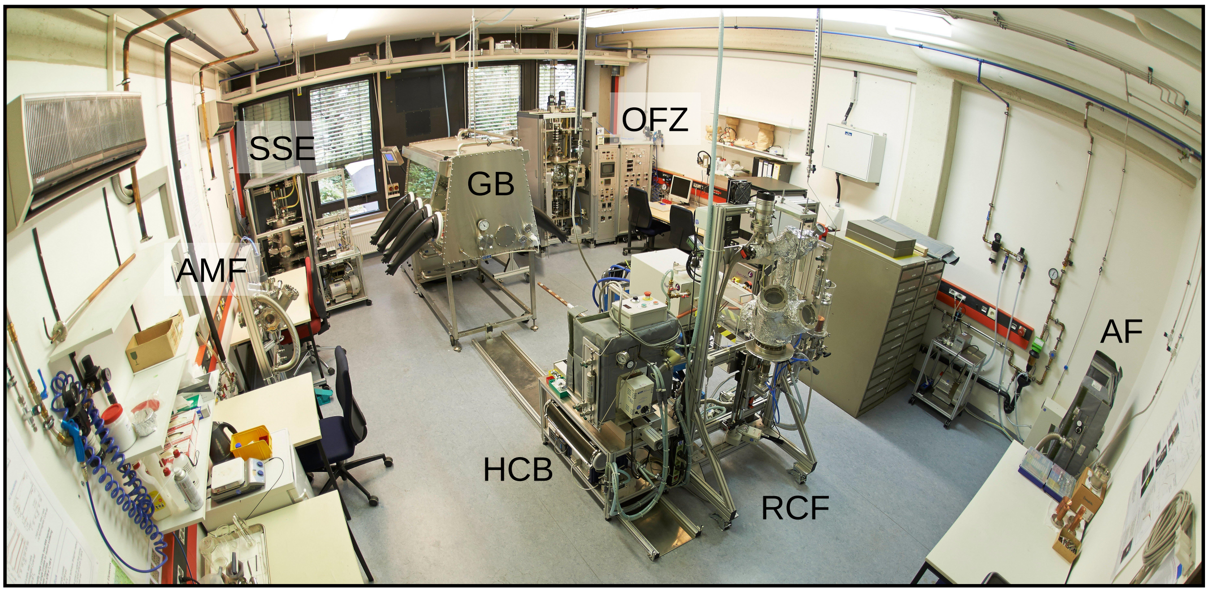

Figure 1.3: Fisheye photograph of the crystal growth laboratory of the chair for the Topology of Correlated Systems. Abbreviations: (GB) glovebox, (HCB) horizontal cold boat furnace, (RCF) rod casting furnace including the setup for large diameter rods (RCF2), (AMF) arc melting furnace, (OFZ) optical float-zoning furnace, (SSE) solid state electrotransport furnace, and (AF) annealing furnace. A central gas supply with a gas storage located on the hallway outside the laboratory has been installed during this thesis.

Our single crystal preparation chain starts from elements purchased with the highest purity available at Alfa Aesar, Ames Laboratory, MaTecK, or smart-elements, respectively. If the elements are sensitive to oxygen or moisture, such as many rare earths, they are packed under argon in glass or stainless steel ampules and are stored as well as handled exclusively inside the argon glovebox. Other elements may require an initial cleaning procedure that involves chemical etching, mechanical grinding, or rod casting. As an example, commercially available 4N (99.99 % pure) manganese flakes are etched in thinned nitric acid, thoroughly cleaned, and cast into a solid rod using the rod casting furnace. While etched pieces of manganese tarnish within minutes, the surface of the cast rod stays metallic.

When deciding how to prepare high-quality intermetallic single crystals out of these high-purity starting elements, many criteria play a role. The various preparation processes available in the crystal growth laboratory of the chair for the Topology of Correlated Systems are depicted in the flow chart in Fig. 1.4. The two preparation routes used most often in this thesis are marked in red and described below. Further paths are addressed in Secs. 1.4, 1.5, and 2.1.3.

Whenever possible, polycrystalline material is synthesized by inductive melting mainly for two reasons. First, inductive heating is very gentle and controlled, in particular if compared to arc melting. Second, water-cooled copper crucibles in both the horizontal cold boat furnace (HCB) and the rod casting furnace (RCF) drastically reduce the risk of contaminating the sample as compared with methods based on hot crucibles like the Bridgman technique. To be treatable in our inductively heated furnaces, at least one of the educts has to be metallic with a diameter of at least ~1 mm. Ideally, the target compound is also metallic permitting that the

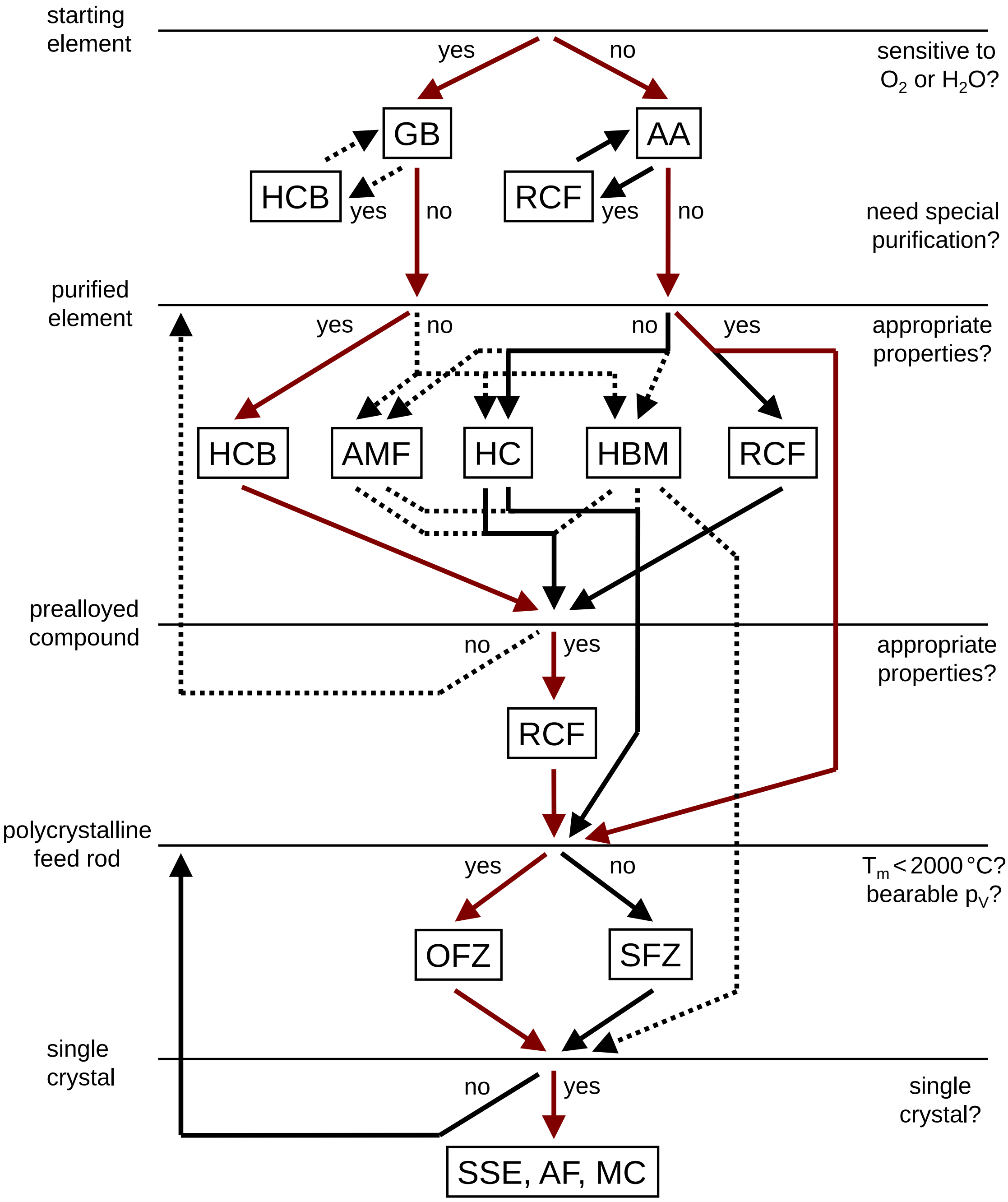

Figure 1.4: Flow chart of the crystal growth processes available in the crystal growth laboratory of the chair for the Topology of Correlated Systems. Abbreviations: (GB) glovebox, (AA) ambient air, (HCB) horizontal cold boat furnace, (RCF) rod casting furnace, (AMF) arc melting furnace, (HC) hot crucible in the HCB, (HBM) horizontal Bridgman method in the HCB, (OFZ) optical floating zone furnace, (SFZ) smart floating zone furnace at the IFW Dresden, (SSE) solid state electrotransport furnace, (AF) annealing furnace, and (MC) metallurgical characterization. Red lines mark the most common connections, solid black lines mark connections that also have been used during this thesis. Dashed black lines mark other possible connections.

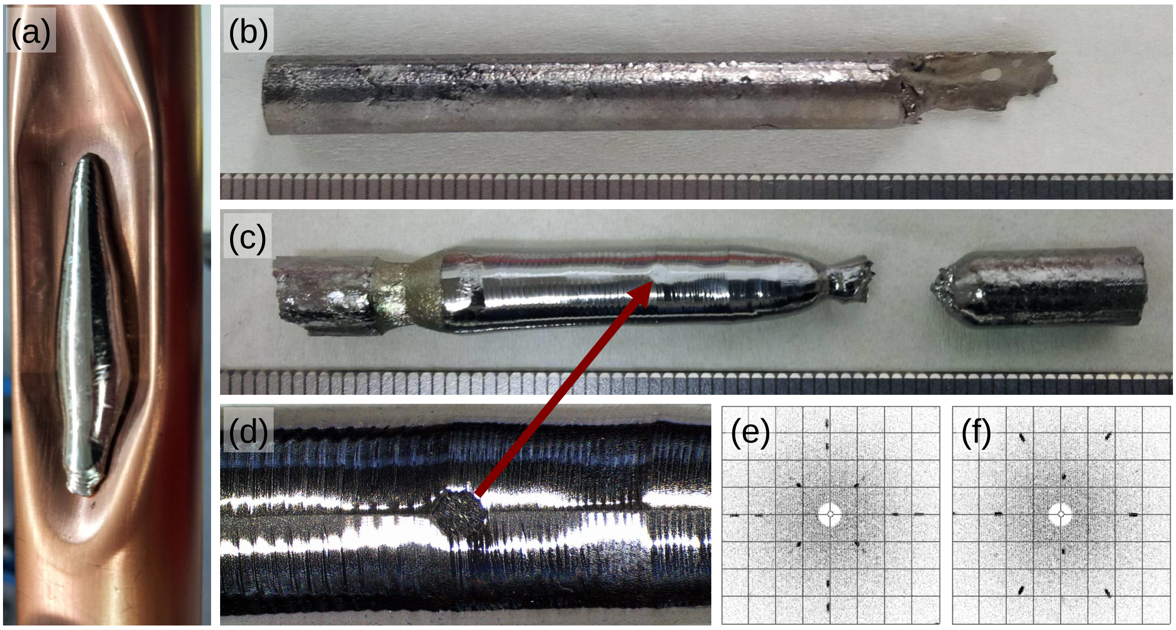

Figure 1.5: Preparation steps for $CeNi_2Ge_2$ as carried out by Georg Benka for his master's thesis [63]. (a) CeNi synthesized from high purity elements using the horizontal cold boat furnace loaded from the argon glovebox. (b) Polycrystalline $CeNi_2Ge_2$ feed rod cast in the rod casting furnace combining stoichiometric amounts of CeNi, Ni, and Ge. (c) Float-zoned $CeNi_2Ge_2$, where the growth direction was from bottom to top. (d) Close-up view of the central part of the $CeNi_2Ge_2$ single crystal. Note the shiny metallic surface and the pronounced $\langle 001 \rangle$ facet. (e) Fourfold Laue pattern of a $\langle 001 \rangle$ surface. (f) Twofold Laue pattern of a $\langle 100 \rangle$ cut.

sample is remelted several times. Powder components pose a challenge and need to be addressed individually, e.g., by mechanically pressing them into pellets. The melting temperatures, T_m, in general should not exceed 2000 °C to be meltable in the currently available setups. Finally, it is advantageous if the boiling point of the lowest melting educt is higher than the melting point of the highest melting educt. These criteria are summarized as 'suitable properties' in Fig. 1.4.

The power for the induction melting is provided by a CELES MP 50 kW radio-frequency generator at frequencies between 100 kHz and 400 kHz. Sample temperatures between 350 °C and 2500 °C may be monitored with an IMPAC IGA 140 MB 25 L pyrometer in all of the crystal growth apparatus used, except the image furnace.

As a typical example for a ternary rare earth compound we illustrate the crystal growth of $CeNi_2Ge_2$, where we follow the red path on the left side of Fig. 1.4. This growth was performed by Georg Benka during his master's thesis [63]. We start from 5N5 high-purity cerium (Ames Laboratory) stored in our glovebox as well as 4N5 nickel and 6N germanium (both MaTecK). First, for the synthesis of CeNi stoichiometric amounts of cerium and nickel were prepared in the glovebox. Utilizing the metal bellow load-lock, we load both elements into the horizontal cold boat furnace. After pumping to ultra-high vacuum, the cold boat system was filled with 1.1 bar high-purity argon and CeNi was finally synthesized by means of radio-frequency induction, cf. Fig. 1.5(a). CeNi, unlike elemental cerium, is not sensitive to oxygen or moisture. Neither in this preparation step nor in the following steps of the crystal growth process we observed evaporation losses. Second, the resulting CeNi pill was combined in the rod casting furnace with the remaining nickel and germanium to obtain stoichiometric $CeNi_2Ge_2$. Here, after pumping to ultra-high vacuum and flooding with 1.7 bar high-purity argon, we cast a polycrystalline feed rod of 6 mm diameter and ∼50 mm length, see Fig. 1.5(b). The steps described above are repeated to cast a seed rod of ∼20 mm length.

Third, feed and seed rod were mounted into the image furnace. The system was thoroughly pumped, baked, and eventually flooded with 3 bar of 6N argon additionally purified with a hot getter furnace. Subsequently, the polycrystalline rods were optically float-zoned at a rate of 5 mm/h while counter-rotating at 6 rpm. At the beginning of the growth process a necking was introduced to promote grain selection. The float-zoned crystal, shown in Figs. 1.5(c) and 1.5(d), exhibits a shiny metallic surface and pronounced facets oriented perpendicular to the tetragonal $\langle 001 \rangle$ axis. The yellowish taint of the final molten zone may indicate a tiny amount of impurities that gathered in the liquid phase and was not incorporated into the crystal. Such a behavior is commonly observed and one of the main advantages of float-zoning in general.

If at room temperature all educts are rather insensitive to oxygen or moisture, the crystal growth process may be short cut along the red path on the right side of Fig. 1.4. This is the case for many transition metal compounds. Potentially after an initial cleaning procedure, elements with 'suitable properties' may be placed directly in the rod casting furnace where a feed rod as well as a seed rod are cast. The growth process is in turn finalized by optical float-zoning. After the actual growth the crystalline quality may be improved by annealing or solid state electrotransport. In the end, a metallurgical characterization is carried out and suitable samples for the investigation of various physical properties are prepared.

1.3 High-purity crystal growth environment

A clean growth environment is one of the key ingredients when trying to prepare high-quality single crystals. In the growth process of an intermetallic compound typical sources of contamination are: (i) remaining air when the system is opened to air for sample changes, (ii) remaining impurities in the inert gas, (iii) the overall leak rate of the recipient, (iv) emission of absorbed molecules by the walls of the vacuum system, and (v) evaporation of the sample and, if used, of a hot crucible. These sources will be addressed in further detail in the following.

For the highest purity achievable it is usually ideal to perform all steps of the crystal growth process in ultra-high vacuum. A remaining pressure of 10^{-7} mbar to 10^{-10} mbar, i.e., the range that is available in our crystal growth apparatus, translates to an impurity concentration of 0.1 ppb to 0.1 ppt compared to ambient pressure. Moreover, pumping may be continued while the sample is heated and thus contributions of the sources (iii) to (v) may be reduced. For most intermetallic compounds, however, crystal growth in vacuum is not favorable since at least one component exhibits a rather high vapor pressure and hence is subject to serious evaporation losses. These losses may be drastically reduced by means of an inert gas atmosphere. Since the crystal growth system may not be pumped continuously when using an inert atmosphere, special care has to be exercised to avoid unnecessary contamination of the sample. An atmosphere of 1 bar of 6N argon, i.e., the cleanest suitable gas commonly available in gas bottles, translates to an impurity concentration of 1 ppm which is far worse than the corresponding ultra-high vacuum. Commercial gas purifiers utilizing inorganic media like metallic sponges either at room temperature or heated to a few hundred degree Celsius allow to further reduce the impurity level of the inert gas. During this thesis a central gas supply was installed providing 6N argon for all crystal growth apparatus as well as high purity oxygen and nitrogen for the image furnace. The glovebox is supplied with 5N argon. At every crystal growth apparatus the 6N argon may be additionally treated by a SAES MicroTorr MC190 point-of-use room temperature gas purifier at a nominal flow rate of up to 5 slpm. As a result, remaining impurity concentrations below 1 ppb may be achieved.

The overall leak rate of the vacuum chamber may be improved greatly in an all-metal sealed setup. Additionally, the latter allows for a thorough pumping in combination with a careful bake-out prior to the gas filling which dramatically reduces the emissions from the walls. The bake-out is typically carried out at ∼180 °C for a day or longer. In contrast, in many conventional crystal growth apparatus the inert atmosphere is inserted via a purging process, i.e., the system is pumped to some 10^{-1} mbar to 10^{-4} mbar and flooded with inert gas a few times. While this process reduces remaining contaminations from opening the system to levels far below the impurity concentration of the inert gas, the emission of absorbed molecules from the inner walls of the recipient may not be suppressed sufficiently.

Especially if samples are kept hot over long periods of time, e.g., in the image furnace, in the annealing furnace, or in the solid state electrotransport furnace, outgassing by the sample and by the vacuum chamber can never be avoided completely. A common way to prevent contamination of the growth environment by these mechanisms is the application of a flowing gas atmosphere. This method, however, possesses an inherent risk of air back-diffusing into the growth chamber and a large amount of gas is consumed. A continuous circulation and purification of the inert gas bypasses these issues and the repetition of the gas purification may ultimately lead to an improved gas quality.

For this purpose, we have converted an adixen AMP007 Holweck type molecular drag pump into a circulation pump. The viton sealing rings in the aluminum housing were replaced by bespoke flanges utilizing lead seals. The ACT 100 controller unit has been modified to reduce the speed to about 10 % to 20 % of its nominal value of 27000 rpm by adjusting a potentiometer while a fan provides additional cooling. This way, the inert argon atmosphere in the crystal growth apparatus may be continuously circulated over a NuPure Omni 40 hot getter furnace at a rate of a few tenths of a liter per minute, i.e., at the optimal flow rate of getter furnace. As a result, the impurity concentrations of the inert atmosphere may be kept constant during long term experiments. The circulation pump project has been started as part of the diploma thesis of Ralf Korntner [64]. The design has been completed and installed at the image furnace as part of this thesis. The results of first tests are promising, whereas long-term tests including a detailed gas analysis are planned for the future. If these tests are successful a similar continuous gas purification setup will be implemented in the other systems of the crystal growth laboratory of our group.

1.4 Argon glovebox, horizontal cold boat, and arc melting furnace

Elements and compounds that are sensitive to air or moisture require special care in order to avoid the contamination of the sample in every step of its preparation process. This section addresses the apparatus of our preparation chain that allow to handle such materials and is organized as follows. In Sec. 1.4.1 we briefly account for the argon glovebox purchased as part of thesis. Subsequently, Secs. 1.4.2 and 1.4.3 are concerned with the horizontal cold boat furnace and the metal bellows load-lock used to load the cold boat from the glovebox. An arc melting furnace that may be docked to the glovebox was finally designed by Georg Benka as part of his master's thesis [63] and is described in Sec. 1.4.4.

1.4.1 Commercial glovebox

Starting point for our materials preparation chain under high-purity growth conditions is a bespoke commercial glovebox from Jacomex. This glovebox provides an argon atmosphere containing about 1 ppm oxygen and 1 ppm water that is continuously circulated and purified. A version with eight gloves, four each on the front and the rear of the box, was chosen to provide the required working space. An automatic load-lock with a diameters of 400 mm and a manual load-lock with a diameter of 150 mm are located on one side of the glovebox. A third bespoke load-lock system was installed on the opposite side of the glovebox. This lock consists of an ISO-K100 flange of 70 mm length and a plug that may be tightened manually. A manometer and a three-way valve are connected for purging. The horizontal cold boat furnace or the arc melting furnace may be connected to this load-lock. For the cold boat we use a custom highly flexible metal bellows stabilized by telescope rods. The arc melting furnace is connected with a CF DN100 plate valve in combination with a short U-profile bellow to adapt the length.

1.4.2 Inductively heated horizontal cold boat furnace

A horizontal cold boat furnace is a versatile and simple device that, in combination with a radio-frequency generator, is widely used to heat and melt metallic specimens. Central part of our horizontal cold boat furnace, shown in Fig. 1.6, is a water-cooled copper tube with four molds of different sizes. Samples are placed in the molds either directly or inside crucibles made of high-melting metals, ceramics, or quartz glass. After closing and pumping the vacuum system, the samples are heated by radio-frequency induction. The water cooling prevents the cold boat from melting and reduces its reactivity during the sample preparation. To achieve sufficient heating for the synthesis of a typical intermetallic compound at least one of the constituents needs to be metallic and of a size in the millimeter range. Crucibles made of tungsten, tantalum, or molybdenum thereby allow for the indirect heating of powder or insulating samples.

Besides a large range of materials that may be treated with this cold boat system, one of its major advantages is its simple design. We realized a compact and all-metal sealed design on top of a Duniway V60 ion getter pump. In combination with an external turbomolecular pump backed by a scroll pump and a two-part heating tent we reach pressures of the order of 10^{-10} mbar. Up to 1.2 bar of argon may subsequently be applied. For sample loading and removal, a quartz glass tube welded onto a standard CF DN40 glass-to-metal seal is demounted. The horizontal movement with respect to the coil of the radio-frequency oscillator circuit that is necessary to reach different molds during the melting process is provided through a linear actuator on which the entire vacuum setup is mounted.

The high versatility of the setup is further enhanced by a water-cooled pulling rod for a horizontal Bridgman single crystal growth that may replace the cold boat, see Fig. 1.6(c). Here, cold welded tantalum ampules may either be used as hot crucibles directly or together with inner crucibles out of alumina (Al_2O_3) or zirconia (ZrO_2).

1.4.3 Metal bellows load-lock

While many compounds may be loaded into the horizontal cold boat furnace under ambient conditions, special care has to be taken if elements are involved that are highly sensitive to oxygen or moisture. For the high-purity synthesis of compounds based on these elements we

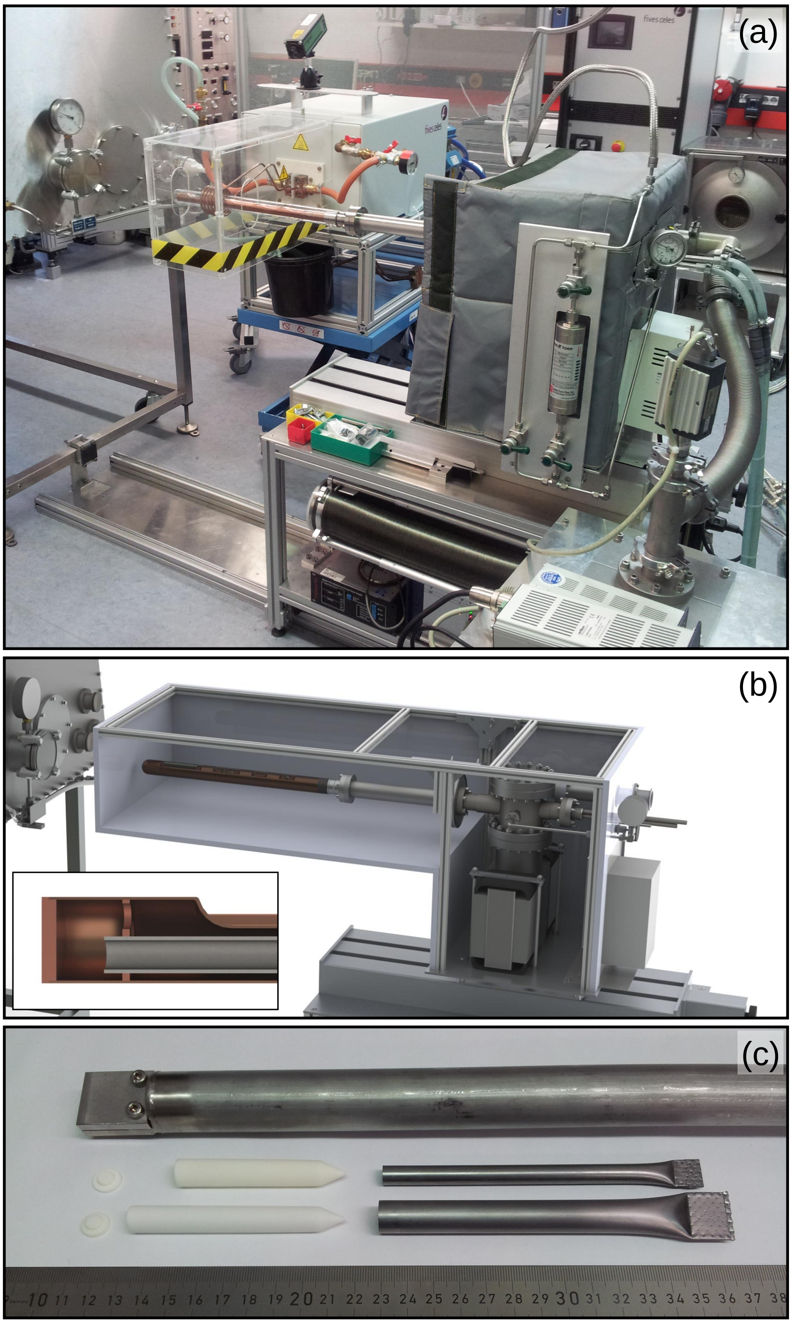

Figure 1.6: Glovebox and horizontal cold boat furnace. (a) Total view of the horizontal cold boat furnace including its permanently installed part of the heating tent and the gas purification system. The custom load-lock of the glovebox is visible on the left. A two-part guide rail provides the room to maneuver for the loading process where the part closer to the glovebox is removed if the arc melting furnace is attached to the latter. (b) Isometric view of the horizontal cold boat system. The inset shows a cut-away view of the tip of the central water-cooled cold boat. (c) Water-cooled pulling rod for horizontal Bridgman growth. Tantalum ampules are used as hot crucibles directly or together with inner crucibles out of alumina or zirconia.

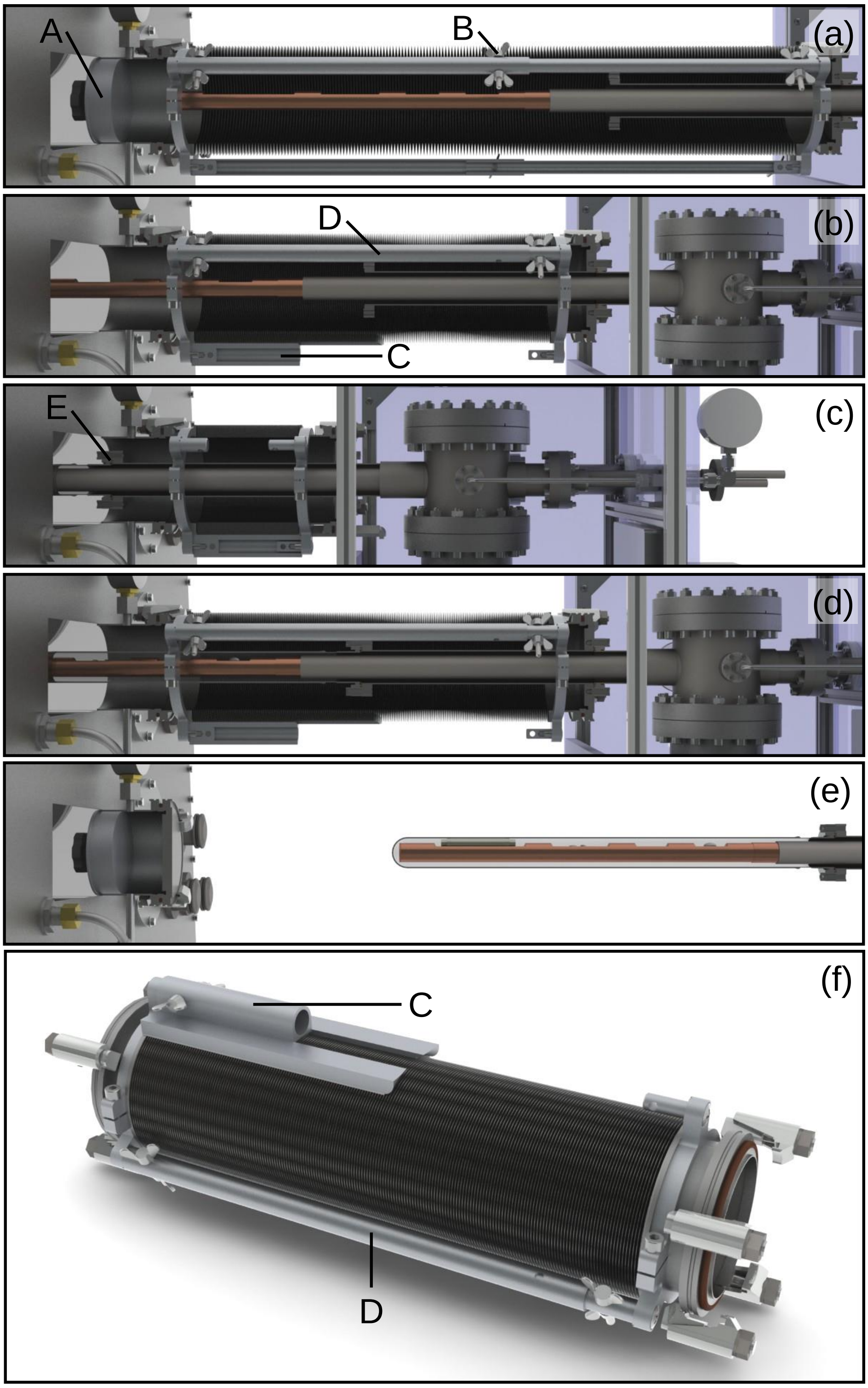

Figure 1.7: Schematic depiction of the loading process of the glovebox and the horizontal cold boat furnace. (a)–(e) Five steps of the loading process. (f) Isometric view onto the bottom side of the metal bellows load-lock system corresponding to steps (b) and (d). See text for details.

have developed a metal bellows load-lock system. This load-lock enables us to connect the cold boat system to our glovebox, load the samples under an inert atmosphere, and close the system under the argon environment inside the glovebox. Subsequently, the cold boat furnace is detached from the glovebox and pumped to ultra-high vacuum. Starting from this point, the samples are treated the same way as if they had been loaded under ambient conditions.

The load-lock consists of a highly flexible metal bellows with ISO-K100 flanges and is stabilized by telescope rods and a sled, respectively. An adapter flange is permanently installed on the cold boat furnace between the glass-to-metal seal and the central vacuum chamber. This flange connects the load-lock with the cold boat system and provides the necessary space for the compressed bellows. The horizontal movement required for the docking process exceeds the capacity of the linear actuator that is used to move the cold boat during sample preparation. The cold boat system including its linear actuator therefore is mounted on top of a guide rail which permits to shift the system manually.

In the following we will describe the docking process in detail. Fig. 1.7(a) shows a cut-away view of the glovebox and the cold boat furnace without its glass tube dismounted. Both systems are connected through the bespoke metal bellow fixed at maximum elongation. The metal bellow and the cold boat system are evacuated and flooded with argon from the glovebox at least three times. After this purging, as depicted in Fig. 1.7(b), the plug (A) at the ISO flange of the glovebox and the fixations of the metal bellow (B) are removed. Subsequently, the cold boat system is moved towards the glovebox until the metal bellow is nearly half way compressed. At this position, the lower rod of the telescope rack of the metal bellow is replaced by a sled (C). After detaching the two upper rods of the telescope rack (D) the metal bellow is compressed completely, as illustrated in Fig. 1.7(c). The educts for the sample preparation are loaded into the cold boat system within the inert atmosphere of the glovebox and the latter is closed at the glass-to-metal seal (E). Subsequently, cf. Fig. 1.7(d), steps (b) and (a) are repeated vice versa. Finally, after removing the metal bellow lock as depicted in Fig. 1.7(e), the cold boat system is ready to be pumped to ultra-high vacuum.

Taken together, the cold boat furnace combined with the metal bellow lock allows for a very controlled pre-melting of intermetallic compounds, in particular if elements sensitive to air or moisture are involved. Metallic as well as non-metallic crucibles extend the range of materials to be handled. We note that samples alloyed in the cold boat system sometimes exhibit a rather poor homogeneity due to the temperature gradient between the top of the sample and the cold copper mold. Moreover, the ingot cannot be flipped without opening the system. This disadvantage, however, is completely overcome if the compound is processed further in the rod casting furnace.

1.4.4 Arc melting furnace

The material preparation chain under inert atmosphere further includes an arc melting furnace, shown in Fig. 1.8, that was developed as part of the master's thesis of Georg Benka [63]. Here, the sample heating is carried out by an argon plasma that is ignited between a tungsten tip electrode and a grounded plate, i.e., an elaborate version of tungsten inert gas welding. While standard arc melting furnaces are widely used for sample preparation and are commercially available, we have designed an all-metal sealed furnace that may be loaded from the glovebox.

Central part of the arc melting furnace is a copper plate (A) providing molds of various sizes and shapes. This plate is tightly bolted to a water-cooled CF DN160 flange (B) at the bottom of a bespoke sample chamber. The electrode consists of a lanthanum doped tungsten tip (C)

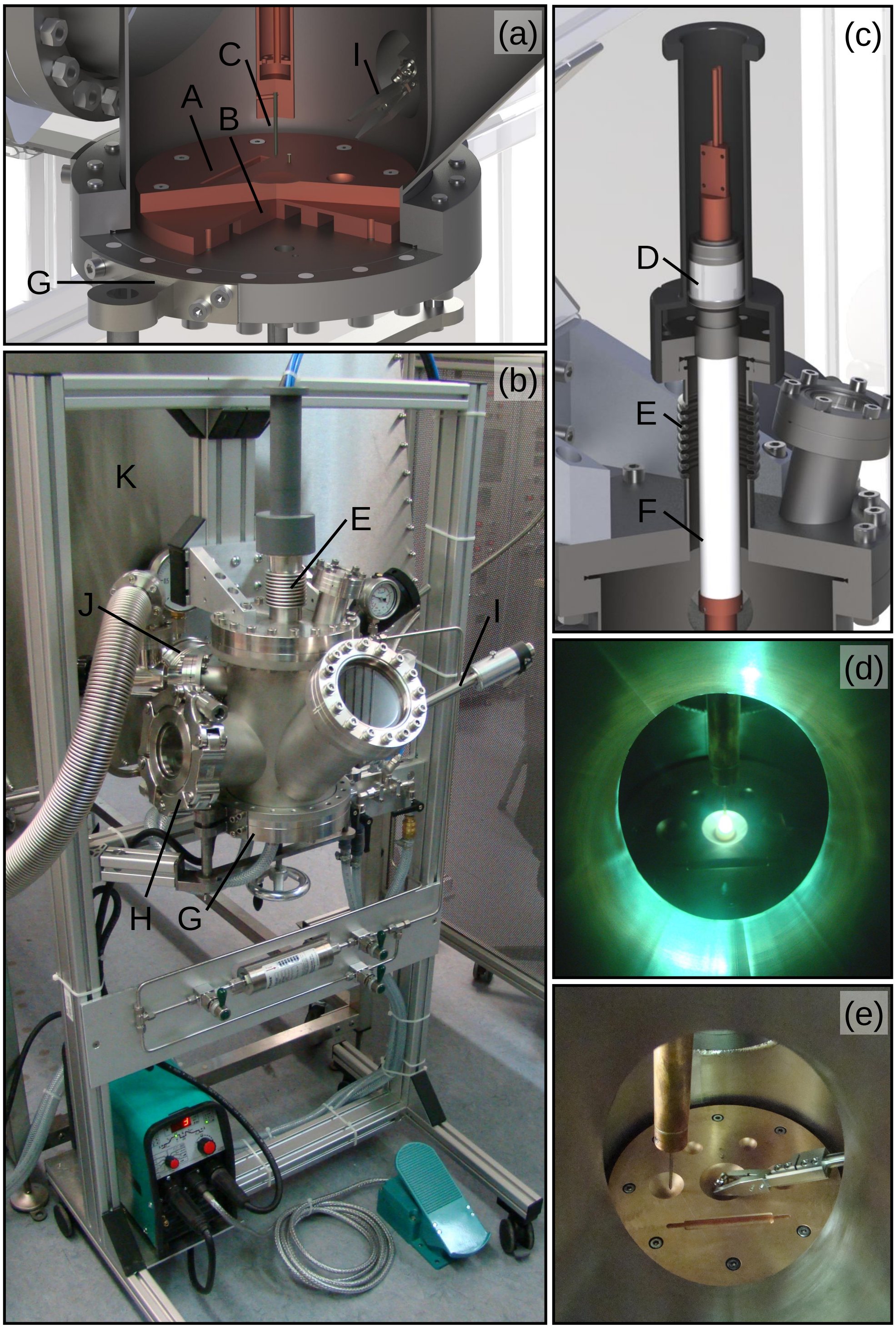

Figure 1.8: All-metal sealed arc melting furnace. (a) Cut-away view of the lower part of the sample chamber. (b) Overall view of the arc melting furnace as docked to the glovebox. (c) Cut-away view of the the top flange. (d) View through the front window during melting. (e) Flipping a sample using the wobble stick. See text for details. Pictures taken by Georg Benka [63].

attached to a water-cooled current feedthrough (D). Horizontal and vertical movement of the electrode is made possible by a DN40 U-profile bellow welded to the DN160 flange at the top of the recipient (E). The electrode is electrically insulated by Stycast 2762 and a sleeve made of polyether ether ketone (PEEK) (F). Electrical power is supplied by a Merkle MobiTIG 190 DC welding transformer. The bottom flange of the system is pivotable to the front (G). This way, easy access is provided for cleaning of the vacuum chamber, loading and unloading of samples, as well as replacing the copper plate or the tip of the electrode. A VACOM Quick-CF DN100 port tightened by a clamping chain located on the left side of the vacuum chamber (H) permits quick access, i.e., to load or unload a sample. Windows at the front and the top of the vacuum chamber as well as in the Quick-CF flange provide optical access. A pyrometer may be attached to the CF DN40 window at the top. In addition, a wobble stick for sample manipulation is included on the right-hand side of the system (I). Thus, without opening the system, one may flip alloyed pills and collect fragments that may have been created during melting.

A CF DN100 plate valve at the back of the chamber (J) is used to connect the arc melting furnace to the glovebox (K), where a short U-profile bellow with one CF DN100 and one ISO-K DN100 flange serves for adaption of the length. Purging is provided from the glovebox. Subsequently, the plate valve is opened and the elements are loaded from the glovebox via a bespoke shovel. The wobble stick may be used to move sample pieces in the molds of the copper plate. After the plate valve is closed, or after a regular sample loading from ambient air, the system is pumped by a turbomolecular pump backed by a scroll pump. In combination with permanently installed heating tapes pressures in the range of 10^{-7} mbar may be reached within a day. Finally, the system is flooded with up to 1.2 bar of high-purity argon. Other than the cold boat system, the arc melting furnace may stay docked to the glovebox during the melting process which permits a high sample output even when handling elements sensitive to air or moisture.

Studies that require a large number of high quality polycrystalline samples, e.g., extended doping studies, are one possible application of the arc melting furnace. Moreover, this furnace is used if very high temperatures are necessary or if insulating samples need to be heated without hot crucibles. Bespoke copper plates with oblong shaped or large-diameter cylindrical molds permit a direct preparation of feed rods for float-zoning or targets for thin film growth, respectively. Finally, metallic and non-metallic ampules may be sealed under inert atmosphere.

1.5 Inductively heated rod casting furnace

The rod casting furnace was developed in three steps. First, Andreas Neubauer built a viton sealed furnace that was inspired by a similar setup at the IFW in Dresden [60]. Second, Wolfgang Münzer overhauled the design [61]. He constructed the metal-sealed central vacuum chamber and connected the pulling rod with a highly flexible metal bellow. However, in this version the crucible was sealed by two viton o-rings. Third, a metal-sealed Hukin crucible and the corresponding cooling water supply flange were developed during my diploma thesis [62] and the early stages of this thesis. The final setup is shown in Figs. 1.9(a) and 1.10 and will be described in the following.

Central part is a water-cooled Hukin copper crucible on a CF DN63 steel flange, see Figs. 1.9(b) and 1.10(C). Eight M8 screws are used to attach the crucible to a support flange providing cooling water. For the preparation of feed rods of intermetallic compounds high-purity starting elements are placed inside the crucible and heated via radio-frequency induction. Electromag-

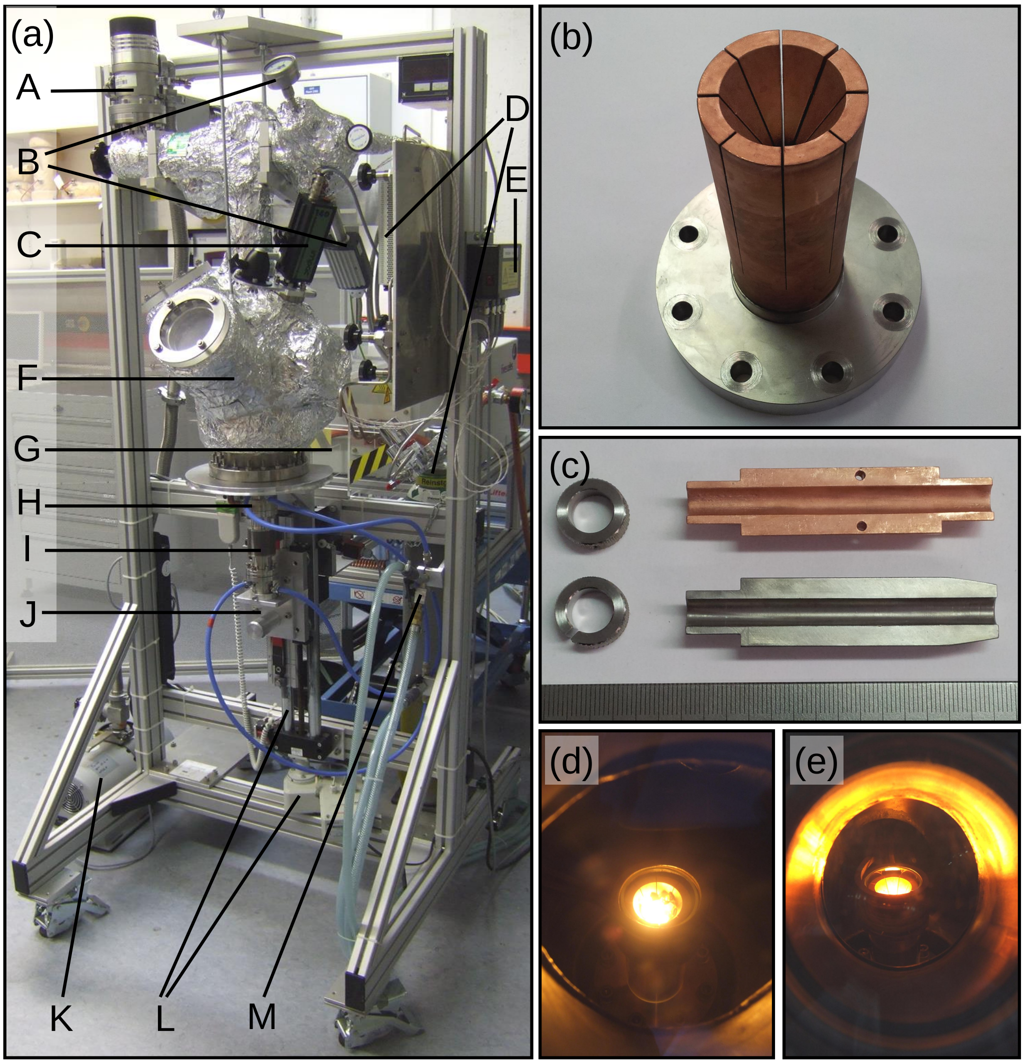

Figure 1.9: All-metal sealed rod casting furnace. (a) Complete system comprised of the following components: (A) turbo molecular pump, (B) pressure gauges, (C) pyrometer, (D) gas handling and purification system, (E) heating tape controller, (F) vacuum chamber, (G) radio-frequency oscillator circuit, (H) central support flange, (I) highly flexible metal bellow, (J) pulling rod on top of a manually movable sled, (K) roughing pump, (L) linear actuator for sample mounting, (M) cooling water supply. (b) Hukin type cold crucible hard-soldered onto a CF DN63 steel flange. (c) One half of a copper and a steel casting mold with clamping rings. The scale is in millimeter. (d) Left viewing port. (e) Front viewing port.

netic levitation reduces the contact between the sample and the crucible during melting, keeping the contamination of the sample to a minimum. A water-cooled pulling rod retains the melt in the crucible. After all starting elements are melted the radio-frequency heating is turned off. The sample cools down and solidifies inside the crucible. The resulting pill is flipped by pushing the pulling rod upwards and is subsequently remelted. Repeating this process several times ensures an excellent mixing of the starting elements maximizing the compositional homogeneity

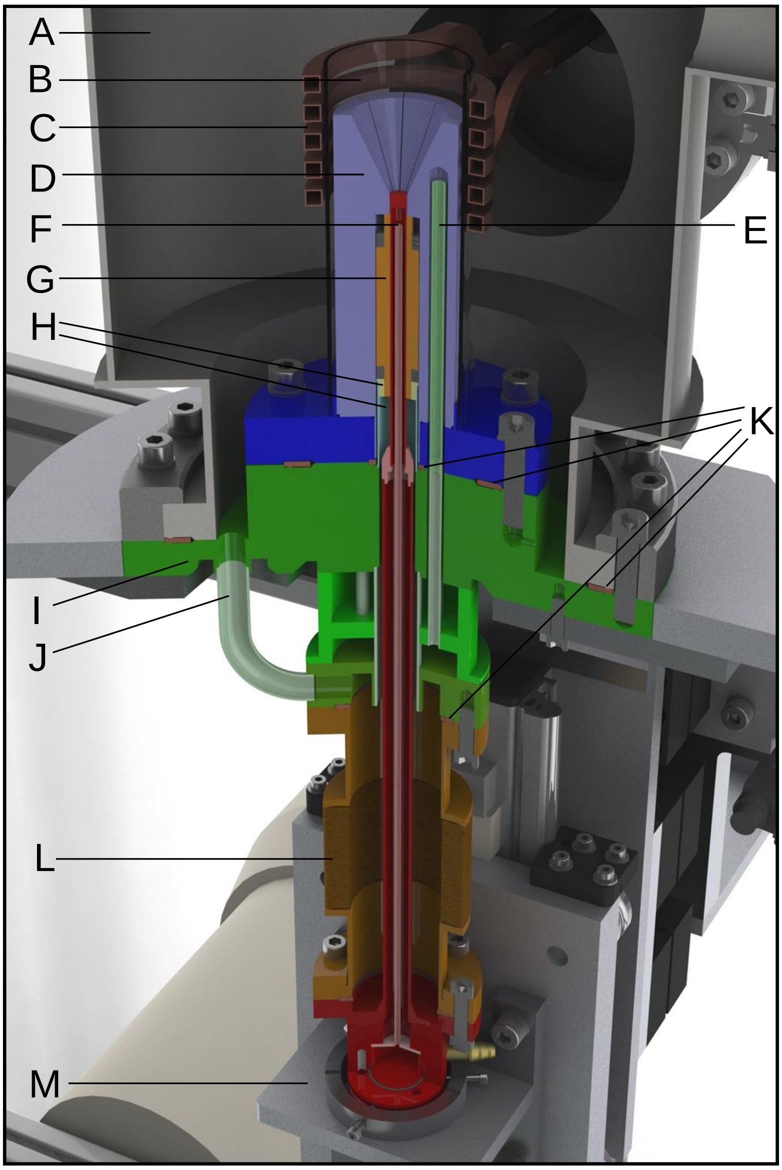

Figure 1.10: Cut-away view of the central part of the rod casting furnace. Inside the vacuum chamber (A) a glass tube (B) serves as electrical insulation between the radio-frequency induction coil (C) and the water-cooled Hukin type cold crucible (D, blue). The latter consists of a copper upper (bright blue) and a steel lower part (dark blue). Inside the crucible the flow of the cooling water is guided by thin steel tubes (E). The sample material inside the crucible may be manipulated through a water-cooled pulling rod (F, red) and cast into a two-part mold (G, orange), which is hold in place by two spacers (H). The water support for the crucible is delivered through a central flange (I, green) that also includes a bypass (J). Standard CF copper sealings (K) connect the central flange with its neighboring parts. A highly flexible metal bellow (L, brown) and a sled (M) allow for a manual movement of the pulling rod.

of the sample. For casting a rod, the pill is melted a final time and a sudden downward movement of the pulling rod permits the melt to drop into the casting mold, see Fig. 1.9(c), where a polycrystalline rod of 6 mm diameter and a length of up to 70 mm forms. The required vertical movement of the pulling rod of about 100 mm is made possible by a highly flexible COMVAT metal bellows in combination with a manually movable sled.

The crucible is mounted in a bespoke stainless steel vacuum chamber. Two DN100 windows permit to monitor the melting process, as depicted in Figs. 1.9(d) and 1.9(e), while a DN35 viewing port allows for measurements of the sample temperature using a pyrometer. For sample preparation the system is evacuated using a Leybold Turbovac 50 turbomolecular pump backed by a Varian SH-110 scroll pump. In combination with permanently installed heating tapes and a bespoke heating jacket pressures in the range of 10^{-8} mbar may be reached. Finally, the system may be flooded with high-purity argon at pressures up to 3 bar.

For the removal of the cast rod and the mounting of new starting elements the connection between the support flange and the vacuum chamber is opened. Subsequently, the entire lower part of the furnace, including the crucible and its water support as well as the pulling rod and its sled, are lowered by about 300 mm with a Rose+Krieger EPX30 linear actuator. After emptying the cooling water circuit using pressurized air, the crucible is removed. Unscrewing the eight steel tubes that deliver the cooling water, see Fig. 1.10(E), eventually permits easy access to the casting mold. Finally, after a thorough cleaning of all parts, the system is reassembled.

The rod casting furnace is mainly used for the purification of starting elements and the casting of polycrystalline feed rods for optical float-zoning. For both applications it is beneficial that oxides in general possess a higher melting temperature and a lower mass density compared to the corresponding pure metals. Hence, any oxide contaminants tend to float on top of the melt and remain in the crucible when the rod is cast.

During the course of this thesis the rod casting furnace has been adapted for the preparation of rods with diameters of 8 mm and 10 mm, respectively, and lengths up to 90 mm. This refurbishment in particular included the design of a modified pulling rod. In the latter the tip and the base are connected via a bespoke micro CF style copper sealing, which allows to change the tip within minutes and without removing the pulling rod from the casting furnace.

1.6 Optical floating zone furnace

Most of the single crystal growth reported in this thesis was carried out by means of optical float-zoning. In our crystal growth laboratory a commercial four mirror image furnace from Crystal Systems Incorporate is used that has been heavily modified to be all-metal sealed and bakeable by Christian Pfleiderer and collaborators at the University of Karlsruhe, cf. Fig. 1.11. Bespoke heating jackets were purchased by Andreas Neubauer during his Ph.D. thesis [60]. As a result, using a turbomolecular pump in combination with a careful bake-out of the system, pressures in the range of 10^{-8} mbar are accessible. Alternatively, up to 10 bar of inert gas may be applied. The refurbishment of the image furnace is described in detail in Refs. [60, 65]. In the following the focus is placed on the all-metal sealed setup where certain details are mentioned as they are important for the implementation of the electrotransport option addressed in Sec. 1.7.4.

In the image furnace the light of four halogen lamps, with a power between 150 W and 1500 W each, is focused on the sample by four ellipsoidal mirrors. Usually, the smallest lamps that are sufficient for the creation of a molten zone are used as they provide the sharpest focus. The maximum operating temperature specified is 2200 °C. This value, however, depends on the

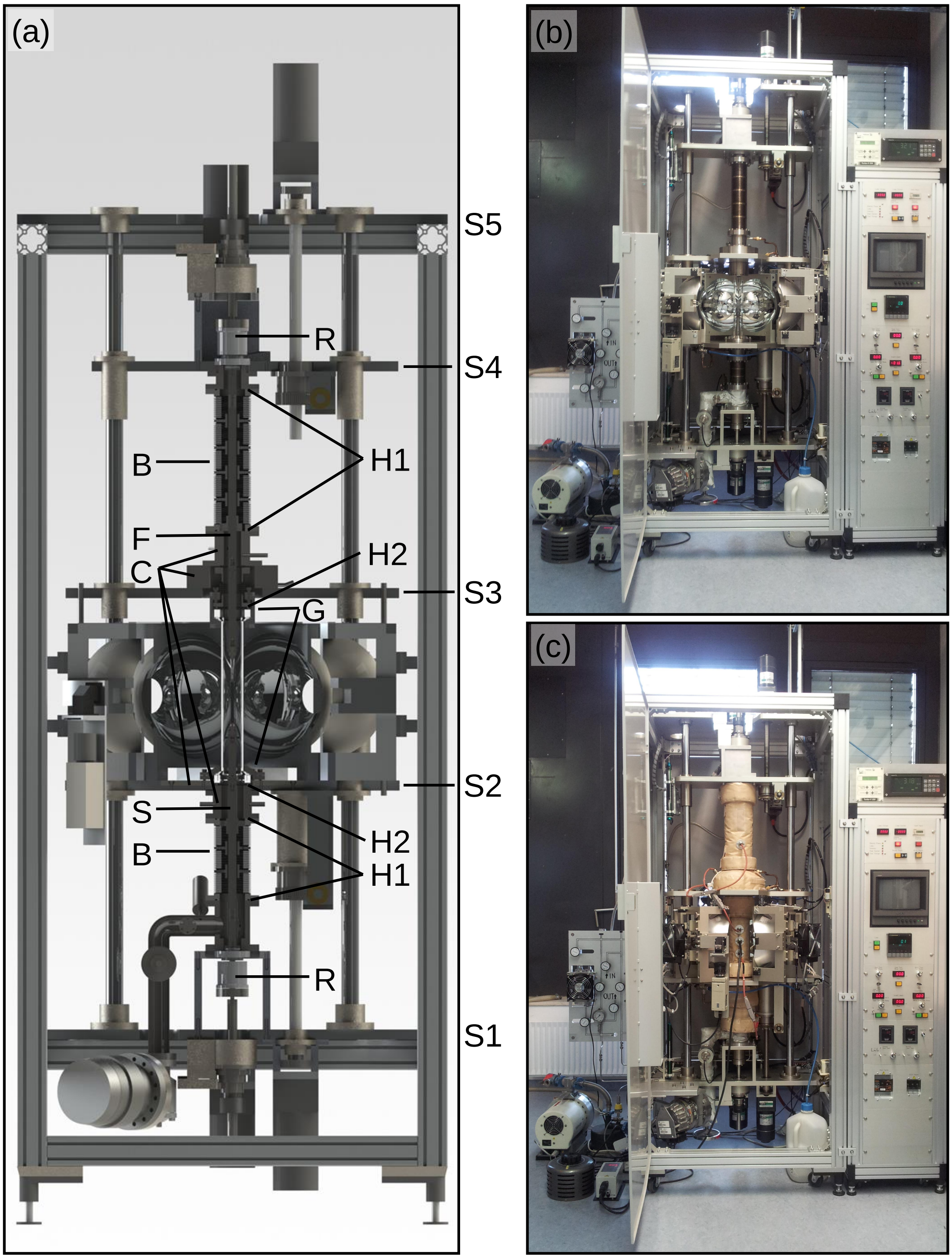

Figure 1.11: All-metal sealed image furnace. (a) Technical drawing of the image furnace made as preparatory work for the integration of electrotransport into optical float-zoning. (B) metal bellow, (C) water-cooled part, (F) shaft for feed rod, (G) quartz glass assembly, (H1)–(H2) Helicoflex sealing, (R) rotation feedthrough, (S) shaft for seed rod, and (S1)–(S5) stage. (b) Image furnace as it was used throughout this thesis. (c) Image furnace with its bespoke heating jackets.

specific properties of the sample and the inert gas pressure. It was not reached when trying to grow the transition metal diborides described in Sec. 2.1.3. Growth rates between 0.1 mm/h and 18.8 mm/h may be applied by vertically moving the mirror stage (consisting of S2 and S3). High-pressure metal bellows (B) provide the necessary room for this translation. Typically, the growth is performed from bottom to top where the upper rod, also referred to as feed, provides the material that crystallizes on the lower rod, also referred to as seed. The rate at which the sample material is added to the molten zone and as a result the diameter of the growing crystal may be regulated by moving the upper stage (S4). All-metal sealed magnetic rotation feedthroughs (R) allow for the individual rotation of the seed rod and feed rod in both directions with up to 56 rpm.

The all-metal sealing of the furnace is achieved via special Helicoflex HN 130 o-rings (H1) made of aluminum and Nimonic that replace the original viton o-rings. The quartz glass inside the mirror stage was embedded into a custom assembly utilizing Helicoflex HNV 290 P sealings (H2) made of aluminum, Inconel 600, and Nimonic. Additionally, the water cooling of the system (C) has been optimized to permit an efficient removal of remaining water using pressurized air prior to a bake-out.

The system is assembled in the following order. First, the mirror stage is moved to a relatively low position while stage four (S4) is moved to the upmost position. After mounting the seed rod together with the upper part of the lower shaft (S) the quartz glass assembly (G) is introduced into the mirror stage from above. Angular resilient adjustment couplings from Maedler installed into the shafts allow for the bending of the upper metal bellow and hence an improved accessibility. Subsequently, the feed rod is mounted together with the lower part of the upper shaft (F). Finally, the quartz glass assembly is screwed onto the upper metal bellow before stage four is lowered and the Helicoflex sealing between the quartz glass assembly and stage two (S2) is tightened. For the removal of the sample the procedure is followed in the reverse order. As preparatory work for combining electrotransport and optical float-zoning, the existing image furnace setup as depicted in Fig. 1.11(a) has been constructed in SolidWorks in collaboration with Stefan Giemsa.

High pressure floating zone furnace

The melting temperatures of the transition metal diborides grown in this thesis exceed the accessible temperature range of the image furnace described above. Thus, we utilized the high pressure crystal growth furnace, the so-called Smart Floating Zone (SFZ), at the Institut für Werkstoffforschung (IFW) in Dresden in collaboration with Christian Blum and Sabine Wurmehl.

The SFZ is an image furnace using the light of a single 7 kW xenon arc lamp that is focused into the crystal growth chamber via two ellipsoidal mirrors. Central part of the chamber is a single-crystalline sapphire cylinder with 3 cm wall thickness and 3 cm inner diameter permitting the application of pressures of up to 150 bar. High inert gas pressures in general reduce evaporation losses which, besides the high melting temperatures, represent an additional challenge for the single crystal growth of transition metal diborides. However, the design of the pressure vessel of the SFZ allows for a small diameter connection to a turbomolecular pump only and the system is neither metal-sealed nor bakeable. Typically, after evacuating the system to some 10^{-4} mbar the growth process takes place in a flowing atmosphere. As inert gas we used 5N argon additionally purified by a titanium getter furnace leading to an oxygen content of less than 0.1 ppm. A shutter may be moved into the light path that permits to measure the temperature of the sample with a two-color pyrometer stroboscopically [66]. For the diborides the zone surface temperature was in good agreement with the binary phase diagrams reported in Ref. [57].

1.7 Apparatus for annealing and electrotransport

As a final step of the growth process, the crystalline quality of a sample may be improved by a post-growth treatment. A very common technique is annealing, i.e., keeping the sample at elevated temperatures below the melting point for up to weeks. Further methods include zone refining, i.e., multiple float-zoning runs on the same sample, and solid state electrotransport. In the latter high currents, usually of the order of ∼500 A translating to current densities of the order of 10^7 A/m^2, are passed through a solid metallic specimen. The application of similar currents on a sample during its float-zoning, albeit being technically demanding, promises to combine the advantages of both methods while at the same time bolstering their efficiency.

This section is organized as follows. In Sec. 1.7.1 we start with an account for the annealing furnace designed by Georg Benka. Subsequently, Sec. 1.7.2 introduces the concept of electrotransport before Sec. 1.7.3 describes the construction of a solid state electrotransport furnace. This furnace was partly constructed as a testing ground for various components for the implementation of an electrotransport option into our all-metal sealed image that is finally illustrated in Sec. 1.7.4.

1.7.1 Annealing furnace

Annealing in general refers to a heat treatment that alters the properties of a specimen. In solid state research annealing in particular is used to relieve strain, heal defects, and improve compositional homogeneity. In some compounds, mostly in congruent ones, an annealing of polycrystalline material may already lead to the formation of grains with a size in the millimeter range. Moreover, carefully chosen annealing routines, sometimes combined with a quenching of the sample, i.e., a rapid cooling after the heat treatment, may stabilize certain compositional or structural phases. Examples include single-crystal neodymium [67] or the weak itinerant ferromagnet Ni_3Al [68, 69]. As the sample is kept at elevated temperatures over an extended period of time, the annealing requires a clean atmosphere. For this purpose, intermetallic samples are mostly sealed under argon in small quartz glass ampules, while the heating is carried out by a tube furnace. The permeability of quartz glass, however, significantly increases with increasing temperature limiting the maximum process temperature to ∼1000 °C.

Hence, as an addition to our high purity material preparation chain, Georg Benka set up a custom annealing furnace during his master's thesis [63]. This furnace, shown in Fig. 1.12, is based on a commercial Knudsen effusion cell (A) that is typically used to evaporate the educts in molecular beam epitaxy. The Knudsen cell is designed for ultra-high vacuum environments, is mounted on a standard CF DN40 flange, and reliably provides temperatures between 200 °C and 1400 °C. The actual crucible (B) is made of pyrolytic boron nitride and possesses a volume of ∼35 cm^3. The cell is surrounded by a bespoke water-cooled radiation shield (C) with the option of a lid made of pyrolytic boron nitride and copper (not shown). The compact vacuum chamber of the annealing furnace is based on a CF DN100 four-way-cross, to which a Quick-CF flange (D) at the top permits easy access for sample changes. The combination of all-metal sealed connections, an ion getter pump (E), pre-pumping via an external turbomolecular pump backed by a scroll pump, and a bake-out via a bespoke heating tent allows for an ultimate vacuum of 10^{-10} mbar. Up to 1.2 bar high-purity argon may be applied as inert atmosphere.

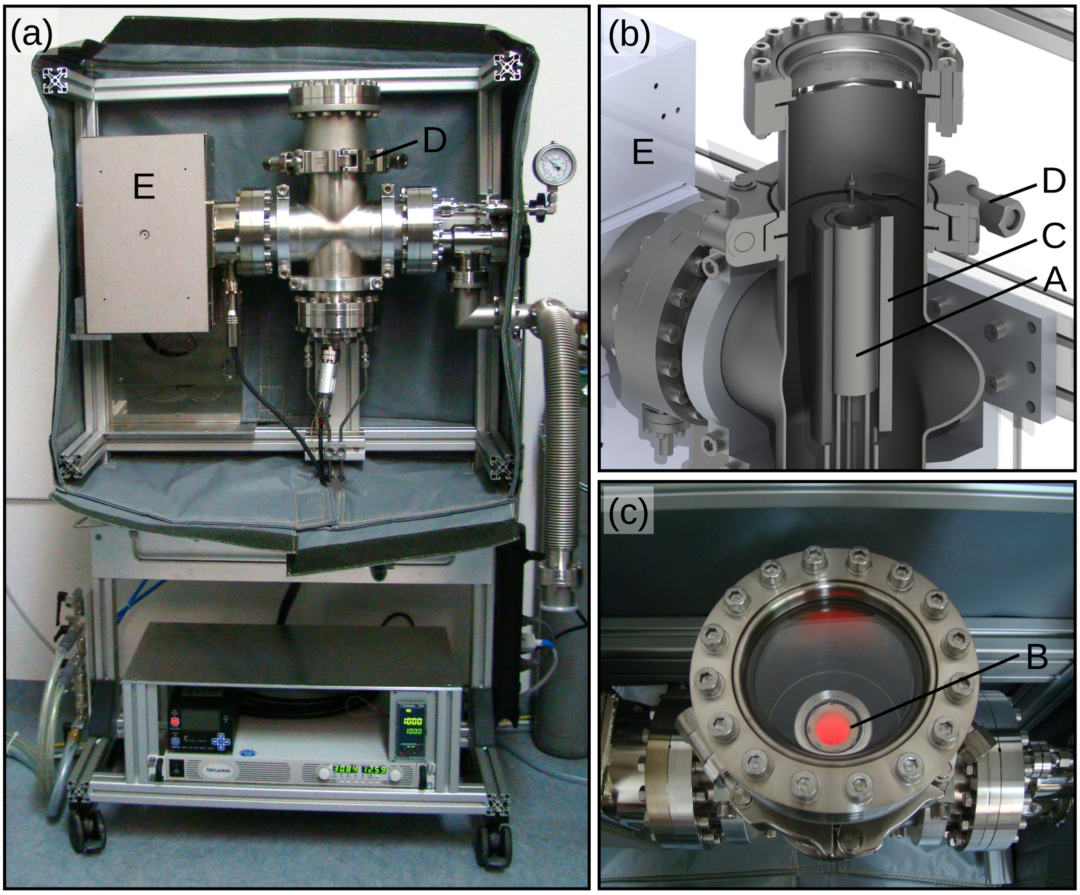

Figure 1.12: Annealing furnace based on a Knudsen effusion cell. (a) Overall system. (b) Cutaway view of the central part of the annealing furnace. (c) View through the window while the Knudsen cell is heated. (A) Knudsen cell, (B) crucible out of pyrolytic boron nitride, (C) water-cooled shroud, (D) Quick-CF flange, and (E) ion getter pump.

1.7.2 Introduction to electrotransport

If an electric field is applied to a conducting samples, a migration of atomic cores accompanies the dominant flow of electrons. In applied semiconductor physics this process is referred to as electromigration and is unwanted since it leads to the degradation of conductor lines and ultimately to the failure of electronic devices. However, this phenomenon can also by exploited to purify metallic specimens where it is called electrotransport or solid state electrotransport, as it is usually performed on solids. An overview of the theoretical and phenomenological understanding of electrotransport is given in Refs. [70, 71]. In the following, the main concepts will be summarized.

As depicted schematically in Fig. 1.13, two opposing forces need to be considered if an electric field is applied to a metallic sample. On the one hand, the electrostatic force pulls the positively charged atomic cores towards the cathode. On the other hand, the flowing electrons scatter on the cores thereby creating a force that drags them towards the anode. The direction and speed of the resulting movement is dependent on the size of the electric field and the current den-

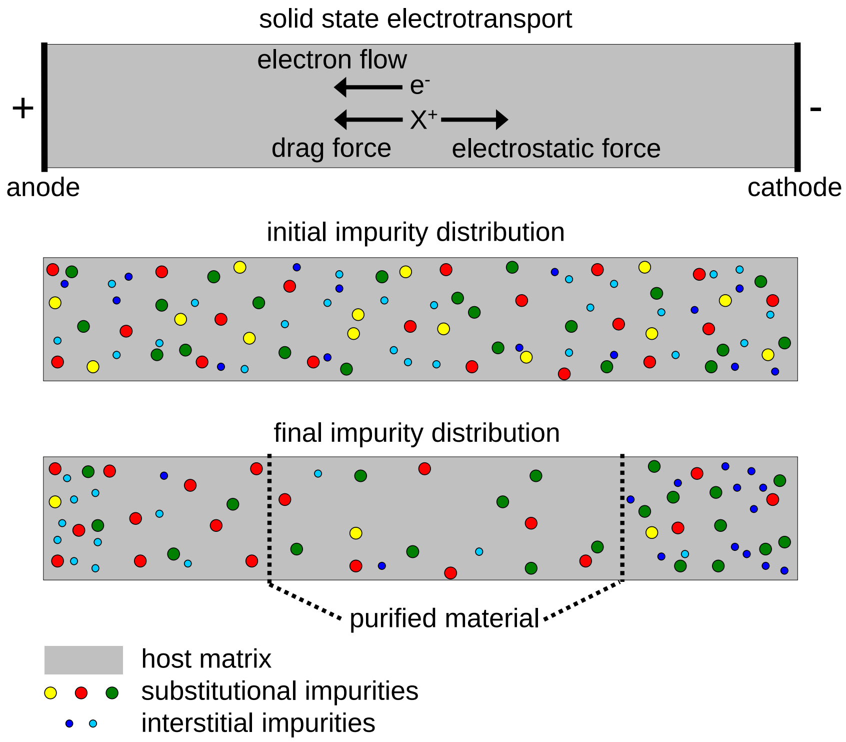

Figure 1.13: Schematic diagram of solid state electrotransport. An electric field applied to a metallic sample most prominently leads to a flow of electrons. Via scattering these electrons exert a drag force on the positively charged atomic cores while the electrostatic force acts in the opposite direction. The resulting drift of the cores is dependent on the material combination of atomic core and host matrix and may be used to purify the middle part of a metallic bar.

sity, respectively, as well as on the material combination of atomic core and host matrix. Since within a given matrix, in general, some impurities drift towards the cathode and some towards the anode, the middle part of the specimen is purified while the contaminations accumulate at the ends of the bar. Typical transport velocities per field, given in units of m^2/Vs, are of the order of 10^{-14} to 10^{-12} for the matrix constituents, 10^{-11} to 10^{-10} for substitutional dopants, and 10^{-10} to 10^{-7} for interstitial dopants [70]. Hence, electrotransport is efficient in sweeping out interstitial impurities (small circles in Fig. 1.13) whereas the removal of substitutional contaminations (large circles in Fig. 1.13) is a very slow process. In transition metal or rare earth elements and compounds interstitial sites are usually occupied by small atoms like hydrogen, carbon, nitrogen, or oxygen, while heavier contamination elements substitute matrix atoms.

The electron flow in the sample in fact also leads to ohmic heating which ultimately limits the maximum electric field applicable and, as a result, the maximum electrotransport velocity. The typical process temperature is around 90 % of the melting temperature. In good metals this value usually is reached at a field of a few volt per meter or a dc current of a few hundred amp, respectively. Consequently, electrotransport is always accompanied by an annealing process that leads, e.g., to the evaporation of volatile impurities (yellow and light blue circles in Fig. 1.13) [72], to the reduction of structural defects, and to grain growth in polycrystalline material. Moreover, the mobility of impurities is significantly increased at elevated temperatures. Still, the ohmic heating also results in a few constraints that need to be considered. First, since solid state electrotransport is a continuous process that requires extended periods of time, usually between a few days and several months, a very clean environment is indispensable. Otherwise the sample might getter more impurities from the atmosphere than are removed by the electrotransport. Furthermore, high (and/or inhomogeneously distributed) initial impurity concentrations in the sample may induce very high local resistances during electrotransport and may either limit the maximum current or lead to a melting and dripping-off of the sample. If the vapor pressure of the sample prohibits the usage of an ultra-high vacuum environment, an inert atmosphere of similar purity has to be applied. Though the inert gas prevents a continuous pumping of the recipient, it also introduces additional cooling and a more homogeneous temperature distribution along the sample. As a result, the applicable maximum current increases.

Solid state electrotransport may be applied to polycrystalline and single-crystalline material. Together with zone refining it is one of the state of the art techniques for the preparation of the highest purity material from all except for the high vapor pressure rare earth elements, e.g., used at the Ames Laboratory [73–76]. To the best of our knowledge, the only solid state electrotransport on a compound reported so far, was carried out on single-crystal $CeNi_2Ge_2$ by Braithwaite *et al.* [77]. They applied a current density of $\sim$1000 A/cm^2 for one week in a vacuum of 10^{-10} mbar and achieved a residual resistivity of less than 1 $\mu\Omega$cm for current along the a-axis.

In compounds, other than in pure elements, the migration of the constituents has to be taken into account. We assume that the corresponding transport velocities are comparable to the transport of matrix constituents or substitutional dopants in elemental hosts. Therefore, electrotransport may still be a valuable tool for removing interstitial impurities. However, while electrotransport continuously improves the quality of the central part of an elemental specimen, in binary and ternary compounds the purification on shorter time scales due to the removal of interstitial impurities has to be balanced with the degradation of the sample on longer time scales due to a change of the stoichiometry along its length caused by the migration of the matrix elements.

Some of the difficulties of solid state electrotransport, like the very long operating times leading to evaporation losses or the compositional issues in binary and ternary compounds, may be avoided by performing electrotransport and float-zoning in parallel. This way, synergy effects between both techniques may be observed. Impurities in general possess a higher solubility as well as a much higher mobility in the molten state when compared to the solid state. Hence, the impurity atoms not only concentrate in the molten but are also efficiently pushed away from the crystallization front by an electric current reducing their concentration at the liquid-solid interface and less impurities are built into the growing crystal. The compositional issues that arise for binary or ternary compounds in solid state electrotransport may be buffered and regulated within the molten zone. Furthermore, if a single crystal is required, float-zoning, float-zoning needs to be carried out anyhow. Performing electrotransport in parallel reduces the time the sample is kept at elevated temperatures to a minimum which is desirable when handling compounds that involve volatile constituents. In addition, the current that is passed through the sample may be used as an after-heater and as a parameter to adjust the temperature gradient along the growth direction.

In the early 1990s, a pioneering study by King and Brown combined electrotransport with inductively heated float-zoning [78]. Though the authors mention possible issues that may emerge from the combination of these two techniques, some of them exclusively arise for inductive heating, they demonstrate its high potential by improving the residual resistivity ratio (RRR) of nickel by a factor of up to four for current parallel to the growth direction. Malang *et al.* utilized electrotransport together with electron-beam heated zone refining in niobium [79]. Here, the authors report an additional increase of the RRR by a factor of two for current parallel to the float-zoning direction compared to zone refining alone. For the antiparallel combination they observe a decrease of the RRR by roughly a factor of two. Moreover, as expected for electrotransport effects, the RRR was dependent on the position along sample. The integration of an electrotransport option into an image furnace is technically demanding but promises to combine the beneficial temperature profile produced by optical heating with the advantages of a parallel operation of float-zoning and electrotransport described above. Keeping the feed and seed rods rotatable, which was neither implemented by King and Brown nor by Malang *et al.*, allows for a control of the molten zone. The realization of such an electrotransport option for our all-metal sealed image furnace was accomplished within this thesis and is described in Sec. 1.7.4.

1.7.3 Solid state electrotransport furnace

As a part of this thesis and as a step towards the integration of electrotransport into optical float-zoning we have designed a solid state electrotransport setup, shown in Fig. 1.14. The basis for the high purity environment is provided by an existing vacuum chamber and a Varian VacIon Plus 300 StarCell ion getter pump (A). In combination with all-metal sealed connections, an external turbomolecular pump backed by a scroll pump, and a bake-out using a bespoke heating tent a vacuum of 10^{-10} mbar is easily achievable. Up to 1.2 bar argon are used as inert atmosphere, where a SAES MicroTorr MC190 gas purifier (B) ensures a nominal impurity concentration of <1 ppb. A water-cooled copper radiation shield (C) prevents the recipient from heating during the electrotransport process, while a small hole permits to monitor the sample temperature optically or by a pyrometer.

The actual electrotransport setup is mounted on the CF DN200 top flange of the vacuum system. This way, easy access for sample changes is provided by lifting the top flange using a Rose+Krieger EDX50 linear actuator (D), cf. Fig. 1.14(b). The actuator may not be heated above 80 °C and is removed prior to a bake-out. A TDK-Lambda Genesys GEN 8-600 5 kW dc power supply (E) provides currents up to 600 A at voltages of up to 8 V and is connected via $40 \times 10\,\mathrm{mm}^2$ copper ribbon cables. Using a constant voltage mode prevents feedback loops that eventually lead to the melting of the sample. Two CF DN40 high-current feedthroughs (F) transport the current onto massive copper rods (G) with a diameter of 20 mm. A design using massive leads was favored over a setup using water-cooled current-carrying pipes as this furnace also served as test setup for the integration of an electrotransport option into our image furnace where current needs to be fed onto rotating shafts.

The sample is contacted by bespoke two-part tungsten sample holders tightened by M2 molybdenum screws, see Fig. 1.14(d). The same design is also used for the sample holders of the electrotransport option in the image furnace. Tungsten was chosen as it combines a very high thermal stability with a relatively low resistivity. The sample holders are in turn connected to the current leads by four copper stranded wires, each with a diameter of 5 mm. The flexibility of the wires compensates for the thermal expansion of the sample and the currents leads. The same design is also used for the sample holders of the electrotransport option within the image furnace. A CF DN40 linear translator (H) located on the top flange allows to adjust for sample lengths up to 120 mm. The solid state electrotransport furnace was tested on single-crystal cobalt. Fig. 1.14(e) depicts the glowing sample while ~400 A are passed through it. No technical problems were observed. Extensive electrotransport studies including a detailed chemical

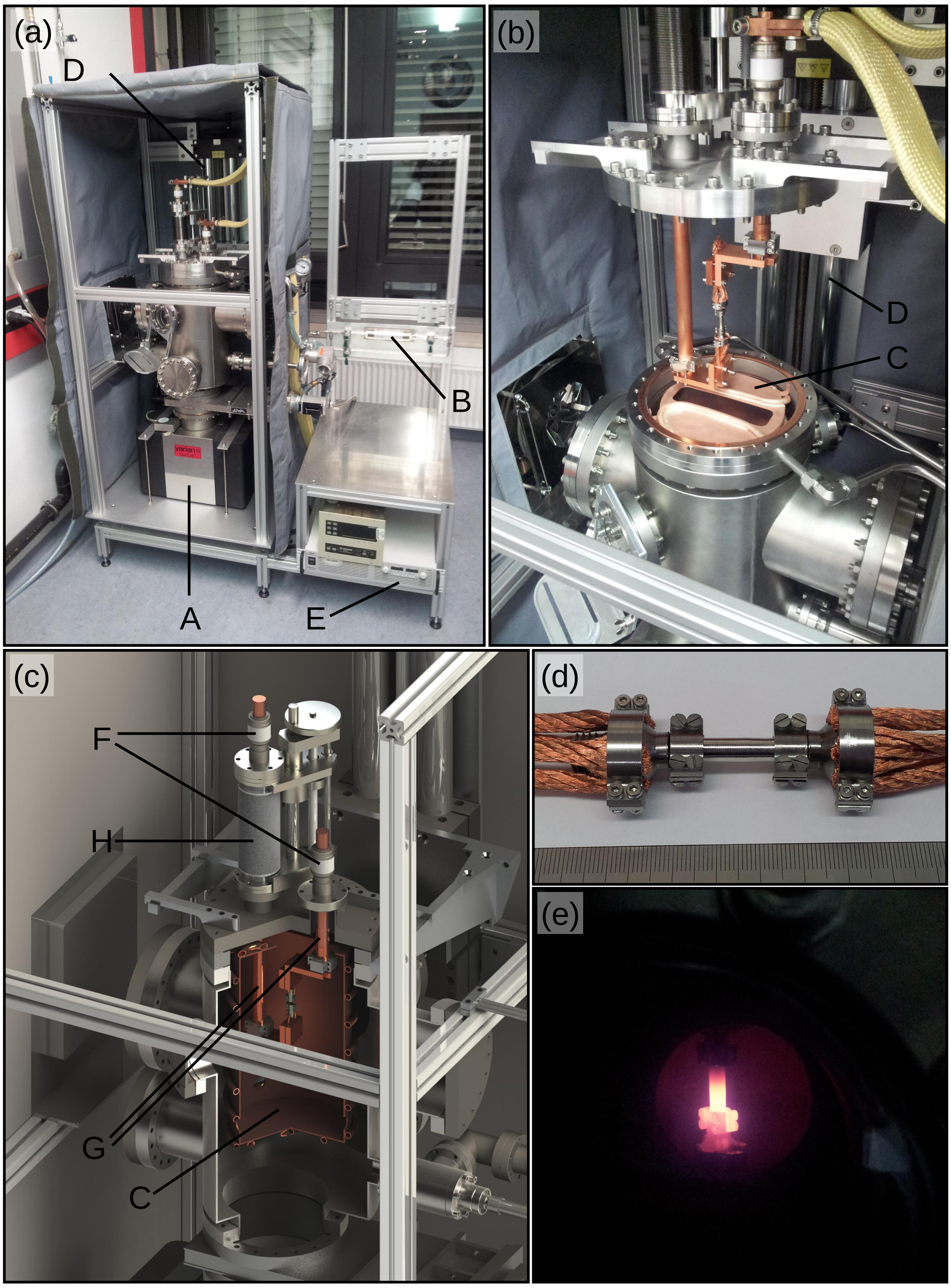

Figure 1.14: Solid state electrotransport furnace. (a) Total view. The all-metal sealed setup resides on top of an ion getter pump and is enclosed by a heating tent. The linear actuator necessary for sample changes is removed during the bake-out and is stored on the right side of the rack. (b) Lifted top flange during sample mounting. (c) Cut-away view of the system and the water-cooled radiation shield. (d) Single-crystalline cobalt sample fixed in tungsten sample holders with copper strands attached. The scale is in millimeter. (e) View through the window while passing ~400 A through the cobalt sample. See text for (A) through (H).

analysis of the sample will be addressed in future studies, e.g., utilizing the prompt gamma ray activation analysis (PGAA) available at Forschungsreaktor München II (FRM II), also referred to as Heinz Maier-Leibnitz Zentrum (MLZ).

1.7.4 Integration of electrotransport into optical float-zoning

In this section we address the major technical challenges of the implementation of an electrotransport option into an all-metal sealed image furnace. First of all, in order to allow for a straightforward and reliable operation, we decided for a setup with permanently installed current feedthrough units (U) that will be described in detail below. Moreover, using the shafts as solid current leads permits to keep the process of mounting and demounting of samples essentially unchanged and avoids the technical complexities associated with feeding cooling water into a rotating shaft in ultra-high vacuum. Thus, if no current is passed through the sample, the image furnace may be used in the same way as it was used prior to the integration of the electrotransport option.

Fig. 1.15 shows the modifications that were necessary to provide the height for two current feedthrough units. In the lower part, i.e., below the mirror stage (consisting of S2 and S3), the rotation feedthrough (R) was moved below the first stage (S1). The corresponding motor required to set the rack of the image furnace on top of aluminum blocks (AB) of 60 mm height. A new base flange (BF), to which the turbomolecular pump, the pressure gauges, and the inert gas inlet are attached, was designed using mostly standard CF components. In the upper part, i.e., above the mirror stage, the rotation feedthrough (R) was placed on a small rack on top of stage four (S4). The open construction permits easier access compared to the previous version.

Along with these modifications we replaced the expensive and delicate Helicoflex HN 130 sealings (H1) by standard CF copper sealings. The Helicoflex HNV 290 P sealings (H2) that connect the quartz glass with its neighboring parts are unchanged. In a first step, the water-cooled parts of the vacuum system below (C1) and above (C2) the mirror stage were re-designed. In a second step, depicted in Fig. 1.16, new high pressure metal bellows (up to 5 bar) were developed in collaboration with COMVAT. As a consequence, the adjacent parts were replaced. Besides being sealed with standard DN40 copper rings, the new bellows offer a large pumping cross-section as they are stabilized by an external guidance. Previously, stabilization rings in conjunction with the shafts prevented the bellows from bending at high pressures at the expense of a drastic reduction of the pumping cross-section. For the operation of the electrotransport option, however, it is indispensable to avoid contact between the stabilization rings and the current leading part of the shaft. While these constrains could eventually be addressed with the old bellows, as described below, the new design circumvents this issue completely.

The crucial parts of the electrotransport option are two bespoke feedthrough units that allow to pass up to 400 A of dc current into the ultra-high vacuum chamber of the image furnace, cf. Fig. 1.17. While the actual feed through can be accomplished by standard CF DN40 high current feedthroughs (U1), a major technical issue involved the transmission of the current onto rotating shafts that allow for an axial movement of about 100 mm in an ultra-high vacuum compatible environment. The transmission system was developed in collaboration with RIE-TECH and is connected to the actual feedthrough by massive copper components (U2). In each feedthrough unit two brass blocks of 80 mm height (U3) support sets of 40 U-shaped nickel silver springs with hard gold droplets on both ends (U4). The springs press the droplets onto a hard gold plated solid copper shaft (U5) transmitting a current of up to 2.5 A per droplet. A spacer (I1) made of the high-temperature resistant and low outgassing polyimide TECASINT 2011 insulates the

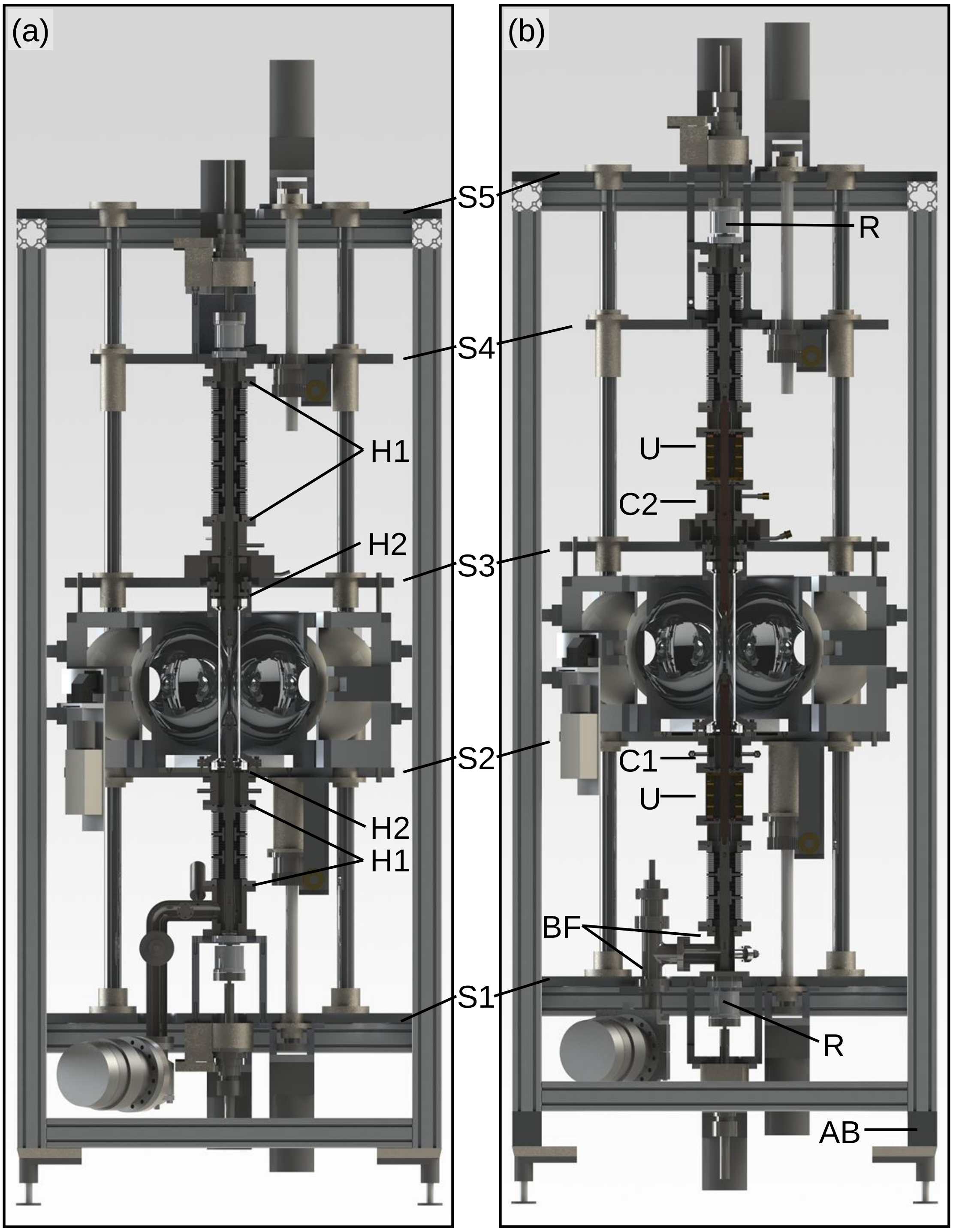

Figure 1.15: Design of the all-metal sealed image furnace. (a) Setup as used for all crystal growth processes performed as part of this thesis, see also Fig. 1.11. (b) Setup after the integration of an electrotransport option. Several modifications provide the necessary height for two current feedthrough units. (AB) aluminum block, (BF) basis flange, (C1)–(C2) water-cooled part, (H1)–(H2) Helicoflex sealing, (R) rotation feedthrough, (S1)–(S5) stages, and (U) current feedthrough unit.

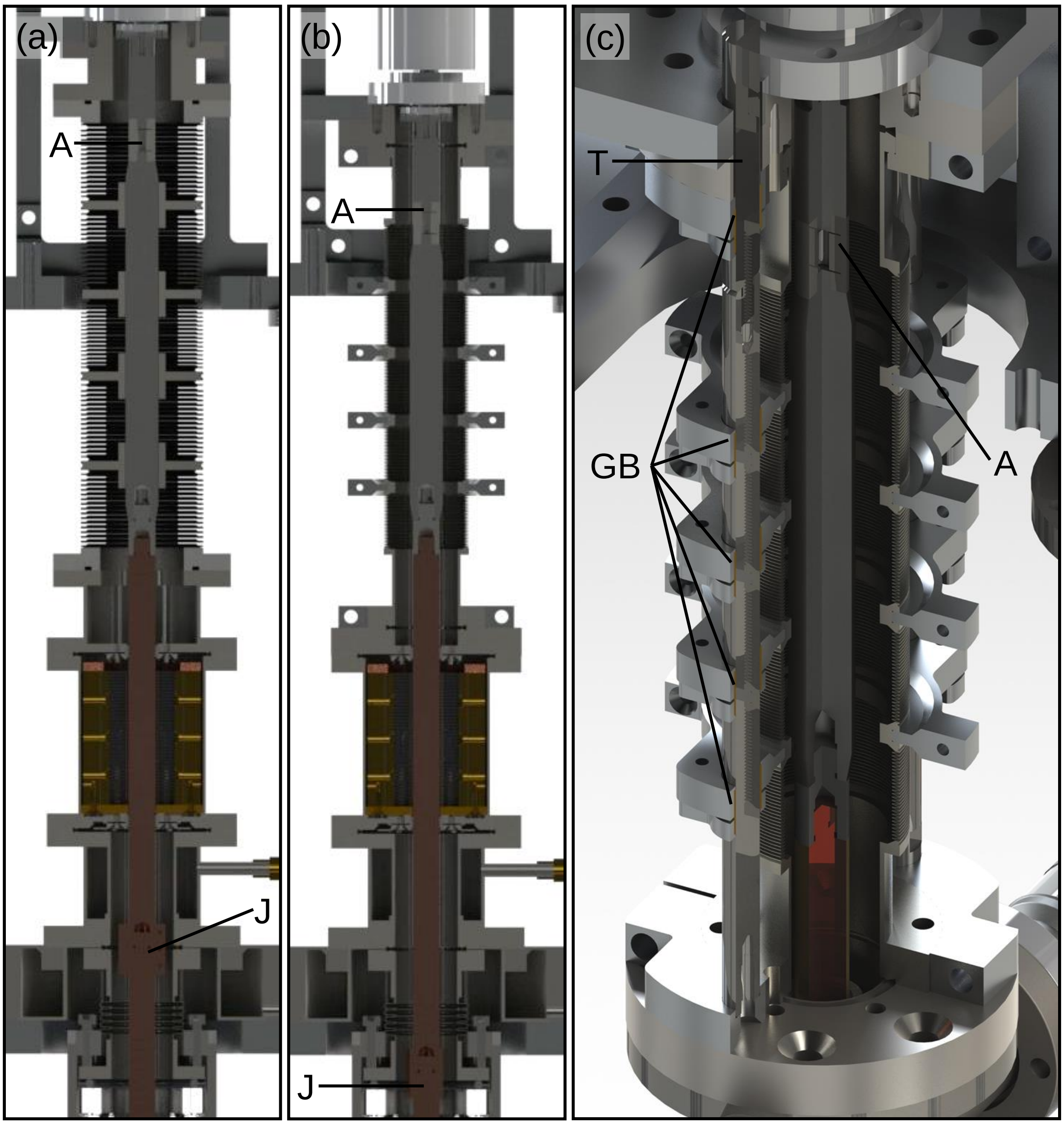

Figure 1.16: High pressure metal bellows with external guides. (a) Upper part of the image furnace with the original bellows. (b) Upper part of the image furnace with the new bellows. The position of the joints (J) in the upper shaft had to be adjusted as the free length of these high pressure bellows corresponds to their maximum length. In the lower shaft only the bellow and the adjacent parts were replaced (not shown). (c) Isometric cut-away view of the upper bellow. Both the top part of the guidance rail (T) and the shaft incorporate an adjustment coupling (A) to provide the mechanical flexibility necessary for sample changes. The glide bearings of the guidance (GB) are made of polyphenylene sulfide to ensure bakeability up to 200 °C.

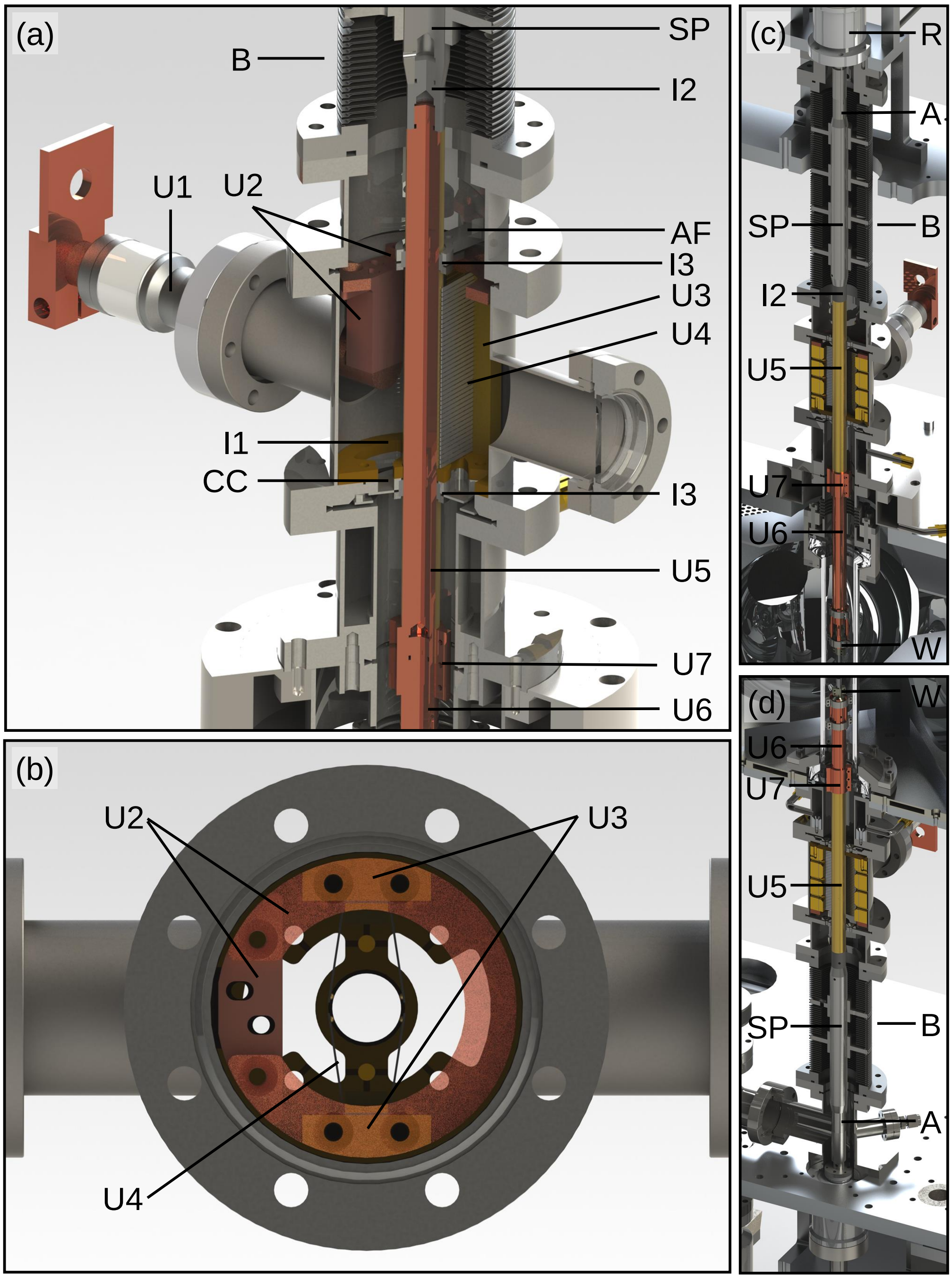

Figure 1.17: Electrotransport setup in the all-metal sealed image furnace. (a) Cut-away view of the feedthrough unit that allows to pass up to 400 A into the ultra-high vacuum chamber and onto the rotating shaft. The setup uses bespoke sliding contacts. (b) Top view of the feedthrough unit. (c) Cut-away view of the upper part of the image furnace. (d) Cut-away view of the lower part of the image furnace. (A) adjustment coupling, (B) metal bellow, (CC) cover, (I1)–(I3) insulating part, (R) rotation feedthrough, (SP) steel part of the shaft, (U1)–(U7) current bearing part, and (W) tungsten sample holder.

current bearing parts from the housing.

The gold plated shaft is continued by a solid copper rod (U6) where a copper sleeve (U7) enhances the electrical contact at their joining. At its other end, a small intermediate piece (I2) made of TECASINT 2391 electrically insulates the gold plated shaft from the steel part of the shaft (SP) that in turn is connected to the all-metal rotation feedthrough (R). TECASINT 2391 corresponds to TECASINT 2011 with the addition of 15 % MoS_2 providing a very small coefficient of friction. The same material is used for two slide bearings (I3) just above and below the transmission system. To provide easy access to the actual feedthrough unit one of the slide bearings is built into the adapter flange (AF) directly adjacent to the unit. In combination with adjustment couplings (A) from Maedler (torsionally stiff, angular and transverse resilient) installed into the steel parts of the shafts, these slide bearings ensure a reliable current transmission and allow for a precise alignment of the seed and feed rod. The diameters and lengths of the different parts of the shafts were carefully optimized in order to permit the vertical movement necessary for the float-zoning while at the same time stabilizing the bellows (B). The two-part tungsten sample holders (W) are based on a design used for conventional float-zoning. The lower holder is tightly screwed to the lower shaft where additional clamped copper strands ensure an excellent electrical contact. The upper holder is mounted via such copper strands only hence providing the mechanical flexibility required during crystal growth.

A custom cover (CC) protects the transmission system from sample material dripping down and from serious evaporation by the sample, respectively, while retaining a large pumping cross-section. The feedthrough units are connected with their neighboring parts using standard CF DN63 sealings and dead volumes are drilled if they were not avoidable. In combination with the bakeability of the entire vacuum system (including the external guidance of the new bellows) this allows for ultra-high vacuum compatible conditions. The water-cooled parts of the system are placed between the feedthrough units and the mirror stage, hence reducing the thermal stress on the the transmission system. The latter may resist temperatures exceeding 300 °C during operation. The currents up to 400 A at voltages of up to 8 V are provided by a TDK-Lambda Genesys GEN 8-400 3.2 kW dc power supply and transported to the feedthrough units via $40 \times 10\,\mathrm{mm}^2$ copper ribbon cables.

1.8 Metallurgical characterization and low-temperature properties

As part of this thesis various experimental methods were used to characterize samples metallurgically and to determine their low-temperature properties. Techniques that were extensively used throughout this thesis are described in the following while other techniques are briefly summarized as part of the presentation of the corresponding data.

1.8.1 Experimental methods for metallurgical characterization

A metallurgical characterization of a sample may be carried out at various steps of the crystal growth process. In most cases, however, we focus on float-zoned specimens, that are labeled by the acronym 'OFZ' in combination with a consecutive number. We usually start the characterization by means of x-ray Laue diffraction in backscattering geometry. This way, we determine whether and where there are large grains or single-crystalline sections in the float-zoned ingot. Albeit x-ray diffraction is only surface sensitive, it usually gives an appropriate first impression and together with polished lateral cuts allows to plan the further steps of the sample preparation. The investigation of a polished longitudinal cut of quenched last zone is crucial for the optimization of the growth parameters, especially in non-congruent compounds.

If single-crystalline sections are identified, x-ray Laue diffraction in combination with a wire saw is used to prepare oriented samples. Rough cuts may also be made by means of spark erosion. Standardized cutting patterns yielding typical samples for various experimental techniques (magnetization, susceptibility, specific heat, electrical transport, thermal transport) and the major field configurations were developed for cubic, tetragonal, orthorhombic, and hexagonal materials. Depending on the measurement methods to be applied, the samples surfaces are kept as cut, ground, or polished. Polished specimens usually reach a mean surface roughness below 10 Å, as indicated by atomic force microscopy data [80]. The sample preparation is mostly carried out by Susanne Mayr in the central crystal laboratory of the TUM.

The composition of our samples is stated as weighted in at the beginning of the crystal growth process. Direct measurements of the composition have been carried out by means of energy dispersive x-ray spectroscopy (EDX) on a scanning electron microscope. For typical intermetallic compounds, the setups available at the Walther-Meißner-Institut (WMI) or the Radiochemie München (RCM) allow for the detection of contamination or doping elements on a percent level and for the determination of relative changes of composition. The latter has been demonstrated conclusively on single crystals of helimagnetic transition metal monosilicides with an intended compositional gradient along their growth direction [60]. Impurity phases that accumulate at grain boundaries or surfaces can also be identified as has been shown for an iron rich impurity phase in Fe_2TiSn [60, 81]. The absolute concentrations of matrix elements, however, often may not be determined with sufficient precision.

Powder x-ray diffraction (XRD) in reflexion geometry was performed on a Siemens D5000. XRD is used to determine the crystalline structure and the lattice constants of a certain compound. Moreover, impurity phases and their relative quantities may be identified. A detailed refinement of the data may yield information about certain types of disorder [82]. When searching for a known impurity phase, XRD can be very sensitive as we have demonstrated in Sec. 2.2.3 for Mn_2Sb in CuMnSb together with Saskia Gottlieb-Schönmeyer. For a fast and reliable grinding of the XRD samples we purchased a Retsch CryoMill, i.e., a swing mill that can cool the samples with liquid nitrogen to increase their brittleness. When synthesizing ternary compounds with unknown metallurgical phase diagrams, XRD provides fast information about the feasibility of a single crystal growth. After the constituent elements have been melted together or a feed rod has been cast, a small portion of the material is milled and a diffractogram is recorded. If most of the sample already possess the desired phase, one may assume that the compound either melts congruently or forms through a weakly peritectic reaction. Hence, a single crystal growth via float-zoning is promising.

Neutron diffraction on the single crystal diffractometers RESI and HEiDi as well as on the powder diffractometer SPODI was carried out by Björn Pedersen, Martin Meven, and Anatoliy Senyshyn. Here, other than with x-ray techniques, the bulk of the sample is investigated and one can clearly distinguish whether the sample consists of a single crystal or of several grains, even if they are just separated by small-angle boundaries. The crystalline structure and mosaicity, the lattice constants, as well as the orientation of the single crystal (or, if present, of several grains) may be determined. A detailed analysis reveals information about different forms of impurities and disorder [81]. Moreover, neutron diffraction is also used to determine magnetic structures as, for instance, applied to the antiferromagnetic order in CrB_2 and CuMnSb by Alexander Regnat, cf. Sec. 2, or the complex order in $EuPtSi_3$ [83].

Finally, measurements of some physical properties may also be a highly suited probe for the quality or composition of a certain sample. As an example, the sensitivity of a magnetization or susceptibility measurement often by far excels direct metallurgical characterization techniques like XRD or EDX when trying to detect ferromagnetic impurities in a non-ferromagnetic host substance. This circumstance has been exploited, e.g., for the detection of Mn_2Sb in CuMnSb or $Fe_{67}Ti_{25}Sn_8$ in Fe_2TiSn as described in Sec. 2.2.3 and Refs. [60, 81], respectively. A commonly used characteristic for sample quality in metals is the residual resistivity ratio (RRR), i.e., the room temperature electrical resistance, $\rho(T = 300\,\mathrm{K})$, divided by the extrapolated zero-temperature resistance, ρ_0. The residual resistance ρ_0 is dominated by electron-impurity scattering. Thus, a low value of ρ_0 corresponding to a large RRR is associated with a high sample quality. While the RRR is easily accessible and often gives a sensible first impression of the quality of a sample, it can, in fact, only be used for comparing samples from the same compound. Moreover, different types of impurities or defects may affect the electron-impurity in different ways. For this reason, a high RRR does not necessarily translate to a small impurity density but to a small density of impurities that are effective in contributing to ρ_0. This will be discussed further in Sec. 3.2.1.

1.8.2 Experimental methods at low temperatures

Most of the experimental low-temperature data shown in this thesis were measured in a Quantum Design physical properties measurement system (PPMS). A PPMS is a helium-4 cryostat that serves as platform for different insets allowing for the determination of various physical quantities. It provides temperatures from 1.8 K up to 400 K for measurements of the specific heat as well as various transport properties (electrical resistivity, Hall effect, thermal conductance, Seebeck coefficient). For measurements of the magnetization and the ac susceptibility the maximum temperature is restricted to 350 K. Two PPMSs were used, one with a 9 T and one with a 14 T superconducting magnet, where the latter was purchased and brought into service during this thesis.

Magnetization and susceptibility in the PPMS

The dc magnetization and the ac susceptibility are measured in the PPMS using the AC Measurement System (ACMS) option. Besides the measurement electronics, this option consists of two parts: (i) an inset containing an ac drive coil, an ac drive compensation coil reducing background, and a set of detection coils used for magnetization and susceptibility measurements, as well as (ii) a servo motor permitting the adjustment of the vertical position of the sample and providing the vertical movement used to detect the dc magnetization via an extraction technique. Using the same set of hardware allows for alternating measurements of the dc magnetization and the ac susceptibility during the same temperature or field sweep, respectively. Bespoke sample holders made of Delrin, see Figs. 1.18(a) and 1.18(b), enable us to quickly mount samples reproducibly in defined orientations, are mechanically stable at low temperatures, and produce sufficiently small background signals.

The magnetization signal may be averaged over up to 50 extractions, where we typically use five repetitions. The ac susceptibility may be recorded at an excitation frequency in the range from 10 Hz to 10 kHz at an excitation amplitude of 0.17 µT to 1.7 mT. Real and imaginary part of the susceptibility are measured simultaneously. Larger excitation frequencies and amplitudes lead to larger signals, but the amplitude should always be small compared to the typical width of the phase transitions in field. When choosing the excitation frequency, in particular for low-resistance samples, the skin depth of the excitation field, $\delta = \sqrt{2\rho/\omega\mu}$ with

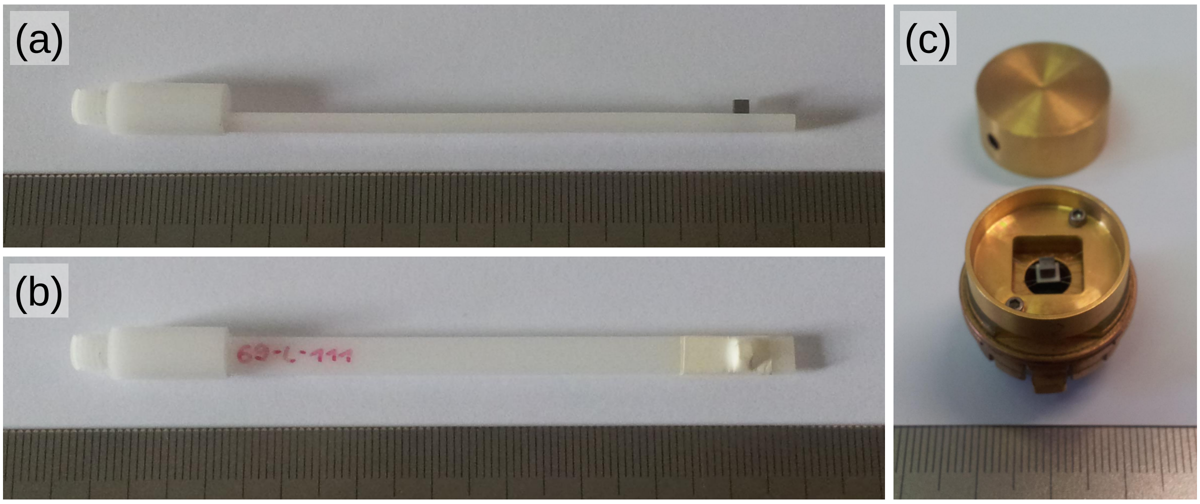

Figure 1.18: Sample mounting for measurements in the PPMS. (a) Sample holder for magnetization and susceptibility measurements. A cubic sample of MnSi is glued on the holder using GE Varnish. The magnetic field is applied along the long axis of the sample holder. (b) Top view of the sample holder. The sample is covered by a Teflon tape soaked with thinned GE Varnish. The label ”69-l-111” refers to the name of the sample, OFZ69-3-2-6-l, mounted for field along $\langle 111 \rangle$. (c) Puck for specific heat measurements. Here, the magnetic field is applied perpendicular to the white sample platform. All scales are in millimeter.

$\mu = \mu_0 \mu_r = \mu_0(1+\chi)$, needs to be considered as δ should be significantly larger than the sample dimensions. Moreover, if slow dynamics play a role, the response of the sample may also be dependent on time scales accessible by excitations at frequencies between 10 Hz and 10 kHz, i.e., on time scales of 0.1 ms to 0.1 s. Typical examples include spin glasses and compounds in which macroscopic magnetic domains are moved. As low-frequency limit of the ac susceptibility one can derivate a susceptibility from the measured magnetization. For field sweeps this corresponds to $\mathrm{d}M/\mathrm{d}H$. Measuring two temperature sweeps at slightly different applied field values allows for the calculation of $\Delta M/\Delta H$ as an analogon to a temperature sweep of the ac susceptibility.

Typically, measurements as a function of field are performed step-wise, i.e., the magnetic field is kept constant during the actual data collection. If not stated else, measurements as a function of temperature are recorded while heating the sample at a rate of 0.1 K/min to 3 K/min. The acquisition of one data point usually requires ∼15 s.

Specific heat in the PPMS

The specific heat may be measured in the PPMS by a conventional small heat pulse technique and by a quasi-adiabatic large heat pulse technique. In both cases, the sample is mounted onto a platform of $3 \times 3\,\mathrm{mm}^2$ out of Al_2O_3 using Apiezon N grease for measurements below room temperature and Apiezon H grease for measurements above, see Fig. 1.18(c). The platform contains a resistive heater and a thermometer connected via platinum wires. The latter also serve as mechanical suspension of the platform and as its thermal link to the cold bath.

For specific heat measurements in the PPMS a heat pulse is applied to the sample by the

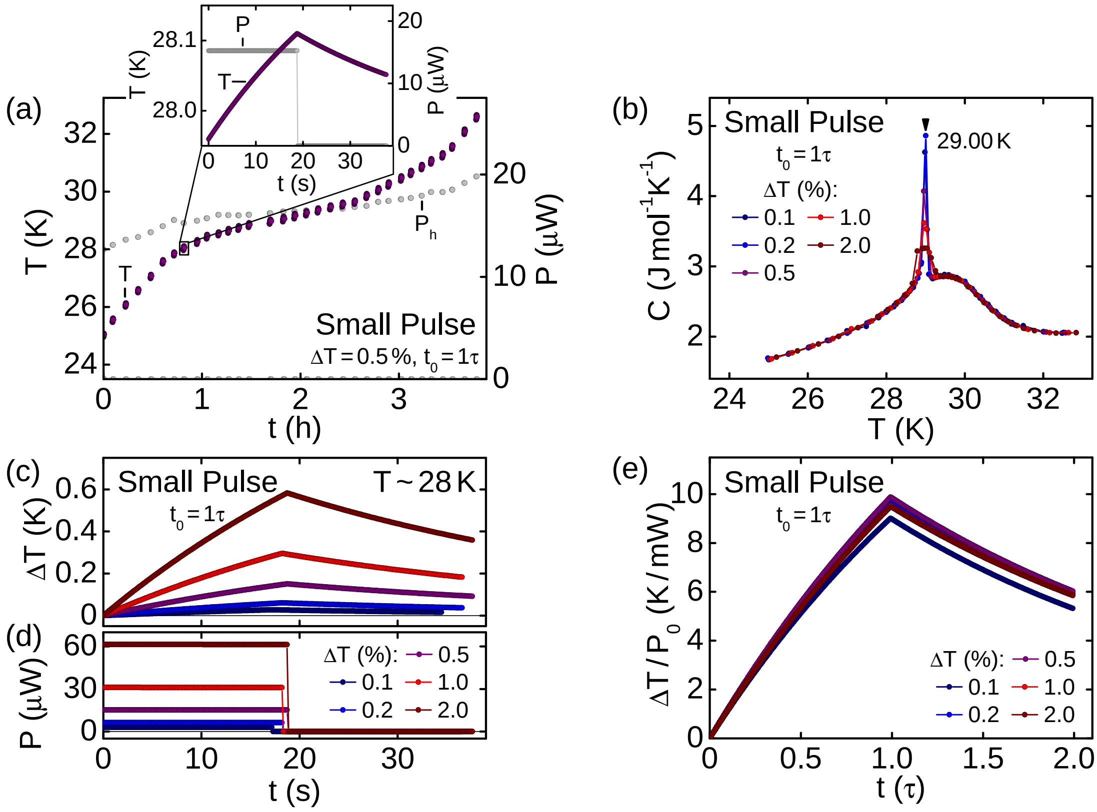

Figure 1.19: Specific heat measurements in the PPMS using small heat pulses. As example we address the magnetic phase transition of MnSi at $T_c = 29\,\mathrm{K}$, see Sec. 3 for further details on the material. (a) Sample temperature, T, and heater power, P, as a function of time for small pulses covering the temperature range around the phase transition. The inset depicts a single pulse. (b) Specific heat data resulting from the pulses shown in panel (a) and from measurements with small pulses of different size. (c) Temperature rise of the sample, ΔT, as a function of time for different pulse sizes. (d) Corresponding heater power. (e) Temperature rise divided by the constant power, P_0, as a function of time in units of the characteristic time constant τ.

resistive heater while the system remains at a constant temperature, the bath temperature T_b. The sample temperature, T, is logged as a function of time, t, both while heating at a constant power, P_0, and while cooling after switching off the heater. Each pulse consists of 256 data points, independent of its size or length. In the following we briefly describe the small heat pulse method, cf. Fig. 1.19, as well as the quasi-adiabatic large heat pulse method, cf. Fig. 1.20. As example we use measurements on a single-crystalline cube of MnSi with a mass of 48.50 mg in zero field. Here, we in particular focus on temperatures around the fluctuation-induced first-order transition at $T_c = 29\,\mathrm{K}$, cf. Secs. 3.1.2 and 3.3.2.

For the small pulse technique heat pulses of a size, ΔT, of about 0.1 % to 2 % of the current sample temperature are applied, see Fig. 1.19(a). In order to extract the specific heat of the sample, two fitting routines may be used: (i) the simple one-tau model, which assumes an ideal thermal contact between the platform and the sample, and (ii) the more sophisticated two-tau model, which accounts for a finite thermal coupling between the sample, the platform, and the grease between them. The results of both routines are compared and the method yielding the smallest fit deviations is employed, which usually is the two-tau model.

- If the thermal contact between the platform and the sample is ideal, the temperature of the latter obeys:
  $$C_{\mathrm{tot}}\frac{\mathrm{d}T}{\mathrm{d}t} = -K_{\mathrm{w}}\left(T - T_{\mathrm{b}}\right) + P(t)$$
  Here, the total heat capacity, C_{tot}, is assumed to be constant during the measurement and K_{w} is the thermal conductance of the supporting wires as determined by a calibration. The equation is solved by exponential functions with a characteristic time constant $\tau = C_{\mathrm{tot}}/K_{\mathrm{w}}$. This time constant determines the length of the heat pulse, t_0, and therefore is estimated prior to the actual measurement, once from a calibration file and subsequently from the previous pulse. Typically, pulse lengths of 1τ are used, except for very small samples where 2τ are recommended. Subtracting the addenda, i.e., the specific heat of the empty sample puck as measured separately, from C_{tot} finally yields the specific heat of the sample.

- If the thermal contact between sample and platform is finite, their temperatures may differ and a short second time constant is required that accounts for the thermal coupling between them. As a consequence, the corresponding heat capacities are treated individually, where the indices ’p’ and ’s’ refer to the platform and the sample, respectively:
  $$C_{\mathrm{p}}\frac{\mathrm{d}T_{\mathrm{p}}}{\mathrm{d}t} = K_{\mathrm{g}}\left(T_{\mathrm{s}}(t) - T_{\mathrm{p}}(t)\right) - K_{\mathrm{w}}\left(T_{\mathrm{p}}(t) - T_{\mathrm{b}}\right) + P(t)$$
  $$C_{\mathrm{s}}\frac{\mathrm{d}T_{\mathrm{s}}}{\mathrm{d}t} = -K_{\mathrm{g}}\left(T_{\mathrm{s}}(t) - T_{\mathrm{p}}(t)\right)$$
  Again, the heat capacities are assumed to be constant during the measurement, while K_{g} is the thermal conductance between the sample and platform due to the grease. The heat capacity of the platform is extracted from the addenda.

In order to cover a certain temperature range, many small pulses are subsequently applied at different temperatures resulting in specific heat data as a function of temperature as depicted in Fig. 1.19(b). Increasing the pulse size reduces the scatter of the data points but also leads to a smearing of sharp anomalies that arise, for instance, at first-order phase transitions. Figs. 1.19(c), 1.19(d), and 1.19(e) show that increased sizes of the heat pulses are accomplished by linearly increased heater power while the length and shape and length of the pulses remains essentially unchanged. Prior to each measurement, the system waits until the platform temperature is stable, i.e., during one time constant the latter changes by less than the given settling accuracy, which usually is 1 % of the current temperature.

The addenda file mentioned above is created by once measuring the heat capacity of the empty sample platform including a small amount of grease. Heat pulses of 2 % size and 2τ length are used, where ∼40 data point permit to cover the temperature range from 1.8 K to 300 K. A polynomial interpolation finally yields addenda values for any temperature in this given range. The influence of finite fields on the empty sample holder, in particular below ∼10 K, requires addenda measurements for several magnetic fields.

In the large pulse technique typical heat pulses have a size of 30 % of the sample temperature and are applied over times of 3τ, see Fig. 1.20(a). Kinks in these raw data already indicate the

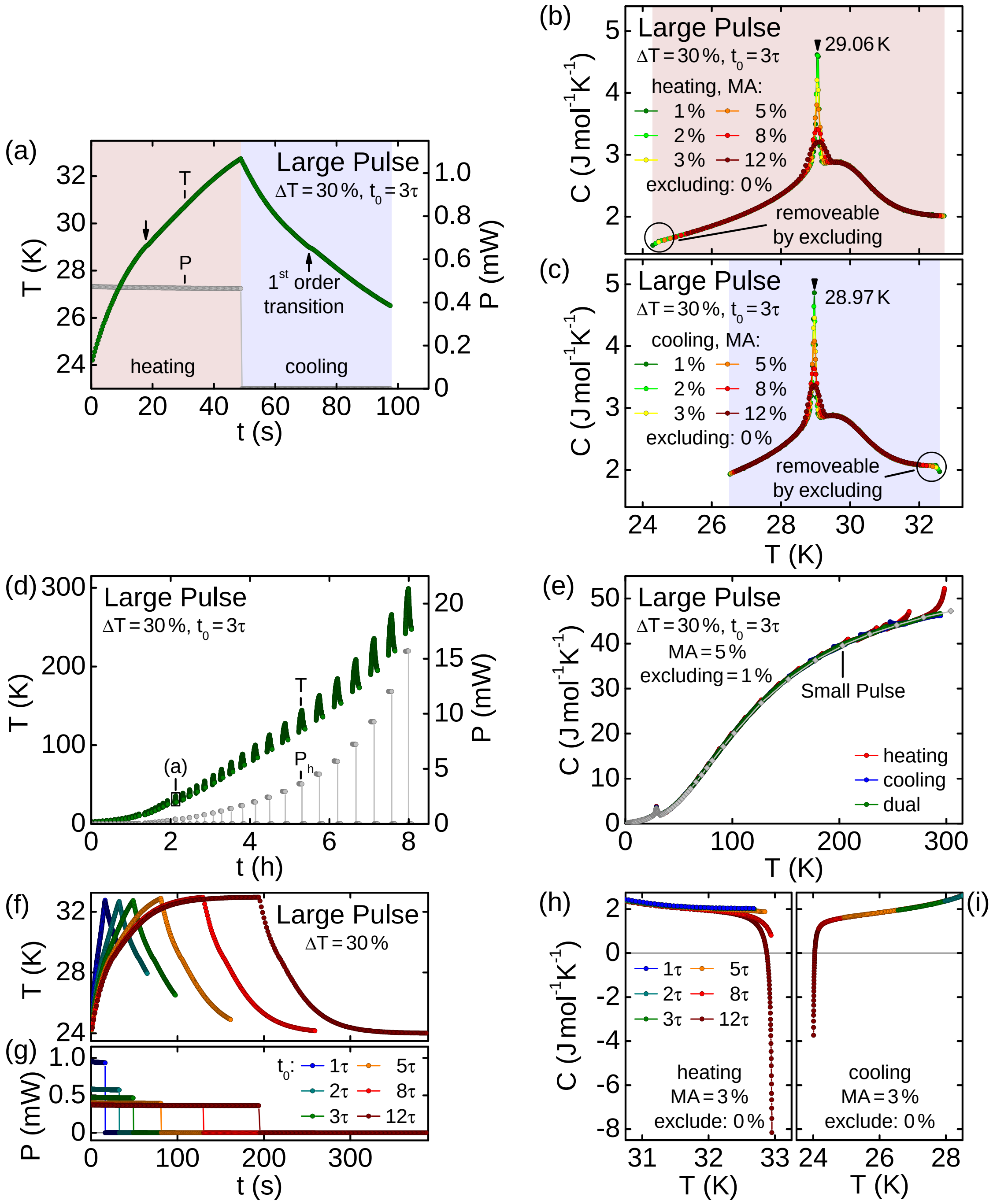

Figure 1.20: Specific heat measurements in the PPMS using large heat pulses. (a) Sample temperature, T, and heater power, P, as a function of time for a single pulse. (b)–(c) Specific heat calculated from panel (a) using the heating and the cooling curve, respectively. Moving averages (MA) of different window size were applied. (d) Large heat pulses covering temperatures from 2 K to 300 K. (e) Specific heat calculated from panel (f). For comparison, small heat pulse data are shown (diamonds). (f)–(i) The saturation of the sample temperature due to very long pulse lengths, t_0, may lead to spurious tails in the specific heat data.

presence of first-order phase transitions as marked by the black arrows. After the measurement has been carried out, the specific heat is derived using the PPMS software. Assuming an ideal thermal contact between the platform and the sample the following equation is used:

$$C_{\mathrm{tot}}(T) = \frac{-K_{\mathrm{w}}\,(T - T_{\mathrm{b}}) + P(T)}{R(T)}$$

Here, $R(T) = \mathrm{d}T/\mathrm{d}t$ is the slope of the temperature curve. The heating curve, where $P(T) = P_0$, and the cooling curve, where $P(T) = 0$, are treated individually. Subsequently, the addenda is subtracted. Figs. 1.20(b) and 1.20(c) depict the resulting specific heat data. Usually, a moving average over 1 % to 10 % of the data points in a relaxation curve is applied. Larger moving averages reduce the scatter of the data points and cause a smearing of sharp anomalies, similar to an increased pulse size in the small heat pulse method. In contrast to the latter, however, the moving average is applied after the actual data collection. Excluding the first up to 5 % of every pulse from the analysis accounts for irregularities that arise from switching the heater on and off, respectively. Taken together, usually ∼120 specific heat data points are extracted from one large heat pulse. We note that there is currently no implementation of the two-tau model for the analysis of large heat pulses.

In order to combine the data from multiple pulses, a considerable overlap in temperature is required for neighboring pulses, usually some 50 %. Hence, covering temperatures from T_{min} to T_{max} with heat pulses of a size of 30 % typically requires $N \gtrsim 1 + 17\log(T_{\mathrm{max}}/T_{\mathrm{min}})$ logarithmically spaced starting temperatures. As shown in Fig. 1.20(d), for instance, some 40 pulses are sufficient to densely cover the temperature range from 1.8 K to 300 K.

In particular for these fast scans over large temperature intervals the heat capacity may also be derived using the so-called dual slope method. Here, the heating curve, indexed 'h', and the cooling curve, indexed 'c', are combined:

$$C_{\mathrm{tot}}(T) = \frac{P_{\mathrm{h}}(T) - P_{\mathrm{c}}(T)}{R_{\mathrm{h}}(T) - R_{\mathrm{c}}(T)}$$

This calculation eliminates the influence of the thermal conductance of the supporting wires and the bath temperature, which becomes advantageous especially at higher temperatures, cf. Fig. 1.19(e). The combination of the data from both curves, however, requires an interpolation of temperatures which reduces the number of data points extracted from a single heat pulse, typically by a factor 2 to 5. Moreover, in particular around first-order phase transitions, the specific heat of the sample may differ between the heating and the cooling curve which yields erroneous results if combined. We have empirically observed that in most cases an analysis of the cooling curves is suited best to resolve pronounced features while the dual slope method is preferable for fast scans over large temperature intervals.

We note that spurious downturns or upturns of the specific heat may emerge at the high-temperature (low-temperature) end of a heating (cooling) curve as depicted in Figs. 1.19(h) and 1.19(i). These artifacts are clearly correlated to a saturation of the sample temperature during the pulse for large t_0, i.e., a vanishing slope $\mathrm{d}T/\mathrm{d}t$. Pulse lengths between 2τ and 5τ typically yield the most reliable results. Heat pulses distinctively larger than 30 % lead to incorrect specific heat data due to the lacking account for the temperature dependence of the wire conductance K_{w} during one pulse and due to the large temperature difference between sample and bath necessitating radiation corrections.

The peak positions as extracted from the small heat pulse method, the heating curve of a large heat pulse, and the corresponding cooling curve may deviate. For the MnSi sample investigated the corresponding values are 29.00 K, 29.06 K, and 28.97 K, respectively, i.e., the shift is about 0.3 % of the sample temperature. Such deviations may be either caused intrinsically by the thermal hysteresis at a first-order phase transition or extrinsically, e.g., by temperature gradients arising during the large heat pulse. The lacking dependence of the peak position on the pulse size for measurements with small heat pulses implies that the shift observed in MnSi is, at least dominantly, caused extrinsically. We note that in the same experimental setup a thermal hysteresis of up to 15 %, presumably of intrinsic nature, was observed in HoCu [84].

In summary, the small pulse technique is reliable and simple, while the large pulse technique may allow to quickly obtain high-resolution specific heat data. If the samples are large enough (typically $m > 10\,\mathrm{mg}$) and the thermal coupling between the sample and the platform is sufficient, data recorded with both methods are perfectly consistent with each other, cf. Refs. [85, 86]. In the same amount of time, however, the large pulse method produces up to three orders of magnitude more data points. This high output renders detailed studies feasible that require a large number of field values and/or a high temperature resolution.

Further techniques

For the study of the antiferromagnets $\mathrm{CrB_2}$, $\mathrm{MnB_2}$, and CuMnSb electrical transport and magnetization measurements were carried out by Alexander Regnat as part of his Ph.D. thesis. Electrical resistivity was measured either in an Oxford Instruments 14/16 T flow cryostat (1.5 K to 300 K) or a cryogen-free adiabatic demagnetization 12 T cryostat (0.1 K to 300 K) using a low-frequency lock-in technique. Magnetization, in addition to the PPMS, was recorded in an Oxford Instruments 9 T vibrating sample magnetometer (2.5 K to 300 K). Furthermore, thermal conductivity was measured in the 14 T PPMS by Marlies Gangl during her master's thesis [87]. Experimental details of these techniques are briefly addressed in Secs. 2.1.4 and 2.2.4.

For the determination of the residual resistivity of a large number of $\mathrm{Mn}_{1+x}\mathrm{Si}$ specimens, a dipstick was designed for the usage in a standard liquid helium transport dewar. Most of the according measurements were carried out by Sina Zeytinoglu as part of an internship, cf. Sec. 3.2.1.

Demagnetization effects

The magnetic field values throughout this thesis, if not stated otherwise, are applied field values. However, in (ferro-)magnetic materials demagnetization effects have to be taken into account. This is especially important if data from samples with different shapes are compared, e.g., when determining a magnetic phase diagram. In general, the internal magnetic field, $\boldsymbol{H}_{\mathrm{int}}$, is calculated as $\boldsymbol{H}_{\mathrm{int}} = \boldsymbol{H}_{\mathrm{ext}} - \mathbf{N}\boldsymbol{M}(\boldsymbol{H}_{\mathrm{ext}})$ with the 3×3 demagnetization matrix $\mathbf{N}$ that obeys $\mathrm{tr}\,\{\mathbf{N}\} = 1$ in SI units. In many cases, however, the scalar equation $H_{\mathrm{int}} = H_{\mathrm{ext}} - NM(H_{\mathrm{ext}})$ is sufficient where for field along the z-direction the matrix entry N_{zz} is referred to as N.

For a proper account of the dipolar interactions in the cubic chiral helimagnets, cf. Sec. 3.1.5, the demagnetization perpendicular to the applied field is also of importance and we distinguish $N_x = N_{xx}$, $N_y = N_{yy}$, and $N_z = N_{zz}$. Most samples investigated in this thesis may be approximated very well as rectangular prisms in which the demagnetization factors are analytically calculable for fields applied along the edges [88, 89]. Note that for the measured ac susceptibility, $\chi_{\mathrm{ac}}^{\mathrm{ext}}$, not only the field scale but also the absolute value of the susceptibility depends on demagnetization effects via the applied excitation field $H_{\mathrm{ac}}^{\mathrm{ext}}$.

In the cubic helimagnets discussed in Chapter 3, the susceptibility is essentially constant in the helimagnetic part of the magnetic phase diagram, i.e., below the transition temperature T_c and below the transition from the conical to field-polarized state at H_{c2}. Here, one may approximate the magnetization using the measured susceptibility in the conical state $M(H_{\text{ext}}) \approx \chi_{\text{con}} H_{\text{ext}}$ leading to $H_{\text{int}} = H_{\text{ext}}\,(1 - N\chi_{\text{con}})$. If the magnetization and a second quantity, e.g., electrical resistivity, are determined on samples with differing demagnetization factors, N_1 and N_2, the formula to calculate the internal field of the second sample extents to:

$$H_{\text{int},2} = H_{\text{ext},2}\left(1 - N_2\,\frac{\chi_{\text{con},1}}{1 - \chi_{\text{con},1}(N_1 - N_2)}\right)$$

Above H_{c2} one may, in first approximation, assume the magnetization as saturated and thus $M(H_{\text{ext}}) \approx \chi_{\text{con}} H_{c2}$ leading to $H_{\text{int}} = H_{\text{ext}} - N\chi_{\text{con}} H_{c2}$ with the constant offset $N\chi_{\text{con}} H_{c2}$.

1.9 Summary of crystals grown

During the course of this thesis about 80 float-zonings were performed. About 60 of them produced large single crystals or at least grains of a few millimeter size, i.e., samples suitable for further investigations. In the following the growth attempts are grouped with respect to their material class, namely transition metal monosilicides, Heusler compounds, transition metal diborides, and rare earth compounds. In most cases only one or two crystals were grown from a certain compound and polycrystalline seed rods were used. For MnSi and Cu_2MnAl, however, we established the growth of oriented single crystals of 10 mm diameter, to the best of our knowledge for the first time. Here, oriented seed rods were cut from ingots previously float-zoned or prepared via a Bridgman technique. In addition to the materials addressed below, three cobalt single crystals were grown together with Saskia Gottlieb-Schönmeyer and Marein Rahn. These crystals were initially used for the tests of the solid state electrotransport furnace. Growth attempts of Ni_3Al (with Dorothea Mallinger), Bi_2Se_3 (with Saskia Gottlieb-Schönmeyer), and YMn_2 were not successful. A full list of float-zoned materials is given in Table 1.1.

Transition metal monosilicides

Most of the $3d$ transition metal monosilicides and monogermanides crystallize in the cubic $B20$ structure. These $B20$ compounds are a class of cubic binary and pseudo-binary intermetallics that possess the space group $P2_13$ lacking inversion symmetry. During this thesis, the largest number of float-zonings were carried out on the helimagnetic monosilicides, (Mn,Fe,Co)Si, where all attempts yielded large single crystals. Firstly, the growth of large single crystals of the doped compounds $Mn_{1-x}Fe_xSi$ ($x = 0.02$, 0.04, 0.06, 0.08, 0.10, 0.12, 0.16, 0.19, 0.22), $Mn_{1-x}Co_xSi$ ($x = 0.02$, 0.04), and $Fe_{1-x}Co_xSi$ ($x = 0.10$, 0.35, 0.50) that was started during the diploma thesis of the author [62] was completed. Secondly, the growth parameters for pure MnSi were optimized using different initial manganese contents, $Mn_{1+x}Si$, and different growth rates, cf. Sec. 3.2.1. Thirdly, several single crystals of MnSi with a diameter of 10 mm were grown utilizing $\langle 100\rangle$, $\langle 110\rangle$, $\langle 111\rangle$, and $\langle 211\rangle$ oriented seed crystals, cf. Sec. 3.2.2.

Additionally, three large single crystals of the isostructural compound $Fe_{1+x}Si$ ($x = 0$, -0.01, 0.01) were prepared by Ralf Korntner and Michael Wagner [64, 90]. FeSi is no helimagnet but a strongly correlated semiconductor [91]. The growth attempts of the isostructural yet metallurgically far more complex compounds CrGe and $FeGe_{1-y}Si_y$ ($y = 0.15$) were not successful.

compound	OFZ number	sc	d	gr	col	comments
$Mn_{1-x}Fe_xSi$	32–35, 42, 51–53, 99, 100, 127	yes	6	5		$0.02 \leq x \leq 0.22$
$Mn_{1-x}Co_xSi$	36, 37, 40	yes	6	5		$x = 0.02, 0.04$
$Fe_{1-x}Co_xSi$	43, 44, 58	yes	6	5		$x = 0.10, 0.35, 0.50$
MnSi	54, 59	yes	6	5		
$Mn_{1+x}Si$	65-68, 71, 81, 83	yes	6	5		$-0.01 \leq x \leq 0.04$
$Mn_{1+x}Si$	69, 70, 82, 84	yes	6	2		$0.01 \leq x \leq 0.04$
$Mn_{1+x}Si$	103	yes	10	5		$x = 0.015$, $\langle 110 \rangle$ seed
MnSi	120, 122, 126	yes	6	5	GB	oriented seeds
MnSi	110, 111, 119, 124, 125, 128	yes	10	10	GB	oriented seeds
CrGe	62	no	6	0.5		traveling solvent
$Fe_{1+x}Si$	63, 93, 94	yes	6	5	RK, MW	$x = -0.01, 0, 0.01$
Mn_3Si	56, 76, 77	no	6	1–2	AN, DM	traveling solvent
Fe_2TiSn	64	yes	6	0.3	AN, RK	traveling solvent
NiMnSb	73, 79	yes	6	5		
YAuPb	74	no	6	5	SG	
$CuMnSb_{1+x}$	75, 98	yes	6	5		$x = 0, 0.035$
Cu_2MnAl	87, 90, 96	yes	8, 10	10		OFZ96: $\langle 110 \rangle$ seed
Mn_2RhSn	121	no	6	1–5	OM	
Co_2TiSn	123	yes	6	0.3–1	MG	
$Cr^{11}B_2$	SFZ118, SFZ162	yes	4–5	5–8	CB	IFW Dresden
$V^{11}B_2$	SFZ156	grains	4–5	5–8	CB	IFW Dresden
$Mn^{11}B_2$	SFZ158	yes	4–5	5–8	CB	IFW Dresden
$CeXAl_3$	60, 88, 106	yes	6	5	CF	X = Au, Cu, Pt
$CeXAl_3$	89, 105, 115	grains	6	5	CF	X = Ag, Pd
$CeAl_2$	101	yes	6	5	CF	
Ce_2XGe_6	91, 92	no	6	5	RB	X = Mn, Cu
$EuPtSi_3$	97, 102	grains	6	5, 1	RB	
HoCu	95	yes	6	5	MW	
ErCu, TmCu	104, 107	grains	6	5	MR	
$CeNi_2Ge_2$	108	yes	6	5	GB	
$CeCu_5Au$	109	yes	6	5	GB	
Ni_3Al	78	no	6	1	DM	
Bi_2Se_3	85	no	6	5	SG	
Co	86, 113, 114	yes	6	5–10	SG, MR	
Nd	112, 116	no	6.4	5–10	MR	
MnFe	117	grains	6	1	FG	
YMn_2	118	no	~6	5		

Table 1.1: Summary of float-zoned materials. Single crystallinity (sc), diameter (d), and growth rate (gr) are stated. Collaborators (col): Andreas Neubauer (AN), Christian Blum (CB), Christian Franz (CF), Dorothea Mallinger (DM), Frederik Georg (FG) Georg Benka (GB), Marlies Gangl (MG), Marein Rahn (MR), Michael Wagner (MW), Olga Meshcheriakova (OM), Ralf Korntner (RK), and Saskia Gottlieb-Schönmeyer (SG).

Heusler compounds

Heusler compounds are a large class of cubic intermetallics, cf. also Sec. 2.2. They may be distinguished into full-Heuslers (empirical formula X_2YZ) crystallizing in the $L2_1$ structure with space group $Fm\bar{3}m$ and half-Heuslers (empirical formula XYZ) crystallizing in the $C1_b$ structure with space group $F\bar{4}3m$. As the perhaps most prominent characteristic, an astonishingly large variety of physical properties may be realized within this class of compounds rendering them interesting for both fundamental and applied research. However, most Heuslers are subject to various forms of disorder that sensitively influence or even determine the properties of the compound [82].

The most important Heusler material for this thesis was the antiferromagnet CuMnSb. To the best of our knowledge, we managed to grow the first two single crystals of this compound, one from stoichiometric feed rods and one from feed rods with a slight antimony excess of 0.035. Details are described in Sec. 2.2.3. Two single crystals of the half-metallic ferromagnet NiMnSb were grown for measurements of the minority and majority spin Fermi surface using spin-polarized angular correlation of annihilation radiation (ACAR) performed by Hubert Ceeh and Josef Weber at the positron source NEPOMUC at FRM II [92]. A large single crystal of

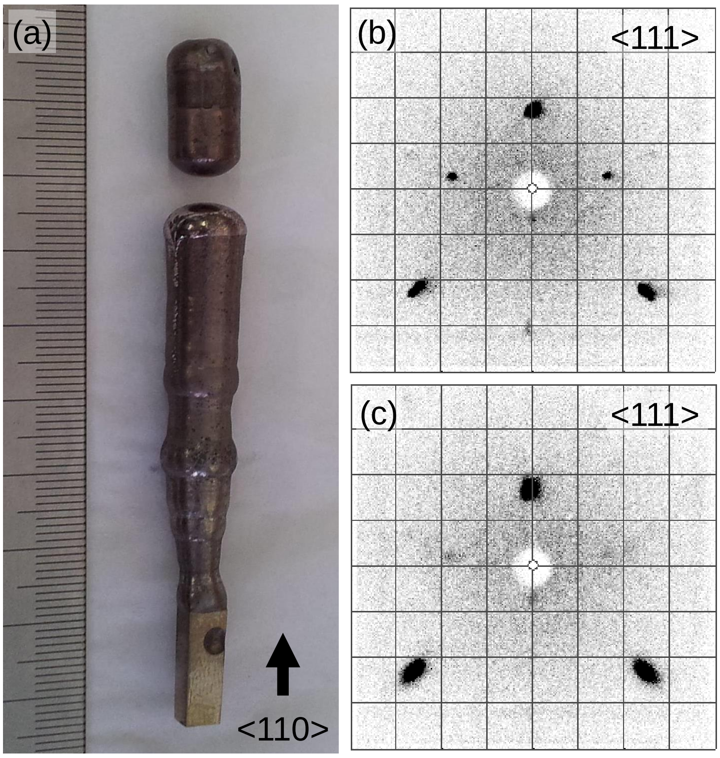

Figure 1.21: Float-zoned single crystal of Cu_2MnAl. (a) A single crystal seed grown by the Bridgman technique was used with a ⟨110⟩ axis along the growth direction (from bottom to top). (b) Threefold Laue pattern from a ⟨111⟩ surface perpendicular to the growth direction taken from the float-zoned single crystal. (c) Corresponding Laue pattern from the seed crystal. The broader peaks indicate a larger crystalline mosaicity.

the peritectically forming Fe_2TiSn was grown together with Ralf Korntner at a rate of 0.3 mm/h successfully completing a study by Andreas Neubauer [60, 64]. Furthermore, a large single crystal of the ferromagnet Co_2TiSn, to best of our knowledge the first grown so far, has been prepared together with Marlies Gangl at a rate of 1 mm/h [87]. The traveling solvent float-zoning attempts of Mn_3Si with Andreas Neubauer and Dorothea Mallinger yielded no single-crystalline material, in contrast to a previous study [60]. The growth of YAuPb, together with Saskia Gottlieb-Schönmeyer, and Mn_2RhSn, in collaboration with Olga Meshcheriakova from the Max Planck Institut für Chemische Physik fester Stoffe, was not successful.

Finally, we have grown multiple single crystals of the full-Heusler compound Cu_2MnAl. This material was the first described by Friedrich Heusler in 1903 when he pointed out that Cu_2MnAl is ferromagnetic albeit its constituent elements are not [93]. In fact, Cu_2MnAl is a ferromagnet with a Curie temperature of $T_C = 622\,\mathrm{K}$ [94], that is used as a polarizing neutron monochromator [95–97]. For this purpose plates of $\sim 40 \times 20 \times 4\,\mathrm{mm}^3$ with a $\langle 111 \rangle$ axis perpendicular to the large surface are needed. Until now, these single crystals have only be supplied by the Institut Laue-Langevin (ILL) where the crystals are grown with the Bridgman technique in crucibles of some 100 mm diameter [98, 99]. Here, every batch consists of several grains of different size and orientation which requires an extensive and expensive characterization.

In contrast, single crystal growth by means of float-zoning not only has the potential for higher crystalline quality [100], but also offers the possibility to use oriented seed crystals. This way, the amount of work that is necessary to prepare oriented plates is drastically reduced. Fig. 1.21 shows a Cu_2MnAl single crystal of 10 mm diameter over about 40 mm of length that was float-zoned at a rate of 10 mm/h with a $\langle 110 \rangle$ direction along the cylinder axis. In first tests, performed by Georg Brandl on the diffractometer MIRA at FRM II, this sample achieved a polarization efficiency of $P \approx 93\,\%$. This value is comparable to the efficiency of a large plate ($60 \times 30 \times 4\,\mathrm{mm}^3$) grown with the Bridgman method tested under similar conditions [100].

Transition metal diborides

Many transition metal and rare earth diborides possess the rather simple layered hexagonal $C32$ structure with space group $P6/mmm$. All of them show metallic behavior, often in combination with ferromagnetism, antiferromagnetism, or superconductivity. For this thesis two large single crystals of CrB_2 and one of MnB_2 were float-zoned together with Christian Blum and Sabine Wurmehl at the IFW Dresden. The growth of VB_2 yielded large grains. The diboride feed rods were prepared by sintering a mixture of the high-purity elements in powder form using bespoke tungsten crucibles and the horizontal cold boat. For all three compounds, the usage of boron isotopically enriched to 99 % ^{11}B for the first time permits comprehensive neutron scattering studies on single crystals. Details of the growth process are described in Sec. 2.1.3. In addition, Georg Benka has prepared polycrystalline samples of various transition metal and rare earth $C32$ diborides by means of arc melting as part of his master's thesis [63].

Rare earth compounds

The high potential of the single crystal preparation chain described in this chapter becomes especially evident if rare earth elements are handled that are sensitive to air, such as cerium or europium. Here, for the first time, the sample loading under inert atmosphere was utilized in the preparation of the non-centrosymmetric heavy fermion compounds $CeXAl_3$ (X = Ag, Au, Cu, Pd, Pt) by Christian Franz as part of his Ph.D. thesis [101]. Starting from the argon glovebox, 5N5 cerium and 6N aluminum were loaded onto the horizontal cold boat and melted. The resulting $CeAl_2$ pill was combined with the remaining aluminum and the precious metal X within the rod casting furnace. For palladium and platinum pellets out of high-purity 4N5 powder were pressed inside the glovebox using a custom mechanical press. After float-zoning we obtained large single crystals of $CeAuAl_3$, $CePtAl_3$, and $CeCuAl_3$ as well as large grains of $CeAgAl_3$ and $CePdAl_3$. Additionally, a large single crystal of $CeAl_2$ was prepared. Using a similar procedure carried out by Georg Benka during his master's thesis [63] yielded large single crystals of $CeCu_5Au$ (via $CeCu_2$) and $CeNi_2Ge_2$ (via CeNi). The growth of Ce_2MnGe_6 and Ce_2CuGe_6, both using Ce_5Ge_3 as intermediate compound, was not successful [102].

The search for topological non-trivial spin textures motivated the growth of several systems. The first candidate was the non-centrosymmetric tetragonal compound $EuPtSi_3$. So far only tin flux Bridgman single crystal growth was reported resulting in thin platelets with tin inclusions [103]. Our growth, carried out together with Ralitsa Bozhanova as part of her master's thesis, yielded single crystal grains of several millimeter in size [102]. The second class of compounds were cubic rare earth copper systems that exhibit very complex magnetic phase diagrams [104]. A large single crystal of HoCu was grown together with Michael Wagner. In addition, several large grains of the isostructural compounds ErCu and TmCu were prepared by Marein Rahn as part of his master's thesis [84]. For the third candidate, neodymium, no grain selection was accomplished. The growth of the fourth system, the solid solution MnFe performed by Frederick Georg during an internship, yielded large grains.

1.10 Summary and outlook

In summary, we have developed a versatile single crystal preparation chain for intermetallic compounds in a high-purity inert atmosphere thus providing ultra-high vacuum compatible conditions. The key part of the preparation chain is a customized image furnace with an integrated electrotransport option. The polycrystalline float-zoning feed rods usually are prepared in an inductively heated rod casting furnace. A horizontal cold boat furnace and an arc melting furnace that both may be docked to and loaded from an argon glovebox permit the pre-alloying and handling of air sensitive elements. Finally, a post-growth treatment of float-zoned ingots may be carried out in a solid state electrotransport furnace or in an annealing furnace. All systems are all-metal sealed, bakeable, and are pumped by turbomolecular pumps or ion getter pumps, respectively. The high-purity inert atmosphere is supplied by a central gas handling system utilizing point-of-use gas purifiers. Using the preparation chain, we have grown large high-quality single crystals of transition metal monosilicides, Heusler compounds, transition metal diborides, as well as various binary and ternary rare earth compounds.

CHAPTER 2

The itinerant antiferromagnets CrB_2 and CuMnSb

One class of materials that was studied intensively as part of this thesis are candidates for weak itinerant antiferromagnetism, i.e., materials with comparably low transition temperatures and small ordered moments in which the magnetism is carried by the conduction electrons. While in local-moment insulators low transition temperatures despite nominally strong interactions may be caused by competing interactions or geometric frustration, in itinerant magnets the coupling of collective spin excitations to the particle-hole continuum may be responsible. These dispersive spin fluctuations were taken into account by a self-consistent quantitative model that was developed in the course of extensive studies of the weak itinerant ferromagnets in the 1980s [105–107]. Here, d-electron ferromagnets, such as $ZrZn_2$, Ni_3Al, and MnSi, provide weak counterparts to iron, nickel, and cobalt which allowed for careful experimental comparison with theory. In contrast, there is a lack of equivalent weak itinerant d-electron systems in correspondence to antiferromagnets like chromium. Possible candidates, for instance, comprise of the metallic Heusler compound Mn_3Si or the cubic pyrite NiS_2. The magnetic order in Mn_3Si, however, is rather complex [108, 109] and NiS_2 is an electrical insulator at ambient pressure which exhibits strong geometric frustration [110].

As part of this thesis we have prepared high-quality single crystals of the hexagonal $C32$ compound CrB_2 and investigated its low-temperature properties by means of the resistivity, the Hall effect, the magnetization, and the specific heat. Our results suggest that CrB_2, albeit being subject to geometric frustration, is the perhaps closest antiferromagnetic analog of the class of weak itinerant ferromagnets so far. The usage of ^{11}B enabled us to start extensive elastic and inelastic neutron scattering studies for the first time. In addition, the first large single crystal of the high-temperature antiferromagnet MnB_2 was prepared and its low-temperature properties were investigated.

We have also grown the first single crystals of the half-Heusler antiferromagnet CuMnSb, one from stoichiometric feed rods and one with an antimony excess of 0.035. After a detailed metallurgical characterization, we have collected magnetization, specific heat, electrical resistivity, Hall effect, thermal conductivity, as well as both elastic and inelastic neutron scattering data. Strangely, CuMnSb combines typical properties of local-moment and itinerant magnets in a rather unique manner. The results from a stoichiometric single crystal are consistent with those from polycrystals including the presence of a tiny amount of an impurity phase [111, 112]. The latter was suppressed by the small excess of antimony in the second crystal grown, resulting in an increased Néel temperature and a spin canting that emerges deep within the antiferromagnetic state.

The work reported in this chapter was carried out as part of the various collaborations. While the preparation of all feed rods as well as the float-zoning of CuMnSb were performed by myself, the diborides were float-zoned at the IFW in Dresden together with Christian Blum and Sabine Wurmehl. X-ray powder diffraction was carried out together with Saskia Gottlieb-Schönmeyer and supplemented by energy dispersive x-ray spectroscopy on CuMnSb in collaboration with Florian Kortmann at the Radiochemie München. All float-zoned ingots were studied by x-ray Laue diffraction, cut with a wire saw, and carefully polished to size by Susanne Mayr. Elastic neutron diffraction on the instruments RESI, HEiDi, and SPODI were performed by Alexander Regnat as part of his Ph.D. thesis in collaboration with Björn Pedersen, Martin Meven, and Anatoliy Senyshyn from the Heinz Maier-Leibnitz Zentrum (MLZ). Recently, a detailed study by means of single crystal and powder x-ray diffraction was started together with Klaudia Hradil from the Technische Universität Wien and Anatoliy Senyshyn. Specific heat measurements on CrB_2 as well as specific heat, susceptibility, and magnetization measurements on VB_2, MnB_2, and CuMnSb were carried out as part of this thesis. The magnetization of CrB_2 as well as the electrical resistivity and Hall effect shown in this chapter were measured by Alexander Regnat as part of his Ph.D. thesis. Thermal transport measurements on CuMnSb were performed by Marlies Gangl as part of her master's thesis [87]. Detailed studies of the torque magnetization of the diborides revealing distinct de Haas-van Alphen frequencies were carried out by Matthias Brasse and Stephan Albert from the group of Prof. Dirk Grundler as part of their Ph.D. theses. Inelastic neutron scattering experiments on CrB_2 and CuMnSb were performed by Georg Brandl as part of his Ph.D. thesis.

This chapter is organized in two parts. Sec. 2.1 addresses the single crystal growth of transition metal diborides and the low-temperature properties of CrB_2. Moreover, we account for our first results on MnB_2. The second part, Sec. 2.2, is concerned with a corresponding study on CuMnSb. Here, a comprehensive metallurgical analysis had to be carried out prior to the investigation of the low-temperature properties. Eventually, the chapter ends with a summary and an outlook in Sec. 2.3.

2.1 CrB_2: weak itinerant antiferromagnetism par excellence

In analogy to weak itinerant ferromagnets like $ZrZn_2$, Ni_3Al, and MnSi one expects certain characteristics for a weak itinerant antiferromagnet including

- a low absolute value of the resistivity,
- a low Néel temperature T_N of up to a few ten Kelvin,
- a small ordered moment in the order of a few tenth of a Bohr magneton,
- a Curie-Weiss dependence of the susceptibility above T_N with a fluctuating moment that by far exceeds the ordered moment, and
- an unsaturated magnetization up to the highest fields studied.

CrB_2 essentially meets all of these criteria. In our high-quality single crystals we observe a typical metallic resistivity with a residual value of a few µΩcm, a comparably low Néel temperature of

$T_N = 88.5\,K$, a small ordered moment $m_s \approx 0.5\,\mu_B$/f.u. contrasted by a large fluctuating moment of $m_{\mathrm{eff}} \approx 2.0\,\mu_B$/f.u., and a remarkable stability of the magnetic order in fields up to 14 T. Taken together, this behavior suggests that $C32$ compound CrB_2 maybe is the closest antiferromagnetic analog to the weak itinerant ferromagnets reported so far. However, the Curie-Weiss temperature Θ_{CW} excels T_N by far suggesting an important additional role of geometric frustration in this hexagonal system. Thus, CrB_2 is identified as a material in which the interplay of geometric frustration and weak itinerant magnetism may be studied in a pure metal. Moreover, in the light of the conventional high-temperature superconductivity in the isostructural MgB_2, we consider the possible implications for the interplay of itinerant antiferromagnetism with superconductivity in non-magnetic CrB_2, i.e., if the magnetism is suppressed via pressure or substitutional doping.

This section is based on Ref. [113] and organized as follows. In Sec. 2.1.1 we start with a short overview about the class of $C32$ diborides. After accounting for previous studies in CrB_2 in Sec. 2.1.2, we describe the single crystal growth of the transition metal diborides CrB_2, MnB_2, and VB_2 in Sec. 2.1.3. Subsequently, Sec. 2.1.4 presents our results on the low-temperature properties of CrB_2 and Sec. 2.1.5 reports first data on MnB_2.

2.1.1 Introduction to the C32 diborides

The hexagonal $C32$ diborides, MB_2, where M is a transition metal or rare earth element, first have attracted interest due to their high mechanical and thermal stability, high chemical inertness, and high electrical as well as thermal conductivity [114, 115]. In recent years, additional scientific interest has been generated by a wide range of unusual electronic and magnetic properties. This class of compounds thereby offers a unique opportunity to trace the emergence of all of these phenomena in an essentially unchanged crystallographic environment. Thus, before turning to the antiferromagnets CrB_2 and MnB_2, we start with a review of the salient features of the $C32$ diborides in general.

The layered crystal structure of the $C32$ diborides belongs to the space group $P6/mmm$ as depicted in Fig. 2.1. However, other than for instance in the cuprate superconductors, the layering displays strong interlayer interactions and represents essentially a dense packing. The boron layers form hexagons, where each boron has 3 nearest neighbors. The transition metal or rare earth atoms are located in the center above the boron hexagons and possess 12 boron nearest neighbors. In turn, the structural and electronic properties require consideration of the B-B, M-B, and M-M bonding as addressed in several electronic structure calculations [116–119]. In a first approximation the boron orbitals may be viewed in terms of an in-plane $2sp^2$ hybrid and an out-of-plane $2p_z$ orbital. A strong σ-bonding of the sp^2 hybrids leads to a large splitting of $\sim$25 eV between the bonding and the anti-bonding states. The narrower π-bonded p_z band resides in the resulting gap.

The perhaps most spectacular electronic property in the class of $C32$ diborides is the conventional electron-phonon mediated superconductivity in MgB_2 [30, 120]. In this compound, the magnesium $3s$ orbitals form a broad band above the Fermi level close to the top of the sp^2 anti-bonding band. Due to a weak out-of-plane dispersion the resulting Fermi surface has a cylindrical shape. Two aspects of the superconductivity in MgB_2 are especially fascinating. First, it displays a record high $T_c = 39.5\,K$ for an electron-phonon mediated superconductor, which originates in the E_{2g} optical phonon of the in-plane motion of the boron atoms that strongly couples to electrons in the two-dimensional σ-band. Second, MgB_2 is an ideal example for multi-gap superconductivity in which two almost independent condensates, associated with the σ-bands and the π-bands, respectively, have different superconducting properties and

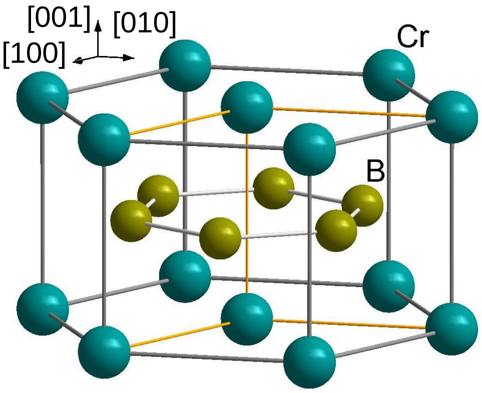

Figure 2.1: Crystal structure of the $C32$ diborides, space group $P6/mmm$. As an example CrB$_2$ is shown. The structure is characterized by an alternating sequence of closest-packed chromium layers and honeycomb boron layers along the hexagonal [001] direction. The boron sheets are isostructural to graphite.

transition temperatures [121]. Presently, MgB$_2$ appears to be the only superconductor amongst the stoichiometric $C32$ diborides. In NbB$_2$ off-stoichiometry plays an important role [122–124] whereas the report of superconductivity in ZrB$_2$ polycrystals presumably arise from a ZrB$_{12}$ impurity phase [125, 126]. OsB$_2$ and RuB$_2$ are superconductors but crystallize in the orthorhombic $Pmmn$ structure [127–129].

Unlike superconductivity, magnetic order is observed in quite a few $C32$ compounds. The rare earth based systems TbB$_2$, DyB$_2$, HoB$_2$, ErB$_2$, and TmB$_2$ order ferromagnetically at low temperatures [130], whereas antiferromagnetism like in YbB$_2$ is less common [131]. In contrast, the transition metal diborides CrB$_2$ and MnB$_2$ are both antiferromagnets, as will be discussed in Secs. 2.1.4 and 2.1.5. The antiferromagnetism in CrB$_2$ is well established and fully corroborated by the results of the work performed as part of this thesis. In MnB$_2$, however, the onset of antiferromagnetism at $T_N = 670\,\mathrm{K}$ is followed by a putative ferromagnetic transition at $T_C = 157\,\mathrm{K}$ that, in fact, may be attributed to a tilting of the antiferromagnetic unit cells [132–134]. The origin of the magnetic order as well as further instabilities of the electronic structure have so far not been explored in these systems. In particular, two questions have not been addressed appropriately yet: are the magnetic properties better described from a local-moment or an itinerant-electron point of view and to which extent does the geometric frustration, that may be expected from the hexagonal crystal structure, play a role?

2.1.2 Introduction to CrB$_2$

Now, we turn to CrB$_2$ for which early nuclear magnetic resonance (NMR) [135] and susceptibility studies [136] identified antiferromagnetism below $T_N \approx 88\,\mathrm{K}$. The character of this order was addressed in further NMR studies on powder samples suggesting that CrB$_2$ is located intermediate between local-moment and weak itinerant magnetism [137–139]. Measurements of the magneto-volume effect showed a thermal expansion coefficient in the paramagnetic region of CrB$_2$ that is comparable to weak itinerant ferromagnets like ZrZn$_2$ hence supporting an itinerant character [140].

Several studies addressed the electronic structure of CrB$_2$ [116–119, 141]. As one of the results, in Ref. [116] Liu *et al.* predicted a nesting of the Fermi surface that results in spin density wave ordering along the c-axis with $\boldsymbol{q} = 0.26\,\boldsymbol{q}_{001}$, $q_{001} = 2\pi/c$. The authors refer to their Ref. 6 for powder neutron diffraction revealing a weak maximum at $0.74q_{001}$, interpreted as $q_{001} - q$, as well as tiny maxima at $0.58q_{001}$ and $1.15q_{001}$, which are attributed to spurious signals or higher harmonics. In contrast, based on single crystal neutron diffraction Funahashi *et al.* suggested cycloidal magnetic order with a small magnetic moment of $0.5\,\mu_B$/f.u. along an in-plane wave vector $\boldsymbol{q} = 0.285\,\boldsymbol{q}_{110}$, $q_{110} = 2\pi/\frac{a}{2}$ [142]. These findings are complemented by a recent NMR study on single crystals that suggest combination of incommensurate and a commensurate magnetic order [143].

As a congruently melting compound the preparation of CrB_2 is, in principle, straightforward [144]. While early studies were mainly carried out on arc-melted or sintered polycrystals [132, 145–147], later the growth of single crystals was reported by means of float-zoning with radio-frequency [141, 143, 148] or optical heating [149]. Single crystals were also prepared from a high-temperature aluminum solution [150]. Yet, two major constraints limit the sample quality. First, the high melting temperature of CrB_2 of about 2150 °C in combination with the high vapor pressure of boron leads to considerable losses that may result in off-stoichiometric samples. Second, in essentially all previous studies fairly pronounced Curie tails in the low-temperature susceptibility were observed, most likely due to iron impurities that stem from the starting elements [141, 149, 151]. An exception is Ref. [148] which is also the only study that addressed the anisotropy of the resistivity and the susceptibility.

Central goal of the study reported in the following was to investigate the intrinsic properties of high-quality single crystals of CrB_2 and to confirm whether their antiferromagnetism in fact has weak itinerant character. The starting point was the growth of large single crystals of CrB_2 by a solid-state reaction of high-purity elements followed by an optical float-zoning under a high-pressure argon atmosphere. All data collected so far, consistently suggest an excellent sample quality. In addition, the usage of 99 % enriched ^{11}B powder allows for detailed neutron scattering experiments that clearly outmatch the study by Funahashi *et al.* in Ref. [142] carried out on samples containing natural boron and hence the excellent neutron absorber ^{10}B. Before we account in detail for our measurements of the electrical resistivity, the Hall effect, the magnetization, and the specific heat that identify CrB_2 as a remarkable example for weak itinerant antiferromagnetism with geometric frustration, we briefly summarize further research carried out on the same single crystals.

First, elastic neutron scattering data from the single-crystal diffractometers RESI and HEiDi at FRM II are essentially consistent with the incommensurate spin order reported by Funahashi *et al.* in Ref. [142]. These data, however, also hint towards the possible existence of a weakly distorted sevenfold super-cell within the basal plane and await a full refinement [153]. Second, inelastic neutron scattering studies at the cold triple-axis spectrometer PANDA at FRM II reveal the presence of an abundance of strongly damped spin excitations both above and below T_N [154]. Third, at temperatures down to 0.3 K and magnetic fields up to 14 T the angular dependences of three distinct de Haas-van Alphen frequencies of the torque magnetization have been recorded [152].

As part of the latter study, the Fermi surface of antiferromagnetic CrB_2 was calculated in the local density approximation using the generalized gradient approximation of the exchange and correlation functionals. The lowest energy was achieved for a cycloidal magnetic ordering wave vector $\boldsymbol{q} = 0.3\,\boldsymbol{q}_{110}$, in agreement with the magnetic ordering vector determined experimentally. A comparison of the resulting Fermi surface, see Fig. 2.2, with the de Haas-van Alphen data suggests that two of the observed oscillations arise from electron-like Fermi surface sheets formed by bands with strong boron $p_{x,y}$ character, while the third may be related to chromium d bands.

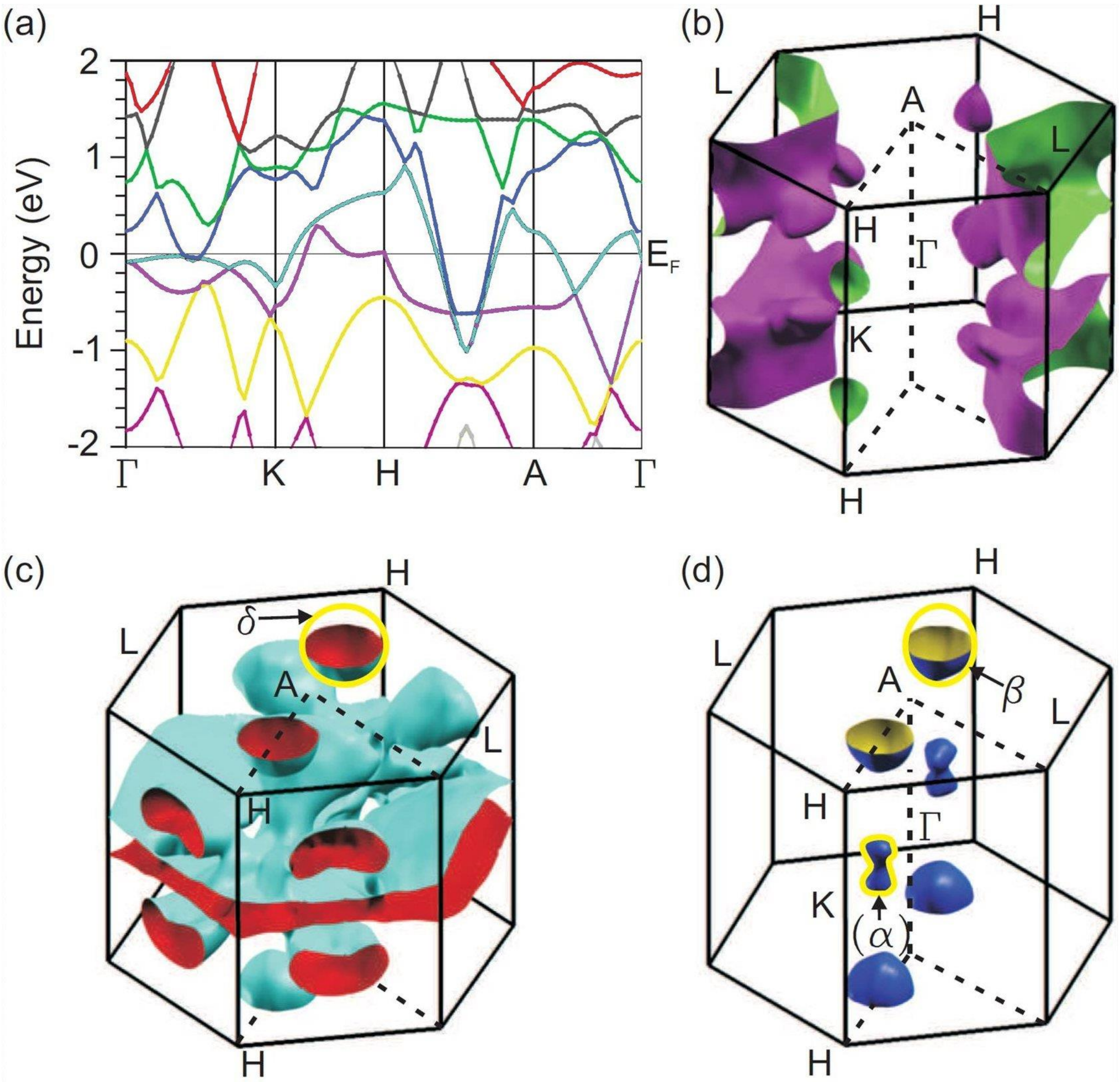

Figure 2.2: Calculated electronic structure of CrB_2 with a cycloidal magnetic ordering wave vector $\boldsymbol{q} = 0.3\,\boldsymbol{q}_{110}$. (a) Band structure of CrB_2 around the Fermi energy, E_F. In total, three bands cross E_F (purple, cyan, blue). (b) Fermi surface sheet originating from the purple band. It consists of a single connected structure centered around the L point at the boundary of the first Brillouin zone and predominantly has chromium d character. (c) Fermi surface sheet originating from the cyan band. Two ball-shaped, boron p-derived pockets are present between the A- and the H-points, where the shape is quite insensitive to magnetic order. The remaining sheets of this band exhibit a complicated structure and possess chromium d character. (d) Fermi surface sheet originating from the blue band. The two ball-shaped pockets are also predominantly of boron p character and very insensitive to the magnetic order, whereas the two dumbbell-shaped pockets are chromium d-like and thus very sensitive to the exact form of the ordering. The yellow circles mark the extremal orbits α, β, and δ that correspond to the experimentally observed de Haas-van Alphen frequencies. Figure taken from Ref. [152].

The calculated electronic structure moreover indicates that MgB_2 and CrB_2 share some general features. The details in the vicinity of the Fermi level, however, are quite different due to the presence of narrow (∼4 eV) partially filled chromium $3d$ bands that, in turn, are a prerequisite for the magnetic order at low temperatures. Compared to MgB_2 the boron p_z states in CrB_2 are pushed away from the Fermi level while the sp^2 bands acquire three-dimensional character leading to quasi-spherical Fermi pockets. Finally, our calculations identify CrB_2 as a covalent compound that has less in common with chromium oxide than with chromium metal.

2.1.3 Single crystal growth

The growth of the single crystals of the transition metal diborides took place in two steps. After the preparation of feed rods with a stoichiometric composition, the actual single crystal growth was carried out by optical float-zoning. In contrast to the other intermetallic compounds grown in the course of this thesis, however, the high melting temperatures of both boron and the resulting diboride as well as the availability of high-purity boron in powder form only required the development of a sintering process for the feed rods.

The synthesis of CrB_2 started from 4N5 chromium powder (100–325 mesh) and 4N5 boron powder (<140 mesh). The high purity minimizes contaminations by iron impurities, which may be traced to the chromium and boron used in commercially available CrB_2 powder and which were present in most samples reported in literature. Additionally, the boron was 99 % ^{11}B-enriched to permit comprehensive neutron scattering studies of the magnetic and structural properties [153, 154]. Stoichiometric amounts of these powders were thoroughly mixed and filled into a bespoke two-component tungsten crucible with an inner diameter of 6 mm and a length of 90 mm. This crucible was then mounted on the horizontal cold boat. After carefully pumping the system and filling it with 1.1 bar of high-purity argon, the crucible was heated by radio-frequency induction. As the powder reached a temperature of ∼1500 °C a metallic rod formed by an exothermic solid state reaction, cf. Fig. 2.3(a) and 2.3(b). The heating and cooling of the tungsten crucible was carried out in less than ten minutes. The sintered CrB_2 rod had an estimated density of $\sim 2.6\,\mathrm{g/cm^3}$, i.e., ∼50 % of the density of crystalline CrB_2, which proved to be sufficient for the float-zoning.

Because of the high melting temperature of CrB_2, which exceeds the temperatures reachable in our image furnace, the optical float-zoning of the sintered rods had to be performed with the high-pressure crystal growth furnace (Smart Floating Zone, SFZ) at IFW Dresden. During the growth at a rate of ∼6 mm/h a flowing argon atmosphere of 15 bar was applied, while seed and feed rod were counter-rotating at rates of 8.5 rpm and 8.5 rpm to 13 rpm, respectively. The surface temperature of the zone of ∼2200 °C during the growth agrees with the binary phase diagram reported by Okamoto [155].

Two samples of CrB_2 were float-zoned. The first growth, SFZ118, resulted in a CrB_2 crystal that exhibits a shiny metallic surface and well developed large facets. After the first 5 mm of growth complete grain selection had taken place resulting in a single crystal grain across the entire rod. Shown in Fig. 2.3(d) and 2.3(e) are typical Laue x-ray pictures of surfaces perpendicular to the c-axis and the a-axis, respectively. While the picture along the c-axis displays the characteristic sixfold symmetry, the a-axis appears to show a fourfold symmetry. Closer inspection confirms, however, the expected twofold symmetry as the lattice constants a and c in CrB_2 are very similar. Neutron single-crystal diffraction at the diffractometer RESI and HEiDi at FRM II revealed good single crystallinity. The hexagonal lattice constants of $a = 2.972$ Å and $c = 3.083$ Å are in close agreement with values reported in the literature

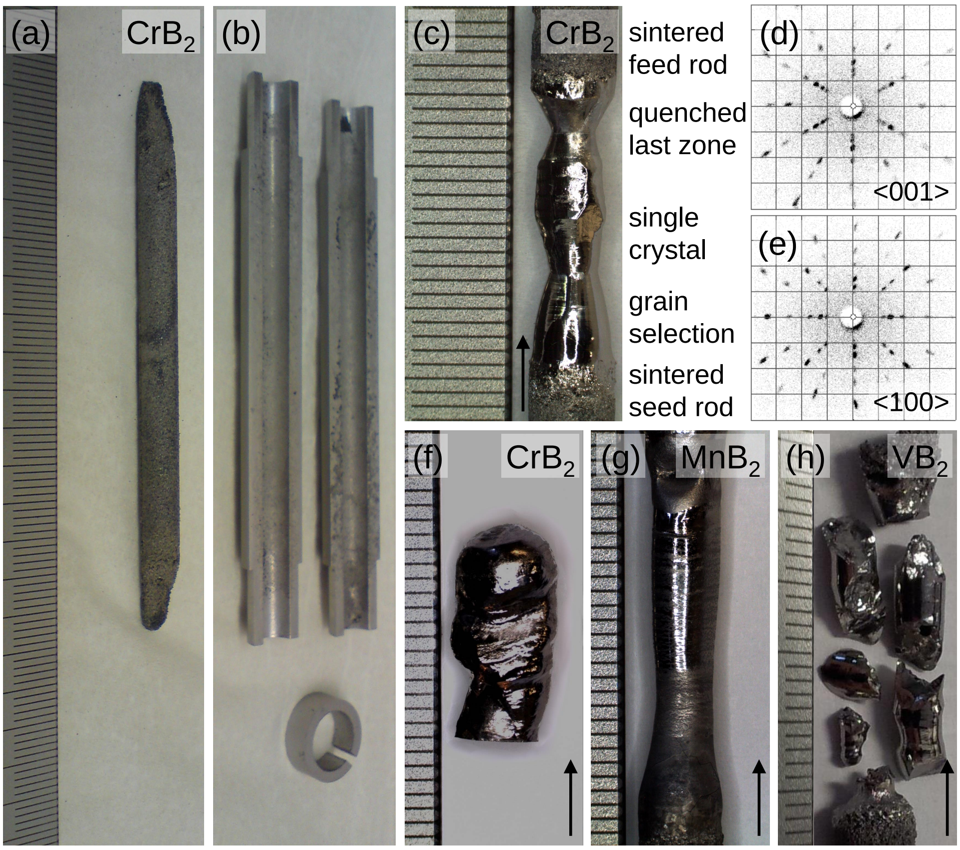

Figure 2.3: Single crystal growth of transition metal diborides. (a) Sintered CrB_2 feed rod. (b) Tungsten crucible for sintering the feed rods from powder ingredients. (c) CrB_2 rod after optical float-zoning (SFZ118). Large facets and a clean metallic surface indicate high sample quality. The growth direction was from bottom to top. (d) Laue x-ray diffraction pattern along the c-axis showing the characteristic sixfold symmetry. (e) Laue x-ray diffraction pattern along the a-axis of the same part of the ingot. The characteristic twofold symmetry demonstrates that the single-crystal grain extends across the cross-section of the ingot. (f) Second CrB_2 rod after float-zoning (SFZ162). (g) MnB_2 rod after optical float-zoning. (h) VB_2 after optical float-zoning.

$a_{\text{lit}} = 2.969\,\text{Å}$ and $c_{\text{lit}} = 3.066\,\text{Å}$ [119]. The float-zoned part of a second growth of CrB_2, SFZ162, is depicted in Fig. 2.3(f) and yielded several large grains that, however, exhibit small-angle grain boundaries. Samples cut from SFZ118 were used for the bulk and resistivity measurements presented below as well as for the neutron scattering and de Haas-van Alphen studies mentioned above. Samples from SFZ162 were used for further resistivity and the Hall effect measurements. The resistivity data is in excellent agreement for both crystals establishing that our single crystal growth of CrB_2 leads to highly reproducible results.

In addition to CrB_2, single-crystal samples of MnB_2 and VB_2 were prepared using a crystal growth procedure similar to the one described above. While the low-temperature properties of MnB_2 are reported in Sec. 2.1.5, VB_2 was used as a non-magnetic, metallic reference compound for the analysis of our specific heat data. At first, pre-cast 4N manganese rods crushed to powder in an agate mortar or 2N8 vanadium powder (<325 mesh), respectively, were combined with the

99 % enriched ^{11}B powder. After filling the ingredients in the tungsten crucibles the solid state reaction was triggered at temperatures of ∼1300 °C and ∼1800 °C, respectively. The sintering of MnB_2 only resulted in short rods of up to 10 mm length. However, due to its comparably low melting temperature of ∼2000 °C, a solid feed rod of MnB_2 was cast from the resulting pieces in the inductively heated rod casting furnace at IFW Dresden. As both manganese and boron are subject to serious evaporation losses, the subsequent float-zoning of MnB_2 in the SFZ was carried out at up to 80 bar of argon pressure. The float-zoned rod is depicted in Fig. 2.3(g) and contained a single crystal grain across the entire rod. In contrast to the other diborides, the growth direction was along an a-axis. The cross-section is significantly flattened along the c-axis and the latter rotates by ∼4° along the ∼10 mm of the single crystal as observed by x-ray Laue diffraction.

The sintered seed and feed-rods of VB_2 could not properly be float-zoned due to their very high melting temperature of ∼2750 °C, see Fig. 2.3(h). Nevertheless we obtained a strongly textured, nearly single-crystalline sample of VB_2. Laue x-ray diffraction established several grains in this piece with a small orientation mismatch of a few degree, sufficient for the studies reported here.

Neutron absorption of boron

Neutrons in general possess a rather small interaction cross-section with matter requiring large sample volumes for neutron scattering experiments, in particular for inelastic ones. In order to achieve the maximum scattered intensity, the ideal thickness of the sample needs to balance the scattering cross-section of the material with its absorption cross-section, where certain isotopes require a separate consideration. One of these isotopes is ^{10}B, which displays a very high neutron absorption cross-section $\sigma_{\mathrm{B10}} = 3835\,\mathrm{b}$ for thermal neutrons as compared to ^{11}B ($\sigma_{\mathrm{B11}} = 0.0055\,\mathrm{b}$) and natural chromium ($\sigma_{\mathrm{Cr}} = 3.05\,\mathrm{b}$). Natural boron consists of 19.9 % ^{10}B and 80.1 % ^{11}B. The resulting absorption coefficient $\Sigma^{\mathrm{abs}}_{\mathrm{nat}} = 65.2\,\mathrm{cm}^{-1}$ of CrB_2 prepared with natural boron therefore implies a transmission of $1.5 \cdot 10^{-3}$ or $4.5 \cdot 10^{-14}$ of the initial neutron intensity through a plate of 1 mm thickness or a cylinder of 6 mm diameter, respectively. For the 99 % isotopically enriched ^{11}B used in our study the absorption coefficient reduces to $\Sigma^{\mathrm{abs}}_{\mathrm{B11}} = 3.40\,\mathrm{cm}^{-1}$, which in turn increases the transmission ratio to 0.71 and 0.20 for the 1 mm plate and 6 mm cylinder, respectively. For comparison, the study by Funahashi *et al.* was performed on a thin platelet of 0.23 mm thickness prepared with natural boron [142]. While this thin sample achieved a transmission ratio of 0.22, at the same time the sample volume was drastically decreased. Comparable results may be obtained for MnB_2 ($\sigma_{\mathrm{Mn}} = \sigma_{\mathrm{Mn55}} = 13.3\,\mathrm{b}$) and VB_2 ($\sigma_{\mathrm{V}} = 5.08\,\mathrm{b}$). All absorption cross-sections were excerpted from the website of the Center for Neutron Research of the National Institute of Standards and Technology (NIST) [156] which in turn refers to Ref. [157].

2.1.4 Low-temperature properties of CrB_2

In the following we describe the low-temperature properties of high-quality single crystals of CrB_2 as determined by means of the electrical resistivity, Hall effect, magnetization, and specific heat. All data are consistent with a very high sample quality and identify CrB_2 as maybe the best example for weak itinerant antiferromagnetism reported so far. Moreover, we account for the role of geometric frustration and anisotropies that arise from the hexagonal crystal structure and discuss possible implications for superconductivity in non-magnetic CrB_2.

Experimental details and outline of the results

For measurements of the electrical transport and the thermodynamic bulk properties of CrB_2, samples were cut from the single-crystal ingots using a wire saw and carefully polished. All bulk measurements (magnetization, ac susceptibility, and specific heat) as well as the de Haas-van Alphen study reported in Ref. [152] were carried out on a single-crystalline cuboid of $2.5 \times 2.2 \times 0.9\,\mathrm{mm}^3$ with its faces oriented along $\langle 001\rangle$, $\langle 100\rangle$, and $\langle 210\rangle$. For the electrical transport and the Hall effect measurements thin platelets were prepared, $1 \times 0.5 \times 0.3\,\mathrm{mm}^3$ and $2.0 \times 1.0 \times 0.2\,\mathrm{mm}^3$ in size. The platelets had faces oriented along $\langle 001\rangle$, $\langle 210\rangle$, and $\langle 100\rangle$ for current along the hexagonal c-axis or along $\langle 100\rangle$, $\langle 210\rangle$, and $\langle 001\rangle$ for current along the hexagonal a-axis, respectively. Gold wires of a diameter of 25 µm were spot welded onto the samples for the excitation current and the voltage pick up. The geometry factors were determined from digital photographs recorded with an optical microscope. A conservative estimate of the resulting accuracy is ∼25 %.

The electrical resistivity, ρ_{xx}, was measured by Alexander Regnat as part of his Ph.D. thesis in a cryogen-free adiabatic demagnetization cryostat at temperatures down to ∼100 mK. A digital lock-in technique was used at an excitation frequency of 22.08 Hz and at low excitation currents using a four-terminal set up. A separate set of measurements was conducted in a 14 T superconducting magnet system at temperatures down to ∼2.3 K using a six-terminal configuration for simultaneous measurements of the longitudinal resistivity and the Hall effect. The Hall resistivity, ρ_{xy}, was inferred from the transverse voltage pick-up, and corresponds to the antisymmetric signal contribution under magnetic field. The longitudinal resistivity obtained in the four- and six-terminal measurements were in excellent agreement with each other. The magnetization was measured in an Oxford Instruments vibrating sample magnetometer with an oscillation frequency of 62.35 Hz and an amplitude of roughly 1 mm by Alexander Regnat as part of his Ph.D. thesis. The specific heat was finally measured in a Quantum Design physical properties measurement system with a standard small heat-pulse method. Heat pulses, if not stated otherwise, had an amplitude of 0.5 % of the bath temperature. Both cryostats provided temperatures down to ∼2 K and magnetic fields up to 9 T.

The presentation of our results is organized as follows. We report, in this order, data on the electrical resistivity, the Hall effect, the magnetization, and the specific heat. These data are analyzed and discussed where we point out evidence for the formation of weak itinerant antiferromagnetism in the presence of strong geometric frustration. Finally, we consider possible implications for superconductivity in non-magnetic CrB_2 before we summarize our findings.

Electrical resistivity

We start our presentation of the experimental results with typical resistivity data of our CrB_2 single crystals in zero magnetic field depicted in Fig. 2.4. With decreasing temperature the resistivity, ρ_{xx}, decreases monotonically for both current directions and limits to small residual values, ρ_0, of a few µΩcm. At high temperatures ρ_{xx} is larger for current along the c-axis than for current along the a-axis, while the situation is reversed around 60 K. For the samples investigated we calculate residual resistivity ratios (RRR) of 11 and 16 for current along the a-axis as well as of 31 and 33 for current along the c-direction. To the best of our knowledge, these values are the highest reported in the literature so far [146, 148].

The temperature dependence of ρ_{xx} changes with decreasing temperature abruptly from a sub-linear to a super-linear dependence at a pronounced kink that marks the onset of itinerant

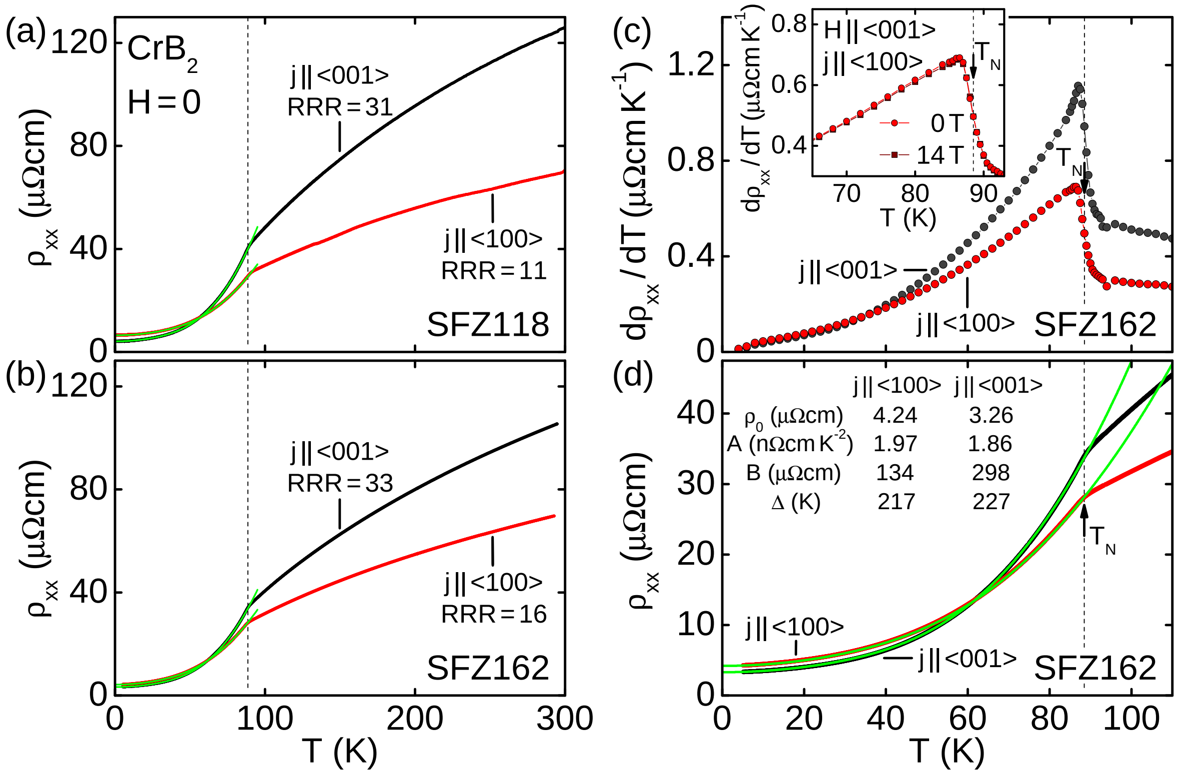

Figure 2.4: Temperature dependence of the electrical resistivity of CrB$_2$. (a) Electrical resistivity for current parallel to the *a*-axis and the *c*-axis. Data of samples prepared from SFZ118 are shown. A pronounced kink marks the antiferromagnetic transition at the Néel temperature T_N. (b) Electrical resistivity for samples prepared from SFZ162 revealing essentially identical behavior. (c) Derivative of the resistivity with respect to the temperature, $\mathrm{d}\rho_{xx}/\mathrm{d}T$. The inset shows $\mathrm{d}\rho_{xx}/\mathrm{d}T$ for zero field and an applied field of 14 T along the *c*-axis. (d) Close-up view of the resistivity below T_N for both current directions as fitted with a model combining Fermi liquid behavior and scattering by spin waves with a slightly anisotropic spin wave gap (green solid lines).

antiferromagnetism. We determine the Néel temperature from the first derivative of the resistivity, $\mathrm{d}\rho_{xx}/\mathrm{d}T$, as depicted in Fig. 2.4(c), where $T_\mathrm{N} = 88.5\,\mathrm{K}$ is the same for both current directions and samples. This value of T_N is in excellent agreement with previous studies [135, 148]. The narrow temperature range of the change in $\mathrm{d}\rho_{xx}/\mathrm{d}T$ provides additional evidence of the high compositional and structural homogeneity of our samples.

In order to account for the detailed temperature dependence of ρ_{xx}, we compare it to related compounds. Around the onset of the spin density wave order in chromium [158, 159] and the onset of the hidden order in the heavy fermion compound URu$_2$Si$_2$ [160, 161], the temperature dependence of ρ_{xx} display a small, well-developed maximum preceding a pronounced drop. This maximum has been interpreted as the formation of a super-zone gap. The resistivity of CrB$_2$, however, lacks such a maximum.

The sub-linear dependence of $\rho_{xx}(T)$ at high temperatures stems from a combination of the scattering of conduction electrons by phonons and an abundance of spin fluctuations as observed in the specific heat presented below. For $T < T_\mathrm{N}$ the super-linear dependence can be accounted

		SZF118		SZF162	
quantity	unit	$\boldsymbol{j} \parallel a$	$\boldsymbol{j} \parallel c$	$\boldsymbol{j} \parallel a$	$\boldsymbol{j} \parallel c$
ρ_0	$\mu\Omega$cm	6.48	4.12	4.24	3.26
A	nΩcm/K^2	1.76	2.12	1.97	1.86
B	$\mu\Omega$cm	127	355	135	298
Δ	K	212	226	217	227
RRR	-	11	31	16	33

Table 2.1: Key parameters for CrB_2 inferred from the temperature dependence of the electrical resistivity of samples from SFZ118 and SFZ162 as well as current along the a-axis and the c-axis. A Fermi liquid ground state was fitted that develops a spin wave gap below T_N.

for extremely well by the formation of spin density wave type order as shown in Fig. 2.4(d). Here, we consider three contributions: (i) a constant term ρ_0 accounting for impurity scattering, (ii) the quadratic temperature dependence AT^2 of a Fermi liquid accounting for electron-electron scattering including Umklapp processes, and (iii) an exponential term accounting for electron-spin-wave scattering [161]. The latter is obtained by inserting a dispersion $\omega(\boldsymbol{k})$ with a spin wave gap Δ into the linearized Boltzmann equation for $T \ll \Delta$ [162]. As the three terms arise from different scattering mechanisms the scattering rates may be added in the spirit of Matthiessen's rule, giving

$$\rho_{xx}(T) = \rho_0 + AT^2 + B\frac{T}{\Delta}\left(1 + 2\frac{T}{\Delta}\right)\exp\left[-\frac{\Delta}{T}\right]$$

Fitting our experimental data of SFZ162 we find $A^a = 1.97\,\mathrm{n\Omega cm/K^2}$ and $A^c = 1.86\,\mathrm{n\Omega cm/K^2}$ for current along a-axis and the c-axis, respectively. These values are not uncommon for d-band metals, as discussed below, and are smaller than the value reported by Guy, who used a quadratic temperature dependence only to fit data from a polycrystalline sample [147]. We obtain slightly anisotropic values for the spin wave gap, $\Delta^a = 217\,\mathrm{K}$ and $\Delta^c = 227\,\mathrm{K}$, consistent with the weak magnetic anisotropy seen in the magnetization presented below. Fitting the transport data of samples from the second crystal, SFZ118, yields essentially the same set of parameters as summarized in Tab. 2.1. Thus, fits to four independent sets of data, two current directions each for two single-crystal ingots, lead to consistent parameter values underscoring the validity of the model used. In addition, the results show the high reproducibility of our single crystal growth procedure hence allowing to readily combine results from different high-quality samples of CrB_2.

Hall effect and magnetoresistance

In view of the strong spin fluctuations inferred from the resistivity, as well as the specific heat and magnetization presented below, one might expect a strong response to applied magnetic fields rapidly quenching these spin fluctuations. This effect is well-established in a large number of d-electron and f-electron compounds [9] and, as the fluctuations are strongest around the phase transition, implies a pronounced suppression of the ordering temperature under applied magnetic fields. In stark contrast, in CrB_2 the transition temperature, T_N, does not change in applied fields of up to 14 T, as shown in the inset of Fig. 2.4(c). This lack of field dependence

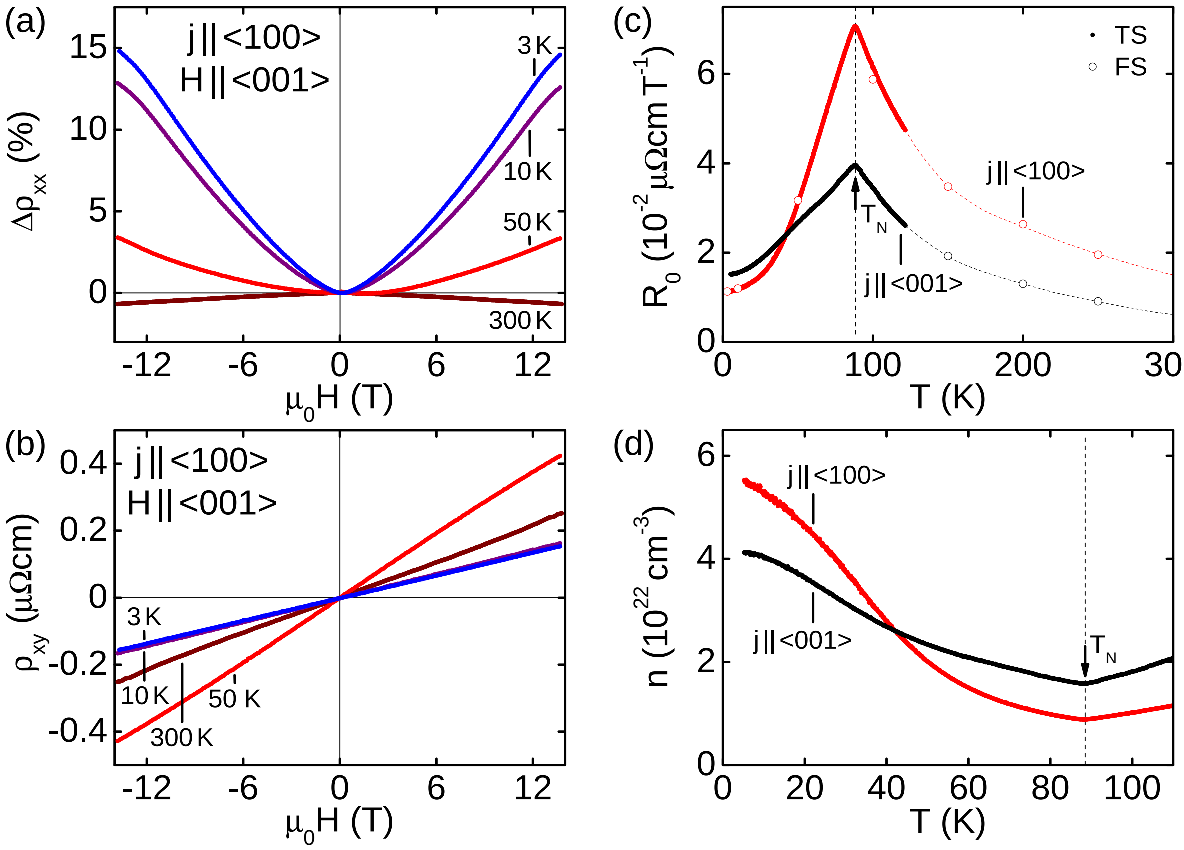

Figure 2.5: Hall effect and magnetoresistance of CrB$_2$ as measured on samples from SFZ162. (a) Magnetoresistance, $\Delta\rho_{xx} = [\rho_{xx}(H)/\rho_{xx}(H=0)] - 1$, for current parallel to the a-axis and field along the c-axis. (b) Hall resistivity, ρ_{xy}, as a function of field for different temperatures exhibiting linear behavior up to 14 T. (c) Normal Hall coefficient, R_0, as a function of temperature for current parallel to the a-axis and the c-axis. For both directions a pronounced maximum is observed at the Néel temperature $T_\mathrm{N} = 88.5$ K. Data extracted from measurements as a function of temperature at fixed fields of ±6 T (solid symbols) and from measurements as a function of field at fixed temperatures (open symbols) are in excellent agreement. Dashed lines are guides to the eye. (d) Effective carrier density, n, as calculated from the data in panel (c).

is characteristic for itinerant antiferromagnetism and also observed in systems such as CuMnSb or Mn$_3$Si.

Typical data of the magnetoresistance of CrB$_2$ reveal conventional, albeit weak, changes of ρ_{xx} up to 14 T, the highest field studied, as illustrated in Fig. 2.5(a). The magnetoresistance, $\Delta\rho_{xx} = [\rho_{xx}(H)/\rho_{xx}(H=0)] - 1$, displays a quadratic field dependence, $\rho_{xx} \propto H^2$, over nearly the entire field range with a weakly temperature dependent prefactor. At low temperatures $\Delta\rho_{xx}$ is positive and reaches 15 % at 14 T, while it decreases with increasing temperature and finally becomes negative, -1 % at 14 T and 300 K.

The Hall resistivity as measured at selected temperatures, see Fig. 2.5(b), displays a linear field dependence described by $\rho_{xy} = R_0\mu_0 H$ with essentially no anomalous Hall contributions up to 14 T. For detailed information on the temperature dependence of the Hall effect we have performed temperature sweeps in fields of ±6 T up to 125 K. The associated linear Hall coefficient, R_0, is shown in Fig. 2.5(c), where open symbols correspond to data derived from field sweeps. The absolute values of R_0 extracted from temperature and field sweeps are in excellent agreement with each other and with the values from a previous study [148]. For increasing temperature R_0 increases and displays a sharp cusp at the Néel temperature $T_N = 88.5$ K, followed by a decrease. The Hall coefficients for field in the easy plane ($\boldsymbol{j} \parallel \langle 001\rangle$) and along the hard axis ($\boldsymbol{j} \parallel \langle 100\rangle$) are qualitatively similar. Their temperature dependencies cross around 40 K such that the former is about a factor of two larger at and above T_N.

From the Hall coefficient $R_0 = (ne)^{-1}$ one may calculate an averaged charge carrier concentration n, as depicted in Fig. 2.5(d). Here, e corresponds to the charge of an electron. The positive value of R_0 is characteristic of electron conduction with an absolute value typical for a good metallic state. The increase of n with decreasing temperature below T_N suggests that multiple bands, presumably with both electron-like and hole-like character, are present at the Fermi level and are affected differently as a function of temperature. This picture is consistent with the calculated electronic structure of CrB$_2$ reported in Ref. [152]. We finally note, that the temperature dependence of n shows a faint S-shape with a point of inflection around ∼40 K that may correspond to an additional temperature dependence in the specific heat. The latter suggests excitations beyond the simple formation a spin wave gap as presented below in the section about the specific heat.

Magnetization

The magnetization, shown in Fig. 2.6, provides additional evidence for the excellent sample quality. Namely, in the low-temperature limit the magnetization lacks the pronounced increase that has been reported in essentially all previous studies [141, 149, 151]. It was long suspected that this increase represents a Curie tail due to magnetic impurities which, for the case of CrB$_2$, most likely stem from the iron content in the chromium and boron used for the sample preparation. This conjecture is supported by the absence of the Curie tail in our samples, which were grown from high-purity chromium and boron, with a very low concentration of transition metal and rare earth impurities. Hence, as we will explain in the following, the high purity of our samples reveals the intrinsic temperature dependence of the magnetization in CrB$_2$. The latter strongly supports the formation of weak itinerant antiferromagnetism coinciding with the effects of geometric frustration.

Fig. 2.6(a) depicts the magnetization as a function of temperature at constant fields, i.e., the uniform magnetization at zero wave vector ($q = 0$). The absolute value is small and only varies slightly between 2 K and 300 K with a clear cusp at the Néel temperature $T_N = 88.5$ K. This value is in excellent agreement with the transition temperature observed in the electrical resistivity and the specific heat presented below. Both the qualitative shape of the magnetization curve and the position of the maximum remain unchanged in fields up to 9 T along the a-axis or the c-axis. Hence, like in CuMnSb or Mn$_3$Si [109, 111, 112], neither the field dependence (not shown) nor the temperature dependence provide evidence for a spin-flop transition. This high stability of the antiferromagnetic order may be attributed to a large dominant energy scale in combination with a very weak coupling of an an external magnetic field to the finite wave vector order, as typical for itinerant magnetism. The weak character of the magnetism is underscored by the fact that the absolute value of the magnetization at 9 T in CrB$_2$ is roughly an order of

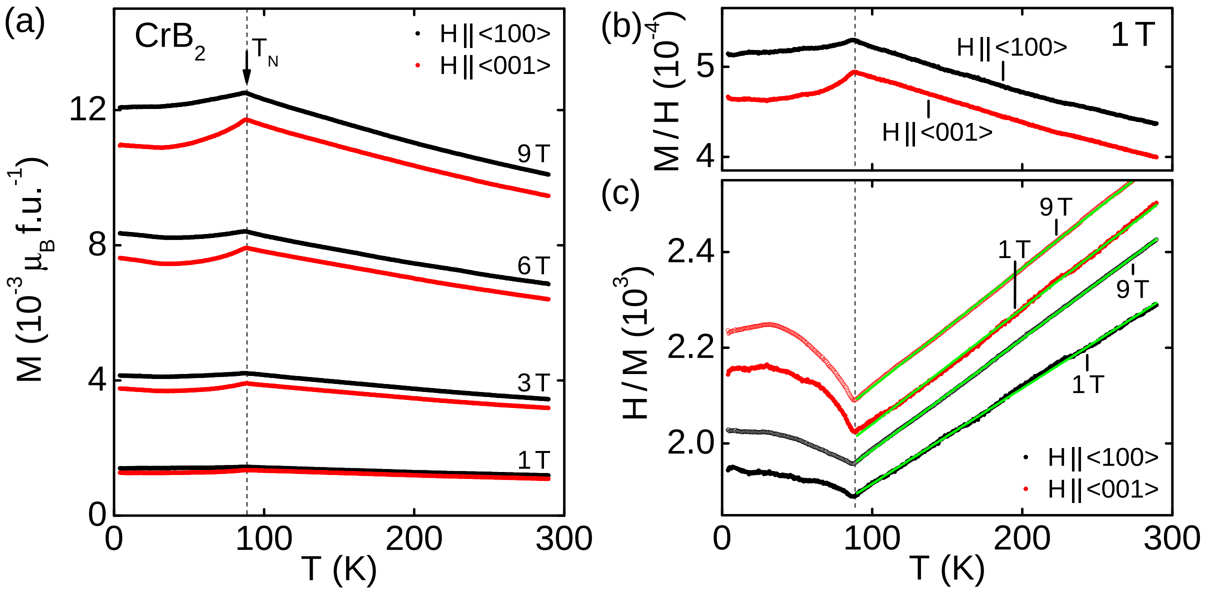

Figure 2.6: Magnetization of CrB$_2$ as a function of temperature. (a) Magnetization for fields up to 9 T displaying a clear kink at the Néel transition. The absolute values are small. The crystalline c-direction corresponds to the magnetic hard axis. No qualitative changes are observed up to the highest fields studied. (b) Normalized magnetization, M/H, for $\mu_0 H = 1\,\mathrm{T}$ and both field directions. At low temperatures there is no sign of a Curie tail. (c) Inverse normalized magnetization, H/M, for both field directions as well as for $\mu_0 H = 1\,\mathrm{T}$ and $\mu_0 H = 9\,\mathrm{T}$. The solid green lines are Curie-Weiss fits for temperatures $T > 90\,\mathrm{K}$.

magnitude smaller than in CuMnSb or Mn$_3$Si.

Fig. 2.6(b) shows the normalized magnetization, M/H, as a function of temperature, which provides an approximation for the susceptibility, dM/dH. The absolute value is small, positive, and of the order of $5 \cdot 10^{-4}$ for the parameter range studied. The magnetization and the susceptibility for field along the crystalline a-direction are about 10 % larger than for field along the c-axis. This behavior indicates a very weak anisotropy with an easy hexagonal basal plane and a hard c-axis, consistent with Tanaka *et al.* [148]. Recently, the magnetic anisotropies in several $C32$ diborides were addressed by means of measurements of the susceptibility and electronic structure calculations [141]. While the absolute value of the susceptibility of several non-magnetic diborides was reproduced from the first-principles calculations, the magnetic anisotropy and the temperature dependence of the susceptibility in CrB$_2$ were not accounted for.

The inverse normalized magnetization, H/M, is finally depicted in Fig. 2.6(c). For both field directions it follows a Curie-Weiss dependence between T_{N} and room temperature, i.e., the highest temperature measured. The slope of the linear temperature dependence stays essentially unchanged in the field range studied. We thereby extract a very large negative Curie-Weiss temperature $\Theta_{\mathrm{CW}} = -(750 \pm 50)\,\mathrm{K}$ and a large effective fluctuating moment $m_{\mathrm{eff}} = (2.0 \pm 0.1)\,\mu_{\mathrm{B}}/\mathrm{f.u.}$, in agreement with earlier reports [132, 148]. The anisotropy of Θ_{CW} is small when compared with the uncertainties in extrapolating its absolute value. The large value of Θ_{CW} suggests very strong antiferromagnetic interactions as the dominant energy scale which is consistent with the lack of any noticeable field dependence up to the highest fields studied. At the same time Θ_{CW} exceeds by far the value of T_N, where the ratio $f = -\Theta_{CW}/T_N$ is widely considered as a measure of the strength of geometric frustration. Large values of f imply a strong suppression of long-range order and hence strong geometric frustration. We obtain $f \approx 8.5$ for CrB_2 which is characteristic of strong but not very strong ($f > 10$) geometric frustration [17].

Moreover, the large fluctuating moment exceeds the ordered moment $m_s \approx 0.5\,\mu_B$/f.u. inferred in previous nuclear magnetic resonance and neutron scattering studies by a factor of four. A similar enhancement is one of hallmarks of the weak itinerant ferromagnets such as MnSi, Ni_3Al, or $ZrZn_2$. In the 1980s, inelastic neutron scattering studies in these systems eventually revealed strong damping of collective spin excitations through the coupling to the particle-hole continuum as a new mechanism leading to Curie-Weiss behavior. As an antiferromagnetic system, CrB_2 appears to display the largest enhancement of m_{eff}/m_s reported to date, which in its own right motivates detailed neutron scattering studies of the spin excitations in CrB_2 [154].

Specific heat

Shown in Fig. 2.7 is the specific heat of CrB_2 as a function of temperature. Perhaps most prominent, a clear lambda anomaly is located at the Néel transition, characteristic of a second-order phase transition. No changes are observed in fields up to 9 T. Measurements with two different sizes of heat pulses, 0.1 % and 0.5 %, lead to identical data confirming that the shape of the anomaly is intrinsic to the sample and not a result of the experimental method. Using a conventional entropy conserving construction (gray shaded areas) provides a Néel temperature $T_N = 88.5\,K$ in remarkable agreement with the resistivity and magnetization measurements. It is important to emphasize, that the width of the transition of roughly $\pm 1.5\,K$ corresponds to $\pm 1.5\,\%$, which is actually quite small and perfectly consistent with the excellent sample quality seen in the other properties.

In the low-temperature limit, where lattice contributions to the specific heat freeze out, we observe a Sommerfeld coefficient $\gamma_0 = 13\,mJ/mol\,K^2$, in agreement with the literature [136]. This value is larger than for non-magnetic diborides but typical for d-electron systems with moderate or strong electronic correlations [119, 143]. Up to 9 T there is no shift of the low-temperature specific heat. This stability contrasts the pronounced suppression on similar field scales occurring in a wide range of d-electron and f-electron systems, also referred to as field-induced quenching of spin fluctuations, but is consistent with other itinerant antiferromagnets like CuMnSb or Mn_3Si.

At higher temperatures, lattice contributions may no longer be neglected, where the Dulong-Petit high-temperature limit corresponds to $C_{DP} = 9R = 74.83\,J/mol\,K$ with the universal gas constant R. Unfortunately, due to the large phonon contributions already present at T_N, the formation of the spin wave gap seen in the resistivity may not be inferred directly from the temperature dependence of the specific heat. In order to obtain at least a rough estimate of the lattice contributions in CrB_2, the specific heat of VB_2 is used as a non-magnetic isostructural reference, see Fig. 2.7(a). Compared to a simple Debye model with a Debye temperature $\Theta_D = 950\,K$, the specific heat of VB_2 reveals additional phonon contributions for intermediate temperatures, that may be attributed, for instance, to the reduced dimensionality of the layered crystal structure. Here, Θ_D was chosen such that the slope of the Debye contribution approaches that of the specific heat of CrB_2 and VB_2 at high temperatures. The value of Θ_D is similar to values reported for other diborides [163].

After subtracting the specific heat of VB_2, which displays a Sommerfeld coefficient $\gamma_0 =$

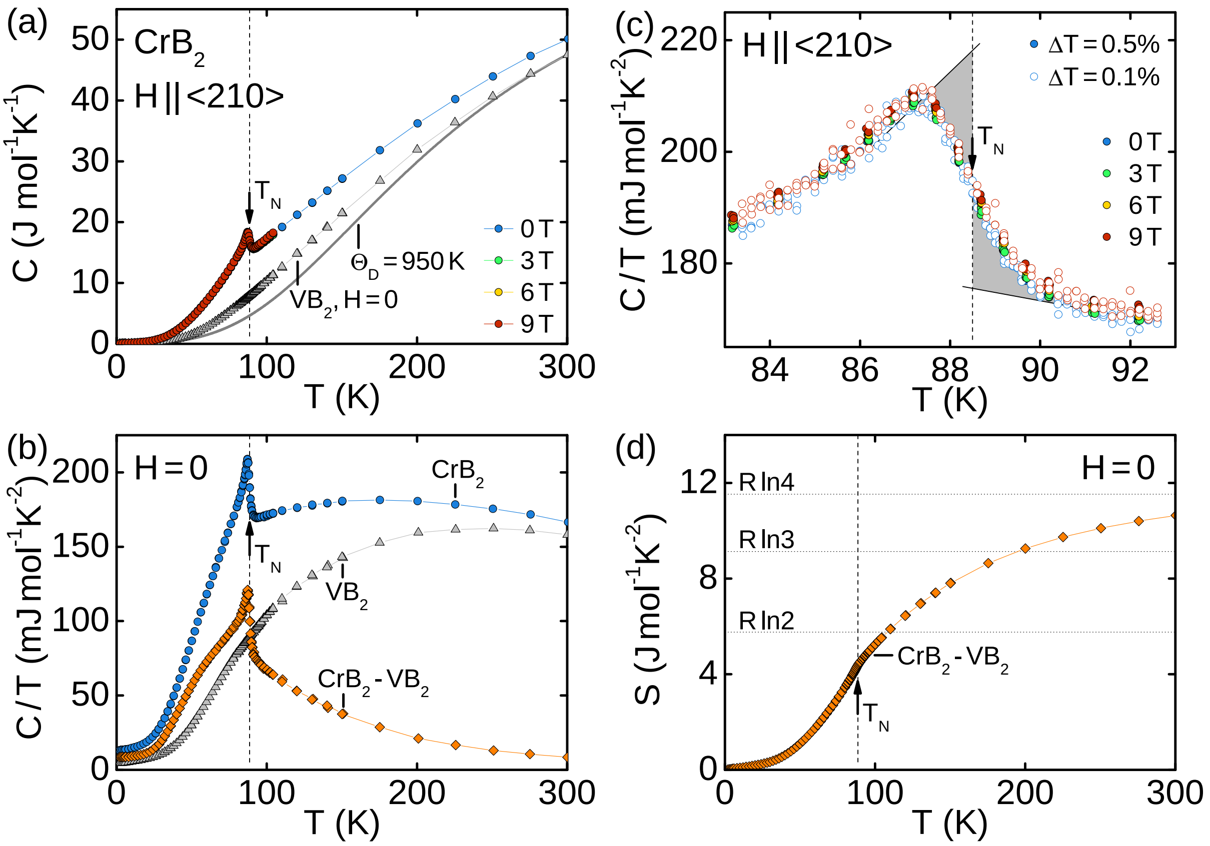

Figure 2.7: Specific heat of CrB$_2$ as a function of temperature. (a) In the specific heat a pronounced anomaly is present at the Néel transition. The specific heat hardly changes in fields up to 9 T. The Dulong-Petit limit corresponds to $9R = 74.83\,\mathrm{J/mol\,K}$. (b) Specific heat divided by temperature, C/T. Data are shown for CrB$_2$ and VB$_2$, where the latter is used for an estimate of the lattice contribution in CrB$_2$. (c) Specific heat divided by temperature around the Néel transition in more detail. An entropy conserving construction yields the Néel temperature $T_N = 88.5\,\mathrm{K}$. Measurements with heat pulses of 0.1 % of the current temperature (open symbols) reproduce data measured with 0.5 % heat pulses. (d) Magnetic contribution to the entropy. The lattice contribution was inferred from VB$_2$.

4 mJ/mol K^2, from the specific heat of CrB$_2$ two unusual features emerge. These features are insensitive to the precise quantitative value of specific heat of VB$_2$ and are resolved best in C/T as illustrated in Fig. 2.7(b). First, for $T > T_N$ the specific heat of CrB$_2$ still includes substantial magnetic contributions pointing at the presence of very strong spin fluctuations. This observation is qualitatively consistent with the large effective fluctuating moment, m_{eff}, inferred from the Curie-Weiss dependence of the inverse normalized magnetization and will be discussed in more detail below. Second, for $T < T_N$ the magnetic contribution to the specific heat displays a negative curvature around ∼50 K. Thus, the temperature dependence is clearly more complex than the exponential dependence anticipated for the straightforward formation of a spin wave gap.

In fact, in a large number of systems the temperature dependence of the electronic contribution to the specific heat, C_{el}/T, and the derivative of the resistivity, $\mathrm{d}\rho_{xx}/\mathrm{d}T$, resemble each other. This behavior may be expected when the scattering that determines the electrical transport follows Fermi's golden rule and the corresponding density of states dominates the specific heat. In CrB_2, however, $\mathrm{d}\rho_{xx}/\mathrm{d}T$ lacks any changes of its curvature around $\sim 50\,\mathrm{K}$, cf. Fig. 2.4(c). Taken together, these observations hint towards the emergence of additional excitations in the specific heat that do not affect the resistivity and may be related to the effects of geometric frustration. Interestingly, a temperature dependence that is reminiscent of the behavior of CrB_2 is observed in the specific heat of UGe_2, where it has inspired speculations about an incipient charge density wave instability [164]. The microscopic origin of such a putative coupled spin and charge density wave order, however, may be completely different for UGe_2 and CrB_2. Notably, rather one-dimensional aspects of the crystal structure in the former case are opposed by a nesting-driven wave order, like in pure chromium [159], for the latter case.

Finally, an estimate of the temperature dependence of magnetic contributions to the entropy of CrB_2 is given in Fig. 2.7(d). Here, C/T was integrated numerically after subtracting the specific heat of VB_2 as estimate of lattice contributions. At high temperatures the entropy appears to approach a value of $R\ln 4$, which suggests a Cr^{3+} configuration, i.e., $[\mathrm{Ar}]\,3d^3$ with half-filled t_{2g} orbitals and a total spin $J = S = 3/2$. Unfortunately, it is presently not possible to provide a microscopic underpinning for this conjecture since the existing band structure calculations cannot capture the physics of fluctuating local moments. A more careful account of the magnetic entropy released at high temperatures and its consistency with the fluctuating Curie-Weiss moment therefore has to await further experimental and theoretical exploration.

Discussion and speculations

In the following we speculate on the broader implications of our experimental results. We find a consistency of the properties of CrB_2 with the Kadowaki-Woods ratio in other systems [165, 166] and extrapolate the behavior of non-magnetic CrB_2 at zero temperature from its paramagnetic state above T_{N}. A logarithmic temperature dependence of the specific heat implies a ratio of the Sommerfeld coefficient in the normal state, γ_{norm}, and the average inverse fluctuation lifetime, $\hbar\Gamma_{\mathrm{ave}}$, that is perfectly consistent with several other materials [167]. The corresponding spin fluctuation temperature, T_{SF}, suggests a critical temperature $T_c \sim 10\,\mathrm{K}$ for magnetically mediated superconductivity in non-magnetic CrB_2. The discovery of such a state may provide the long-sought link between the heavy fermion superconductivity in f-electron compounds and the high-T_c superconductivity in the cuprates [168].

We start our discussion with the Kadowaki-Woods ratio, i.e., the ratio of the coefficient of the quadratic temperature dependence of the resistivity, A, to the square of the coefficient of the linear temperature dependence of the specific heat, γ^2 [165]. This empirical classification considers the consistency of a wide range of materials exhibiting strong electronic correlations with Fermi liquid theory. Here, A probes the cross-section of the quasiparticle-quasiparticle scattering, i.e., the imaginary part of the self-energy, whereas γ represents the effective quasiparticle mass connected to the real part of the self-energy. In turn, the Kadowaki-Woods ratio is only meaningful, if the self-energy is essentially momentum independent [166]. In the antiferromagnetic state at low temperatures, where we have also taken into account the scattering by impurities and the formation of a spin wave gap, we determine $A^a = 1.76\,\mathrm{n\Omega cm/K^2}$ and $A^c = 2.12\,\mathrm{n\Omega cm/K^2}$, respectively, as well as a Sommerfeld coefficient $\gamma_0 = 13\,\mathrm{mJ/mol\,K^2}$. These values are typical for d-electron systems. Nevertheless, as shown in Fig. 2.8, the resulting Kadowaki-Woods ra-

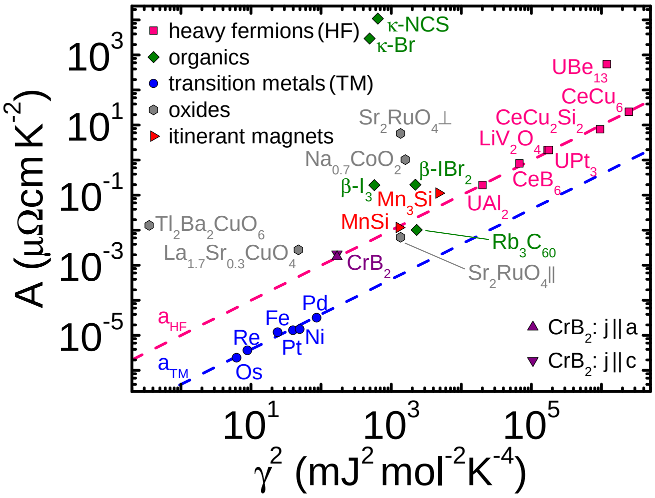

Figure 2.8: Kadowaki-Woods plots of selected d-electron and f-electron compounds as presented in Ref. [166]. The Kadowaki-Woods ratio of CrB_2 is close to the value $a_{\mathrm{HF}} = 10\,\mu\Omega\mathrm{cm}\,\mathrm{mol}^2\mathrm{K}^2/\mathrm{J}^2$ observed in heavy fermion compounds (upper dashed line) and distinctively differs from the value $a_{\mathrm{TM}} = 0.4\,\mu\Omega\mathrm{cm}\,\mathrm{mol}^2\mathrm{K}^2/\mathrm{J}^2$ observed in transition metals (upper dashed line).

tio, $a = A/\gamma^2$, corresponds to that of f-electron heavy fermion systems, while it differs clearly from transition metal elements. MnSi, which is in first approximation a prime example for weak itinerant ferromagnetism, shows the same Kadowaki-Woods ratio, whereas the ratio for Mn_3Si slightly differs [169]. Other itinerant magnets such as CuMnSb [112], $ZrZn_2$ [50, 170], or Ni_3Al [171–173] exhibit non-Fermi liquid behavior.

In a next step, we address the possible properties of non-magnetic CrB_2 as extrapolated from its paramagnetic state above T_{N}. Here, a large fluctuating Curie-Weiss moment and a large magnetic contribution to the specific heat provide consistent evidence for an abundance of strong spin fluctuations. In the following we assume two-dimensional fluctuations in a three-dimensional system, which we justify by the layered crystal structure of CrB_2, the weak easy-plane magnetic anisotropy, and the anisotropic resistivity. Therefore, in the spirit of the framework of the self-consistently renormalized spin fluctuation theory, the additional contribution to the specific heat in the normal state, i.e., after subtraction of the specific heat of VB_2, is expected to vary logarithmically as $C_{\mathrm{mag}}/T = \gamma_{\mathrm{norm}} \ln(T_{\mathrm{SF}}/T)$. As shown in Fig. 2.9(a), we find reasonable agreement with the experimental data, where the deviation at the highest temperatures may be attributed to the inaccuracy of the subtraction of the lattice contribution. We extract for the normal state of CrB_2 a Sommerfeld coefficient of $\gamma_{\mathrm{norm}} \approx 70\,\mathrm{mJ/mol\,K}^2$ and a spin fluctuation temperature $T_{\mathrm{SF}} \approx 257\,\mathrm{K}$. The latter corresponds to an average fluctuation rate $\hbar\Gamma_{\mathrm{ave}} = k_{\mathrm{B}}T_{\mathrm{SF}} \approx 22\,\mathrm{meV}$.

In the self-consistently renormalized Ginzburg-Landau theory of itinerant-electron magnets the dynamical susceptibility associated with the relaxation frequency spectrum is parametrized in terms of a single-pole function at the magnetic ordering wave vector. Material-specific parameters describe the damping and spin wave stiffness across the Brillouin zone. Assuming this ansatz, the normal state contribution to the specific heat, γ, scales with an average fluctuation rate, Γ_{ave}. Empirically, this relationship has been demonstrated by Hayden *et al.* [167] for a

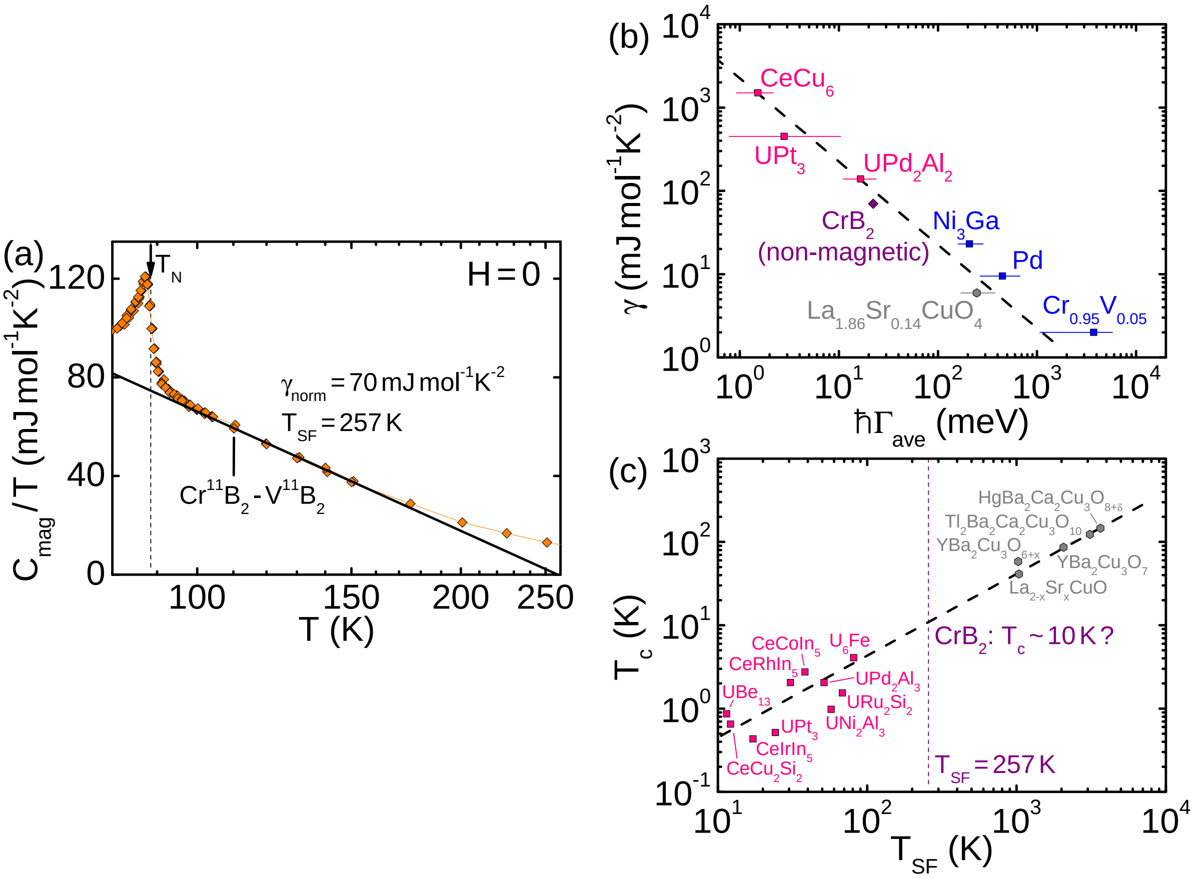

Figure 2.9: Estimate of the average fluctuation rate for non-magnetic CrB$_2$. (a) Magnetic contribution to the specific heat of CrB$_2$ at high temperatures over a logarithmic temperature scale. A fit corresponding to $C_{\mathrm{mag}}/T = \gamma_{\mathrm{norm}} \ln(T_{\mathrm{SF}}/T)$ (solid line) yields an estimate of the Sommerfeld coefficient expected for non-magnetic CrB$_2$, $\gamma_{\mathrm{norm}} = 70\,\mathrm{mJ/mol\,K^2}$, and a spin fluctuation temperature, $T_{\mathrm{SF}} = 257\,\mathrm{K}$. (b) Correlation between the Sommerfeld coefficient, γ, and the average fluctuation rate, Γ_{ave}, for various compounds. The figure has been reproduced from Ref. [167]. An estimated for non-magnetic CrB$_2$ is inferred from the specific heat. (c) Correlation between the superconducting transition temperature, T_c, and the spin fluctuation temperature, T_{SF}, for heavy fermion and cuprate superconductors. The figure has been reproduced from Ref. [168]. An extrapolation implies a possible transition temperature $T_c \sim 10\,\mathrm{K}$ for magnetically mediated superconductivity in non-magnetic CrB$_2$.

wide range materials comprising ferromagnetic and antiferromagnetic compounds as reproduced in Fig. 2.9(b). In CrB$_2$ we estimate from the spin fluctuation temperature T_{SF} an average fluctuation rate $\hbar\Gamma_{\mathrm{ave}} = k_{\mathrm{B}}T_{\mathrm{SF}} \approx 22\,\mathrm{meV}$ for the normal state. The resulting ratio of γ_{norm} and Γ_{ave} agrees remarkably well with the empirical observation by Hayden *et al.* hence suggesting that the assumptions made above are justified.

Finally, the possible occurrence of spin fluctuation mediated superconductivity has been discussed in a wide range of materials, see, e.g., Ref. [31]. Here, the superconducting instability requires a number of factors to be satisfied, namely: (i) a spin fluctuation spectra that is fairly well focused in energy and momentum, (ii) dominant momentum contributions that match sections of the Fermi surface to promote superconductive pairing, and (iii) transverse and longitudinal components that are pair-forming. As a consequence, the superconducting transition temperature, T_c, may be expected to scale with the width of the relaxation frequency spectrum as measured by a characteristic spin fluctuation temperature T_{SF}. In this context, the heavy fermion and cuprate superconductors may be empirically related by plotting the superconducting transition temperature T_c against the spin fluctuation temperature T_{SF} as reproduced in Fig. 2.9(c) [4, 168]. If we speculate, that all microscopic factors promoting magnetically mediated superconductivity may indeed be satisfied for non-magnetic CrB$_2$, this empirical relationship suggests a critical temperature of $T_c \sim 10\,\mathrm{K}$. This hypothesis, however, presumes that the antiferromagnetic order in CrB$_2$ has been suppressed, e.g., through the application of hydrostatic or uniaxial pressure, and that the normal state properties in the zero-temperature limit of antiferromagnetism may be inferred from the normal state at ambient pressure as outlined above. Furthermore, this a prediction ignores, for instance, the possible effects of geometric frustration that may play a role in CrB$_2$ as implied by the magnetization.

Perhaps most excitingly, the spin fluctuation temperature T_{SF}, that we have inferred in our study, places CrB$_2$ between the heavy-fermion and the cuprate superconductors. Thus, given the simplicity of CrB$_2$, discovery of a superconducting state may provide a missing link that identifies magnetically mediated superconductivity as a universal phenomenon in a wide range of materials. The structural similarity with the conventional two-band superconductor MgB$_2$ promises fresh insights on the perhaps most important hidden agenda in this field—the interplay of structural and magnetic degrees of freedom for superconductivity.

Summary

In conclusion, we have prepared high-quality single crystals of CrB$_2$ using a solid state reaction of chromium and boron powder followed by optical float-zoning. For the first time, large ^{11}B-enriched crystals were grown. The excellent quality of our samples is evident from (i) the shiny, faceted appearance of the float-zoned ingot, (ii) Laue x-ray and neutron diffraction, (iii) the hitherto highest residual resistivity ratios reported in the literature, (iv) the absence of a Curie tail in the magnetization, (v) well developed anomalies at the magnetic transition in the specific heat and the derivative of resistivity, as well as (vi) the observation of quantum oscillations [152].

The bulk and transport properties of our high-purity single crystals of CrB$_2$ reveal the characteristics of weak itinerant antiferromagnetism par excellence. The key properties include strong spin fluctuations with a large fluctuating moment of $2.0\,\mu_{\mathrm{B}}/\mathrm{f.u.}$ contrasted by a small ordered moment of $0.5\,\mu_{\mathrm{B}}/\mathrm{f.u.}$, a comparably small transition temperature $T_{\mathrm{N}} = 88.5\,\mathrm{K}$, and a remarkable stability of the magnetic order in fields up to 14 T. As an additional aspect, we note that the susceptibility points at the presence of strong geometric frustration. Finally, our data indicate the possible existence of magnetically mediated superconductivity in CrB$_2$ if the antiferromagnetic order is suppressed with (clean) non-thermal control parameters. Taken together, these findings identify CrB$_2$ as a fascinating material for future studies.

2.1.5 Low-temperature properties of MnB$_2$

In the following we summarize the magnetic properties of the $C32$ compound MnB$_2$ as reported in the literature and briefly discuss our first results on the low-temperature properties of single-crystal specimens. Early magnetization and susceptibility data on MnB_2 indicated weak ferromagnetism below $\sim$150 K with an ordered moment of $\sim 0.2\,\mu_B$/f.u. and a Curie-Weiss moment of $\sim 2\,\mu_B$/f.u. [132, 174]. Later on, Kasaya and coworkers questioned this assumption by means of nuclear magnetic resonance, magnetization, and resistivity measurements [133, 175]. They revealed that the putative itinerant ferromagnetism at low temperatures in fact arises from the tilting of antiferromagnetically ordered in-plane moments of $\sim 3\,\mu_B$/f.u. with a Néel temperature $T_N = 760\,K$. The tilting is explained on the basis of a *s*-*d* exchange interaction. The proposed magnetic order was corroborated by a neutron diffraction study that established ferromagnetically coupled moments of $2.6\,\mu_B$/f.u. within the basal plane. Consecutive planes order antiferromagnetically with respect to each other resulting in a doubling of the magnetic unit cell along the *c*-axis [134]. While first studies of the electronic structure of MnB_2 either neglected the magnetism [117, 118] or presumed an itinerant character [119], recent calculations [176, 177] suggest that MnB_2 is an interesting example for Kübler's covalent magnetism. In the latter, the magnetism is caused by spin-dependent changes in the covalent interactions between the *d*-states of neighboring transition metal atoms [178].

Most of previous experimental studies in MnB_2 were carried out on sintered polycrystalline samples that contained impurity phases, namely MnB_4 or Mn_3B_4. Only for the determination of the magnetic anisotropy Kasaya and Hihara examined tiny single-crystal platelets of $0.5 \times 0.5 \times 0.05\,mm^3$ with the *c*-axis along the shortest edge. Here, the authors observed that the magnetization is slightly larger for field along the *c*-axis. These samples were prepared by sublimating sintered polycrystals in sealed silica tubes [133]. In contrast, to the best of our knowledge, we have grown the first large single crystal of MnB_2. As explained in Sec. 2.1.3, in this crystal the *c*-axis rotates by $\sim 0.4\,°$/mm around an the *a*-axis. Still, using ^{11}B allows for comprehensive neutron scattering studies that clearly outperform the experiments reported in Ref. [134], where sintered MnB_2 powder prepared from natural boron and containing an impurity phase (MnB_4) was mixed with vanadium powder to achieve sufficient neutron transmission.

For all measurements reported in the following, we used a single-crystalline cuboid of $2.8 \times 2.7 \times 1.7\,mm^3$ oriented along $\langle 210 \rangle$, $\langle 100 \rangle$, and $\langle 001 \rangle$. The relatively large absolute value of the magnetization in MnB_2 at low temperatures requires an account for demagnetization effects, where the demagnetization factors for field along the *a*-axis and the *c*-axis correspond to $N_a = 0.283$ and $N_c = 0.283$, respectively. In the field sweeps of the magnetization, the internal field values were calculated as $H_{int} = H_{ext} - NM(H_{ext})$. The absolute value of the zero-field susceptibility was determined as $\chi_{ac}^{int} \approx \chi_{ac}^{ext}/(1 - N\mathrm{Re}\,\chi_{ac}^{ext})$.

Shown in Fig. 2.10(a) is the specific heat of MnB_2 as a function of temperature in zero field. To the best of our knowledge, such data has not been reported so far. A relatively low Sommerfeld coefficient of $\gamma_0 = 3\,mJ/mol\,K^2$ is characteristic for weak or no electronic correlations. Perhaps most important, however, in the temperature range studied, 2 K to 300 K, no anomalies are observed. In contrast, the real and the imaginary part of the ac susceptibility gradually increase with decreasing temperature as shown in Figs. 2.10(b) and 2.10(c), where a pronounced rise sets in around $T \sim 130\,K$, consistent with the literature. This gradual increase, in combination with the absence of anomalies in the specific heat, implies either that the corresponding phase transition is strongly broadened, e.g., due to geometric frustration on the hexagonal lattice, that the entropy release associated with the transition is tiny, or that the spin structure smoothly rearranges via a crossover.

The absolute value of the susceptibility in zero field is higher for field along the *a*-axis. This observation is corroborated by the field dependence of the magnetization, shown in Fig. 2.10(d), where the slope in small fields is larger for field along the *a*-axis. With increasing field, a distinct

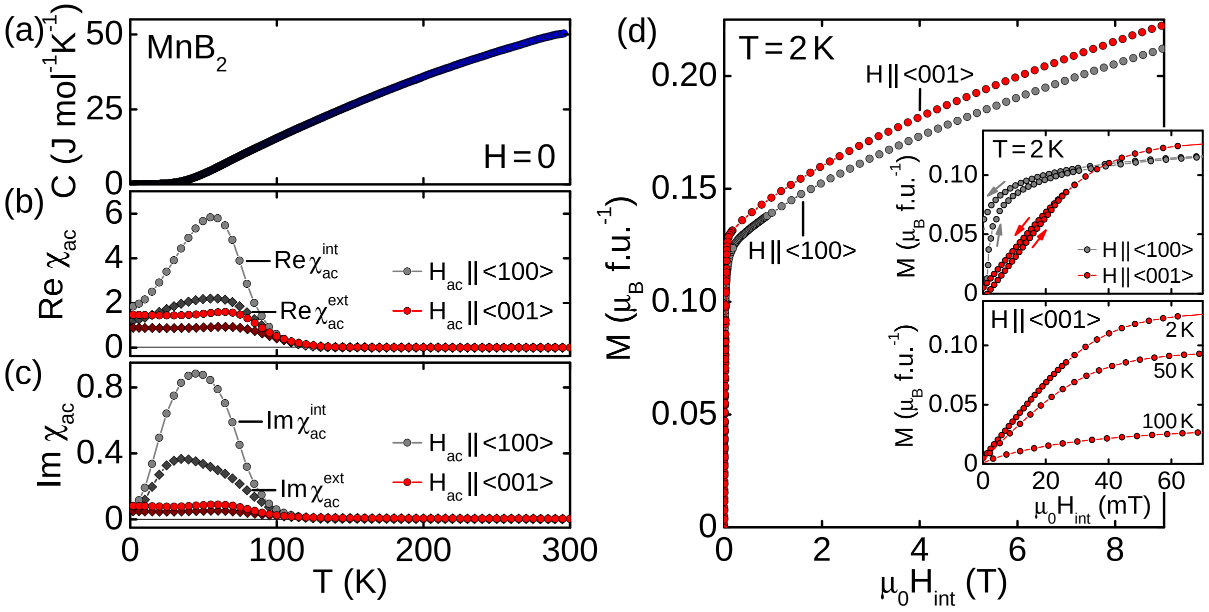

Figure 2.10: Low-temperature properties of MnB$_2$. (a) Specific heat as a function of temperature in zero field. No anomalies are observed between 2 K and 300 K. (b) Real part of the ac susceptibility in zero field. For decreasing temperature a significant increase appears below $T \sim 130$ K for ac field along both the a-axis or the c-axis. (c) Imaginary part of the ac susceptibility in zero field. Significant dissipation occurs at low temperatures. (d) Magnetization as a function of field up to 9 T at low temperatures. The magnetization stays unsaturated up to the highest fields studied. The inset shows the presence of hysteresis at low fields (upper panel) and the evolution of the magnetization with increasing temperature for field along the a-axis (lower panel).

change of slope is observed at ~10 mT and ~40 mT for field parallel to the a-axis and the c-axis, respectively. At high fields, finally, the absolute value of the magnetization for field along the c-axis exceeds the a-axis value by ~5 %. Around 40 mT the magnetization curves for the different field direction cross each other. Up to the highest fields studied, the magnetization stays unsaturated and small compared to the local moments of 2.6 μ_B/f.u. determined from neutron scattering. At low temperatures, a small hysteresis occurs where the loops possess a total width of ~3 mT for both field directions. With increasing temperature both the hysteresis and the absolute values of the magnetization decrease.

Combining our magnetization data with the neutron diffraction data from Legrand and Neov [134], we finally speculate on the possible spin order of MnB$_2$ at low temperatures and discuss the implications for the magnetic interactions in this compound. In the following we will assume localized manganese moments [177]. These moments order ferromagnetically within a basal plane, whereas consecutive planes couple antiferromagnetically. As no information on the orientation of the moments within the easy basal plane is available, we expect that they point either along the ⟨100⟩ or the ⟨210⟩ directions. Due to the the hexagonal crystal structure, three equivalent domains exist. We propose that these domains are of macroscopic size and populated equally.

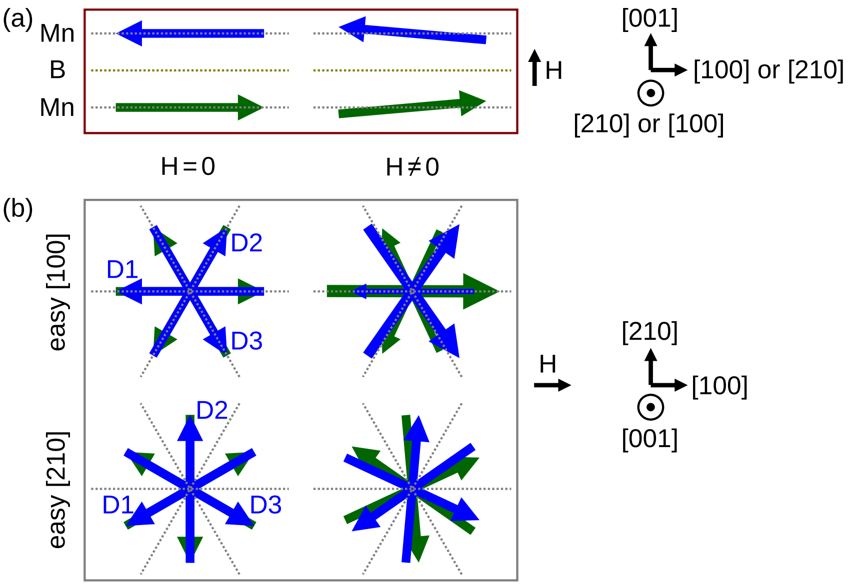

Figure 2.11: Schematic depiction of the possible spin configuration of MnB_2. (a) View perpendicular to the c-axis. In zero field, neighboring ferromagnetically coupled manganese layers (blue and green arrows) order antiferromagnetically under 180° with each other. If field is applied along the c-axis, the net magnetic moment of a plane tilts towards the field direction. (b) View along the c-axis. The three equivalent in-plane domains (marked as D1–D3) are populated equally. Easy in-plane axes are either the $\langle 100 \rangle$ or the $\langle 210 \rangle$ directions. If field is applied in the basal plane, a rotation of the domains within the manganese layers, a change of the domain population (depicted by the size of the arrows), or a combination thereof occurs.

For magnetic field along the c-axis, as schematically illustrated in Fig. 2.11(a), the net magnetic moments of the manganese layers are slightly tilted out of the basal plane giving rise to a small absolute value of the magnetization. For clarity, only one of the in-plane domains is depicted. In this field configuration, the Zeeman energy competes with (i) the easy-plane anisotropy of the local moments and (ii) the antiferromagnetic exchange of neighboring layers as the angle between the moments of these layers falls below 180°. For field within the basal plane, see Fig. 2.11(b), the net magnetization may stem from a small rotation of the ferromagnetic layers towards the field, from a change of (sublattice) domain population in favor of domains along the field, or from a combination thereof. Here, the Zeeman energy needs to be compared with (i) the presumably weak in-plane anisotropy and (ii) the antiferromagnetic exchange of neighboring layers as the in-plane angle between the corresponding sublattices differs from 180°. Changes of the population of certain sublattice domains may also require the consideration of the effects of geometric frustration. The complex interplay of these interactions, that scale in distinct ways with the magnetic field and the two angles introduced above, finally leads to the field dependence of the magnetization observed in the experiment. Here, the comparably small absolute value and the missing saturation of the magnetization up to 9 T imply that strong interactions are involved as the local moments smoothly tilt towards the field direction.

In summary, according to the first specific heat, magnetization, and susceptibility data on single-crystal samples determined as part of this thesis, MnB_2 is a local-moment antiferromagnet with a Néel transition far above room temperature. At low temperatures a canting of the magnetic structure evolves where no corresponding anomaly is observed in the specific heat. These results are fully consistent with previous reports on polycrystalline material in the literature [133, 134, 177]. In combination with our findings on CrB_2, cf. Sec. 2.1.4, the data on MnB_2 suggest that adding one electron may transform the weak itinerant antiferromagnet CrB_2 into the high-temperature local-moment antiferromagnet MnB_2. This remarkable difference underscores that $C32$ diborides are a promising playground for the investigation of a wide range of electronic and magnetic properties. An ongoing project on MnB_2 thereby concerns the investigation of its detailed magnetic structure by means of single crystal neutron diffraction in applied magnetic fields as carried out by Alexander Regnat as part of his Ph.D. thesis. Samples of a few millimeter in size allow for a compensation of the screwing of the c-axis in our single-crystal ingot. Moreover, measurements of the torque magnetization performed by Stephan Albert as part of his Ph.D. thesis will permit to quantify the magnetic anisotropies in MnB_2. Here, the observation of distinct de Haas-van Alphen frequencies, in combination with band structure calculations, will also allow us to determine the Fermi surface of MnB_2, cf. Ref. [152] for an analogous study on CrB_2.

2.2 CuMnSb: between local and itinerant antiferromagnetism

The prediction of half-metallic ferromagnetism in NiMnSb [179] and Co_2-based alloys [180] in 1983 was a major source of scientific interest in magnetic Heusler compounds in recent decades. Half-metallic materials are metallic for one spin direction while they are semiconducting for the other thus exhibiting complete spin polarization at the Fermi level, cf. Fig. 2.12. The corresponding density of states naturally gives rise to (itinerant) ferromagnetism with integral magnetic moments ($4\,\mu_\mathrm{B}$/f.u. in the case of NiMnSb). In contrast, half-metallic antiferromagnetism seems to be excluded by the full spin polarization, but may be accomplished in the form of a perfectly balanced ferrimagnet [181]. Materials with a high spin polarization accompanied by a vanishing magnetic moment are highly desirable for spintronic applications as they, for instance, do not give rise to stray fields and are less sensitive to external magnetic fields [82]. However, materials that appear to be promising candidates in the cubic half-Heusler structure, like CrMnSb, Mn_2Sb, or FeMnSb, do not crystallize in that structure and hence, if they form at all, possess differing magnetic and electronic properties.

The related compound CuMnSb is one of the few known half-Heusler compounds exhibiting antiferromagnetism that may not be clearly attributed to local moments, cf. Sec. 2.2.1. In fact, the order shares characteristics of both itinerant and localized magnetism. Speculations about half-metallicity [111], however, were ended by band structure calculations [182]. Still, the presence of antiferromagnetism with a comparably low transition temperature neighboring high-temperature ferromagnets, such as the half-metallic NiMnSb, indicates the importance of spin fluctuations in CuMnSb. Thus, understanding the nature of magnetism in CuMnSb may not only help to design antiferromagnetic Heusler compounds with distinct properties for applications but may also bring fresh insights to a wider field of research where spin fluctuations play an important role including, for instance, the high-T_c superconductors.

To the best of our knowledge, however, so far only polycrystalline material was studied. This constraint hindered the determination of the intrinsic properties of CuMnSb as Heusler compounds, in general, are very sensitive to disorder and defects. CuMnSb specimens, in particular, tend to form the ferrimagnetic impurity phase Mn_2Sb, which may in turn be suppressed by

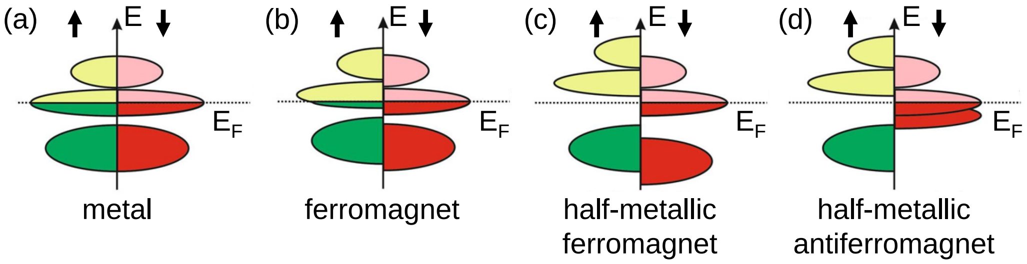

Figure 2.12: Schematic band structure of itinerant magnets. (a) Non-magnetic metal. The band structure is symmetric for both spin directions. (b) Ferromagnetic metal. The bands for the two spin directions are shifted with respect to each other. As a result, the majority charge carriers (red) possess a higher density of states at the Fermi level, E_F, leading to a finite polarization. (c) Half-metallic ferromagnet. The Fermi level is located within a gap of the minority band structure, i.e., it is semiconducting, while the majority bands remain metallic. Full spin polarization is observed. (d) Half-metallic antiferromagnet, also referred to as completely compensated half-metallic ferrimagnet. Multiple bands contribute to the majority density of states at E_F leading to a full spin polarization while the corresponding magnetic moments cancel out. Figure adapted from Ref. [82].

a slight antimony excess [183]. In this thesis, we managed to grow the first single crystals of CuMnSb, one from feed rods with stoichiometric composition and one from feed rods with an antimony excess of 0.035. Measurements of the low-temperature properties of these crystals confirm the peculiar combination of magnetic properties observed in polycrystals. Furthermore, within the antiferromagnetic state of phase-pure CuMnSb a transition was identified for the first time that could be attributed to a canting of the spin structure.

This section is organized as follows. In Sec. 2.2.2 we begin with a brief introduction to Heusler compounds where we focus on reports of antiferromagnetism in this class of materials. Subsequently, we give an overview of the previous studies on polycrystalline CuMnSb in Sec. 2.2.2 before turning to the preparation of single crystals in Sec. 2.2.3. Finally, in Sec. 2.2.4 we describe the low-temperature properties of our single-crystalline samples and discuss how the behavior is influenced by the initial antimony content.

2.2.1 Introduction to antiferromagnetic Heusler compounds

Heusler compounds are a class of cubic intermetallics that comprise more than 1500 known members [82]. Two subclasses are distinguished. Full-Heuslers possess an empirical formula X_2YZ. Their $L2_1$ crystal structure with the space group $Fm\bar{3}m$, see Fig. 2.13(a), consists of four interpenetrating face-centered cubic sublattices, each shifted by a quarter of a room diagonal. In half-Heusler compounds, described by XYZ, one of the fcc sublattices stays vacant and hence these materials lack inversion symmetry. The resulting $C1_b$ structure belongs to the space group $F\bar{4}3m$, see Fig. 2.13(b). Quaternary and also certain ternary compounds exhibit an inverse Heusler structure also belonging space group $F\bar{4}3m$. The corresponding empirical formula may be denoted as $(XY)X'Z$, where in quaternary cases different elements occupy the X and X' sites.

The X, Y, and Z atoms may be selected from most transition metals, post-transition metals,

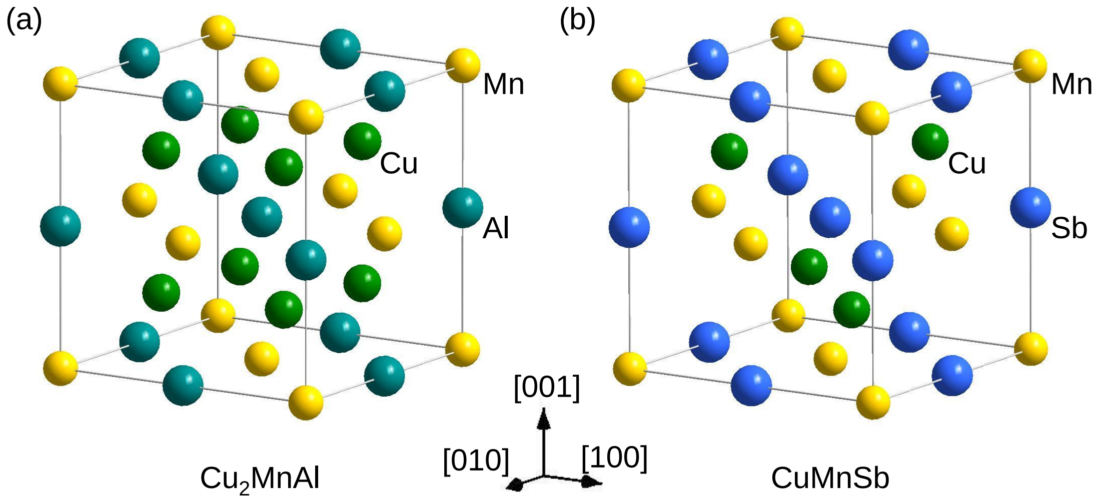

Figure 2.13: Crystal structure of the Heusler compounds. (a) Full-Heusler compound in the cubic $L2_1$ crystal structure with the space group $Fm\bar{3}m$ using the example of Cu_2MnAl. The structure may be described by four interpenetrating face-centered cubic sublattices that are shifted by a quarter of a room diagonal with respect to each other. (b) Half-Heusler compound in the cubic $C1_b$ crystal structure with the space group $F\bar{4}3m$ using the example of CuMnSb. Here, one of the sublattices is not occupied.

metalloids, or lanthanides, as well as from lithium, beryllium, and magnesium. This tremendous selection allows to realize a rich variety of physical properties reaching from metallic to insulating behavior and from diamagnetism to ferromagnetism. Further examples include superconductors, thermoelectrics, heavy fermion compounds, and shape memory alloys [82], even topological insulators are predicted [184, 185]. Since all of these properties may be achieved within the same crystal structure so-called all-Heusler-devices are a promising goal for future research. At the same time, however, Heusler compounds are prone to various forms of disorder that often alternate or even determine the behavior of the compound. Moreover, materials that are predicted to possess certain properties in a cubic structure may, in fact, crystallize in tetragonal, orthorhombic, or hexagonal modifications with distinctly differing properties. These modified structures, as well as cubic structures that are subject to strong antisite disorder and hence an altered symmetry are often also alluded to as Heusler compounds. In the following, however, we restrict ourselves to compounds with the $L2_1$ and $C1_b$ structures.

Antiferromagnetism in Heusler compounds is not uncommon, though not as prevalent as ferromagnetism. For this overview, we group known antiferromagnetic full-Heuslers and half-Heuslers into three categories, namely compounds that are based on (i) $5f$ or $6f$ elements, (ii) heavy $4d$ or $5d$ transition metals, and (iii) light $3d$ transition metals. In most cases only polycrystalline samples were investigated.

In f-electron systems antiferromagnetism occurs, for instance, in many members of the RYZ and RY_2Z series with R selected from many rare earths or uranium, Y = Ni, Pd, and Z = Sn, Pb, Sb, Bi [186–188]. In these compounds, the magnetism is carried by the localized f-electrons. Typical Néel temperatures, T_N, are in the order of a few Kelvin with gadolinium-based (up to nearly 20 K) and uranium-based (several ten Kelvin) materials as high-temperature exceptions [189, 190]. Members of the RPd$_2$Sn and RPd$_2$Pb families also show superconductivity [189, 191–193], where in ErPd$_2$Sn and YbPd$_2$Sn a coexistence of superconductivity and long-range order is discussed [194, 195].

Examples for antiferromagnetism in $4d$ and $5d$ full-Heusler compounds include Pt$_2$MnAl, Pt$_2$MnGa, Pd$_2$MnAl, and Pd$_2$MnIn with Néel temperatures that range from 75 K to 240 K [196–198]. The antiferromagnetism in the $5d$ half-Heusler IrMnGa is sensitive to the detailed composition and structural disorder [197, 199]. In contrast, PdMnTe seems to be a robust $5d$ half-Heusler antiferromagnet. It exhibits commensurate antiferromagnetism with ordered moments of $2.5\,\mu_\mathrm{B}$/f.u. below $T_\mathrm{N} \sim 20\,\mathrm{K}$ and fluctuating moments of $\sim 5.4\,\mu_\mathrm{B}$/f.u. in its paramagnetic regime [200–202]. In combination with the large magnetization observed in high fields, $3.5\,\mu_\mathrm{B}$/f.u. at 45 T, the commensurate structure suggests a rather localized character of the magnetism in this compound [111].

Known $3d$-based antiferromagnets are presently limited to Mn$_3$Si and CuMnSb. In contrast, the putative evidence for antiferromagnetism in Cu$_2$MnSb [203] may indeed be attributed to an CuMnSb impurity phase [112]. The antiferromagnetism in Fe$_2$VSi [204] seems to be related to a tetragonal distortion [205] or disorder [206]. For Mn$_3$Si, also written as $\mathrm{Mn}_2^{\mathrm{II}}\mathrm{Mn}^{\mathrm{I}}\mathrm{Si}$, Néel temperatures between 21 K and 26 K were reported, presumably due to differing compositions. Below T_N, a complex incommensurate helical structure propagates along the crystalline $\langle 111 \rangle$ axes, where $\boldsymbol{q} = 0.425\,\boldsymbol{q}_{111}$ and $q_{111} = 2\pi\sqrt{3}/a$ [108]. Higher harmonics emerge below 9 K [207]. The Mn^{I} and $\mathrm{Mn}^{\mathrm{II}}$ sites carry ordered moments of $1.7\,\mu_\mathrm{B}$ and $0.2\,\mu_\mathrm{B}$, respectively [108]. The structure is turned commensurate by $\sim 10\,\%$ substitutional doping of chromium on the Mn^{I} sites or iron on the $\mathrm{Mn}^{\mathrm{II}}$ sites [208, 209]. Density functional theory calculations indicate that the magnetic structure in Mn$_3$Si arises from a competition between direct antiferromagnetic interaction of the Mn^{I} moments and indirect ferromagnetic interaction of the same moments mediated by the $\mathrm{Mn}^{\mathrm{II}}$ sublattice [210]. The incommensurate nature of the order, its high stability with respect to fields up to 50 T [111, 169, 211], as well the magnetic excitations [212–214] and transport properties [215] in Mn$_3$Si consistently suggest an itinerant character of the magnetism. The nearly integral moment per unit cell ($\sim 2.1\,\mu_\mathrm{B}$/f.u.) in combination with calculations of the density of states hint towards possible half-metallicity [109, 216, 217]. Single crystals have been prepared via the Bridgman method [108], optical float-zoning [65], and induction-heated float-zoning [218].

2.2.2 Introduction to CuMnSb

At room temperature CuMnSb crystallizes in the cubic $C1_b$ half-Heusler structure with a lattice constant $a = (6.07 \pm 0.02)\,\text{Å}$ [219, 220]. With increasing temperature around 480 °C a volume decreases of $\sim 1.5\,\%$ is accompanied by an increase of the electrical resistivity by a factor of two [221, 222]. These observations may be related to an order-disorder transition where, e.g., some atomic sites in the empty sublattice get occupied. At a comparably low temperature of $T_m = 793\,°\mathrm{C}$ the compound melts.

In the late 1960s, CuMnSb was identified as maybe the first example of antiferromagnetic order in a Heusler compound [223]. At low temperatures, a commensurate structure was found with ordered moments of $(3.9 \pm 0.1)\,\mu_\mathrm{B}$/f.u., $\boldsymbol{q} = 0.5\,\boldsymbol{q}_{111}$, and $q_{111} = 2\pi\sqrt{3}/a$ [224]. Here, manganese moments oriented along a $\langle 111 \rangle$ direction align ferromagnetically within the corresponding $\langle 111 \rangle$ plane. These planes, in turn, couple antiferromagnetically with their neighboring planes. The studies by Bœuf *et al.* [112], Endo [183], and Helmholdt *et al.* [199] reported varying values of the Néel temperature T_N (50 K, 55 K, and 62 K), of the fluctuating moment m_eff ($6.3\,\mu_\mathrm{B}$/f.u.,

$5.6\,\mu_B$/f.u., and $5.2\,\mu_B$/f.u.), as well as of the Curie-Weiss temperature Θ_{CW} (-250 K, -160 K, and -120 K). These discrepancies presumably are caused by small differences between the compositions of the samples studied. In any case, the value of Θ_{CW} clearly exceeds T_N which hints towards a possible influence of geometric frustration. In the metallic system CuMnSb, the latter may be induced by disorder as corroborated by the large residual resistivity $\rho_0 \sim 50\,\mu\Omega$cm and the corresponding residual resistivity ratio of about 4 [112, 221, 225, 226]. Such values are not uncommon for Heusler compounds and characteristic for the presence of considerable amounts of disorder. In Ref. [112] it was also shown that T_N increases as a function of pressure by $\sim$0.4 K/kbar.

As already pointed out by Endo in 1970, in arc-melted samples prepared from stoichiometrically weighted educts the susceptibility usually exhibits a broad maximum around 200 K [183]. He attributed this anomaly to the presence of an impurity phase, namely Mn_2Sb or copper-doped $Mn_{2-x}Cu_xSb$ [227]. Mn_2Sb crystallizes in the tetragonal $C38$ structure with the space group $P4/nmm$ and orders ferrimagnetically below $T_C = 550$ K [228]. Its anisotropy changes from an easy c-axis at high temperatures to an easy basal plane at $T = 240$ K resulting in an increased susceptibility. Endo also demonstrated that an initial antimony excess of a few percent is sufficient to suppress the formation of the Mn_2Sb impurity phase while keeping the lattice constant of the host unchanged.

Despite these metallurgical complexities, a qualitatively consistent picture of the antiferromagnetism in CuMnSb may be drawn. The result, however, combines properties that are believed to be the hallmarks of either local-moment or itinerant magnetism [109, 112]. Large ordered moments that are only slightly smaller than the fluctuating moments and, in particular, the commensurate magnetic structure clearly indicate local-moment magnetism. In contrast, the typical metallic resistivity as well as the high stability of the antiferromagnetic order in magnetic fields, similar to Mn_3Si, are characteristics of itinerant magnetism, cf. Ref. [111] (see also CrB_2 in Sec. 2.1.4). Half-metallicity, finally, is suggested by the integer value of the order moment and the recovery of ferromagnetic order by doping only a few percent of nickel or palladium on the copper sites [183, 229]. The latter is expected for a half-metallic antiferromagnet as it is, in fact, a delicately balanced ferrimagnet. Yet, electronic structure calculations, that reproduce the antiferromagnetically ordered moments of $4\,\mu_B$/f.u., hint towards a small, semi-metallic (not to be confused with half-metallic) density of states at the Fermi level with a finite minority band occupation [182]. Moreover, a large electron mass enhancement is predicted due to spin fluctuations while the hole masses stay normal [182, 230].

So far, only polycrystalline samples were studied in the literature, mostly prepared via arc melting. The properties of Heusler compounds, however, are in general very sensitive to various forms of disorder and CuMnSb in particular tends to the formation of the ferrimagnetic impurity phase Mn_2Sb. Central goal of the study reported in the following thereby was to identify the intrinsic properties of phase-pure single crystals of CuMnSb. We utilized optical float-zoning to prepare the first bulk single crystals, one from feed rods with stoichiometric composition and on from feed rods with an antimony excess of 0.035. A detailed metallurgical characterization revealed that even single-crystalline samples from the first ingot, in the following referred to as CuMnSb-A, contain a tiny volume fraction of Mn_2Sb whereas phase purity was confirmed for the second ingot, in the following referred to as CuMnSb-B. Measurements of the thermodynamic bulk and transport properties for both specimens essentially confirm the peculiar combination of magnetic properties extracted from the measurements on polycrystals. In addition, a second transition at $T^* \sim 30$ K is established within the antiferromagnetically ordered state of CuMnSb-B.

Before presenting the abovementioned results in detail, however, we briefly summarize the findings of first elastic and inelastic neutron scattering experiments that are readily permitted in CuMnSb due to its large magnetic moments. Measurements carried out by Alexander Regnat in collaboration with Björn Pedersen and Anatoliy Senyshyn on the single crystal diffractometer RESI at FRM II for both CuMnSb-A and CuMnSb-B indeed are consistent with the commensurate spin order reported by Forster *et al.* in Ref. [224]. Additionally, in CuMnSb-B below T^* peaks of magnetic intensity emerge on commensurate positions where vanishing intensity is expected for magnetic moments along the $\langle 111 \rangle$ axes. This intensity may, for instance, be attributed to a canting of the magnetic structure by $\sim 10^\circ$ where the microscopic origin of such a canting is yet to be resolved. Inelastic data from the thermal neutron triple-axis spectrometer EIGER at the Paul Scherrer Institut (PSI) measured by Georg Brandl on CuMnSb-B revealed that with decreasing temperature a gap develops at T_N and reaches $\sim 2.5\,\mathrm{meV}$ at low temperatures. No anomalies are observed around T^*. For finite momentum k, the magnonic excitations evolve rather isotropic. Contributions of strong magnetic fluctuations remain visible far above T_N, i.e., at least up to 150 K.

2.2.3 Single crystal growth

For the single crystal growth of CuMnSb we utilized the preparation chain as described in Sec. 1. The tendency of CuMnSb to form the impurity phase Mn_2Sb, however, demanded an especially careful metallurgical characterization. Even tiny amounts of the ferrimagnetic Mn_2Sb, below the usual detection limit of energy dispersive x-ray spectroscopy or conventional powder x-ray diffraction, may delicately influence the behavior of the antiferrmagnetic host. Thus, we combined powder x-ray diffraction with long exposure times and measurements of the magnetic as susceptibility to confirm the phase purity of our CuMnSb specimens.

The single crystal growth of CuMnSb started from 6N copper pieces, pre-cast 4N manganese rods, and 6N antimony shots. First, polycrystalline feed rods were prepared in the inductively heated rod casting furnace, cf. Figs. 2.14(a) and 2.14(b). Subsequently, these rods were optically float-zoned at a rate of 5 mm/h in a high-purity argon atmosphere of 2.5 bar while seed and feed rod were counter-rotating at 6 rpm. The process was carried out two times, once with a stoichiometric initial composition denoted as OFZ75, see Fig. 2.14(c), and once with an antimony excess of 0.035 yielding OFZ98, see Fig. 2.14(d). Both growth attempts resulted in clean metallic rods without facets. Presumably due to the relatively low melting temperature of $\sim 800\,^\circ\mathrm{C}$, no evaporation losses were observed during the growth process. In both ingots, the last $\sim 15\,\mathrm{mm}$ of the float-zoned material were identified as single crystals across the whole cross-section of the rod by means of x-ray Laue diffraction, where typical patterns are shown in Figs. 2.14(e) through Figs. 2.14(g). Data from the neutron single crystal diffractometer RESI confirmed the single crystallinity of the investigated specimens. In the following the single crystals prepared from OFZ75 and OFZ98 will be referred to as CuMnSb-A and CuMnSb-B, respectively.

We begin our account for the detailed metallurgical characterization of CuMnSb with the growth from stoichiometric feed rods. Here, on a polished surface of the single-crystal ingot no impurity phases were detected by means of energy dispersive x-ray spectroscopy carried out by Saskia Gottlieb-Schönmeyer in collaboration with Florian Kortmann at the Radiochemie München. The corresponding scanning electron pictures are shown in Figs. 2.14(h) through 2.14(j). A corresponding investigation on arc-melted polycrystals by Bœuf *et al.* in Ref. [112] revealed $\sim 1\,\%$ of copper and $\sim 0.1\,\%$ of a manganese rich (Mn,Sb)-phase, presumably Mn_2Sb. Similar to the latter study, standard x-ray powder diffraction performed on both as-cast and

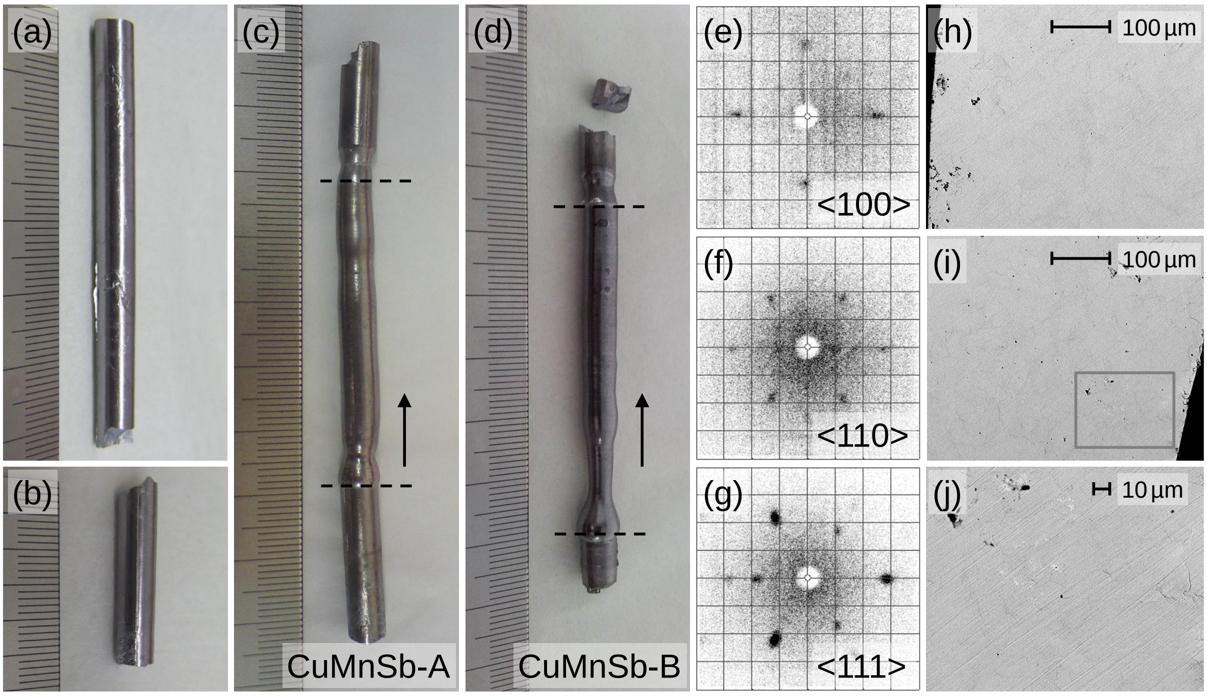

Figure 2.14: Single crystal growth of CuMnSb. (a) Float-zoning feed rod prepared in the inductively heated rod casting furnace. (b) Float-zoning seed rod. (c) CuMnSb after optical float-zoning using stoichiometric feed rods (OFZ75), also referred to as CuMnSb-A. (d) CuMnSb after optical float-zoning using feed rods with an antimony excess of 0.035 (OFZ98), also referred to as CuMnSb-B. The vertical dashed lines indicate the beginning and the end of the float-zoning. Growth direction was from right to left. The last ∼15 mm of both growths yielded single crystals across the whole cross-section. (e)–(g) Laue x-ray diffraction pattern of OFZ75 along a $\langle 100\rangle$, a $\langle 110\rangle$, and a $\langle 111\rangle$ axis. Fourfold, twofold, and threefold symmetries, respectively, are observed as expected for a cubic crystal structure. (h)–(j) Scanning electron microscope pictures of a polished surface of the single-crystal ingot of OFZ75. Panel (j) displays a blow-up of panel (i).

float-zoned samples shows within the resolution limit phase-pure CuMnSb in the $C1_b$ half-Heusler structure, see Figs. 2.15(a) and 2.15(c). These patterns were recorded on a Siemens D5000 in reflection geometry with counting times of 15 s per data point.

In contrast, if we expose the samples for 600 s per data point and focus on angles where Bragg peaks are expected from the tetragonal $C38$ compound Mn_2Sb but not from the cubic CuMnSb, tiny fractions of impurity phases are resolved. These data are depicted in blue in Figs. 2.15(b) and 2.15(d), where the peak intensities are smaller than the noise floor of the standard diffractogram (open gray circles). To the best of our knowledge, for the first time these data directly identify crystalline Mn_2Sb as an impurity phase in CuMnSb. Besides the peaks that may clearly be attributed to Mn_2Sb, further maxima arise that are marked by black arrows and probably stem from further unidentified impurity phases. Though we refrain from a full refinement of the data, we estimate that the volume fraction of the impurity phases is below 1 %. Float-zoning distinctively diminishes the concentrations of all impurity phases, but

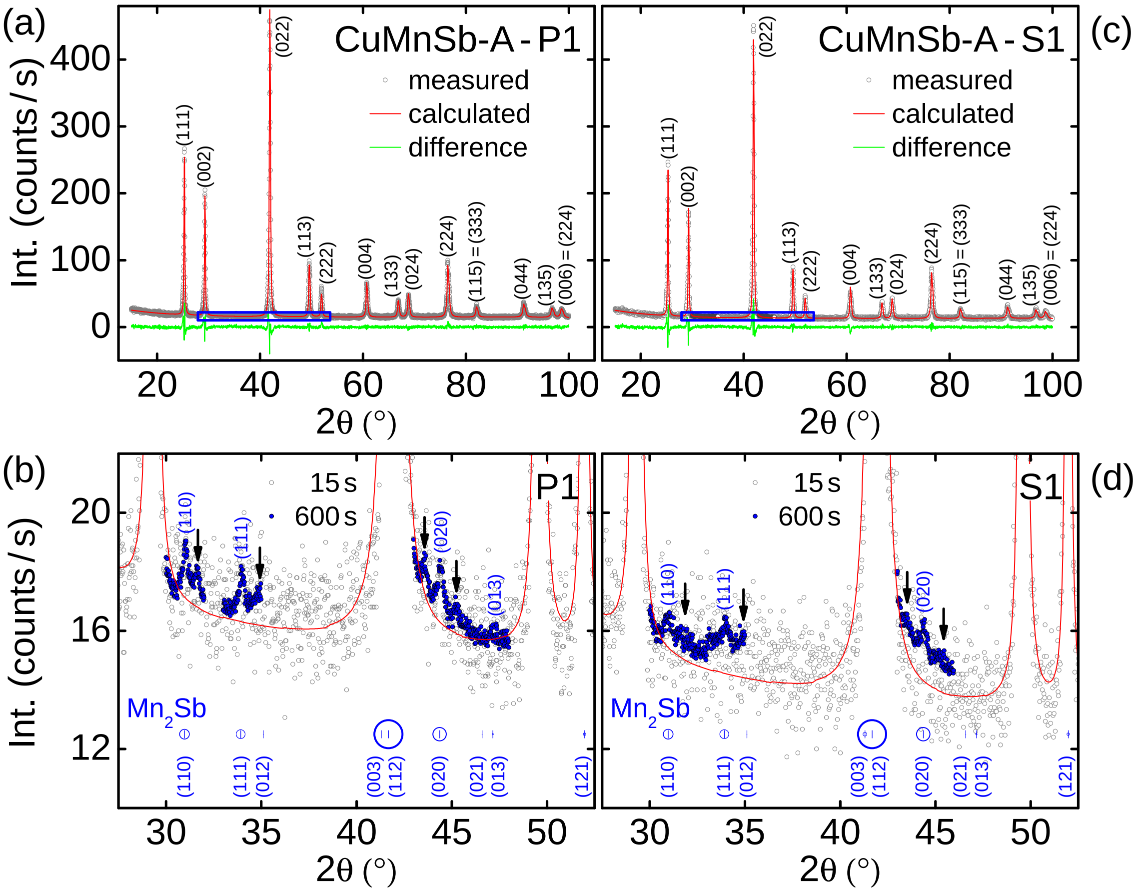

Figure 2.15: X-ray powder diffraction data of CuMnSb prepared from a stoichiometric initial weight. (a) As-cast samples already form essentially phase-pure in the $C1_b$ half-Heusler structure. Also shown are data calculated with the Rietveld method (red) and the difference of measured and calculated data (green). (b) High exposure time data of an as-cast specimen. The area depicted corresponds to the blue box in panel (a). The blue vertical lines mark expected peak positions for $MnSb_2$, the circles indicate their intensity. Tiny amounts of Mn_2Sb (blue) and further unidentified impurity phases (black arrows) are present. (c) Float-zoned samples also crystallize in the $C1_b$ half-Heusler structure. (d) High exposure time data of a float-zoned specimen.

in particular Mn_2Sb remains present, potentially in form of precipitates.

As introduced above, the ferrimagnetic order in Mn_2Sb changes its easy axis around 240 K. The resulting magnetic susceptibility probes very sensitively the presence of this impurity phase. Therefore, we have measured the zero-field ac susceptibility in a Quantum Design physical properties measurement system at an excitation frequency of 911 Hz and with an excitation amplitude of 1 mT. Figs. 2.16(a) and 2.16(b) show the real and the imaginary part of the ac susceptibility as a function of temperature for various polycrystalline (P) and single-crystalline (S) specimens of CuMnSb. In all samples studied, an anomaly around $T_N \sim 50$ K indicates the onset of antiferrmagnetic order, which will be discussed in further detail in Sec. 2.2.4. In

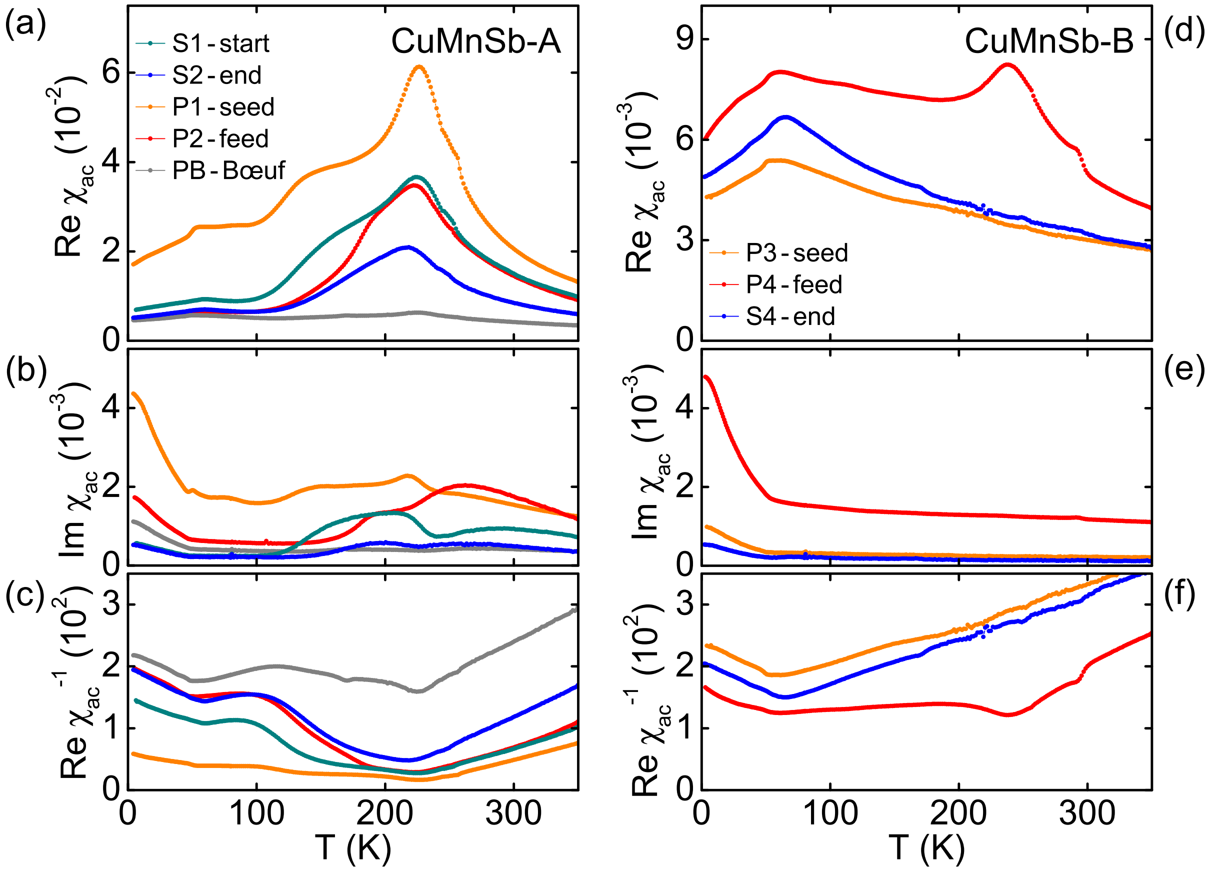

Figure 2.16: Temperature dependence of the ac susceptibility for polycrystalline and single-crystalline samples of CuMnSb. (a) Real part of CuMnSb-A. For all samples studied an anomaly around $T_{\mathrm{N}} \sim 50\,\mathrm{K}$ marks the Néel transition of CuMnSb. The broad maximum around 200 K may be attributed to a small volume fraction of the ferrimagnetic impurity phase $\mathrm{Mn_2Sb}$ which is reduced but still present in float-zoned specimens. (b) Imaginary part of CuMnSb-A. (c) Inverse susceptibility of CuMnSb-A. The intrinsic Curie-Weiss behavior of CuMnSb is masked by the contributions from $\mathrm{Mn_2Sb}$. (d) Real part of CuMnSb-B. Note the different scale compared to panel (a). No signatures are observed around 200 K. For comparison, data taken on a sample prepared for Ref. [112] is shown (gray). (e) Imaginary part of CuMnSb-B. (f) Inverse susceptibility of CuMnSb-B. Curie-Weiss behavior is observed above T_{N}.

the following, we concentrate on the behavior at higher temperatures, i.e., $T > T_{\mathrm{N}}$, where the susceptibility is dominated by a broad maximum.

In the polycrystalline samples (P1, P2) with nominally stoichiometric composition the maximum peaks at ~225 K and additional shoulders emerge on its low-temperature (~150 K) and its high-temperature side (~250 K). These features may be attributed to, potentially slightly doped, $\mathrm{Mn_2Sb}$ or further magnetically ordering impurity phases. In float-zoned specimens (S1, S2) the absolute value of the susceptibility and hence the volume fraction of the impurity phases decreases. Furthermore, in particular at the end of the single-crystalline ingot (S2), the shoulders are largely suppressed whereas a peak centered at ~220 K remains. This observation is consistent with our x-ray diffraction data, where float-zoning reduces the amount of Mn_2Sb and largely suppresses all further impurity phases. A comparison of the beginning (S1) and the final part (S2) of the ingot suggests that the phase purity of CuMnSb improves during the course of the float-zoning. The maximum at $\sim$220 K, however, still indicates the presence of a sizeable amount of Mn_2Sb that, for instance, masks the intrinsic Curie-Weiss-like linear temperature dependence expected for CuMnSb above T_N, see 2.16(c).

In contrast, as pointed out by Endo [183], an antimony excess of a few percent in the initial composition drastically reduces the formation of Mn_2Sb leaving the Néel transition as the only salient feature in the temperature dependence of the susceptibility, see Figs. 2.16(d) through 2.16(f). While one of the as-cast polycrystals (P4) exhibits comparably small maxima at 240 K and 290 K, the other polycrystalline (P3) as well as the single-crystalline (S4) sample exhibit essentially no parasitic contributions. For the study of the low-temperature properties of the host compound CuMnSb presented below, we focus on two samples: (i) the single-crystalline sample from CuMnSb-A with the smallest volume fraction of impurity phases (S2) and (ii) the single-crystalline sample from CuMnSb-B (S4). The latter is assumed to be free of (magnetic) impurity phases.

For comparison, we also show data from a polycrystalline sample (PB) out of the batch studied by Bœuf *et al.* in Ref. [112]. It displays a relatively low absolute value of the susceptibility indicating small impurity phase concentrations, but a qualitative temperature dependence that is located between our polycrystalline samples P1 and P4. A possible explanation thereby is the evaporation of manganese during the arc melting which results in a small shift of the composition of the originally stoichiometric sample.

Taken together, our detailed metallurgical characterization demonstrates that special care has to be taken when investigating the intrinsic properties of the antiferromagnet CuMnSb. The tendency to form various impurity phases, in particular Mn_2Sb, implies that the ternary compound CuMnSb forms through a slightly peritectic reaction. This assumption is corroborated by the lack of grain selection during the first $\sim$30 mm of both float-zoning processes. The latter indeed may have been self-flux traveling solvent growths that required the corresponding time to adjust the composition of the molten zone. We note that an investigation of the metallurgical phase diagram of the ternary copper-manganese-antimony system, for instance by means of differential thermal analysis, would allow to clarify how CuMnSb is crystallizing. Such a study, however, lies beyond the scope of this thesis.

2.2.4 Low-temperature properties

In the following we present our study of the low-temperature properties of single-crystalline CuMnSb by means of magnetization, specific heat, electrical resistivity, Hall effect, and thermal transport. For both single crystals available, CuMnSb-A and CuMnSb-B, the data show a peculiar combination of magnetic properties that are believed to be the hallmarks of either local or itinerant antiferromagnetism, largely consistent with reports on polycrystalline material. Moreover, in the bulk and transport properties of CuMnSb-B we identify previously unrecognized signatures that may be related to a canting of the magnetic structure as implied by first neutron scattering results. It is yet unresolved, whether the intrinsic behavior of CuMnSb is best accounted for by our single crystal CuMnSb-A, which still contains a tiny volume fraction of Mn_2Sb, or by our single crystal CuMnSb-B, where the microscopic distribution of the excess antimony is unknown. Thus, we address the properties of both specimens in parallel.

Experimental details and outline of the results

After identifying the single-crystalline sections of the float-zoned crystals, the ingots were oriented by means of x-ray Laue diffraction. Discs with their axis along a crystalline $\langle 110 \rangle$ direction were cut from the end of the ingots of CuMnSb-A (labeled S2) and CuMnSb-B (labeled S4). From these discs bars of $6 \times 1 \times 1\,\mathrm{mm}^3$ with $\langle 100 \rangle \times \langle 110 \rangle \times \langle 110 \rangle$ orientations were prepared for measurements of the magnetization, the susceptibility, the specific heat, and the thermal conductivity. For the study of the electrical resistivity and the Hall effect platelets were cut from the same discs. They had a size of $6 \times 1 \times 0.2\,\mathrm{mm}^3$ with $\langle 100 \rangle \times \langle 110 \rangle \times \langle 110 \rangle$ orientations for field along $\langle 110 \rangle$ and current along $\langle 100 \rangle$ as well as of $3 \times 1 \times 0.2\,\mathrm{mm}^3$ with $\langle 110 \rangle \times \langle 100 \rangle \times \langle 110 \rangle$ for field along $\langle 100 \rangle$ and current along $\langle 110 \rangle$. Demagnetization effects were neglected in CuMnSb due to the small absolute value of the magnetization.

The magnetization was measured in a 9 T Oxford Instruments vibrating sample magnetometer with an oscillation frequency of 62.35 Hz and an amplitude of roughly 1 mm by Alexander Regnat as part of his Ph.D. thesis. The ac susceptibility was detected in a 9 T Quantum Design physical properties measurement system (PPMS) using a excitation frequency of 911 Hz and an excitation amplitude of 1 mT. The specific heat was measured in a 14 T PPMS with a conventional small-pulse method using heat pulses of 0.5 % of the current sample temperature. For measurements of the thermal conductivity, as carried out by Marlies Gangl as part of her master's thesis [87], flattened silver wires of 0.25 mm diameter were glued onto the bar-shaped samples in a four-terminal configuration (heater, hot thermometer, cold thermometer, cold bath) using silver epoxy. Utilizing the thermal transport option of the 14 T PPMS heat pulses of ~3 % of the current temperature were applied, while the temperature was continuously swept from 300 K to 2 K at a rate of 0.5 K/min. Measurements of the electrical resistivity and the Hall effect were performed by Alexander Regnat as part of his Ph.D. thesis in a 14 T Oxford Instruments cryostat. For this purpose, gold wires of 25 µm diameter were spot welded onto the samples in a standard six-terminal configuration. A digital lock-in technique was used at an excitation frequency of 22.08 Hz and at low excitation currents. The electrical resistivity, ρ_{xx}, and the Hall resistivity, ρ_{xy}, were inferred from a symmetrization and an anti-symmetrization of the measured longitudinal and transverse voltage pick-up, respectively. All geometry factors were determined from digital photographs recorded with an optical microscope. A conservative estimate of the resulting error yields 25 %.

The presentation of our results is organized as follows. Data are shown for a nominally stoichiometric sample, CuMnSb, and for a sample with antimony excess, $\mathrm{CuMnSb}_{1.035}$. We begin with the bulk properties, i.e., magnetization and specific heat, in fields up to 14 T. Subsequently, the transport properties, namely the electrical resistivity, the Hall effect, and the thermal conductivity, are addressed. We conclude with a short summary of our findings.

Magnetization and specific heat

We start our account for the low-temperature properties of CuMnSb with the magnetization as a function of temperature. As shown in Fig. 2.17(a), for all field values and field directions studied the magnetization in CuMnSb-B shows qualitatively identical behavior. With decreasing temperature the magnetization increases monotonically until it reaches its maximum value at the Néel temperature $T_{\mathrm{N}} = 55\,\mathrm{K}$. A further decrease of the temperature reduces the magnetization again. An additional shoulder around $T^{*} \approx 30\,\mathrm{K}$ arises only in CuMnSb-B and will be discussed in detail below. The absolute values of the magnetization are relatively small, as typical for an antiferromagnet, but not as tiny as in the weak itinerant antiferromagnet CrB_2, cf. Sec. 2.1.4.

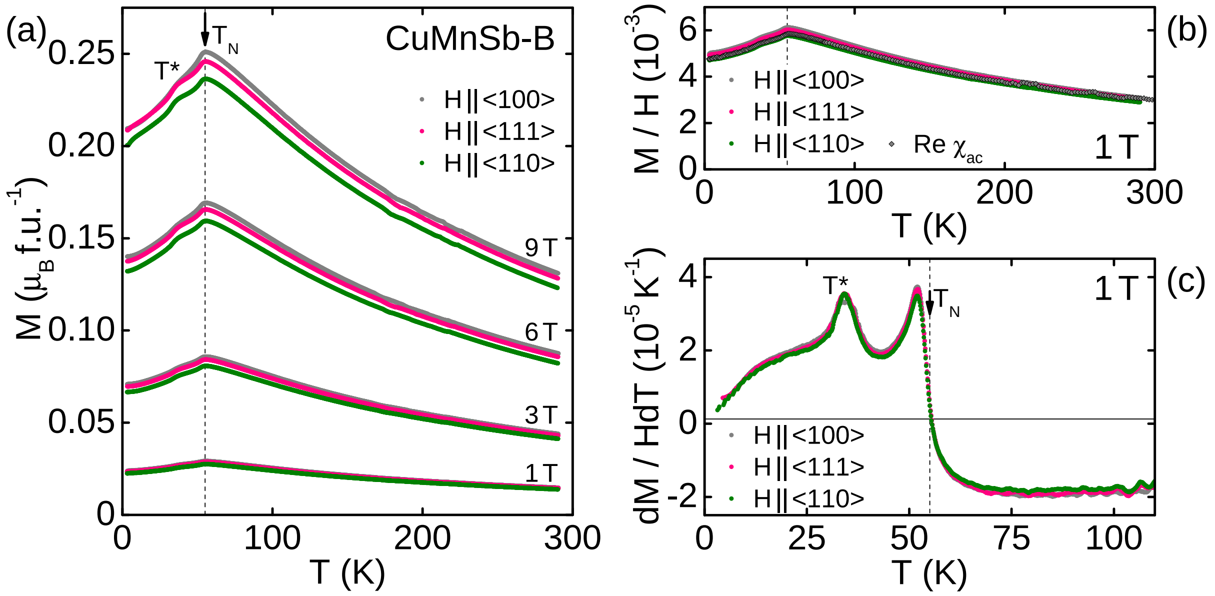

Figure 2.17: Magnetization of CuMnSb-B for field along the major crystallographic axes. (a) Magnetization as a function of temperature in fields up to 9 T. Qualitatively similar behavior is observed for all field values and directions studied. The anisotropy is of the order of ∼5 %. (b) Normalized magnetization, M/H, for an applied field of 1 T as an approximate of the susceptibility dM/dH. For comparison the real part of the ac susceptibility, Re χ_{ac}, is shown for field along a ⟨100⟩ axis (diamonds). (c) Temperature derivative of the normalized magnetization. Essentially isotropic behavior is observed.

For all temperature and field values, the magnetization is largest for field along a ⟨100⟩ direction while it is smallest for field parallel to a ⟨110⟩ axis. The difference, however, is in the order of ∼5 % and hence small, as expected for a cubic compound. The anisotropy in CuMnSb-A is comparable (not shown).

The influence of the almost linear increase of the magnetization as a function of field may be compensated by plotting the normalized magnetization M/H, see Fig. 2.17(b). Due to the linear field dependence this quantity is also a proper estimate of the susceptibility dM/dH. The anomalies at low temperatures eventually are best resolved in the derivative with respect to the temperature, dM/HdT, that is depicted in Fig. 2.17(c). However, neither the Néel transition at T_{N}, which is defined as zero crossing of dM/HdT, nor the anomaly at T^* are dependent on the field direction. Thus, in the following we concentrate on the normalized magnetization for field along the ⟨100⟩ axis.

In CuMnSb-A, see Fig. 2.18(a), with increasing temperature the normalized magnetization, M/H, exhibits a cusp at $T_{\mathrm{N}} = 49$ K, consistent with the value from Bœuf *et al.* [112]. Above T_{N} in small fields (1 T) a broad maximum is observed that may be attributed to the impurity phase Mn$_2$Sb. With increasing field the absolute value of M/H is reduced and the maximum at high temperatures is gradually suppressed until in large fields (9 T) an essentially Curie-Weiss-like temperature dependence of M/H is recovered. We extract a fluctuating moment $m_{\mathrm{eff}} \approx 3.4\,\mu_{\mathrm{B}}$/f.u. and a Curie-Weiss temperature $\Theta_{\mathrm{CW}} \approx -300$ K. In contrast, the cusp in normalized magnetization of CuMnSb-B, cf. Fig. 2.18(d), is located at $T_{\mathrm{N}} = 55$ K, consistent

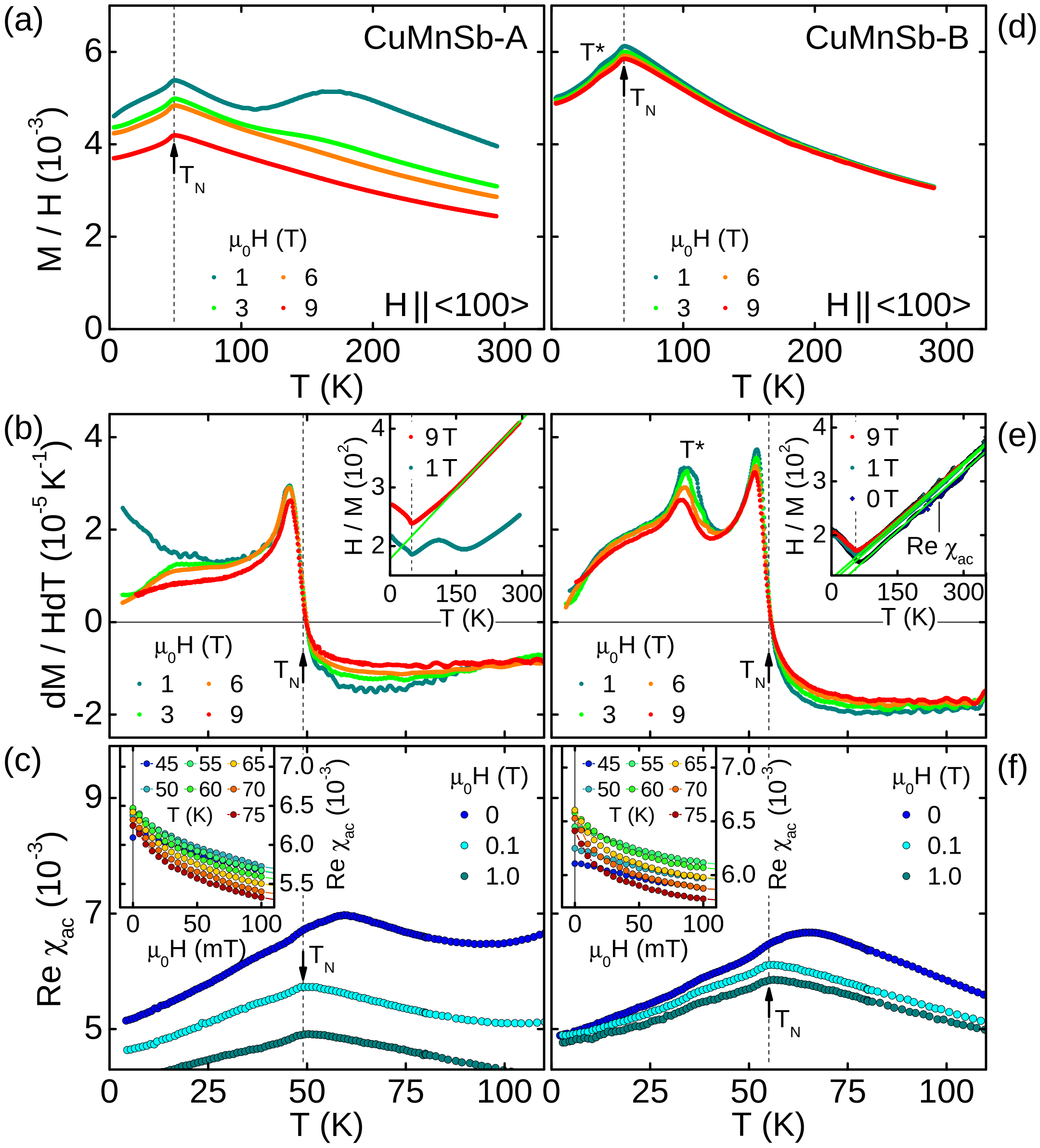

Figure 2.18: Magnetization and susceptibility of CuMnSb. (a) Normalized magnetization, M/H, of CuMnSb-A as a function of temperature. In high fields a cusp at $T_\mathrm{N} = 49\,\mathrm{K}$ dominates. The broad maximum above T_N in smaller fields stems from the impurity phase Mn_2Sb. (b) Temperature derivative of M/H for CuMnSb-A. The inset shows the inverse normalized magnetization. The solid green lines are Curie-Weiss fits for $T \gg T_\mathrm{N}$. (c) Real part of the ac susceptibility of CuMnSb-A. In zero-field a change of slope at T_N is superimposed by a maximum at $T_\mathrm{N} + 10\,\mathrm{K}$. The inset shows the corresponding field dependence and the suppression of the maximum at $\sim$50 mT. (d) Normalized magnetization, M/H, of CuMnSb-B. A cusp at $T_\mathrm{N} = 55\,\mathrm{K}$ dominates in all fields studied. (e) Temperature derivative of M/H for CuMnSb-B. In addition to T_N, a second anomaly is present around $T^* \approx 30\,\mathrm{K}$. (f) Real part of the ac susceptibility of CuMnSb-B.

with the value reported by Endo [183]. Above T_N, a Curie-Weiss-like temperature dependence is observed for all fields studied. Independent from the magnetic field applied, we derive $m_\mathrm{eff} = (3.95 \pm 0.05)\,\mu_\mathrm{B}/\mathrm{f.u.}$ and $\Theta_\mathrm{CW} = -(160 \pm 8)\,\mathrm{K}$. From the ac susceptibility in zero field we extract $m_\mathrm{eff} = 3.99\,\mu_\mathrm{B}/\mathrm{f.u.}$ and $\Theta_\mathrm{CW} = -132\,\mathrm{K}$. For all samples investigated, the fluctuating moments are slightly smaller than the literature values (between $6.3\,\mu_\mathrm{B}/\mathrm{f.u.}$ and $5.2\,\mu_\mathrm{B}/\mathrm{f.u.}$), while the Curie-Weiss temperatures are essentially consistent with the large spread of values reported in the literature (between -250 K and -120 K), cf. Refs. [112, 183, 199].

In our phase-pure single crystal CuMnSb-B the size of the fluctuating moment exactly corresponds to the ordered moment as detected in neutron scattering experiments [224] strongly favoring a local-moment scenario of the antiferromagnetism. The discrepancy with respect to the single crystal CuMnSb-A may be related to its remaining volume fraction of impurity phases. The contributions of the latter may alter the detailed temperature dependence of the magnetic susceptibility even in high fields and presumably are also responsible for the large spread of values reported in literature. A typical local-moment scenario in CuMnSb-B, however, is questioned by the high stability of the magnetic order in applied fields, which is generally associated with itinerant magnets. Furthermore, the value of the ratio $f = -\Theta_\mathrm{CW}/T_\mathrm{N} \approx 3$ hints towards a possible role of geometric frustration. The latter may, for instance, be caused by various forms of disorder, which in Heusler compounds are commonly present even in the highest-quality single crystals available.

Now, we compare the temperature derivatives of the normalized magnetization, $\mathrm{d}M/H\mathrm{d}T$, for CuMnSb-A and CuMnSb-B shown in Figs. 2.18(b) and 2.18(e). The signature of the Néel transition is qualitatively similar for both specimens, but a second peak appears around $T^* \approx 30\,\mathrm{K}$ only in CuMnSb-B. With increasing field, the height of the peak decreases whereas its temperature position hardly shifts. As explained above, first neutron scattering results hint towards a canting of the magnetic structure at T^*, where our magnetization data exclude any sizeable ferromagnetic net moment.

Another puzzling property emerges in the ac susceptibility as a function of temperature in small fields as depicted in Figs. 2.18(c) and 2.18(f) for CuMnSb-A and CuMnSb-B, respectively. While in zero field at T_N only a weak change of slope is observed, the susceptibility reaches a rather pronounced maximum about 10 K above T_N. Already tiny fields of ~50 mT are sufficient to quench this additional contribution, cf. data for 0.1 T, and lead to a temperature dependence in the susceptibility that in turn hardly changes up to the highest fields studied. The additional contribution also results in a shift of the inverse susceptibility, see the inset of Fig. 2.18(e), where the zero-field data exhibit a similar slope but a lower absolute value of Θ_CW when compared to data recorded in field. Qualitatively similar observations are made for polycrystalline and single-crystalline samples of both CuMnSb-A and CuMnSb-B suggesting that the maximum of the ac susceptibility around $T_\mathrm{N} + 10\,\mathrm{K}$ is intrinsic. Our finding may also explain the high Néel temperature $T_\mathrm{N} = 62\,\mathrm{K}$ reported by Helmholdt *et al.* [199]. No corresponding anomalies are found at $T_\mathrm{N} + 10\,\mathrm{K}$ in the other quantities measured in zero field (specific heat, electrical resistivity, thermal conductivity, elastic and inelastic neutron scattering), as will be presented below.

From the first inelastic neutron scattering data measured at EIGER, we know that at least in CuMnSb-B magnetic fluctuations persist up to temperatures well above T_N. Contributions from these fluctuations may, in general, result in an enhanced susceptibility. This explanation, however, is questioned by the fact that fields of ~50 mT are already enough to suppress the additional susceptibility, in particular when taking into account the stability of the magnetic order up to the highest fields studied. A typical glassy state may also be excluded as the

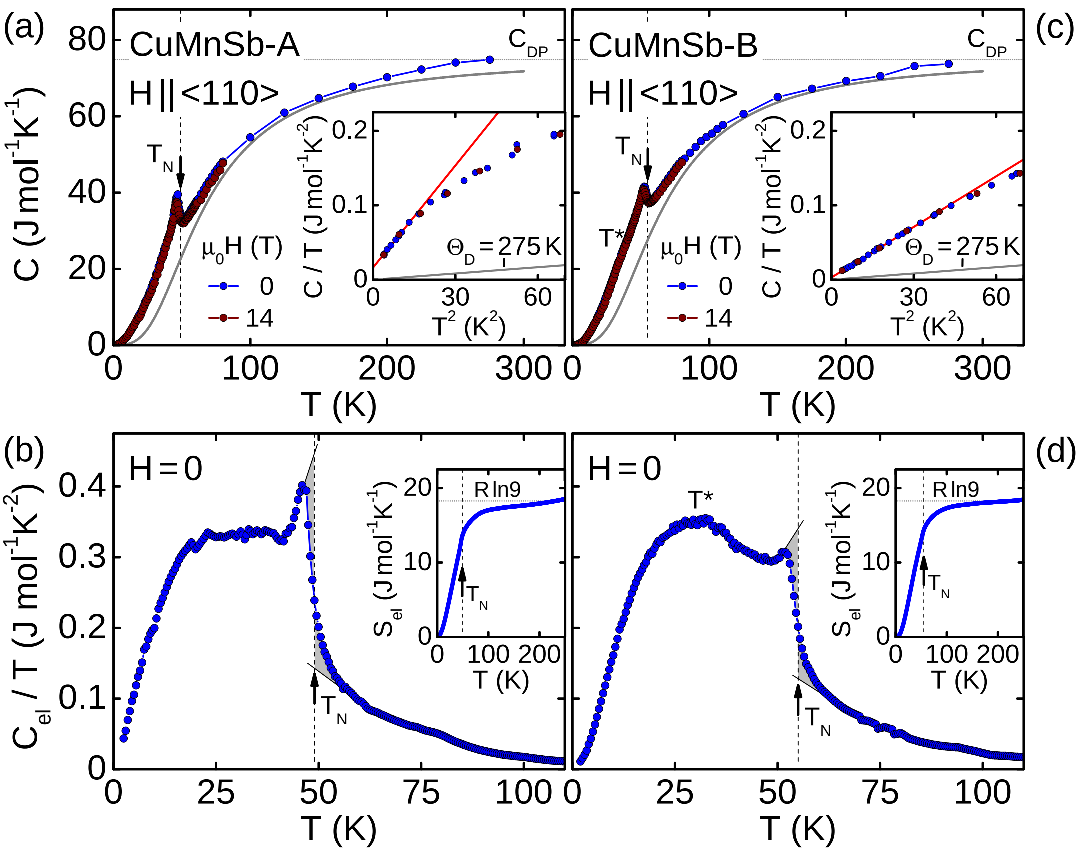

Figure 2.19: Specific heat of CuMnSb. (a) Specific heat of CuMnSb-A as a function of temperature. A pronounced lambda anomaly is present at T_{N}. Also shown is a Debye model with $\Theta_{\mathrm{D}} = 275\,\mathrm{K}$ (solid gray line). The Dulong-Petit limit corresponds to $9R = 74.83\,\mathrm{J/mol\,K}$. The inset depicts the low-temperature extrapolation of the specific heat divided by temperature, C/T, over a quadratic temperature scale (solid red line). In fields up to 14 T essentially no changes are observed. (b) Electronic contribution to the specific heat of CuMnSb-A divided by temperature, C_{el}/T. The inset shows the electronic contribution to the entropy. (c) Specific heat of CuMnSb-B. (d) Electronic contribution to the specific heat of CuMnSb-B divided by temperature.

maximum lacks any pronounced dependency on the excitation frequency or the cooling and field history (not shown). Hence, the origin of increased susceptibility above T_{N} in small fields is yet unknown.

Now, we turn to the specific heat depicted in Fig. 2.19. The most salient feature is a clear lambda anomaly at the Néel transition indicating a second-order phase transition. An entropy conserving construction, cf. gray shading in Figs. 2.19(b) and 2.19(d), yields $T_{\mathrm{N}} = 49\,\mathrm{K}$ and $T_{\mathrm{N}} = 55\,\mathrm{K}$ for CuMnSb-A and CuMnSb-B in excellent agreement with our magnetization data. In a field of 14 T the transition temperatures decrease by at most $\sim 0.5\,\mathrm{K}$. This stability of the magnetic order is a characteristic of itinerant magnetism.

In the low-temperature limit, where lattice contributions may be neglected, we obtain surprisingly different Sommerfeld coefficients $\gamma_0 = 15.4\,\mathrm{mJ/mol\,K^2}$ and $\gamma_0 = 3.2\,\mathrm{mJ/mol\,K^2}$ for CuMnSb-A and CuMnSb-B, respectively. The value for CuMnSb-A is consistent with earlier reports on polycrystals [112, 230] and typical for d-electron systems with moderate or strong electronic correlations like the weak itinerant antiferromagnet CrB_2. The contribution from the small volume fraction of Mn_2Sb is below $0.3\,\mathrm{mJ/mol\,K^2}$ and hence negligible [231]. In stark contrast, the small value of γ_0 in CuMnSb-B is reminiscent of systems with weak or no electronic correlations such as the local-moment antiferromagnet MnB_2. For both samples fields up to 14 T do not influence γ_0. We note that glassy states, other than geometrically frustrated systems, in principle may lead to contributions that are constant in C/T [17, 232]. If the glassiness is caused by disorder, the larger value of γ_0 in CuMnSb-A implies a larger amount of disorder as consistent with the transport properties presented below. Still, while susceptibility data suggest the presence of geometrical frustration, at low temperatures we find no signs for glassiness. Taken together, the large discrepancy of γ_0 between CuMnSb-A and CuMnSb-B remains puzzling and is not reflected in other quantities.

With increasing temperature, lattice contributions to the specific heat gain importance. In both CuMnSb-A and CuMnSb-B they may be approximated by a Debye model with $\Theta_\mathrm{D} = 275\,\mathrm{K}$, where the Dulong-Petit limit at high temperatures is $9R = 74.83\,\mathrm{J/mol\,K}$ and R is the universal gas constant. After subtraction of this phonon contribution, the remaining specific heat divided by temperature, C_el/T, is shown in Figs. 2.19(b) and 2.19(d). Below the lambda anomaly at T_N, C_el/T possesses a rather unusual shape that may not be described by an exponential fit taking into account the formation a gap in the excitation spectrum. Instead, a plateau above $\sim$20 K in CuMnSb-A evolves into a broad maximum around $T^* \approx 30\,\mathrm{K}$ in CuMnSb-B where it may be related to the spin canting detected via neutron scattering. The presence of this plateau in CuMnSb-A indicates that a tendency towards a spin canting may already be present but is suppressed, for instance, by pinning due to the ferrimagnetic impurity phase Mn_2Sb.

Finally, we calculate the electronic contribution to the entropy, S_el, by numerically integrating C_el/T. Around T_N the largest part of entropy has been released and the slope of S_el distinctly changes. Still, contributions even well above T_N indicate the presence of spin fluctuations as consistent with our first inelastic neutron scattering data. At high temperatures, however, S_el for both CuMnSb-A and CuMnSb-B approaches $R\ln 9$ which may be anticipated for a state with localized moments of $4\,\mu_\mathrm{B}$.

Electrical resistivity, Hall effect, and thermal conductivity

The main results of the investigation of the thermodynamic bulk properties of CuMnSb-A and CuMnSb-B are corroborated by the transport data presented in the following. Figs. 2.20(a) and 2.20(d) show the temperature dependence of the electrical resistivity, ρ_{xx}, in zero field. Starting from a value of $\sim$150 µΩcm at room temperature, with decreasing temperature ρ_{xx} monotonically decreases as expected for a metal. At low temperatures ρ_{xx} saturates at a residual resistivity $\rho_0 = 45.2\,\mu\Omega\mathrm{cm}$ and $\rho_0 = 36.7\,\mu\Omega\mathrm{cm}$ for CuMnSb-A and CuMnSb-B, respectively. The residual resistivity ratio is 4.2 for both samples. These values of ρ_0 are comparatively high for transition metal compounds in general, but typical for Heusler compounds indicating the presence of, for instance, antisite disorder. Still, our values are smaller than all values reported in the literature [112, 221, 225, 226] hinting at a reduced defect concentration in our single-crystalline samples, in particular for CuMnSb-B.

The onset of antiferromagnetic order at T_N is accompanied by a distinct change of slope in both CuMnSb-A and CuMnSb-B. The latter is best resolved in the temperature derivative of

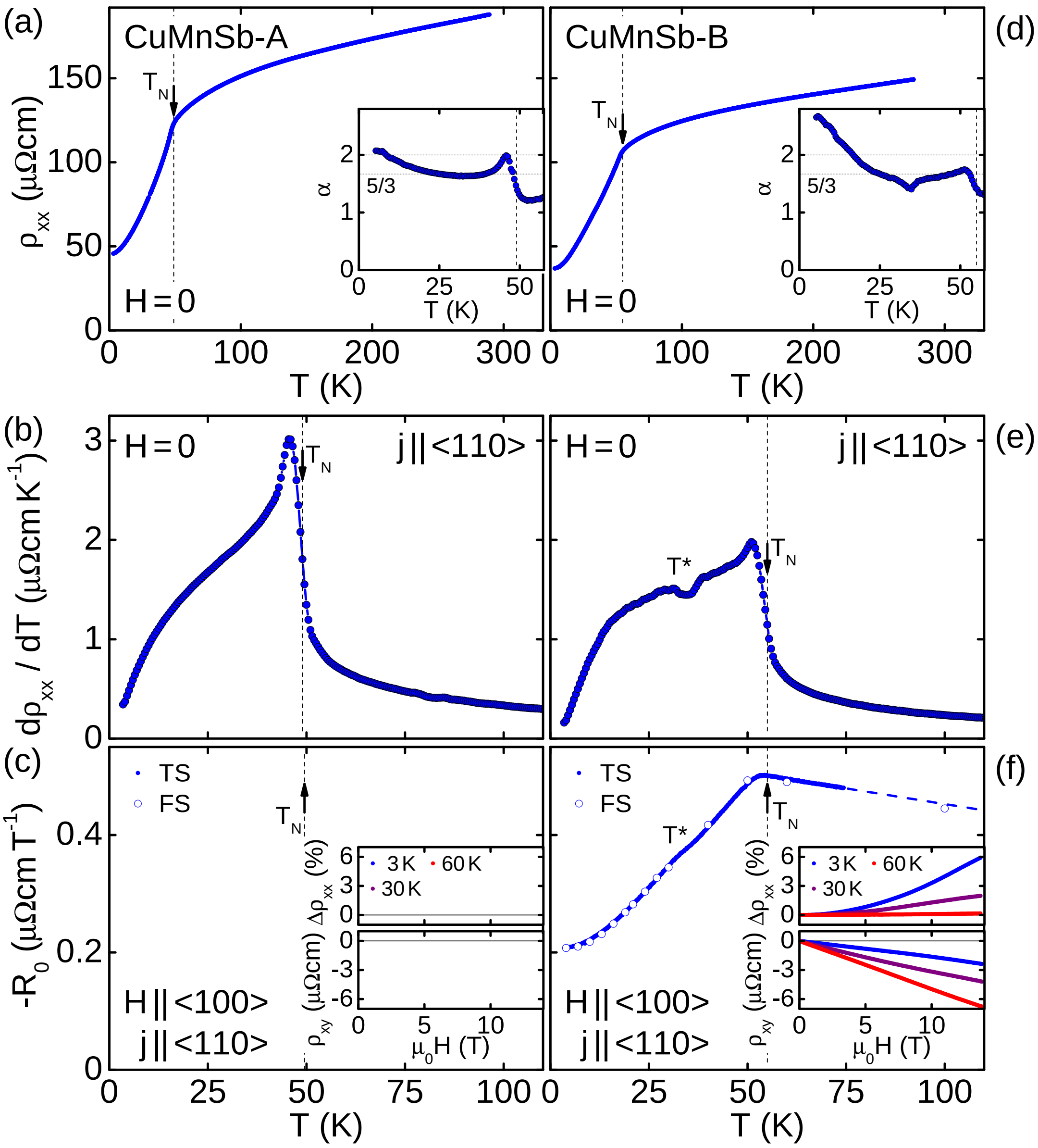

Figure 2.20: Electrical resistivity and Hall effect of CuMnSb. (a) Longitudinal resistivity, ρ_{xx}, of CuMnSb-A as a function of temperature in zero field. A distinct change of slope is observed at the onset of antiferromagnetic order at T_N. The inset shows the exponent, α, of a sliding fit to the resistivity data. (b) Temperature derivative of the longitudinal resistivity, $\mathrm{d}\rho_{xx}/\mathrm{d}T$, for CuMnSb-A. (c) Temperature dependence of the normal Hall coefficient, R_0, of CuMnSb-A measured at $\pm 3\,\mathrm{T}$. The insets depict the magnetoresistance, $\Delta\rho_{xx} = [\rho_{xx}(H)/\rho_{xx}(H=0)] - 1$, and the essentially linear field dependence of the Hall resistivity, ρ_{xy}. (d) Longitudinal resistivity of CuMnSb-B. (e) Temperature derivative of the longitudinal resistivity of CuMnSb-B. An anomaly is observed around $T^* \approx 30\,\mathrm{K}$. (f) Temperature dependence of the normal Hall coefficient of CuMnSb-B.

the resistivity, $\mathrm{d}\rho_{xx}/\mathrm{d}T$, shown in Figs. 2.20(b) and 2.20(e). Using a definition that resembles the entropy conserving construction applied to the specific heat in Fig. 2.19, the transition temperature is in excellent agreement with the other quantities measured. In CuMnSb-B an additional dip is observed around $T^* \approx 30\,\mathrm{K}$. The qualitative shape of $\mathrm{d}\rho_{xx}/\mathrm{d}T$ resembles the electronic contribution to the specific heat, C_{el}/T, including a pronounced change of slope around $\sim$20 K, cf. Figs. 2.19(b) and 2.19(d). Hence, we may assume that Fermi's golden rule applies to the dominant scattering mechanism of the electrical resistivity and that the corresponding density of states determines the specific heat.

As a consequence, similar to the specific heat and in contrast to CrB_2, the resistivity may not be described by an exponential fit that considers the formation of a spin wave gap. Instead, we have fitted the resistivity below T_{N} by the expression $\rho_{xx}(T) = \rho_0 + AT^{\alpha}$. While ρ_0 covers the scattering of the charge carriers on impurities, the second term accounts for scattering between the charge carriers where $\alpha = 2$ is expected for the electron-electron scattering of a conventional Fermi liquid. We have determined the evolution of the exponent α as a function of temperature by applying a sliding fit to our data, i.e., fitting over temperature intervals of 3 K that are consecutively shifted by 0.5 K. Around T_{N} the fit looses its validity.

At low temperatures in CuMnSb-A a Fermi liquid exponent $\alpha \approx 2$ is extracted, whereas a relatively stable $T^{5/3}$ dependence persists from intermediate temperatures up to nearly T_{N}. This finding compares to the value $\alpha = 1.8$ obtained by Bœuf and coworkers [112]. In CuMnSb-B at low temperatures we get $\alpha \approx 8/3$ clearly exceeding the expectation for a Fermi liquid. With increasing temperature α decreases until it settles at a value of $\sim 5/3$, similar to CuMnSb-A. An additional anomaly emerges around the spin canting at T^*. Surprisingly, an exponent $\alpha = 5/3$ is also observed in a marginal Fermi liquid that arises on the border of metallic ferromagnetism in three dimensions [50]. The drastic change of α as a function of temperature in both CuMnSb-A and CuMnSb-B, however, implies that a simple power law is not sufficient to describe the dominant scattering mechanisms. In fact, the different scattering mechanisms may even be linked with each other and hence Matthiessen's rule may not be applicable.

In field, both CuMnSb-A and CuMnSb-B exhibit a weak positive magnetoresistance, $\Delta\rho_{xx} = [\rho_{xx}(H)/\rho_{xx}(H = 0)] - 1$, that reaches 6 % at low temperatures and 14 T. With increasing temperature the magnetoresistance decreases and becomes negative between 60 K and 100 K. The Hall resistivity, ρ_{xy}, is essentially linear as a function of field in the field and temperature range studied. As a consequence, the temperature dependence of the associated linear Hall coefficient, R_0, is most effectively extracted from temperature sweeps in fixed fields as shown for ±3 T in Figs. 2.20(c) and 2.20(f). Data obtained from fitting field sweeps in the range ±4 T are in excellent agreement. With increasing temperature the absolute value of R_0 increases up to a cusp around T_{N}. In CuMnSb-B an additional weak S-shape emerges around $T^* \approx 30\,\mathrm{K}$. From R_0 we calculate an averaged charge carrier concentration, $n = (R_0 e)^{-1}$, in the order of $-2 \cdot 10^{21}\,\mathrm{cm}^{-3}$. For a metal, this value is relatively low suggesting a small density of states at the Fermi level while the negative sign alludes to a dominantly hole-like conduction. These findings are fully consistent with the prediction of semi-metallicity with heavy electron masses and normal hole masses by Jeong *et al.* [182].

Finally, we briefly address the thermal conductivity, κ, displayed in Fig. 2.21. As a function of decreasing temperature κ monotonically decreases. At the Néel transition a pronounced kink is observed in CuMnSb-A, whereas in CuMnSb-B the slope just slightly changes. The absolute value of κ is higher for CuMnSb-B, as expected for a sample with a smaller defect concentration. These findings are corroborated by the thermal resistivity $w = L_0 T/\kappa$, where $L_0 = 2.443 \cdot 10^{-8}\,\mathrm{W\Omega/K^2}$ is the Sommerfeld value of the Lorenz number. While the data for

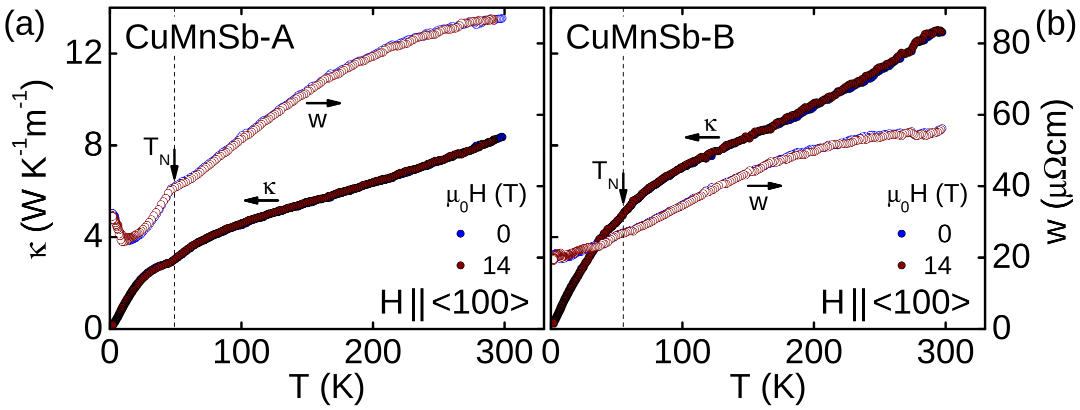

Figure 2.21: Thermal conductivity of CuMnSb. (a) Thermal conductivity of CuMnSb-A as a function of temperature. A clear kink marks the onset of antiferromagnetic order at T_{N}. No changes are occur in fields up to 14 T. The open symbols show the thermal resistivity $w = L_0 T/\kappa$. (b) Thermal conductivity of CuMnSb-B. In contrast to CuMnSb-A, at T_{N} only a faint change of slope is observed.

CuMnSb-B show essentially no anomalies, in CuMnSb-A a pronounced kink is observed at T_{N} and w increases with decreasing temperature below ∼15 K. Consistent with a higher sample quality in CuMnSb-B, the absolute value of the residual thermal resistivity, w_0, is higher for CuMnSb-A. In general, the absolute value of the thermal resistivity is smaller than the electrical resistivity which suggests that the transport properties in CuMnSb are dominated by large-k scattering processes. In fields up to 14 T the behavior hardly changes.

Summary

In conclusion, we have prepared the first two single crystals of the half-Heusler compound CuMnSb. A detailed metallurgical analysis revealed the presence of the ferrimagnetic impurity phase Mn_2Sb on a sub-percent level even in single-crystalline samples if prepared from stoichiometric feed rods, referred to as CuMnSb-A. In the second crystal, referred to as CuMnSb-B, the formation of Mn_2Sb was completely suppressed by a slight initial excess of 0.035 yielding phase-pure single-crystalline material. Since it is not yet clear whether the intrinsic properties of CuMnSb are best accounted for by CuMnSb-A or CuMnSb-B, we have carried out a comprehensive study of both.

The antiferromagnetic order below a Néel temperature, T_{N}, of 49 K and 55 K in CuMnSb-A and CuMnSb-B, respectively, shares characteristics that are believed to be the hallmarks of either local-moment or itinerant magnetism. Thereby, we largely confirm results from the literature gathered on polycrystalline material, e.g., in Refs. [112, 183]. In our phase-pure single crystal CuMnSb-B, however, the susceptibility exhibits a Curie-Weiss temperature dependence above T_{N} already in zero field. The size of the fluctuating moment, $m_{\mathrm{eff}} \approx 4\,\mu_{\mathrm{B}}$/f.u., is identical to the ordered moment obtained from neutron scattering [224] and consistent with the magnetic entropy released at high temperatures. Together with the commensurate magnetic structure, this finding is a strong argument in favor of local-moment magnetism. In contrast, as typical for an itinerant magnet, the order is very stable up to the highest fields studied. Contributions from spin fluctuations persist up to at least ∼$3T_{\mathrm{N}}$ in both inelastic neutron scattering data and the magnetic entropy. An enhanced ac susceptibility about 10 K above T_N may also hint towards the presence of strong magnetic fluctuations, but surprisingly is quenched already in tiny fields of ~50 mT. The possible influence of disorder-induced geometric frustration is finally indicated by a large Curie-Weiss temperature, Θ_{CW}, that outmatches T_N be roughly a factor of 3. As expected for a cubic compound the anisotropy is very weak.

The electrical and thermal transport properties of CuMnSb-A and CuMnSb-B include pronounced contributions from scattering on defects, as typical for Heusler compounds, and may not by accounted for by conventional Fermi liquid theory. From Hall resistivity data we extract a comparably small charge carrier concentration with dominantly hole-like character, consistent with a semi-metallic density of states at the Fermi level as predicted in Ref. [182]. Finally, in the phase-pure single crystal CuMnSb-B anomalies were identified in the bulk and transport properties around $T^* \approx 30$ K, i.e., deep within the antiferromagnetic state. First neutron diffraction data suggest a canting of the spin structure below T^* that presumably had been suppressed in previous studies, e.g., by pinning due to the ferrimagnetic impurity phase Mn_2Sb.

CuMnSb so far is the only robust Heusler antiferromagnet based on light transition metals, apart from Mn_3Si with its complex magnetic structure. Still, the microscopic origin of the peculiar combination of magnetic properties, the spin canting below T^*, and the enhanced susceptibility just above T_N in tiny fields is yet unresolved making CuMnSb a fascinating subject for future studies. Unraveling the uncommon antiferromagnetism in CuMnSb may deepen the understanding of itinerant antiferromagnetism in general and may finally allow to design (antiferromagnetic) Heusler compounds for both fundamental and applied research.

2.3 Summary and outlook

In summary, this chapter addressed two classes of intermetallics that exhibit a large variety of electronic and magnetic properties in a comparably simple crystallographic environment—the hexagonal $C32$ diborides and the cubic Heusler compounds. In this thesis, however, we focused on the antiferromagnetic materials CrB_2, MnB_2, and CuMnSb.

Utilizing the preparation chain described in Sec. 1, we have grown two large single crystals of CrB_2, the first large single crystal of MnB_2, and large grains of VB_2 as a non-magnetic reference. The usage of ^{11}B for the first time permits extensive neutron scattering studies. Furthermore, the first two single crystals of half-Heusler compound CuMnSb have been prepared. After a careful metallurgical characterization combining various x-ray, neutron, and microscopy techniques with the magnetic susceptibility and the electrical resistivity, the low-temperature properties of these crystals were investigated comprehensively. These studies were carried out by means of measurements of the magnetization, the ac susceptibility, the specific heat, the electrical and thermal transport, as well as the Hall effect, and were supported by first elastic as well as inelastic neutron scattering data.

This way, we have established CrB_2 as a prime example for weak itinerant antiferromagnetism. Its characteristic properties include a typical metallic resistivity, a comparably low Néel temperature, an incommensurate magnetic structure, a small ordered moment contrasted by a large fluctuating moment, and a remarkable stability of the magnetic order up to the highest fields studied. An additional role of geometric frustration is suggested by the large Curie-Weiss temperature that exceeds the Néel temperature by far. Our bulk and transport data also allow for a discussion of the possible implications for the interplay of itinerant antiferromagnetism and superconductivity in non-magnetic CrB_2. Replacing chromium by the neighboring transition metal manganese finally leads to MnB_2 which is also antiferromagnetic, but in contrast to CrB_2 shows local-moment magnetism with a high ordering temperature. At low temperatures the magnetic structure cants and evolves a ferrimagnetic net moment.

For CuMnSb, one of the few transition metal based Heusler antiferromagnets, we confirmed the peculiar combination of magnetic properties reported for polycrystals in the literature. While the commensurate magnetic structure with ordered moments that correspond to the fluctuating moments is typical for local-moment magnetism, the high stability of the order in magnetic fields is a strong argument in favor of itinerant magnetism. A comparably high Curie-Weiss temperature alludes to the presence of disorder-induced geometric frustration. A tiny volume fraction of the impurity phase Mn_2Sb was still present in the first single crystals prepared from stoichiometric feed rods, but was suppressed in a second crystal by an initial antimony excess of 0.035. Apart from an increased Néel temperature, however, the latter sample also revealed a spin canting that sets in deep within the antiferromagnetic state. It is not yet clear whether the emergence of this phenomenon was previously prevented by the ferrimagnetic Mn_2Sb or whether it was introduced by the antimony excess. Thus, details of the intrinsic properties of CuMnSb are yet to be resolved.

Currently, Georg Brandl carries out comprehensive inelastic neutron scattering studies on both single crystals of CuMnSb, whereas Alexander Regnat investigates the influence of hydrostatic pressure. Regarding the diborides, ongoing project comprise the high-temperature properties of MnB_2, the refinement of high-resolution neutron and x-ray diffraction data on CrB_2, and the suppression of magnetism in CrB_2 by applying hydrostatic, uniaxial, or chemical pressure, e.g., in the $Cr_{1-x}V_xB_2$ system. As part of his Ph.D. thesis, Georg Benka will finally address magnetism and superconductivity in various transition metal and rare earth diborides, where one example concerns the localization of magnetism in the $Cr_{1-x}Mn_xB_2$ system.

CHAPTER 3

The cubic chiral helimagnets MnSi, $Fe_{1-x}Co_xSi$, and Cu_2OSeO_3

The cubic Dzyaloshinskii-Moriya driven helimagnets represent the second class of materials that was investigated as part of this thesis. MnSi, the most prominent member of this material class, has been studied extensively for decades. Still, the identification of the so-called A-phase as the first example of a Skyrmion lattice in a bulk solid state system [12] recently added a further fascinating aspect to the research on the cubic chiral helimagnets.

The contribution of this thesis consisted in the growth of a large number of single crystals, especially from the archetypical compound MnSi. The influence of the growth parameters on its crystalline quality and as a result on its physical properties was investigated. Customized samples for various projects at our institute and for external collaborators were prepared. Moreover, the magnetic phase diagrams of MnSi, $Mn_{1-x}Fe_xSi$, $Fe_{1-x}Co_xSi$, and Cu_2OSeO_3 were investigated in great detail by means of measurements of the magnetization, the ac susceptibility, and the specific heat. Besides addressing several fundamental questions regarding the nature and dynamics of the magnetic phases and the transitions between them, our results form the basis for future studies of this class of compounds and related materials.

The chapter will start in Sec. 3.1 with a general introduction to the cubic chiral helimagnets and the Skyrmion lattice, followed by material-specific descriptions of the state of the art. Next, Sec. 3.2 addresses the single crystal growth of the cubic chiral helimagnets and the influence of the growth parameters on the crystalline quality of MnSi. The detailed investigation of the magnetic phase diagram of MnSi by means of magnetization and susceptibility measurements is presented in Sec. 3.3.1. In Sec. 3.3.2 we report a high-resolution specific heat study on MnSi and $Mn_{1-x}Fe_xSi$. The magnetic phase diagrams of $Fe_{1-x}Co_xSi$ and its dependence on the field and temperature history are described in Sec. 3.3.3. The chapter concludes with a summary and an outlook in Sec. 3.4.

3.1 Introduction

The cubic chiral helimagnets are a class of compounds that exhibits long-wavelength helimagnetic order and shares a qualitatively similar magnetic phase diagram. Well-known representatives are the (pseudo-)binary $B20$ transition metal monosilicides and monogermanides MnSi,

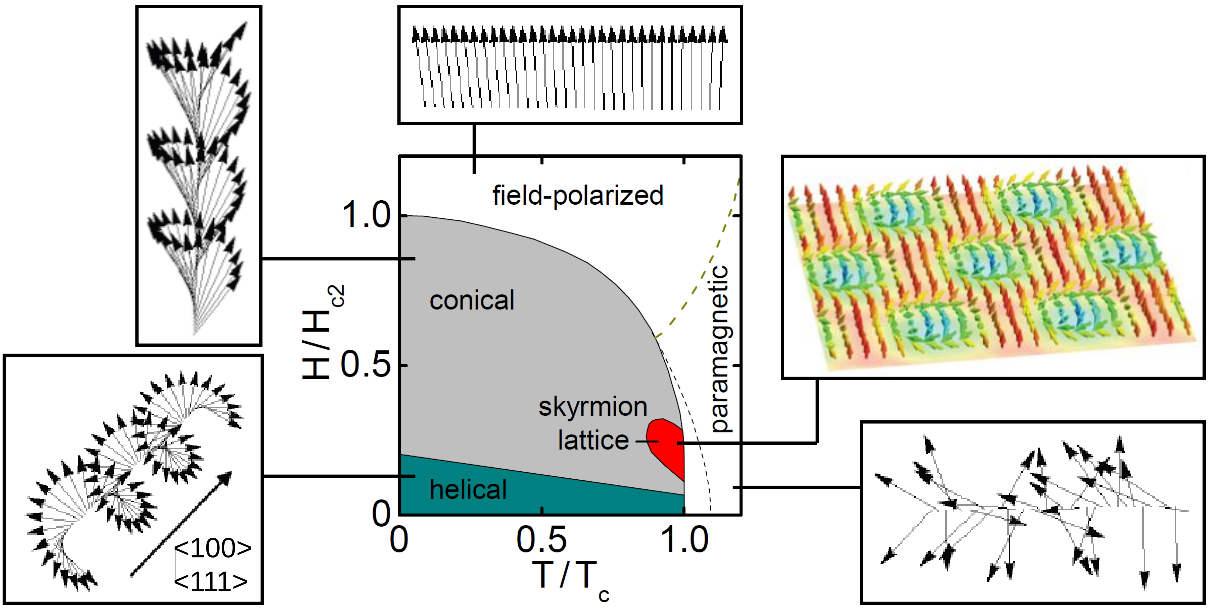

Figure 3.1: General phase diagram of the cubic chiral helimagnets (center). The abscissa and the ordinate are given in units of the helimagnetic transition temperature, T_c, and the zero-temperature value of the transition field into the field-polarized state, H_{c2}, respectively. Also shown are schematic depictions of the spin arrangements in the different magnetic states. For the schematic depictions I wish to thank Markus Garst.

$Mn_{1-x}Fe_xSi$, $Mn_{1-x}Co_xSi$, $Fe_{1-x}Co_xSi$, FeGe, MnGe, and mixtures thereof, as well as the insulator Cu_2OSeO_3. These compounds crystallize in the space group $P2_13$ that lacks inversion symmetry allowing for two crystalline enantiomers. In the following we will give a brief overview of the salient properties of the cubic chiral helimagnets where we refer to the detailed descriptions in Secs. 3.1.1 through 3.1.10 for references.

The long-wavelength helimagnetic order observed in these compounds originates in a well-understood set of hierarchical energy scales. On the strongest scale ferromagnetic exchange interactions favor parallel spin alignment. On intermediate scales the Dzyaloshinskii-Moriya spin-orbit interactions arise due to the lack of inversion symmetry of the crystal structure favoring perpendicular spin alignment. In competition with the stronger ferromagnetic exchange a helical modulation is stabilized. The chirality of the Dzyaloshinskii-Moriya interaction and thus of the helical modulation is fixed by the enantiomer of the crystal structure. Finally, on the weakest energy scale higher-order spin-orbit couplings, also referred to as crystal electric field effects or cubic anisotropies, align the propagation vectors of the helical modulations along certain crystallographic directions. We note that the local-moment insulator Cu_2OSeO_3 represents an exceptional case for strongest energy scale. Here, three ferromagnetically aligned Cu^{2+} moments pair up antiferromagnetically with a fourth Cu^{2+} moment giving rise to an effectively ferrimagnetic exchange.

The hierarchy of energy scales results in a common magnetic phase diagram, as shown in Fig. 3.1, albeit the cubic chiral helimagnets comprise metals, semiconductors, and insulators for which the transition temperatures, transition fields, and helix wavelengths vary by roughly two

compound	x or y	T_c (K)	$\mu_0 H_{c2}$ (T)	λ_h (Å)	$\boldsymbol{q}$ $[H=0]$	$\Gamma_c \cdot \gamma_m$	references
MnSi	-	29	0.6	180	$\langle 111 \rangle$	$+1$	[12, 233]
$Mn_{1-x}Cr_xSi$	<0.15	<29	?	180–200	?	?	[234]
$Mn_{1-x}Fe_xSi$	<0.15	<29	$\lesssim$0.6	90–180	$\langle 111 \rangle$	$+1$	[85, 235, 236]
$Mn_{1-x}Co_xSi$	<0.07	<29	$\lesssim$0.6	90–180	$\langle 111 \rangle$	?	[85, 237]
$Mn_{1-x}Ni_xSi$	<0.05	<29	?	?	?	?	[238]
$MnSi_{1-y}Ge_y$	~0.01	40	0.75	160	$\langle 111 \rangle$	?	[239]
FeGe	-	278	0.2	700	$\langle 111 \rangle \to \langle 100 \rangle$	-1	[240, 241]
$Fe_{1-x}Cr_xGe$	0.15, 0.25	<278	?	620	?	?	[234]
$FeSi_{1-y}Ge_y$	0.25–1	100–278	?	?	?	?	[242]
MnGe	-	170	12	30	$\langle 100 \rangle$	$+1$	[241, 243]
$Mn_{1-x}Fe_xGe$	0–1	100–278	?	30–3000	?	$+1 \to -1$	[241, 244]
$Cr_{1-x}Mn_xGe$	0.17, 0.19	~13	0.05	~370	$\langle 100 \rangle$	?	[245–247]
$Fe_{1-x}Co_xSi$	0.05–0.8	<50	<0.15	300–2300	$\langle 100 \rangle$	-1	[233, 248–250]
Cu_2OSeO_3	-	58	0.1	620	$\langle 100 \rangle$	?	[42, 251]

Table 3.1: Summary of the cubic chiral helimagnets known to date. Comprehensively studied compounds are shown in black, sporadically investigates compounds in gray. We state the helimagnetic transition temperature, T_c, the zero-temperature value of the transition field into the field-polarized state, H_{c2}, and the helix wavelength, λ_h, as well as the easy axis of the propagation vector, $\boldsymbol{q}$. The latter changes in FeGe as a function of temperature. Also given is the product of the crystalline chirality, Γ_c, and the magnetic chirality, γ_m. The product $\Gamma_c \cdot \gamma_m = \pm 1$ is fixed by the sign of the Dzyaloshinskii-Moriya constant.

orders of magnitude, cf. Tab. 3.1. At high temperatures, all compounds are paramagnetic. At low temperatures and zero field we observe multi-domain helical order. The propagation vector of each of these domains is aligned along one of the crystallographic directions determined by the weak cubic magnetic anisotropies. Under an applied magnetic field the domain population changes and the helical state eventually transforms into the conical state with a single domain of spin spirals propagating along the magnetic field. In addition, the spins tilt towards the field direction resulting in a conical shape of the spirals, i.e., the conical state is analogous to the spin-flop state of a conventional antiferromagnet. Increasing the field further leads to the closing-up of the spins and eventually to a field-polarized state.

In recent years, however, the perhaps largest scientific interest has been attracted by a small phase pocket at intermediate fields just below the helimagnetic transition temperature, T_c, that is historically referred to as A-phase. The pocket was identified to be the first example of a Skyrmion lattice in three-dimensional solid state system. This Skyrmion lattice consists of topologically non-trivial spin whirls that arrange in a regular hexagonal lattice in a plane perpendicular to the applied magnetic field and form Skyrmion lines along the field.

The following section is organized as follows. After describing the helimagnetic phases and their transitions as a function of temperature and field in Secs. 3.1.1, 3.1.2, and 3.1.3, we summarize the present understanding of the Skyrmion lattice phase in Sec. 3.1.4. After an account for the collective excitations in the cubic chiral helimagnets in Sec. 3.1.5, we turn to material specific aspects. We start with the most heavily investigated compound, the itinerant helimagnet MnSi, in Sec. 3.1.6 and MnSi doped with iron or cobalt in Sec. 3.1.7. We continue with the strongly doped semiconductor $Fe_{1-x}Co_xSi$ in Sec. 3.1.8 and the insulator Cu_2OSeO_3 in Sec. 3.1.9. Finally, Sec. 3.1.10 completes this section with a short summary on the transition metal monogermanides FeGe and MnGe.

3.1.1 Ginzburg-Landau model of the cubic chiral magnets

In the following subsections we account for the helical, the conical, the field-polarized, and the paramagnetic state. We start with a short summary of their theoretical description using a Ginzburg-Landau ansatz and continue with recent experimental and theoretical studies on the phase transitions between these states. Here, Sec. 3.1.2 describes the transition between the paramagnetic and the helical state in zero field while Sec. 3.1.3 addresses the field-induced phase transitions between the helical, the conical, and the field-polarized state. Albeit some complexities unfold around these phase transitions, the behavior is in perfect agreement with the predictions of the Ginzburg-Landau framework and may be used to quantitatively determine the material-specific parameters required in this model. The account of the Ginzburg-Landau model presented here follows the Supplementary information of Ref. [252].

When treating the cubic chiral helimagnets theoretically, the Ginzburg-Landau free energy density may be split in two parts $f = f_0 + f_{\mathrm{cub}}$, where the free energy functional is given as the integral $\mathcal{F} = \int \mathrm{d}^3\boldsymbol{r} f$. The first term, f_0, includes the ferromagnetic exchange, the Dzyaloshinskii-Moriya interaction as the highest order spin-orbit coupling term, and the Zeeman term as the response on an external magnetic field. It may be written as:

$$f_0 = \frac{1}{2}\boldsymbol{\psi}(r - J\nabla^2)\boldsymbol{\psi} + D\boldsymbol{\psi}(\nabla \times \boldsymbol{\psi}) + \frac{u}{4!}(\boldsymbol{\psi}^2)^2 - \mu_0\mu\boldsymbol{\psi}\boldsymbol{H}$$

We choose the three component order parameter field, $\boldsymbol{\psi}$, with dimensionless units yielding a magnetization density $\boldsymbol{M} = \mu\boldsymbol{\psi}$ with $\mu = \mu_{\mathrm{B}}/\mathrm{f.u.}$, i.e., a single Bohr magneton per formula

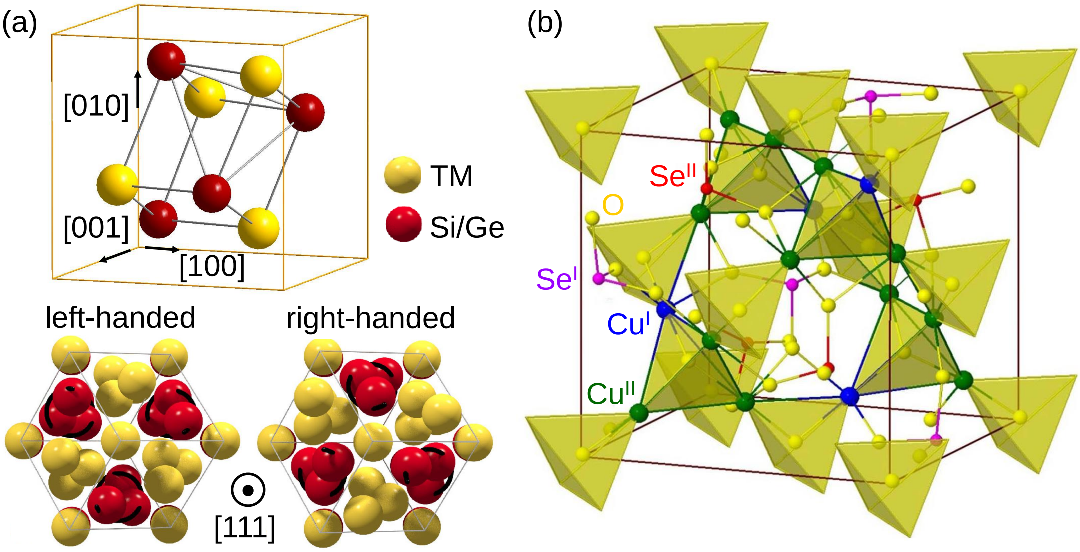

Figure 3.2: Crystal structure of the cubic chiral helimagnets. Both the $B20$ compounds and Cu_2OSeO_3 crystallize in the space group $P2_13$. (a) $B20$ structure of the transition metal (TM) monosilicides and monogermanides. The transition metal atoms are for instance chromium, manganese, iron, and cobalt or, as a dopant, nickel. The atomic positions are $(u,u,u)a$, $(\frac{1}{2}+u,\frac{1}{2}-u,-u)a$, $(\frac{1}{2}-u,-u,\frac{1}{2}+u)a$, and $(-u,\frac{1}{2}+u,\frac{1}{2}-u)a$ with the lattice constant a. In MnSi one obtains $u_{\mathrm{Mn}} = 0.863$ and $u_{\mathrm{Si}} = 0.155$ for a left-handed metal sublattice or $u_{\mathrm{Mn}} = 0.137$ and $u_{\mathrm{Si}} = 0.845$ for a right-handed TM sublattice, respectively [236]. The two crystalline enantiomers may best be discriminated, by viewing the structure along its [111] axis with threefold symmetry. (b) Crystal structure of Cu_2OSeO_3. Pictures adopted from Refs. [236, 253].

unit ($\mu_{\mathrm{B}} > 0$). The parameter r tunes the distance to the phase transition, J is the exchange stiffness and u the interaction parameter of the ferromagnetic exchange. The second term $D\boldsymbol{\psi}(\nabla\times\boldsymbol{\psi})$ corresponds to the Dzyaloshinskii-Moriya interaction with the coupling constant D that is allowed due to the missing inversion symmetry of the crystal structure. The last term describes the Zeeman coupling to a magnetic field $\boldsymbol{H}$. An ansatz for a single conical helix is:

$$\boldsymbol{\psi}(\boldsymbol{r}) = \psi_0\hat{\boldsymbol{\psi}}_0 + \varPsi_{\mathrm{hel}}\hat{\boldsymbol{e}}^-\mathrm{e}^{\mathrm{i}\boldsymbol{Q}\boldsymbol{r}} + \varPsi^*_{\mathrm{hel}}\hat{\boldsymbol{e}}^+\mathrm{e}^{-\mathrm{i}\boldsymbol{Q}\boldsymbol{r}}$$

Here, ψ_0 is the amplitude of the homogeneous magnetization and $\varPsi_{\mathrm{hel}}$ is the complex amplitude of the helical order characterized by the pitch vector $\boldsymbol{Q}$. The vectors $\hat{\boldsymbol{e}}_1\times\hat{\boldsymbol{e}}_2 = \hat{\boldsymbol{e}}_3$ form a normalized dreibein where $\hat{\boldsymbol{e}}^\pm = (\hat{\boldsymbol{e}}_1 \pm \mathrm{i}\hat{\boldsymbol{e}}_2)/\sqrt{2}$ and $\boldsymbol{Q} = Q\hat{\boldsymbol{e}}_3$.

The second term of the free energy density, f_{cub}, contains the spin-orbit coupling of second or higher order, breaking the rotation symmetry of f_0 already in zero field.

$$f_{\mathrm{cub}} = \frac{J_{\mathrm{cub}}}{2}\left[(\partial_x\psi_x)^2 + (\partial_y\psi_y)^2 + (\partial_z\psi_z)^2\right] + \ldots$$

This leading-order term of the cubic anisotropies, where $J_{\mathrm{cub}} \ll J$, implies that the easy axis of the helical propagation vector is either a $\langle 100\rangle$ or a $\langle 111\rangle$ direction as first pointed out by Bak and Jensen [254]. As the field is increased the Zeeman term gains importance and finally overcomes the cubic anisotropies, stabilizing the conical state with the propagation vector parallel to the magnetic field, in analogy to the spin-flop transition of a conventional antiferromagnet. In order to account for more subtle effects, further terms of the cubic anisotropies need to be considered, where the non-centrosymmetric space group $P2_13$ selects the terms allowed. The allowed symmetry operations comprise threefold rotations around one specific $\langle 111\rangle$ direction, three screw axes consisting of a 180° rotation around a $\langle 100\rangle$ axis followed by a $(\frac{1}{2}, \frac{1}{2}, 0)a$ non-primitive translation, and combinations thereof [255]. The corresponding crystal structures are depicted in Fig. 3.2. They may form in two enantiomers with different crystalline chirality, Γ_c. As the sign of the Dzyaloshinskii-Moriya constant is given for a certain compound, the crystalline chirality determines the magnetic chirality, γ_m, i.e., the product $\Gamma_c \cdot \gamma_m$ is fixed to either $+1$ or -1 [233, 236, 241, 256].

While the terms $\mathcal{F}_0$ and $\mathcal{F}_{\text{cub}}$ are sufficient to describe the ground state of the helical, the conical, the field-polarized, and the paramagnetic phase, specific issues require the consideration of further contributions. These may be summarized as follows:

- Just above the helimagnetic ordering temperature a fluctuation-disordered regime emerges in which strongly interacting chiral fluctuations lead to non-analytic corrections to the free energy functional, cf. Sec. 3.1.2. These terms finally drive the phase transition first-order [257].

- It has been noticed theoretically that the stabilization of the Skyrmion lattice with respect to the conical state may be accounted for by thermal fluctuations, cf. Sec. 3.1.4. Here, the leading correction arises from Gaussian fluctuations around the mean-field spin configurations of the conical and the Skyrmion lattice state, $\boldsymbol{\psi}_{\text{MF}}$, respectively.

  $$\mathcal{G}_{\text{fluc}} \approx \frac{1}{2} \log \det \left(\frac{\delta^2 \mathcal{F}}{\delta \boldsymbol{\psi} \delta \boldsymbol{\psi}} \right) \bigg|_{\boldsymbol{\psi}_{\text{MF}}}$$

  Close to the helimagnetic ordering temperature long-range fluctuations dominate and a cutoff $|\boldsymbol{k}| < 2\pi/a$ is used where a is the lattice constant. Interestingly, both short-range and long-range fluctuations favor the Skyrmion lattice for intermediate magnetic fields [12].

- A proper description of the collective excitations finally requires consideration of dipolar interactions, cf. Sec. 3.1.5. In Fourier space the corresponding free energy functional may be expressed using the inverse susceptibility $\chi^{-1}_{\text{dip},ij}$.

  $$\mathcal{F}_{\text{dip}} = \frac{1}{2} \sum_{\boldsymbol{k}} \psi_i(-\boldsymbol{k}) \chi^{-1}_{\text{dip},ij}(\boldsymbol{k}) \psi_j(\boldsymbol{k})$$

  $$\chi^{-1}_{\text{dip},ij}(\boldsymbol{k}) = \mu_0 \mu^2 \begin{cases} \frac{\boldsymbol{k}_i \boldsymbol{k}_j}{\boldsymbol{k}^2} & \text{if } |\boldsymbol{k}| \gg 1/L \\ N_{ij} & \text{if } |\boldsymbol{k}| \ll 1/L \end{cases}$$

  Fourier components with momenta larger than the inverse of the linear size of the sample, L, interact via dipolar interactions. For smaller momenta, the dipolar susceptibility is determined by the demagnetization matrix N_{ij} that obeys $\operatorname{tr}\{N\} = 1$ in SI units [252].

3.1.2 Brazovskii-type phase transition

In the following, we address the onset of helimagnetic order as a function of temperature in zero field. As a consequence of the very weak magnetic anisotropies the corresponding transition in

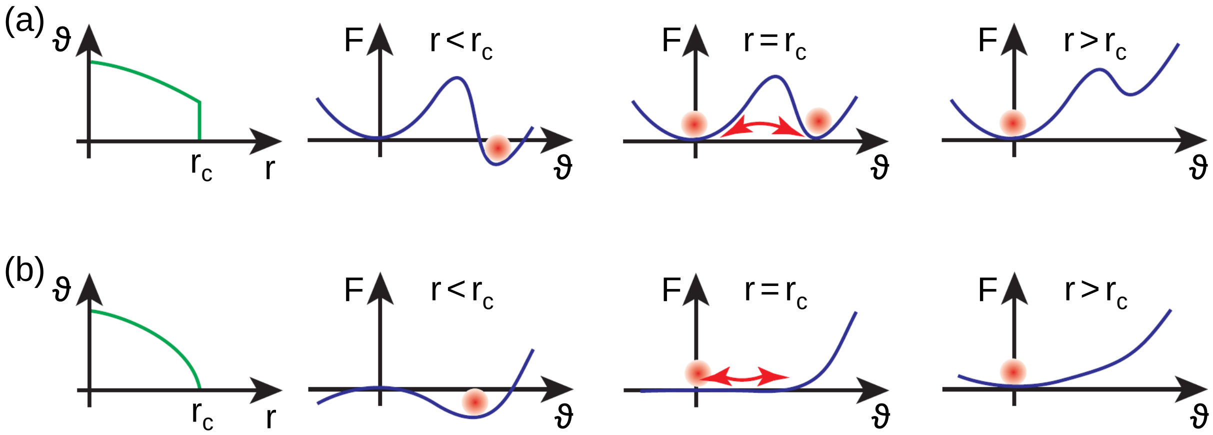

Figure 3.3: Classification of phase transitions. (a) First-order transition. The order parameter, ϑ, varies discontinuously as a function of the control parameter, r. With increasing r the systems jumps from one local minimum of the free energy, F, to a degenerate one as the critical value, r_c, is reached. (b) Second-order transition. Here, ϑ changes continuously as a function of r. The flat free energy landscape leads to strong fluctuations that drive the systems into a smoothly developing global minimum. For classical phase transitions the control parameter is the temperature. Possible control parameters for quantum phase transitions include pressure, uniaxial stress, electric field, magnetic field, or composition. Figure adapted from Ref. [258].

MnSi may be described within a fluctuation-induced first-order Brazovskii scenario, as recently demonstrated by Janoschek *et al.* in Ref. [257] and reviewed below.

In general, phase transitions may be characterized as first-order or second-order according to Ehrenfest, see Fig. 3.3. At first-order transitions the system transits from one local minimum of the free energy to another one accompanied by a discontinuous change of the order parameter and the release of latent heat. Typically, phase coexistence phenomena are observed at first-order transitions while fluctuations of the order parameter may be neglected. In contrast, at second-order transitions the order parameter changes continuously accompanied by strong fluctuations that extend over increasing length scales as the transition is approached. The divergence of the corresponding correlation length may typically be described in terms of universal scaling laws for observables that depend only on the symmetry of the system but not on its microscopic details [259]. An abundance of critical fluctuations, however, may change the nature of the phase transition, if the phase space available for the critical degrees of freedom is large enough. The system then avoids the critical point and the large entropy associated with the fluctuations by realizing a (fluctuation-induced) first-order transition.

In a seminal theoretical paper, Brazovskii considered the consequences of critical fluctuations becoming soft on a finite manifold in reciprocal space, in particular on a sphere, instead of just on a point as, e.g., for a ferromagnet [260]. The large phase space volume leads to interactions between the critical fluctuations that strongly suppress the correlation length and, finally, trigger a fluctuation-induced first-order transition. The Brazovskii-type scenario was discussed for a wide range of systems including weakly anisotropic antiferromagnets [260], weak crystallization [261], liquid crystals [262, 263], the Rayleigh-Bénard convective instability [264], pion condensates in neutron stars [265], and Bose-Einstein condensates [266]. Experimental realizations, however, have so far remained scarce with diblock copolymers as one example [267, 268] as the relevant fluctuations are difficult to resolve [269]. In a recent study involving neutron scattering, susceptibility, and specific heat measurements, we provided strong evidence that the helimagnetic transition in MnSi is driven first order by the interactions between isotropic critical fluctuations, consistent with the predictions by Brazovskii. Preliminary data imply that the same scenario may also be applicable to $Mn_{1-x}Fe_xSi$ for $x < 0.12$ as well as to Cu_2OSeO_3 [270]. Hence, a Brazovskii-type phase transition appears to be a rather general characteristic of the cubic chiral helimagnets. In contrast, for Cu_2OSeO_3 an analysis of the renormalization of the zero-field ac susceptibility recently suggested that a Wilson-Fischer scenario may be applicable [271].

Brazovskii-type phase transition in MnSi

As introduced above, the magnetic phase diagram of the cubic chiral helimagnets may be explained by a hierarchy of energy scales. The ferromagnetic exchange J is followed by the Dzyaloshinskii-Moriya interaction $D \sim \mathcal{O}(\lambda_{\mathrm{SO}})$ as highest order term in spin-orbit coupling λ_{SO} and the cubic anisotropies $J_{\mathrm{cub}} \sim \mathcal{O}(\lambda_{\mathrm{SO}}{}^2)$ of at least second order in λ_{SO}. This hierarchy of energy scales translates into a hierarchy of correlation lengths, $\xi_{\mathrm{cub}} \gg \xi_{\mathrm{DM}} \gg \xi_{\mathrm{FM}}$. Hence, if the helimagnetic transition is approached from high temperatures, $T \gg T_c$, the fluctuations are initially ferromagnetic and their correlation length ξ is short. With decreasing temperature and thus increasing ξ, the Dzyaloshinskii-Moriya length scale $\xi_{\mathrm{DM}} \sim J/D$ is reached and isotropic chiral fluctuations emerge on a sphere of radius $Q = D/J$ in reciprocal space. A further increase of ξ above ξ_{cub} eventually results in a preference of momentum along certain crystallographic directions.

On the mean-field level the paramagnetic-to-helimagnetic phase transition is expected to be second-order. Interactions between the helimagnetic fluctuations, however, lead to non-analytic corrections in the Ginzburg-Landau free energy functional. These terms drive the transition first-order where the exact mechanism depends on the strength of the interaction between the fluctuations, as described by the additional Ginzburg scale ξ_{Gi}. Three scenarios may be distinguished; (i) the Bak-Jensen scenario for weak interactions ($\xi_{\mathrm{Gi}} \gg \xi_{\mathrm{cub}} \gg \xi_{\mathrm{DM}}$) [254], (ii) the Brazovskii scenario for intermediate interactions ($\xi_{\mathrm{cub}} \gg \xi_{\mathrm{Gi}} \gg \xi_{\mathrm{DM}}$) [260], and (iii) the Wilson-Fisher scenario for strong interactions ($\xi_{\mathrm{cub}} \gg \xi_{\mathrm{DM}} \gg \xi_{\mathrm{Gi}}$). Albeit MnSi has been investigated for decades, the nature of the helimagnetic phase transition is still subject to a controversial discussion that will be reviewed in further detail in Sec. 3.1.6. Multiple scenarios have been proposed including an extended Bak-Jensen scenario [273, 274], blue phases [275], or a Skyrmion liquid [276, 277]. In the following, however, we will show that the experimental data in MnSi is in remarkable agreement with the Brazovskii scenario, as the minimal theoretical model.

Typical zero-field small-angle neutron scattering data are shown in Fig. 3.4(a). Well above the onset of helimagnetic order, i.e., at $T_2 \approx T_c + 1.5\,\mathrm{K}$ which is also referred to as T^*, a sphere of intensity with a radius corresponding to the helical pitch, Q, condensates and grows in intensity as the temperature is lowered. Below $T_c \approx 29.0\,\mathrm{K}$ the distinct intensity maxima of the helical order are visible along the crystalline $\langle 111 \rangle$ directions. The weak maxima along $\langle 100 \rangle$ and $\langle 110 \rangle$ arise due to double scattering. As expected for a first-order transition, a tiny fraction of helimagnetic order survives up to $T \sim T_c + 0.2\,\mathrm{K}$.

The inverse correlation length $\kappa = \xi^{-1}$, depicted in Fig. 3.4(b), is extracted from fits of modified Lorentzian profiles to radial q-scans (blue symbols) and the measured susceptibility (black symbols). The difference with respect to the extended Bak-Jensen scenario employed by

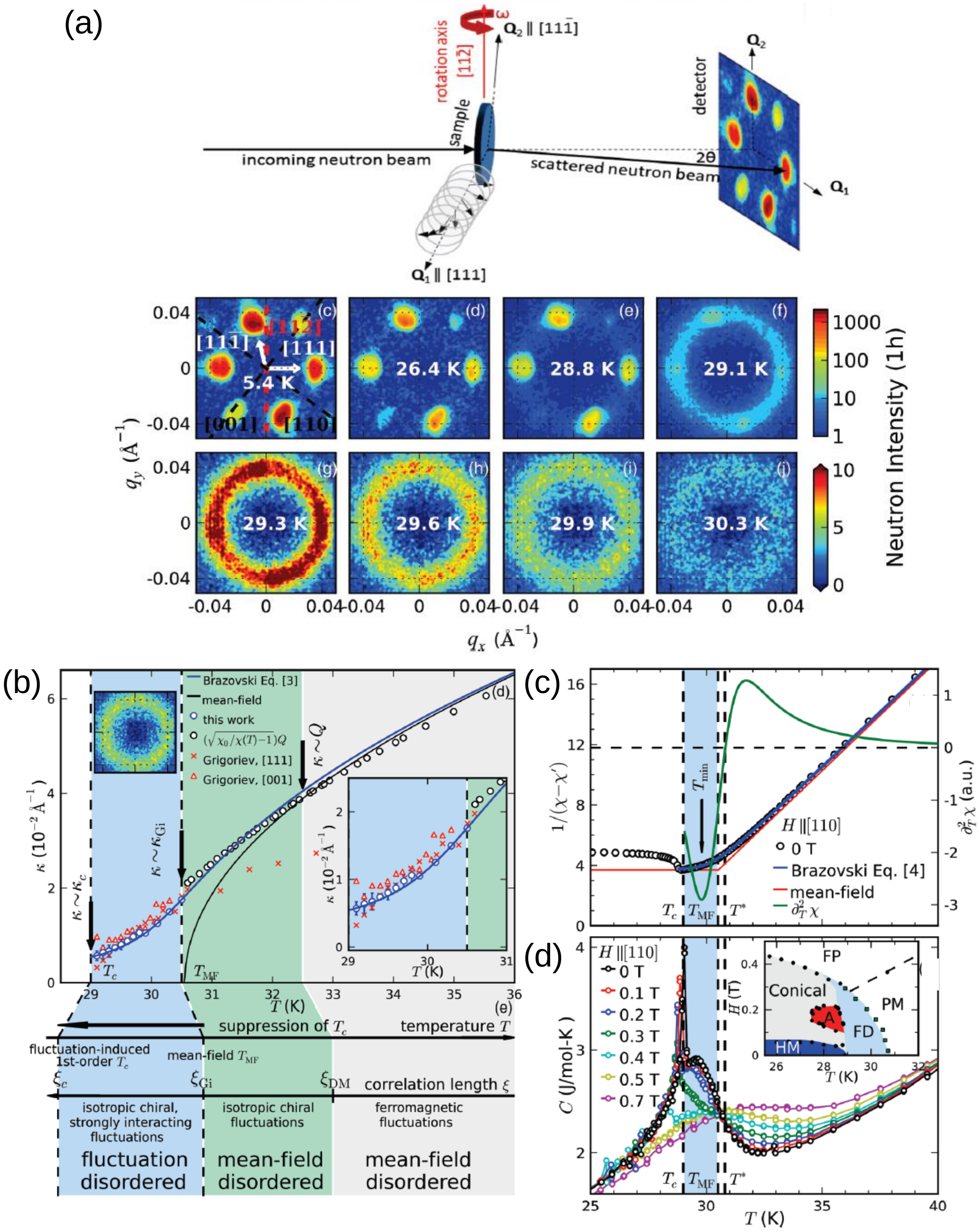

Figure 3.4: The helimagnetic phase transition in MnSi at $T_c \approx 29.0\,\mathrm{K}$. (a) Small-angle neutron scattering setup and typical intensity patterns below (top) and above T_c (bottom). (b) Inverse magnetic correlation length, κ, as a function of temperature. Also shown are data from Ref. [272] (Grigoriev, red) and data calculated from the ac susceptibility (black). A fit according to the Brazovskii scenario is in remarkable agreement with the data (blue line). Mean-field behavior is recovered for $T \gg T_c$ (black line). (c) Inverse ac susceptibility as a function of temperature. (d) Specific heat in fields up to 1 T. The inset shows the magnetic phase diagram. Figure compiled from Ref. [257].

interaction	energy density	ϵ (μeV/Å^3)	ratio
ferromagnetic	$\epsilon_{\mathrm{FM}} = J/{a_{\mathrm{f.u.}}}^2$	336	1
Dzyaloshinskii-Moriya	$\epsilon_{\mathrm{DM}} = JQ^2$	4.3	10^{-2}
Ginzburg	$\epsilon_{\mathrm{Gi}} = J{\kappa_{\mathrm{Gi}}}^2$	1.0	10^{-3}
cubic anisotropies	$\epsilon_{\mathrm{Cub}} = \lvert J_{\mathrm{cub}}\rvert Q^2/2$	0.1	10^{-4}

Table 3.2: Hierarchy of energy scales in MnSi around the helimagnetic transition at T_c. The volume occupied by one formula unit of MnSi is ${a_{\mathrm{f.u.}}}^3 = 24.018\,\text{Å}^3$. See Ref. [257] for further details.

Grigoriev *et al.* (red symbols) concerns the detailed treatment of the cubic anisotropies. For large temperatures mean-field behavior is observed (black line) and the system is dominated by ferromagnetic fluctuations (gray shading). With decreasing temperature, i.e., as the correlation length overcomes ξ_{DM} isotropic chiral fluctuations get increasing spectral weight (green shading). As the helimagnetic phase transition is approached even further and the correlation length exceeds ξ_{Gi} the interaction between the chiral fluctuations suppresses the mean-field transition temperature, T_{MF}, and leads to a fluctuation-disordered regime between the fluctuation-induced first-order transition at T_c and the crossover at $T_2 \approx T_{\mathrm{MF}}$ (blue shading).

The characteristic length scales of the system may also be derived from the neutron scattering data. At T_c we find $\xi_{\mathrm{DM}} \approx 26\,\text{Å}$ and $\xi_{\mathrm{cub}} \approx 169\,\text{Å}$. The finite correlation length at the transition $\xi_c = {\kappa_c}^{-1} \approx 200\,\text{Å}$ is similar to ξ_{cub}, i.e., the first-order transition occurs before the influence of the cubic anisotropies on the fluctuations has fully developed. This fact contradicts the Bak-Jensen scenario and favors a Brazovskii-type transition. A fit of $\kappa(T)$ accounting for the Brazovskii renormalization is in excellent agreement with the experimental data (blue line) and yields a mean-field transition temperature $T_{\mathrm{MF}} \approx 30.5\,\mathrm{K}$ and a Ginzburg length scale $\xi_{\mathrm{Gi}} \approx 53\,\text{Å}$. Thus, consistent with the Brazovskii scenario, we find $\xi_{\mathrm{cub}} > \xi_{\mathrm{Gi}} > \xi_{\mathrm{DM}}$.

A Brazovskii-type transition is corroborated also by thermodynamic data, namely ac susceptibility and specific heat. At high temperatures we observe a Curie-Weiss like behavior in the susceptibility, cf. Fig. 3.4(c) for the inverse susceptibility. With decreasing temperature a point of inflection emerges at T_2, while the onset of helical order at T_c is indicated by a pronounced kink. The susceptibility for $T > T_c$ again is in remarkable agreement with the predictions from the Brazovskii scenario (blue line). In the mean-field approximation (red line) the transition is expected at $T_{\mathrm{MF}} > T_c$. The specific heat, see Fig. 3.4(d), shows a first-order δ-spike at T_c in zero field. The peak resides on top of a broad shoulder that is characterized by a crossing point in small fields at T_2 as observed in many correlated systems [85, 278, 279]. This so-called Vollhardt invariance is connected to a point of inflection in the susceptibility in the limit of small fields ($M \approx \chi H$) via a Maxwell relation, $0 = \partial C/\partial H|_{T_2} = T\partial^2 M/\partial T^2|_{T_2} \approx TH\partial^2\chi/\partial T^2|_{T_2}$. In the cubic chiral magnets, both the turning point in the susceptibility and the crossing point in the specific heat are consequences of the same phenomenon—the strong Brazovskii renormalization of the correlation length due to the interaction between the chiral fluctuations.

Susceptibility and specific heat data extracted from a recent classical Monte Carlo study are fully consistent with the experimental findings and hence the Brazovskii scenario [280]. A further test of the Brazovskii scenario concerns the influence of a magnetic field which is predicted to quench the interactions between the critical fluctuations, thereby changing the transition from first-order to second-order at a tricritical point. As part of this thesis, we have demonstrated the existence of such a tricritical point in the magnetic phase diagram of MnSi and $Mn_{1-x}Fe_xSi$ up to $x = 0.10$from measurements of the specific heat, cf. Sec. 3.3.2. Finally, using the parameters obtained in the study by Janoschek *et al.* we are able to quantify the hierarchy of energy scales in the case of MnSi as summarized in Tab. 3.2.

3.1.3 Phase transitions as a function of field

Around the helical-to-conical transition at H_{c1} a rather complex behavior emerges from the cubic anisotropies and the interplay between macroscopic helical domains. In the stoichiometric cubic helimagnets the details of the transition mainly depend on three factors; (i) the orientation of the applied magnetic field, (ii) the field and temperature history of the sample, as well as (iii) the sample quality. Still, combining the Ginzburg-Landau approach presented above with a qualitative account for the physics of helical domains enables us to describe the comprehensive set of magnetization data shown in Fig. 3.5. These data were collected by Michael Wagner on a spherical sample of MnSi, in order to eliminate the influence of inhomogeneous or anisotropic demagnetization effects [281]. Together with transverse susceptibility measured by Felix Rucker [282] and small-angle neutron scattering data on both the helical-to-conical transition and the Skyrmion lattice measured by Alfonso Chacon [281, 283] and Tim Adams [284, 285], respectively, the prefactors of various cubic anisotropy terms may be determined quantitatively. While a detailed account will be given elsewhere, the main results on the helical-to-conical transition are summarized in the following.

We begin the description with the state obtained after zero-field cooling where the equivalent helical domains along the easy axes are populated equally, i.e., the four $\langle 111 \rangle$ axes in the case of MnSi, see Fig. 3.5(a). With increasing field, domains that enclose larger angles with the magnetic field are depopulated in favor of the domains closer to the field direction, while the pitch of the latter smoothly rotates towards the field direction, cf. Ref. [286]. Once the conical state has been stabilized in an applied magnetic field, the domains of the helical state that enclose smaller angles with the field direction display a higher population under reduction of the applied field. For field directions close to the easy axis, at low temperatures no multi-domain helical state is recovered. Just below the helimagnetic ordering temperature T_c, however, a re-population of all helical domains is observed (not shown) that might be attributed to an increased amount of thermal fluctuations [85].

The transition to the helical state as a function of decreasing field, i.e., approached from the single-domain conical state, may either be a symmetry-breaking second-order transition or a crossover. The former is the case if the magnetic field is applied along a direction where two or more of the easy axes enclose the same smallest angle with respect to the magnetic field, while the latter is the case for all other field direction. Magnetic field along the hard $\langle 100 \rangle$ axis in MnSi represents a special case as all four $\langle 111 \rangle$ axes enclose the same angle with the magnetic field. Here, a double transition is observed that may be explained as follows, cf. Ref. [281] for corresponding small-angle neutron scattering data. First, the single conical domain splits into two sets of domains that increasingly tilt towards opposing $\langle 110 \rangle$ directions as the field is decreased. In a second step, these domains separate into four sets of helical domains that finally lock in at the crystalline $\langle 111 \rangle$ axes. As shown in Sec. 3.2.1, the details of this double transition are dependent on the sample quality. If the helical-to-conical transition is approached from the multi-domain helical state at low fields, a comparably broad anomaly is observed. This smearing may presumably be attributed to the fact that helical domain walls, which resemble topological defects, are hard to destroy once they have formed. Their pinning to defects may

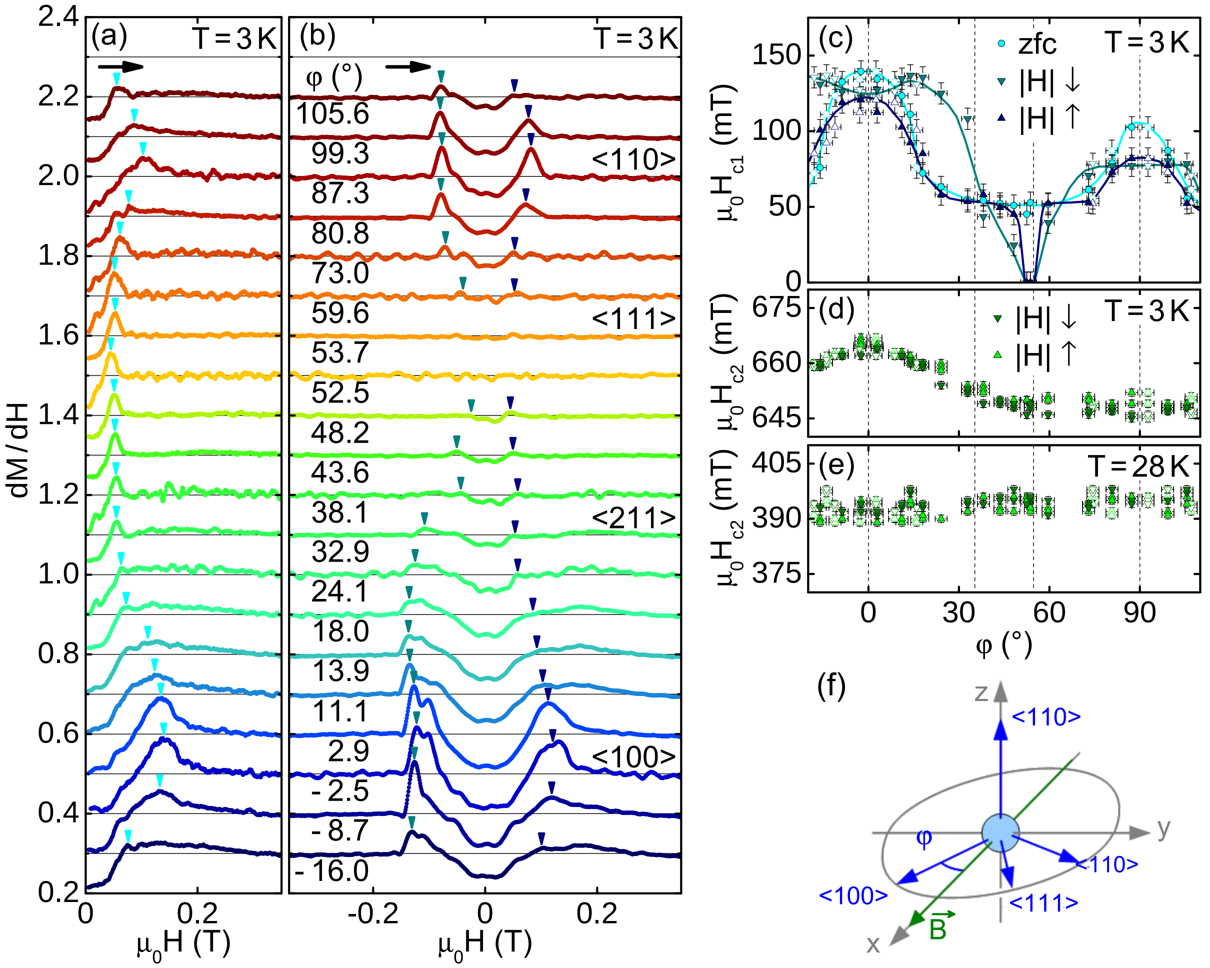

Figure 3.5: Orientation and history dependence of the field-induced transitions in MnSi measured on a spherical sample. (a) The susceptibility calculated from the measured magnetization, $\mathrm{d}M/\mathrm{d}H$, as a function of field at low temperatures for different field orientations after zero-field cooling. For clarity data have been shifted vertically by a constant value of 0.1. (b) Susceptibility for increasing fields starting from -1 T, i.e., from the field-polarized state. (c) Orientation dependence of the transition field between the helical and the conical state, H_{c1}, for different field histories. (d) The upper critical field, H_{c2}, as a function of field orientation at low temperatures. (e) Just below the helimagnetic ordering temperature, H_{c2} is isotropic. (f) Schematic depiction of the definition of the angle φ.

play an additional role. In any case, as will be shown in Sec. 3.3.1, the reorientation of the macroscopic helical domains is a very slow process.

In doped compounds like $Mn_{1-x}Fe_xSi$, $Mn_{1-x}Co_xSi$, or $Fe_{1-x}Co_xSi$ a helical state that is comparable to the stoichiometric compounds forms after zero-field cooling. However, once a field has been applied that was sufficient to stabilize the conical state, no long-range-ordered helical state is recovered for all crystallographic directions [80, 85, 287]. This behavior may be due to the large amount of structural disorder present in these systems.

In contrast to the complex behavior around H_{c1}, for all cubic chiral helimagnets the transition between the conical and the field-polarized state is a conventional second-order transition belonging to the XY-universality class [86]. Here, the complex amplitude of the helical order, Ψ_{hel}, corresponds to the two-dimensional ordering vector. The cubic anisotropies lead to a tiny orientation dependence of H_{c2}, where the difference of about 3 % observed in MnSi at low temperatures disappears near T_c.

3.1.4 The Skyrmion lattice phase

In recent years the perhaps largest scientific interest for the cubic chiral helimagnets has been attracted by a phase pocket historically referred to as the A-phase. The existence of this pocket in MnSi just below T_c in intermediate fields was reported already in the 1970s [289–291]. The detailed microscopic spin structure, however, remained puzzling until 2009 when a small-angle neutron scattering study revealed that the A-phase represents the first realization of a Skyrmion lattice in a bulk solid state system [12]. Subsequently, similar observations were made in other cubic chiral helimagnets [251, 287, 292–294]. The concept of Skyrmions was originally introduced around 1960 by Tony Skyrme for the description of neutrons and protons as discrete entities emerging from a continuous nuclear field [295–297]. Besides its application in particle physics [298], the concept also has been applied to quantum Hall states [299–304], Bose-Einstein condensates [305, 306], and liquid crystals [307].

The Skyrmion lattice in the chiral helimagnets consists of a regular arrangement of spin whirls that may essentially be described by the phase-locked superposition of three helices under 120° in a plane perpendicular to the applied magnetic field in combination with a ferromagnetic component along the field. This spin texture possesses a non-trivial topology, i.e., it cannot be continuously transformed into a topologically trivial state such as a paramagnet, ferromagnet, or helimagnet. The associated winding number of the structure, Φ, is an integer and the integral of the Skyrmion density, ϕ_i, over a magnetic unit cell.

$$\phi_i = \frac{1}{8\pi}\epsilon_{ijk}\hat{\psi} \cdot \partial_j \hat{\psi} \times \partial_k \hat{\psi}$$

Here, ϵ_{ijk} is the antisymmetric unit tensor and $\hat{\psi} = \boldsymbol{M}(\boldsymbol{r})/M(\boldsymbol{r})$ is the orientation of the local magnetization.

Along the field direction the quasi two-dimensional structure is repeated forming Skyrmion lines as depicted in Fig. 3.6(a). Thus, in small-angle neutron experiments a sixfold pattern of the magnetic structure may be seen, if the magnetic field is applied parallel to the neutron beam, cf. Figs. 3.6(b) and 3.6(c). Such a setup is also used for the investigation of the flux line lattices in type-II superconductors [308], with which the lattice of Skyrmion lines shares some similarities. In earlier experiments the magnetic field and the neutron beam had been applied perpendicular to each other so that, depending on the crystalline orientation, two or no spots were observed perpendicular to the field direction. As a result, the A-phase was erroneously discussed as a paramagnetic pocket [309], a single-Q spin-flop state [286], a sinusoidal structure [310], or a Bose condensation of spin waves [311]. The wave vector in the Skyrmion lattice has essentially the same absolute value as in the helical state. Due to the hexagonal structure, in real space this translates to a distance between two neighboring Skyrmion cores, i.e., a Skyrmion lattice constant, that is a factor of $2/\sqrt{3} \approx 1.15$ larger than the helix wavelength.

Energetically the Skyrmion lattice may be accounted for within a standard Landau-Ginzburg approach when properly taking into account thermal fluctuations [12]. This finding was recently

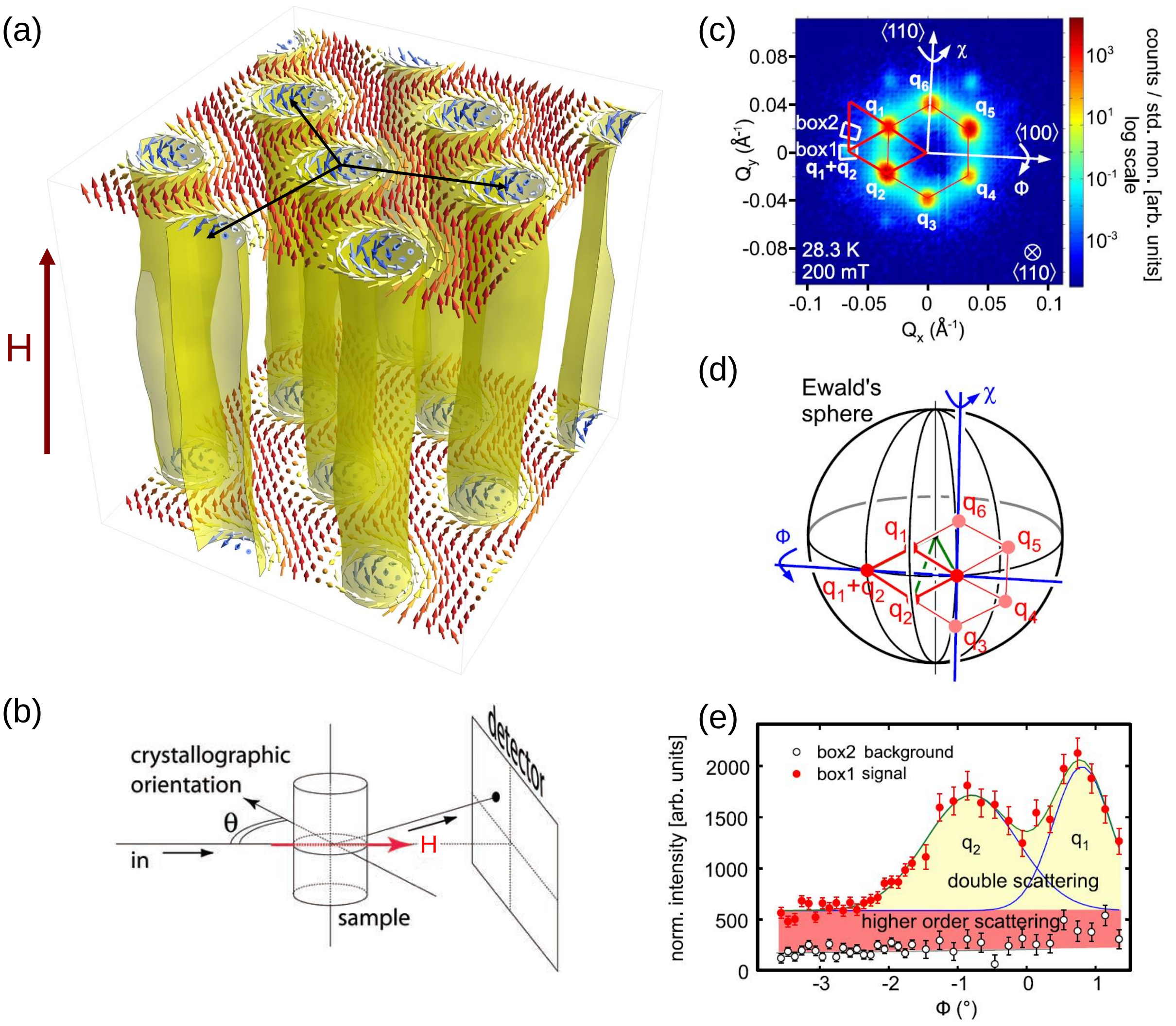

Figure 3.6: Skyrmion lattice in the cubic chiral helimagnets. (a) Schematic depiction of the spin structure of the Skyrmion lattice phase. The three propagation vectors are indicated by the black arrows. Along the field direction Skyrmion lines are formed. (b) Field configuration used in small-angle neutron scattering experiments to detect the sixfold pattern of the Skyrmion lattice. The magnetic field and the incoming neutron beam are parallel to each other. (c) Typical sixfold pattern obtained as a sum over a rocking scan around ϕ. The weak spots at high q-values (box 1) arise from double scattering and higher-order scattering. (d) Definition of the angles ϕ and χ used in Renninger scans. (e) The Renninger scans allow the distinguish between double scattering and higher-order scattering. Pictures adapted from Refs. [12, 80, 288].

confirmed by classical Monte Carlo simulations reproducing the magnetic phase diagram observed experimentally [280]. Consistently, the Skyrmion lattice forms rather independent from the underlying crystalline lattice. In addition, the cubic anisotropies lead to minor modifications, namely (i) an anisotropic temperature and field extent of the Skyrmion lattice phase pocket [281, 312, 313], (ii) an easy axis in the plane perpendicular to the magnetic field along which one of the propagation vectors aligns, and (iii) a slight misalignment of up to a few degree between the magnetic field and the Skyrmion lines for most field directions [285]. The influence of uniaxial pressure on the stability of the various phases is a topic of ongoing research [314, 315]. In contrast, in a seminal study Bogdanov and coworkers predicted the existence of a Skyrmion lattice for anisotropic non-centrosymmetric materials in the presence of a magnetic field [316, 317]. They concluded that in cubic compounds the Skyrmion lattice would be metastable, neglecting the influence of thermal fluctuations. The latter also holds true for a competing theoretical scenario that proposes the stabilization of a Skyrmion lattice by a combination of a softened modulus of the magnetization and uniaxial anisotropies [318, 319].

A detailed small-angle neutron scattering study utilizing a configuration that minimizes demagnetization effects revealed a resolution-limited rocking width of the intensity maxima of the Skyrmion lattice that corresponds to a correlation length in excess of several hundred micrometer [288]. Furthermore, so-called Renninger scans permitted to distinguish between higher-order and parasitic double scattering, cf. Figs. 3.6(c) through 3.6(e). The presence of higher-order scattering for itself indicated a weak particle-like character of the Skyrmions, while its evolution as a function of temperature and field underlined the long-range crystalline nature of the Skyrmion lattice and, in particular, the phase-locked multi-Q nature of the modulation at heart of the non-trivial topological winding.

Topological Hall effect and spin transfer torque

A particularly exciting consequence of the non-trivial topology arises for the interplay of conduction electrons with the Skyrmion lattice. When an electric current is passed through the Skyrmion lattice, the spin of a conduction electron adiabatically follows the smoothly varying

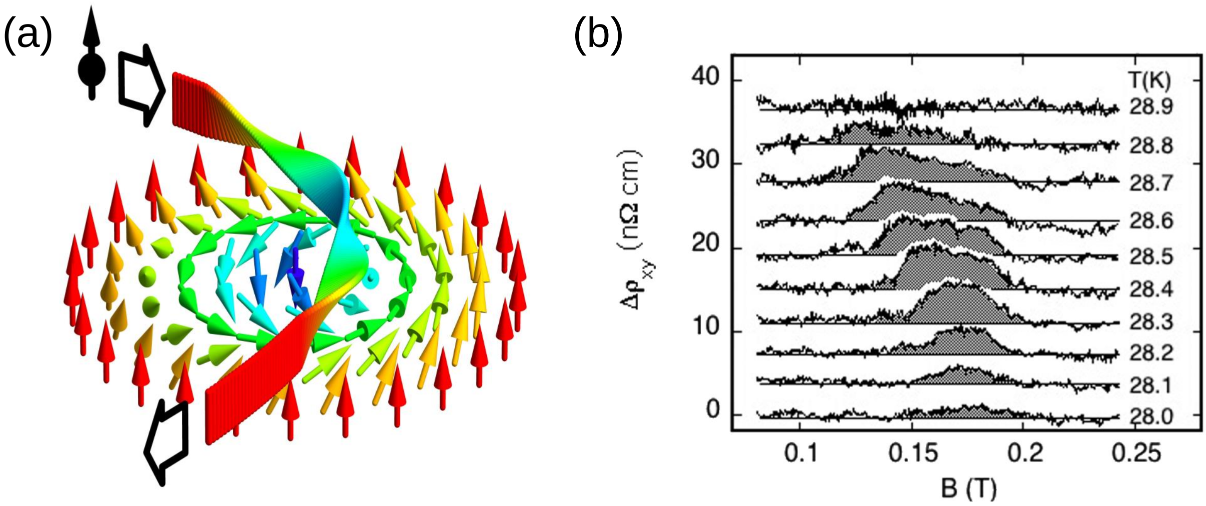

Figure 3.7: Coupling of electric currents to the Skyrmion lattice. (a) The spin of a conduction electron adiabatically follows the local magnetization of a Skyrmion thereby collecting a Berry phase. (b) Topological Hall contribution, $\Delta\rho_{xy}$, in the Skyrmion lattice phase of MnSi. The normal and anomalous Hall contribution scaling with the field and the magnetization, respectively, have been subtracted empirically. Pictures taken from Refs. [320, 321].

magnetic texture as schematically depicted in Fig. 3.7(a). As a consequence, the electron collects a Berry phase in real space [321, 322]. The Berry phase is given by the solid angle covered by $\hat{\psi} = \hat{\psi}(\boldsymbol{r}, t)$ which wraps once around a unit sphere for a Skyrmion. It can be rewritten [323–325] as an effective Aharonov-Bohm phase associated with an emergent magnetic and electric field, $B_i^e = \frac{\hbar}{2}\epsilon_{ijk}\hat{\psi} \cdot \partial_j\hat{\psi} \times \partial_k\hat{\psi}$ and $E_i^e = \hbar\hat{\psi} \cdot \partial_i\hat{\psi} \times \partial_t\hat{\psi}$, respectively, with $\partial_i = \partial/\partial r_i$ and $\partial_t = \partial/\partial t$. Thus, the deflection of the electrons may be described and detected in terms of a topological Hall effect, as first reported for MnSi, cf. Fig. 3.7(b). We note that the intrinsic anomalous Hall effect, present across the whole magnetic phase diagram, may be treated as a Berry phase in momentum space [326–328] and that even mixed contributions may play an important role [329–331].

Using the charge carrier spin polarization P and assuming the absence of intraband (spin-flip) scattering, while interband (non-spin-flip) scattering is captured by the normal Hall constant R_0, the topological Hall contribution may be estimated as $\Delta\rho_{xy,\mathrm{top}} = PR_0B_{\mathrm{eff}}$. The emergent Aharonov-Bohm field, B_{eff}, is topologically quantized as it is given by the product of the flux quantum that each Skyrmion carries, $\phi_0 = h/e$, and the Skyrmion density ϕ. Thus, the sign of the topological Hall contribution allows to distinguish between Skyrmions ($\varPhi = +1$) and anti-Skyrmions ($\varPhi = -1$). At least in MnSi the latter is the case, i.e., the center spin is antiparallel to the applied magnetic field. Note that the formula given above for $\Delta\rho_{xy,\mathrm{top}}$ is just a rough approximation, as the bands at Fermi surface may contribute to the topological Hall effect in different ways. Moreover, as a function of temperature the polarization as well as the Skyrmion lattice constant may change and at finite temperatures spin-flip scattering processes partly suppress the intrinsic value of $\Delta\rho_{xy,\mathrm{top}}$ [330].

The effective coupling of electric currents to the magnetic structure, together with the exceptional long-range order of the Skyrmion lattice and the resulting very weak collective pinning to defects, allows for the manipulation of the magnetic structure already at ultra-low current densities. Above a threshold current density of the order of $10^6\ \mathrm{A/m^2}$ in MnSi the whole Skyrmion lattice depins and starts to drift. Using numerical simulations, Iwasaki *et al.* revealed that the Skyrmion motion exhibits a universal current-velocity relation that is (on the scale of the study) unaffected by impurities and non-adiabatic effects [333]. Flexible shape-deformations of individual Skyrmions and the Skyrmion lattice permit to avoid pinning centers. Moreover, spin transfer torque effects are also predicted in the helical state, however, above a defect dependent threshold current of the order of $10^{10}\ \mathrm{A/m^2}$ and with a current-velocity relation that depends on material specific parameters [333]. The latter is also observed in conventional spin transfer torque experiments where domain walls are moved through ferromagnetic nanostructures, typically at currents of the order of $10^{10}\ \mathrm{A/m^2}$ to $10^{12}\ \mathrm{A/m^2}$ [334, 335, 335–338].

Theoretically, the spin transfer torque effects in the cubic chiral helimagnets may be accounted for by the Landau-Lifshitz-Gilbert equation using the Thiele approach [332, 339]. Here, a Magnus force perpendicular to the current direction and a dissipative drag force along it are balanced by pinning forces, e.g., due to defects. The Magnus force represents the effective Lorentz force arising from the emergent magnetic field $\boldsymbol{B}^e$ and leads to a certain angle between the current direction and the drift direction of the Skyrmion lattice. According to Faraday's law of induction, a moving Skyrmion, which supports exactly one quantum of magnetic flux, induces an emergent electric field $\boldsymbol{E}^e$ that inherits the topological quantization [325]. These electric fields can be directly measured as a putative suppression of the topological Hall signal as depicted in Figs. 3.8(a) and 3.8(b) [322]. For these experiments, a dc current sufficient to move the Skyrmions ($\sim 10^6\ \mathrm{A/m^2}$) was superimposed with a small ac current ($\sim 10^3\ \mathrm{A/m^2}$) for measuring the Hall effect with a lock-in technique.

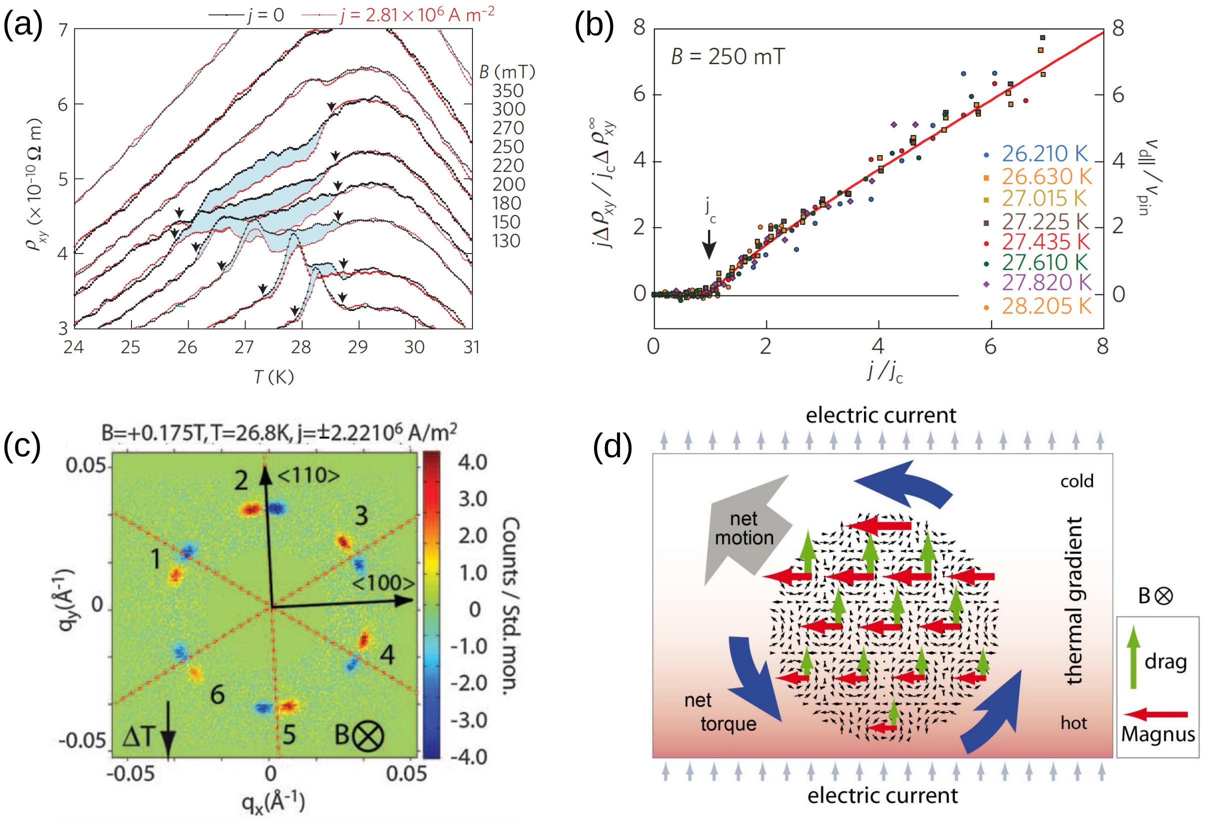

Figure 3.8: Manipulation of the Skyrmion lattice by electric currents. (a) Hall effect as a function of temperature in MnSi without (black) and with (red) the application of a dc current in the order of 10^6 A/m^2. (b) Drift velocity of the Skyrmion lattice as a function of the dc current density, where a critical current density j_c is required to unpin the magnetic structure. Using normalized units a universal behavior is observed for different temperatures. (c) Difference of two small-angle neutron scattering patterns for current applied in opposite directions in the presence of a temperature gradient. (d) Schematic depiction of the forces leading to the rotation of the scattering pattern. Pictures taken from Refs. [322, 332].

In the presence of a gradient of the local charge carrier spin polarization, the movement of the magnetic structure above the threshold current density may also be observed in small-angle neutron scattering, cf. Figs. 3.8(c) and 3.8(d) [332, 340]. A variation the local polarization enters the prefactors of the Magnus force and the drag force creating a net torque on the magnetic structure between the sample regions with high and low polarization. As a consequence, the sixfold small-angle neutron scattering pattern rotates, where the rotation sense depends on the direction of the magnetic field, the current, and the polarization gradient. If the gradient is steep enough to allow for a rotation of 15° hence overcoming the weak pinning of the propagation vectors in the Skyrmion lattice due to cubic anisotropies, a continuous rotation of large Skyrmion domains is predicted [341]. Experimentally, the local polarization gradient may for example be produced by a gradient of the temperature [332] or the magnetic field. Moreover, a thermal gradient caused by irradiating the sample with a light or an electron beam may lead to a ratchet motion of the Skyrmion lattice [342]. In Cu_2OSeO_3 the magnetoelectric coupling promises further ways to manipulate the Skyrmion lattice, e.g., via the application of electric fields, as will be explained in Sec. 3.1.9.

Real-space observation and unwinding by magnetic monopoles

The Skyrmion lattice and its manipulation by electric currents has also been observed in real space. For this purpose, Tokura *et al.* used Lorentz force transmission electron microscopy which images the local distribution of the magnetic moments perpendicular to the electron beam [40–42, 343]. The measurements were performed on electron-transparent wedges prepared from bulk samples (<100 nm). In these samples the hexagonal Skyrmion lattice was observed in a large part of the magnetic phase diagram as the conical state is energetically unfavorable for very thin samples in an out-of-plane field, cf. Fig. 3.9(a) [344]. With increasing sample thickness bulk behavior is recovered [41]. In a further study of FeGe the authors also demonstrated the direct observation of spin transfer torque effects on a Skyrmion lattice near room temperature [345]. Finally, at the border of the regular Skyrmion lattice state, single Skyrmions were spotted in a helimagnetic or a field-polarized background, respectively, suggesting regimes of phase coexistence. The first-order phase boundary between the Skyrmion lattice and the neighboring states, the resulting regime of phase coexistence, and the slow response therein will be addressed in Secs. 3.3.1 and 3.3.2, cf. also Refs. [86, 313]. Recently, the spin structure of the helical and the Skyrmion lattice state was also mapped in three dimensions by means of electron holography [346].

In addition, magnetic force microscopy was used to image the Skyrmion lattice in real space, cf. Fig. 3.9(b) through Fig. 3.9(d) [80]. Here, the distribution of magnetic moments perpendicular to the sample surface is detected by essentially measuring their stray field with an atomic force microscope equipped with a ferromagnetically coated tip. By means of this complimentary technique the surface of bulk samples (as in the present study), thin films including their substrates, or whole devices may be investigated. In addition, in this study we addressed the question how the topologically non-trivial Skyrmion lattice may emerge from and decay into a topologically trivial helimagnetic state. When starting from a regular Skyrmion lattice state and decreasing the magnetic field, two neighboring Skyrmion lines associated with two flux quanta, $\sum|\Phi| = 2$, coalesce and form an elongated structure ($|\Phi| = 1$). Monte Carlo simulations showed that these changes of topology are controlled by singular magnetic point defects. They can be viewed as quantized magnetic monopoles and antimonopoles, which provide sources and sinks of one quantum of emergent magnetic flux, respectively. Finally, small-angle neutron scattering data proved that the behavior at the surface of the sample is characteristic for its bulk. The moving emergent monopoles are expected to induce electric currents and, following Ref. [347], are dyon-like objects in terms of the effective fields, i.e., they have both electric and magnetic charge.

Skyrmions in thin films

Especially since the discovery of the Skyrmion lattice in the bulk cubic chiral helimagnets, thin films of these compounds are also heavily investigated both experimentally and theoretically. The creation, manipulation, and the dynamics of Skyrmions in thin films [348–351, 351–355], nanowires [356, 357], and eventually patterned nanostructures [358–362] of chiral helimagnets or other compounds offer great potential for future applications [363]. For instance, it is predicted that single Skyrmions may be created by the injection of currents that are either spin-

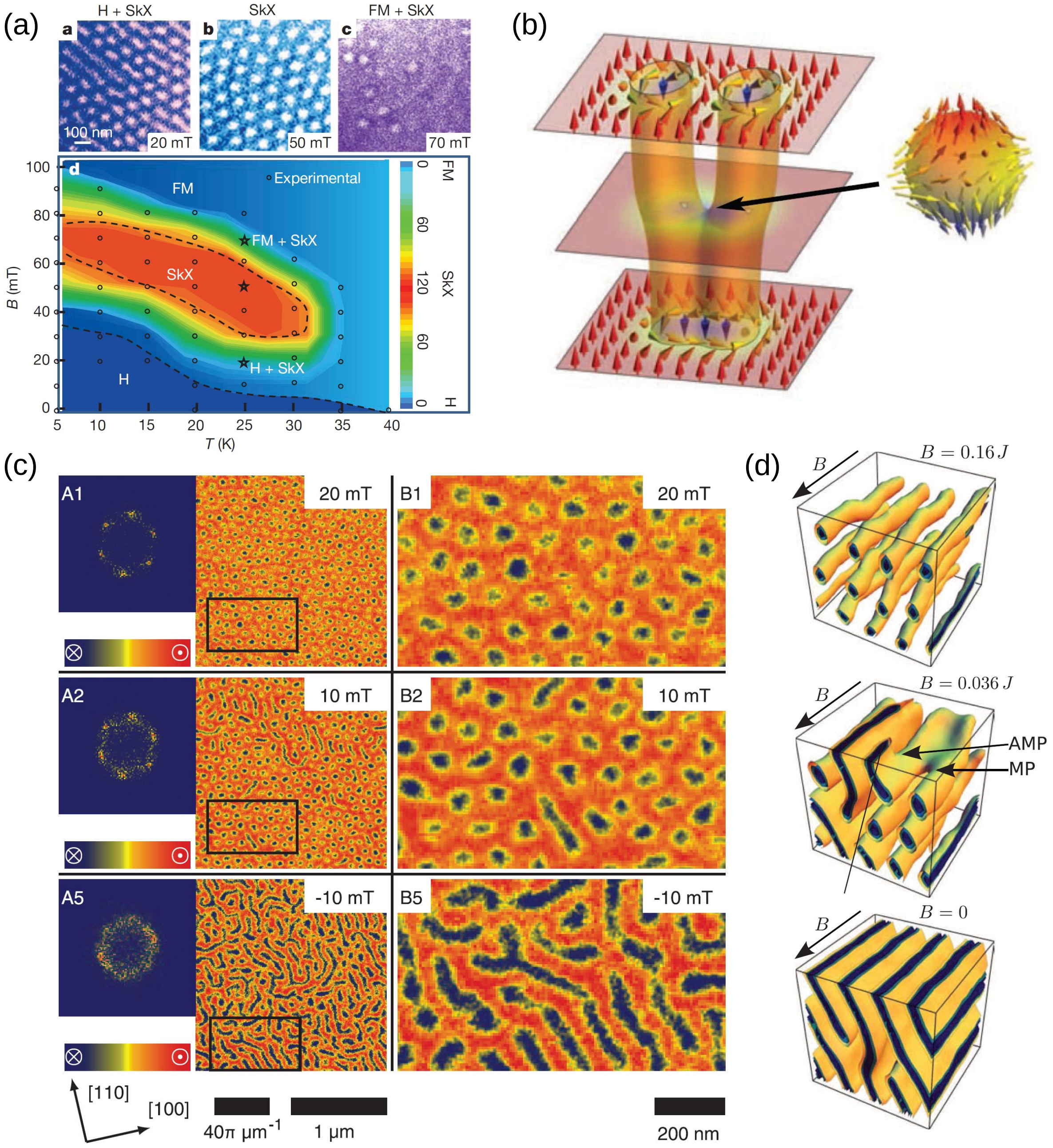

Figure 3.9: Real-space observation of the Skyrmion lattice. (a) Lorentz force transmission electron microscopy images of $\mathrm{Fe}_{1-x}\mathrm{Co}_x\mathrm{Si}$ ($x = 0.50$) and the magnetic phase diagram derived thereof. (b) Magnetic (anti-)monopoles act as sources (sinks) of magnetic flux and merge neighboring Skyrmion lines. (c) Left column: Magnetic force microscopy images of $\mathrm{Fe}_{1-x}\mathrm{Co}_x\mathrm{Si}$ ($x = 0.50$) after field cooling to 10 K for decreasing fields (top to bottom). The insets show the Fourier transformations of the real-space pictures resembling small-angle neutron scattering data. Right column: Blow-ups of the regions marked with black rectangles. (d) Monte Carlo simulations reveal that the Skyrmion lines merge in the bulk via monopoles (MP) and antimonopoles (AMP) as the field strength B is decreased. Pictures taken from Refs. [40, 80].

polarized [364] or combined with constricted geometries [365]. The topological stability and the small size of the Skyrmions promise devices for ultra-dense information storage and spintronics [366, 367]. In addition, the unique collective excitations of the magnetic textures that will be addressed in the following subsection allow for the design of conceptually new microwave devices [368, 369]. Furthermore, metallurgically complex systems with interesting properties such as FeGe (high T_c) or MnGe (small λ_h) may be accessible in the form of thin films [370]. Currently, however, even fundamental aspects are discussed controversially, e.g., in Refs. [349, 371, 372].

Solid state research on the Skyrmions, however, is not exclusively carried out on cubic chiral helimagnets. Result from completely different systems may thereby stimulate each other. In thin films, where the inversion symmetry is already broken by the surface, up to now three mechanisms are known that may stabilize Skyrmions: (i) the Dzyaloshinskii-Moriya interaction in the cubic chiral helimagnets, as discussed above, leading to Skyrmion lattice constants in the order of 10 nm to 100 nm, (ii) four-spin exchange interactions leading to an atomic-scale Skyrmion lattice ($\sim$1 nm), or (iii) long-ranged magnetodipolar interactions stabilizing Skyrmions with a typical size of $\sim$1 µm. A fascinating example for the second case are iron monolayers on top of an iridium $\langle 111 \rangle$ surface where an atomic-scale Skyrmion lattice evolves as ground state in zero field [24]. By adding palladium and a magnetic field, a state is stabilized where the Skyrmions may be created and annihilated individually [25]. The formation of Skyrmions in field is also predicted for FePt on top of a platinum $\langle 111 \rangle$ surface [373]. The third scenario occurs in thin ferromagnetic layers with the easy axis perpendicular to the film. Here, examples include individual Skyrmions created by laser pulses [374, 375] and lattices of double-twisted Skyrmions with random helicity in doped hexagonal barium ferrite ($BaFe_{12-x-0.05}Sc_xMg_{0.05}O_{19}$, $x = 0.16$) with field normal to the film [376]. Recently, Skyrmion-like magnetic clusters with random chirality have also been observed in the ferromagnetic manganite $La_{0.5}Ba_{0.5}MnO_3$ above $T_C \approx 310$ K, where a thermally activated repeated reversal of the magnetic chirality occurs around 360 K [377].

3.1.5 Collective excitations

In the following subsection, we will first summarize our recent study of the collective excitations of the cubic chiral helimagnets by means of cryogenic microwave spectroscopy including a quantitative theoretical description, cf. Ref. [252]. Subsequently, in the view of these results, we will account for previous studies at small momenta and address the excitation spectra as measured at large momenta.

The magnetic structures in the cubic chiral helimagnets give rise to a set of collective excitations that are schematically depicted in Fig. 3.10. In the topologically trivial helical and conical states the low-lying excitations arise from a local precession of the spins. The resulting compressional wave either propagates parallel (+Q) or antiparallel (−Q) to the propagation vector of the helix. The direction of the local precession of the spins is fixed by the sign of the gyromagnetic ratio. In the Skyrmion lattice state three fundamental modes arise; two gyration modes where the Skyrmion core precesses collectively either counter-clockwise or clockwise as well as a breathing mode. The latter may only be excited if the excitation possesses momentum along the applied magnetic field. The gyration modes as well as the modes in the conical and the helical state require momentum perpendicular to the applied field and the helical pitch vector, respectively.

Energetically, the excitations may be treated by the Ginzburg-Landau approach discussed in Sec. 3.1.1, if properly taking into account dipolar interactions. Hence, the free energy density

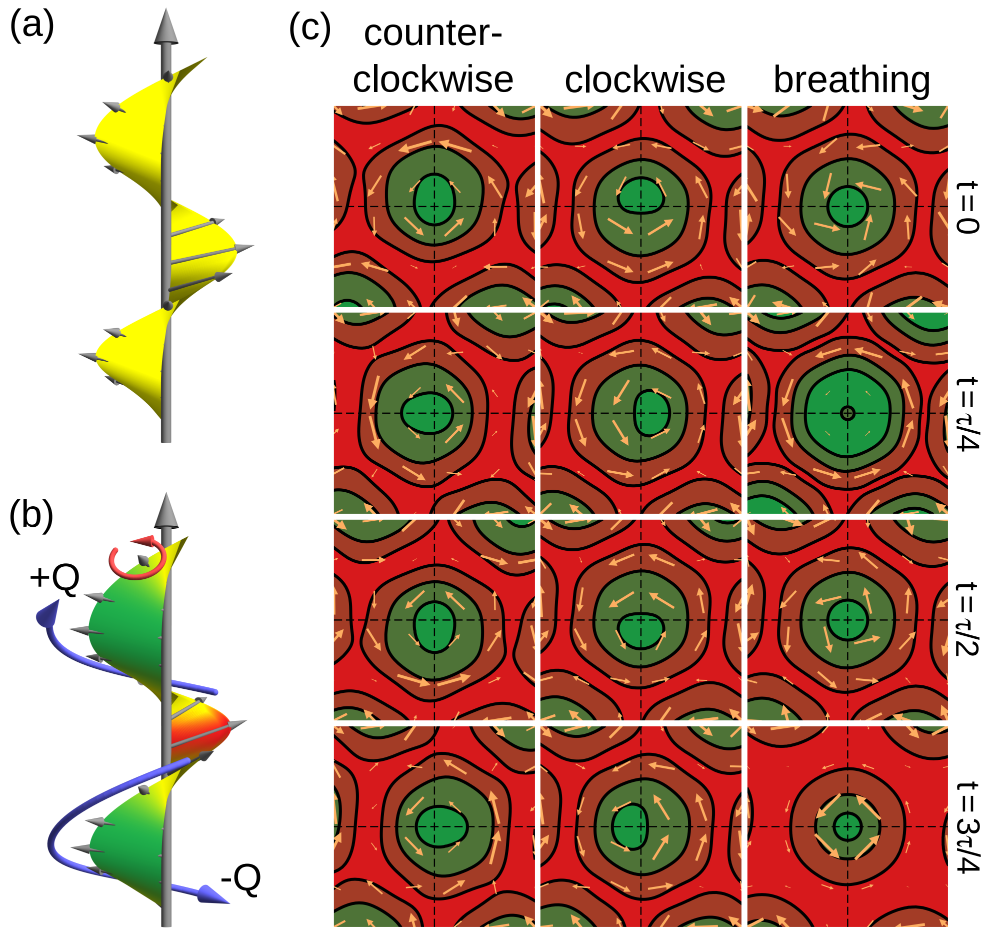

Figure 3.10: Collective excitations in the cubic chiral helimagnets. (a) Conical spiral in equilibrium. (b) Excited conical spiral. The local precession of the spins (red arrow) translates to a compressional wave that propagates either parallel (+Q) or antiparallel (−Q) to the propagation vector of the helix (gray arrow). (c) The two gyration modes and the breathing mode of the Skyrmion lattice phase. The color indicates the distribution of the out-of-plane moments parallel (red) and antiparallel (green) to the magnetic field. Pictures taken from Ref. [252].

may be expressed as $f = f_0 + f_{\text{cub}} + f_{\text{dip}}$. The magnetic resonances are then determined with the help of the equation of motion for the magnetization $\partial_t M = -\gamma M \times B_{\text{eff}}$. Here, $\gamma = g\mu_{\text{B}}/\hbar$ with $\mu_{\text{B}} > 0$ is the gyromagnetic ratio and the effective local field is given by the functional derivative $B_{\text{eff}} = -\partial\mathcal{F}/\partial M$. In equilibrium the magnetization minimizes the free energy so that $B_{\text{eff}}|_{\text{eq}} = 0$. Linearizing the equation around the equilibrium configuration allows to determine the eigenmodes and eigenfrequencies, where we first focus on excitations with a vanishing wave vector, k.

The resulting excitation spectra, see Fig. 3.11, including the spectral weight of the different modes are dependent only on material specific parameters and geometry of the sample. The material specific parameters are easily accessible from experiments and comprise the essentially constant magnetic susceptibility in the conical state, χ_{con}, the gyromagnetic factor, g, and the temperature dependent critical field between the conical and the field-polarized state, $H_{c2}(T)$. It turns out that χ_{con} quantifies the influence of the dipolar interactions. The two other parameters g and $H_{c2}(T)$ may be combined to the critical internal field energy $E_{\text{CF}}(T) = g\mu_0\mu_{\text{B}}H^{\text{int}}_{c2}(T)$ which fixes the absolute values of the resonance frequencies and inherits its weak temperature dependence mainly from $H_{c2}(T)$. The tiny temperature dependence of the gyromagnetic factor may usually be neglected. The sample shape finally enters via the effects of the demagnetizing fields that distinctly influence both the frequency and the weight of the modes and that are covered by the demagnetization factors N_x, N_y, and N_z. Here, we approximate the magnetization as $M \approx \chi_{\text{con}}H$ for $H < H_{c2}$ and $M \approx \chi_{\text{con}}H_{c2}$ for $H \geq H_{c2}$.

In the field-polarized state a single excitation mode arises that corresponds to a standard ferromagnetic resonance and may be described by the Kittel formula [378].

$$\hbar\omega = |g|\mu_0\mu_{\text{B}}H_{c2}\sqrt{[h + (N_x - N_z)\chi_{\text{con}}][h + (N_y - N_z)\chi_{\text{con}}]}$$

Here, the field is applied along the z-direction and $h = H/H_{c2}$. The two excitation modes in the conical phase may also described analytically. One solution of the rather longish expression, ω^+, smoothly connects to the Kittel mode of the field-polarized state at H_{c2} while the spectral weight of the other branch, ω^-, vanishes in this limit. When taking into account the cubic anisotropies in the helical state, the mean magnetization is in general not longitudinal to the pitch vector. Hence, the two excitation modes need to be obtained numerically with the strength of the cubic anisotropy, J_{cub}, as an additional material specific parameter. In the Skyrmion lattice state, finally, the three excitation modes are also evaluated numerically.

Experimentally, we have recorded these resonances by means of cryogenic microwave spectroscopy. Here, polished bulk single crystals of the cubic chiral helimagnets MnSi, $\text{Fe}_{1-x}\text{Co}_x\text{Si}$ ($x = 0.20$), and Cu_2OSeO_3 with different sample shapes and crystalline orientations were put on top of a coplanar waveguide. In combination with a vector network analyzer sinusoidal radio-frequency currents at frequencies between 10 MHz and 26.5 GHz were applied at a small excitation wave vector of $k_{\text{CPW}} = 9.4 \cdot 10^{-6}\,\text{Å}^{-1}$. The corresponding wave length is large compared to the intrinsic length scales in the chiral helimagnets and one may therefore consider a homogeneous excitation field. In the setup used the main contribution of the excitation field lies perpendicular to the dc magnetic field and hence the breathing mode of the Skyrmion lattice was not excited. The transmission of the microwave is measured as a function of the excitation frequency at fixed temperatures and magnetic fields. After the subtraction of a reference spectrum recorded at large fields, minima may be attributed to resonant excitations. Plotting the corresponding frequencies as a function of field yields the data shown in Fig. 3.11 which are in excellent agreement with the theoretical model.

Prior to our work summarized above, the collective excitations in the cubic chiral helimagnets have been addressed in several studies. Early spin resonance work on MnSi [379] and FeGe [380] carried out at fixed frequencies resolved two modes in the conical phase and a single excitation in the ferromagnetic state [381]. In MnSi additionally one of the Skyrmion modes was resolved. These seminal studies clearly predated the large scientific interest in the chiral helimagnets in recent years. This constraint essentially also holds true for a similar study carried out at high frequencies in the field-polarized state of Cu_2OSeO_3 [382]. The modes within the Skyrmion lattice state have first been predicted by Mochizuki who also pointed out that the Skyrmion lattice may even be melted by an intense irradiation of circularly polarized microwaves [383]. Petrova and Tchernyshyov addressed the gyration modes analytically, however, by treating the Skyrmion lattice as superposition of three helices [384]. In a comprehensive but purely

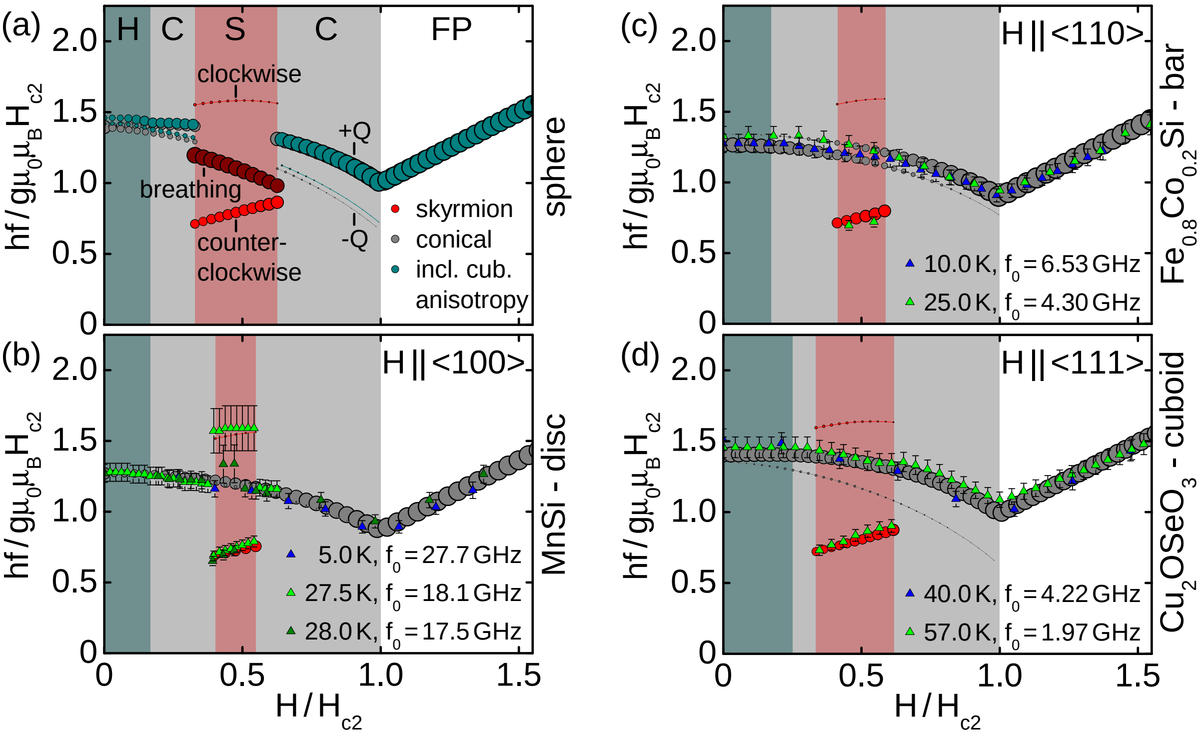

Figure 3.11: Excitation spectra across the magnetic phase diagram of the cubic chiral helimagnets. (a) Expected excitation spectrum for a spherical sample and a field scan crossing the helical (H), the conical (C), the Skyrmion lattice (S), and the field-polarized (FP) state. The size of the points reflects their spectral weight. The analytic solution neglecting the cubic anisotropies as well as the numeric solution taking them into account are shown for the topologically trivial states. (b)–(d) Experimental data on MnSi, $Fe_{1-x}Co_xSi$, and Cu_2OSeO_3 for different crystallographic orientations and sample geometries are in excellent agreement with the theory. Pictures taken from Ref. [252].

qualitative study, Onose and coworkers investigated the excitations in the insulator Cu_2OSeO_3 using stripline wave guides [385]. At low temperatures the two modes in the conical state were resolved. At temperatures within the Skyrmion lattice state they detected one of the low-lying gyration modes as well as the breathing mode for magnetic dc fields perpendicular and parallel to the excitation field, respectively. Following theoretical predictions, in this multiferroic compound the collective modes may also be excited by electric fields [368, 386], cf. Sec. 3.1.9. Recently, also the different modes of single Skyrmions in a ferromagnetic background were considered [387].

A comprehensive inelastic neutron scattering study on MnSi in zero field addressed excitations with large momenta k in the regime $2Q_\mathrm{h} \lesssim k$, where $Q_\mathrm{h} = 2\pi/\lambda_\mathrm{h}$ corresponds to the wave vector of the helix. [388]. Here, multiple strongly coupled bands of helimagnons arise as an universal property of long-wavelength helimagnets. For excitations along $\boldsymbol{Q}_\mathrm{h}$ three modes centered at $k = 0$ and $k = \pm Q_\mathrm{h}$ emerge that disperse linear for $k_\parallel \ll Q_\mathrm{h}$ and quadratic for $k_\parallel \gg Q_\mathrm{h}$. With increasing momentum perpendicular to $\boldsymbol{Q}_\mathrm{h}$ the modes are mixed. In the limit $k_\perp \gg Q_\mathrm{h}$ typically some $\sqrt{k_\perp/Q_\mathrm{h}}$ modes with equally spaced energies are excited. Their dispersion is essentially independent of $k_{\|}$ for $k_{\|} < \sqrt{k_{\perp} Q_{\mathrm{h}}}$ which results from repeated Umklapp scattering that prohibits the motion of the spin excitations parallel to $\boldsymbol{Q}_{\mathrm{h}}$. The complex spectra obtained experimentally finally are the superposition of contributions from the different helical domains.

These observations were complemented by a recent study on $Fe_{1-x}Co_xSi$ ($x = 0.20$), where we demonstrated that helimagnons may also be optically excited by a laser pulse [389]. The oscillation of the local magnetization and its decay were monitored by time-delayed probe pulses measuring the Kerr rotation on the surface of the sample time-resolved. The temperature and field dependence of the signal were in agreement with the magnetic phase diagram. The Gilbert damping parameter, $\alpha = (2\pi f_0 \tau_{\mathrm{K}}) = 0.4 \pm 0.1$, was calculated from the decay time of the oscillation, τ_{K}. The frequency of the resonance at low temperatures, f_0, is in good agreement with the cryogenic microwave spectroscopy data.

Taken together, a proper account for dipolar interactions and demagnetization effects permits a quantitative and universal description of the collective modes in the cubic chiral helimagnets. Their excitation and detection may be carried out by various methods. Perhaps most excitingly, however, the tailored gigahertz response of the self-organized spin textures may be exploited for magnonics, i.e., spin-wave-based electronics, that so far were dependent on nanopatterning and bespoke demagnetizing fields [390, 391]. Coplanar waveguides, which may be readily integrated into thin film heterostructures, thereby allow for a study of such devices due to their small but finite excitation wave vector distribution centered at k_{CPW}.

3.1.6 MnSi: a weak itinerant helimagnet

In this subsection, we summarize the properties of the metallic $B20$ compound MnSi, which is the archetypical and most investigated cubic chiral helimagnet. We start with an account for its ambient pressure properties and the historical development of the research carried out over the past five decades. In the second part, we briefly address the pressure-induced suppression of magnetic order.

MnSi exhibits long-range magnetic order below $T_c \approx 29\,\mathrm{K}$ [289, 392–394], which was identified as long-wavelength helimagnetism with an easy $\langle 111 \rangle$ axes in the 1970s [254, 290, 395–397]. The helix wavelength, λ_{h}, increases from $\sim$165 Å at T_c to $\sim$180 Å at lowest temperatures [257, 311, 395]. After zero-field cooling the four helical $\langle 111 \rangle$ domains are populated equally. With increasing field the conical state, which compares to the spin-flop state of a conventional antiferromagnet, is reached at $\mu_0 H_{c1} \sim 0.1\,\mathrm{T}$ before the system enters a field-polarized state at $\mu_0 H_{c2} \sim 0.6\,\mathrm{T}$. Just below T_c and in fields of $\sim$0.2 T a small phase pocket, historically referred to as A-phase, was discovered early on [289–291]. Its microscopic nature, however, remained enigmatic until it was identified as a Skyrmion lattice in recent years [12], cf. Sec. 3.1.4.

MnSi was the first experimental example of a material which exhibits a spin spiral based on the Dzyaloshinskii-Moriya interaction [398–400]. The resulting correlation of the chirality of the crystal lattice, Γ_c, and the spin structure, γ_m, was revealed a few years later (in MnSi: $\Gamma_c \cdot \gamma_m = +1$) [401–403]. In the 1970s and 80s, however, the different energy scales were addressed as separate issues and the helical order was considered as a small distortion of an otherwise ferromagnetic state that occupies just a tiny fraction of the Brillouin zone. MnSi thereby turned out to be one of the prime examples for weak itinerant ferromagnetism, along with Ni_3Al, $ZrZn_2$, and very few further compounds. Its behavior could be described quantitatively with a phenomenological model taking into account the spectrum of thermal spin fluctuations [105–107, 404], which for the first time were detected over the entire Brillouin zone in MnSi [405, 406]. Further key characteristics include the strong Curie-Weiss dependence in the paramagnetic state with a large fluctuating moment of $\sim 2.2\,\mu_{\mathrm{B}}$/f.u. by far exceeding the ordered moment of $\sim 0.4\,\mu_{\mathrm{B}}$/f.u. and the unsaturated, non-linear magnetization up to highest fields studied (33 T) [407].

Despite the intense research, the nature of the phase transition from paramagnetism at high temperatures to helimagnetism at low temperatures is still debated controversially. While it was initially interpreted as second order [289], more detailed bulk and transport data clearly established a first-order transition with the release of a tiny latent heat at T_c [211, 408–410]. A broad shoulder in the specific heat in the vicinity of T_c [211] hinted towards the importance of chiral fluctuations that were detected above T_c by means of inelastic neutron scattering [272, 411]. A Vollhardt invariance at $T_2 \approx T_c + 1$ suggested strong renormalization effects arising from the interaction between these fluctuations [85, 278, 279]. The latter leads to a fluctuation-induced first-order transition as recently explained within a Brazovskii scenario [257] that was favored over an extended Bak-Jensen scenario [273, 274], cf. Sec. 3.1.2. Further scenarios include (i) a Skyrmion liquid phase [276, 277] as a generic precursor phenomenon in Dzyaloshinskii-Moriya-driven helimagnets [318] and (ii) a so-called magnetic blue phase, which is a complex form of long-range order that was motivated by an amorphous lattice of Skyrmions observed in Monte Carlo simulations [275].

Pressure dependence

The behavior of MnSi as a function of hydrostatic pressure was intensively studied in the last two decades. The first studies were motivated by the search for a marginal breakdown of Fermi liquid theory at a pressure-induced quantum phase critical point [413]. With increasing pressure the helimagnetic transition temperature T_c is suppressed and finally vanishes at a critical pressure of $p_c = 14.6\,\mathrm{kbar}$, cf. Fig. 3.12(a). At $p^* \approx 12\,\mathrm{kbar}$, however, the transition turns distinctly first-order and itinerant metamagnetism under applied magnetic fields appears [414–416], i.e., at p_c there is no conventional second-order quantum critical point but a first-order quantum phase transition [417]. Moreover, nuclear magnetic resonance [418] and muon spin resonance data [419] suggest a magnetic phase separation for $p > p^*$ where a decreasing volume fraction of helimagnetic order tracks the transition extracted from bulk and transport measurements [413, 420–424].

In addition, neutron scattering [412] reveals partial magnetic order in a pocket above p_c. In combination with the lack of observable relaxation in muon data [419], a dynamic character on a timescale between 10^{-10} s and 10^{-11} s is implied. This partial order is depicted in Fig. 3.12(b) and characterized by a sphere of intensity in reciprocal space with a radius corresponding to the helical pitch and broad maxima along the crystalline $\langle 110 \rangle$ directions. It was named due to its analogy with liquid crystals and inspired several theoretical studies searching for complex spin structures in MnSi [318, 425–430].

Despite the lack of quantum criticality, Fermi liquid theory, which properly accounts for the behavior at lower pressures, breaks down above p_c. Here, an extended temperature, pressure, and field regime of non-Fermi liquid behavior emerges, where the resistivity shows a $T^{3/2}$ dependence instead of the T^2 dependence of a Fermi liquid at least up to $p \approx 3p_c$ [431–433]. This behavior contrasts the excellent quantitative description of MnSi as a weak itinerant magnet and, among other scenarios, columnar fluctuations were discussed as a possible origin [434, 435]. Moreover, at intermediate pressures a large topological Hall signal was reported [436]. In a recent study [11, 330], we established a clear connection between the topological Hall effect in the Skyrmion lattice at ambient pressure and a large topological Hall signal in the non-Fermi liquid regime above p_c, cf. Fig. 3.12(c). As the transition temperature decreases the Skyrmion lattice state forms at lower

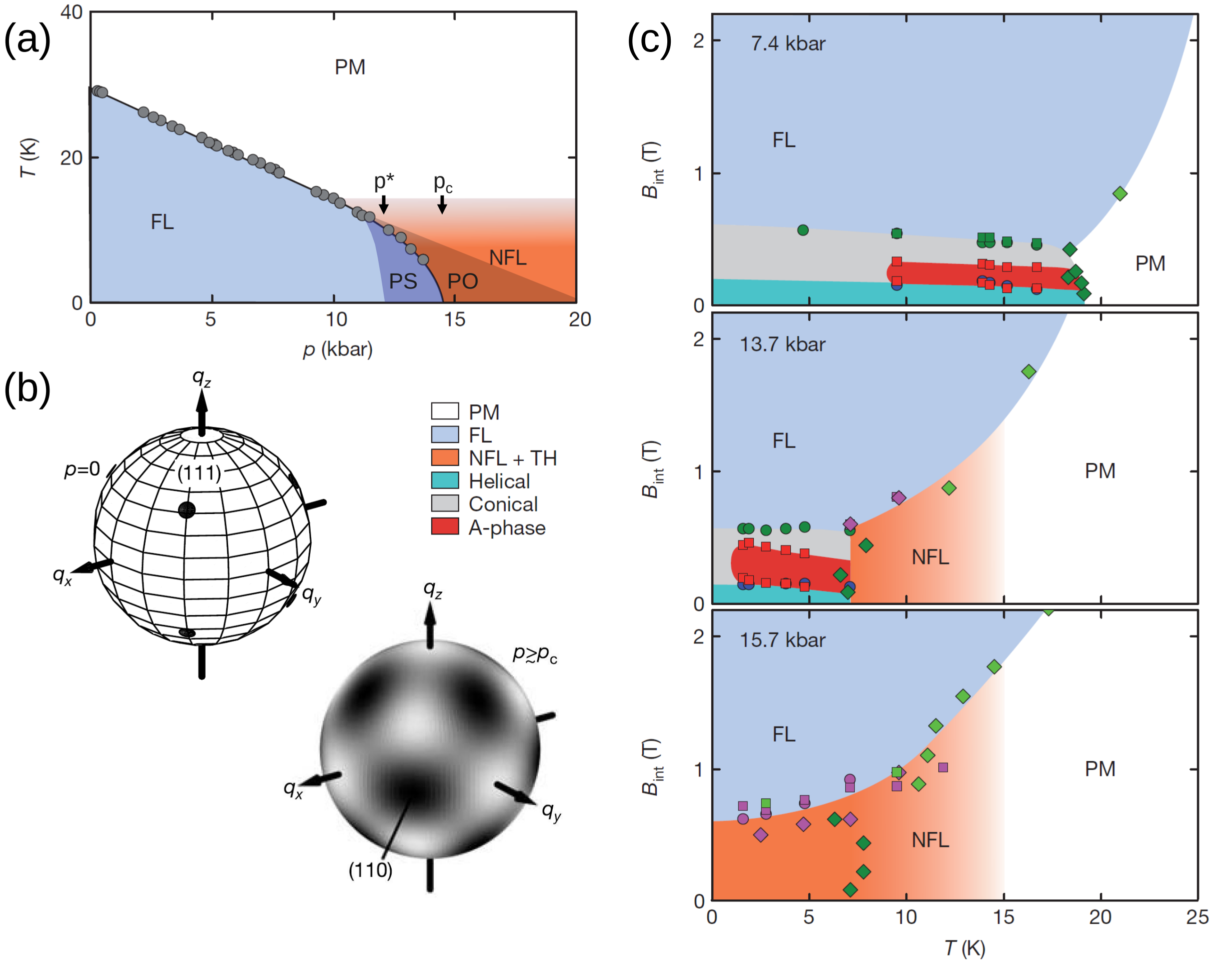

Figure 3.12: MnSi under hydrostatic pressure. (a) Temperature-pressure phase diagram. We distinguish the following regimes: Fermi liquid (FL), non-Fermi liquid (NFL), paramagnet (PM), phase separation (PS), and partial order (PO). (b) Schematic depiction of zero-field neutron intensity observed at low temperatures in reciprocal space at ambient pressure (left) and in the partially ordered state (right). (c) Magnetic phase diagrams at $p < p^*$ (top), $p_0 < p < p_c$ (middle), and $p > p_c$ (bottom). With respect to ambient pressure, the transition temperature, T_c, is suppressed but the phase diagram at first stays qualitatively similar. For $T_c \lesssim 12\,\mathrm{K}$ a regime with NFL resistivity and a large topological Hall (TH) contribution emerges for $T_c < T \lesssim 12\,\mathrm{K}$ (orange shading). Pictures taken from Refs. [11, 412].

temperatures. Thus, spin-flip scattering is suppressed and the topological Hall contribution approaches its intrinsic value of $\sim 50\,\mathrm{n\Omega cm}$ whereas at ambient pressure only some $\sim 4\,\mathrm{n\Omega cm}$ are observed [321]. The coincidence of the extent of the topological Hall signal and the non-Fermi liquid resistivity suggests empirically that spin correlations with non-trivial topological character, that may somehow be associated with the partial magnetic order, drive the breakdown of Fermi liquid theory.

3.1.7 $Mn_{1-x}Fe_xSi$: substitutional doping of MnSi

Substitutional doping is often referred to as the application of chemical pressure. In general, hydrostatic pressure shrinks the lattice constant and thereby alters the band structure and finally the density of states at the Fermi level. The situation under doping is more complex as it may vary the lattice constant and the number of electrons per formula unit. In addition, doping introduces disorder to the system.

In MnSi substitutional doping of neighboring transition metals onto the manganese sites results in a suppression of the helimagnetic ordering temperature. It was demonstrated that the decisive factor is the number of valance electrons per formula unit where doping with iron, cobalt, and nickel results in a universal behavior [85, 238]. Doping with chromium, i.e., reducing the number of valance electrons, leads to a suppression of T_c comparable to iron doping [234]. Taken together, this dependence suggests that the shift of the Fermi level is the dominant mechanism responsible for the change of the physical properties, that the Fermi energy in MnSi is located near a local extremum of the density of states, and that the band structure is only moderately modified by the doping.

In the following we focus on the properties under doping with iron, see Fig. 3.13(a). Here, the lattice constant decreases roughly linear with increasing doping level as expected from Vegard's law and, in contrast to hydrostatic pressure, there is no anomaly as the magnetic order is suppressed [417, 437, 438]. If we neglect all but the strongest energy scale, the ferromagnetic exchange, the suppression of itinerant ferromagnetism in $Mn_{1-x}Fe_xSi$ agrees remarkably well with the predictions of spin fluctuation theory. In particular, the ferromagnetic transition temperature, T_C, extrapolated from Arrott plots at high fields or Curie plots at high temperatures, and the ordered moment at zero temperature, $m_{s,0}$, vanish continuously as $T_C \propto {m_{s,0}}^{3/2}$, see Fig. 3.13(b) [85, 106]. This behavior contrasts the dependence of $m_{s,0}$ as a function of pressure [413, 415, 439] and suggests the existence of an underlying ferromagnetic quantum critical point as a function of doping. However, the extrapolated temperature T_C is always between the fluctuation-induced first-order transition at T_c, also referred to as T_1, and the Vollhardt invariance at T_2 as introduced in the Brazovskii scenario, cf. Sec. 3.1.2. Thus, the putative quantum critical point at $x_{C,\mathrm{Fe}} \approx 0.19$ is masked by the influence of the smaller energy scales and a series of quantum phase transitions [85]. In a recent neutron scattering study this phenomenon was referred to as chiral criticality [274].

As the transition temperature is suppressed, the magnetic phase diagram as extracted from magnetization, susceptibility, specific heat, and small-angle neutron scattering stays qualitatively unchanged up to concentrations of $x \sim 0.5x_C$ [85, 235, 237, 292, 440], consistent with early data [248, 441]. The field scale stays essentially unchanged while the helix wavelength decreases by roughly a factor of two and hence considerably more than in MnSi under hydrostatic pressure [442]. As one of the consequences, the pronounced Skyrmion lattice state gives rise to a large topological Hall effect that gets as large as $\sim 50\,\mathrm{n}\Omega\mathrm{cm}$ [443] and that is subject to spin transfer torque effects [444]. Due to the increased amount of disorder, the residual resistivity increases with x [101, 248, 445] and a proper helical state only is observed after zero-field cooling. The transition field H_{c1} increases essentially linearly with decreasing temperature. At higher concentrations, $x_{\mathrm{Fe}} \leq 0.12$, the signatures in susceptibility and small-angle neutron scattering data are drastically smeared out. In the specific heat the anomaly from the fluctuation-induced first-order Brazovskii-type transition vanishes for $0.10 < x_{\mathrm{Fe}} < 0.12$, cf. Sec. 3.3.2 or Ref. [270] for corresponding neutron scattering data. Therefore, the underlying mechanisms seem to alter significantly as the putative quantum critical point at x_C is approached, combined with or

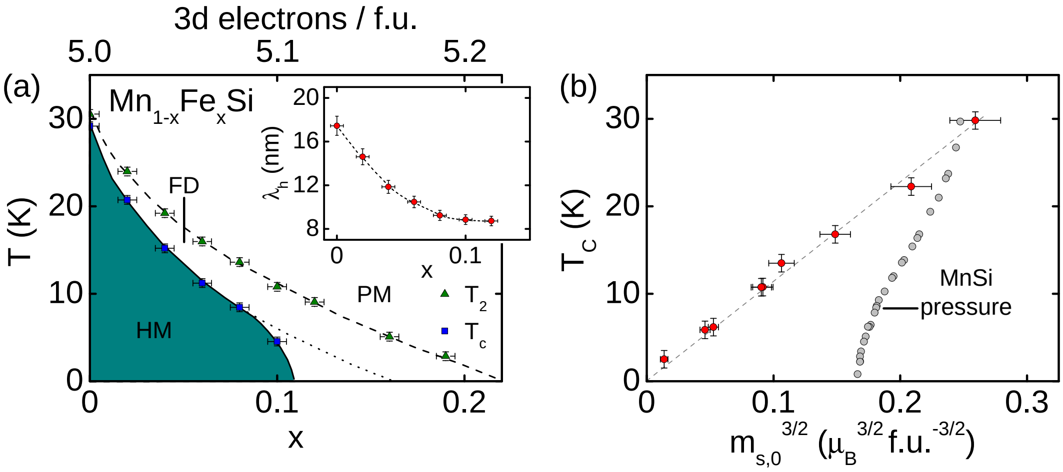

Figure 3.13: Suppression of helimagnetism in $Mn_{1-x}Fe_xSi$. (a) Compositional phase diagram with paramagnetism (PM), helimagnetism (HM), and a fluctuation-disordered regime (FD). Using the upper abscissa essentially yields a universal phase diagram for $Mn_{1-x}Fe_xSi$, $Mn_{1-x}Co_xSi$, and $Mn_{1-x}Ni_xSi$ [238]. The inset shows the helix wavelength, λ_{h}, as a function of the iron content. (b) The transition temperature extrapolated from high fields, T_{C}, vanishes continuously with the zero-temperature ordered moment, $m_{s,0}$. The Plots are reproduced from Refs. [85, 270]. Data as a function of pressure are taken from Refs. [413, 414, 439].

caused by an increasing amount of disorder in the system [85, 446]. Though, for $x_{\mathrm{Fe}} = 0.12$ a large topological Hall signal survives and suggests the presence of structures with non-trivial topology albeit no long-range order is identified in neutron scattering [443]. Taken together, the behavior largely resembles the situation under hydrostatic pressure [11, 330] and needs to be addressed in further studies.

The application of negative pressure, i.e., the enlargement of the lattice constant by an isoelectric substitutional doping of ~1 % germanium on the silicon site, results in an increase of the transition temperature and transition fields by ~30 % [239]. This effect may be related to similar observations in single-crystal thin films of MnSi grown on top of silicon substrates, where the lattice mismatch causes a comparable distortion [349, 447]. A less pronounced shift of the transition temperature was reported for polycrystalline material [448]. Apart from helimagnetism, especially iron-rich $Mn_{1-x}Fe_xSi$ and $Fe_{1-x}Co_xSi$ are also investigated for their unconventional metallic properties and anomalies of the Hall effect [437, 449–451]. Moreover, in $Mn_{1-x}Co_xSi$ a spin-glass ground state is reported for $x > x_C$ [238].

3.1.8 $Fe_{1-x}Co_xSi$: a strongly doped semiconductor

In the pseudo-binary $B20$ compound $Fe_{1-x}Co_xSi$ helimagnetism exists in a large composition range, $0.05 \lesssim x \lesssim 0.8$ [248, 450, 455], albeit the parent compounds FeSi and CoSi are a paramagnetic insulator [456] and a diamagnetic metal [393], respectively. Starting from the strongly correlated insulator FeSi [91], an insulator-to-metal transition takes place around $x \approx 0.02$ [453]. Due to the comparably high absolute value of the electrical resistivity and an upturn at low temperatures, however, helimagnetic $Fe_{1-x}Co_xSi$ is often referred to as a strongly doped semi-

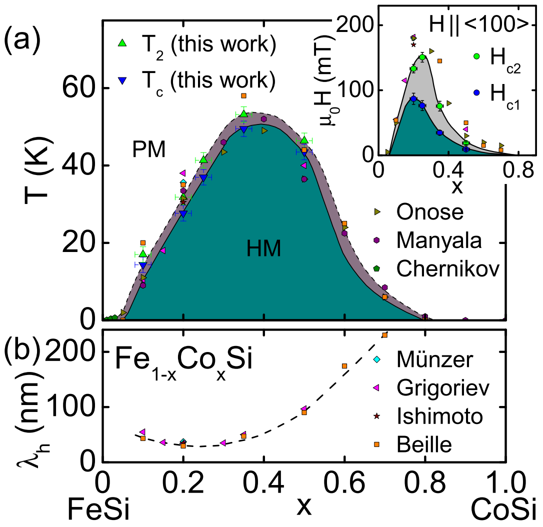

Figure 3.14: Helimagnetism in $\mathrm{Fe}_{1-x}\mathrm{Co}_x\mathrm{Si}$. (a) Compositional phase diagram with paramagnetism (PM) and helimagnetism (HM). $\mathrm{Fe}_{1-x}\mathrm{Co}_x\mathrm{Si}$ exhibits helimagnetism with transition temperatures up to ∼50 K over a wide compositional range. See Sec. 3.3.3 for details. The inset depicts the low-temperature transition fields H_{c1} and H_{c2}. (b) Helix wavelength, λ_h, as a function of cobalt content x. The values are taken from Refs. [248, 249, 287, 450, 452–454].

conductor [248, 249, 437]. Its lattice constant decreases almost linearly from $a = 4.48$ Å in FeSi to $a = 4.45$ Å in CoSi [437].

Compared to the stoichiometric helimagnets, $\mathrm{Fe}_{1-x}\mathrm{Co}_x\mathrm{Si}$ offers the opportunity to vary the characteristic parameters of the helimagnetism over a wide range via compositional tuning while the magnetic phase diagrams stays qualitatively similar. As summarized in Fig. 3.14, the helimagnetic transition temperature reaches up to ∼50 K, the critical fields assume values up to ∼150 mT, and the helix wavelength ranges from about 300 Å to more than 2000 Å. Only after zero-field cooling a proper helical state is observed. $\mathrm{Fe}_{1-x}\mathrm{Co}_x\mathrm{Si}$ displays easy $\langle 100 \rangle$ axes that, especially for larger cobalt contents, are less pronounced than in other cubic chiral helimagnets [80, 454]. For $x = 0.20$ a helical pitch along $\langle 110 \rangle$ was identified in Ref. [287]. The latter study also revealed the existence of a Skyrmion lattice in $\mathrm{Fe}_{1-x}\mathrm{Co}_x\mathrm{Si}$ that is sensitive on the field and temperature history. While the reversible pocket of Skyrmion lattice state is comparable to other chiral helimagnets, field-cooling may result in a metastable extension down to lowest temperatures, cf. also Sec. 3.3.3. A similar behavior was later also discovered in low-quality MnSi samples under applied pressure [330]. Moreover, depending on the field direction, two Skyrmion lattice domains with different in-plane orientations were observed leading two a twelvefold small-angle scattering pattern [457].

Due to the wide range of transition temperatures, transition fields, and helix wavelengths, cf. also Sec. 3.3.3, $\mathrm{Fe}_{1-x}\mathrm{Co}_x\mathrm{Si}$ is suitable for studies by various experimental techniques. As an example, the large helix wavelength of $\mathrm{Fe}_{1-x}\mathrm{Co}_x\mathrm{Si}$ with $x \sim 0.5$ allowed for the first real-space observation of the helical order [458] and the Skyrmion lattice state [40] in a chiral helimagnet using Lorentz force transmission electron microscopy. Moreover, in combination with the metastable extension of the Skyrmion lattice, the large wavelength enabled us to resolve the unwinding of the Skyrmion lines by magnetic monopoles in a magnetic force microscopy study [80]. The collective excitation spectra in $Fe_{1-x}Co_xSi$ may also be tuned considerably [252, 389].

Recently, it was speculated whether in $Fe_{1-x}Co_xSi$ the magnetic chirality, γ_m, changes as a function of cobalt content [256]. This postulated spontaneous symmetry breaking, however, was disproved in a subsequent study that correlated the crystalline chirality, $\mathit{\Gamma}_c$, of a single crystal to the random chirality of the seed crystal used for its growth. The magnetic chirality is finally inherited from the crystalline chirality, where $\mathit{\Gamma}_c \cdot \gamma_m = -1$ in $Fe_{1-x}Co_xSi$ [250].

3.1.9 Cu_2OSeO_3: a magnetoelectric insulator

The copper-oxo-selenite Cu_2OSeO_3 crystallizes in the space group $P2_13$ [459], i.e., in the same non-centrosymmetric space group as the binary $B20$ compounds. The primitive unit cell, see Fig. 3.2(b) or Fig. 3.15(a), possesses a lattice constant $a = 8.930\,\text{Å}$, contains eight formula units, and is composed of four building blocks [253, 460, 461]. The sixteen Cu^{2+} ions are distributed into twelve Cu^{I} sites around which the oxygen ions form trigonal bipyramids and four Cu^{II} sites that are surrounded by oxygen square pyramids. The CuO_5 polyhedra are connected by sharing edges and corners. The eight Se^{4+} ions are split into two crystallographically non-equivalent groups, four Se^{I} and four Se_{II}. Around these ions two different types of SeO_3 lone pair trigonal pyramids form that share corners with the CuO_5 polyhedra.

Magnetically, on the strongest scale Cu_2OSeO_3 shows ferrimagnetic order of the spin-$\frac{1}{2}$ Cu^{2+} ions. Here, the ferromagnetically aligned moments on the Cu^{I} sites couple antiferromagnetically to the ions on the Cu^{II} sites leading to a 3:1 ratio [253, 382, 462–464]. No breaking of the ferrimagnetic coupling is observed up to 55 T [465]. The corresponding exchange constant are $J_{\mathrm{FM}} = -50\,\mathrm{K}$ and $J_{\mathrm{AFM}} = 65\,\mathrm{K}$ [253]. The ferrimagnetism is superimposed by a long-wavelength helical modulation based on the Dzyaloshinskii-Moriya interaction with $\lambda_{\mathrm{h}} = 620\,\text{Å}$ [42]. Cu_2OSeO_3 shows a magnetic phase diagram similar to the helimagnetic $B20$ compounds with $T_c \approx 58\,\mathrm{K}$, $\mu_0 H_{c2} \approx 0.1\,\mathrm{T}$, an easy axes of the helical pitch along $\langle 100 \rangle$, and a delicate pinning within the Skyrmion lattice state [251, 293]. As a function of pressure the transition temperature increases by $\sim 0.3\,\mathrm{K/kbar}$ [465]. A recent study using resonant soft x-ray diffraction further suggested that the Cu^{I} and Cu^{II} sites may form individual but coupled Skyrmion lattices that are rotated by a few degree with respect to each other giving rise to a moiré pattern [466]. The latter, however, was not confirmed in a study using magnetic force microscopy [467].

Magnetoelectric coupling

In Cu_2OSeO_3, as an insulating compound, the space group $P2_13$ does not permit spontaneous electric polarization but piezoelectricity, piezomagnetism, and a magnetoelectric effect, where the application of a magnetic field may induce a electric polarization and vice versa. In addition, a significant magnetocapacitance and a magnetodielectric effect are observed at the onset of magnetic order while not being accompanied by any symmetry-lowering crystalline distortions or lattice strains [53, 463, 468–470]. Instead, the magnetoelectric coupling is related to the Dzyaloshinskii-Moriya driven helimagnetism [471, 472]. The polarization may be described in a d-p hybridization model [473–476], where the covalency between copper d and oxygen p orbitals is modulated according to the local magnetization direction via the spin-orbit interaction which leads to a local electric dipole along the bond direction [386].

A coupling between ferroelectricity and a helical spin order was also identified in other com-

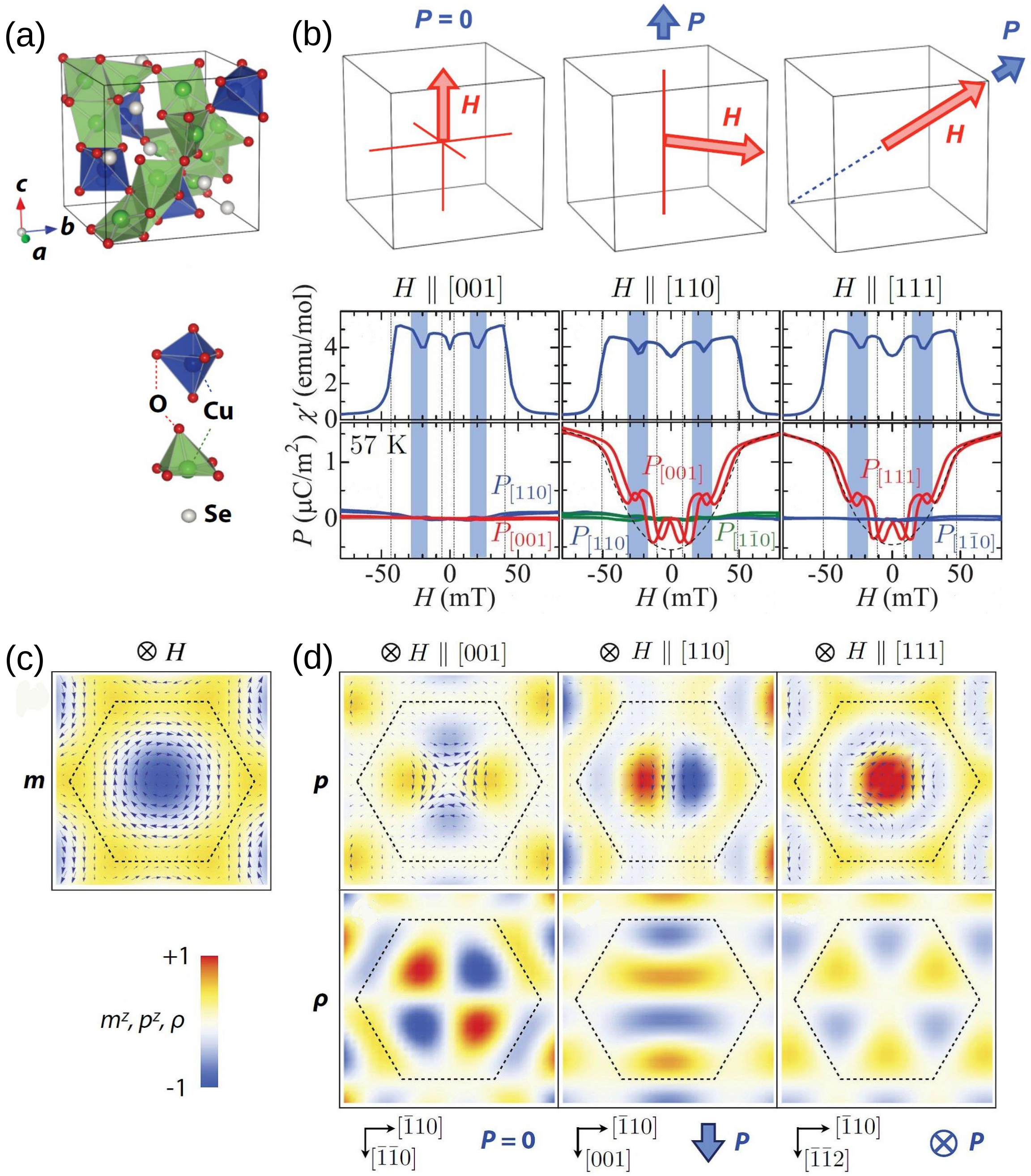

Figure 3.15: Magnetoelectric coupling in Cu_2OSeO_3. (a) Crystalline structure. (b) Depending on the orientation, an applied magnetic field, $\boldsymbol{H}$, may or may not induce an electric polarization, P, across the different magnetic phases. The Skyrmion lattice regime is shaded in blue. In contrast, the magnetic susceptibility, χ, is rather isotropic. (c) Calculated spatial distribution of the local magnetization, $\boldsymbol{m}$, in the Skyrmion lattice in a plane perpendicular to $\boldsymbol{H}$ which is essentially independent from the crystalline orientation. (d) Local electric polarization, $\pm p$, and local electric charge, ρ, for magnetic field along the major axes. The color scale encodes the out-of-plane components of $\boldsymbol{m}$ and $\boldsymbol{p}$ as well as ρ. Figure compiled from Ref. [386].

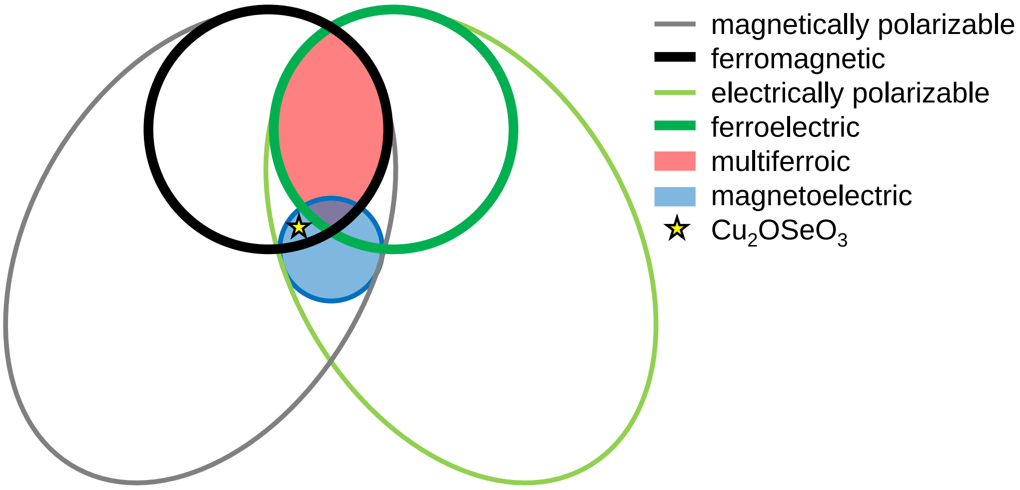

Figure 3.16: Classification of ferroic materials. Ferromagnets are a subset of magnetically polarizable materials which also include paramagnets or antiferromagnets. The same holds true for their electrical analogs. Compounds that exhibit both ferromagnetic and ferroelectric order are referred to as multiferroics (red shading). Magnetoelectric coupling (blue shading) is an independent phenomenon. In principle, it may emerge in any material that is both magnetically and electrically polarizable and in practice it arises in most of them, either directly or via strain [18].

pounds [19, 477–480], where it often allows for a control of the magnetic structure via the application of electric fields [481–483]. Cu_2OSeO_3, albeit being non-polar, possesses a magnetically induced electrical polarization in finite fields and, in particular, within the Skyrmion lattice state as depicted in Fig. 3.15(b). Moreover, the magnetoelectric susceptibility, i.e., the response of the dc magnetization to an ac electric field, allows to track the magnetic phase diagram [484]. Hence, though Cu_2OSeO_3 actually is a (heli-)ferrimagnetic magnetoelectric, cf. Fig. 3.16, it is often referred to as a multiferroic as it offers the hitherto unique opportunity to manipulate a topologically non-trivial entity with a magnetoelectric nature using various external control parameters.

Depending on the orientation of the magnetic field, the Skyrmion lattice may exhibit an electric polarization along or perpendicular to the Skyrmion lines and each Skyrmion may locally carry electric dipole or quadrupole moments, cf. Figs. 3.15(c) and 3.15(d) [386]. As a result, the eigenmodes of the Skyrmion lattice in Cu_2OSeO_3 [385] are magnetically active to an ac magnetic field and electrically active to an ac electric field resulting in an increased dynamical magnetoelectric coupling at the corresponding resonances (~GHz). An interference between the two activation processes may finally lead to unparalleledly large directional dichroism as the absorption of the electromagnetic wave by the Skyrmion lattice changes by up to ~20 % when the incident direction is reversed [368]. This so-called non-reciprocal directional dichroism has been detected experimentally and renders conceptually new microwave diodes or other devices possible [369].

Further manipulation concepts include position-dependent electric fields that induce a Hall motion of the Skyrmions [485] or the application of a temperature gradient on an insulating thin film resulting in a drift of Skyrmions towards the high-temperature region in contrast to conventional particle diffusion [486]. This movement is caused by a magnonic spin transfer torque [487, 488], its direction is reversed if the hot region gets paramagnetic, and an electric ac current is induced that depends on the precise nature of the magnetoelectric coupling [489]. Moreover, it was demonstrated that the sixfold neutron scattering pattern of the Skyrmion lattice state may be rotated by the application of an electric field [490]. The strong dependence of this effect on the temperature and fields history, however, implies that it may be related to the delicate domain structure of the Skyrmion lattice in bulk Cu_2OSeO_3.

3.1.10 FeGe and MnGe: helimagnets with complex metallurgy

The helimagnetic $B20$ monogermanides FeGe and MnGe possess high transition temperatures of 278 K and ~170 K, respectively. Unfortunately, unlike their monosilicide siblings, they exhibit very complex metallurgical phase diagrams that prevent a sample preparation from the melt. FeGe forms from solid educts through a peritectoid reaction [56] and MnGe is in fact not a stable phase at ambient pressure [491]. Hence, the latter may only be synthesized at pressures of a few gigapascal yielding polycrystalline material with a few percent of impurity phases [492–494]. The same technique is also employed for the preparation of polycrystalline FeGe as well as $Mn_{1-x}Fe_xGe$ [241, 244]. In addition, single crystals of FeGe with a size of ~1 mm may be grown via chemical vapor transport [52, 58]. Epitaxial thin films were prepared by magnetron sputtering [370].

Furthermore, CoGe was also synthesized in the $B20$ structure under high pressure [495]. It orders magnetically around 120 K and possesses a small fluctuating moment of $0.26\,\mu_B$/f.u. but has not been investigated in further detail yet [492].

FeGe: high-temperature sibling of MnSi

The magnetic properties of cubic FeGe highly resemble that of the archetypical cubic chiral helimagnet MnSi, despite of an almost tenfold increase of the transition temperature. As typical for an itinerant magnet, a large fluctuating Curie-Weiss moment of $2.1\,\mu_B$/f.u. compares to an ordered moment of $1\,\mu_B$/f.u. [496, 497]. Below the transition temperature $T_c = 278\,\mathrm{K}$, in zero field a helical state is observed that is transformed into a conical state around $H_{c1} \sim 0.02\,\mathrm{T}$ and finally into a field-polarized state at $H_{c2} \sim 0.2\,\mathrm{T}$ [498]. In contrast to MnSi, the easy axes of the helical order with $\lambda_h \sim 700\,\text{Å}$ changes from $\langle 111 \rangle$ at low temperatures to $\langle 100 \rangle$ at high temperatures, where a pronounced temperature hysteresis is observed with $T_{\mathrm{down}} = 211\,\mathrm{K}$ and $T_{\mathrm{up}} = 245\,\mathrm{K}$ [240]. As a function of pressure, the helimagnetic order is suppressed until it vanishes at $p_c \approx 19\,\mathrm{GPa}$, followed by a non-Fermi liquid resistivity with a $T^{3/2}$ temperature dependence above p_c [499].

In recent years, the Skyrmion lattice in FeGe attracted interest as it allows for the observation [41] and manipulation [345] of Skyrmions near room temperature, cf. Fig. 3.17. Due to the complex metallurgy of FeGe and the resulting lack of samples, however, research on bulk single crystals of FeGe is currently mainly reported by the group of Wilhelm and coworkers without the possibility to confirm their results. From ac susceptibility, specific heat, and small-angle neutron scattering data they construct a very complex magnetic phase diagram that includes multiple pockets in the A-phase as well as various precursor phenomena and mesophases above T_c, see Fig. 3.18(a) [294, 500–502]. They attribute this complexity to the softening of the magnetization modulus, to the confinement of helical, solitonic, or Skyrmionic units, and to a crossover of the intersoliton coupling from repulsive to attractive [318, 503]. However, the interpretation by

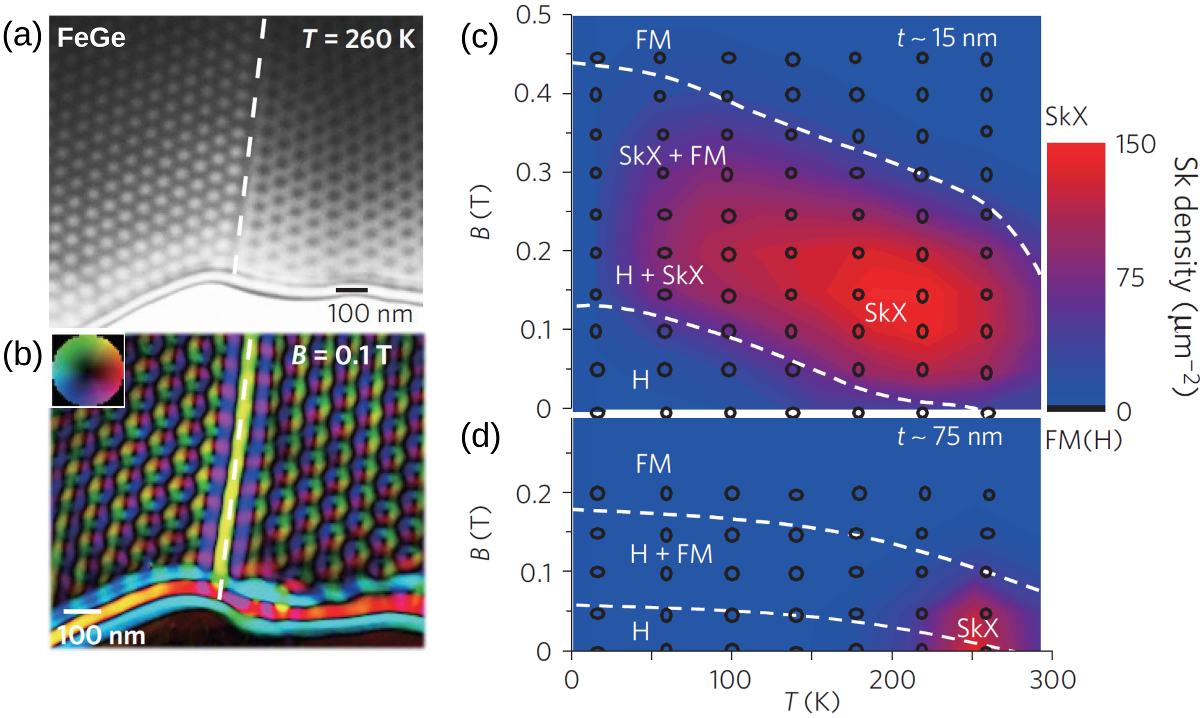

Figure 3.17: Skyrmion lattice near room temperature in FeGe. (a) Lorentz transmission electron microscope data of the Skyrmion lattice in a thin wedge of FeGe at 260 K in small fields. Two crystalline grains with opposite crystalline chirality are visible. (b) Lateral magnetization distribution. (c) Magnetic phase diagram for a sample of 15 nm thickness showing an extended regime of Skyrmion lattice state. (d) Magnetic phase diagram for a sample of 75 nm thickness being reminiscent of the bulk cubic chiral helimagnets. Pictures taken from Ref. [41].

Wilhelm and coworkers may be questioned, as they empirically define non-coinciding transitions in temperature and field sweeps motivated by a theoretically proposed magnetic phase diagram with multiple phase pockets.

The data, in fact, are highly reminiscent of data measured in other cubic chiral helimagnets such as MnSi, $Mn_{1-x}Fe_xSi$, or Cu_2OSeO_3, in particular when taking into account the irregular shape of the small samples which causes ill-defined demagnetizing fields. As depicted in Fig. 3.18(b), the results from susceptibility and neutron scattering measurements may be accounted for by a single pocket of Skyrmion lattice phase. This pocket is separated from the conical state by a first-order transition that is accompanied by a regime of phase coexistence with non-vanishing dissipation, consistent with the findings for other helimagnets presented in Ref. [313] and Sec. 3.3. No microscopic evidence, neither in real nor in reciprocal space, hints towards the existence of previously unresolved spin structures. Moreover, the specific heat in small fields is characterized by a small peak on top of a broad shoulder, as anticipated from a Brazovskii-type fluctuation-induced first-order transition. Taken together, the available data clearly suggest that FeGe indeed is the high-temperature analogon of MnSi—without hints for further complexities.

When doping silicon on the germanium site of FeGe, the transition temperature slowly de-

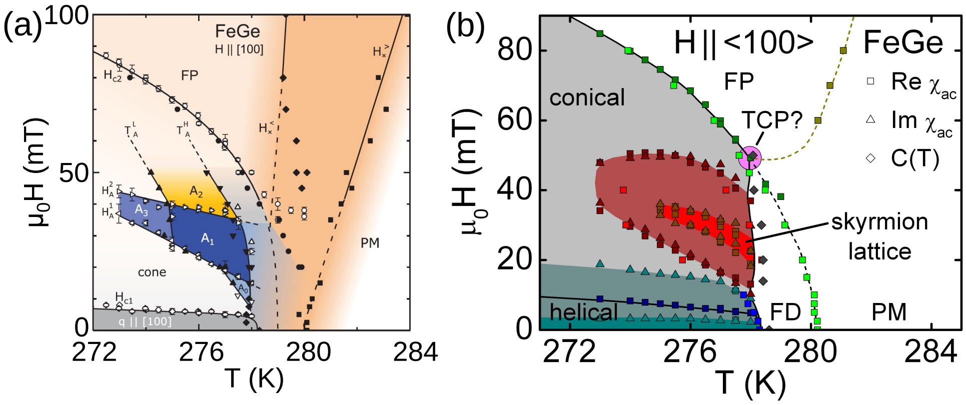

Figure 3.18: Magnetic phase diagram of FeGe. (a) Phase diagram for field along $\langle 100 \rangle$ with multiple phase pockets and precursor phenomena taken from Ref. [500]. (b) Phase diagram for field along $\langle 100 \rangle$ determined in accordance with the definitions given in Ref. [313] for MnSi. A single pocket of Skyrmion lattice is bordered by a broad regime of phase coexistence, as typical for a sample that is subject to large demagnetization effects. The transition in zero field is consistent with the Brazovskii scenario. Susceptibility data from Refs. [500, 501] and specific heat data from Ref. [502] were used. The phase diagram is also consistent with recent neutron scattering data [294]. A temperature discrepancy of the maximum in the specific heat in Refs. [501, 502] indicates that care has to be taken when combining data from different samples as the transition temperature T_c presumably is related to the detailed sample composition, cf. Sec. 3.2.1 for a corresponding study on $\mathrm{Mn}_{1+x}\mathrm{Si}$.

creases. The magnetic order in $\mathrm{FeGe}_{1-y}\mathrm{Si}_y$ finally disappears around $y \sim 0.75$ where also a metal-to-insulator transition is observed [242].

MnGe: short-wavelength helimagnet

In contrast to FeGe, the magnetic properties of MnGe potentially differ from the other cubic chiral helimagnets. Due to its complex metallurgy, however, all measurements so far had to be carried out on polycrystalline samples containing a few percent of impurity phases. The magnetic properties of these impurities, as well as defects or stress caused by the high-pressure synthesis, may mask or alter the intrinsic properties of single-phase single crystals of MnGe. Fig. 3.19(a) shows the magnetic phase diagram extracted from measurements of the magnetization, the Hall resistivity, and the longitudinal resistivity [243, 493]. A comparable large transition temperature, $T_c \sim 170\,\mathrm{K}$, and a very high upper critical field of $H_{c2} \sim 12\,\mathrm{T}$ are observed. An ordered moment of some $2\,\mu_\mathrm{B}/\mathrm{f.u.}$ suggests a rather localized character of the magnetism. Compared to the other cubic chiral helimagnets, the helix wavelength is relatively short and significantly changes from $\sim$30 Å to $\sim$60 Å with increasing temperature, see Fig. 3.19(b) [243, 493, 494]. The easy axes for the helices probably are the $\langle 100 \rangle$ directions [243]. As a function of pressure the transition temperature of MnGe decreases monotonically until the magnetism finally vanishes above 10 GPa. The helix wavelength and the ordered moment also decrease saturating at values of 20 Å and $0.7\,\mu_\mathrm{B}/\mathrm{f.u.}$ above $\sim$6 GPa [504].

Large topological Hall signals of $\sim$200 nΩcm are reported across essentially the whole helimag-

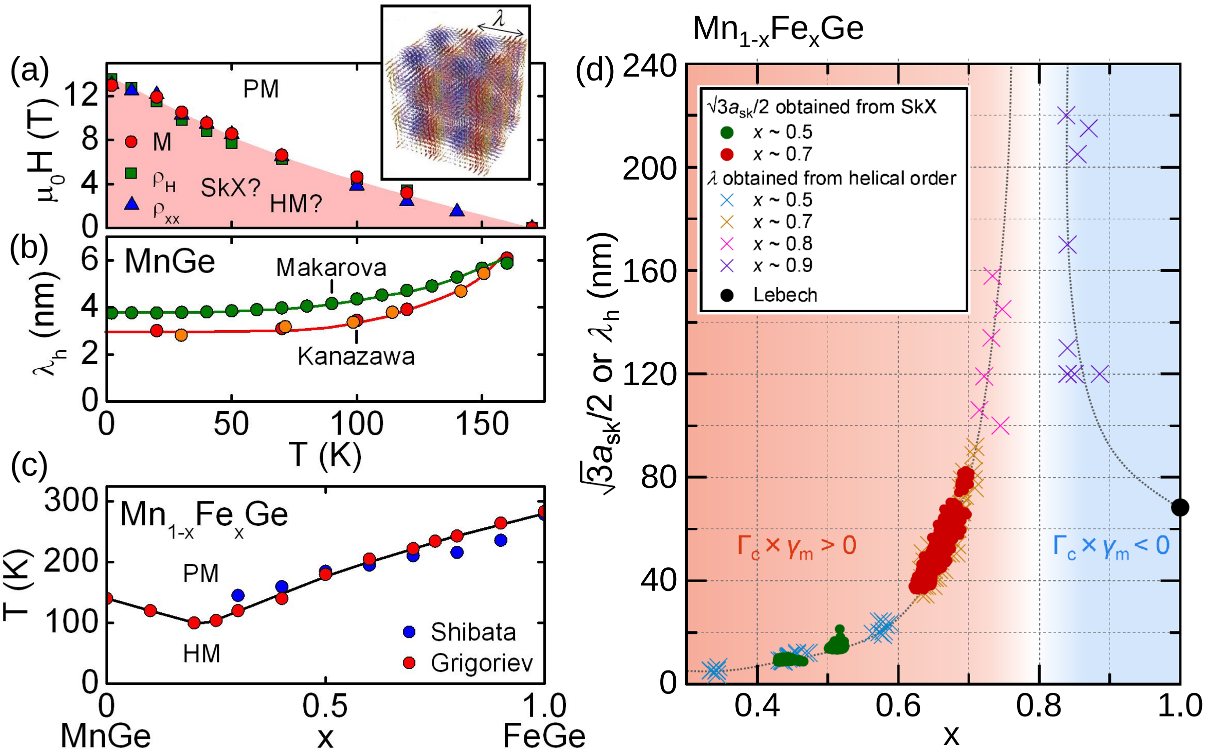

Figure 3.19: Helimagnetism in MnGe and $\mathrm{Mn}_{1-x}\mathrm{Fe}_x\mathrm{Ge}$. (a) Magnetic phase diagram of MnGe as derived from magnetization, M, Hall resistivity, ρ_H, and longitudinal resistivity, ρ_{xx}. A simple cubic Skyrmion lattice state (SkX) is proposed for MnGe and depicted in the inset. (b) Helix wavelength, λ_{h}, in MnGe as a function of temperature. (c) Compositional phase diagram of $\mathrm{Mn}_{1-x}\mathrm{Fe}_x\mathrm{Ge}$ showing paramagnetism (PM) above and helimagnetism (HM) below T_c. (d) Helix wavelength, λ, and the corresponding length extracted from the Skyrmion lattice, $\sqrt{3}a_{\mathrm{sk}}/2$, in $\mathrm{Mn}_{1-x}\mathrm{Fe}_x\mathrm{Ge}$ as a function of the iron content x. Around $x \sim 0.8$ the wavelength diverges as the relation between the crystalline and the magnetic chirality is inverted and the Dzyaloshinskii-Moriya constant changes sign. Data and pictures taken from Refs. [240, 241, 243, 244, 493, 494].

netic part of the magnetic phase diagram at ambient pressure, where the size of the topological Hall effect is attributed to the short helix period in MnGe [493]. These Hall data, as well as topological Nernst effect data [505], may be accounted for best by a three-dimensional simple cubic lattice of Skyrmions that possibly persists as a ground state in zero field. Small-angle neutron scattering in magnetic fields revealed intensity perpendicular to the field, reminiscent of the intensity distribution of a Skyrmion lattice [243].

Other than in the monosilicides, the doped series $\mathrm{Mn}_{1-x}\mathrm{Fe}_x\mathrm{Ge}$ orders magnetically for all compositions. Simultaneously, the product of the crystalline and the magnetic chirality, $\Gamma_c \cdot \gamma_m$, inverts from MnGe (+1) to FeGe (−1). The associated sign change of the Dzyaloshinskii-Moriya constant as a function of the iron content x has recently been monitored in both real [244] and reciprocal space [241]. Starting from MnGe, the helix wavelength hardly changes up to $x \sim 0.4$ while the transition temperature decreases, see Figs. 3.19(c) and 3.19(d). For $0.4 \lesssim x \lesssim 0.8$ both the helix wavelength and the transition temperature increase with x and a regular hexagonal Skyrmion lattice is resolved in Lorentz force transmission electron microscopy. Around $x \approx 0.8$ the helix wavelength diverges as the Dzyaloshinskii-Moriya constant vanishes and changes sign giving rise to an essentially ferromagnetic state. For $0.8 \lesssim x$, finally, the increase of the absolute value of the Dzyaloshinskii-Moriya again results in a shrinking helix wavelength.

3.2 Single crystal growth

During the course of this thesis we have prepared a large number of single crystals from various $B20$ transition metal monosilicides including the helimagnet MnSi, the strongly correlated insulator FeSi, as well as the pseudo-binary helimagnets $\mathrm{Mn}_{1-x}\mathrm{Fe}_x\mathrm{Si}$, $\mathrm{Mn}_{1-x}\mathrm{Co}_x\mathrm{Si}$, and $\mathrm{Fe}_{1-x}\mathrm{Co}_x\mathrm{Si}$. All these compounds form congruently making them ideally suited for a growth from the melt. MnSi, on which the main focus was placed, melts congruently at about 1270 °C and more than 20 float-zoning attempts all yielded large single crystals as summarized in Tab. 3.3. However, manganese possesses a high vapor pressure that leads to evaporation losses even when using an inert atmosphere of a few bar pressure. The molten zone is expected to buffer these losses to a certain degree. Empirically, however, we have observed a large spread of residual resistivity ratios (RRRs) between the few crystals float-zoned prior to this study. Samples from one crystal, OFZ54, show a very high RRR ~ 300. At the same time, the helimagnetic ordering temperature, T_c, in samples from this ingot is about 1 K smaller than the values reported in literature while the other magnetic properties are similar, e.g., when comparing Ref. [85] with Ref. [313].

The following section is divided into two parts. First, motivated by the findings mentioned above, we have carried out a comprehensive study of the influence certain growth parameters on the crystalline quality and the magnetic properties of MnSi that is presented in Sec. 3.2.1. We thereby established a correlation between the initial manganese content of the feed rods, the RRR of the single-crystal ingot, and the magnetic behavior of the ingot. Second, as shown in Sec. 3.2.2, oriented seed crystals were utilized to prepare large oriented single crystals of up to 70 mm length and 10 mm diameter, e.g., for the use in inelastic neutron scattering experiments.

3.2.1 Influence of the growth parameters

All MnSi sample used throughout this thesis were grown by means of optical float-zoning. In the following we elaborate on a systematic investigation of the influence of two growth parameters, namely the initial composition of the feed rods and the float-zoning velocity, on the magnetic properties of the resulting single-crystal $\mathrm{Mn}_{1+x}\mathrm{Si}$. Therefore, besides the sample preparation we have carried out measurements of the residual resistivity ratio (RRR), the susceptibility, and the specific heat. We show that a slight excess of manganese leads to the highest RRR while the float-zoning velocity possesses no major impact. The magnetic properties of the $\mathrm{Mn}_{1+x}\mathrm{Si}$ samples, in general, are very similar. We observe a slight continuous decrease of the helimagnetic transition temperature, T_c, with increasing manganese excess, x. In addition to this general trend, a few samples exhibit transition temperatures that are 1 K to 2 K smaller than expected together with an exceptionally high RRR. Moreover, we observe a significant smearing of the signatures at T_c and at the boundary of the Skyrmion lattice state in the ac susceptibility and the specific heat of manganese-rich samples. The initial manganese content also delicately influences the details of the helical-to-conical transition which is governed by the interplay of cubic anisotropies, the physics of helical domains, and defect pinning.

OFZ	x	d (mm)	l_{sc} (mm)	v (mm/h)	or.	comment
16	0	6	25	5	no	RRR $\sim$ 80, W. Münzer
54	0	6	15	5	no	RRR $\sim$ 300, pc at top
59	0	6	30	5	no	RRR $\sim$ 80
65	-0.01	6	25	5	no	
66	0	6	20	5	no	
67	0.01	6	20	5	no	
68	0.02	6	30	5	no	
69	0	6	20	2	no	
70	0.01	6	15	2	no	
71	-	6	25	5	no	$x = -0.01 \rightarrow 0.02$
81	0.03	6	25	5	no	
82	0.03	6	15	2	no	
83	0.04	6	10	5	no	pc at top
84	0.04	6	10	2	no	
103	0.015	10	35	5	$\langle 110 \rangle$	seed: Bridgman
110	0	10	40	5	$\langle 110 \rangle$	seed: start of OFZ103
111	0	10	70	10	$\langle 110 \rangle$	seed: start of OFZ110
119	0	10	30	5	$\langle 110 \rangle$	seed: start of OFZ111
120	0	6	25	5	$\langle 100 \rangle$	seed: bar from OFZ110
122	0	6	15	5	$\langle 211 \rangle$	seed: bar from OFZ110
124	0	10	40	10	$\langle 100 \rangle$	seed: start of OFZ120
125	0	10	35	10	$\langle 211 \rangle$	seed: start of OFZ122
126	0	6	5	5	$\langle 111 \rangle$	seed: bar from OFZ110
128	0	10	25	10	$\langle 111 \rangle$	seed: start of OFZ126

Table 3.3: Summary of the $Mn_{1+x}Si$ single crystals grown or used in this thesis. The table states the OFZ number, the initial manganese excess x, the crystal diameter d, the length of the single crystal cylinder at full diameter l_{sc}, the float-zoning speed v at which this cylinder was grown, the crystalline orientation along the growth direction (if applicable), and additional comments. OFZ16 was grown by Wolfgang Münzer during his diploma thesis [61]. OFZ54 and OFZ83 grew single crystalline after the initial grain selection at first. However, in the middle of float-zoned rod x-ray Laue indicated a polycrystal (pc) albeit no peculiarities were observed during the float-zoning. For the gradient crystal OFZ71 a $Mn_{1+x}Si$ seed rod with $x = -0.01$ and a feed rod with $x = 0.02$ were used.

Our results, in combination with extremely pure 5N8 manganese recently purchased from Alfa Aesar, might allow us to prepare MnSi single crystals of ultra-high quality. This way, samples with a large spread of RRRs are available for future studies. Such studies, for instance, may address the connection between the crystalline quality and the threshold current in spin transfer torque experiments, as currently carried out by Christoph Schnarr as a part of his Ph.D. thesis.

Experimental details and outline of the results

Many factors may influence the quality of a single crystal during its growth. In order to systematically address two distinct parameters, the initial manganese content and the float-zoning speed, we kept all other growth parameters unchanged. At first, polycrystalline feed rods of 6 mm diameter and a nominal composition of $\mathrm{Mn}_{1+x}\mathrm{Si}$ with $x = -0.01$, 0, 0.01, 0.02, 0.03, and 0.04 were prepared in the inductively heated rod casting furnace from pre-cast 4N manganese and 6N silicon. Prior to its usage the system was pumped to $\sim 10^{-6}$ mbar and filled with $\sim$1.5 bar additionally purified 6N argon. The feed rods were mounted into the image furnace, the system was pumped to $\sim 10^{-7}$ mbar, and filled with $\sim$2.5 bar additionally purified 6N argon. The float-zoning was carried out at a rate of 2 mm/h or 5 mm/h, respectively, while the seed rod and the feed rod were counter-rotating at 6 rpm. The resulting crystals are depicted in Fig. 3.20. In order to promote grain selection, a necking was introduced at the beginning of all growth attempts at 5 mm/h.

The crystals were investigated by means of x-ray Laue diffraction revealing single crystallinity from the end of the necking to the last quenched zone for all growth attempts except OFZ83. This growth attempt yielded single crystalline material at first, but became polycrystalline again in the middle of float-zoned rod although no peculiarities were observed during the float-zoning. Discs of 1 mm thickness with their large surfaces perpendicular to $\langle 110\rangle$ were cut from the beginning and the end of the single-crystal ingots. Two platelets of $\sim 5 \times 1 \times 0.2\,\mathrm{mm}^3$ oriented along $\langle 100\rangle \times \langle 110\rangle \times \langle 110\rangle$ were prepared from every disc. The RRRs of these samples were determined as the ratio between the room temperature resistance and the resistance at 4.2 K using a custom dipstick and a liquid helium dewar. Gold wires of 25 µm diameter were spot-welded onto the samples in a standard 4-point configuration for current along the long edge. Data were recorded using a lock-in technique at an excitation frequency of $\sim$22 Hz and an excitation amplitude of 5 mA. A large part of these measurements were performed as part of a RISE project (Research Internships in Science and Engineering) by Sina Zeytinoglu.

Samples for measurements of the ac susceptibility and the specific heat were cut from the same discs and from neighboring parts of the ingots. The magnetic properties of about 40 samples with masses of $\sim$2 mg to $\sim$150 mg were probed by measurements of the ac susceptibility in zero field. An excitation frequency of 911 Hz and an excitation amplitude of 1 mT along a crystalline $\langle 110\rangle$ axis were used. The absolute value of the susceptibility were not corrected for demagnetization effects. The ac susceptibility in field was investigated on cubes with 1 mm edge length and two surfaces perpendicular to $\langle 100\rangle$ and four surfaces perpendicular to $\langle 110\rangle$, respectively. These cubes were prepared from the beginning of the growths at 5 mm/h for each manganese content available. The field was applied after initial zero-field cooling. The specific heat was measured for field along a $\langle 110\rangle$ axis using the large pulse technique. The field dependence of susceptibility calculated from the magnetization, $\mathrm{d}M/\mathrm{d}H$, was determined from magnetization data collected at field steps of 1 mT. Subsequently, the data were numerically derivated and smoothed by a fifth-order Sovitzky-Golay algorithm over 40 data points.

The presentation of our results is organized as follows. First, we account for the evolution of the RRR of $\mathrm{Mn}_{1+x}\mathrm{Si}$ as a function of the manganese content, the growth speed, and the position within the single-crystal ingot. Zero-field ac susceptibility data and the transition temperature derived thereof are presented for a large number of samples. Subsequently, we show ac susceptibility and specific heat data in small applied fields for representative samples before the helical-to-conical transition at low temperatures is addressed. Finally, we briefly summarize our findings.

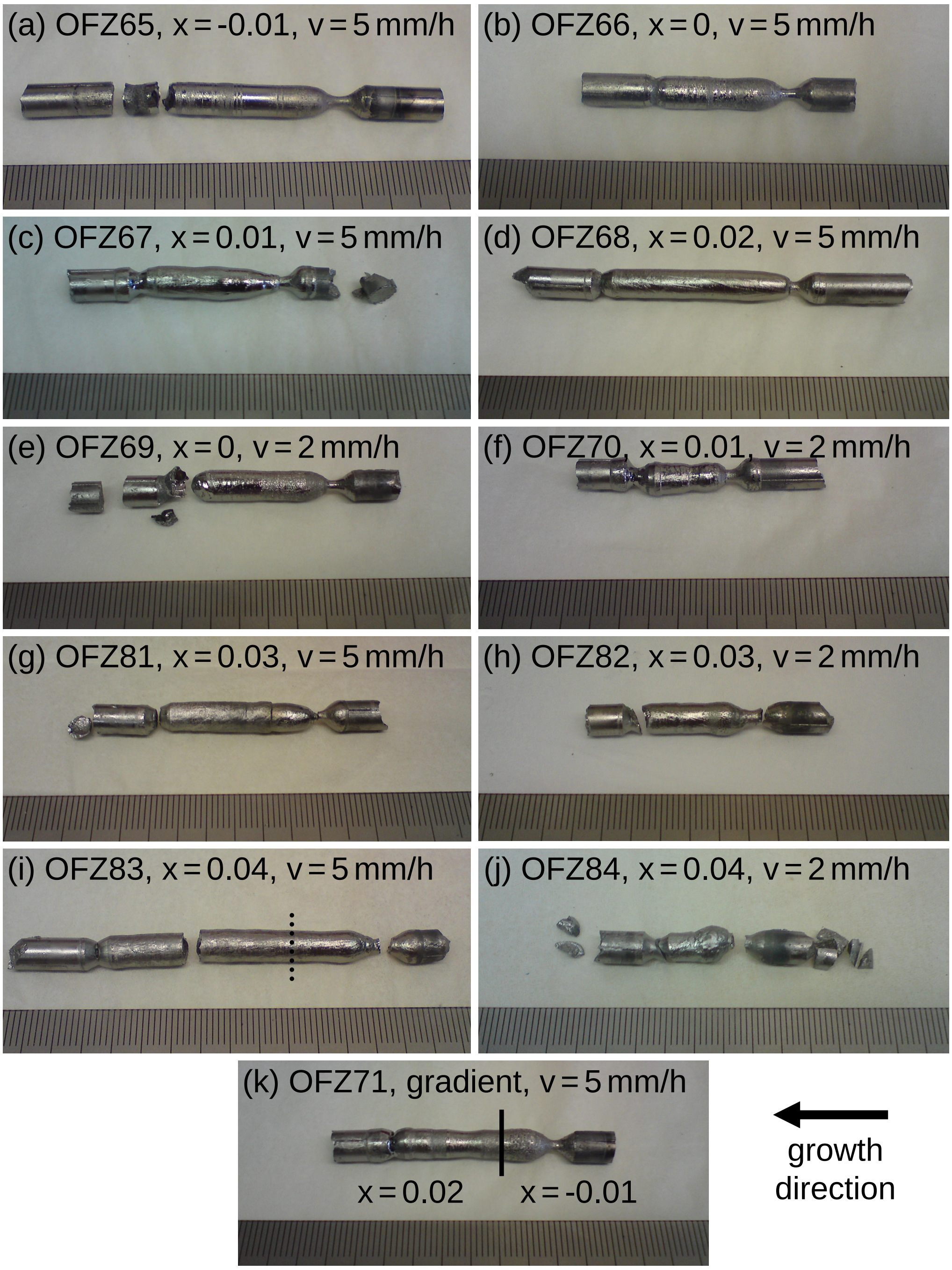

Figure 3.20: Float-zoned single crystals of $Mn_{1+x}Si$. The growth number (OFZ), the manganese excess x, and the float-zoning speed v are stated in each panel. Growth direction was from right to left. For OFZ83 the dotted line marks the border between single-crystalline part (right) and the polycrystalline part (left) of the float-zoned ingot. For the gradient crystal OFZ71 the solid line marks the initial juncture of the seed rod ($x = -0.01$) and the feed rod ($x = 0.02$). All scales are in millimeter.

Residual resistivity ratio

We start our description with the RRR as a function of the manganese content displayed in Fig. 3.21 and Tab. 3.4. Data taken on samples from the beginning and the end of a single-crystal ingot are shown in blue and red, respectively. For manganese deficient specimens, $x = -0.01$, we observe a comparably low RRR of about 40 that increases with increasing x. A slight manganese excess of 1 % (end) to 2 % (start) leads to the highest RRR. For higher values of x the RRR again drops back to about 40. Samples cut from the same disc usually show similar RRRs, except for OFZ81 where variations up to ∼30 % are observed. Moreover, the RRR varies between the beginning and the end of the same growth, where the latter tends to possess a lower RRR. A variation of the growth velocity between 2 mm/h (open symbols) and 5 mm/h (solid symbols) has no significant influence on the RRR.

These observations may be explained when considering the metallurgical phase diagram of manganese-silicon system, cf. Fig. 1.2(a). MnSi melts congruently and has a compositional homogeneity range of $-0.008 < x < 0.020$ where it crystallizes in the $B20$ structure [57]. In fact, a composition with $x \neq 0$ unavoidably leads to an increased amount of defects, e.g., manganese vacancies or antisite defects with silicon atoms on manganese sites for $x < 0$ as well as silicon vacancies or antisite defects with manganese atoms on silicon sites for $x > 0$. During a float-zoning the molten zone buffers small deviations from the stoichiometric composition stemming from the feed rod. The continuous insertion of a deficiency or an excess of one element, however, shifts the equilibrium at the liquid-solid interface and ultimately leads to the incorporation of the abovementioned defects. If the composition of the feed material is outside the homogeneity range, the accumulation of one of the constituent elements in the molten zone may lead to an

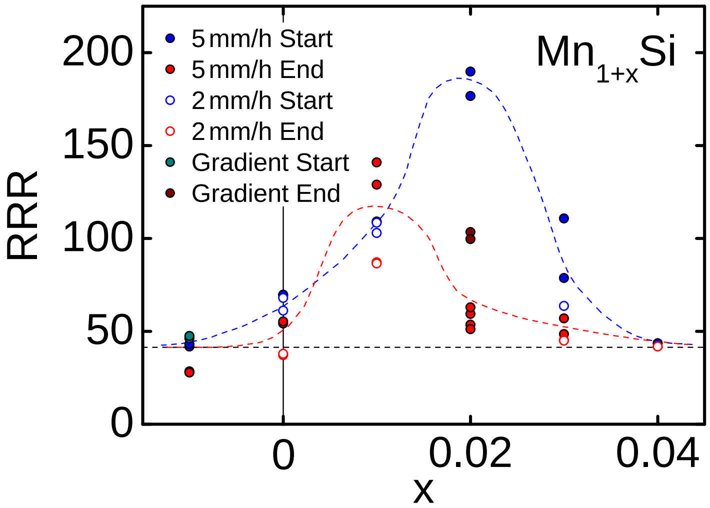

Figure 3.21: Residual resistivity ratio (RRR) of $Mn_{1+x}Si$ as a function of the initial manganese excess, x. The legend states the float-zoning velocity and the position within the single crystal that the measured samples was cut from. 'Gradient' refers to the crystal OFZ71 that was started from seed and feed rods with $x = -0.01$ and $x = 0.02$, respectively. In general, a slight excess of manganese leads to the highest RRR, as consistent with the evaporation of manganese during the growth process. The dashed lines are guides to the eye.

sample	x	v (mm/h)	RRR	comment
OFZ65-3-1-c1, -c2	-0.01	5	41.8, 43.1	start
OFZ65-3-3-c1, -c2	-0.01	5	28.4, 27.8	end
OFZ66-3-1-c1, -c2	0	5	69.4, 69.7	start
OFZ66-3-3-c1, -c2	0	5	54.2, 55.3	end
OFZ67-3-1-c1, -c2	0.01	5	108.8, 109.1	start
OFZ67-3-3-c1, -c2	0.01	5	128.9, 140.9	end
OFZ68-3-1-c1, -c2	0.02	5	176.6, 189.2	start
OFZ68-3-3-c1, -c2	0.02	5	53.6, 51.1	end
OFZ68-3-3-1-c1, -c2	0.02	5	59.3, 62.9	end
OFZ69-3-1-c1, -c2	0	2	61.1, 68.0	start
OFZ69-3-3-c1, -c2	0	2	37.1, 37.9	end
OFZ70-3-1-c1, -c2	0.01	2	108.5, 102.9	start
OFZ70-3-3-c1, -c2	0.01	2	87.1, 86.5	end
OFZ71-3-1-c1, -c2	-0.01	5	46.2, 47.5	gradient start
OFZ71-3-3-c1, -c2	0.02	5	103.5, 99.7	gradient end
OFZ81-3-1-c1, -c2	0.03	5	78.7, 110.7	start
OFZ81-3-3-c1, -c2	0.03	5	48.5, 57.0	end
OFZ82-3-1-c1	0.03	2	63.6	start
OFZ82-3-3-c1, -c2	0.03	2	45.3, 45.0	end
OFZ83-3-1-c1	0.04	5	43.5	start
OFZ84-3-3-c2	0.04	2	41.9	end

Table 3.4: Summary of the $Mn_{1+x}Si$ samples investigated for their RRR. The table states the name, the initial manganese excess x, the float-zoning speed v, and the RRR of the samples. We note that platelets cut from the same disc of a single crystal ingot, for instance OFZ65-3-1-c1 and OFZ65-3-1-c2, exhibit very similar RRRs.

interruption of the crystal growth. This scenario might be applicable to OFZ83.

The RRRs of samples with very low ($x = -0.01$) and very high ($x = 0.04$) manganese content suggest that defects caused by manganese deficiency and excess contribute to the electron-impurity scattering in a similar way. The smallest defect concentrations associated with the highest RRRs are expected for samples with a stoichiometric composition but are observed for a slight manganese excess. Unlike silicon, however, manganese is subject to evaporation during the growth process due to its high vapor pressure. The reduction of the manganese content in the float-zoned crystal by 1 % to 2 % with respect to the initial manganese content of the feed rods is thereby plausible. The higher RRR of samples from the begin of a single-crystal ingot compared to its end may finally be attributed to the way these sections were cooled. At first the single crystal steadily cools down as the heat source and with it the molten zone is traversed through the feed rods. At the end of the growth, the movement of the heat source is stopped and the heating power is gradually reduced to zero by hand within roughly an hour. Thus, the end of the single-crystal ingot is cooled in a less controlled and steady manner probably inducing stress and defects. Motivated by these observations, a future study will systematically address the influence of annealing on the crystalline quality and the RRR of $Mn_{1+x}Si$.

Susceptibility in zero field

The magnetic properties of about 40 samples of $Mn_{1+x}Si$ were investigated by means of the ac susceptibility in zero field as summarized in Tab. 3.5. Data for a conventional MnSi sample, i.e., a sample comparable to the samples used throughout literature (OFZ66-3-0-g with $x = 0$

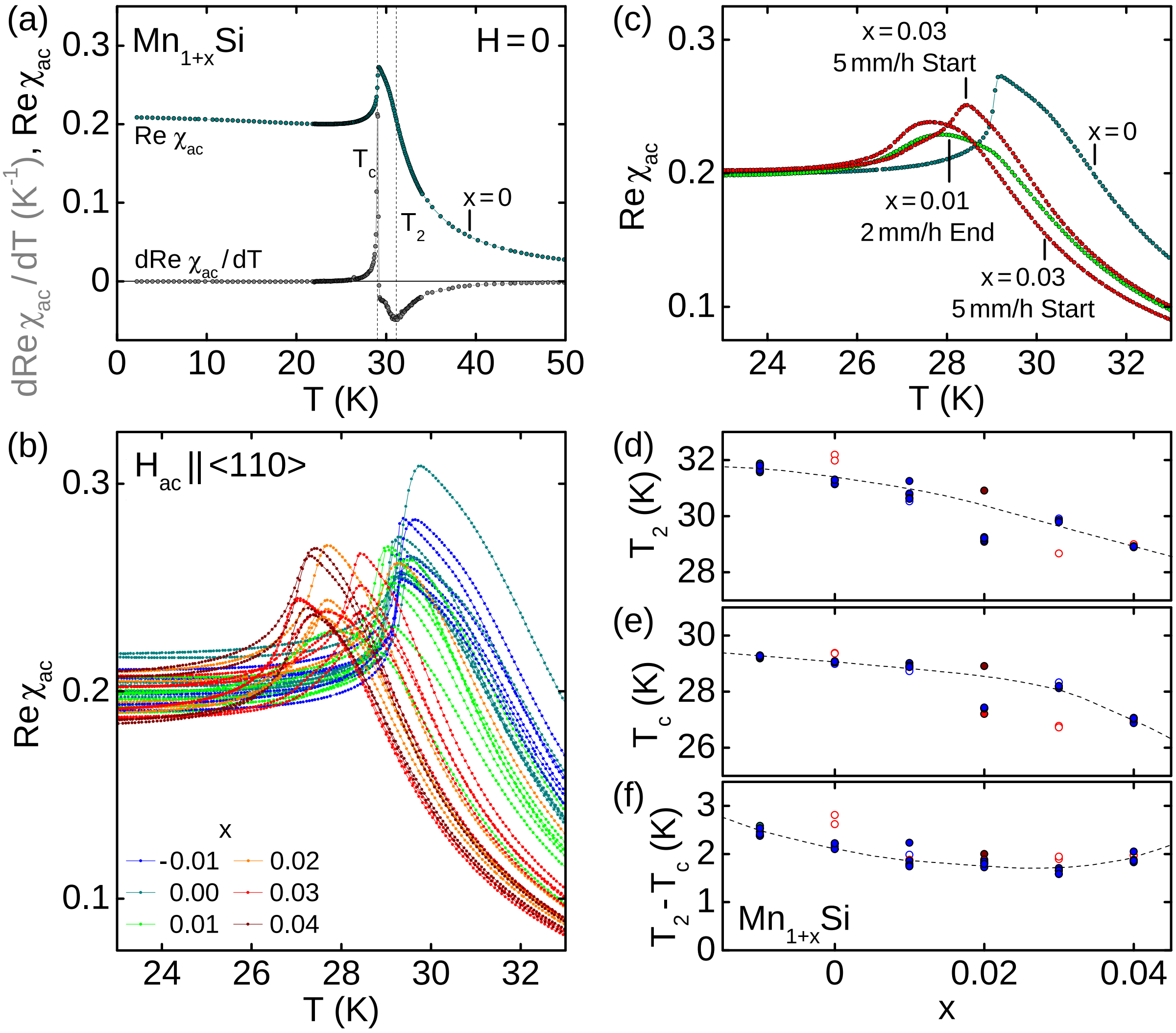

Figure 3.22: Temperature dependence of the ac susceptibility of $Mn_{1+x}Si$ in zero field. (a) Susceptibility and its derivative for a conventional MnSi sample ($x = 0$) defining the temperatures T_c and T_2. (b) Susceptibility for a large number of $Mn_{1+x}Si$ samples, cf. Tab. 3.5. Qualitatively similar behavior is observed. (c) A few samples show a significantly broadened transition or an additional point of inflection below T_c and were excluded from the further analysis. (d)–(f) Evolution of the temperatures T_2, T_c, and the width of the fluctuation-disordered regime, $T_2 - T_c$, as a function of the manganese content, x. In general, T_2 and T_c decrease monotonically with increasing x. Samples that show exceptionally low transition temperatures tend to possess a RRR considerably exceeding 100.

sample	x	RRR	m (mg)	T_c (K)	T_2 (K)	$T_2 - T_c$ (K)	comment
OFZ65-3-1-b	-0.01	42	32.35	29.254	31.719	2.465	
OFZ65-3-1-g	-0.01	42	5.83	29.277	31.806	2.529	
OFZ65-3-1-Large	-0.01	42	78.80	29.221	31.632	2.411	
OFZ65-3-1-Small	-0.01	42	29.45	29.272	31.806	2.534	
OFZ66-3-0	0	70	10.86	29.084	31.304	2.220	
OFZ66-3-0-b	0	70	40.98	29.048	31.253	2.205	
OFZ66-3-0-g	0	70	5.71	29.030	31.134	2.104	
OFZ66-3-1	0	70	71.91	29.066	31.289	2.223	
OFZ67-3-1	0.01	109	10.19	29.015	31.250	2.235	
OFZ67-3-1-b	0.01	109	47.90	28.928	30.788	1.860	
OFZ67-3-1-g	0.01	109	6.11	28.875	30.650	1.775	
OFZ68-3-2	0.02	183	86.38	27.43	29.221	1.791	
OFZ68-3-2-g	0.02	183	5.52	27.394	29.203	1.809	
OFZ68-3-2	0.02	183	86.38	27.43	29.221	1.791	
OFZ68-3-3-1	0.02	61	136.25	27.204	29.086	1.882	
OFZ69-3-1	0	65	67.65	28.979	31.134	2.155	
OFZ69-3-3-Large	0	38	46.03	28.358	31.979	2.621	
OFZ69-3-3-Small	0	38	2.56	28.376	32.185	2.809	
OFZ70-3-1-Large	0.01	106	109.73	28.824	30.806	1.982	
OFZ70-3-1-Small	0.01	106	11.07	28.730	30.531	1.801	
OFZ70-3-3-Large	0.01	87	129.98	28.875	30.755	1.880	
OFZ70-3-3-Small	0.01	87	14.73	26.997	29.633	2.636	broad transition
OFZ71-3-1-Large	-0.01	47	145.84	29.185	31.564	2.379	
OFZ71-3-1-Small	-0.01	47	6.58	29.290	31.874	2.584	
OFZ71-3-3	0.02	102	11.10	28.911	30.910	1.999	
OFZ81-3-1-b	0.03	95	62.78	28.117	29.824	1.707	
OFZ81-3-1-g	0.03	95	6.52	28.188	29.842	1.654	
OFZ81-3-1-Large	0.03	95	15.57	28.203	29.788	1.585	shoulder below T_c
OFZ81-3-1-Small	0.03	95	11.61	26.947	29.272	2.325	broad transition
OFZ82-3-1	0.03	64	134.43	28.326	29.910	1.584	
OFZ82-3-3-Large	0.03	45	95.23	26.774	28.669	1.895	
OFZ82-3-3-Small	0.03	45	11.35	26.723	28.669	1.946	
OFZ83-3-1	0.04	44	7.67	27.066	28.893	1.827	
OFZ83-3-1-b	0.04	44	17.77	26.878	28.928	2.050	
OFZ83-3-1-g	0.04	44	6.12	27.015	28.893	1.878	
OFZ84-3-3-Large	0.04	42	81.02	26.947	28.928	1.981	
OFZ84-3-3-Small	0.04	42	2.24	27.033	28.997	1.964	

Table 3.5: Summary of the Mn$_{1+x}$Si samples investigated by means of ac susceptibility in zero field. The table shows the name, the initial manganese x, and the mass m of the samples. The RRR is estimated from samples cut from the same disc of a single crystal ingot, cf. Tab. 3.4. For each sample we state the transition temperatures T_c and T_2 as well their difference $T_2 - T_c$. See text for details.

and RRR $\sim$ 70), are depicted in Fig. 3.22(a). At high temperatures MnSi is paramagnetic. With decreasing temperature a crossover into the fluctuation-disordered regime is observed at a temperature T_2 followed by a fluctuation-induced first-order transition into the helical state at T_c. Here, the transition temperatures are defined as points of inflection.

In Fig. 3.22(b) we show the susceptibility of about 40 samples of $\mathrm{Mn}_{1+x}\mathrm{Si}$. In general, very similar behavior is observed with a tendency for smaller transition temperatures with increasing manganese content (blue to red). The spread of about 15 % in the absolute values essentially may be explained by the sample shapes and the resulting difference of the demagnetization factors. In a few small samples with masses of less than ~10 mg cut from the skin of the single-crystal ingots, the susceptibility around the helimagnetic phase transition is either significantly smeared or shows a double structure, cf. Fig. 3.22(c). These effects might be attributed to compositional inhomogeneities or mechanical stress induced during the cutting of these samples. The corresponding data were excluded from the further analysis.

The temperatures T_2 and T_c are summarized in Figs. 3.22(d) and 3.22(e). For samples cut from the same disc T_c varies by less than 0.1 K, the variation of T_2 is slightly larger. The readout errors of T_2 and T_c are estimated to be ±0.15 K and ±0.05 K, respectively. Within the concentration range studied the transition temperatures rather systematically decrease with increasing x. Some samples, however, show transition temperatures that are 1 K to 2 K smaller than expected. These samples tend to display a RRR considerably exceeding 100. The difference $T_2 - T_c$, i.e., the temperature width of the fluctuation-disordered regime, is shown in Fig. 3.22(f). With 2.5 K it is largest for manganese deficiency and exhibits a shallow minimum of 1.8 K for a slight manganese excess. Here, exceptionally low values of T_2 and T_c cancel out. As introduced in Secs. 3.1.6 and 3.1.7, the suppression of the helimagnetic transition temperature is also observed as a function of hydrostatic or chemical pressure. Thus, the small decrease of the transition temperatures as well as the change of the temperature width of the fluctuation-disordered regime may be related to a minor variation of the number of valence electrons or the lattice constant, respectively.

Susceptibility and specific heat in applied magnetic fields

In the following we discuss the influence of the initial manganese excess of $\mathrm{Mn}_{1+x}\mathrm{Si}$ on the helical, the conical, and the Skyrmion lattice state, as well as on the transitions between them. Fig. 3.23(a) recapitulates the zero-field susceptibility for cubes of 1 mm edge length prepared from the starting section of every growth. Hence, also the demagnetization factors are kept unchanged for all samples and orientations. The general behavior is very similar. Neglecting the specimen with $x = 0.02$, the helimagnetic transition is continuously shifted to lower temperatures with increasing x. The cube with $x = 0.02$, however, possesses a very low transition temperature where samples cut from the same disc exhibit a high RRR $\sim$ 200. Moreover, for $x \geq 0.02$ the anomaly at T_c is broadened, in particular its low-temperature flank.

Fig. 3.23(b) depicts the ac susceptibility in an applied field of 0.2 T, i.e., for a field value giving rise to the Skyrmion lattice state. At low temperatures we observe the constant susceptibility of the conical state. For field along $\langle 100\rangle$ (open symbols), where the temperature and field extent of the Skyrmion lattice state is largest, cf. Sec. 3.3, a pronounced plateau of reduced susceptibility arises just below T_c as the characteristic of the Skyrmion lattice. For $x \geq 0.02$ the borders of the plateau are smeared, similar to the helimagnetic transition in zero field. With field along $\langle 110\rangle$ (closed symbols) we still observe a pronounced minimum for $x \leq 0.01$, while for $x \geq 0.02$ only a shallow rounded dip remains. Measurements at different field values (not

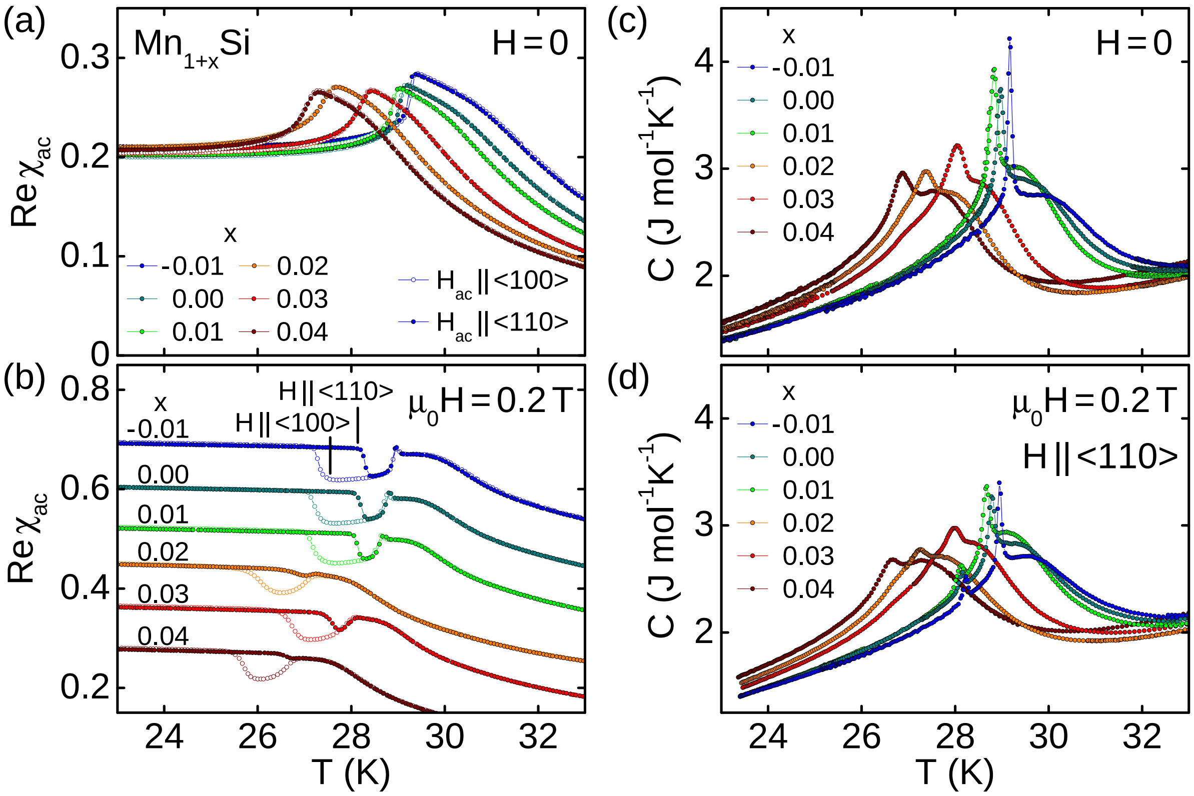

Figure 3.23: Evolution of the temperature dependence of the ac susceptibility and the specific heat of $Mn_{1+x}Si$ as a function of the manganese content, x. (a) Susceptibility in zero field. Data are independent from the orientation of the excitation field. (b) Susceptibility in a field around the high-field boundary of the Skyrmion lattice. For clarity data have been offset by 0.08. (c) Specific heat in zero field. (d) Specific heat in a field around the high-field boundary of the Skyrmion lattice. The signatures at transition between the helical state and the fluctuation-disordered regime as well as at the boundary of the Skyrmion lattice state are broadened for $x \geq 0.02$.

shown) reveal that for $x = 0.02$ and $x = 0.04$ a signal comparable to $x = 0.03$ is observed for $\mu_0 H = 180\,\mathrm{mT}$ suggesting a slight reduction of the field extent of the Skyrmion lattice pocket in the manganese-rich samples.

These observations are corroborated by our specific heat measurements shown in Figs. 3.23(c) and 3.23(d). In zero field, the specific heat of MnSi exhibits a sharp peak at the helimagnetic ordering temperature, T_c, that sits on top of a broad shoulder characterized by a Vollhardt invariance at a temperature T_2. The values of T_c and T_2 derived from the specific heat are in very good agreement with the values from the ac susceptibility. With increasing manganese content, similar to behavior in the ac susceptibility, the transition temperatures are shifted to smaller values and the peak at T_c is increasingly smeared out. This evolution is especially pronounced for $x \geq 0.02$, where the sample with $x = 0.02$ again shows exceptionally low values of T_c and T_2. In fields giving rise to the Skyrmion lattice, the peak at T_c is split into two peaks its low temperature and its high-temperature boundary, T_{A1} and T_{A2}, cf. Sec. 3.3.2. In accordance with the behavior in zero field, we observe a pronounced anomaly at T_{A1} for $x \leq 0.01$ while for

$x \geq 0.02$ only faint features remain, presumably due to a significant broadening of the transition.

In previous studies Pfleiderer [211] as well as Stishov and Petrova [506] showed that in MnSi the RRR of a sample influences the detailed shape of the specific heat, C, and the derivative of the electrical resistivity, $\mathrm{d}\rho/\mathrm{d}T$, around the helimagnetic phase transition. The authors of the latter study argue that the sharpness of the peak emerging in C and $\mathrm{d}\rho/\mathrm{d}T$, instead of the RRR, should be employed as the indicator for the quality of a sample, where a narrow phase transition is attributed to a high crystalline quality. However, using the sharpness of the helimagnetic phase transition alone is as arbitrary and questionable as using the RRR since there is currently no microscopic evidence directly linking the structural quality of a sample with either the RRR or the width of the phase transition.

Field-induced transition between the helical and the conical state

Finally, we address the field-induced transition between the helical and the conical state at low temperatures. As introduced in Sec. 3.1.1, this transition is driven by the interplay between the Zeeman energy, the cubic anisotropies, and the physics of helical domains. For the latter, the pinning of domains and, in particular, domain walls to defects are an important aspect. Hence, the density and type of defects present in a given sample are expected to delicately influence the details of the helical-to-conical phase transition, as consistent with our study of $\mathrm{Mn}_{1+x}\mathrm{Si}$ reported in the following. In contrast, the transition between the conical and the field polarized state exhibits no dependence on the manganese excess x (not shown).

After zero-field cooling MnSi is in the helical state with four equally occupied domains propagating along the crystalline $\langle 111 \rangle$ directions. If a magnetic field is applied the system undergoes a transition into the conical state with a single domain along the field direction. Fig. 3.24 illustrates the transition between the helical and the conical state for field along $\langle 100 \rangle$. Here, all four $\langle 111 \rangle$ axes include the same angle with the field direction and the most complex situation is observed. A suitable probe to determine details of the transition is the susceptibility calculated from the measured magnetization, $\mathrm{d}M/\mathrm{d}H$, cf. Figs. 3.24(a) and 3.24(b). This quantity, as will be addressed in detail in Sec. 3.3.1, covers the slow processes occurring in the transition regime and is not tracked by the ac susceptibility. Corresponding microscopic information is extracted from small-angle neutron scattering and will be reported elsewhere [281].

First, we describe the behavior of a standard MnSi sample ($x = 0$) when sweeping the field from large positive to large negative fields, cf. branch (2) and (3) in Fig. 3.24(c). If the transition is approached from the high-field side, i.e., from the single-domain conical state, a sharp increase of $\mathrm{d}M/\mathrm{d}H$ reaches its maximum before a second peak emerges at slightly lower field values. This double structure may be explained from higher-order cubic anisotropy terms as introduced in Sec. 3.1.1. At the high-field peak the single conical domain splits into two domains that gradually tilt towards certain crystalline $\langle 110 \rangle$ directions selected by the non-centrosymmetric $P2_13$ space group. At the low-field peak these two domains split into four helical domains that finally lock onto the four $\langle 111 \rangle$ axes. If the field is further decreased to negative values and hence the helical-to-conical transition is approached from the multi-domain helical state, we observe a broadened peak with a less pronounced high-field flank when compared to branch (2). The minimum of the susceptibility around zero field is also clearly asymmetric. This behavior may be attributed to the complicated interplay between the macroscopic helical domains, their domain walls, and pinning thereof that superposes the transition triggered by the competition between the crystalline anisotropy and the Zeeman energy.

In the real part of the ac susceptibility, $\mathrm{Re}\,\chi_{\mathrm{ac}}$, we observe a tiny cusp and a kink at the

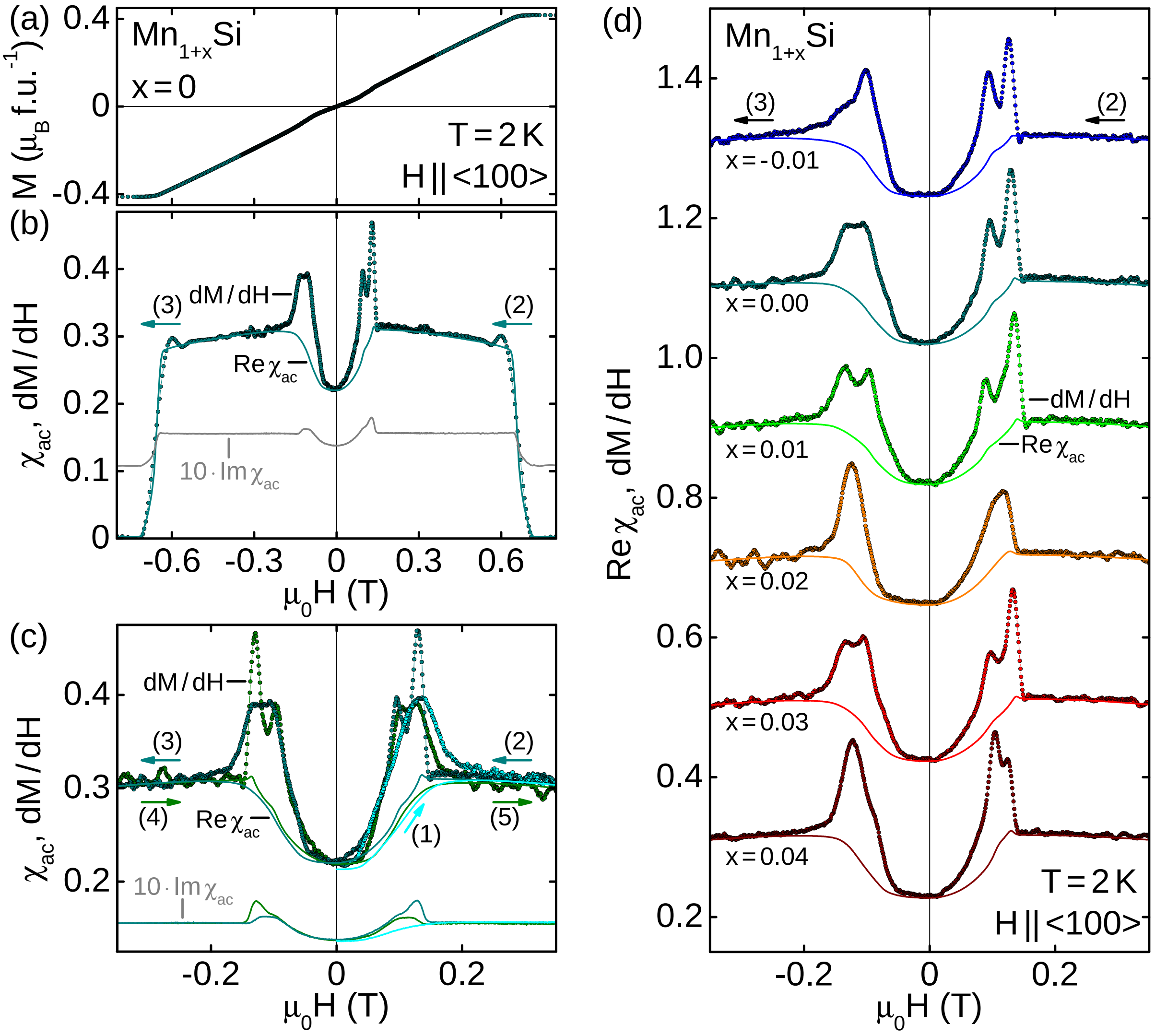

Figure 3.24: Evolution of the field-induced transition from the helical to the conical state in $Mn_{1+x}Si$ as a function of the manganese content, x, at 2 K for field along ⟨100⟩. (a) Field dependence of the magnetization for a conventional MnSi sample ($x = 0$). (b) Real and imaginary part of the ac susceptibility (solid lines) as well as the susceptibility calculated from the magnetization (circles). The oscillations around $\mu_0 H_{c2} \approx \pm 0.7\,\mathrm{T}$ are artifacts from the smoothing algorithm. The arrow marks the sweep direction. (c) Hysteretic behavior at low fields for a full field cycle after initial zero-field cooling; (1) 0 T to +0.9 T, (2) +0.9 T to 0 T, (3) 0 T to −0.9 T, (4) −0.9 T to 0 T, and (5) 0 T to +0.9 T. (d) Real part of the ac susceptibility (solid lines) and susceptibility calculated from the magnetization (circles) for $Mn_{1+x}Si$ with different manganese contents.

positions of the double peak in branch (2), a rounded signature in branch (3), as well as a small general asymmetry between the two branches. The imaginary part, $\mathrm{Im}\,\chi_{ac}$, is small and behaves similar. As depicted in Fig. 3.24(c) the susceptibility is mirrored if the field is swept in the opposite direction, i.e., (2) is analogous to (4) and (3) is analogous to (5). For field along ⟨100⟩ the situation after zero-field cooling, marked (1), essentially corresponds to the situation for increasing field, marked (3) and (5), respectively.

Changing the manganese content in $Mn_{1+x}Si$ finally alters the defect arrangement in the sample and as a consequence the detailed shape of the transition regime, cf. Fig. 3.24(d). For instance, for $x = 0.01$ and $x = 0.03$ a clear double structure is observed also in branch (3). Again, the sample with $x = 0.02$ differs most from the others as it shows no pronounced double structure in branch (2), albeit a small cusp is present. However, all samples share a clear asymmetry between the branches for decreasing and increasing absolute values of the field. Note that the misalignment between the applied field and the crystalline ⟨100⟩ axis of the sample is estimated to be smaller than 2°, i.e., all samples were measured clearly within the solid angle around the ⟨100⟩ direction in which a double structure was observed in a spherical sample of standard MnSi ($x = 0$), cf. Sec. 3.1.1.

Summary

In summary, we have float-zoned a series of $Mn_{1+x}Si$ single crystals with varying manganese content ($-0.01 \leq x \leq 0.04$) at growth rates of 2 mm/h and 5 mm/h. We established a clear correlation between the initial composition and the RRR of a single-crystal $Mn_{1+x}Si$ sample, while the variation of the growth rate had no significant effect. The RRR peaks for a slight initial manganese excess of $x = 0.01$ to $x = 0.02$ which possibly connects to the compensation of the evaporation losses of manganese during the growth process. Differences between the beginning and the end of a single-crystal ingot may be attributed to different cooling rates. The influence of annealing and various cool-down profiles will be subject to a future study.

In general, the magnetic behavior of the $Mn_{1+x}Si$ samples highly resembles each other. Qualitatively very similar magnetic phase diagrams are observed including a single pocket of Skyrmion lattice phase for all samples studied. With increasing x, however, the helimagnetic transition is decreased by up to ~2 K, where samples with exceptional high RRRs exhibit exceptional low transition temperatures. The decrease of the transition temperatures is reminiscent of the behavior as a function of hydrostatic [330] or chemical pressure [85], respectively. In the susceptibility and the specific heat the signatures of the phase transitions get smeared for large manganese contents ($x \geq 0.02$). Finally, also the field-induced transition between the helical and the conical state at low temperatures is sensitive on the composition of the $Mn_{1+x}Si$ sample as expected for a regime that is strongly affected by the defect pinning of macroscopic helical domains and their domain walls.

Our investigations reveal that the determination of sample quality is a difficult task for MnSi as, for example, the RRR may not be directly linked to the sharpness of the helimagnetic phase transition in the specific heat. While the former is commonly used as a criterion for sample quality in many metallic system, the latter was suggested by Stishov and Petrova [506]. We assume, however, that different types of defects influence the electron-impurity scattering, the broadening of thermodynamic signatures at phase transitions, and the pinning of helical domains in distinctively different ways. Hence, microscopic defect studies will be required to clarify this issue. Corresponding measurements by means of positron lifetime spectroscopy are currently carried out by Markus Reiner as part of his Ph.D. thesis. Preliminary data suggest that the specimens may be divided into two categories, manganese-poor with $x \leq 0.01$ and manganese-rich with $x \geq 0.02$, where the samples in one group show a similar defect structure. In addition, an increasing manganese content continuously reduces the amount of open-volume defects.

3.2.2 Large oriented single crystals of MnSi

As part of this thesis, we have prepared large single crystals of MnSi with their growth direction along major crystallographic axes, see Fig. 3.25. For the growth of the first ingot we cut a

Figure 3.25: Float-zoned single crystals of MnSi with major crystallographic directions along their axes. Oriented single crystals were used as seeds. All scales are in millimeter.

$4 \times 4 \times 15\,\mathrm{mm}^3$ bar with a $\langle 110 \rangle$ along its long edge from a large Bridgman grown MnSi single crystal provided by Peter Böni. This bar was used as seed rod for the float-zoning of four polycrystalline feed rods of 10 mm diameter cast in the inductively heated rod casting furnace. As a result, single-crystal cylinders with their axis along $\langle 110 \rangle$, 10 mm diameter, and up to 70 mm length are available (OFZ103, OFZ110, OFZ111, and OFZ119). The feed rod of OFZ103 possessed a manganese excess of $x = 0.015$. Seed crystals of $2 \times 2 \times 9\,\mathrm{mm}^3$ with their long edge along $\langle 100 \rangle$, $\langle 211 \rangle$, and $\langle 111 \rangle$ were cut from OFZ110. Oriented single crystals of 6 mm diameter (OFZ120, OFZ122, and OFZ126) were grown on top of these seeds that in turn served as seed crystals for the preparation of $\langle 100 \rangle$ (OFZ124), $\langle 211 \rangle$ (OFZ125), and $\langle 111 \rangle$ (OFZ128) oriented single crystals of 10 mm diameter.

Taken together, single-crystal cylinders of ~30 mm height and 10 mm diameter are provided for inelastic neutron scattering studies under uniaxial pressure along $\langle 100 \rangle$, $\langle 110 \rangle$, $\langle 111 \rangle$, and $\langle 211 \rangle$, respectively. Furthermore, the $\langle 110 \rangle$ oriented single-crystal cylinder of ~70 mm height and 10 mm diameter resulting from OFZ111 is an ideal sample for various inelastic and elastic neutron scattering techniques. The remaining single-crystal ingots, finally, allow for the preparation of bespoke samples for many future experiments.

3.3 Details of the magnetic phase diagrams

As has been pointed out in the introduction, the magnetic phase diagrams of the cubic chiral helimagnets share many similarities and, in general, are well-known and well-understood. Nevertheless, there are competing scenarios for the explanation of certain aspects. At ambient pressure, this in particular concerns (i) the nature of the phase transition between paramagnetism and helimagnetism and (ii) the mechanism stabilizing the Skyrmion lattice. Thus, as part of this thesis, extensive measurements of the magnetization, the ac susceptibility, and the specific heat of the cubic chiral helimagnets were carried out to resolve these issues and to establish a sound basis for further studies. Our data prove to be fully consistent with a Brazovskii-type fluctuation-induced first-order transition between the paramagnetic and the helimagnetic state and a single pocket of Skyrmion lattice phase that is stabilized by thermal fluctuations.

The following section is divided into three parts. In Sec. 3.3.1, we start with simultaneous measurements of the magnetization and ac susceptibility in high-quality single-crystal MnSi. These measurements show a single pocket of Skyrmion lattice phase for all major crystallographic directions. Additionally, we observe regimes of slow dissipative processes at the phase boundaries between the helical, the conical, and the Skyrmion lattice state. Exploratory measurements in $\mathrm{Mn}_{1-x}\mathrm{Fe}_x\mathrm{Si}$, $\mathrm{Fe}_{1-x}\mathrm{Co}_x\mathrm{Si}$, and $\mathrm{Cu}_2\mathrm{OSeO}_3$ suggest that these findings are a universal characteristic of the cubic chiral helimagnets. The second part, Sec. 3.3.2, is concerned with high-resolution measurements of the specific heat in MnSi yielding two main results. First, the Skyrmion lattice phase is bordered by first-order phase boundaries and possesses a higher entropy compared to the surrounding conical state. Second, there is a tricritical point at intermediate fields in strong support of a fluctuation-induced first-order transition in zero field. Corresponding data for $\mathrm{Mn}_{1-x}\mathrm{Fe}_x\mathrm{Si}$ reveal similar behavior up to $x = 0.10$ while no first-order transition is observed for higher doping levels. Finally, Sec. 3.3.3 addresses the magnetic phase diagrams of $\mathrm{Fe}_{1-x}\mathrm{Co}_x\mathrm{Si}$ where we emphasize the dependence on the magnetic field and temperature history. In combination with the large compositional range that exhibits helimagnetic order, this history dependence allows to optimize the properties of $\mathrm{Fe}_{1-x}\mathrm{Co}_x\mathrm{Si}$ with respect to the requirements of future experiments.

3.3.1 Single-pocket Skyrmion lattice and slow susceptibility response

In the following we report simultaneous measurements of the magnetization and ac susceptibility in high-quality single-crystal MnSi. In particular, we explore the importance of the excitation frequency, the excitation amplitude, the sample shape, and the crystallographic orientation. Consistent with earlier reports, we observe a helical, a conical, and a single pocket of Skyrmion lattice phase as well as a field-polarized, a paramagnetic, and a fluctuation-disordered regime for all configurations studied. Additionally, regimes of slow dissipative processes emerge at the phase boundaries between the helical, the conical, and the Skyrmion lattice state, where the real part of the ac susceptibility, $\mathrm{Re}\,\chi_{\mathrm{ac}}$, does not track the susceptibility calculated from the magnetization, $\mathrm{d}M/\mathrm{d}H$, and is dependent on the excitation frequency and amplitude. Measurements in $Mn_{1-x}Fe_xSi$, $Fe_{1-x}Co_xSi$, and Cu_2OSeO_3 suggest that all cubic chiral helimagnets show similar behavior in χ_{ac} and $\mathrm{d}M/\mathrm{d}H$. A more detailed account of these results is given in Refs. [313, 507].

The work on MnSi reported in this subsection was partly motivated by a series of recent studies by Wilhelm and coworkers claiming evidence for a complex magnetic phase diagram in FeGe with various phase pockets and mesophases near the helimagnetic phase transition [500–502]. As pointed out in Sec. 3.1.10, we have derived a magnetic phase diagram for FeGe using the published data in combination with the definitions as applied to MnSi, $Mn_{1-x}Fe_xSi$, $Fe_{1-x}Co_xSi$, and Cu_2OSeO_3. The resulting phase diagram strongly questions the interpretation by Wilhelm and coworkers since it corresponds to that of a typical cubic chiral helimagnets being subject to large demagnetization effects. The small-angle neutron scattering data in Ref. [294] are also fully consistent with a single pocket of Skyrmion lattice state bordered by a regime of phase coexistence, although Moskvin *et al.* interpret these data as confirmation for the existence of at least two different Skyrmionic pockets.

Experimental details and outline of the results

We have carried out measurements on four high-quality samples of MnSi. The RRR of samples from the same float-zoned ingot exceeded 300 and as a consequence we observed a relatively low $T_c \approx 28\,\mathrm{K}$, cf. Sec. 3.2.1. The dimensions and the orientations of the MnSi samples were selected to cover all major crystallographic directions and a large spread of demagnetization factors. Most data were collected on a bar of $6 \times 1 \times 1\,\mathrm{mm}^3$ with its long edge and the applied field parallel to a crystalline $\langle 100 \rangle$ direction, referred to as Sample 1. This configuration minimizes demagnetization effects. The role of the crystallographic direction was checked on two cubes of 1 mm edge length. In Sample 2 two surfaces were perpendicular to $\langle 100 \rangle$ and four surfaces were perpendicular to $\langle 110 \rangle$. Sample 3 had two surfaces aligned perpendicular to $\langle 110 \rangle$, $\langle 111 \rangle$, and $\langle 211 \rangle$, respectively. This way, all major crystallographic directions could be compared while keeping the demagnetization unchanged. Sample 4 was a thin platelet of $0.115 \times 3 \times 1\,\mathrm{mm}^3$ edge length with its short edge and the applied field parallel to $\langle 100 \rangle$. Thus, the influence of the demagnetization was investigated for field along $\langle 100 \rangle$ on Samples 1, 2, and 4 exhibiting demagnetization factors of $N_1 = 0.074$, $N_2 = N_3 = 0.333$, and $N_4 = 0.837$.

In addition, we have performed exploratory measurements of $Mn_{1-x}Fe_xSi$, $Fe_{1-x}Co_xSi$, and Cu_2OSeO_3 suggesting that our findings in MnSi are universal for the class of cubic chiral helimagnets. The samples of $Mn_{1-x}Fe_xSi$ ($x = 0.04$) and $Fe_{1-x}Co_xSi$ ($x = 0.20$) were bars of $6 \times 1 \times 1\,\mathrm{mm}^3$ with their long edge and the applied field parallel to a crystalline $\langle 100 \rangle$ direction, i.e., analogous to Sample 1. For Cu_2OSeO_3 a vapor-transport-grown crystal was measured that had facets along major crystallographic axes. The sample was approximated as a cube of ~3 mm

	compound	shape	x-direction	y-direction	z-direction	N
1	MnSi	bar	6 mm, $\langle 100 \rangle$	1 mm, $\langle 110 \rangle$	1 mm, $\langle 110 \rangle$	0.074
2	MnSi	cube	1 mm, $\langle 100 \rangle$	1 mm, $\langle 110 \rangle$	1 mm, $\langle 110 \rangle$	0.333
3	MnSi	cube	1 mm, $\langle 110 \rangle$	1 mm, $\langle 111 \rangle$	1 mm, $\langle 211 \rangle$	0.333
4	MnSi	platelet	0.115 mm, $\langle 100 \rangle$	3 mm, $\langle 100 \rangle$	1 mm, $\langle 110 \rangle$	0.837
5	$Mn_{1-x}Fe_xSi$, $x = 0.04$	bar	6 mm, $\langle 100 \rangle$	1 mm, $\langle 110 \rangle$	1 mm, $\langle 110 \rangle$	0.074
6	$Fe_{1-x}Co_xSi$, $x = 0.20$	bar	6 mm, $\langle 100 \rangle$	1 mm, $\langle 110 \rangle$	1 mm, $\langle 110 \rangle$	0.074
7	Cu_2OSeO_3	~cube	3 mm, $\langle 111 \rangle$	3 mm, $\langle 110 \rangle$	3 mm, $\langle 211 \rangle$	0.333

Table 3.6: Samples investigated in this study. The magnetic field was applied along the x-direction and hence $N = N_x$.

edge length. The field was applied along a crystalline $\langle 111 \rangle$ direction, i.e., the hard axis for the helix in Cu_2OSeO_3. The samples are finally summarized in Tab. 3.6.

The magnetization and the ac susceptibility were measured in a 9 T Quantum Design physical properties measurement system. To permit simultaneous measurements of both quantities, the temperature and field were changed stepwise, i.e., at each given temperature and field value the magnetization and the ac susceptibility were consecutively measured before the next temperature or field value was approached. The ac excitation field, which was only turned on during the data acquisition, was set to a frequency between 10 Hz and 10 kHz at an excitation amplitude between 0.1 mT and 1 mT. At temperatures around the Skyrmion lattice state MnSi typically shows a resistivity of ~30 µΩcm [11]. The resulting estimated skin depth $\delta_{\mathrm{MnSi}}(28\,\mathrm{K}) = 0.26 \cdot f^{-1/2}\,\mathrm{m\,s^{-1/2}}$ leads to a minimal value of 2.6 mm at 10 kHz which is considerably larger than the relevant sample dimensions. Compared to MnSi, the larger resistivity of the other compounds investigated results in larger skin depths.

The presentation of our results is organized as follows. First, we begin with the typical magnetic field and temperature dependencies of the magnetization and the susceptibility in MnSi and define the phase transitions and crossovers inferred from these data. Subsequently, the influence of the excitation frequency and amplitude on the real and imaginary part of the ac susceptibility are summarized. The role of the crystallographic orientation and the demagnetization effects are discussed and followed by the magnetic phase diagrams for field along all major axes. Finally, results for $Mn_{1-x}Fe_xSi$, $Fe_{1-x}Co_xSi$, and Cu_2OSeO_3 are shown before we sum up our findings.

Magnetic field and temperature dependence of the magnetization and the susceptibility

Due to the rather complex shape of the magnetization (and the susceptibility) landscape of MnSi around the Skyrmion lattice state, it is helpful to present at first a qualitative summary as a guide of the essential features. Hence, we begin with Figs. 3.26(a) and 3.26(b) showing a schematic depiction of the magnetization as a function of magnetic field and temperature. At low temperatures the magnetization is essentially that of a weak itinerant ferromagnet with vanishing hysteresis. The magnetization of the Skyrmion lattice is characterized by a slightly tilted plateau bordered by a discontinuous first-order step that is smeared out in the experimental data. Thus, two steps can be observed as a function of increasing field, marked by trace (I). As a function of increasing temperature, however, the behavior is more complex. For a temperature scan near the upper field boundary of the Skyrmion lattice phase, depicted by trace (II), the magnetization

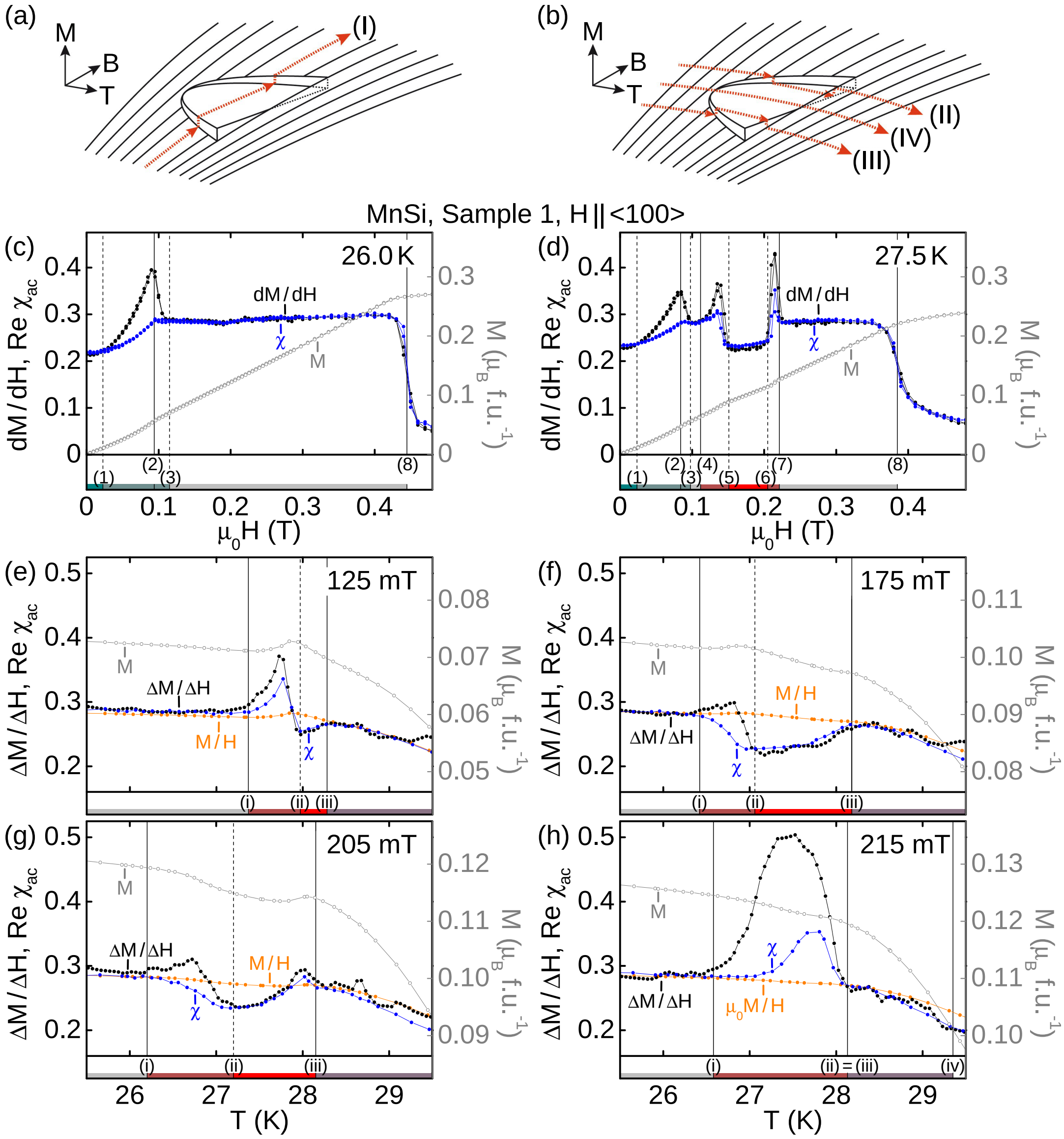

Figure 3.26: Magnetization and susceptibility of MnSi around the Skyrmion lattice phase. (a)–(b) Schematic depiction of the magnetization as a function of temperature and magnetic field. In the regime of the Skyrmion lattice phase the magnetization is characterized by a tilted plateau bordered by a discontinuous first-order step. The traces illustrate typical scans as a function of magnetic field or temperature. In the experimental data the discontinuous steps are smeared out. (c)–(d) Comparison of the magnetic field dependence of the magnetization, M (gray), the susceptibility calculated from the magnetization, $\mathrm{d}M/\mathrm{d}H$ (black), and the real part of the ac susceptibility, $\mathrm{Re}\,\chi_{\mathrm{ac}}$ (blue). (e)–(h) Comparison of the corresponding temperature dependences including the ratio M/H (orange).

name	label	signature in $\mathrm{d}M/\mathrm{d}H$	signature in $\mathrm{Re}\,\chi_{\mathrm{ac}}$	signature in $\mathrm{Im}\,\chi_{\mathrm{ac}}$
H_{c1}^{-}	(1)	begin $\mathrm{d}M/\mathrm{d}H \neq \mathrm{Re}\,\chi_{\mathrm{ac}}$	begin $\mathrm{d}M/\mathrm{d}H \neq \mathrm{Re}\,\chi_{\mathrm{ac}}$	begin of small peak
H_{c1}	(2)	peak	point of inflection	small peak
H_{c1}^{+}	(3)	end $\mathrm{d}M/\mathrm{d}H \neq \mathrm{Re}\,\chi_{\mathrm{ac}}$	end $\mathrm{d}M/\mathrm{d}H \neq \mathrm{Re}\,\chi_{\mathrm{ac}}$	end of small peak
H_{A1}^{-}	(4)	begin of peak	begin of deviation from $\mathrm{Re}\,\chi_{\mathrm{ac}}$ in conical phase	begin of peak
H_{A1}^{+}	(5)	begin of plateau of reduced $\mathrm{d}M/\mathrm{d}H$	begin of plateau of reduced $\mathrm{Re}\,\chi_{\mathrm{ac}}$	end of peak
H_{A2}^{-}	(6)	end of plateau of reduced $\mathrm{d}M/\mathrm{d}H$	end of plateau of reduced $\mathrm{Re}\,\chi_{\mathrm{ac}}$	begin of peak
H_{A2}^{+}	(7)	end of peak	end of deviation from $\mathrm{Re}\,\chi_{\mathrm{ac}}$ in conical phase	end of peak
H_{c2}	(8)	point of inflection	point of inflection	small peak

Table 3.7: Summary of characteristic transition and crossover fields of MnSi and the associated labels used in the figures. The signatures in $\mathrm{d}M/\mathrm{d}H$ were used to define the actual field values, which correspond within the accuracy of our data to the signatures in $\mathrm{Re}\,\chi_{\mathrm{ac}}$ and $\mathrm{Im}\,\chi_{\mathrm{ac}}$. Values extracted from data recorded for increasing and decreasing magnetic field are in excellent agreement. The small peaks at H_{c1} and, in particular, H_{c2}, were not resolved in the study reported in Ref. [313] but in subsequent studies, see Refs. [282, 508]. Note that our definition of H_{A1}^{-} and H_{A2}^{+} corresponds to values referred to as H_{A1} and H_{A2} in the literature.

is slightly reduced within the Skyrmion lattice state. In contrast, for a temperature scan in the vicinity of the lower boundary, depicted by trace (III), a shallow maximum may be observed. For intermediate field values within the Skyrmion lattice state, depicted by trace (IV), tiny or no features are obtained. This is a purely accidental effect and explains the putative observation of two phase pockets near the helimagnetic transition of MnSi in a pioneering magnetization study by Kadowaki *et al.* [291]. In this study two distinct phase pockets were inferred from two kinks in the temperature dependence of the magnetization.

Figs. 3.26(c) and 3.26(d) show the typical magnetic field dependence of the magnetization and the susceptibility at temperatures below and in the Skyrmion lattice state, respectively. Data for both increasing and decreasing fields are shown, where the field sweeps were started at -1 T and +1 T for increasing and decreasing fields, respectively.

At first, we account for the magnetization starting from zero field at low temperatures where it increases almost linearly. Well below the helimagnetic transition temperature, T_c, the initial quasi-linear increase for $H < H_{c1} \sim 0.1\,\mathrm{T}$ arises from an increasing anharmonicity of the helical modulation, a slight reorientation of the helical modulation, and changes of domain population as seen in neutron scattering studies [286, 311]. Depending on field direction the reorientation at H_{c1} represents a crossover or a symmetry-breaking second-order phase transition, cf. Sec. 3.1.1. In contrast, for $H > H_{c1}$ the linear increase has a slightly larger slope and is a characteristic of a closing-in of the spin-flop phase (the conical phase) up the transition to the field-polarized ferromagnetic state at H_{c2}. Just below T_c, a plateau of diminished slope is observed at intermediate fields, $\mu_0 H \sim 0.2\,\mathrm{T}$, as the characteristic of the Skyrmion lattice state. The helical, the conical, and the Skyrmion lattice state are connected by small transition regimes of increased

name	label	signature in $\Delta M/\Delta H$	signature in $\mathrm{Re}\,\chi_{\mathrm{ac}}$	signature in $\mathrm{Im}\,\chi_{\mathrm{ac}}$
T_{A1}^{-}	(i)	begin of maximum	begin of deviation from $\mathrm{Re}\,\chi_{\mathrm{ac}}$ in conical phase	begin of peak
T_{A1}^{+}	(ii)	end of maximum	end $\Delta M/\Delta H \neq \mathrm{Re}\,\chi_{\mathrm{ac}}$	end of peak
T_{A2}^{+}	(iii)	end of deviation from $\Delta M/\Delta H$ in conical phase	end of deviation from $\mathrm{Re}\,\chi_{\mathrm{ac}}$ in conical phase	no signature
T_{c2}	(iv)	point of inflection	point of inflection	no signature

Table 3.8: Summary of characteristic transition and crossover temperatures of MnSi and the associated labels used in the figures. The signatures in $\Delta M/\Delta H$ were used to define the actual field values, which correspond within the accuracy of our data to the signatures in $\mathrm{Re}\,\chi_{\mathrm{ac}}$ and $\mathrm{Im}\,\chi_{\mathrm{ac}}$. Values extracted from data recorded for increasing and decreasing temperatures are in excellent agreement. Note that our definition of T_{A1}^{-} and T_{A2}^{+} corresponds to values referred to as T_{A1} and T_{A2} in the literature.

slope.

Deviations from the quasi-linear field dependence of the magnetization are best seen in the susceptibility. Here, we compare the real part of the ac susceptibility measured at an excitation frequency of 10 Hz and an excitation amplitude of 0.1 mT, $\mathrm{Re}\,\chi_{\mathrm{ac}}$, with the susceptibility calculated from the measured magnetization, $\mathrm{d}M/\mathrm{d}H$. The small excitation frequency and amplitude were chosen to disturb the system as little as possible. Deep in the helical, the conical, the Skyrmion lattice, or the field-polarized state both quantities are in agreement with each other. At the phase transitions between the helical, the conical, and the Skyrmion lattice state, however, $\mathrm{d}M/\mathrm{d}H$ shows pronounced maxima that are not tracked by $\mathrm{Re}\,\chi_{\mathrm{ac}}$.

At the helical-to-conical transition we attribute this deviation to the slow response that arises from the reorientation of the large helical domains. We define the transition field H_{c1} as the maximum in $\mathrm{d}M/\mathrm{d}H$. The borders of the surrounding regime of slow response, H_{c1}^{-} and H_{c1}^{+} marked as (1) and (3), are characterized by the merging of $\mathrm{d}M/\mathrm{d}H$ and $\mathrm{Re}\,\chi_{\mathrm{ac}}$. Around the Skyrmion lattice state similar deviations between $\mathrm{d}M/\mathrm{d}H$ and $\mathrm{Re}\,\chi_{\mathrm{ac}}$ are observed. However, at this first-order transition the slow response is attributed to the nucleation process of topologically non-trivial Skyrmions in the conical phase, i.e., a regime of phase coexistence that accompanies the first-order transition. Here, the lower field boundary of the Skyrmion lattice state is described by H_{A1}^{-} and H_{A1}^{+}, marked as (4) and (5), and the upper field boundary by H_{A2}^{-} and H_{A2}^{+}, marked as (6) and (7). The outer limits, H_{A1}^{-} and H_{A2}^{+}, reflect the definition of the phase boundaries used in earlier studies [85, 414]. In contrast, a high-precision study of the specific heat reported in Sec. 3.3.2 reveals that in fact the inner boundaries, H_{A1}^{+} and H_{A2}^{-}, coincide with the peaks of the first-order transition between the conical and the Skyrmion lattice state. The second-order transition between the conical and the field-polarized state at H_{c2} is marked as (8).

These observations are supported by typical temperature dependences of the magnetization and the susceptibility for field values within the Skyrmion lattice state presented in Figs. 3.26(e) through 3.26(h). Data are shown after an initial zero-field cool. The qualitative evolution of the magnetization can be accounted for by the schematic picture given in Fig. 3.26(b). Features that arise from the Skyrmion lattice state are again best seen in the susceptibility. In order to infer the temperature dependence of the susceptibility from the measured magnetization, we have measured $M(T)$ at field values that differed by 5 mT and computed $\Delta M/\Delta H$ as a reasonable

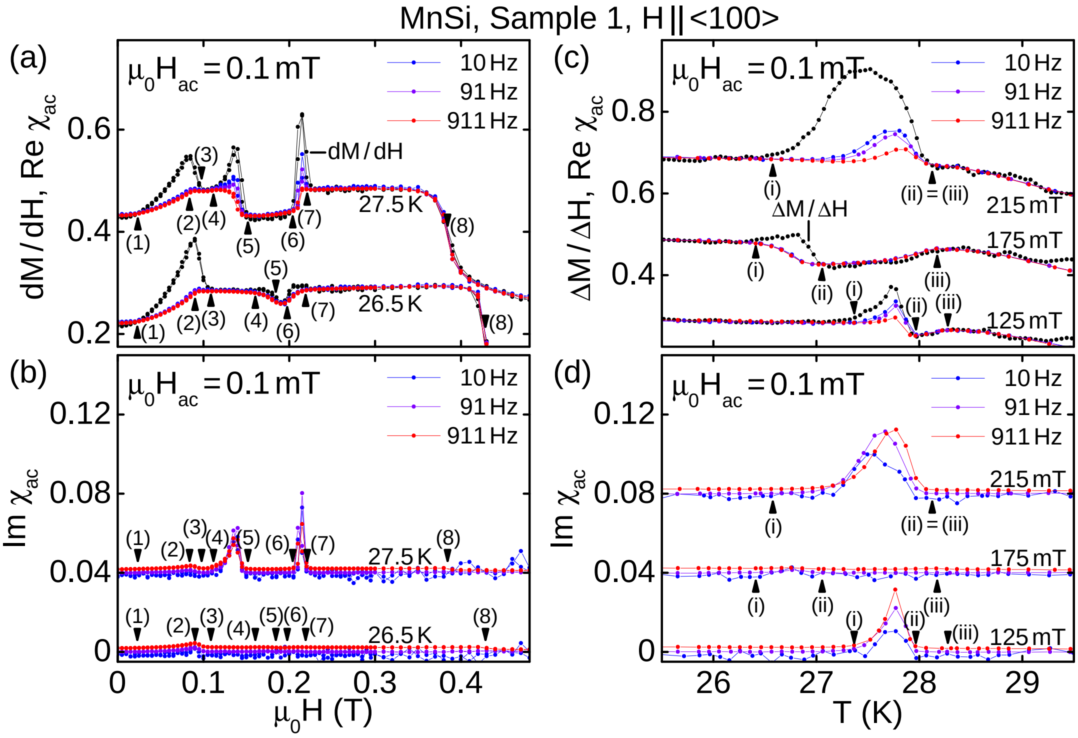

Figure 3.27: Typical magnetic field and temperature dependence of the susceptibility inferred from the magnetization, $\mathrm{d}M/\mathrm{d}H$, and the real and imaginary parts of the ac susceptibility, $\mathrm{Re}\,\chi_{\mathrm{ac}}$ and $\mathrm{Im}\,\chi_{\mathrm{ac}}$, for various excitation frequencies. Data were recorded for an excitation amplitude of 0.1 mT. Curves have been shifted by constant values for clarity.

approximation of $\mathrm{d}M/\mathrm{d}H$.

Consistent with the behavior as a function of field, deep within the different states $\Delta M/\Delta H$ and $\mathrm{Re}\,\chi_{\mathrm{ac}}$ agree very well whereas a discrepancy is observed around the low-temperature boundary of the Skyrmion lattice state, i.e., between T_{A1}^{-} and T_{A1}^{+} marked as (i) and (ii). At the border between the Skyrmion lattice state and the fluctuation-disordered regime at T_{A2}, marked as (iii), both quantities coincide. The pronounced maximum at the high-field boundary of the Skyrmion lattice state, see Fig. 3.26(h), arises due to the vanishing slope of this boundary as a function of temperature. Hence, a temperature sweep may cut solely through the transition regime. The crossover between the fluctuation-disordered and the paramagnetic regime at higher temperatures is finally indicated in $\mathrm{Re}\,\chi_{\mathrm{ac}}$ by a point of inflection at T_{c2}, marked as (iv). The detailed definitions of the transition fields and temperatures are summarized in Tabs. 3.7 and 3.8.

Influence of the excitation frequency and amplitude on the ac susceptibility

In the following, the influence of the excitation frequency and amplitude on the ac susceptibility will be discussed. Fig. 3.27 shows typical magnetic field and temperature dependences of the real and the imaginary part of the ac susceptibility. Data were measured at three different frequencies, namely 10 Hz, 91 Hz, and 911 Hz, using a small excitation amplitude of 0.1 mT. The susceptibility calculated from the measured magnetization, $\mathrm{d}M/\mathrm{d}H$ and $\Delta M/\Delta H$, respectively,

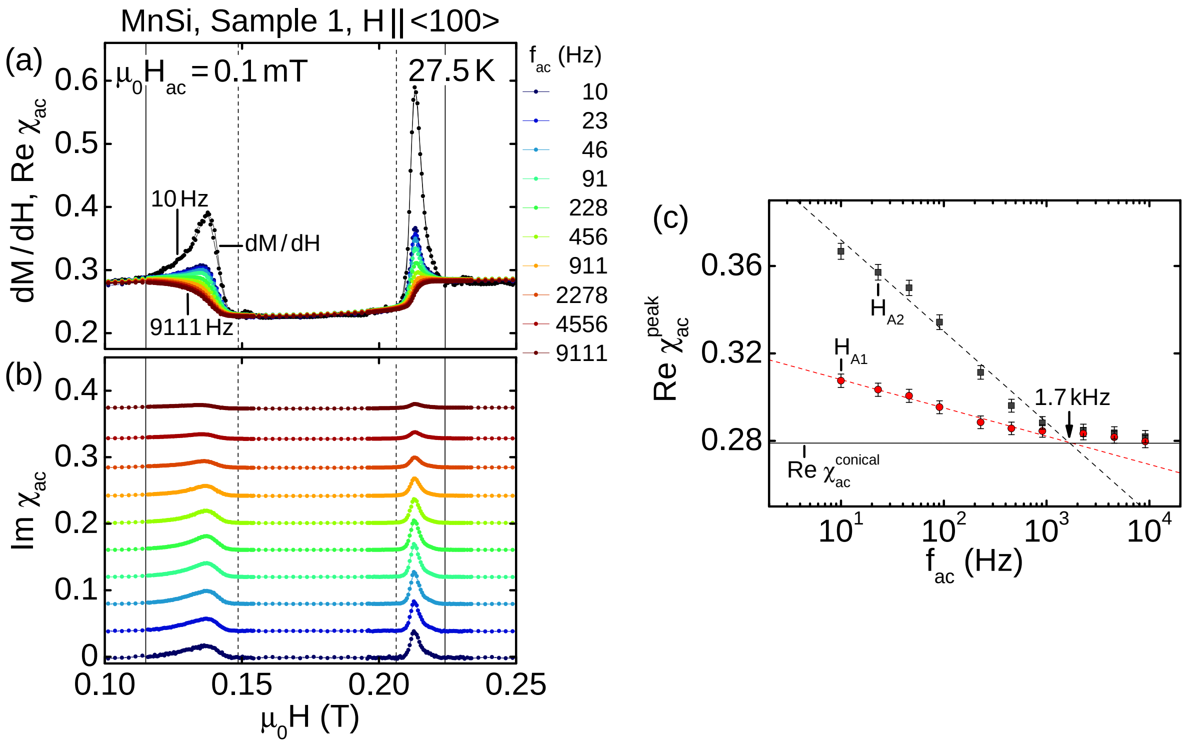

Figure 3.28: Comparison of the susceptibility calculated from the magnetization, $\mathrm{d}M/\mathrm{d}H$, and the ac susceptibility at a wide range of different frequencies. (a) The maxima at the lower and upper boundary of the Skyrmion lattice phase, H_{A1} and H_{A2}, decrease dramatically with increasing frequency and vanish altogether for very large frequencies. (b) The maxima in the imaginary part of the susceptibility at the phase boundaries also decrease substantially with increasing frequency. (c) Frequency dependence of the height of the peak in the ac susceptibility at H_{A1} and H_{A2}.

is added for comparison.

As depicted in Fig. 3.27(a) the maximum in $\mathrm{d}M/\mathrm{d}H$ at the helical-to-conical transition has already vanished in Re χ_{ac} at an excitation frequency of 10 Hz. Increasing the excitation frequency further leaves Re χ_{ac} unchanged. In contrast, the maxima in $\mathrm{d}M/\mathrm{d}H$ that encompass the Skyrmion lattice state are still partly visible in Re χ_{ac} at an excitation frequency of 10 Hz and suppressed with increasing frequency. The influence of the excitation frequency on the temperature dependence of the ac susceptibility depicted in Fig. 3.27(c) corroborates this observation. Taken together, while the time scales at the boundary of the Skyrmion lattice state and at the helical-to-conical transition are both slow, the latter are distinctly slower. This quantitative difference substantiates the assumption that these time scales arise from different mechanisms. At the helical-to-conical transition, which is second-order or a crossover, the slow reorientation of large helical domains is responsible. Around the Skyrmion lattice state the slow response emerges due to a regime of phase coexistence encompassing the first-order phase transition, e.g., droplets of Skyrmion lattice that persist within a conical spin texture and vice versa.

The imaginary part of the ac susceptibility, Im χ_{ac}, supports this distinction, see Figs. 3.27(b) and 3.27(d). Im χ_{ac} exhibits pronounced maxima in the transition regime between the conical and the Skyrmion lattice state while being essentially zero elsewhere. A finite imaginary part of the susceptibility is associated with dissipation. Around the Skyrmion lattice state, the latter stems from the nucleation process of topologically non-trivial Skyrmions in the conical phase (or vice versa) eventually triggering the first-order transition. The lack of hysteresis within the resolution of the methods used may be attributed to a very weak pinning. In contrast, the helical-to-conical transition is not accompanied by a substantial $\mathrm{Im}\,\chi_{\mathrm{ac}}$. Finally, we also checked the influence of different excitation amplitudes between 0.1 mT and 1 mT at a fixed excitation frequency of 10 Hz (not shown). Compared to the variation of the excitation frequency similar changes of the ac susceptibility are observed in the transition regimes; cf. Figs. 5 and 9 in Ref. [313].

Finally, Fig. 3.28 addresses the frequency dependence of the real and imaginary part of the ac susceptibility around the boundaries of the Skyrmion lattice state in detail. With increasing frequency the heights of peaks at the lower and the upper field boundary of the Skyrmion lattice state, H_{A1} and H_{A2}, are continuously decreasing in both $\mathrm{Re}\,\chi_{\mathrm{ac}}$ and $\mathrm{Im}\,\chi_{\mathrm{ac}}$. On a logarithmic frequency scale, shown in Fig. 3.28(c), both maxima decrease linearly and vanish around a characteristic frequency $f_A \sim 1.7\,\mathrm{kHz}$ where the value of the susceptibility in the conical phase is reached. In contrast, the ac susceptibility at the helical-to-conical transition shows no peak and no difference for a variation of the excitation frequency between 10 Hz and 10 kHz. This implies that in MnSi the characteristic frequency of this transition, f_{c1}, is below 10 Hz and hence $f_{c1} \ll f_A$. In principle, it would be instructive to compare these frequencies for samples with different RRR and therefore different defect pinning. As the transition temperatures, however, are also dependent on the RRR as shown in Sec. 3.2.1, the comparison of equivalent points in the magnetic phase diagram is difficult for samples with different RRR.

Influence of the sample shape, the orientation, and the cooling history

All data shown so far were collected on Sample 1 for field along a crystalline $\langle 100 \rangle$ axis, i.e., for field along the long edge of a bar hence minimizing the effects of the demagnetization fields. Fig. 3.29 summarizes the influence of the shape and orientation of the sample on the behavior of MnSi. A larger demagnetization factor, N, simultaneously leads to an increase of the transition fields and to a decrease of the absolute value of the measured susceptibility. Both effects can be readily corrected by properly taking into account the demagnetization effects, cf. Sec. 1.8.2. Additionally, in samples with very large demagnetization factors or irregular shaped surfaces the signatures at the phase boundaries smear out significantly, in particular around the Skyrmion lattice state. Such a behavior is clearly observed in Sample 4, a thin platelet with its short edge along the field. The broadening may be attributed to a large spread of the size and orientation of the demagnetization fields within the sample. Thus, different parts of the sample are subject to different effective magnetic fields.

Changing the field direction has two decisive effects. First, the characteristic field value for the helical-to-conical transition is largest for field along $\langle 100 \rangle$, the hard axis of the magnetic pitch, and smallest for field along $\langle 111 \rangle$, the soft axis of the magnetic pitch. Second, the extent of the Skyrmion lattice phase, especially with respect to temperature, is largest for field along $\langle 100 \rangle$ and smallest for field along $\langle 111 \rangle$. In both cases, field along $\langle 110 \rangle$ leads to an intermediate behavior. These observations are fully consistent with the leading-order cubic anisotropy terms as explained in Sec. 3.1.1. The cooling history, finally, has no influence on the behavior of MnSi, with exception of well-understood changes in the domain population in the helical state at low temperatures, cf. Fig. 10 in Ref. [313].

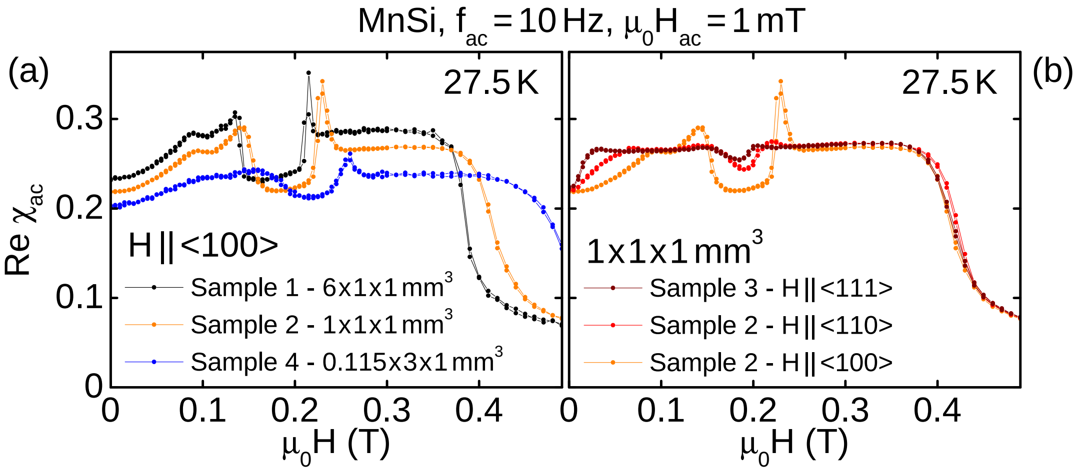

Figure 3.29: Typical ac susceptibility data for different sample shapes and orientations as a function of the applied field. Data were recorded with an excitation frequency of 10 Hz and an excitation amplitude of 1 mT. (a) Real part of the ac susceptibility, Re χ_{ac}, for three different sample geometries. The pronounced qualitative and quantitative discrepancies for different sample shapes are purely due to demagnetizing fields. (b) Real part of the ac susceptibility, Re χ_{ac}, for a cubic sample shape and field along the major crystallographic directions. Discrepancies are purely due to the influence of the cubic anisotropies.

Magnetic phase diagrams

As one of the main results of our study, we have carefully determined the magnetic phase diagrams of MnSi for field along ⟨100⟩, ⟨110⟩, and ⟨111⟩, see Fig. 3.30. Data are shown on an internal magnetic field scale, i.e., after correcting for demagnetization effects. The phase diagram for field along ⟨100⟩ contains data taken on Samples 1, 2, and 4, which are in excellent agreement. Due to the significant broadening of the signatures at the boundary of the Skyrmion lattice state in Sample 4 caused by the large demagnetization effects, the corresponding data were omitted.

In general, our phase diagrams are fully consistent with earlier reports. As explained in Sec. 3.2.1, the comparably small absolute values of the transition temperatures may be attributed to the high RRR of the measured sample which does not interfere with our further results. Below the helimagnetic ordering temperature, T_c, we observe the helical, the conical, and a single pocket of Skyrmion lattice phase for all major crystallographic directions. The small differences between the different orientations are explained by the leading-order cubic anisotropy terms. At high fields or temperatures MnSi is in a field-polarized (FP) or a paramagnetic state (PM), respectively. The fluctuation-disordered regime (FD), previously also referred to as intermediate regime, that arises as a consequence of the Brazovskii-type fluctuation-induced first-order transition in zero field will be accounted for in detail in Sec. 3.3.2. In addition to these six well-established phases and regimes we have, for the first time, resolved regions of slow response encompassing the helical and the Skyrmion lattice state. This slow response may be attributed to the slow reorientation of large helical domains and the nucleation process of topologically non-trivial Skyrmions in the conical phase (or vice versa), respectively.

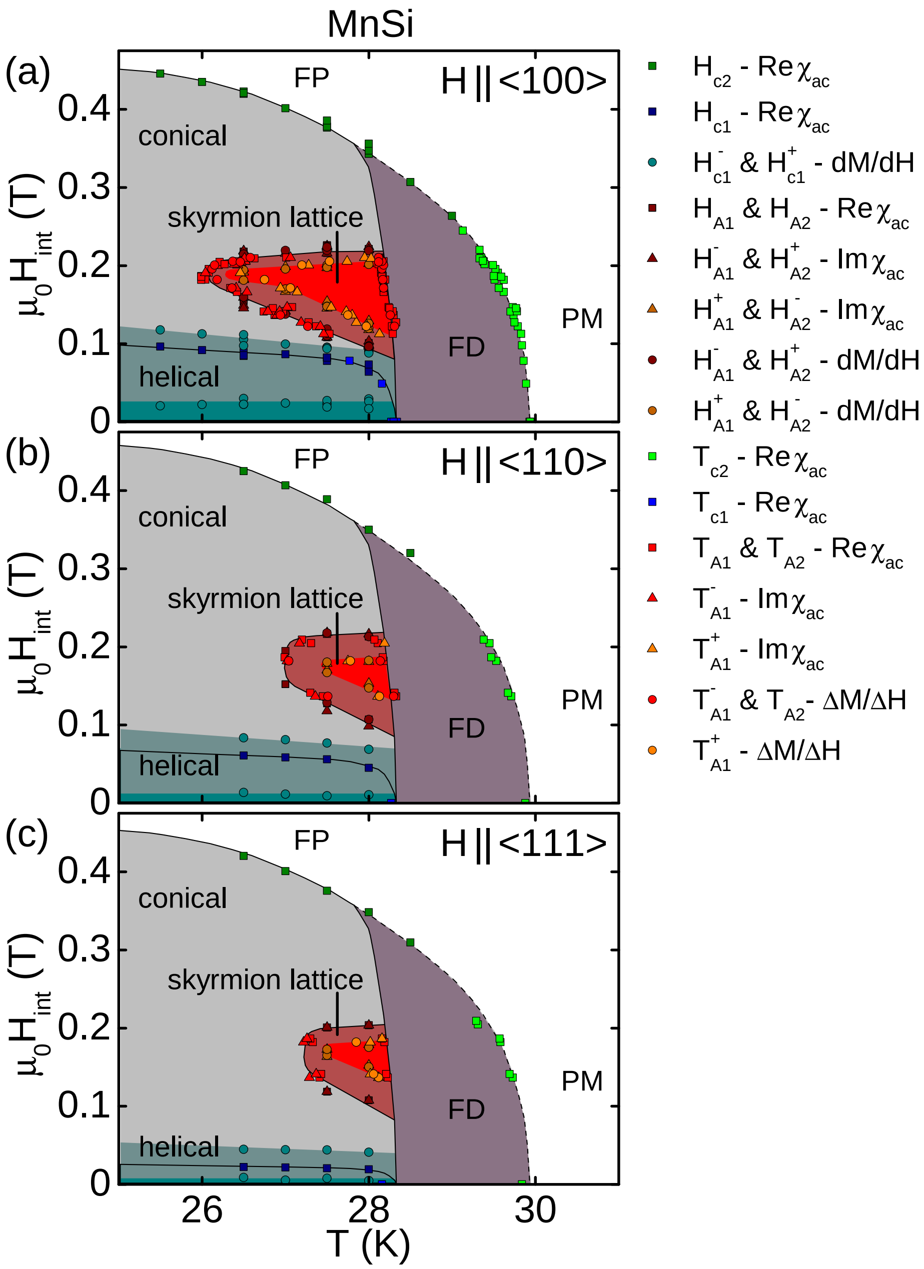

Figure 3.30: Magnetic phase diagram of MnSi for field along different crystallographic directions. Phase diagrams are shown as a function of internal field; the effects of demagnetizing fields have been corrected. We distinguish the following regimes: helical order, conical order, Skyrmion lattice, fluctuation-disordered (FD), paramagnetic (PM), and field-polarized (FP). The dashed line between the FD and the PM regime represents a crossover. The crossover separating the FP from the PM regime has not been tracked. The dark red shading at the first-order transition between the conical and Skyrmion lattice phase marks a regime of phase coexistence with finite Im χ_{ac}.

Relevance for other cubic helimagnets: $Mn_{1-x}Fe_xSi$ and $Fe_{1-x}Co_xSi$

As explained in the introduction, substitutional doping of MnSi with iron or cobalt suppresses the helimagnetic ordering temperature. In the case of $Mn_{1-x}Fe_xSi$ with $x = 0.04$ the transition temperature decreases to $T_c \approx 15\,\mathrm{K}$, while the magnetic phase diagram is still strongly reminiscent of pure MnSi. The left column of Fig. 3.31 shows the typical magnetic field dependence of the susceptibility for $Mn_{1-x}Fe_xSi$ with $x = 0.04$ for a temperature well below T_c and two temperatures crossing the Skyrmion lattice state. After zero-field cooling (zfc), see Fig. 3.31(a), the data are very similar to pure MnSi, with the same general features at the helical-to-conical transition at H_{c1} and at the border of the Skyrmion lattice phase. The maxima in the susceptibility calculated from the magnetization, $\mathrm{d}M/\mathrm{d}H$, are again not tracked by the real part of the ac susceptibility, $\mathrm{Re}\,\chi_{\mathrm{ac}}$. However, in contrast to pure MnSi, a variation of the excitation frequency between 10 Hz and 911 Hz has no influence on $\mathrm{Re}\,\chi_{\mathrm{ac}}$. Hence, the characteristic frequency at the boundary of the Skyrmion lattice, f_A, is shifted to a value well below 10 Hz.

In addition, compared to MnSi, there are some differences at the helical-to-conical transition. Well below T_c after zero-field cooling H_{c1} increases almost linearly with decreasing temperature

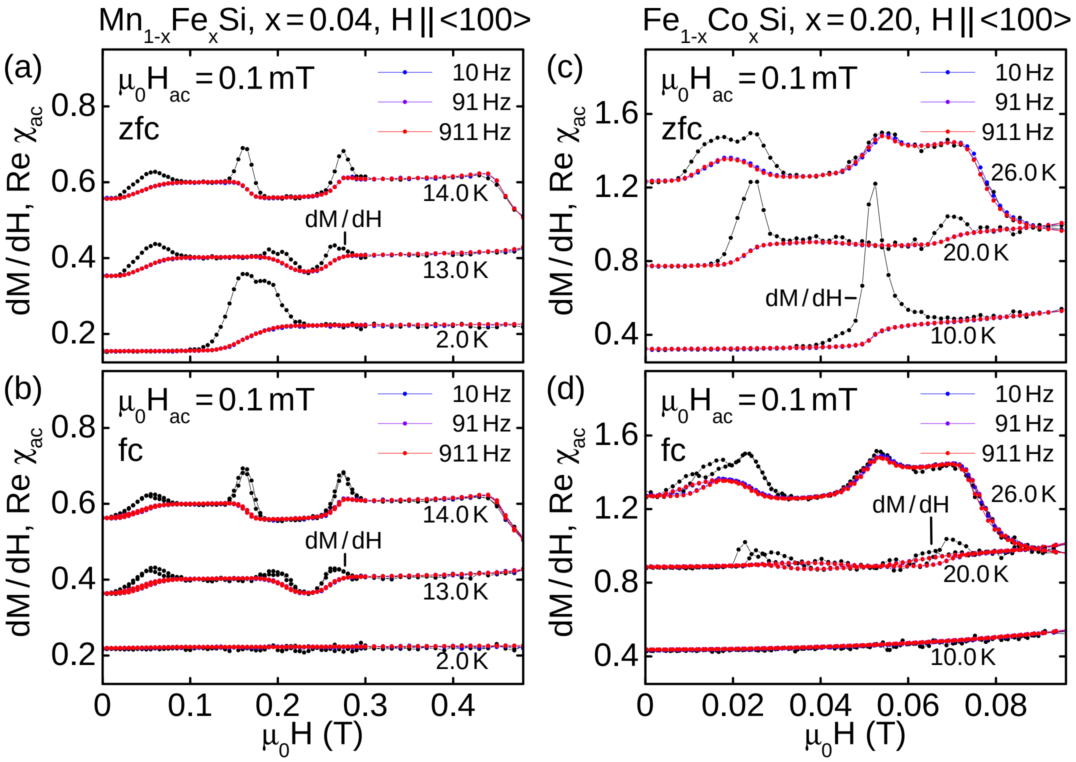

Figure 3.31: Comparison of the susceptibility calculated from the magnetization, $\mathrm{d}M/\mathrm{d}H$, with the real part of the ac susceptibility, $\mathrm{Re}\,\chi_{\mathrm{ac}}$, for $Mn_{1-x}Fe_xSi$ ($x = 0.04$) and $Fe_{1-x}Co_xSi$ ($x = 0.20$). (a) Data for $Mn_{1-x}Fe_xSi$ after zero-field cooling. (b) Data for $Mn_{1-x}Fe_xSi$ after field cooling. (c) Data for $Fe_{1-x}Co_xSi$ after zero-field cooling. (d) Data for $Fe_{1-x}Co_xSi$ after field cooling. The same qualitative differences are observed as in MnSi with an additional discrepancy between different cooling histories.

in $Mn_{1-x}Fe_xSi$ while H_{c1} is essentially temperature independent in MnSi. Moreover, once a field $H > H_{c1}$ is applied in $Mn_{1-x}Fe_xSi$ the susceptibility value of the conical state is observed down to zero field, see Fig. 3.31(b). Here, field cooled (fc) denotes scans that start at -1 T and +1 T for increasing and decreasing fields, respectively. At low temperatures there are no anomalies in $\mathrm{d}M/\mathrm{d}H$ or in $\mathrm{Re}\,\chi_{\mathrm{ac}}$ that may be attributed to a transition at H_{c1}. In the vicinity of T_c the behavior after zero-field cooling is recovered which may be attributed to the effects of thermal excitations into the helical state. Taken together, the behavior of $Mn_{1-x}Fe_xSi$ is consistent with an increased amount of disorder that in turn leads to a stronger defect related pinning when compared to pure MnSi.

For the strongly doped semiconductor $Fe_{1-x}Co_xSi$ corresponding susceptibility data after zero-field cooling and after field cooling, i.e., for scans starting at ±0.3 T, are displayed in Figs. 3.31(c) and 3.31(d). Apart from a small hysteresis within the Skyrmion lattice state, the behavior of $Fe_{1-x}Co_xSi$ with $x = 0.20$ highly resembles that of $Mn_{1-x}Fe_xSi$ with $x = 0.04$. The hysteresis in the phase diagram of $Fe_{1-x}Co_xSi$ will be addressed in detail in Sec. 3.3.3.

Relevance for other cubic helimagnets: Cu_2OSeO_3

We finally consider the insulating helimagnet Cu_2OSeO_3. Fig. 3.32 depicts typical magnetization and susceptibility data for Cu_2OSeO_3 at a low temperature and at a temperature just below the helimagnetic transition temperature, T_c. The field is applied along the ⟨111⟩ direction, i.e., the hard axis for the helical pitch. This configuration is comparable to field along the ⟨100⟩ axis in MnSi. Data for both increasing and decreasing fields are shown, where the field sweeps were started at -0.2 T and +0.2 T for increasing and decreasing fields, respectively.

In general, the behavior of Cu_2OSeO_3 is highly reminiscent of MnSi, albeit the underlying

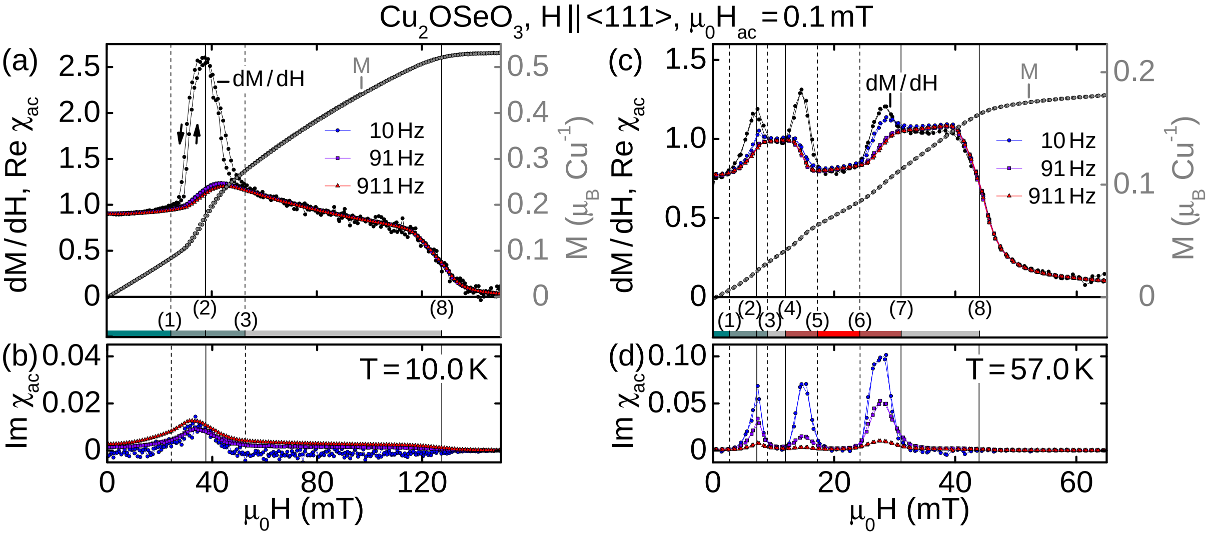

Figure 3.32: Comparison of the susceptibility calculated from the magnetization, $\mathrm{d}M/\mathrm{d}H$, with the real and imaginary part of the ac susceptibility, $\mathrm{Re}\,\chi_{\mathrm{ac}}$ and $\mathrm{Im}\,\chi_{\mathrm{ac}}$, respectively, for Cu_2OSeO_3. (a) Real and (b) imaginary part of the ac susceptibility at a temperature well below T_c. (c) Real and (d) imaginary part of the ac susceptibility at a temperature just below T_c, i.e., in the Skyrmion lattice state.

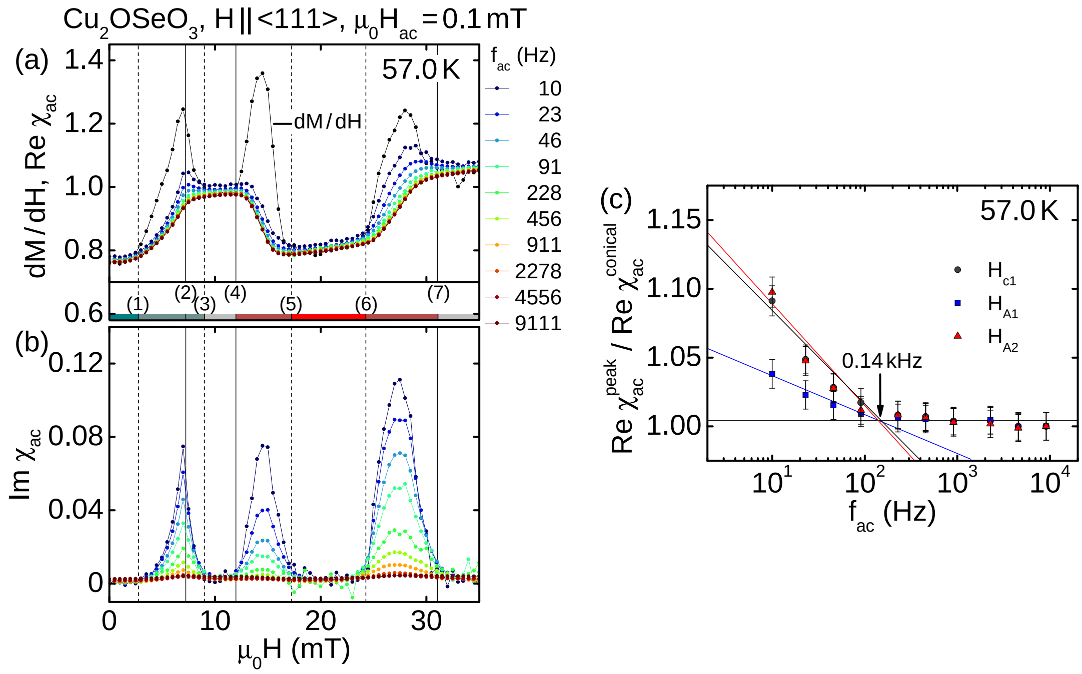

Figure 3.33: Comparison of the susceptibility calculated from the magnetization, $\mathrm{d}M/\mathrm{d}H$, and the ac susceptibility at a wide range of different frequencies for Cu_2OSeO_3. (a) The maxima at the helical-to-conical transition, H_{c1}, as well as at the lower and upper boundary of the Skyrmion lattice phase, H_{A1} and H_{A2}, decrease dramatically with increasing frequency and vanish altogether for large frequencies. (b) The maxima in the imaginary part of the susceptibility at the phase boundaries also decrease substantially with increasing frequency. (c) Frequency dependence of the height of the peak in the ac susceptibility at H_{c1}, H_{A1}, and H_{A2}.

crystal structure is more complex and the material is a local-moment ferrimagnetic insulator. In particular, other than in the doped compounds $Mn_{1-x}Fe_xSi$ and $Fe_{1-x}Co_xSi$, the properties of Cu_2OSeO_3 are not influenced by the field and temperature history, apart from well-understood changes of the domain population in the helical state. As a result, for the field configuration shown in Fig. 3.32, the behavior after initial zero-field cooling is essentially identical with the sweep for increasing field after field cooling (not shown). This missing hysteresis in the stoichiometric compound Cu_2OSeO_3 strongly corroborates the assumption that the history dependence in the doped materials may be attributed to doping-induced disorder.

Small but noticeable differences compared to MnSi concern the helical-to-conical transition at H_{c1}. On the one hand, like in the doped compounds, the size of H_{c1} is dependent on the temperature. On the other hand, at temperatures near T_c, $\mathrm{Re}\,\chi_{\mathrm{ac}}$ exhibits a small maximum around H_{c1} for low excitation frequencies that vanishes with increasing frequency. This frequency dependence around H_{c1} is not observed in MnSi, $Mn_{1-x}Fe_xSi$, and $Fe_{1-x}Co_xSi$ or in Cu_2OSeO_3 at low temperatures. The faster response to an external stimulus may be attributed to a softening or a smaller size of the helical domains which in turn may be caused by the increased amount of thermal fluctuations at higher temperatures. This explanation is supported by the imaginary part of the ac susceptibility, $\mathrm{Im}\,\chi_{\mathrm{ac}}$, shown in Fig. 3.32(d). Here, at temperatures just below

T_c a pronounced maximum emerges around H_{c1} which indicates the presence of considerable dissipation. With increasing excitation frequency the maximum is suppressed.

The detailed frequency dependence of the real and imaginary part of the ac susceptibility at the helical-to-conical transition and the boundaries of the Skyrmion lattice state in Cu_2OSeO_3 are addressed in Fig. 3.33. With increasing frequency the height of the peaks in $\mathrm{Re}\,\chi_{\mathrm{ac}}$ and $\mathrm{Im}\,\chi_{\mathrm{ac}}$ at the upper and the lower boundary of the Skyrmion lattice state, H_{A1} and H_{A2}, are continuously decreasing. In contrast to MnSi, however, also the helical-to-conical transition at H_{c1} shows a similar frequency dependence. On a logarithmic frequency scale, depicted in Fig. 3.28(c), all three maxima decrease linearly and vanish around a characteristic frequency $f_A \approx f_{c1} \sim 0.14\,\mathrm{kHz}$ where the susceptibility reaches the value of the susceptibility in the conical phase. The peak height is normalized to the corresponding value in the conical state. In MnSi, the characteristic frequency f_A is one order of magnitude larger, while even just below T_c the value of f_{c1} is well below $10\,\mathrm{Hz}$. The coincidence of the characteristic frequencies f_A and f_{c1} in Cu_2OSeO_3 may just be accidental as they arise from different underlying mechanisms. The slow reorientation of macroscopic helical domains at a symmetry-breaking second-order transition (for field along $\langle 111 \rangle$) is responsible for f_{c1}, whereas f_A is related to a regime of phase coexistence encompassing a first-order phase transition.

Summary

In conclusion, we have carried out detailed simultaneous measurements of the magnetization as well as of the real and imaginary part of the ac susceptibility in high-quality single-crystal MnSi. Data were recorded as a function of temperature, magnetic field, crystalline orientation, excitation frequency, excitation amplitude, as well as temperature and field history. We observe a helical, a conical, and a single pocket of Skyrmion lattice phase together with a field-polarized, a paramagnetic, and a fluctuation-disordered regime for all crystallographic directions studied. Our observations are fully consistent with earlier reports including microscopic studies, especially small-angle neutron scattering, and the small anisotropies between the different crystallographic directions may be explained by the leading-order cubic anisotropy terms.

For the first time, we have identified regimes of slow dissipative processes at the phase boundaries between the helical, the conical, and the Skyrmion lattice state, where the real part of the ac susceptibility does not track the susceptibility calculated from the magnetization, $\mathrm{d}M/\mathrm{d}H$, and is dependent on the excitation frequency and amplitude. The slow response arises from the slow reorientation of large helical domains and the nucleation process of topologically non-trivial Skyrmions within the conical phase (or vice versa), respectively. Exploratory measurements in $Mn_{1-x}Fe_xSi$, $Fe_{1-x}Co_xSi$, and Cu_2OSeO_3 suggest that the results gathered on MnSi are a universal characteristic of the cubic chiral helimagnets and question the recent claim of a very complex magnetic phase diagram in FeGe [500] as explained in Sec. 3.1.10.

3.3.2 Specific heat of the Skyrmion lattice and field-induced tricritical point

In the following we report a high-resolution specific heat study of MnSi and $Mn_{1-x}Fe_xSi$ using a quasi-adiabatic large heat pulse method, where the part on MnSi is based on a recent publication, cf. Ref. [86]. Data were recorded at finely spaced temperature and field values enabling us to resolve clear first-order specific heat anomalies bordering a single pocket of Skyrmion lattice state. These signatures establish the Skyrmion lattice unambiguously as a thermodynamic phase. As expected for a state that is stabilized by thermal fluctuations, it exhibits a larger entropy than the surrounding conical state. Moreover, we establish the existence of a field-induced tricritical point located at the high-field end of the fluctuation-disordered regime. This tricritical point is a consequence of the helimagnetic Brazovskii-type transition at zero field and arises as the magnetic field quenches the interactions between the critical fluctuations, thereby changing the transition from first to second order. In $Mn_{1-x}Fe_xSi$ up to $x = 0.10$ qualitatively unchanged behavior is observed indicating the general applicability of our findings for the class of cubic chiral helimagnets. For $x = 0.12$, however, no specific heat anomalies associated with first-order transitions are detected. The related question if samples with $x \geq 0.12$ develop long-range order at all is currently pursued by Jonas Kindervater as part of his Ph.D. thesis by means of neutron resonance spin-echo spectroscopy.

During the publication of our results, we became aware of another specific heat study of MnSi [509] also detecting the Skyrmion lattice phase and a change of the transition from first to second order. This work, however, lacks the experimental resolution and the in-depth interpretation of our study. Moreover, some years ago Lamago *et al.* reported a signature of the A-phase in the specific heat, but based on only a few data points [312]. We note that, despite the lack of resolution, data shown in both reports are consistent with our results as presented below.

Experimental details and outline of the results

The data discussed in the first part of this subsection were collected on a MnSi sample that had the shape of a parallelepiped of roughly $4 \times 1.5 \times 1\,\mathrm{mm}^3$ where the field was applied along the short side, i.e., parallel to a crystalline $\langle 110 \rangle$ axis. The specific heat measurements were carried out in a 14 T Quantum Design physical properties measurement system. The heat pulses had a size of 30 % of the sample temperature. The data shown here were inferred from the cooling curves by applying a moving average over 3 % of the data points in a relaxation curve and excluding the first 1 % of every pulse from the analysis. To complete the magnetic phase diagram, ac susceptibility was measured on the same sample for the same orientation at an excitation frequency of 911 Hz and an excitation amplitude of 1 mT. These data were in excellent agreement with the data reported in the previous subsection. A small systematic offset between the sample thermometers was accounted for by shifting the temperature scale of the susceptibility by -0.1 K. The influence of the sample orientation on the specific heat was checked on two cubes of 2 mm edge length. In the first cube two surfaces were perpendicular to $\langle 100 \rangle$ and four surfaces were perpendicular to $\langle 110 \rangle$. The second cube had two surfaces aligned perpendicular to $\langle 110 \rangle$, $\langle 111 \rangle$, and $\langle 211 \rangle$, respectively. The RRR of samples from the same ingot as the three MnSi samples was 70. The samples of $Mn_{1-x}Fe_xSi$ ($x = 0.02$, 0.04, 0.06, 0.08, 0.10 and 0.12) were quarters of a disc with a radius of 3 mm and a thickness of 1 mm. The field was applied along the latter and along a $\langle 110 \rangle$ axis.

The presentation of our results is organized as follows. After the presentation of the specific heat data of MnSi for field along $\langle 110 \rangle$, we derive the associated magnetic phase diagram and discuss the entropy released at the phase transitions. Subsequently, the influence of the crystallographic orientation on the detailed shape of the phase boundaries is accounted for. Finally, the specific heat study of $Mn_{1-x}Fe_xSi$ is presented, before we summarize our findings.

Specific heat of MnSi

Shown in Fig. 3.34(a) are typical specific heat data of MnSi in the vicinity of the helimagnetic phase transition as a function of temperature for a wide range of magnetic fields. Our data

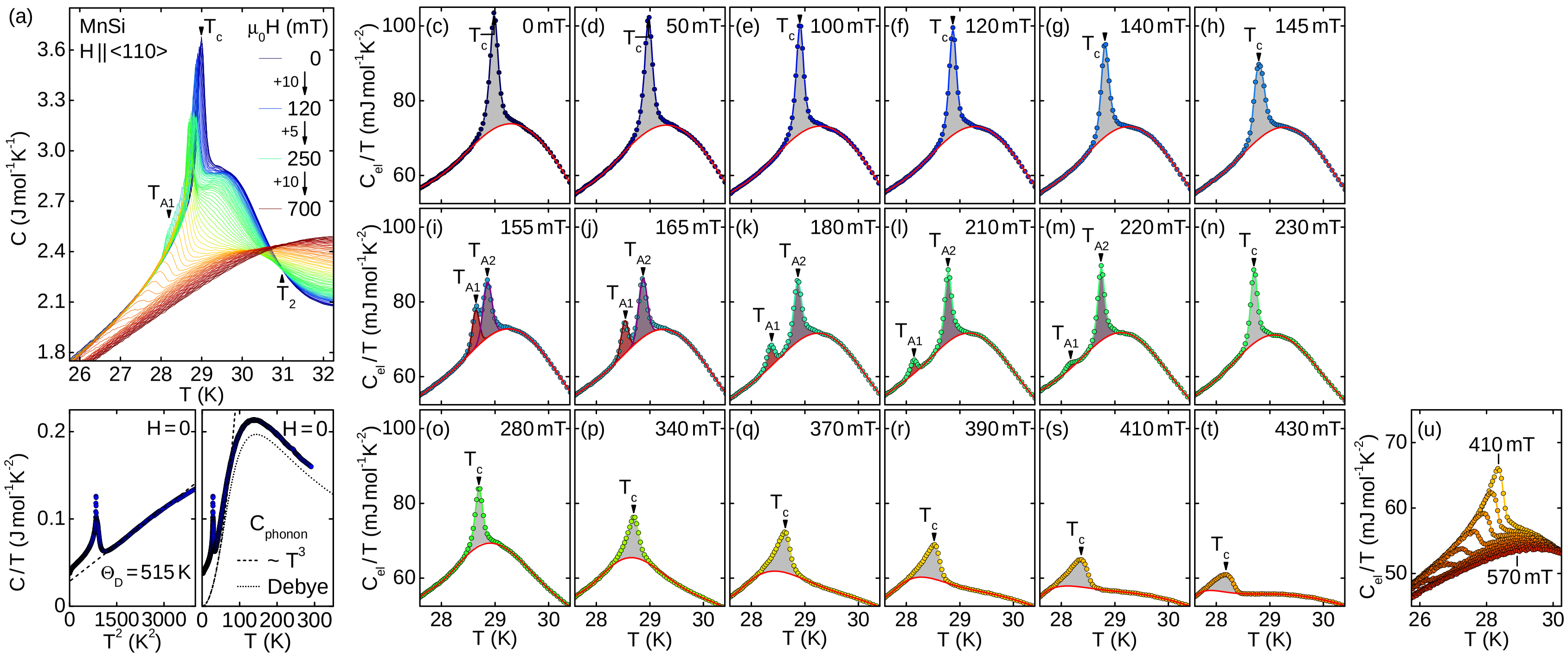

Figure 3.34: Specific heat of MnSi as a function of temperature for magnetic fields up to 0.7 T along the $\langle 110 \rangle$ axis. At $H = 0$ the narrow peak at the helimagnetic transition, marked T_c, resides on top of a broad shoulder. In small fields the shoulder is characterized by a Vollhardt invariance at T_2. In the field range of the Skyrmion lattice, the peak at T_c splits into two peaks where we mark the lower temperature peak as T_{A1}. (a) Data as measured. (b) C/T versus T^2 to illustrate the lattice subtraction. (c)–(u) Specific heat over temperature after subtraction of lattice contributions. Solid lines represent polynomial estimates of the background at temperatures far away from the anomalies of the transition.

are in excellent agreement with previous reports for the field values available [85]. In zero magnetic field, a sharp peak at the onset of helimagnetic order, marked as T_c, resides on top of a broad shoulder. For small fields H, this shoulder is characterized by a Vollhardt invariance at a temperature T_2, i.e., $\partial C/\partial H|_{H=0} = 0$ [85, 257, 278, 279]. With increasing field, a second peak emerges in the range of the Skyrmion lattice, marked as T_{A1}. For even larger fields the peak at T_c shifts to lower temperatures and changes its character from first to second order. In our high-resolution specific heat study, the thermodynamic signatures of the Skyrmion lattice were clearly resolved for the first time establishing it unambiguously as a thermodynamic phase. There is no evidence suggesting the formation of mesophases or other complexities.

The phonon contribution to the specific heat may be inferred from the cubic temperature dependence of $C(T)$ in the range $T_2 < T < 50\,\mathrm{K}$, see solid and dashed line in Fig. 3.34(b). The corresponding Debye temperature $\Theta_{\mathrm{D}} = 515\,\mathrm{K}$ is in excellent agreement with previous work [85] and, in combination with a numerically integrated Debye ansatz, describes the behavior of MnSi remarkably well (dotted line). Recently, Stishov and coworkers derived a Debye temperature $\Theta_{\mathrm{D}} = 660\,\mathrm{K}$ from powder neutron diffraction of the phonon density of states and density functional calculations [510] as well as from measurements of the elastic constants [511]. This large value of Θ_{D}, however, disagrees with previous results from the same group [409, 512] and is strongly questioned as it leads to a phonon contribution to the specific heat that differs distinctly from the experimentally observed low-temperature form of the specific heat. In the following, we subtract a lattice contribution with $\Theta_{\mathrm{D}} = 515\,\mathrm{K}$ to determine the detailed field dependence of the electronic contribution to the specific heat divided by temperature, C_{el}/T, close to the helimagnetic transition. The resulting data are illustrated in the remaining panels of Fig. 3.34.

In small applied fields the shape of the peak at T_c is well approximated as a symmetric Gaussian with typical values of the full width at half maximum of $\Delta T_c \sim (0.15 \pm 0.02)\,\mathrm{K}$. This is characteristic of the latent heat of a slightly broadened first-order transition where we attribute the broadening to imperfections of the sample. The peak resides as an additional feature on a broad shoulder, cf. Fig. 3.34(c) through 3.34(h). Up to 140 mT the peak at T_c is essentially unchanged, while its position slightly moves to lower temperatures. Around 145 mT a second peak appears at a temperature T_{A1}. This peak clearly shifts to lower temperatures with increasing field and decreases in size until it vanishes above ~230 mT, cf. Figs. 3.34(i) through 3.34(n). In the field range for which two peaks are observed, we denote the maximum of the peak at the higher temperature as T_{A2}. The shape and size of the peak at T_{A2} as well as the values of T_{A2} are essentially unchanged in this field range. The broadening around 145 mT is due to the initial overlap of the two peaks which are well described at all fields by Gaussians of widths similar to ΔT_c. Finally, for field values exceeding the regime of the Skyrmion lattice, the shape of the specific heat anomaly changes drastically, see Figs. 3.34(o) through 3.34(u). Here the maximum is again denoted as T_c. For a field around 400 mT the anomaly is clearly asymmetric, characteristic of a mean-field lambda anomaly. At the same time, the broad shoulder on which the peak resides moves to lower temperatures. For even larger fields, the lambda anomaly displays some rounding as shown in Fig. 3.34(u) which may be attributed to the field dependence of T_c; i.e., temperature scans cut the phase boundary under a shallow angle.

Shown in Fig. 3.35 is the phase diagram as inferred from our specific heat and susceptibility data, which is fully consistent with earlier reports, cf. Sec. 3.3.1. However, the distinct specific heat anomalies allow us to (i) determine the borders between the fluctuation-disordered regime and the helimagnetic states with unrivaled resolution, (ii) identify a field-induced tricritical point, and (iii) establish unambiguously the first-order boundary of the Skyrmion lattice state.

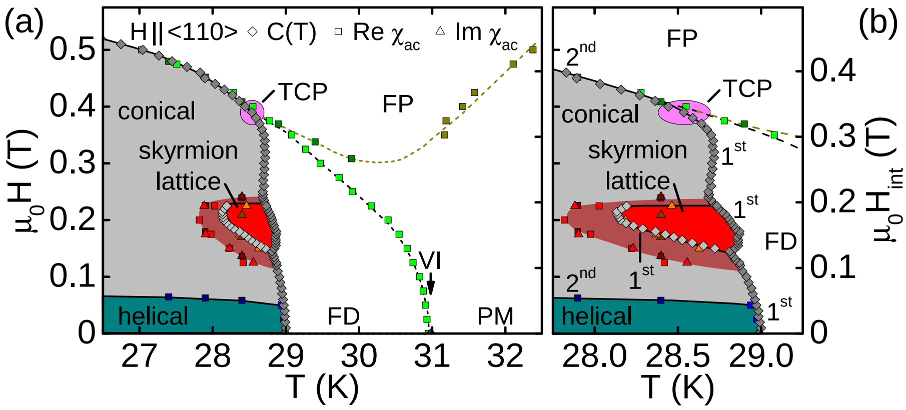

Figure 3.35: Magnetic phase diagram of MnSi for field along $\langle 110 \rangle$ as derived from the specific heat (diamonds), as well as the real part (squares) and imaginary part (triangles) of the ac susceptibility; cf. also Sec. 3.3.1. We distinguish the following regimes: helical order, conical order, Skyrmion lattice, fluctuation-disordered (FD), paramagnetic (PM), and field-polarized (FP). Phase transitions and crossover lines are marked as solid and dashed lines, respectively. In the shaded coexistence regime between the conical and Skyrmion lattice phase, a finite Im χ_{ac} is observed, characteristic of hysteresis associated with a first-order transition. The ordinate on the right-hand side reflects an estimate of the internal field. Panel (b) shows an enlarged section of panel (a) where we state the order of the phase transitions.

For small magnetic fields, the specific heat displays a crossover with decreasing temperature from an uncorrelated paramagnetic (PM) to a fluctuation-disordered (FD) regime. The latter is characterized by strongly interacting chiral fluctuations that eventually induce a first-order Brazovskii-type transition to the magnetically ordered state [257]. This interaction suppresses the correlation length and thus induces a point of inflection in the susceptibility, $\partial^2\chi/\partial T^2 = 0$. Its position defines the crossover line between the paramagnetic and fluctuation-disordered regimes which meets the Vollhardt invariance (VI) for $H \to 0$. At high magnetic fields, where the interaction between the chiral paramagnons is quenched, the transition to the conical phase is of second order. Consequently, there must exist a fluctuation-induced tricritical point (TCP) at intermediate fields where the transition changes from first to second order. From general scaling arguments, one expects the crossover between the paramagnetic and fluctuation-disordered regime to merge with the phase boundary at this singular tricritical point. Moreover, the crossover line between the paramagnetic and the field-polarized (FP) regime observed in the susceptibility also emanates from the tricritical point. Taken together, this allows us to estimate $T_{\mathrm{TCP}} \approx 28.5\,\mathrm{K}$ and $\mu_0 H_{\mathrm{TCP}} \approx 390\,\mathrm{mT}$ corresponding to an internal field $\mu_0 H^{\mathrm{int}}_{\mathrm{TCP}} \approx 340\,\mathrm{mT}$. Around the tricritical point, the shape of the specific heat anomaly changes from being a symmetric Gaussian to a mean-field-like asymmetric lambda anomaly. A detailed analysis of the corresponding entropy to be presented below confirms the position of the tricritical point.

By decreasing the temperature further within the fluctuation-disordered regime, a first-order transition either to the helimagnetic, the conical, or the Skyrmion lattice phase is observed depending on the applied field. In the field range of the Skyrmion lattice, two first-order anomalies at T_{A1} and T_{A2} with $T_{A1} < T_{A2}$ are found as a function of temperature. This establishes the Skyrmion lattice unambiguously as a thermodynamic phase. As explained in the previous

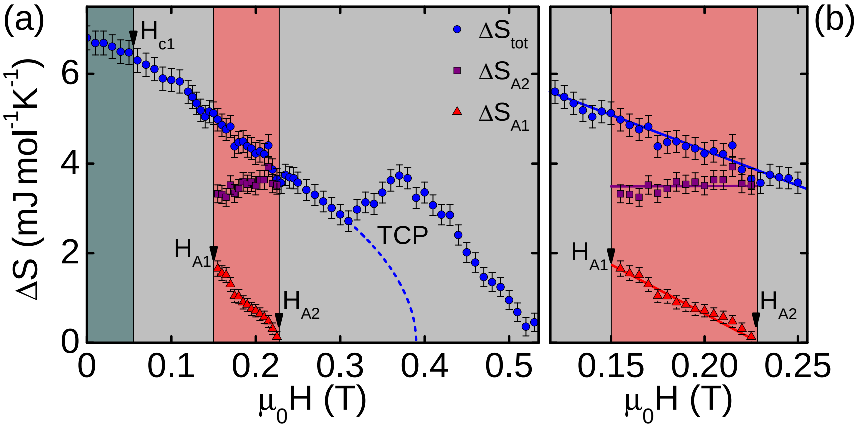

Figure 3.36: Entropy ΔS_{tot} inferred from the specific heat anomalies at T_c, T_{A1}, and T_{A2}. Error bars reflect conservative estimates of the uncertainties of the background subtraction. (a) For small fields, ΔS_{tot} essentially corresponds to the latent heat and decreases linearly. Near the tricritical point, critical fluctuations contribute to ΔS_{tot} resulting in a local maximum. The dashed line indicates an estimate of the latent heat that vanishes at $\mu_0 H_{\mathrm{TCP}} \approx 390\,\mathrm{mT}$. (b) Expanded view of the regime of the Skyrmion lattice state.

subsection, cf. Sec. 3.3.1, the dissipative part of the ac susceptibility, $\mathrm{Im}\,\chi_{\mathrm{ac}}$, is quite different at these two transitions. Whereas at the fluctuation-induced first-order transition at T_{A2} no significant contribution to $\mathrm{Im}\,\chi_{\mathrm{ac}}$ is observed, a comparatively broad coexistence regime with a substantial $\mathrm{Im}\,\chi_{\mathrm{ac}}$ encompasses the T_{A1} line, displayed as shaded region between the conical and Skyrmion lattice phase in Fig. 3.35(b). The finite dissipation derives from the nucleation process of topologically nontrivial Skyrmions within the conical phase [80], which eventually triggers the first-order transition at T_{A1}.

Furthermore, considering the relationship of Clausius-Clapeyron, $\mathrm{d}T/\mathrm{d}\mu_0 H = -\Delta M/\Delta S$, the negative slope of $T_{A1}(H)$ at the lower boundary of the Skyrmion lattice phase implies an increase of entropy as $\Delta M > 0$. In contrast, there is no difference of entropy when exiting the Skyrmion lattice phase at larger fields, as the slope is practically infinite. Therefore, the Skyrmion lattice phase possesses a larger entropy than the conical phase. This conjecture is supported by the detailed phase boundary between the ordered phases and the fluctuation-disordered regime shown in Fig. 3.35(b), where T_{A2} is shifted towards higher temperatures as expected of a thermodynamical state with a larger entropy than the competing conical phase.

After subtracting a background to C_{el}/T determined by a polynomial fit, shown as red lines in Fig. 3.35, the shaded areas were integrated to determine the entropy released at the phase transitions, ΔS. The resulting field dependence of ΔS is summarized in Fig. 3.36(a), while Fig. 3.36(b) shows the field range of the Skyrmion lattice in further detail. The error bars are estimated by a systematic variation of the background contribution, cf. Figs. 3.37 and 3.38. The conclusions discussed in the following are not sensitive to the precise choice of the background. For fields exceeding ~300 mT the anomaly becomes broader and the absolute size of ΔS depends more sensitively on the choice of the background, but the general evolution of ΔS remains unaffected. We denote the entropy released near T_c by ΔS_{tot}. In the field range of the Skyrmion lattice, the entropies of the anomalies at T_{A1} and T_{A2} are referred to as ΔS_{A1} and ΔS_{A2},

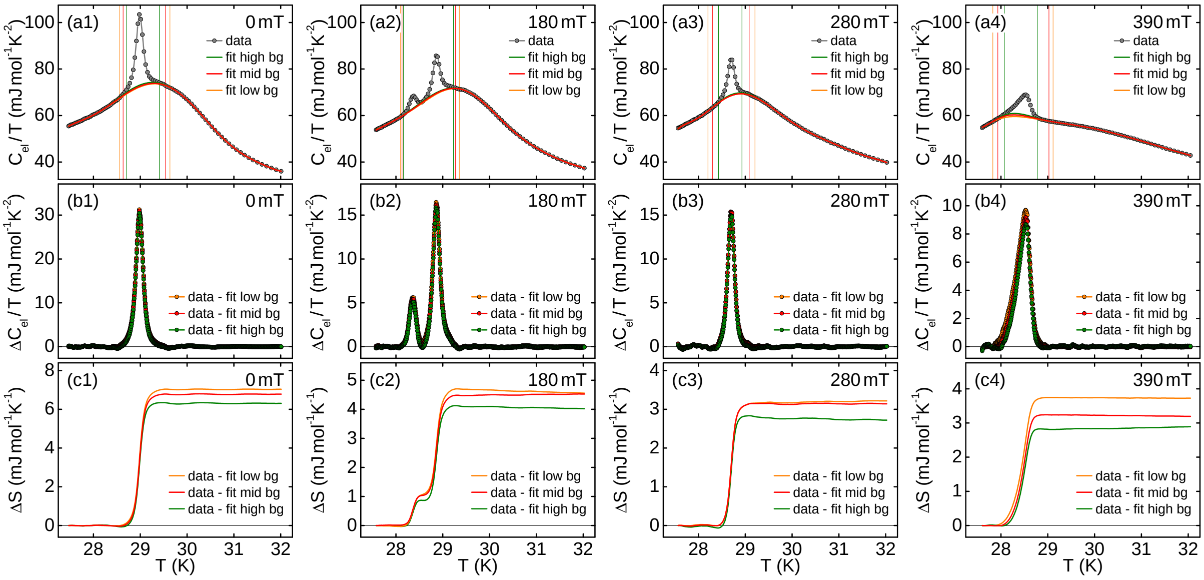

Figure 3.37: Typical specific heat data and step-by-step analysis to determine the change of entropy at the anomalies. Columns correspond to the same field value. The top row shows the data as measured after subtracting a phonon contribution. The green, red, and orange vertical lines indicate the temperature interval for which data were excluded when determining the high, middle, and low background contribution (solid lines). The center row shows the specific heat data after subtracting the different choices of background. The bottom row displays the entropy as inferred from the specific heat anomaly by numerical integration. Data points in Fig. 3.36 were determined from the non-zero plateau values, whereas the variation of these values with the choice of background defines the error bars.

respectively, where ΔS_{tot} is determined as the sum of ΔS_{A1} and ΔS_{A2}. Note that ΔS_{tot} is basically the latent heat for the transitions at small fields, whereas ΔS_{tot} corresponds to the entropy released near the second-order transition for $H \gtrsim H_{\mathrm{TCP}}$.

The latent heat determined this way is in quantitative agreement with Clausius-Clapeyron. On the one hand, from the magnetic phase diagram we extract for the lower boundary of the Skyrmion lattice phase $\mathrm{d}T/\mathrm{d}(\mu_0 H) = -(12 \pm 1)\,\mathrm{K/T}$, corresponding to $\mathrm{d}T/\mathrm{d}(\mu_0 H_{\mathrm{int}}) = -(14 \pm 1)\,\mathrm{K/T}$ after correcting for demagnetizing fields. On the other hand, we observe around the low-field and high-temperature boundary of the Skyrmion lattice phase a change of entropy $\Delta S_{A1} = (1.5 \pm 0.2)\,\mathrm{mJ/mol\,K}$. From magnetization data we estimate for the change at the first-order transition $\Delta M = (3.4 \pm 1) \cdot 10^{-3}\,\mu_{\mathrm{B}}/\mathrm{f.u.} = (1.3 \pm 0.4)\,\mathrm{kA/m}$ implying $-\Delta M/\Delta S_{A1} = -(13 \pm 4)\,\mathrm{K/T}$. In comparison, at the upper field boundary ΔM is similar to the value at the lower boundary while $\Delta S_{A1} \to 0$, consistent with the absence of a noticeable slope.

Finally, also the field dependence of the entropy released at the phase transitions shown in Fig. 3.36 yields several important pieces of information. For small fields, ΔS_{tot} can be identified with the latent heat of the first-order transitions and it decreases monotonically from its zero-field value, 6.8 mJ/mol K, across all phases up to ~300 mT. Second, the unchanged monotonic decrease across the Skyrmion lattice phase implies that its entropy is larger than that of the conical phase as conjectured above. The field dependence originates from the transition between

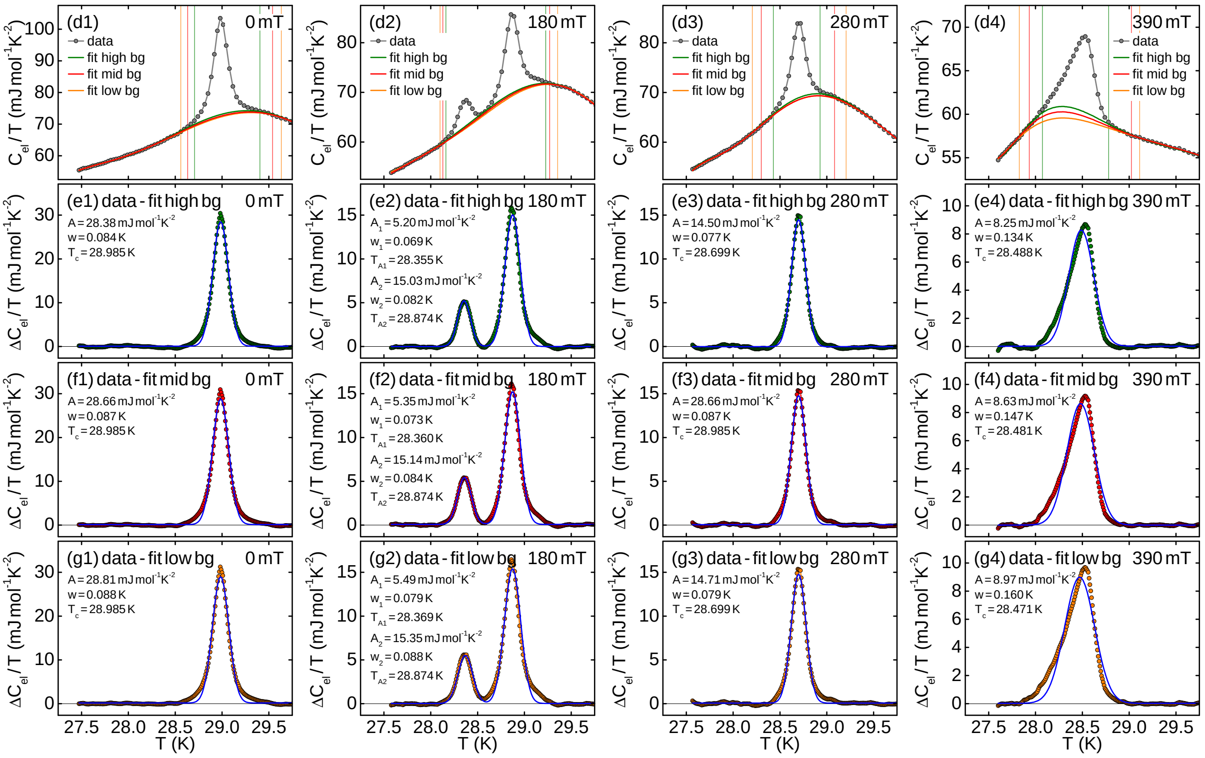

Figure 3.38: Typical specific heat data and Gaussian fits of the anomalies. Columns correspond to the same field value. The first row is a close-up view of the data depicted in the first row of Fig. 3.37. The second, third, and fourth row show the specific heat anomalies after subtracting the high, middle, and low background, respectively. The thin blue lines represent (double) Gaussian fits to guide the eye, $\Delta C/T|_{\mathrm{Gauss}} = y_0 + A\exp\left[-(T-T_c)^2/2w^2\right]$. The parameters of the fits, A, w, and T_c, are shown in each panel. The offset y_0 is below $0.1\,\mathrm{mJ/mol\,K^2}$ and thus negligible. Independent of the background subtracted, the shape of the anomaly changes with increasing field from a symmetric essentially Gaussian shape to an asymmetric shape, which clearly cannot be fitted by a Gaussian.

the Skyrmion lattice and the conical state at T_{A1}, while ΔS_{A2} stays essentially unchanged. As ΔS_{A1} vanishes with increasing field, the Skyrmion lattice phase becomes thermodynamically unfavorable above H_{A2}. Third, near the tricritical point, critical fluctuations start to contribute to ΔS_{tot} resulting first in an increase as a function of H. In a mean-field approximation, the precise function for the latent heat depends on microscopic parameters but is bounded by two power laws $\Delta S_{\mathrm{latent\ heat}} \propto (H_{\mathrm{TCP}} - H)^x$ as $H \rightarrow H_{\mathrm{TCP}}$ with $x = 1$ and $x = 0.5$, respectively. The latter is shown as a dashed line in Fig. 3.36(a) and yields a value for H_{TCP} that is consistent with the value estimated from the evolution of the crossover lines.

Specific heat of MnSi: Influence of the orientation

The influence of the sample orientation on the specific heat was checked on two cubes. Hence, the magnetic field was applied along the crystallographic ⟨100⟩, ⟨110⟩, ⟨111⟩, and ⟨211⟩ directions

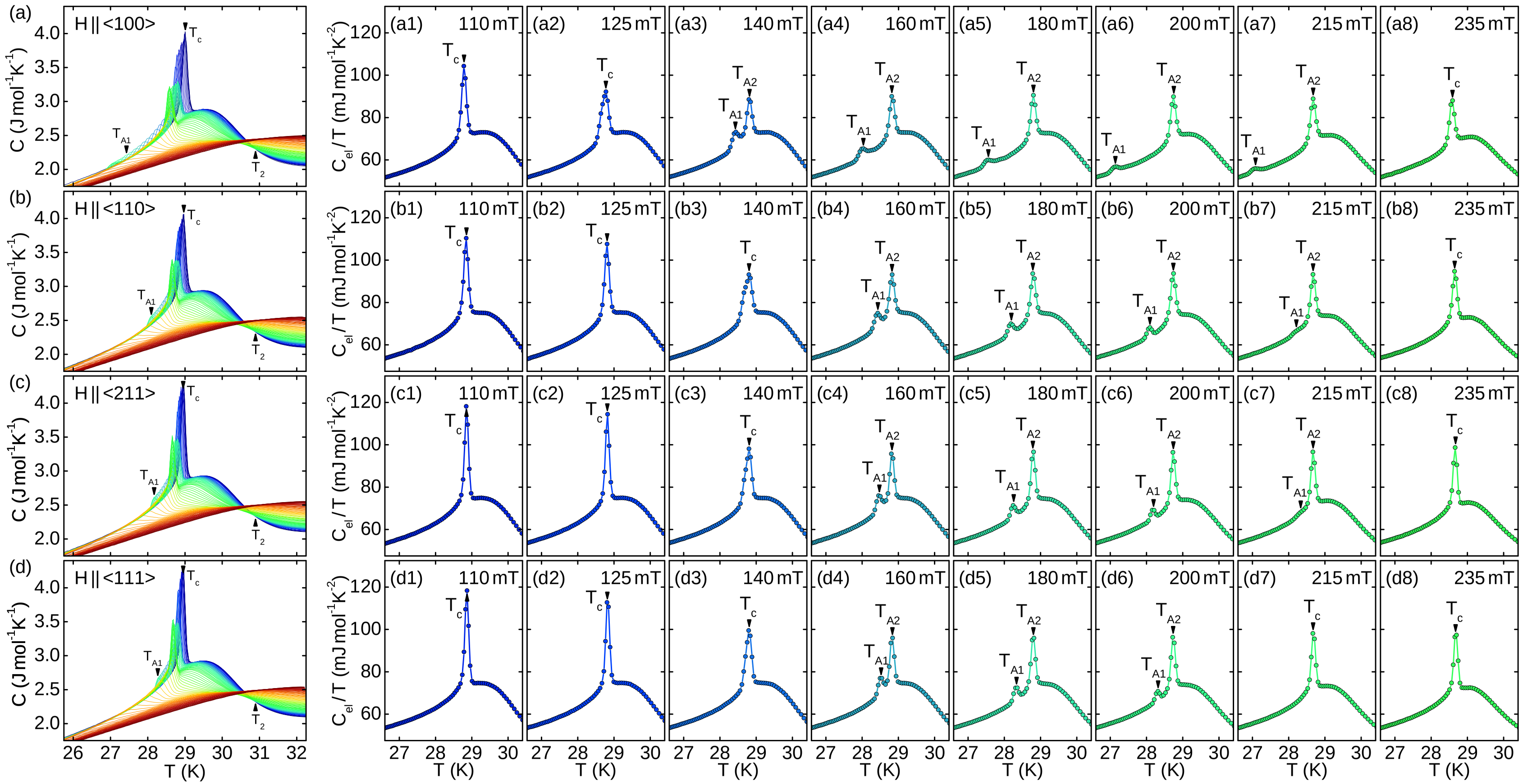

Figure 3.39: Influence of the crystalline orientation on the specific heat of MnSi. (a)–(d) Specific heat as a function of temperature for magnetic fields up to 0.7 T along the major crystallographic axes. In general, the specific heat is rather isotropic. (a1)–(d8) Specific heat over temperature after subtraction of lattice contributions for fields along the major crystallographic axes and field values around the Skyrmion lattice state. The temperature and field extent of the Skyrmion lattice phase varies being largest for field along ⟨100⟩ and smallest for field along ⟨111⟩.

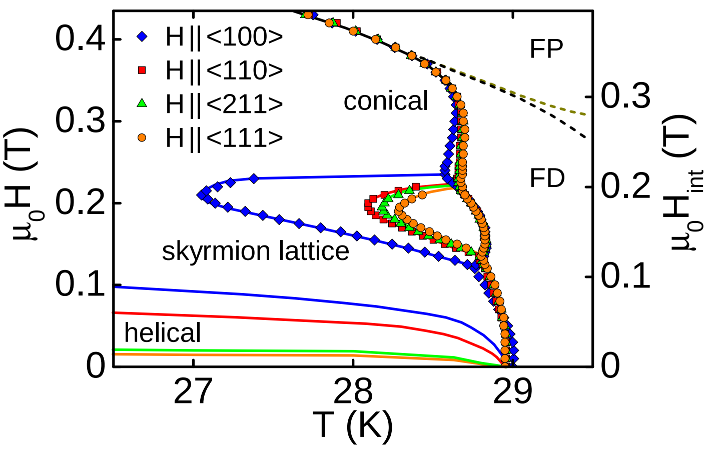

Figure 3.40: Magnetic phase diagram of MnSi for field along ⟨100⟩, ⟨110⟩, ⟨111⟩, and ⟨211⟩ as derived from the specific heat. Data were collected on two cubic samples resulting in the same demagnetization effects for all directions studied. The boundary between the helical and the conical state was determined from a comprehensive magnetization study on a spherical sample [281].

while keeping the demagnetization effects unchanged. In general, the specific heat data of MnSi shown in Fig. 3.39(a) through 3.39(d) are rather isotropic and very similar to the data presented in Fig. 3.35. This behavior may be expected since the cubic anisotropies, which break the rotational symmetry of the interactions in the cubic chiral helimagnets, represent the weakest energy scale. The lattice contribution to the specific heat is well described by a Debye model with $\Theta_D = 515\,K$ for all orientations studied. The only prominent difference between the field configurations concerns the temperature and field extent of the Skyrmion lattice phase as depicted in detail in the remaining panels of Fig. 3.39. This observation is consistent with earlier reports and the susceptibility data in Sec. 3.3.1. Furthermore, also the transition between the helical and the conical state is dependent on the direction of the applied field, as addressed in a comprehensive magnetization study on a spherical sample [281]. However, the helical and the conical state may not be discriminated from specific heat data.

Taken together, the orientation dependence of the specific heat essentially may be captured within the magnetic phase diagram in Fig. 3.40. While the phase diagram of MnSi in general is rather isotropic, the extent of the helical and the Skyrmion lattice state is largest for field along ⟨100⟩ and smallest for ⟨111⟩, as consistent with the leading-order cubic anisotropy terms. Note that for the field extent of the Skyrmion lattice phase for field along ⟨111⟩, the high-temperature boundary of the Skyrmion lattice, T_{A2}, is congruent for all field directions studied. Compared to the other directions, for field along ⟨100⟩ the field extent of the Skyrmion lattice state is distinctively larger and the non-linearity of the boundary between the fluctuation-disordered regime and the helimagnetic states is more pronounced. Though this behavior is consistent with the cubic anisotropies, the discrepancy of the transition temperature in zero field is unexpected and not yet explained. An influence of the sample quality, however, can be excluded, since the measurements for field along the ⟨100⟩ and along the ⟨110⟩ direction were performed on the same sample. Moreover, the same sample platform with the same set of thermometers was used for all measurements.

Specific heat of $Mn_{1-x}Fe_xSi$

Substitutional doping of MnSi with iron or cobalt suppresses the helimagnetic transition temperature, while the magnetic phase diagram stays strongly reminiscent of pure MnSi up to doping levels of several percent, cf. Sec. 3.1.7. As depicted in Fig. 3.41, the specific heat of $Mn_{1-x}Fe_xSi$ up to $x = 0.10$ in zero field strongly resembles that of MnSi showing a slightly broadened peak, marked as T_c, on top of a broad shoulder. The latter is characterized in small fields by a Vollhardt invariance at T_2. For $x = 0.12$ the peak, i.e., the characteristic of the fluctuation-induced first-order Brazovskii-type transition, has vanished suggesting that the underlying mechanisms has significantly altered. This assumption is corroborated by small-angle neutron scattering experiments. For $x = 0.10$ and temperatures below T_c broadened maxima of intensity are ob-

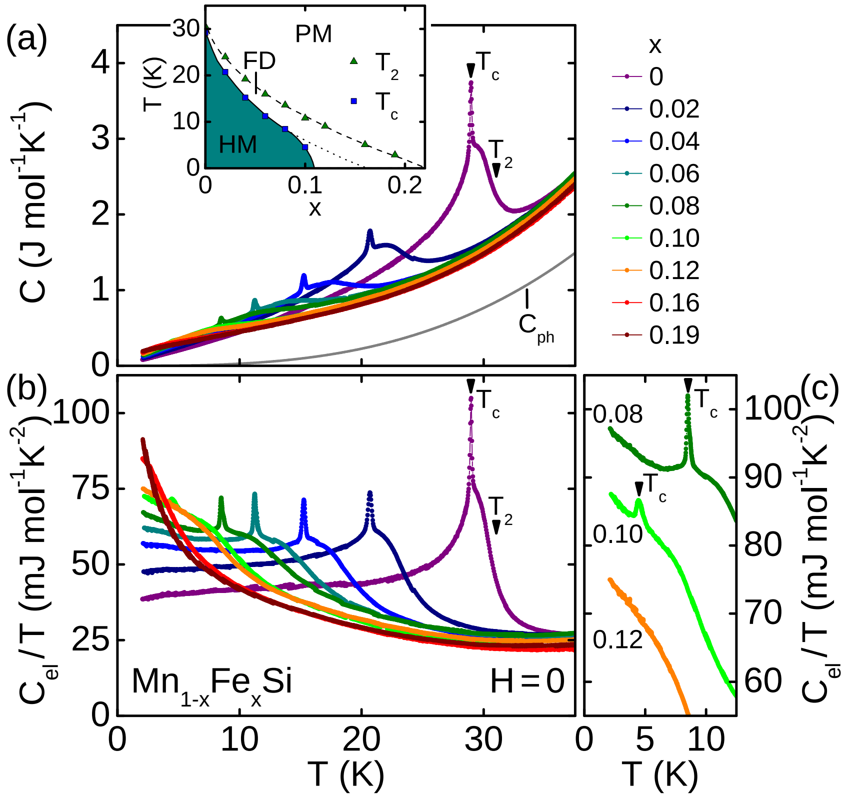

Figure 3.41: Specific heat of MnSi and $Mn_{1-x}Fe_xSi$ as a function of temperature in zero field. (a) With increasing iron content the helimagnetic order is suppressed. The phononic contribution, C_{ph}, stays unchanged for all concentrations studied (solid gray line). The inset shows the compositional phase diagram of $Mn_{1-x}Fe_xSi$ where we observe a helimagnetic phase (HM) and a paramagnetic phase (PM) separated by a fluctuation-disordered regime (FD). (b) Electronic contribution to the specific heat divided by temperature. The height of the peak at T_c stays essentially constant for $0.02 \leq x \leq 0.08$ after decreasing in size upon initially doping with iron. (c) Electronic contribution to the specific heat divided by temperature for intermediate values of x. For $x = 0.10$ the peak significantly decreases in height, for $x = 0.12$ it has disappeared. For clarity data have been offset by $15\,\mathrm{mJ/mol\,K^2}$.

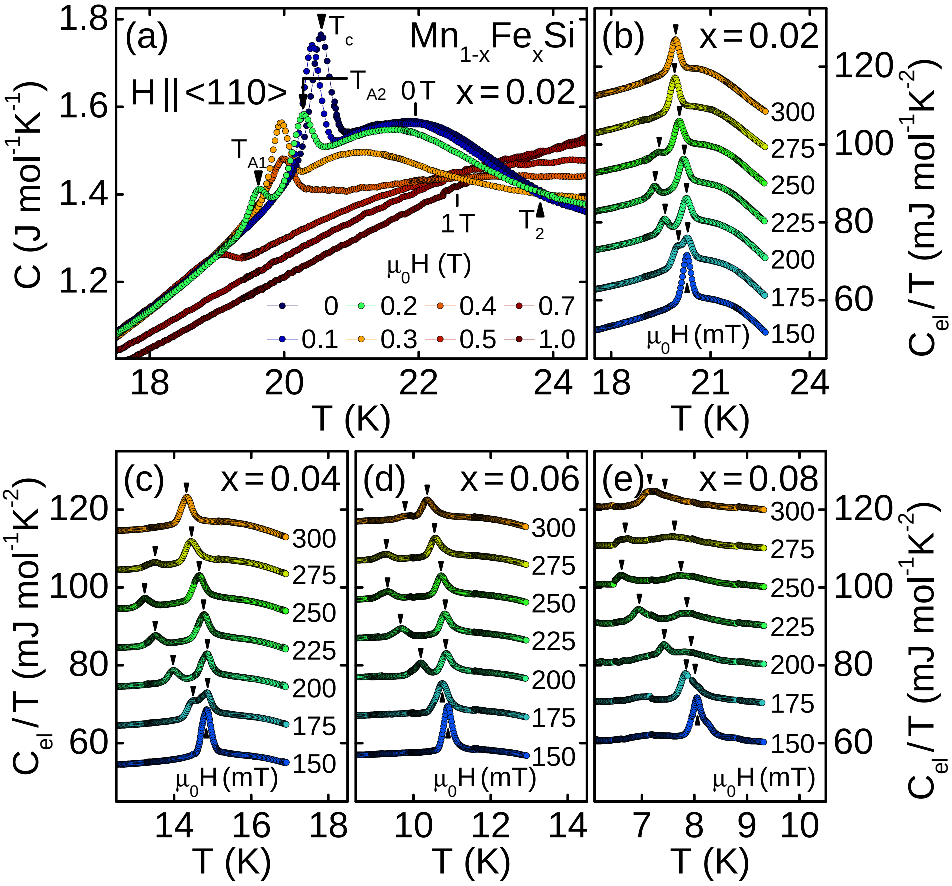

Figure 3.42: Specific heat of $Mn_{1-x}Fe_xSi$ as a function of temperature in magnetic fields. (a) Specific heat for $x = 0.02$ in magnetic fields up to 1 T. The behavior strongly resembles that of MnSi. (b)–(e) Specific heat over temperature after subtraction of lattice contributions in magnetic fields around the Skyrmion lattice phase for $x = 0.02$, 0.04, 0.06, and 0.08, respectively. Two distinct peaks are observed. For clarity data have been offset by 10 mJ/mol K^2.

served in zero field at finite q along the $\langle 111\rangle$ directions characteristic for the helical state. In $Mn_{1-x}Fe_xSi$ with $x = 0.12$ a sphere of weak intensity at finite q appears for $T < T_c$. A preliminary summary of these neutron scattering experiments is reported in Ref. [237], while a more detailed account will be given elsewhere.

In agreement with MnSi, the phonon contribution to the specific heat, C_{ph}, in $Mn_{1-x}Fe_xSi$ can be approximated by a Debye model with $\Theta_D = 515$ K, up to the highest iron contents studied [85]. The electronic part of the specific heat, i.e., after subtraction of the phonon contribution, divided by temperature, C_{el}/T, is shown in Figs. 3.41(b) and 3.41(c). At high temperatures a constant value is observed as expected from Fermi liquid theory. The low-temperature value, γ_0, starts to diverge as the quantum critical concentration is approached. Up to $x = 0.08$, the height of the peak at T_c stays constant after an initial decrease from pure MnSi to $Mn_{1-x}Fe_xSi$ with $x = 0.02$. A detailed consideration of the contributions to the specific heat of MnSi, $Mn_{1-x}Fe_xSi$, and $Mn_{1-x}Co_xSi$ is given in Ref. [85].

When magnetic field is applied to $\mathrm{Mn}_{1-x}\mathrm{Fe}_x\mathrm{Si}$ the specific heat is again highly reminiscent of pure MnSi up to $x = 0.10$ as illustrated in Fig. 3.42(a) for $\mathrm{Mn}_{1-x}\mathrm{Fe}_x\mathrm{Si}$ with $x = 0.02$. In small field a crossing point is observed at T_2, the characteristic of a Vollhardt invariance. With increasing field, the peak at T_c shifts to lower temperatures and at some 0.4 T changes from a slightly broadened essentially Gaussian shape to a clearly asymmetric signature, characteristic of a mean-field lambda anomaly. Thus, as in MnSi, the transition into the helimagnetic state changes its nature from fluctuation-induced first order to mean-field second order at a tricritical point. Above $H = 0.7\,\mathrm{T} > H_{c2}$ there is no anomaly. For field values within the Skyrmion lattice state, i.e., for $\mu_0 H \sim 0.2\,\mathrm{T}$, two distinct peaks are observed where the low-temperature and the high-temperature peak are referred to as T_{A1} and T_{A2}, respectively. The temperature and field evolution of these peaks is comparable to pure MnSi and tracks the phase boundaries of the Skyrmion lattice state, cf. Figs. 3.42(b). For higher iron concentrations, see Figs. 3.42(c) through 3.42(e), the transitions are shifted to lower temperatures while the general behavior stays the same.

Summary

In conclusion, we have used a quasi-adiabatic large heat pulse method to carry out a high-resolution specific heat study in MnSi and $\mathrm{Mn}_{1-x}\mathrm{Fe}_x\mathrm{Si}$. Consistent with earlier reports, in zero field we observe a narrow peak at the onset of helimagnetic order that resides on top of a broad shoulder as one of the key characteristics of the Brazovskii scenario, i.e., a fluctuation-induced first-order transition. Additionally, our data at finely spaced temperatures and magnetic fields allow us to establish two main results.

First, we identify clear specific heat anomalies surrounding a single pocket of Skyrmion lattice phase in MnSi for all major crystallographic directions as well as in $\mathrm{Mn}_{1-x}\mathrm{Fe}_x\mathrm{Si}$ for $x < 0.12$. Combined with an analysis of the entropy released at these anomalies and the detailed shape of the phase boundaries in the magnetic phase diagram, we find clear evidence that the Skyrmion lattice represents a single thermodynamic phase stabilized by thermal fluctuations and bordered by first-order transitions.

Second, the existence of a field-induced tricritical point in MnSi and in $\mathrm{Mn}_{1-x}\mathrm{Fe}_x\mathrm{Si}$ for $x < 0.12$ is deduced from the evolution of the specific heat anomaly at the helimagnetic phase transition. With increasing field the anomaly transforms from a slightly broadened essentially Gaussian shape, characteristic of a first-order transition, to a clearly asymmetric signature, characteristic of a second-order mean-field lambda anomaly. In MnSi the position of the tricritical point is confirmed by the field dependence of the entropy released at the helimagnetic phase transition and the course of the crossover lines in the magnetic phase diagram. This finding is in strong support of the helimagnetic Brazovskii scenario, where the transition has to change from fluctuation-induced first order to second order at a tricritical point as the interactions between the critical fluctuations are quenched by the magnetic field. For $\mathrm{Mn}_{1-x}\mathrm{Fe}_x\mathrm{Si}$ with $x \geq 0.12$ we observe no anomalies that are associated with first-order transitions suggesting that the underlying mechanisms have drastically altered.

3.3.3 Hysteresis in the magnetic phase diagram of $\mathrm{Fe}_{1-x}\mathrm{Co}_x\mathrm{Si}$

In the following we report a study of the magnetization, the ac susceptibility, and the specific heat of optically float-zoned single crystals of $\mathrm{Fe}_{1-x}\mathrm{Co}_x\mathrm{Si}$ in the composition range between $x = 0.20$ and $x = 0.50$. Special emphasis was placed on the determination of the magnetic phase diagrams under the influence of various cooling histories. After zero-field cooling, the phase diagram of all concentrations and field configurations studied resembles that of the archetypal $B20$ helimagnet MnSi. Besides the helical and the conical state, we observe a single pocket of Skyrmion lattice phase just below the helimagnetic ordering temperature. In contrast to MnSi, however, the helical state only appears after zero-field cooling for all field configurations studied. If the sample is cooled in field, the reversible pocket of Skyrmion lattice phase may be extended metastably down to lowest temperatures. Taken together with the large range in which the transition temperatures, the transition fields, and the helix wavelength may be adjusted, this hysteresis allows for an optimization of the parameters of $Fe_{1-x}Co_xSi$ for future experiments.

Experimental details and outline of the results

Large single crystals of $Fe_{1-x}Co_xSi$ were grown during the diploma theses of Wolfgang Münzer ($x = 0.20, 0.25$) [61] and the author ($x = 0.10, 0.35$) [62] as well as within this thesis ($x = 0.50$). Magnetization and ac susceptibility for field along $\langle 100\rangle$ were measured on bars with $6\times 1\times 1\,\mathrm{mm}^3$ and their long axis along $\langle 100\rangle$. This way demagnetizing effects were minimized. The influence of the crystallographic orientation was investigated on cubes of $1\times 1\times 1\,\mathrm{mm}^3$ with two surfaces perpendicular to $\langle 100\rangle$ and four surfaces perpendicular to $\langle 110\rangle$. Heat capacity was measured on quarters of a cylindrical disc with a radius of 3 mm and thickness of 1 mm. The magnetic field was applied perpendicular to its large surface, i.e., parallel to $\langle 110\rangle$. All measurements were carried out in a 9 T Quantum Design physical properties measurement system. The ac susceptibility was recorded at an excitation amplitude of 1 mT and at an excitation frequency of 911 Hz. The specific heat was measured with a standard heat-pulse method, where typical heat pulses were around 1 % of the current sample temperature. All experimental data are shown as a function of applied field, while the phase diagrams inferred from the data are shown as a function of internal field, i.e., after correcting for demagnetizing effects.

The behavior of $Fe_{1-x}Co_xSi$ depends on its temperature and magnetic field history. Therefore, we carefully distinguish four different approach modes for data as a function of temperature. Data are always recorded between 2 K and a temperature well above the helimagnetic ordering temperature.

- Zero-field cool (zfc): The sample is cooled to 2 K in zero field before the desired field value is applied. Data are collected while increasing the temperature.
- Field cool down (fcd): The sample is field cooled in the desired field and data are gathered simultaneously.
- Field cool (fc): After cooling the sample in the desired field, data are recorded while increasing the temperature.
- High-field cool (hfc): The sample is cooled to 2 K in a field larger than the upper critical field, H_{c2}. Subsequently, the desired field is applied and data are measured while increasing the temperature.

For magnetic field sweeps the sample is initially heated well above the helimagnetic ordering temperature and subsequently cooled to the desired temperature in zero field. The data collected during the first increase of the field is consistent with data after zero-field cooling in temperature sweeps. The following sweeps starting at $|H| \gg H_{c2}$ correspond to the situation after high-field cooling.

The presentation of our experimental results is organized as follows. We begin with the behavior of $Fe_{1-x}Co_xSi$ at zero field and high temperatures as well as at high fields and low temperatures, i.e., in the paramagnetic and the field-polarized regime, respectively. This account provides the setting for the field and temperature dependence of the susceptibility observed at low temperatures and small fields. The role of the field and temperature history as well as the dependence on the crystalline orientation are discussed in detail for $x = 0.20$. Subsequently, the magnetic phase diagrams derived from our susceptibility data are presented, before we address the specific heat data and finally summarize our results.

Paramagnetic and field-polarized regime

In general, the behavior of $Fe_{1-x}Co_xSi$ is highly reminiscent of the other cubic chiral helimagnets. In zero field, $Fe_{1-x}Co_xSi$ is paramagnetic at high temperatures and shows helimagnetic order at low temperatures for $0.05 < x < 0.8$. The helimagnetic transition temperature as a function of the cobalt content, x, is depicted in Fig. 3.43(a). It exhibits a maximum value exceeding 50 K around $x = 0.35$. In earlier reports, the transition temperature was defined in various ways and for datasets comprising magnetization [450, 454], ac susceptibility [249, 453], electrical resistivity [248], and small-angle neutron scattering [287, 452]. Hence, we show the temperatures T_c and T_2 inferred from the ac susceptibility, T_{CW} derived from Curie-Weiss plots, and T_{Arr} extracted from Arrott plots. The detailed definitions of these temperatures are given in the following. Bearing in mind that in the literature the transition temperatures were extracted from different quantities and that the definitions are often not stated explicitly, both the earlier reports and our findings are in very good agreement.

The inset of Fig. 3.43(a) depicts the extrapolated zero-temperature values of the transition fields in $Fe_{1-x}Co_xSi$ as a function of the cobalt content x. The transition between the helical and the conical state is referred to as H_{c1}, while H_{c2} marks the transition between the conical and the field-polarized state. The values from earlier reports are usually a few ten millitesla higher than the values in this study. In these reports, however, demagnetizing effects and the influence of the crystalline orientation on H_{c2}, which is relatively large in $Fe_{1-x}Co_xSi$ compared to the other cubic chiral helimagnets, have not been taken into account. The available data on the helical wavelength, λ_{h}, is summarized in Fig. 3.43(b).

The paramagnetic behavior at high temperatures is illustrated in the inverse ac susceptibility in Fig. 3.43(c). Well above the helimagnetic transition, a Curie-Weiss like behavior is observed. The Curie-Weiss temperature, T_{CW}, is a few kelvin higher than the helimagnetic transition temperature, T_c, as extracted from the ac susceptibility or small-angle neutron scattering. In the concentration range studied, the fluctuating moment, m_{CW}, increases linearly from $1\,\mu_{\mathrm{B}}$/f.u. to $2\,\mu_{\mathrm{B}}$/f.u.. The temperature dependence of the ac susceptibility of $Fe_{1-x}Co_xSi$ in zero field is finally depicted in Fig. 3.43(d). Starting from the Curie-Weiss-like susceptibility at high temperatures the susceptibility smoothly increases with decreasing temperature. Consistent with the behavior of MnSi and the helimagnetic Brazovskii scenario, we observe a point of inflection, marked as T_2, before the susceptibility drops from its maximum value to a lower plateau. The kink is referred to as T_c and marks the onset of helical order with helices aligned along certain crystallographic directions. The fluctuation-disordered regime between T_c and T_2 is dominated by strongly interacting chiral fluctuations. The qualitative shape of the susceptibility of $Fe_{1-x}Co_xSi$ is very similar in the concentration range studied. For $x = 0.50$, however, the susceptibility increases linearly for decreasing temperatures within the helical state.

In the following, we describe the situation at low temperatures and high fields, i.e., $|\mu_0 H| >$

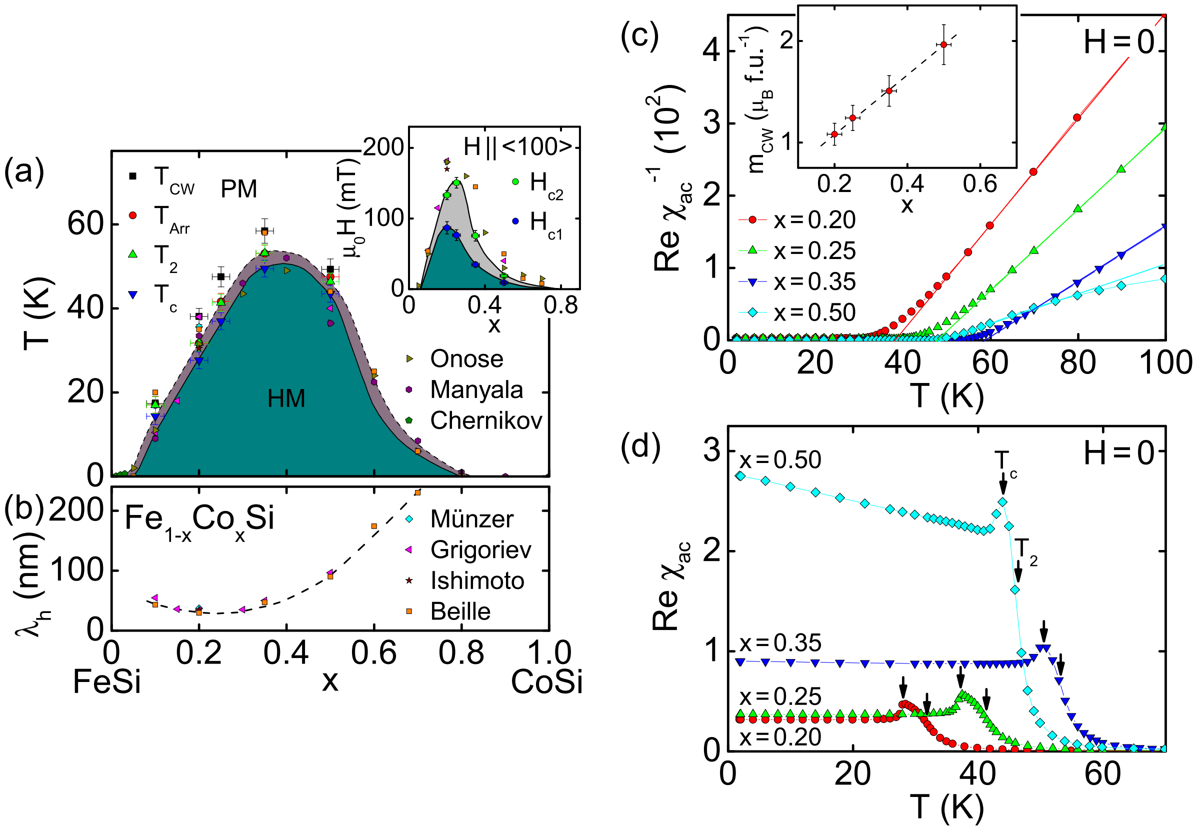

Figure 3.43: Helimagnetism in $Fe_{1-x}Co_xSi$. (a) Compositional phase diagram exhibiting paramagnetism (PM) and helimagnetism (HM). The inset depicts the low-temperature helimagnetic transition fields. (b) Helix wavelength, λ_h, as a function of the cobalt content x. Data are taken from Refs. [248, 249, 287, 450, 452–454]. (c) Temperature dependence of the inverse ac susceptibility revealing Curie-Weiss like behavior at high temperatures. The extrapolated fluctuating moments are shown in the inset. (d) Temperature dependence of the real part of the ac susceptibility. The transitions at T_c and T_2 are defined as kink and as point of inflection, respectively.

0.2 T, where $Fe_{1-x}Co_xSi$ is in a field-polarized state. Here, as shown in Fig. 3.44(a), the magnetization is of the order of $0.2\,\mu_B$/f.u. and stays unsaturated up to 9 T for all concentrations studied. The missing saturation is characteristic of itinerant magnetism and consistent with pure and doped MnSi. For a ferromagnet, one can assume an equation of state $H = aM + bM^3$ with the inverse initial susceptibility a and the mode-coupling parameter b. To derive the spontaneous ordered moment as a function of temperature, $m_s(T)$, isotherms of the magnetization are plotted as H/M versus M^2. Subsequently, the behavior at high fields, i.e., where the helimagnetism is suppressed, may be extrapolated linearly to $H = 0$ yielding $m_s(T)$. This so-called Arrott plot is shown for $x = 0.20$ in Fig. 3.44(b), the corresponding magnetization data are depicted in the inset.

For weak itinerant ferromagnets the spontaneous moments are expected to scale according to $m_s(T)^2 = {m_{s,0}}^2\,(1 - (T/T_{\mathrm{Arr}})^{\alpha})$ with the zero-temperature moment $m_{s,0}$ and the exponent $\alpha = 2$. Fig. 3.44(c) depicts the spontaneous moment, $m_s(T)$, of $Fe_{1-x}Co_xSi$ as a function of

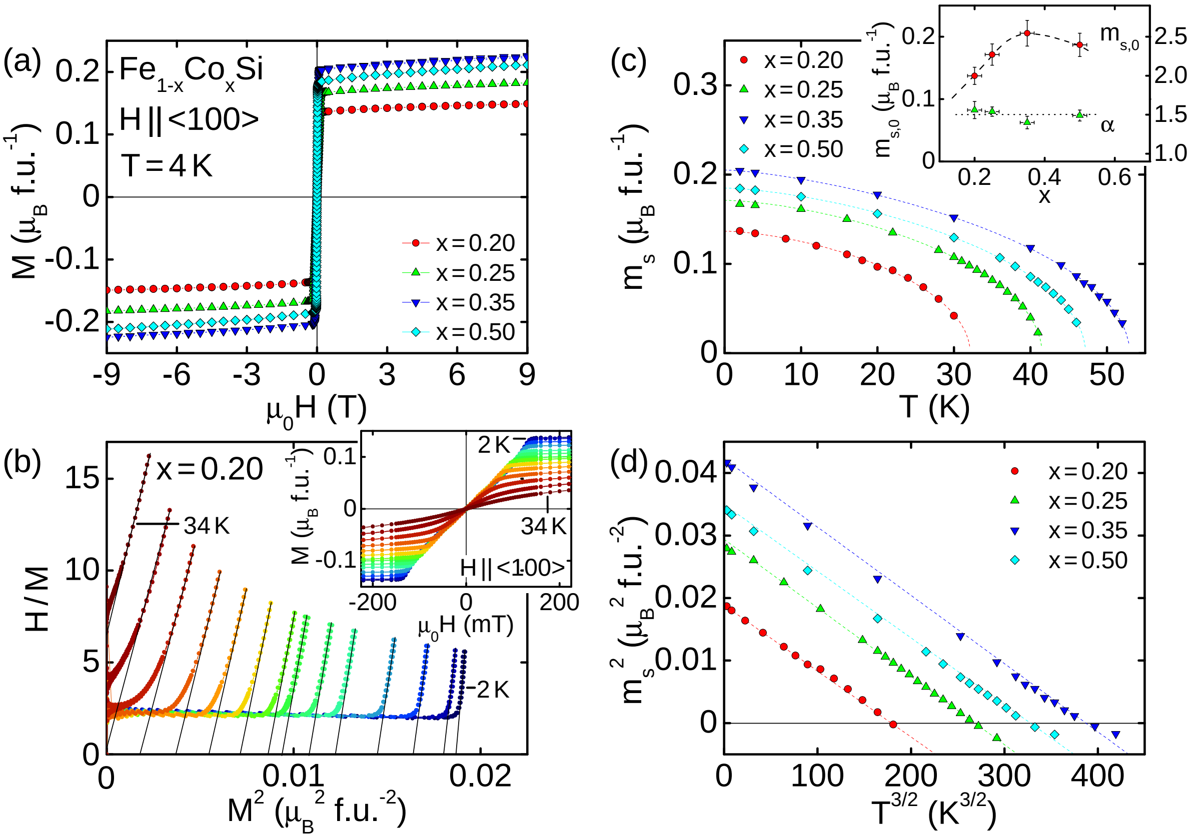

Figure 3.44: Behavior of $\mathrm{Fe}_{1-x}\mathrm{Co}_x\mathrm{Si}$ at high fields and low temperatures. (a) Magnetization of $\mathrm{Fe}_{1-x}\mathrm{Co}_x\mathrm{Si}$ at 4 K as a function of field up to 9 T. We observe an unsaturated magnetization up to the highest fields and down to the lowest temperatures studied. (b) Arrott plot, i.e., magnetic field divided by magnetization versus the square of the magnetization, for $\mathrm{Fe}_{1-x}\mathrm{Co}_x\mathrm{Si}$ with $x = 0.20$. Data are shown for every 2 K up to 34 K, i.e., above T_c. Solid lines represent linear fits to the high-field data. The inset displays the corresponding isothermal magnetization. (c) Temperature dependence of the spontaneous moment, m_s, of $\mathrm{Fe}_{1-x}\mathrm{Co}_x\mathrm{Si}$ as extrapolated from the Arrott plots. The dashed lines are fits according to $m_s(T)^2 = {m_{s,0}}^2\,(1 - (T/T_c)^\alpha)$. The inset depicts the concentration dependence of the zero-temperature spontaneous moment, $m_{s,0}$. The exponent $\alpha = 3/2$ differs from typical itinerant ferromagnets where one expects $\alpha = 2$. (d) Square of the spontaneous moment, m_s^2, as a function of $T^{3/2}$ showing a linear dependence.

temperature. The dashed lines represent fits using the abovementioned formula and the free parameters T_{Arr}, $m_{s,0}$, and α. The intersections with the abscissa mark the characteristic temperatures T_{Arr} that are shown in Fig. 3.43(a). The values of T_{Arr} agree remarkably well with the temperatures T_2 derived from the ac susceptibility. The spontaneous zero-temperature ordered moments, $m_{s,0}$, and the exponents α are depicted in the inset of Fig. 3.44(c). The spontaneous moments are much smaller than the fluctuating Curie-Weiss moments, as characteristic for weak itinerant ferromagnetism. Still, we observe $\alpha = 3/2$ in $\mathrm{Fe}_{1-x}\mathrm{Co}_x\mathrm{Si}$ deviating from the value $\alpha = 2$ expected for weak itinerant ferromagnetism, see Fig. 3.44(d). The latter contrasts the behavior in $Mn_{1-x}Fe_xSi$ and $Mn_{1-x}Co_xSi$ [85, 106].

Magnetization and susceptibility after zero-field cooling

In the helimagnetic regime at low temperatures and small magnetic fields the behavior of $Fe_{1-x}Co_xSi$ is again highly reminiscent of pure and especially doped MnSi. As described in Sec. 3.3.1, the various magnetic states in this part of the phase diagram may be discriminated best by using susceptibility data, where the definitions of the various transition fields and temperatures are summarized in Ref. [313]. Figs. 3.45(a) through 3.45(d) show the typical field dependency of the susceptibility calculated from the magnetization, $\mathrm{d}M/\mathrm{d}H$, and the real part of the ac susceptibility, $\mathrm{Re}\,\chi_{\mathrm{ac}}$, for $Fe_{1-x}Co_xSi$ with $x = 0.20$, $x = 0.25$, $x = 0.35$, and $x = 0.50$, respectively. The lowest temperature measured, 2 K, and a temperature a few kelvin below the helimagnetic transition temperature, T_c, were selected. The magnetic field was applied along the crystalline $\langle 100 \rangle$ direction after an initial zero-field cooling. The behavior of all concentrations studied is qualitatively similar, albeit the critical field and temperature values change significantly.

The description starts with the susceptibility calculated from the magnetization, $\mathrm{d}M/\mathrm{d}H$, at 2 K and in zero field. Here, $Fe_{1-x}Co_xSi$ is in the helical state. With increasing field the susceptibility stays essentially constant for $H < H_{c1}^-$. At H_{c1}^- a pronounced peak starts to evolve that reaches its maximum at H_{c1} and vanishes around H_{c1}^+. For higher fields $Fe_{1-x}Co_xSi$ is in the conical state before it finally enters the field-polarized state for fields exceeding H_{c2}. The real part of the ac susceptibility tracks $\mathrm{d}M/\mathrm{d}H$ except for the peak at the helical-to-conical transition around H_{c1}. As discussed in Sec. 3.3.1, this difference arises from the slow reorientation of the large helical domains. For temperatures just below the helimagnetic transition, in addition two peaks bordering a plateau of reduced susceptibility emerge in $\mathrm{d}M/\mathrm{d}H$ at intermediate fields as the characteristic of the Skyrmion lattice state. These peaks are not tracked by the real part of the ac susceptibility. We mark the beginning and the end of the deviation between $\mathrm{d}M/\mathrm{d}H$ and $\mathrm{Re}\,\chi_{\mathrm{ac}}$ as H_{A1}^- and H_{A1}^+ as well as H_{A2}^- and H_{A2}^+, respectively. At the first-order boundary of the Skyrmion lattice state the slow response is attributed to the nucleation process of topologically non-trivial Skyrmions in the conical phase (or vice versa), i.e., a regime of phase coexistence.

The temperature dependence of the ac susceptibility after zero-field cooling is depicted in Figs. 3.45(e) through 3.45(h) and again is typical of the cubic chiral helimagnets. In zero field, a plateau of comparably low susceptibility at low temperatures is characteristic of the helical state. With increasing temperature, we observe a kink at T_c followed by a point of inflection at T_2. These signatures are associated with the helimagnetic Brazovskii-type transition into an essentially paramagnetic state above T_2, where the intermediate temperature interval $T_c < T < T_2$ is dominated by strongly interacting chiral fluctuations. In small magnetic fields, we observe a transition from the helical state at low temperatures to the conical state at higher temperatures, i.e., to a plateau of higher susceptibility. The transition temperature, T_{c1}, is defined as point of inflection and arises as the critical field of the helical-to-conical transition, H_{c1}, is dependent on temperature in $Fe_{1-x}Co_xSi$. This behavior contrasts pure MnSi and is consistent with $Mn_{1-x}Fe_xSi$, $Mn_{1-x}Co_xSi$, and Cu_2OSeO_3 [85, 251]. Similar to the zero-field data, a point of inflection at T_{c2} marks the crossover between the fluctuation-disordered and the paramagnetic regime. The temperatures T_c and T_2 thereby correspond to the zero-temperature values of T_{c1} and T_{c2}, respectively.

For intermediate fields an additional minimum appears at the high-temperature side of the conical plateau as the characteristic of the Skyrmion lattice state. The transition temperatures,

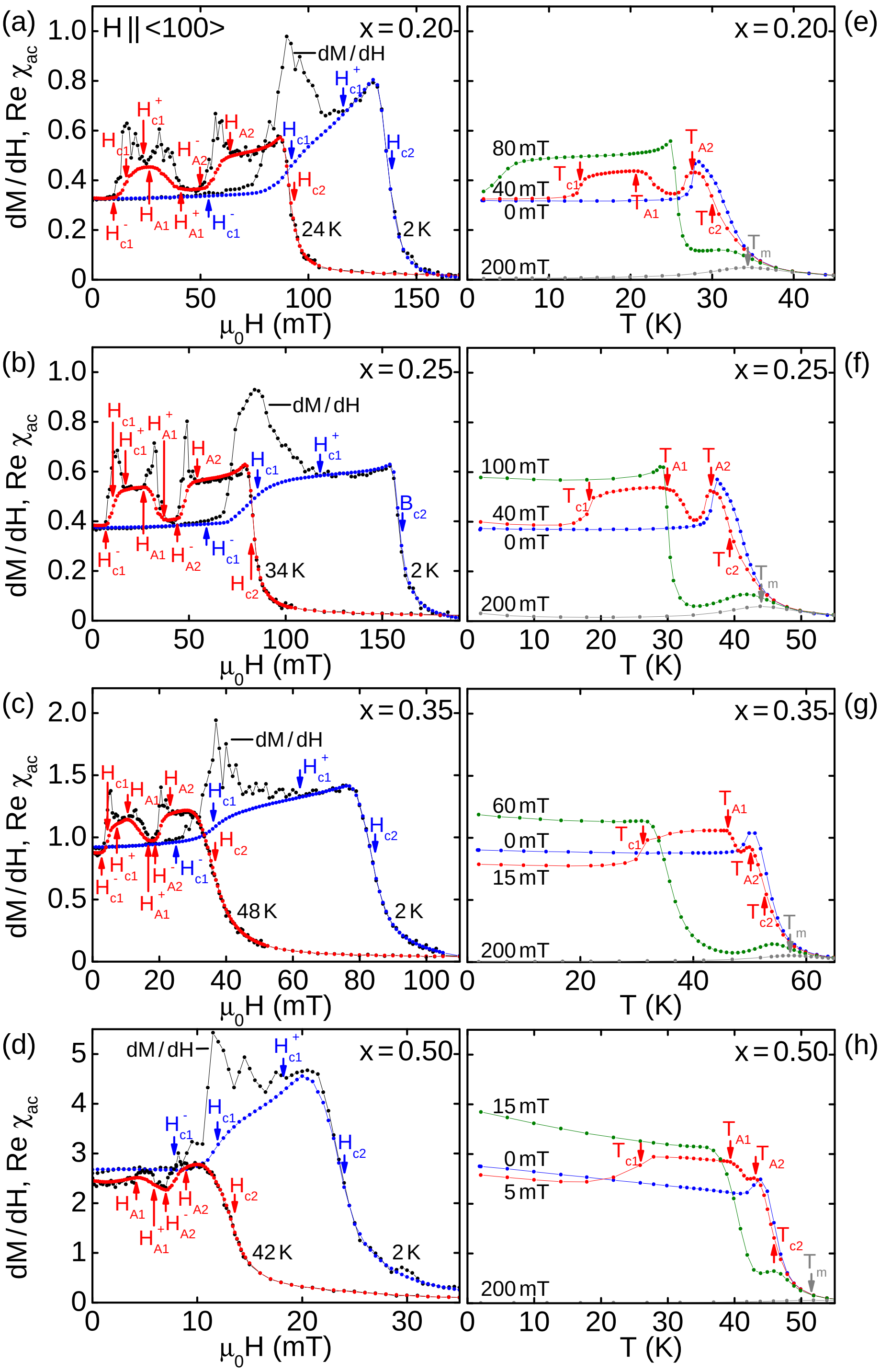

Figure 3.45: Susceptibility of $Fe_{1-x}Co_xSi$ for different cobalt contents. (a)–(d) Field dependence at 2 K (blue) and at a temperature just below the helimagnetic transition (red). In addition to the real part of the ac susceptibility, the susceptibility calculated from the measured magnetization, $\mathrm{d}M/\mathrm{d}H$, is shown (black). (e)–(h) Temperature dependence for zero field (blue) as well as for typical field values within the Skyrmion lattice state (red), the conical state (green), and the field-polarized regime (gray).

T_{A1} and T_{A2}, are defined as beginning and end of the deviation of the susceptibility from the value within the conical state. With increasing cobalt content, x, the signature of the Skyrmion lattice phase becomes less pronounced. Assuming that the difference of the susceptibility between the conical and the Skyrmion lattice state is proportional to the Skyrmion density, ϕ, this observation is a consequence of the increasing helix wavelength, λ_{h}, in the concentration range studied, since $\phi \propto {\lambda_{\mathrm{h}}}^{-2}$. For higher fields the conical plateau remains visible and a shallow maximum emerges at a temperature $T_m > T_{c2}$. This maximum indicates the crossover from the field-polarized state at low temperatures to the essentially paramagnetic state at high temperatures. For fields exceeding H_{c2} the maximum survives and shifts to higher temperatures for increasing magnetic fields.

Role of sample orientation as well as temperature and field history

In the following, we discuss the influence of the crystalline orientation as well as of the field and temperature history on the magnetic properties of $Fe_{1-x}Co_xSi$, as first addressed in a small-angle neutron scattering study by Wolfgang Münzer *et al.* [287]. A detailed account is given for $x = 0.20$, but a similar behavior is observed for all concentrations studied. We start with the susceptibility as a function of field and continue with temperature dependent data.

Figs. 3.46(a) through 3.46(f) show the field dependence of the real and imaginary part of the ac susceptibility for field along $\langle 100 \rangle$, $\langle 110 \rangle$, and $\langle 111 \rangle$. The lowest temperature measured, 2 K (blue), as well as two temperatures around the lower and upper temperature boundary of the Skyrmion lattice phase (green and red) were selected. The open symbols represent data after zero-field cooling; cf. Fig. 3.45. The filled symbols refer to data for decreasing and increasing field, respectively, that start from the field-polarized state, $|H| > H_{c2}$, i.e., corresponding to the situation after high-field cooling in temperature sweeps.

First, we account for the real part of the ac susceptibility depicted in Figs. 3.46(a), 3.46(c), and 3.46(e). At low temperatures after zero-field cooling, the characteristic field of the helical-to-conical transition, H_{c1}, is essentially independent from the orientation. Perhaps most prominent, however, after a field has been applied there is no sign of the helical-to-conical transition for all field directions studied, consistent with small-angle neutron scattering [287]. These observations contrast the stoichiometric compounds MnSi and Cu_2OSeO_3 but are consistent with the doped systems $Mn_{1-x}Fe_xSi$ and $Mn_{1-x}Co_xSi$ suggesting that disorder plays a decisive role. At temperatures just below the helimagnetic ordering temperature, a minimum around zero field emerges that resembles the minimum observed after zero-field cooling and is most pronounced for field along $\langle 100 \rangle$. This signature may be attributed to the re-population of the helical state due to an increased amount of thermal fluctuations and is also occurs in the other cubic chiral helimagnets [85]. In this minimum a small hysteresis between the sweeps for increasing and decreasing field may be observed. While H_{c1} is essentially isotropic, the transition between the conical and the field-polarized state at H_{c2} exhibits reasonable anisotropy. At low temperatures, H_{c2} increases by about 20 % from field parallel $\langle 100 \rangle$ to field parallel $\langle 111 \rangle$. This anisotropy is much larger than for pure or doped MnSi. Still, we observe no hysteresis at H_{c2} within the resolution of our study. The shape of the susceptibility in the conical state slightly changes for different field directions.

At 26 K a Skyrmion lattice state is present at intermediate fields for all field directions studied. At 22 K, we observe no corresponding signatures for field along $\langle 110 \rangle$ and $\langle 111 \rangle$, whereas there is still a Skyrmion lattice for field along $\langle 100 \rangle$. In the latter case, the sweep for increasing and decreasing field slightly deviate from each other where the data after zero-field cooling track the

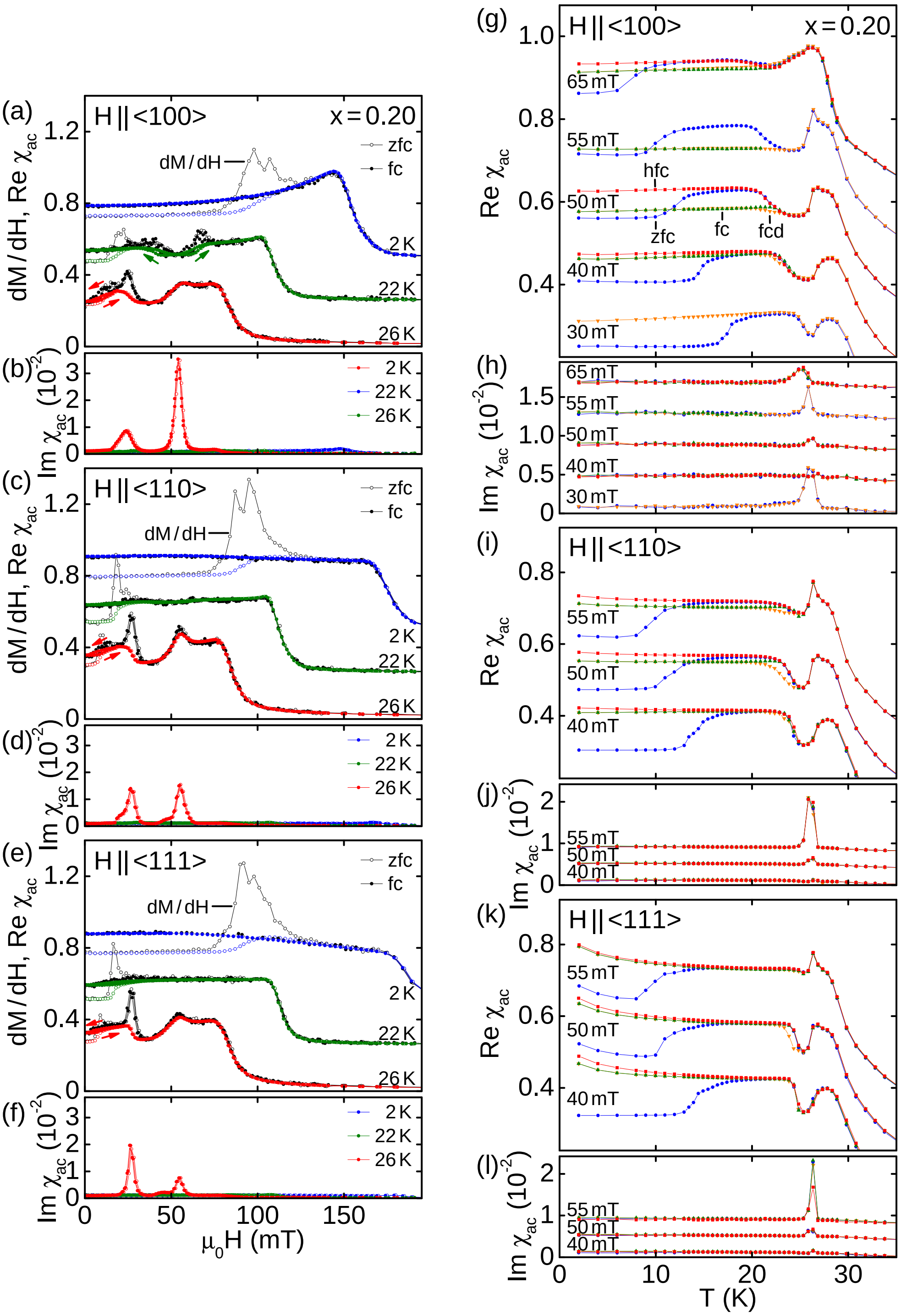

Figure 3.46: Susceptibility of $Fe_{1-x}Co_xSi$ with $x = 0.20$ for field along the $\langle 100 \rangle$, $\langle 110 \rangle$, and $\langle 111 \rangle$ axis. (a)–(f) Field dependence of the real and imaginary part of the ac susceptibility as well as the susceptibility calculated from the magnetization, $\mathrm{d}M/\mathrm{d}H$. Data are shown after initial zero-field cooling (zfc) and for a subsequent field cycle (fc). (g)–(l) Temperature dependence of the real and imaginary part of the ac susceptibility for different cooling histories. For clarity the data have been offset.

sweep for increasing field. Such a hysteresis is unique among the cubic chiral helimagnets. The temperature and field extent of the Skyrmion lattice state and how it is influenced by the cooling history will be addressed in more detail below. The imaginary part of the ac susceptibility is very similar for all directions studied; cf. Figs. 3.46(b), 3.46(d), and 3.46(f). The imaginary part, in general, is small except for pronounced peaks at the transitions between the Skyrmion lattice and the conical state. This finite dissipation is the characteristic of a regime of phase coexistence and consistent with the other cubic chiral helimagnets [313].

The influence of the cooling history, finally, is addressed most efficiently by the susceptibility as a function of temperature illustrated in Figs. 3.46(g) through 3.46(l). Here, we focus on field values in the Skyrmion lattice phase where we distinguish four different cooling histories: zero-field cooling (zfc, blue), field cooling down (fcd, orange), field cooling (fc, green), and high-field cooling (hfc, red).

The helical state at low temperatures is only stabilized after zero-field cooling. The typical signature of the Skyrmion lattice state is a minimum at the high-temperature side of the conical plateau. In this pocket just below T_c, the Skyrmion lattice forms reversible, i.e., independent from the field and temperature history. However, if $Fe_{1-x}Co_xSi$ is field cooled down, this minimum may be extended to lower temperatures. Around its low field boundary the Skyrmion lattice phase may only be enlarged by a few kelvin, while at higher fields the metastable regime may extend down to the lowest temperatures studied. Both the temperature width of the reversible Skyrmion lattice phase pocket and the magnitude of its metastable extension are largest for field along $\langle 100\rangle$ and smallest for $\langle 111\rangle$. For the latter case, the Skyrmion lattice may not be stabilized down to lowest temperatures. The observed phase boundaries, both reversible and metastable, are consistent with small-angle neutron scattering data [287]. After high-field cooling, the helical state is suppressed and the Skyrmion lattice state is only present in the reversible pocket. Hence, e.g., for a field of $\mu_0 H = 50\,\mathrm{mT}$ along $\langle 100\rangle$, either the helical state (after zfc), the Skyrmion lattice state (after fcd), or the conical state (after hfc) may be stabilized. The imaginary part of the susceptibility, depicted in Figs. 3.46(h), 3.46(j), and 3.46(l), is independent of the field and temperature history. Consistent with the field dependent data, the imaginary part shows peaks around the phase boundary of the Skyrmion lattice state, while it is negligible everywhere else.

Magnetic phase diagrams

Finally, the temperature and field dependences of the susceptibility are combined to construct magnetic phase diagrams. Fig. 3.47 summarizes our findings for $Fe_{1-x}Co_xSi$ with $x = 0.20$ after zero-field cooling (left column) and field cooling (right column) for magnetic fields along the major crystallographic directions.

After zero-field cooling, the magnetic phase diagram resembles that of the archetypical chiral helimagnet MnSi. Below the helimagnetic ordering temperature, T_c, we observe a helical state at low fields, a conical state at higher fields, and a Skyrmion lattice state at intermediate fields just below T_c. The transition regimes between the helical, the conical, and the Skyrmion lattice state are dominated by the slow response that stems from the reorientation of large helical domains and a regime of phase coexistence, respectively. At low temperatures and high fields, $Fe_{1-x}Co_xSi$ is field-polarized (FP), at high temperatures and low fields it is essentially paramagnetic (PM). The two regimes are separated by a crossover observed as a shallow maximum in the ac susceptibility. The transition from the paramagnetic to the helimagnetic state occurs via a fluctuation-disordered regime (FD) that is dominated by strongly interacting chiral fluctuations

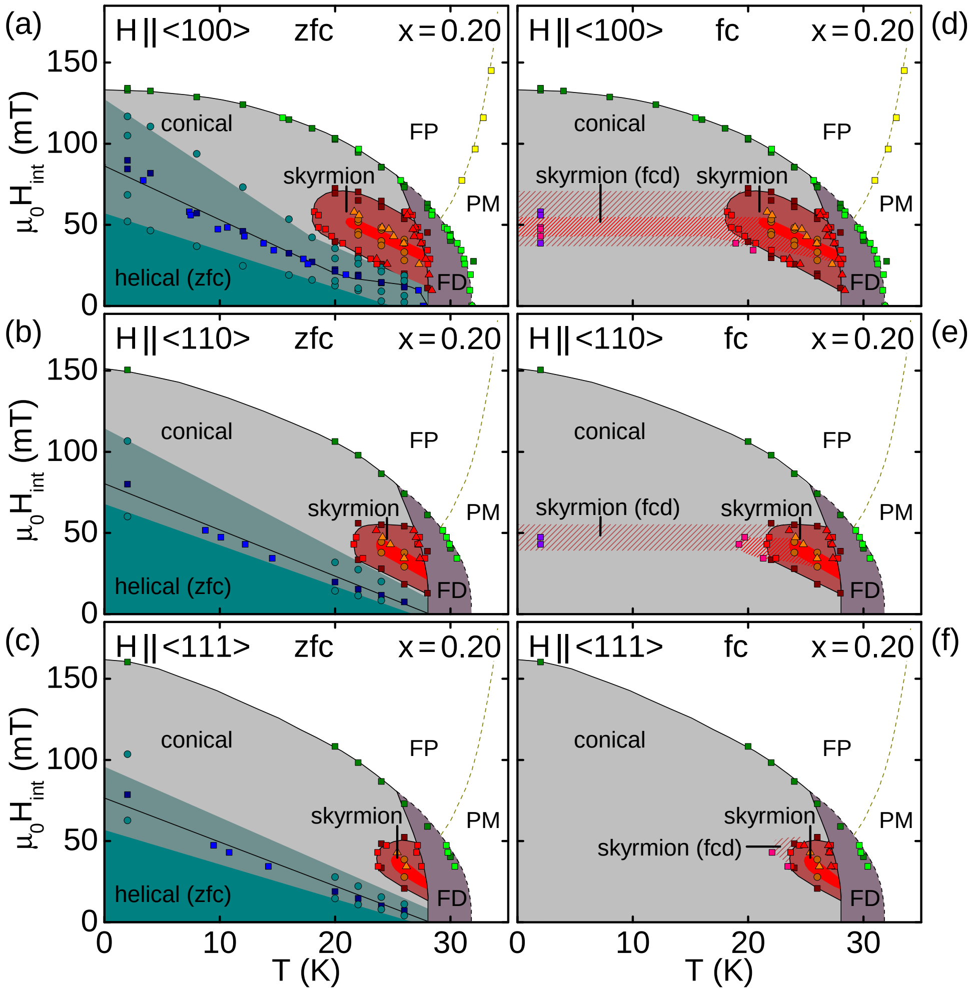

Figure 3.47: Magnetic phase diagram of $Fe_{1-x}Co_xSi$ with $x = 0.20$ for the major crystallographic directions after zero-field cooling (zfc, left column) and field cooling (fc, right column). Data are shown as a function of the internal field. The phase diagrams are rather isotropic. We distinguish the following regimes: helical order, conical order, Skyrmion lattice, fluctuation-disordered (FD), paramagnetic (PM), and field-polarized (FP). A proper helical state is only observed after zero-field cooling. The Skyrmion lattice phase is most pronounced for field along $\langle 100 \rangle$ and may be extended metastably down to the lowest temperatures studied after field cooling. Small-angle neutron scattering as reported in Ref. [287] yielded consistent results.

as described by the helimagnetic Brazovskii scenario [257]. Other than in MnSi, the critical field of the helical-to-conical transition, H_{c1}, increases with decreasing temperature and is essentially independent from the crystallographic orientation. Instead, the transition between the conical and the field-polarized state at H_{c2} shows a comparably strong anisotropy of about 20 % with the smallest value for field along $\langle 100 \rangle$.

The Skyrmion lattice exists reversibly, i.e., independent from the cooling history, in a phase pocket below the helimagnetic ordering temperature T_c. The temperature extent of this pocket

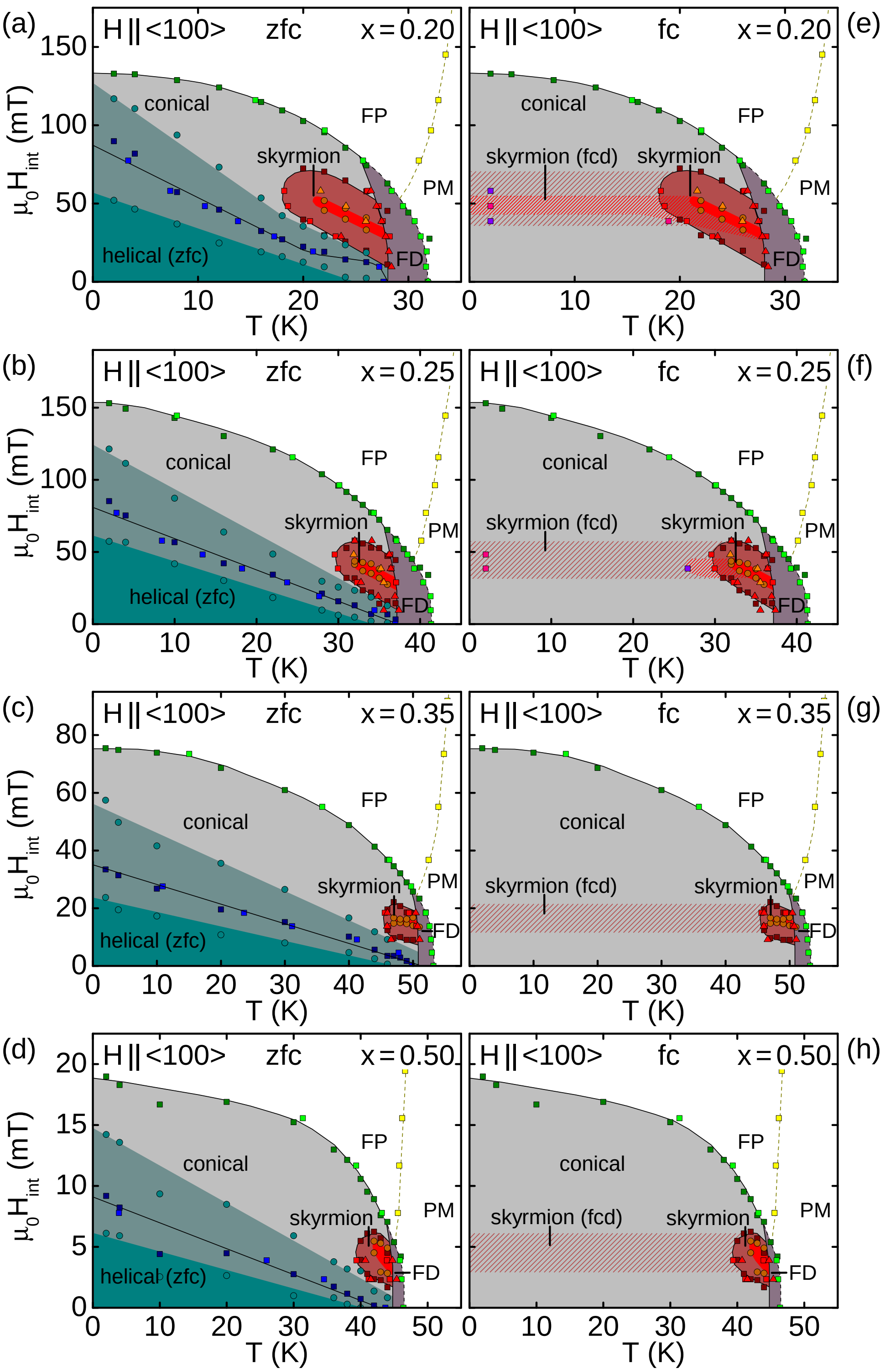

Figure 3.48: Magnetic phase diagram of $Fe_{1-x}Co_xSi$ for various concentrations after zero-field cooling (left column) and field cooling (right column) for field along ⟨100⟩. Data are shown as a function of the internal field. The phase diagrams stay qualitatively similar in the concentration range studied.

is largest for field along ⟨100⟩ and smallest for field along ⟨111⟩. The upper critical field of the Skyrmion lattice decreases with increasing temperature giving rise to a reentrant conical state. For all crystallographic directions the temperature extent of the Skyrmion lattice state, especially in relation to T_c, is large compared with stoichiometric materials exhibiting a Skyrmion lattice, i.e., MnSi, FeGe, and Cu_2OSeO_3.

Considering the leading terms of the cubic anisotropies, the anisotropy of the Skyrmion lattice phase implies an easy ⟨111⟩ axis for the helical pitch in $Fe_{1-x}Co_xSi$ with $x = 0.20$, although H_{c1} shows no direction dependence. In contrast, in small-angle neutron scattering intensity maxima along the ⟨110⟩ axes were detected after zero-field cooling in Ref. [287]. In combination with the pronounced anisotropy of H_{c2}, these observations suggest that an account for the cubic anisotropies in this compound requires the consideration of contributions beyond Bak and Jensen[254], cf. Sec. 3.1.1. In order to address the cubic anisotropies and, in particular, their evolution as a function of the cobalt content, x, corresponding susceptibility and small-angle neutron scattering data are required for $x \neq 0.20$ that will be subject to a future study.

After field cooling, two distinct differences are observed with respect to the behavior after zero-field cooling. First, the helical state is not recovered once a field larger than H_{c1} has been applied for all crystallographic directions. Similar observations in the doped compounds $Mn_{1-x}Fe_xSi$ and $Mn_{1-x}Co_xSi$ [85] suggest that the disorder introduced by doping has a strong influence on the magnetic anisotropy of the helices and the formation and evolution of helical domain walls, respectively. Second, and perhaps more excitingly, after field cooling the Skyrmion lattice in $Fe_{1-x}Co_xSi$ may be stabilized as a metastable state down to the lowest temperatures studied. This extension is most pronounced for field along ⟨100⟩ and weakest for ⟨111⟩. The dense hatching in Fig. 3.47 marks the part of the phase diagram, where the ac susceptibility stays at its lowest value, i.e., where the metastable Skyrmion lattice is most pronounced. This metastability at ambient pressure is hitherto unique within the class of cubic chiral helimagnets.

Fig. 3.48 finally summarizes the magnetic phase diagrams for all concentrations studied. The magnetic field was applied along ⟨100⟩ after zero-field cooling (left column) or field cooling (right column), respectively. While the qualitative shape of all phase diagrams is very similar, the characteristic temperature and field values vary significantly as a function of the cobalt content. All phase diagrams are qualitatively and quantitatively consistent with corresponding results from small-angle neutron scattering [287, 452, 454]. The helimagnetic ordering temperature, T_c, reaches its maximum of more than 50 K around $x = 0.35$, cf. Fig. 3.43(a). For larger and smaller cobalt contents T_c decreases smoothly. The critical field H_{c2} peaks around $x = 0.25$ and shrinks steeply for larger cobalt contents. For the samples with $x = 0.35$ and $x = 0.50$ the signature of the Skyrmion lattice state in the susceptibility is rather shallow which may be attributed to the large helix wavelength leading to a small Skyrmion density. Hence, it is hard to track the differences between different cooling histories. Nevertheless, our data suggest that the same metastable extension of the Skyrmion lattice state is observed as in the low-cobalt samples, $x = 0.20$ and $x = 0.25$. A study using magnetic force microscopy and small-angle neutron scattering not only confirmed this assumption for $x = 0.50$ but also utilized the metastably extended Skyrmion lattice to investigate its decay into a helimagnetic state [80].

Specific heat

The specific heat of $Fe_{1-x}Co_xSi$ as a function of temperature is shown in Fig. 3.49(a) for zero field and fields up to 9 T. In the concentration range studied the specific heat is dominated by the phononic contribution and weakly dependent on the magnetic field. However, small additional

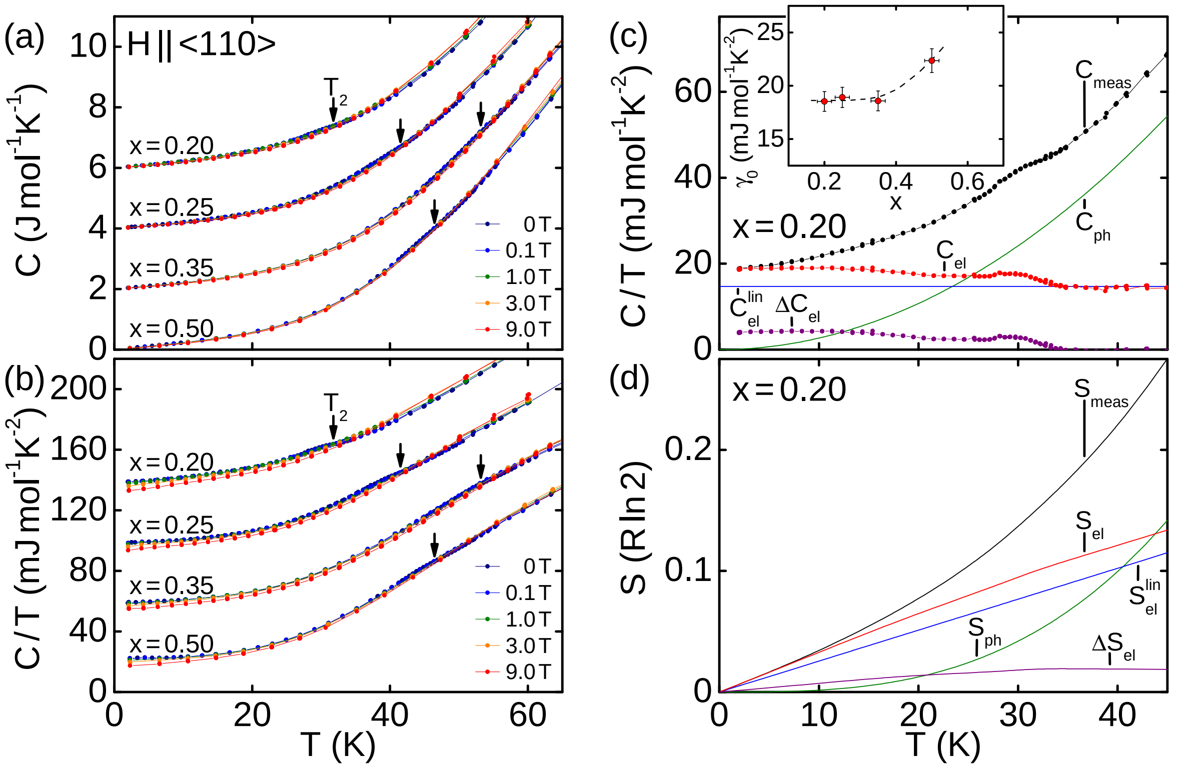

Figure 3.49: Temperature dependence of the specific heat of $Fe_{1-x}Co_xSi$. The magnetic field was applied along $\langle 110 \rangle$. (a) Specific heat as a function of temperature for different cobalt contents. For clarity the data have been offset by 2 J/mol K. A Vollhardt invariance at T_2 is observed in small fields. (b) Specific heat divided by temperature as a function of temperature. For clarity the data have been offset by 40 mJ/mol K^2. (c) Contributions to the specific heat of $Fe_{1-x}Co_xSi$ with $x = 0.20$. See text for details. The inset shows the zero-temperature extrapolation of C/T, γ_0, as a function of cobalt content. (d) Contributions to the entropy of $Fe_{1-x}Co_xSi$ with $x = 0.20$ calculated from the data in panel (c).

contributions arise in the helimagnetically ordered phase, that are best resolved by plotting the specific heat divided by temperature, C/T, as a function of temperature, see Fig. 3.49(b). These additional contributions at low temperatures are suppressed with increasing field.

A crossing point in small fields, labeled T_2, is the characteristic of a Vollhardt invariance [85, 257, 278]. In the helimagnetic Brazovskii scenario, T_2 marks the crossover from an essentially paramagnetic regime at high temperatures to a regime of strongly interacting chiral fluctuations at lower temperatures. This crossover is followed by a fluctuation-induced first-order transition into the helical state at $T_c < T_2$. A peak in the specific heat is thereby expected as a clear signature of the first-order transition that coincides with the onset of helical order. Within the resolution of our study, however, we observe no first-order-like anomaly in the specific heat of $Fe_{1-x}Co_xSi$, whereas helical order with pinned helices is detected in small-angle neutron scattering [80, 287, 454].

The lack of such a specific heat anomaly contrasts the situation in both the itinerant helimagnets MnSi and $Mn_{1-x}Fe_xSi$ (up to $x = 0.10$) as well as in the local-moment helimagnet

Cu_2OSeO_3. In $Mn_{1-x}Fe_xSi$ for $x \geq 0.12$ neither a peak in the specific heat nor the onset of long-range helical order are observed. Hence, the absence of a noticeable peak in combination with clear signatures of T_c and T_2 in the ac susceptibility and the onset of helical order in small-angle neutron scattering represents a unique combination of properties within the class of cubic chiral helimagnets. The absolute value of the electrical resistivity [249], the large difference between the fluctuating moment, $m_{s,0}$, and the fluctuating moment, m_{CW}, as well as the missing saturation of the magnetization up to the highest fields studied consistently indicate that $Fe_{1-x}Co_xSi$ may be viewed as an itinerant system. Compared to MnSi, however, the conduction electron density is smaller yielding comparably small magnetic contributions to the specific heat and the entropy. As a result, a fluctuation-induced first-order anomaly might be present at the transition into the helimagnetic state, but may not be resolvable within the resolution of our study. The large amount of disorder in $Fe_{1-x}Co_xSi$, however, may also masked or a suppress of the first-order character.

An analysis of the different contributions to the specific heat of $Fe_{1-x}Co_xSi$ corroborates the general analogy to MnSi, albeit at a reduced conduction electron density. Corresponding data is shown in Fig. 3.49(c) on the example of $x = 0.20$. Here, C_{meas} is the total measured specific heat. $C_{\mathrm{ph}} \propto T^3$ corresponds to the lattice contribution derived from a Debye model using $\Theta_{\mathrm{D}} = 525\,K$. This value of Θ_{D} is in good agreement with the values observed in pure and doped MnSi [85]. Extrapolating C/T to zero temperature yields $\gamma_0 = 19\,\mathrm{mJ/mol\,K^2}$ for $x = 0.20$. This value is half the size of MnSi and slightly increases for increasing cobalt content, x, as depicted in the inset of Fig. 3.49(c). $C_{\mathrm{el}} = C_{\mathrm{meas}} - C_{\mathrm{ph}}$ corresponds to the total electronic contribution to the specific heat and may be split into two contributions. First, $C_{\mathrm{el}}^{\mathrm{lin}} = \gamma_{\mathrm{fl}} T$ is the linear contribution expected from Fermi liquid theory. Fitting temperatures well above T_2 we extract $\gamma_{\mathrm{fl}} = 15\,\mathrm{mJ/mol\,K^2}$, i.e., a value comparable to pure and doped MnSi. In combination with an electron density that for $x = 0.20$ is by a factor of $\sim$5 smaller than in MnSi [437], this value of γ_{fl} implies a distinct enhancement of the effective mass in $Fe_{1-x}Co_xSi$. Second, $\Delta C_{\mathrm{el}} = C_{\mathrm{el}} - C_{\mathrm{el}}^{\mathrm{lin}}$ covers the remaining specific heat and may be attributed to the additional magnetic contributions. This additional contribution is tiny, which becomes especially obvious when considering the entropy calculated from the specific heat data depicted in Fig. 3.49(d), where ΔC_{el} yields an additional entropy of $\Delta S = 0.02\,R\,\ln 2$. This small magnetic contribution suggests that in $Fe_{1-x}Co_xSi$, compared to the metallic MnSi, only a small number of electrons is involved in the magnetic ordering.

Summary

In summary, we have carried out an extensive study of the magnetization, the ac susceptibility, and the specific heat of single-crystal $Fe_{1-x}Co_xSi$ in the composition range between $x = 0.20$ and $x = 0.50$. Here, for the first time, we have carefully addressed the influence of the crystalline orientation and the cooling history. The magnetic phase diagrams of $Fe_{1-x}Co_xSi$, as one of our key results, are qualitatively similar to the other cubic chiral helimagnets, rather isotropic, and consistent with earlier reports. We observe a helical, a conical, and a single pocket of Skyrmion lattice phase as well as a field-polarized, a paramagnetic, and a fluctuation disordered regime. The phase boundaries between the helical, the conical, and the Skyrmion lattice state are accompanied by regimes slow response. In contrast to the stoichiometric compounds, however, the helical state only appears after zero-field cooling for all field directions studied. Perhaps most excitingly, the Skyrmion lattice may be metastably extended down to the lowest temperatures studied by field cooling the sample. At ambient pressure this behavior is hitherto unique within the class of chiral helimagnets.

The ac susceptibility as well as small-angle neutron scattering data in Ref. [287] are perfectly consistent with a Brazovskii-type fluctuation-induced first-order transition into the helimagnetic state in zero field. Other than in MnSi, $Mn_{1-x}Fe_xSi$ ($x \leq 0.10$), and Cu_2OSeO_3, however, the specific heat only exhibits a crossing point, the Vollhardt invariance, but lacks the first-order anomaly expected within the Brazovskii scenario. As our magnetization and specific heat data consistently suggest an itinerant character of the magnetism, the latter may be associated with a rather small number of electrons that are involved in the magnetic ordering.

The history dependence of $Fe_{1-x}Co_xSi$, in combination with the possibility to vary the transition temperatures, transition fields, and the helix wavelength by roughly one order of magnitude via compositional tuning, allows for optimized samples for future experiments. The potential for such studies has been demonstrated recently by magnetic force microscopy on the surface of a $Fe_{1-x}Co_xSi$ sample with $x = 0.50$ [80]. Here, the Skyrmion lattice was metastably cooled in field down to 10 K and its transformation into a topologically trivial helimagnetic state was investigated as a function of decreasing field. This study required a helix wavelength that is a few times larger than the lateral resolution of the technique (∼20 nm) and transition fields that are well below the coercivity of the magnetic tip (∼100 mT) to prevent its switching during a field cycle. The metastable Skyrmion lattice state finally offered two decisive advantages. First, the magnetic moment increases significantly with decreasing temperature hence substantially increasing the contrast of the magnetic force microscopy data. Second, the strong suppression of thermal fluctuations exposes the generic mechanism of the topological unwinding, i.e., the emergence of singular magnetic point defects that may be viewed as quantized magnetic monopoles.

3.4 Summary and outlook

During the course of this thesis the research on non-trivial spin textures in the cubic chiral helimagnets has evolved tremendously. After the identification of the A-phase in MnSi as a Skyrmion lattice in 2009, similar observations were made in many isostructural materials ranging from metals to insulators and spanning two orders of magnitude in temperature, field, and lateral size. The non-trivial topology of the Skyrmions leads to emergent electrodynamics and allows for a direct manipulation of the spin structure at ultra-low electrical current densities. This research is currently extended to thin films and nanostructured samples as the topological stability and the small size of the Skyrmions as well as their unique collective excitations promise great potential for future applications. In parallel, more fundamental issues are being addressed. For instance, we recently were able to shed new light on the puzzling properties of MnSi around its pressure-induced quantum phase transition by linking the Skyrmion lattice at ambient pressure to the formation of a topological non-Fermi liquid at high pressures [11].

The contributions reported in this thesis were twofold. On the one hand, using the preparation chain described in Chapter 1, a large number of single crystal of MnSi, $Mn_{1-x}Fe_xSi$, $Mn_{1-x}Co_xSi$, and $Fe_{1-x}Co_xSi$ were grown including oriented single crystals of 10 mm diameter and up to 70 mm length for extensive inelastic neutron scattering experiments not mentioned here. From these ingots we have prepared customized samples for various finished and ongoing projects in our group as well as for external collaborators. Additionally, in a systematic study we revealed that the initial manganese content of a $Mn_{1+x}Si$ single crystal is weakly correlated to its helimagnetic transition temperature and to the shape of the thermodynamic signatures at the phase transitions. The magnetic phase diagram in general, however, stays robust. This study also provided samples with a wide spread of residual resistivity ratios that allowed to investigate the influence of defect pinning on the spin transfer torque effects in MnSi [444] and the careful study of evolution of the magnetic phase diagram as a function of hydrostatic pressure [330].

On the other hand, we established a common magnetic phase diagram for the cubic chiral helimagnets by means of magnetization, ac susceptibility, and specific heat measurements. The phase diagram, in particular, involves a single pocket of Skyrmion lattice for all crystallographic directions that is separated from the conical state by a first-order phase transition. The transition is accompanied be a regime of phase coexistence with finite dissipation and slow dynamics. High-resolution specific heat data on MnSi and $\mathrm{Mn}_{1-x}\mathrm{Fe}_x\mathrm{Si}$ enabled us to track the evolution of the phase transitions around the helimagnetic ordering temperature T_c in unprecedented detail. A field-induced tricritical point was identified that is in strong support of a fluctuation-induced Brazovskii-type first-order transition in zero field and a fluctuation-disordered regime just above T_c. Finally, the magnetic phase diagram of the strongly doped helimagnet $\mathrm{Fe}_{1-x}\mathrm{Co}_x\mathrm{Si}$ was mapped. Here, special focus was placed on the pronounced influence of the cooling history in this compound, which allows to metastably extend the Skyrmion lattice to lowest temperatures if the sample is cooled in field. This metastable state was recently exploited to detect the unwinding of the Skyrmion lattice by magnetic monopoles [80]. Supplementary measurements of the bulk and transport properties of cubic chiral helimagnets also supported, for instance, the identification of a Brazovskii-type fluctuation-induced first-order transition in MnSi [257], of long-wavelength helimagnetism and a Skyrmion lattice in $\mathrm{Cu_2OSeO_3}$ [288], and of universal excitation spectra in MnSi, $\mathrm{Fe}_{1-x}\mathrm{Co}_x\mathrm{Si}$, and $\mathrm{Cu_2OSeO_3}$ [252, 389]

Further ongoing projects in our group include, for example, the investigation of the spin-fluctuations in MnSi and $\mathrm{Mn}_{1-x}\mathrm{Fe}_x\mathrm{Si}$ near T_c using high-resolution neutron spin resonance techniques. The main focus, however, currently lies on the Skyrmion lattice. Here, for instance, we study how uniaxial pressure influences its stability, how and on which timescales it decays into a topologically trivial state, how one may tailor its collective excitations, and how it can be manipulated via electric or inhomogeneous magnetic fields. Extending the studies to thin films of the cubic chiral helimagnets is a further goal. Finally, one may speculate whether topologically non-trivial spin structures are a general phenomenon in certain bulk materials and not restricted to compounds that crystallize in the $P2_13$ space group.A promising candidate, for instance, is the metallic helimagnet $\mathrm{SrFeO_3}$ where large contributions to the Hall effect, presumably of topological origin, were observed [513]. However, it is important to note that a topological Hall effect not exclusively occurs in Skyrmion lattices but may also arise in other non-coplanar spin structures [514–517]. Hence, an observation of the magnetic structure in either real or reciprocal space is highly desirable.

Conclusion

This thesis consists of three parts. After an account for the single crystal growth of intermetallics in the first part, the second and third part addressed our investigations of itinerant antiferromagnets and cubic chiral helimagnets. Our main results are summarized in the following.

Chapter 1 described the single crystal growth of intermetallic compounds and, in particular, the preparation chain developed in our group. This chain is dedicated to the growth of high-quality intermetallics by means of optical float-zoning and the synthesis of the required polycrystalline feed rods. All furnaces are all-metal sealed, bakeable, and equipped for the application of a high-purity inert gas atmosphere. As part of this thesis, we have (i) installed a central gas handling system utilizing point-of-use gas purifiers, (ii) commissioned an argon glovebox, (iii) designed a horizontal cold boat system that may be docked to the former using a bespoke metal bellow lock, (iv) completed the all-metal-sealed refurbishment of the rod casting furnace and modified it for crystal diameters up to 10 mm, (v) built a solid state electrotransport furnace, and (vi) implemented an electrotransport option into the all-metal sealed image furnace. Georg Benka, as part of his master's thesis, finally added an annealing furnace and an arc-melting furnace, that may be docked onto the glovebox. Using the preparation chain, during this thesis we have successfully grown about 60 single crystals of transition metal monosilicides, Heusler compounds, transition metal diborides, and various rare earth compounds.

Chapter 2 was concerned with the low-temperature properties of (itinerant) antiferromagnets, namely CrB_2, MnB_2, and CuMnSb. As reported in Sec. 2.1, we have grown the first large single crystals of CrB_2 using ^{11}B to permit extended neutron scattering studies. We have carried out comprehensive measurements of the electrical resistivity, the Hall effect, the magnetization, and the specific heat, as well as first elastic and inelastic neutron scattering experiments. In addition, we have investigated the Fermi surface by de Haas-van Alphen oscillations and band structure calculations. All data confirm an excellent sample quality, with the highest RRR reported so far, and clearly identify CrB_2 as a prime example for weak itinerant antiferromagnetism. Its hallmarks comprise of a typical metallic resistivity, a relatively low Néel temperature, an incommensurate magnetic structure, a small ordered moment contrasted by a large fluctuating moment, and a remarkable stability of the magnetic order up to the highest fields studied. A large Curie-Weiss temperature indicates the presence of strong geometric frustration. Finally, we have discussed possible implications for superconductivity in CrB_2, if the magnetic order is suppressed. We have also prepared the first large single-crystal of MnB_2. In agreement with earlier reports on polycrystals we observe local-moment magnetism with a Néel transition far above room temperature. At low temperatures the commensurate magnetic structure starts to cant giving rise to a finite moment.

The third antiferromagnet of interest was the half-Heusler CuMnSb, see Sec. 2.2, of which we have also grown the first two single crystals. A detailed metallurgical analysis indicated a tiny volume fraction of the ferrimagnetic impurity phase Mn_2Sb in the single crystal prepared from feed rods with stoichiometric composition. This impurity phase, however, was completely suppressed by using feed rods with an antimony excess of 0.035. Magnetization, specific heat, electrical resistivity, Hall effect, and thermal conductivity data recorded on both specimens were complemented by preliminary elastic and inelastic neutron data. Consistent with results on polycrystals, we observe for both samples a commensurate magnetic structure of ordered moments that correspond to the fluctuating moments as characteristic for local-moment magnets. In contrast, the high stability of the magnetic order in fields and magnetic fluctuations that persist up to high temperatures are typical for itinerant magnets. Moreover, a relatively high Curie-Weiss temperature suggests the presence of geometric frustration, probably induced by disorder. In addition, a yet unreported spin-canting emerges in the antiferromagnetic state of phase-pure CuMnSb. Taken together, CuMnSb displays a peculiar combination of magnetic properties that motivates further investigations.

Chapter 3 reported on our investigations of the cubic chiral helimagnets MnSi, $Mn_{1-x}Fe_xSi$, $Fe_{1-x}Co_xSi$, and Cu_2OSeO_3. Here, a detailed introduction in Sec. 3.1 was followed by a study optimizing the growth parameters of MnSi in Sec. 3.2, where we showed that a small initial manganese excess yields the highest residual resistivity ratios. Moreover, oriented single crystals of 10 mm diameter were prepared.

Our research on the low-temperature properties of the cubic chiral helimagnets in Sec. 3.3 may again be divided into three parts. (i) In a first study, cf. Sec. 3.3.1, simultaneous measurements of the magnetization and ac susceptibility were carried out focusing on high-quality single crystals of MnSi. Here, we identified a single pocket of Skyrmion lattice phase for all major crystallographic directions and, in addition, observed regimes of slow dissipative processes at the phase boundaries between the helical, the conical, and the Skyrmion lattice state. Exploratory measurements on other cubic chiral helimagnets indicated that this behavior indeed is universal. (ii) A high-resolution specific heat study on MnSi and $Mn_{1-x}Fe_xSi$ using a large heat pulse technique, cf. Sec. 3.3.2, confirmed the first-order character of the phase transitions around the Skyrmion lattice pocket and corroborated that the Skyrmion lattice is stabilized by thermal fluctuations. The detailed shape of the high-temperature phase boundary of the helimagnetic states was resolved for the first time. We finally established the existence of a field-induced tricritical point that strongly supports a Brazovskii-type fluctuation-induced first-order transition in zero field. (iii) An investigation of the magnetic phase diagrams of $Fe_{1-x}Co_xSi$ ($0.20 < x < 0.50$) by means of magnetization, ac susceptibility, and specific heat was eventually reported in Sec. 3.3.3. These measurements revealed a typical behavior of a cubic chiral helimagnet but with a strong influence of the temperature and field history, where the Skyrmion lattice may be metastably extended down to lowest temperatures if field cooled. In combination with the large range of critical temperatures, critical fields, and helix wavelengths that may be accessed in $Fe_{1-x}Co_xSi$ via compositional tuning, this hysteresis allows for the selection of appropriate samples for a wide range of experiments.

Publications

1. **Quality of Heusler Single Crystals Examined by Depth Dependent Positron Annihilation Techniques**
   C. Hugenschmidt, A. Bauer, P. Böni, H. Ceeh, S. W. H. Eijt, T. Gigl, C. Pfleiderer, C. Piochacz, A. Neubauer, M. Reiner, H. Schut, and J. Weber
   submitted (2014)

2. **Relaxation processes in the reentrant spin glass $\mathrm{Fe}_{14.5}\mathrm{Cr}_{85.5}$**
   J. Repper, W. Häußler, O. Holderer, A. Bauer, S. M. Shapiro, and P. Böni
   submitted (2014)

3. **Scanning probe microscopy in an ultra-low vibration closed-cycle cryostat**
   F. P. Quacquarelli, J. Puebla, T. Scheler, D. Andres, C. Bödefeld, B. Sipos, C. D. Savio, A. Bauer, C. Pfleiderer, A. Erb, and K. Karrai
   submitted (2014)

4. **Universal helimagnon and Skyrmion excitations in metallic, semiconducting, and insulating chiral magnets**
   T. Schwarze, J. Waizner, M. Garst, A. Bauer, I. Stasinopoulos, H. Berger, C. Pfleiderer, and D. Grundler
   submitted (2014)

5. **Low-temperature properties of single-crystal CrB_2**
   A. Bauer, A. Regnat, C. G. F. Blum, S. Gottlieb-Schönmeyer, B. Pedersen, M. Meven, S. Wurmehl, J. Kuneš, and C. Pfleiderer
   Physical Review B **90**, 064414 (2014)

6. **A Raman study of the temperature and magnetic field dependence of electronic and lattice properties in MnSi**
   H.-M. Eiter, P. Jaschke, R. Hackl, A. Bauer, M. Gangl, and C. Pfleiderer
   Physical Review B **90**, 024411 (2014)

7. **Real-Space and Reciprocal-Space Berry Phases in the Hall Effect of $\mathrm{Mn}_{1-x}\mathrm{Fe}_x\mathrm{Si}$**
   C. Franz, F. Freimuth, A. Bauer, R. Ritz, C. Schnarr, C. Duvinage, T. Adams, S. Blügel, A. Rosch, Y. Mokrousov, and C. Pfleiderer
   Physical Review Letters **112**, 186601 (2014)

8. **Superparamagnetic regular nanopillar-like structures studied by grazing incidence X-ray scattering: effect of vertical correlation**
   A. Paul, N. Paul, P. Müller-Buschbaum, A. Bauer, and P. Böni
   Journal of Applied Crystallography **47**, 1065 (2014)

9. **De Haas-van Alphen effect and Fermi surface properties of single-crystal CrB_2**
   M. Brasse, L. Chioncel, J. Kuneš, A. Bauer, A. Regnat, C. G. F. Blum, S. Wurmehl, C. Pfleiderer, M. A. Wilde, and D. Grundler
   Physical Review B **88**, 155138 (2013)

10. **Unwinding of a Skyrmion Lattice by Magnetic Monopoles**
    P. Milde, D. Köhler, J. Seidel, L. M. Eng, A. Bauer, A. Chacon, J. Kindervater, S. Mühlbauer, C. Pfleiderer, S. Buhrandt, C. Schütte, and A. Rosch
    Science **340**, 1076 (2013)

11. **Formation of a topological non-Fermi liquid in MnSi**
    R. Ritz, M. Halder, M. Wagner, C. Franz, A. Bauer, and C. Pfleiderer
    Nature **497**, 231 (2013)

12. **Giant generic topological Hall resistivity of MnSi under pressure**
    R. Ritz, M. Halder, C. Franz, A. Bauer, M. Wagner, R. Bamler, A. Rosch, and C. Pfleiderer
    Physical Review B **87**, 134424 (2013)

13. **Specific Heat of the Skyrmion Lattice Phase and Field-Induced Tricritical Point in MnSi**
    A. Bauer, M. Garst, and C. Pfleiderer
    Physical Review Letters **110**, 177207 (2013)

14. **Fluctuation-induced first-order phase transition in Dzyaloshinskii-Moriya helimagnets**
    M. Janoschek, M. Garst, A. Bauer, P. Krautscheid, R. Georgii, P. Böni, and C. Pfleiderer
    Physical Review B **87**, 134407 (2013)

15. **Polyoxometalate-stabilized, water dispersible Fe_2Pt magnetic nanoparticles**
    K. M. Seemann, A. Bauer, J. Kindervater, M. Meyer, C. Besson, M. Luysberg, P. Durkin, W. Pyckhout-Hintzen, N. Budisa, R. Georgii, C. M. Schneider, and P. Kögerler
    Nanoscale **5**, 2511 (2013)

16. **Observation of Coherent Helimagnons and Gilbert damping in an Itinerant Magnet**
    J. D. Koralek, D. Meier, J. P. Hinton, A. Bauer, S. A. Parameswaran, A. Vishwanath, R. Ramesh, R. W. Schoenlein, C. Pfleiderer, and J. Orenstein
    Physical Review Letters **109**, 247204 (2012)

17. **Magnetic phase diagram of MnSi inferred from magnetization and ac susceptibility**
    A. Bauer and C. Pfleiderer
    Physical Review B **85**, 214418 (2012)

18. **Long-Wavelength Helimagnetic Order and Skyrmion Lattice Phase in Cu_2OSeO_3**
T. Adams, A. Chacon, M. Wagner, A. Bauer, G. Brandl, B. Pedersen, H. Berger, P. Lemmens, and C. Pfleiderer
Physical Review Letters **108**, 237204 (2012)

19. **Emergent electrodynamics of skyrmions in a chiral magnet**
T. Schulz, R. Ritz, A. Bauer, M. Halder, M. Wagner, C. Franz, C. Pfleiderer, K. Everschor, M. Garst, and A. Rosch
Nature Physics **8**, 301 (2012)

20. **Long-Range Crystalline Nature of the Skyrmion Lattice in MnSi**
T. Adams, S. Mühlbauer, C. Pfleiderer, F. Jonietz, A. Bauer, A. Neubauer, R. Georgii, P. Böni, U. Keiderling, K. Everschor, M. Garst, and A. Rosch
Physical Review Letters **107**, 217206 (2011)

21. **Ultra-high vacuum compatible image furnace**
A. Neubauer, J. Bœuf, A. Bauer, B. Russ, H. v. Löhneysen, and C. Pfleiderer
Review of Scientific Instruments **82**, 013902 (2011)

22. **Spin Transfer Torques in MnSi at Ultralow Current Densities**
F. Jonietz, S. Mühlbauer, C. Pfleiderer, A. Neubauer, W. Münzer, A. Bauer, T. Adams, R. Georgii, P. Böni, R. A. Duine, K. Everschor, M. Garst, and A. Rosch
Science **330**, 1648 (2010)

23. **Quantum phase transitions in single-crystal $Mn_{1-x}Fe_xSi$ and $Mn_{1-x}Co_xSi$: Crystal growth, magnetization, ac susceptibility, and specific heat**
A. Bauer, A. Neubauer, C. Franz, W. Münzer, M. Garst, and C. Pfleiderer
Physical Review B **82**, 064404 (2010), recommended as Editor's Choice

24. **Skyrmion lattices in metallic and semiconducting B20 transition metal compounds**
C. Pfleiderer, T. Adams, A. Bauer, W. Biberacher, B. Binz, F. Birkelbach, P. Böni, C. Franz, R. Georgii, M. Janoschek, F. Jonietz, T. Keller, R. Ritz, S. Mühlbauer, W. Münzer, A. Neubauer, B. Pedersen, and A. Rosch
Journal of Physics: Condensed Matter **22**, 164207 (2010)

Acknowledgments

This thesis would not have been possible without the assistance, support, advice, and collaboration of various people. In particular I want to thank:

- First of all, my supervisor Christian Pfleiderer. Thank you for the last four years (well, actually six if we include the diploma thesis and the time as a working student . . .). Albeit the schedule has become denser over the years, you still have been a great mentor. I have learned a lot and had a fantastic time.
- Peter Böni for your nature, your advice, the perfect conditions at your chair, and the enlightening insights to Swiss Neutronics.
- Everybody at E21 for the great atmosphere at work and after work. Thank you for barbecues, sample changes via phone, watching soccer, playing soccer, Christmas parties, brainstorming, rock music, chili con carne, discussing data, bonfires, coding tips, birthday parties, having bad pizza during night sessions, triple d-days, Weißwürscht, skype sessions, burgers in the sun, philosophizing, playing quattroball, cakes & muffins, roasting Lounibär, the two (or three or four) daily coffee breaks, Oktoberfest, discussing technical designs, the school trip to Cambridge, proofreading, and all the other odds and ends. In particular, I want to thank Georg Benka for his enormous help in the crystal growth lab during his master's thesis, Alexander Regnat for the excellent cooperation on the antiferromagnets, and Anna Kusmartseva for her support in the PPMS lab during the last year. Kamsahamnida to Christian Franz, Tim Adams, and Michael Wagner (it has been a long way from the Semestereinführungstage to our Ph.D.). Moreover, I want to thank my officemates Marco Halder and Alfonso Chacon (we really would have had a problem if one of us was listening to hip-hop). Arigato gozaimasu to Kindervater-san, Rucker-san, and Schnarr-san. Thanks to Robert Ritz, Christopher Duvinage, our adoptee Christina Schäffler, Birgit Wiedemann, Patrick Ziegler, Marein Rahn, Jan Spallek, Marlies Gangl, Katharina Lochner, Saskia Gottlieb-Schönmeyer, Dorothea Mallinger, Pau Jorba, and all the other students, postdocs, alumni (especially Andreas Neubauer, Marc Janoschek, and Florian Jonietz), and employees.
- Everybody at FRM II, especially Georg Brandl for the measurements on CrB_2, CuMnSb, and the polarization tests on Cu_2MnAl, Philipp Schmakat for being Schmak Norris,

Tommy Reimann, Sebastian Mühlbauer, Robert Georgii, and Wolfgang Häußler. I also want to thank the positron group of Christoph Hugenschmidt and in particular Hubert Ceeh, Josef Weber, and Markus Reiner for their measurements on the Heusler compounds and $Mn_{1+x}Si$, respectively. Thanks to our crystallographers Martin Meven, Björn Pedersen, and, especially, Anatoliy Senyshyn. I am looking forward to the results on $EuPtSi_3$.

- Katarzyna Danielewicz, Michael Stanger, Andreas Erb and, most notably, Susanne Mayr from central crystal laboratory for cutting, grinding, polishing, orienting, and everything else that is required to prepare samples from a float-zoned ingot.
- Andi Mantwill and, in particular, Stefan Giemsa for their hands-on help in the labs and expert tips on SolidWorks. Manfred Pfaller, Manfred Reiter, and the team of the central workshop, as well as Norbert Heimerl and the apprentices of the precision mechanics for deciphering our drawings and manufacturing everything in time—even if it was on short notice. Herbert Hetzl for the steady support with liquid helium, liquid nitrogen, and high-purity gases.
- Achim Rosch and his theory group at the University of Cologne. Here, in particular I want to thank Markus Garst for countless phone calls and skype sessions and his remarkable understanding of both theory and experiment. Thanks to Karin Everschor-Sitte and Johannes Waizner.
- Dirk Grundler and his group E10 at TUM. Thomas Schwarze for the excellent collaboration on the collective excitations of the chiral helimagnets and Ioannis Stasinopoulos for continuing this project with skill and eagerness. Moreover, I want to thank Matthias Brasse, Stephan Albert, and Marc Wilde for de Haas-van Alphen measurements on the diborides as well as Jan Kuneš from the Academy of Sciences in Prague for his quick band structure calculations.
- Helmuth Berger for providing the Cu_2OSeO_3 samples. The day the first batch arrived felt a bit like all Christmases have come at once.
- Dennis Meier for the collaboration together with Jake Koralek and your groups in Berkeley, for showing my your labs, as well as for introducing me to Jan Seidel.
- Peter Milde, Jan Seidel, and the group of Lukas Eng for the fascinating magnetic force microscopy studies of the helimagnets and the lab tour in Dresden.
- Sabine Wurmehl and Christian Blum for the possibility to float-zone the diborides; Hans-Martin Eiter and Rudi Hackl for the Raman project on MnSi; Klaus Seemann for an interesting collaboration on FePt nanoparticles; Ross Springell and Christian Ruegg for giving me the opportunity to join a synchrotron experiment at ESRF.
- Everybody in Moosburg, Munich, and Neufahrn who contributed to four incredible years.
- Last but not least, my better half, Miriam. Thank you, for being you.

Bibliography

[1] J. G. Bednorz and K. A. Müller, Possible high T_c superconductivity in the Ba-La-Cu-O system, Z. Physik B **64**, 189 (1986).

[2] P. A. Lee, N. Nagaosa, and X.-G. Wen, Doping a Mott insulator: Physics of high-temperature superconductivity, Rev. Mod. Phys. **78**, 17 (2006).

[3] F. Steglich, J. Aarts, C. D. Bredl, W. Lieke, D. Meschede, W. Franz, and H. Schäfer, Superconductivity in the Presence of Strong Pauli Paramagnetism: $CeCu_2Si_2$, Phys. Rev. Lett. **43**, 1892 (1979).

[4] C. Pfleiderer, Superconducting phases of f-electron compounds, Rev. Mod. Phys. **81**, 1551 (2009).

[5] Y. Maeno, H. Hashimoto, K. Yoshida, S. Nishizaki, T. Fujita, J. G. Bednorz, and F. Lichtenberg, Superconductivity in a layered perovskite without copper, Nature (London) **372**, 532 (1994).

[6] K. Takada, H. Sakurai, E. Takayama-Muromachi, F. Izumi, R. A. Dilanian, and T. Sasaki, Superconductivity in two-dimensional CoO_2 layers, Nature (London) **422**, 53 (2003).

[7] Y. Kamihara, T. Watanabe, M. Hirano, and H. Hosono, Iron-Based Layered Superconductor $La[O_{1-x}F_x]FeAs$ ($x = 0.05 - 0.12$) with $T_c = 26\,K$, J. Am. Chem. Soc. **130**, 3296 (2008).

[8] G. R. Stewart, Superconductivity in iron compounds, Rev. Mod. Phys. **83**, 1589 (2011).

[9] G. R. Stewart, Non-Fermi-liquid behavior in d- and f-electron metals, Rev. Mod. Phys. **73**, 797 (2001).

[10] H. v. Löhneysen, A. Rosch, M. Vojta, and P. Wölfle, Fermi-liquid instabilities at magnetic quantum phase transitions, Rev. Mod. Phys. **79**, 1015 (2007).

[11] R. Ritz, M. Halder, M. Wagner, C. Franz, A. Bauer, and C. Pfleiderer, Formation of a topological non-Fermi liquid in MnSi, Nature (London) **497**, 231 (2013).

[12] S. Mühlbauer, B. Binz, F. Jonietz, C. Pfleiderer, A. Rosch, A. Neubauer, R. Georgii, and P. Böni, Skyrmion Lattice in a Chiral Magnet, Science **323**, 915 (2009).

[13] M. Z. Hasan and C. L. Kane, *Colloquium*: Topological insulators, Rev. Mod. Phys. **82**, 3045 (2010).

[14] X.-L. Qi and S.-C. Zhang, Topological insulators and superconductors, Rev. Mod. Phys. **83**, 1057 (2011).

[15] H. Rosner, D. Koudela, U. Schwarz, A. Handstein, M. Hanfland, I. Opahle, K. Koepernik, M. D. Kuz'min, K.-H. Müller, J. A. Mydosh, and M. Richter, Magneto-elastic lattice collapse in YCo_5, Nature Phys. **2**, 469 (2006).

[16] E. A. Yelland, J. M. Barraclough, W. Wang, K. V. Kamenev, and A. D. Huxley, High-field superconductivity at an electronic topological transition in URhGe, Nature Phys. **7**, 890 (2011).

[17] A. P. Ramirez, Strongly geometrically frustrated magnets, Annu. Rev. Mater. Sci. **24**, 453 (1994).

[18] W. Eerenstein, N. D. Mathur, and J. F. Scott, Multiferroic and magnetoelectric materials, Nature (London) **442**, 759 (2006).

[19] S.-W. Cheong and M. Mostovoy, Multiferroics: a magnetic twist for ferroelectricity, Nature Mater. **6**, 13 (2007).

[20] S. Thiel, G. Hammerl, A. Schmehl, C. W. Schneider, and J. Mannhart, Tunable Quasi-Two-Dimensional Electron Gases in Oxide Heterostructures, Science **313**, 5795 (2006).

[21] N. Reyren, S. Thiel, A. D. Caviglia, L. F. Kourkoutis, G. Hammerl, C. Richter, C. W. Schneider, T. Kopp, A.-S. Rüetschi, D. Jaccard, M. Gabay, D. A. Muller, J.-M. Triscone, and J. Mannhart, Superconducting Interfaces Between Insulating Oxides, Science **317**, 1196 (2007).

[22] B. A. Bernevig, T. L. Hughes, and S.-C. Zhang, Quantum Spin Hall Effect and Topological Phase Transition in HgTe Quantum Wells, Science **314**, 1757 (2006).

[23] M. König, S. Wiedmann, C. Brüne, A. Roth, H. Buhmann, L. W. Molenkamp, X.-L. Qi, and S.-C. Zhang, Quantum Spin Hall Insulator State in HgTe Quantum Wells, Science **318**, 766 (2007).

[24] S. Heinze, K. v. Bergmann, M. Menzel, J. Brede, A. Kubetzka, R. Wiesendanger, G. Bihlmayer, and S. Blügel, Spontaneous atomic-scale magnetic skyrmion lattice in two dimensions, Nature Phys. **7**, 713 (2011).

[25] N. Romming, C. Hanneken, M. Menzel, J. E. Bickel, B. Wolter, K. v. Bergmann, A. Kubetzka, and R. Wiesendanger, Writing and Deleting Single Magnetic Skyrmions, Science **341**, 636 (2013).

[26] J. Wang, J. B. Neaton, H. Zheng, V. Nagarajan, S. B. Ogale, B. Liu, D. Viehland, V. V. D. G. Schlom, U. V. Waghmare, N. A. Spaldin, K. M. Rabe, and M. W. R. Ramesh, Epitaxial $BiFeO_3$ Multiferroic Thin Film Heterostructures, Science **299**, 1719 (2003).

[27] R. Ramesh and N. A. Spaldin, Multiferroics: progress and prospects in thin films, Nature Mater. **6**, 21 (2007).

[28] J. E. Geusic, H. M. Marcos, and L. G. V. Uitert, Laser oscillations in Nd-doped yttrium aluminium, yttrium gallium and gadolinium garnets, Appl. Phys. Lett. **4**, 182 (1964).

[29] J. Ninkovic, G. Angloher, C. Bucci, C. Cozzini, T. Frank, D. Hauff, H. Kraus, B. Majorovits, V. Mikhailik, F. Petricca, F. Pröbst, Y. Ramachers, W. Rau, W. Seidel, and S. Uchaikin, $CaWO_4$ crystals as scintillators for cryogenic dark matter search, Nucl. Instrum. Methods Phys. Res. A **537**, 339 (2005).

[30] J. Nagamatsu, N. Nakagawa, T. Muranaka, Y. Zenitani, and J. Akimitsu, Superconductivity at 39 K in magnesium diboride, Nature (London) **410**, 63 (2001).

[31] P. Monthoux, D. Pines, and G. G. Lonzarich, Superconductivity without phonons, Nature (London) **450**, 1177 (2007).

[32] F.-C. Hsu, J.-Y. Luo, K.-W. Yeh, T.-K. Chen, T.-W. Huang, P. M. Wu, Y.-C. Lee, Y.-L. Huang, Y.-Y. Chu, D.-C. Yan, and M.-K. Wu, Superconductivity in the PbO-type structure α-FeSe, P. Natl. Acad. Sci. USA **105**, 14262 (2008).

[33] J. Paglione and R. L. Greene, High-temperature superconductivity in iron-based materials, Nature Phys. **6**, 645 (2010).

[34] C. Castelnovo, R. Moessner, and S. L. Sondhi, Magnetic monopoles in spin ice, Nature (London) **451**, 42 (2008).

[35] L. D. C. Jaubert and P. C. W. Holdsworth, Signature of magnetic monopole and Dirac string dynamics in spin ice, Nature Phys. **5**, 258 (2009).

[36] S. T. Bramwell, S. R. Giblin, S. Calder, R. Aldus, D. Prabhakaran, and T. Fennell, Measurement of the charge and current of magnetic monopoles in spin ice, Nature (London) **461**, 956 (2009).

[37] D. J. P. Morris, D. A. Tennant, S. A. Grigera, B. Klemke, C. Castelnovo, R. Moessner, C. Czternasty, M. Meissner, K. C. Rule, J.-U. Hoffmann, K. Kiefer, S. Gerischer, D. Slobinsky, and R. S. Perry, Dirac Strings and Magnetic Monopoles in the Spin Ice $Dy_2Ti_2O_7$, Science **326**, 411 (2009).

[38] T. Fennell, P. P. Deen, A. R. Wildes, K. Schmalzl, D. Prabhakaran, A. T. Boothroyd, R. J. Aldus, D. F. McMorrow, and S. T. Bramwell, Magnetic Coulomb Phase in the Spin Ice $Ho_2Ti_2O_7$, Science **326**, 415 (2009).

[39] L. Balents, Spin liquids in frustrated magnets, Nature (London) **464**, 199 (2010).

[40] X. Z. Yu, Y. Onose, N. Kanazawa, J. H. Park, J. H. Han, Y. Matsui, N. Nagaosa, and Y. Tokura, Real-space observation of a two-dimensional skyrmion crystal, Nature (London) **465**, 901 (2010).

[41] X. Z. Yu, N. Kanazawa, Y. Onose, K. Kimoto, W. Z. Zhang, S. Ishiwata, Y. Matsui, and Y. Tokura, Near room-temperature formation of a skyrmion crystal in thin-films of the helimagnet FeGe, Nature Mater. **10**, 106 (2011).

[42] S. Seki, X. Z. Yu, S. Ishiwata, and Y. Tokura, Observation of Skyrmions in a Multiferroic Material, Science **336**, 198 (2012).

[43] R. A. Borzi, S. A. Grigera, J. Farrell, R. S. Perry, S. J. S. Lister, S. L. Lee, D. A. Tennant, Y. Maeno, and A. P. Mackenzie, Formation of a Nematic Fluid at High Fields in $Sr_3Ru_2O_7$, Science **315**, 214 (2007).

[44] D. Hsieh, D. Qian, L. Wray, Y. Xia, Y. S. Hor, R. J. Cava, and M. Z. Hasan, A topological Dirac insulator in a quantum spin Hall phase, Nature (London) **452**, 970 (2008).

[45] H. Zhang, C.-X. Liu, X.-L. Qi, X. Dai, Z. Fang, and S.-C. Zhang, Topological insulators in Bi_2Se_3, Bi_2Te_3 and Sb_2Te_3 with a single Dirac cone on the surface, Nature Phys. **5**, 438 (2009).

[46] Y. Xia, D. Qian, D. Hsieh, L. Wray, A. Pal, H. Lin, A. Bansil, D. Grauer, Y. S. Hor, R. J. Cava, and M. Z. Hasan, Observation of a large-gap topological-insulator class with a single Dirac cone on the surface, Nature Phys. **5**, 398 (2009).

[47] Y. L. Chen, J. G. Analytis, J.-H. Chu, Z. K. Liu, S.-K. Mo, X. L. Qi, H. J. Zhang, D. H. Lu, X. Dai, Z. Fang, S. C. Zhang, I. R. Fisher, Z. Hussain, and Z.-X. Shen, Experimental Realization of a Three-Dimensional Topological Insulator, Bi_2Te_3, Science **325**, 178 (2009).

[48] L. W. M. Schreurs, H. M. Weijers, A. P. J. van Deursen, and A. R. de Vroomen, Growth and electrical properties of $ZrZn_2$ single crystals, Mater. Res. Bull. **24**, 1141 (1989).

[49] N. Kimura, M. Endo, T. Isshiki, S. Minagawa, A. Ochiai, H. Aoki, T. Terashima, S. Uji, T. Matsumoto, and G. G. Lonzarich, de Haas-van Alphen Effect in $ZrZn_2$ under Pressure: Crossover between Two Magnetic States, Phys. Rev. Lett. **92**, 197002 (2004).

[50] R. P. Smith, M. Sutherland, G. G. Lonzarich, S. S. Saxena, N. Kimura, S. Takashima, M. Nohara, and H. Takagi, Marginal breakdown of the Fermi-liquid state on the border of metallic ferromagnetism, Nature (London) **455**, 1220 (2008).

[51] S. N. Toubektsis and E. K. Polychroniadis, Growth and structural considerations on single $TlBiSe_2$ crystals, J. Cryst. Growth **84**, 316 (1987).

[52] M. Richardson, The Partial Equilibrium of the Fe-Ge System in the Range 40-72 at. % Ge, and the Crystallisation of some Iron Germanides by Chemical Transport Reaction, Acta Chem. Scand. **21**, 2305 (1967).

[53] V. P. Gnezdilov, K. V. Lamonova, Y. G. Pashkevich, P. Lemmens, H. Berger, F. Bussy, and S. L. Gnatchenko, Magnetoelectricity in the ferrimagnetic Cu_2OSeO_3: symmetry analysis and Raman scattering study, Low Temp. Phys. **36**, 550 (2010).

[54] I. Mazilu, M. Frontzek, W. Löser, G. Behr, A. Teresiak, and L. Schultz, Single crystal growth of the Er_2PdSi_3 intermetallic compound, J. Cryst. Growth **275**, 103 (2005).

[55] H. Okamoto, Mn-Si (Manganese-Silicon), J. Phase Equilib. **12**, 505 (1991).

[56] E. Kato and S. Nunoue, *Fe-Ge (iron-germanium). Phase Diagrams of Binary Iron Alloys* (ASM International, Materials Park, OH, 1993) p. 156.

[57] H. Okamoto, *Desk Handbook: Phase Diagrams for Binary Alloys, Second Edition* (ASM International, 2010).

[58] H. Wilhelm, M. Schmidt, R. Cardoso-Gil, U. Burkhardt, M. Hanfland, U. Schwarz, and L. Akselrud, Structural investigations of ϵ-FeGe at high pressure and low temperature, Sci. Tech. Adv. Mater. **8**, 416 (2007).

[59] P. Villars, A. Prince, and H. Okamoto, *Handbook of Ternary Alloy Phase Diagrams* (ASM International, 1995).

[60] A. Neubauer, *Single crystal growth of intermetallic compounds with unusual low temperature properties*, Ph.D. thesis, Technische Unitversität München (2010).

[61] W. Münzer, *Einkristallzüchtung und magnetische Eigenschaften von MnSi und* $Fe_{1-x}Co_xSi$, Diploma thesis, Technische Unitversität München (2008).

[62] A. Bauer, *Quantenphasenübergänge und Skyrmion-Gitter in* $Mn_{1-x}Fe_xSi$ *und* $Mn_{1-x}Co_xSi$, Diploma thesis, Technische Unitversität München (2009).

[63] G. Benka, *UHV-Compatible Arc Melting Furnace and Annealing Oven for Materials with Exotic Electronic Properties*, Master's thesis, Technische Unitversität München (2013).

[64] R. Korntner, *Suche nach topologischen Effekten in intermetallischen Verbindungen*, Diploma thesis, Technische Unitversität München (2011).

[65] A. Neubauer, J. Bœuf, A. Bauer, B. Russ, H. v. Löhneysen, and C. Pfleiderer, Ultra-high vacuum compatible image furnace, Rev. Sci. Instrum. **82**, 013902 (2011).

[66] G. Behr, R. Voigtlander, A. Horst, R. Morgner, and F. Fischer, German Patent DE 10 2006 019 807.7 (21.04.2006), PCT/EP2007/05157 (07.03.2007).

[67] J. J. Tonnies and K. A. Gschneidner Jr., Preparation of lanthanide single crystals; praseodymium, neodymium, and lutetium, J. Cryst. Growth **10**, 013902 (1971).

[68] N. R. Bernhoeft, G. G. Lonzarich, P. W. Mitchell, and D. M. Paul, Magnetic excitations in Ni_3Al at low energies and long wavelengths, Phys. Rev. B **28**, 422 (1983).

[69] T. I. Sigfusson, N. R. Bernhoeft, and G. G. Lonzarich, The de Haas-van Alphen effect, exchange splitting and Curie temperature in the weak itinerant ferromagnetic Ni_3Al, J. Phys. F **14**, 2141 (1984).

[70] R. G. Jordan, Electrotransport in solid metal systems, Contemp. Phys. **15**, 375 (1974).

[71] P. S. Ho and T. Kwok, Electromigration in metals, Rep. Prog. Phys. **52**, 301 (1989).

[72] Y. Haga, T. Honma, E. Yamamoto, H. Ohkuni, Y. Onuki, M. Ito, and N. Kimura, Purification of Uranium Metal using the Solid State Electrotransport Method under Ultrahigh Vacuum, Jpn. J. Appl. Phys. **37**, 3604 (1998).

[73] D. W. Jones, J. S. Abell, D. Fort, and J. K. Hulbert, Preparation of rare earth materials, crystals and specimens, J. Magn. Magn. Mater. **29**, 20 (1982).

[74] D. Fort, The purification and crystal growth of rare earth metals using solid state electrotransport, J. Less. Comm. Met. **134**, 45 (1987).

[75] C. K. Gupta and N. Krishnamurthy, *Extractive Metallurgy of Rare Earths, Chapter 5* (CRC Press, 2005).

[76] The Ames Laboratory: Rare Earth Metals, https://www.ameslab.gov/rare-earth-metals, U.S. Department of Energy (2013).

[77] D. Braithwaite, T. Fukuhara, A. Demuer, I. Sheikin, S. Kambe, J.-P. Brison, K. Maezawa, T. Naka, and J. Flouquet, Superconductivity, upper critical field and normal state resistivity in $CeNi_2Ge_2$ under pressure, J. Phys.: Condens. Matter **12**, 1339 (2000).

[78] C. A. King and S. V. Brown, The combination of electrotransport and zone refining techniques for the growth and purification of metallic crystals, Rev. Sci. Instrum. **63**, 3185 (1992).

[79] E. U. Malang, C. S. Oglesby, T. Siegrist, and E. Bucher, Purification and single crystal growth of niobium by combined zone refining and electrotransport, Physica B **204**, 363 (1995).

[80] P. Milde, D. Köhler, J. Seidel, L. M. Eng, A. Bauer, A. Chacon, J. Kindervater, S. Mühlbauer, C. Pfleiderer, S. Buhrandt, C. Schütte, and A. Rosch, Unwinding of a Skyrmion Lattice by Magnetic Monopoles, Science **340**, 1076 (2013).

[81] M. Wagner, A. Neubauer, M. Schulz, A. Senyshyn, K. Hradil, A. Bauer, R. Korntner, S. Gottlieb-Schönmeyer, R. Jungwirth, H. Ceeh, C. Hugenschmidt, G. Behr, J. Kübler, S. Chadov, C. Felser, P. Böni, and C. Pfleiderer, Incipient Quantum Criticality in the Zero-Gap Semiconductor Fe_2TiSn, unpublished (2014).

[82] T. Graf, C. Felser, and S. S. P. Parkin, Simple rules for the understanding of Heusler compounds, Prog. Solid State Ch. **39**, 1 (2011).

[83] A. Senyshyn, A. Bauer, C. Franz, R. Bozhanova, S. Gottlieb-Schönmeyer, and C. Pfleiderer, Long wavelength order in non-centrosymmetric $EuPtSi_3$, unpublished (2014).

[84] M. Rahn, *Search for Topological Properties in Multi-k Magnetic Structures*, Diploma thesis, Technische Unitversität München (2013).

[85] A. Bauer, A. Neubauer, C. Franz, W. Münzer, M. Garst, and C. Pfleiderer, Quantum phase transitions in single-crystal $Mn_{1-x}Fe_xSi$ and $Mn_{1-x}Co_xSi$: Crystal growth, magnetization, ac susceptibility, and specific heat, Phys. Rev. B **82**, 064404 (2010).

[86] A. Bauer, M. Garst, and C. Pfleiderer, Specific Heat of the Skyrmion Lattice Phase and Field-Induced Tricritical Point in MnSi, Phys. Rev. Lett. **110**, 177207 (2013).

[87] M. Gangl, *Thermische Transporteigenschaften von $Mn_{1-x}Fe_xSi$*, Master's thesis, Technische Unitversität München (2013).

[88] A. Aharoni, Demagnetizing factors for rectangular ferromagnetic prisms, J. Appl. Phys. **83**, 3432 (1998).

[89] W. Scholz, Calculator for the demagnetizing factor of a uniformly magnetized ferromagnetic prism, http://www.magpar.net/static/magpar/doc/html/demagcalc.html, GNU General Public License (2010).

[90] M. Wagner, *Untersuchung elektronisch korrelierter Systeme mit nicht-trivialer Topologie*, Ph.D. thesis, Technische Unitversität München (to be published in 2014).

[91] M. Arita, K. Shimada, Y. Takeda, M. Nakatake, H. Namatame, M. Taniguchi, H. Negishi, T. Oguchi, T. Saitoh, A. Fujimori, and T. Kanomata, Angle-resolved photoemission study of the strongly correlated semiconductor FeSi, Phys. Rev. B **77**, 205117 (2008).

[92] J. A. Weber, P. Böni, H. Ceeh, M. Leitner, and C. Hugenschmidt, First 2D-ACAR Measurements on Cu with the new Spectrometer at TUM, J. Phys.: Conf. Ser. **443**, 012092 (2013).

[93] F. Heusler, Über die ferromagnetischen Eigenschaften von Legierungen unmagnetischer Metalle, Verhandlungen Der Deutschen Physikalischen Gesellschaft **5**, 219 (1903).

[94] B. Michelutti, R. P. de la Bathie, E. du Tremolet de Lacheisserie, and A. Waintal, Magnetization, magnetocrystalline anisotropy, magnetostriction and elastic constants of the Heusler alloy: Cu_2MnAl, Solid State Commun. **25**, 163 (1978).

[95] W. G. Williams, *Polarized Neutrons* (Clarendon Press, Oxford, New York, 1988).

[96] A. Delapalme, J. Schweizer, G. Couderchon, and R. P. de la Bathie, Étude de l'alliage de Heusler (Cu_2MnAl) comme monochromateur de neutrons polarisés, Nucl. Instrum. Methods **95**, 589 (1971).

[97] A. Freund, R. Pynn, W. G. Stirling, and C. M. E. Zeyen, Vertically focussing Heusler alloy monochromators for polarised Neutrons, Physica B & C **120**, 86 (1983).

[98] P. Courtois, Characterization of Heusler crystals for polarized neutrons monochromators, Physica B **267–268**, 363 (1999).

[99] P. Courtois, B. Hamelin, and K. H. Andersen, Production of copper and Heusler alloy Cu_2MnAl mosaic single crystals for neutron monochromators, Nucl. Instrum. Methods Phys. Res. A **529**, 157 (2004).

[100] A. Neubauer, F. Jonietz, M. Meven, R. Georgii, G. Brandl, G. Behr, P. Böni, and C. Pfleiderer, Optical floating zone growth of high-quality Cu_2MnAl single crystals, Nucl. Instrum. Methods Phys. Res. A **688**, 66 (2012).

[101] C. Franz, *Untersuchung von Quantenphasenübergängen bei fehlender Inversionssymmetrie*, Ph.D. thesis, Technische Unitversität München (2014).

[102] R. Bozhanova, *Single crystal growth of f-electron compounds with unusual low temperature properties*, Master's thesis, Technische Unitversität München (2012).

[103] N. Kumar, S. K. Dhar, A. Thamizhavel, P. Bonville, and P. Manfrinetti, Magnetic properties of $EuPtSi_3$ single crystals, Phys. Rev. B **81**, 144414 (2010).

[104] P. Morin and D. Schmitt, Competition between multi-q antiferromagnetic structures in cubic rare earth-copper compounds, J. Magn. Magn. Mater. **21**, 243 (1980).

[105] T. Moriya, Recent progress in the theory of itinerant electron magnetism, J. Magn. Magn. Mater. **14**, 1 (1979).

[106] G. G. Lonzarich and L. Taillefer, Effect of spin fluctuations on the magnetic equation of state of ferromagnetic or nearly ferromagnetic metals, J. Phys. C: Solid State **18**, 4339 (1985).

[107] T. Moriya, Theory of itinerant electron magnetism, J. Magn. Magn. Mater. **100**, 261 (1991).

[108] S. Tomiyoshi and H. Watanabe, Helical Spin Structure of Mn_3Si, J. Phys. Soc. Jpn. **39**, 295 (1975).

[109] C. Pfleiderer, Are Mn_3Si and CuMnSb antiferromagnetic half-metals? Physica B **329–333**, 1085 (2003).

[110] P. G. Niklowitz, P. L. Alireza, M. J. Steiner, G. G. Lonzarich, D. Braithwaite, G. Knebel, J. Flouquet, and J. A. Wilson, Unconventional resistivity at the border of metallic antiferromagnetism in NiS_2, Phys. Rev. B **77**, 115135 (2008).

[111] M. Doerr, J. Bœuf, C. Pfleiderer, M. Rotter, N. Kozlova, D. Eckert, P. Kerschl, K.-H. Müller, and M. Loewenhaupt, Search for half-metallic antiferromagnetism using pulsed magnetic fields: experimental investigation of Mn_3Si, CuMnSb and PdMnTe, Physica B **346–347**, 137 (2004).

[112] J. Bœuf, C. Pfleiderer, and A. Faißt, Low-temperature properties of the semi-Heusler compound CuMnSb, Phys. Rev. B **74**, 024428 (2006).

[113] A. Bauer, A. Regnat, C. G. F. Blum, S. Gottlieb-Schönmeyer, B. Pedersen, M. Meven, S. Wurmehl, J. Kuneš, and C. Pfleiderer, Low-temperature properties of single-crystal CrB_2, Phys. Rev. B **90**, 064414 (2014).

[114] W. G. Jr. and S. B. Soffer, A galvanomagnetic investigation of TiB_2, NbB_2 and ZrB_2, J. Phys. Chem. Solids **36**, 627 (1975).

[115] D.-C. Tian and X.-B. Wang, Electronic structure and equation of state of TiB_2, J. Phys.: Condens. Matter **4**, 8765 (1992).

[116] S. H. Liu, L. Kopp, W. B. England, and H. W. Myron, Energy bands, electronic properties, and magnetic ordering of CrB_2, Phys. Rev. B **11**, 3463 (1975).

[117] D. R. Armstrong, The electronic structure of the first-row transition-metal diborides, Theor. Chim. Acta **64**, 137 (1983).

[118] X.-B. Wang, D.-C. Tian, and L.-L. Wang, The electronic structure and chemical stability of the AlB_2-type transition-metal diborides, J. Phys.: Condens. Matter **6**, 10185 (1994).

[119] P. Vajeeston, P. Ravindran, C. Ravi, and R. Asokamani, Electronic structure, bonding, and ground-state properties of AlB_2-type transition-metal diborides, Phys. Rev. B **63**, 045115 (2001).

[120] H. J. Choi, D. Roundy, H. Sun, M. L. Cohen, and S. G. Louie, The origin of the anomalous superconducting properties of MgB_2, Nature (London) **418**, 758 (2001).

[121] P. C. Canfield and G. W. Crabtree, Magnesium Diboride: Better Late than Never, Phys. Today **56**, 34 (2003).

[122] A. Yamamoto, C. Takao, T. Masui, M. Izumi, and S. Tajima, High-pressure synthesis of superconducting $Nb_{1-x}B_2$ ($x = 0$–0.48) with the maximum $T_c = 9.2\,\mathrm{K}$, Physica C **383**, 197 (2002).

[123] R. Escamilla, O. Lovera, T. Akachi, A. Durán, R. Falconi, F. Morales, and R. Escudero, Crystalline structure and the superconducting properties of NbB_{2+x}, J. Phys.: Condens. Matter **16**, 5979 (2004).

[124] C. A. Nunes, D. Kaczorowski, P. Rogl, M. R. Baldissera, P. A. Suzuki, G. C. Coelho, A. Grytsiv, G. André, F. Boureé, and S. Okada, The NbB_2-phase revisited: Homogeneity range, defect structure, superconductivity, Acta Mater. **53**, 3679 (2005).

[125] V. A. Gasparov, N. S. Sidorov, I. I. Zver'kova, and M. P. Kulakov, Electron transport in diborides: Observation of superconductivity in ZrB_2, JETP Lett. **73**, 532 (2001).

[126] V. A. Gasparov, N. S. Sidorov, and I. I. Zver'kova, Two-gap superconductivity in ZrB_{12}: Temperature dependence of critical magnetic fields in single crystals, Phys. Rev. B **73**, 094510 (2006).

[127] J. M. Vandenberg, B. T. Matthias, E. Corenzwit, and H. Barz, Superconductivity of some binary and ternary transition-metal borides, Mater. Res. Bull. **10**, 889 (1975).

[128] Y. Singh, A. Niazi, M. D. Vannette, R. Prozorov, and D. C. Johnston, Superconducting and normal-state properties of the layered boride OsB_2, Phys. Rev. B **76**, 214510 (2007).

[129] B. J. Suh, X. Zong, Y. Singh, A. Niazi, and D. C. Johnston, ^{11}B NMR in the layered diborides OsB_2 and RuB_2, Phys. Rev. B **76**, 144511 (2007).

[130] V. V. Novikov and A. V. Matovnikov, Low-temperature heat capacity of dysprosium diboride, J. Therm. Anal. Calorim. **88**, 597 (2007).

[131] V. V. Novikov, T. A. Chukina, and A. A. Verevkin, Anomalies in thermal expansion of rare-earth diborides in the temperature range of magnetic phase transformations, Phys. Solid State **52**, 364 (2010).

[132] M. C. Cadeville, Proprietes magnetiques des diborures de manganese et de chrome: MnB_2 et CrB_2, J. Phys. Chem. Solids **27**, 667 (1966).

[133] M. Kasaya and T. Hihara, Magnetic Structure of MnB_2, J. Phys. Soc. Jpn. **29**, 336 (1970).

[134] E. Legrand and S. Neov, Neutron diffraction study of MnB_2, Solid State Commun. **10**, 883 (1972).

[135] R. G. Barnes and R. B. Creel, Chromium-like antiferromagnetic behavior of CrB_2, Phys. Lett. A **29**, 203 (1969).

[136] J. Castaing, R. Caudron, G. Toupance, and P. Costa, Electronic structure of transition metal diborides, Solid State Commun. **7**, 1453 (1969).

[137] F. Borsa and R. G. Lecander, Enhancement of the B^{11} nuclear relaxation in CrB_2 near the antiferromagnetic transition, Solid State Commun. **20**, 389 (1976).

[138] Y. Kitaoka, H. Yasuoka, T. Tanaka, and Y. Ishizawa, Nuclear magnetic resonance of ^{11}B in CrB_2, Solid State Commun. **26**, 203 (1978).

[139] Y. Kitaoka and H. Yasuoka, NMR Investigations on the Spin Fluctuations in Itinerant Antiferromagnets III. CrB_2, J. Phys. Soc. Jpn. **49**, 493 (1980).

[140] Y. Nishihara, M. Tokumoto, Y. Yamaguchi, and S. Ogawa, Magneto-Volume Effect of the Interant-Electron Antiferromagnet CrB_2, J. Phys. Soc. Jpn. **56**, 1562 (1987).

[141] A. V. Fedorchenko, G. E. Grechnev, A. S. Panfilov, A. V. Logosha, I. V. Svechkarev, V. B. Filippov, A. B. Lyashchenko, and A. V. Evdokimova, Anisotropy of the magnetic properties and the electronic structure of transition-metal diborides, Low Temp. Phys. **35**, 862 (2009).

[142] S. Funahashi, Y. Hamaguchi, T. Tanaka, and E. Bannai, Helical magnetic structure in CrB_2, Solid State Commun. **23**, 859 (1977).

[143] C. Michioka, Y. Itoh, K. Yoshimura, Y. Watabe, Y. Kousaka, H. Ichikawa, and J. Akimitsu, NMR studies of single crystal chromium diboride, J. Magn. Magn. Mater. **310**, e620 (2007).

[144] K. I. Portnoi, V. M. Romashov, and I. V. Romanovich, Diagram of state of the chromium-boron system, Sov. Powder Metall. **8**, 298 (1969).

[145] J. Castaing, P. Costa, M. Heritier, and P. Lederer, Spin fluctuation effects in nearly antiferromagnetic vanadium and chromium diborides, J. Phys. Chem. Solids **33**, 533 (1972).

[146] J. Castaing, J. Danan, and M. Rieux, Calorimetric and resistive investigation of the magnetic properties of CrB_2, Solid State Commun. **6**, 563 (1972).

[147] C. N. Guy, The electronic properties of chromium borides, J. Phys. Chem. Solids **37**, 1005 (1976).

[148] T. Tanaka, H. Nozaki, E. Bannai, Y. Ishizawa, S. Kawai, and T. Yamane, Preparation and properties of CrB_2 single crystals, J. Less-Common Met. **50**, 15 (1976).

[149] G. Balakrishnan, S. Majumdar, M. R. Lees, and D. M. Paul, Single crystal growth of using a high-temperature image furnace, J. Cryst. Growth **274**, 294 (2005).

[150] S. Okada, K. Kudou, K. Iizumi, K. Kudaka, I. Higashi, and T. Lundström, Single-crystal growth and properties of CrB, Cr_3B_4, Cr_2B_3 and CrB_2 from high-temperature aluminum solutions, J. Cryst. Growth **166**, 429 (1996).

[151] J. Bœuf, *Untersuchungen an den antiferromagnetischen Übergangsmetallverbindungen* Mn_3Si*, CuMnSb und PdMnTe*, Ph.D. thesis, Universität (TH) Karlsruhe (2003).

[152] M. Brasse, L. Chioncel, J. Kuneš, A. Bauer, A. Regnat, C. G. F. Blum, S. Wurmehl, C. Pfleiderer, M. A. Wilde, and D. Grundler, De Haas-van Alphen effect and Fermi surface properties of single crystal CrB_2, Phys. Rev. B **88**, 155138 (2013).

[153] A. Regnat, A. Bauer, B. Pedersen, M. Meven, A. Senyshyn, and C. Pfleiderer, Magnetic order of CrB_2 determined by neutron diffraction, unpublished (2014).

[154] G. Brandl, A. Bauer, A. Regnat, A. Schneidewind, P. Böni, and C. Pfleiderer, Inelastic neutron scattering in CrB_2, unpublished (2014).

[155] H. Okamoto, B-Cr (Boron-Chromium), J. Phase Equilib. **24**, 480 (2003).

[156] Center for Neutron Research, http://www.ncnr.nist.gov/resources/n-lengths, National Institute of Standards and Technology (2013).

[157] V. F. Sears, Neutron scattering lengths and cross sections, Neutron News **3**, 26 (1992).

[158] A. L. Trego and A. R. Mackintosh, Antiferromagnetism in Chromium Alloys. II. Transport Properties, Phys. Rev. **166**, 495 (1968).

[159] E. Fawcett, Spin-density-wave antiferromagnetism in chromium, Rev. Mod. Phys. **60**, 209 (1988).

[160] M. W. McElfresh, J. D. Thompson, J. O. Willis, M. B. Maple, T. Kohara, and M. S. Torikachvili, Effect of pressure on competing electronic correlations in the heavy-electron system URu_2Si_2, Phys. Rev. B **35**, 43 (1987).

[161] A. L. Dawson, W. R. Datars, J. D. Garrett, and F. S. Razavi, Electrical transport in URu_2Si_2, J. Phys.: Condens. Matter **1**, 6817 (1989).

[162] N. H. Andersen, *Crystalline Electric Field and Structural Effects in f-Electron Systems* (Plenum, New York, 1980) p. 373.

[163] F. Bouquet, R. A. Fisher, N. E. Phillips, D. G. Hinks, and J. D. Jorgensen, Specific Heat of $Mg^{11}B_2$: Evidence for a Second Energy Gap, Phys. Rev. Lett. **87**, 047001 (2001).

[164] A. Huxley, I. Sheikin, E. Ressouche, N. Kernavanois, D. Braithwaite, R. Calemczuk, and J. Flouquet, UGe_2: A ferromagnetic spin-triplet superconductor, Phys. Rev. B **63**, 144519 (2001).

[165] K. Kadowaki and S. B. Woods, Universal relationship of the resistivity and specific heat in heavy-Fermion compounds, Solid State Commun. **58**, 507 (1986).

[166] A. C. Jacko, J. O. Fjærestad, and B. J. Powell, A unified explanation of the Kadowaki-Woods ratio in strongly correlated metals, Nature Phys. **5**, 422 (2009).

[167] S. M. Hayden, R. Doubble, G. Aeppli, T. G. Perring, and E. Fawcett, Strongly Enhanced Magnetic Excitations Near the Quantum Critical Point of $Cr_{1-x}V_x$ and Why Strong Exchange Enhancement Need Not Imply Heavy Fermion Behavior, Phys. Rev. Lett. **84**, 999 (2000).

[168] T. Moriya and K. Ueda, Antiferromagnetic spin fluctuation and superconductivity, Rep. Prog. Phys. **66**, 1299 (2003).

[169] C. Pfleiderer, J. Bœuf, and H. v. Löhneysen, Stability of antiferromagnetism at high magnetic fields in Mn_3Si, Phys. Rev. B **65**, 172404 (2002).

[170] M. Sutherland, R. P. Smith, N. Marcano, Y. Zou, S. E. Rowley, F. M. Grosche, N. Kimura, S. M. Hayden, S. Takashima, M. Nohara, and H. Takagi, Transport and thermodynamic evidence for a marginal Fermi-liquid state in $ZrZn_2$, Phys. Rev. B **85**, 035118 (2012).

[171] H. Sasakura, K. Suzuki, and Y. Masuda, Magnetization and Electrical Resistivity in Itinerant Electron Ferromagnet Ni_3Al, J. Phys. Soc. Jpn. **53**, 352 (1984).

[172] P. G. Niklowitz, F. Beckers, G. G. Lonzarich, G. Knebel, B. Salce, J. Thomasson, N. Bernhoeft, D. Braithwaite, and J. Flouquet, Spin-fluctuation-dominated electrical transport of Ni_3Al at high pressure, Phys. Rev. B **72**, 024424 (2005).

[173] A. C. Abhyankar and S. N. Kaul, Effect of off-stoichiometry and site disorder on the properties of Ni_3Al: I. Electrical and magneto-transport, J. Phys.: Condens. Matter **20**, 445227 (2008).

[174] L. Andersson, B. Dellby, and H. P. Myers, Ferromagnetic MnB_2, Solid State Commun. **4**, 77 (1966).

[175] M. Kasaya, T. Hihara, and Y. Kōi, NMR Study in MnB_2, J. Phys. Soc. Jpn. **26**, 1549 (1969).

[176] S. Khmelevskyi and P. Mohn, Magnetic ordering in MnB_2: an ab initio study, Solid State Commun. **113**, 509 (2000).

[177] S. Khmelevskyi and P. Mohn, Covalent magnetism, exchange interactions and anisotropy of the high temperature layered antiferromagnet MnB_2, J. Phys.: Condens. Matter **24**, 016001 (2012).

[178] A. R. Williams, R. Zeller, V. L. Moruzzi, C. D. Gelatt, and J. Kübler, Covalent magnetism: An alternative to the Stoner model, J. Appl. Phys. **52**, 2067 (1981).

[179] R. A. de Groot, F. M. Mueller, P. G. van Engen, and K. H. J. Buschow, New Class of Materials: Half-Metallic Ferromagnets, Phys. Rev. Lett. **50**, 2024 (1983).

[180] J. Kübler, A. R. William, and C. B. Sommers, Formation and coupling of magnetic moments in Heusler alloys, Phys. Rev. B **28**, 1745 (1983).

[181] H. van Leuken and R. A. de Groot, Half-Metallic Antiferromagnets, Phys. Rev. Lett. **74**, 1171 (1995).

[182] T. Jeong, R. Weht, and W. E. Pickett, Semimetallic antiferromagnetism in the half-Heusler compound CuMnSb, Phys. Rev. B **71**, 184103 (2005).

[183] K. Endo, Magnetic Studies of Cl_b-Compounds CuMnSb, PdMnSb and Cu_{1-x}(Ni or Pd$)_x$MnSb, J. Phys. Soc. Jpn. **29**, 643 (1970).

[184] S. Chadov, X. Qi, J. Kübler, G. H. Fecher, C. Felser, and S.-C. Zhang, Tunable multifunctional topological insulators in ternary Heusler compounds, Nature Mater. **9**, 541 (2010).

[185] H. Lin, L. A. Wray, Y. Xia, S. Xu, S. Jia, R. J. Cava, A. Bansil, and M. Z. Hasan, Half-Heusler ternary compounds as new multifunctional experimental platforms for topological quantum phenomena, Nature Mater. **9**, 546 (2010).

[186] D. T. Adroja and S. K. Malik, Valence fluctuation and heavy fermion behaviour in rare earth and actinide based compounds, J. Magn. Magn. Mater. **100**, 126 (1991).

[187] K. Gofryk, D. Kaczorowski, T. Plackowski, A. Leithe-Jasper, and Y. Grin, Magnetic and transport properties of the rare-earth-based Heusler phases RPdZ and $R\mathrm{Pd}_2Z$ (Z = Sb, Bi), Phys. Rev. B **72**, 094409 (2005).

[188] F. Casper and C. Felser, Magnetic and Electronic Properties of RENiBi (RE =Pr, Sm, Gd-Tm, Lu) Compounds, Z. anorg. allg. Chem. **634**, 2418 (2008).

[189] C. L. Seaman, N. R. Dilley, M. C. de Andrade, J. Herrmann, M. B. Maple, and Z. Fisk, Superconductivity and magnetism in the Heusler alloys $M\mathrm{Pd}_2\mathrm{Pb}$ (M = rare earth, Th, and U), Phys. Rev. B **53**, 2651 (1996).

[190] K. Gofryk, D. Kaczorowski, and A. Czopnik, Magnetic and transport properties of $\mathrm{UPd}_2\mathrm{Sb}$, Solid State Commun. **133**, 625 (2005).

[191] M. Ishikawa, J.-L. Jorda, and A. Junod, *Superconductivity in d- and f-Band Metals* (Kernforschungszentrum Karlsruhe, Germany, 1982).

[192] J. H. Wernick, G. W. Hull, T. H. Geballe, J. E. Bernardini, and J. V. Waszczak, Superconductivity in ternary Heusler intermetallic compounds, Mater. Lett. **2**, 90 (1983).

[193] M. J. Johnson and R. N. Shelton, Pressure effects on the superconductivity of ternary rare earth palladium Heusler alloys, Solid State Commun. **52**, 839 (1986).

[194] H. A. Kierstead, B. D. Dunlap, S. K. Malik, A. M. Umarji, and G. K. Shenoy, Coexistence of ordered magnetism and superconductivity in $\mathrm{Pd}_2\mathrm{YbSn}$, Phys. Rev. B **32**, 135 (1985).

[195] R. N. Shelton, L. S. Hausermann-Berg, M. J. Johnson, P. Klavins, and H. D. Yang, Coexistence of superconductivity and long-range magnetic order in $\mathrm{ErPd}_2\mathrm{Sn}$, Phys. Rev. B **34**, 199 (1986).

[196] P. J. Webster and R. S. Tebble, Magnetic and Chemical Order in $\mathrm{Pd}_2\mathrm{MnAl}$ in Relation to Order in the Heusler Alloys $\mathrm{Pd}_2\mathrm{MnIn}$, $\mathrm{Pd}_2\mathrm{MnSn}$, and $\mathrm{Pd}_2\mathrm{MnSb}$, J. Appl. Phys. **39**, 471 (1968).

[197] F. A. Hames and J. Crangle, Ferromagnetism in Heusler-Type Alloys Based on Platinum-Group or Palladium-Group Metals, J. Appl. Phys. **42**, 1336 (1971).

[198] C. C. M. Campbell, Hyperfine field systematics in Heusler alloys, J. Phys. F: Met. Phys. **5**, 1931 (1975).

[199] R. B. Helmholdt, R. A. de Groot, F. M. Mueller, P. G. van Engen, and K. H. J. Buschow, Magnetic and crystallographic properties of several $\mathrm{C1}_b$ type Heusler compounds, J. Magn. Magn. Mater. **43**, 249 (1984).

[200] H. Masumoto, K. Watanabe, and S. Ohnuma, New Compounds of the Cl_b, Cl Types of IrMnSb and PdMnTe, New $L2_1$(Heusler) Type of $\mathrm{Ir}_2\mathrm{MnGa}$ Alloys, and Magnetic Properties, J. Phys. Soc. Jpn. **32**, 570 (1972).

[201] H. Masumoto, K. Watanabe, and S. Ohnuma, On Cl_b Type Intermetallic Compound PdMnTe and Its Magnetic Properties, T. Jpn. I. Met. **15**, 135 (1974).

[202] R. B. Helmholdt and K. H. J. Buschow, A neutron diffraction and magnetization study of PdMnTe, J. Less-Common Met. **123**, 169 (1986).

[203] D. P. Oxley, R. S. Tebble, C. T. Slack, and K. C. Williams, An Anti-ferromagnetic Heusler Alloy, Cu_2MnSb, Nature (London) **194**, 465 (1962).

[204] K. Endo, H. Matsuda, K. Ooiwa, and K. Itoh, Antiferromagnetism in a Heusler Alloy Fe_2VSi, J. Phys. Soc.Jpn. **64**, 2329 (1995).

[205] S. N. M. Kawakami and T. Fujita, Tetragonal Deformation in Fe_2VSi at Low Temperatures, J. Phys. Soc.Jpn. **64**, 4081 (1995).

[206] H. Nishihara, K. Ono, K. U. Neumann, K. R. A. Ziebeck, and T. Kanomata, Complex magnetism in Fe_2VSi, Physica B **329–333**, 1107 (2003).

[207] S. Tomiyoshi, E. R. Cowley, and H. Onodera, Anomalous behavior of higher-harmonic spin density waves in Mn_3Si, Phys. Rev. B **73**, 024416 (2006).

[208] E. R. Cowley, S. Tomiyoshi, Y. Yamaguchi, M. Ohashi, and G. Shirane, Magnetic excitations in Fe-doped Mn_3Si, J. Appl. Phys **61**, 3403 (1987).

[209] H. Miki, K. Ohoyama, S. Funahashi, S. Tomiyoshi, and Y. Yamaguchi, Crystallographic and magnetic structure of the itinerant-electron antiferromagnets $Mn_{3-x}T_xSi$ ($T =$Cr, Fe), Physica B **213–214**, 360 (1995).

[210] M. Hortamani, L. Sandratskii, P. Zahn, and I. Mertig, Physical origin of the incommensurate spin spiral structure in Mn_3Si, J. Appl. Phys. **105**, 07E506 (2009).

[211] C. Pfleiderer, Experimental studies of weakly magnetic transition metal compounds, J. Magn. Magn. Mater. **226-230**, 23 (2001).

[212] S. Tomiyoshi, S. Funahashi, and Y. Yamaguchi, Magnetic excitations in Mn_3Si, Physica B & C **120**, 143 (1983).

[213] S. Tomiyoshi, Y. Yamaguchi, M. Ohashi, E. R. Cowley, and G. Shirane, Magnetic excitations in the itinerant antiferromagnets Mn_3Si and Fe-doped Mn_3Si, Phys. Rev. B **36**, 2181 (1987).

[214] Y. Yamaguchi, T. R. Thurston, H. Miki, and S. Tomiyoshi, Paramagnetic scattering of neutrons from an itinerant electron antiferromagnet Mn_3Si, Physica B & C **213–214**, 363 (1995).

[215] F. Steckel, S. Rodan, R. Hermann, C. G. F. Blum, S. Wurmehl, B. Büchner, and C. Hess, Spin density wave order and fluctuations in Mn_3Si: a transport study, arXiv:1309.1636 (2013).

[216] S. Fujii, S. Ishida, and S. Asano, A Half-Metallic Band Structure and Fe_2MnZ ($Z =$Al, Si, P), J. Phys. Soc. Jpn. **64**, 185 (1995).

[217] T. Jeong, Magnetic properties of Mn_3Si from first-principles studies, Physica B **407**, 888 (2012).

[218] R. Hermann, H. Wendrock, S. Rodan, U. K. Rößler, C. G. F. Blum, S. Wurmehl, and B. Büchner, Single crystal growth of antiferromagnetic Mn_3Si by a two-phase RF floating-zone method, J. Cryst. Growth **363**, 1 (2013).

[219] H. Nowotny and B. Glatzl, Neue Vertreter ternärer Verbindungen mit $C1$-Struktur, Monatsh. Chem. **83**, 237 (1952).

[220] L. Castelliz, Über eine Mischkristallreihe zwischen zwei terären Vertretern des $C1$-Typs, Monatsh. Chem. **83**, 1314 (1952).

[221] M. J. Otto, R. A. M. van Woerden, P. J. van der Valk, J. Wijngaard, C. F. van Bruggen, C. Haas, and K. H. J. Buschow, Half-metallic ferromagnets. I. Structure and magnetic properties of NiMnSb and related inter-metallic compounds, J. Phys.: Condens. Matter **1**, 2341 (1989).

[222] S. M. Podgornykh, V. A. Kazantsev, and E. I. Shreder, Thermal expansion of Heussler alloys NiMnSb, CuMnSb, Ni_2MnSb, and Ni_2MnSn, Fiz. Met. Metalloved. **86**, 464 (1997).

[223] K. Endo, T. Ohoyama, and R. Kimura, Antiferromagnetism of CuMnSb, J. Phys. Soc. Jpn. **25**, 907 (1968).

[224] R. H. Forster, G. B. Johnston, and D. A. Wheeler, Studies on the heusler alloys-III. The antiferro-magnetic phase in the Cu-Mn-Sb system, J. Phys. Chem. Solids **29**, 855 (1968).

[225] W. H. Schreiner and D. E. Brandão, Electrical resistivity of the Cl_b alloy CuMnSb, Solid State Commun. **43**, 463 (1982).

[226] M. M. Kirillova, A. A. Makhnev, E. I. Shreder, V. P. Dyakina, and N. B. Gorina, Interband Optical Absorption and Plasma Effects in Half-Metallic XMnY Ferromagnets, Phys. Status Solidi B **187**, 231 (1995).

[227] T. A. Bither, P. H. L. Walter, W. H. Cloud, T. J. Swoboda, and P. E. Bierstedt, New Modified Mn_2Sb Compositions Showing Exchange Inversion, J. Appl. Phys. **33**, 1346 (1962).

[228] M. K. Wilkinson, N. S. Gingrich, and C. G. Shull, The magnetic structure of Mn_2Sb, J. Phys. Chem. Solids **2**, 289 (1957).

[229] I. Galanakis, E. Şaşıoğlu, and K. Özdoğan, Magnetic phase transition in half-metallic CoMnSb and NiMnSb semi-Heusler alloys upon Cu doping: First-principles calculations, Phys. Rev. B **77**, 214417 (2008).

[230] S. M. Podgornykh, S. V. Streltsov, V. A. Kazantsev, and E. I. Shreder, Heat capacity of Heusler alloys: Ferromagnetic Ni_2MnSb, Ni_2MnSn, NiMnSb and antiferromagnetic CuMnSb, J. Magn. Magn. Mater. **311**, 530 (2007).

[231] M. I. Bartashevich, T. Goto, T. Tomita, N. V. Baranov, S. V. Zemlyanski, G. Hilscher, and H. Michor, AF-FRI metamagnetic transition in itinerant $Mn_{2-x}Co_xSb$ system: high-field and high-pressure effects, Physica B **318**, 198 (2002).

[232] D. Meschede, F. Steglich, W. Felsch, H. Maletta, and W. Zinn, Specific Heat of Insulating Spin-Glasses, (Eu,Sr)S, near the Onset of Ferromagnetism, Phys. Rev. Lett. **44**, 102 (1980).

[233] D. Morikawa, K. Shibata, N. Kanazawa, X. Z. Yu, and Y. Tokura, Crystal chirality and skyrmion helicity in MnSi and (Fe,Co)Si as determined by transmission electron microscopy, Phys. Rev. B **88**, 024408 (2013).

[234] E. W. Achu, H. J. Al-Kanani, J. G. Booth, M. M. R. Costa, and B. Lebech, Studies of the incommensurate structures of B20 alloys, J. Magn. Magn. Mater. **177–181**, 779 (1998).

[235] S. V. Grigoriev, V. A. Dyadkin, E. V. Moskvin, D. Lamago, T. Wolf, H. Eckerlebe, and S. V. Maleyev, Helical spin structure of $\mathrm{Mn}_{1-x}\mathrm{Fe}_x\mathrm{Si}$ under a magnetic field: Small angle neutron diffraction study, Phys. Rev. B **79**, 144417 (2009).

[236] S. V. Grigoriev, D. Chernyshov, V. A. Dyadkin, V. Dmitriev, E. V. Moskvin, D. Lamago, T. Wolf, D. Menzel, J. Schoenes, S. V. Maleyev, and H. Eckerlebe, Interplay between crystalline chirality and magnetic structure in $\mathrm{Mn}_{1-x}\mathrm{Fe}_x\mathrm{Si}$, Phys. Rev. B **81**, 012408 (2010).

[237] T. Adams, *Skyrmionengitter und partielle Ordnung in B20 Übergangsmetallverbindungen*, Diploma thesis, Technische Unitversität München (2009).

[238] J. Teyssier, E. Giannini, V. Guritanu, R. Viennois, D. van der Marel, A. Amato, and S. N. Gvasaliya, Spin-glass ground state in $\mathrm{Mn}_{1-x}\mathrm{Co}_x\mathrm{Si}$, Phys. Rev. B **82**, 064417 (2010).

[239] N. Potapova, V. Dyadkin, E. Moskvin, H. Eckerlebe, D. Menzel, and S. Grigoriev, Magnetic ordering in bulk MnSi crystals with chemically induced negative pressure, Phys. Rev. B **86**, 060406 (2012).

[240] B. Lebech, J. Bernhard, and T. Freltoft, Magnetic structures of cubic FeGe studied by small-angle neutron scattering, J. Phys.: Condens. Matter **1**, 6105 (1989).

[241] S. V. Grigoriev, N. M. Potapova, S.-A. Siegfried, V. A. Dyadkin, E. V. Moskvin, V. Dmitriev, D. Menzel, C. D. Dewhurst, D. Chernyshov, R. A. Sadykov, L. N. Fomicheva, and A. V. Tsvyashchenko, Chiral Properties of Structure and Magnetism in $\mathrm{Mn}_{1-x}\mathrm{Fe}_x\mathrm{Ge}$ Compounds: When the Left and the Right are Fighting, Who Wins? Phys. Rev. Lett. **110**, 207201 (2013).

[242] S. Yeo, S. Nakatsuji, A. D. Bianchi, P. Schlottmann, Z. Fisk, L. Balicas, P. A. Stampe, and R. J. Kennedy, First-Order Transition from a Kondo Insulator to a Ferromagnetic Metal in Single Crystalline $\mathrm{FeSi}_{1-x}\mathrm{Ge}_x$, Phys. Rev. Lett. **91**, 046401 (2003).

[243] N. Kanazawa, J.-H. Kim, D. S. Inosov, J. S. White, N. Egetenmeyer, J. L. Gavilano, S. Ishiwata, Y. Onose, T. Arima, B. Keimer, and Y. Tokura, Possible skyrmion-lattice ground state in the B20 chiral-lattice magnet MnGe as seen via small-angle neutron scattering, Phys. Rev. B **86**, 134425 (2012).

[244] K. Shibata, X. Z. Yu, T. Hara, D. Morikawa, N. Kanazawa, K. Kimoto, S. I. Y. Matsui, and Y. Tokura, Towards control of the size and helicity of skyrmions in helimagnetic alloys by spin-orbit coupling, Nature Nano. **8**, 723 (2013).

[245] T. Sato, T. Ando, T. Oku, and M. Furusaka, Itinerant-electron-type helical spin-glass reentrant transition in $\mathrm{Cr}_{0.81}\mathrm{Mn}_{0.19}\mathrm{Ge}$, Phys. Rev. B **49**, 11864 (1994).

[246] T. Sato, T. Ando, T. Oku, and M. Furusaka, Helical-spin-glass reentrant transition in itinerant electron type magnet $\mathrm{Cr}_{1-x}\mathrm{Mn}_x\mathrm{Ge}$, J. Magn. Magn. Mater. **140–144**, 1785 (1995).

[247] T. Sato and K. Morita, The magnetic phase diagram of the itinerant-electron-type helical-spin-glass re-entrant magnet $Cr_{0.81}Mn_{0.19}Ge$, J. Phys.: Condens. Matter **11**, 4231 (1999).

[248] J. Beille, J. Voiron, and M. Roth, Long period helimagnetism in the cubic B20 $Fe_xCo_{1-x}Si$ and $Co_xMn_{1-x}Si$ alloys, Solid State Commun. **47**, 399 (1983).

[249] Y. Onose, N. Takeshita, C. Terakura, H. Takagi, and Y. Tokura, Doping dependence of transport properties in $Fe_{1-x}Co_xSi$, Phys. Rev. B **72**, 224431 (2005).

[250] V. A. Dyadkin, S. V. Grigoriev, D. Menzel, D. Chernyshov, V. Dmitriev, J. Schoenes, S. V. Maleyev, E. V. Moskvin, and H. Eckerlebe, Control of chirality of transition-metal monosilicides by the Czochralski method, Phys. Rev. B **84**, 014435 (2011).

[251] T. Adams, A. Chacon, M. Wagner, A. Bauer, G. Brandl, B. Pedersen, H. Berger, P. Lemmens, and C. Pfleiderer, Long-Wavelength Helimagnetic Order and Skyrmion Lattice Phase in Cu_2OSeO_3, Phys. Rev. Lett. **108**, 237204 (2012).

[252] T. Schwarze, J. Waizner, M. Garst, I. Stasinopoulos, A. Bauer, H. Berger, A. Rosch, C. Pfleiderer, and D. Grundler, Universal helimagnon and Skyrmion excitations in metallic, semiconducting, and insulating chiral magnets, submitted (2014).

[253] M. Belesi, I. Rousochatzakis, H. C. Wu, H. Berger, I. V. Shvets, F. Mila, and J. P. Ansermet, Ferrimagnetism of the magnetoelectric compound Cu_2OSeO_3 probed by ^{77}Se NMR, Phys. Rev. B **82**, 094422 (2010).

[254] P. Bak and M. H. Jensen, Theory of helical magnetic structures and phase transitions in MnSi and FeGe, J. Phys. C: Solid State **13**, L881 (1980).

[255] T. Jeong and W. E. Pickett, Implications of the B20 crystal structure for the magnetoelectronic structure of MnSi, Phys. Rev. B **70**, 075114 (2004).

[256] S. V. Grigoriev, D. Chernyshov, V. A. Dyadkin, V. Dmitriev, S. V. Maleyev, E. V. Moskvin, D. Menzel, J. Schoenes, and H. Eckerlebe, Crystal Handedness and Spin Helix Chirality in $Fe_{1-x}Co_xSi$, Phys. Rev. Lett. **102**, 037204 (2009).

[257] M. Janoschek, M. Garst, A. Bauer, P. Krautscheid, R. Georgii, P. Böni, and C. Pfleiderer, Fluctuation-induced first-order phase transition in Dzyaloshinskii-Moriya helimagnets, Phys. Rev. B **87**, 134407 (2013).

[258] C. Pfleiderer, Why first order quantum phase transitions are interesting, J. Phys.: Condens. Matter **17**, S987 (2005).

[259] K. G. Wilson, The renormalization group and critical phenomena, Rev. Mod. Phys. **55**, 583 (1983).

[260] S. A. Brazovskii, Phase transition of an isotropic system to a nonuniform state, Sov. Phys. JETP **41**, 85 (1975).

[261] S. A. Brazovskii, I. E. Dzyaloshinskii, and A. R. Muratov, Theory of weak crystallization, Sov. Phys. JETP **66**, 625 (1987).

[262] S. A. Brazovskil and S. G. Dmitriev, Phase transitions in cholesteric liquid crystals, Sov. Phys. JETP **42**, 497 (1975).

[263] J. Swift, Fluctuations near the nematic-smectic-C phase transition, Phys. Rev. A **14**, 2274 (1976).

[264] J. Swift and P. C. Hohenberg, Hydrodynamic fluctuations at the convective instability, Phys. Rev. A **15**, 319 (1977).

[265] A. B. Migdal, E. E. Saperstein, M. A. Troitsky, and D. N. Voskresensky, Pion degrees of freedom in nuclear matter, Phys. Rep. **192**, 179 (1990).

[266] S. Gopalakrishnan, B. L. Lev, and P. M. Goldbart, Emergent crystallinity and frustration with Bose-Einstein condensates in multimode cavities, Nature Phys. **5**, 845 (2009).

[267] L. Leibler, Theory of Microphase Separation in Block Copolymers, Macromolecules **13**, 1602 (1980).

[268] F. S. Bates, J. H. Rosedale, and G. H. Fredrickson, Fluctuation effects in a symmetric diblock copolymer near the order-disorder transition, J. Chem. Phys. **92**, 6255 (1990).

[269] K. Binder, Theory of first-order phase transitions, Rep. Prog. Phys. **50**, 783 (1987).

[270] J. Kindervater, W. Häußler, A. Bauer, M. Garst, and C. Pfleiderer, Dynamics at the Brazovskii-type phase transition in $Mn_{1-x}Fe_xSi$, unpublished (2014).

[271] I. Živković, J. S. White, H. M. Rønnow, K. Prša, and H. Berger, Critical scaling in the cubic helimagnet Cu_2OSeO_3, Phys. Rev. B **89**, 060401 (2014).

[272] S. V. Grigoriev, S. V. Maleyev, A. I. Okorokov, Y. O. Chetverikov, R. Georgii, P. Böni, D. Lamago, H. Eckerlebe, and K. Pranzas, Critical fluctuations in MnSi near T_C: A polarized neutron scattering study, Phys. Rev. B **72**, 134420 (2005).

[273] S. V. Grigoriev, S. V. Maleyev, E. V. Moskvin, V. A. Dyadkin, P. Fouquet, and H. Eckerlebe, Crossover behavior of critical helix fluctuations in MnSi, Phys. Rev. B **81**, 144413 (2010).

[274] S. V. Grigoriev, E. V. Moskvin, V. A. Dyadkin, D. Lamago, T. Wolf, H. Eckerlebe, and S. V. Maleyev, Chiral criticality in the doped helimagnets $Mn_{1-y}Fe_ySi$, Phys. Rev. B **83**, 224411 (2011).

[275] A. Hamann, D. Lamago, T. Wolf, H. v. Löhneysen, and D. Reznik, Magnetic Blue Phase in the Chiral Itinerant Magnet MnSi, Phys. Rev. Lett. **107**, 037207 (2011).

[276] C. Pappas, E. Lelièvre-Berna, P. Falus, P. M. Bentley, E. Moskvin, S. Grigoriev, P. Fouquet, and B. Farago, Chiral Paramagnetic Skyrmion-like Phase in MnSi, Phys. Rev. Lett. **102**, 197202 (2009).

[277] C. Pappas, E. Lelièvre-Berna, P. Bentley, P. Falus, P. Fouquet, and B. Farago, Magnetic fluctuations and correlations in MnSi: Evidence for a chiral skyrmion spin liquid phase, Phys. Rev. B **83**, 224405 (2011).

[278] D. Vollhardt, Characteristic Crossing Points in Specific Heat Curves of Correlated Systems, Phys. Rev. Lett. **78**, 1307 (1997).

[279] M. Greger, M. Kollar, and D. Vollhardt, Isosbestic points: How a narrow crossing region of curves determines their leading parameter dependence, Phys. Rev. B **87**, 195140 (2013).

[280] S. Buhrandt and L. Fritz, Skyrmion lattice phase in three-dimensional chiral magnets from Monte Carlo simulations, Phys. Rev. B **88**, 195137 (2013).

[281] M. Wagner, A. Bauer, A. Chacon, M. Halder, M. Garst, and C. Pfleiderer, Detailed determination of the cubic anisotropies in MnSi, unpublished (2014).

[282] F. Rucker, *High Precision Susceptometer for Angle-Resolved Studies of Quantum Phase Transitions*, Diploma thesis, Technische Unitversität München (2013).

[283] A. Chacon, A. Bauer, F. Rucker, M. Garst, and C. Pfleiderer, Domain populations in the helical state of MnSi just below T_c, unpublished (2014).

[284] T. Adams, *Neutronenstreuung an komplexen magnetischen Verbindungen*, Ph.D. thesis, Technische Unitversität München (to be published in 2014).

[285] T. Adams, A. Bauer, R. Georgii, M. Garst, and C. Pfleiderer, Small-angle neutron scattering study of the orientation dependence of the skyrmion lattice in MnSi, unpublished (2014).

[286] B. Lebech, *Recent Advances in Magnetism of Transition Metal Compounds* (World Scientific, Singapore, 1993) p. 167.

[287] W. Münzer, A. Neubauer, T. Adams, S. Mühlbauer, C. Franz, F. Jonietz, R. Georgii, P. Böni, B. Pedersen, M. Schmidt, A. Rosch, and C. Pfleiderer, Skyrmion lattice in the doped semiconductor $Fe_{1-x}Co_xSi$, Phys. Rev. B **81**, 041203 (R) (2010).

[288] T. Adams, S. Mühlbauer, C. Pfleiderer, F. Jonietz, A. Bauer, A. Neubauer, R. Georgii, P. Böni, U. Keiderling, K. Everschor, M. Garst, and A. Rosch, Long-Range Crystalline Nature of the Skyrmion Lattice in MnSi, Phys. Rev. Lett. **107**, 217206 (2011).

[289] E. Fawcett, J. P. Maita, and J. H. Wernick, Magnetoelastic and thermal properties of MnSi, Int. J. Magn. **1**, 29 (1970).

[290] S. Kusaka, K. Yamamoto, T. Komatsubara, and Y. Ishikawa, Ultrasonic study of magnetic phase diagram of MnSi, Solid State Commun. **20**, 925 (1976).

[291] K. Kadowaki, K. Okuda, and M. Date, Magnetization and Magnetoresistance of MnSi. I, J. Phys. Soc. Jpn. **51**, 2433 (1982).

[292] C. Pfleiderer, T. Adams, A. Bauer, W. Biberacher, B. Binz, F. Birkelbach, P. Böni, C. Franz, R. Georgii, M. Janoschek, F. Jonietz, T. Keller, R. Ritz, S. Mühlbauer, W. Münzer, A. Neubauer, B. Pedersen, and A. Rosch, Skyrmion lattices in metallic and semiconducting B20 transition metal compounds, J. Phys.: Condens. Matter **22**, 164207 (2010).

[293] S. Seki, J.-H. Kim, D. S. Inosov, R. Georgii, B. Keimer, S. Ishiwata, and Y. Tokura, Formation and rotation of skyrmion crystal in the chiral-lattice insulator Cu_2OSeO_3, Phys. Rev. B **85**, 220406 (R) (2012).

[294] E. Moskvin, S. Grigoriev, V. Dyadkin, H. Eckerlebe, M. Baenitz, M. Schmidt, and H. Wilhelm, Complex Chiral Modulations in FeGe Close to Magnetic Ordering, Phys. Rev. Lett. **110**, 077207 (2013).

[295] T. H. R. Skyrme, A Non-Linear Field Theory, Proc. R. Soc. Lond. A **260**, 127 (1961).

[296] T. H. R. Skyrme, Particle States of a Quantized Meson Field, Proc. R. Soc. Lond. A **262**, 237 (1961).

[297] T. H. R. Skyrme, A unified field theory of mesons and baryons, Nucl. Phys. **31**, 556 (1962).

[298] G. S. Adkins, C. R. Nappi, and E. Witten, Static properties of nucleons in the Skyrme model, Nucl. Phys. B **228**, 552 (1983).

[299] S. L. Sondhi, A. Karlhede, S. A. Kivelson, and E. H. Rezayi, Skyrmions and the crossover from the integer to fractional quantum Hall effect at small Zeeman energies, Phys. Rev. B **47**, 16419 (1993).

[300] L. Brey, H. A. Fertig, R. Côté, and A. H. MacDonald, Skyrme Crystal in a Two-Dimensional Electron Gas, Phys. Rev. Lett. **75**, 2562 (1995).

[301] A. Schmeller, J. P. Eisenstein, L. N. Pfeiffer, and K. W. West, Evidence for Skyrmions and Single Spin Flips in the Integer Quantized Hall Effect, Phys. Rev. Lett. **75**, 4290 (1995).

[302] E. H. Aifer, B. B. Goldberg, and D. A. Broido, Evidence of skyrmion excitations about $\nu = 1$ in n-modulation-doped single quantum wells by interband optical transmission, Phys. Rev. Lett. **76**, 680 (1996).

[303] K. Yang, S. Das Sarma, and A. H. MacDonald, Collective modes and skyrmion excitations in graphene $SU(4)$ quantum Hall ferromagnets, Phys. Rev. B **74**, 075423 (2006).

[304] J. Alicea and M. P. A. Fisher, Graphene integer quantum Hall effect in the ferromagnetic and paramagnetic regimes, Phys. Rev. B **74**, 075422 (2006).

[305] U. A. Khawaja and H. Stoof, Skyrmions in a ferromagnetic Bose-Einstein condensate, Nature (London) **411**, 918 (2001).

[306] L. S. Leslie, A. Hansen, K. C. Wright, B. M. Deutsch, and N. P. Bigelow, Creation and Detection of Skyrmions in a Bose-Einstein Condensate, Phys. Rev. Lett. **103**, 250401 (2009).

[307] J. Fukuda and S. Žumer, Quasi-two-dimensional Skyrmion lattices in a chiral nematic liquid crystal, Nat. Commun. **2**, 246 (2011).

[308] S. Mühlbauer, C. Pfleiderer, P. Böni, M. Laver, E. M. Forgan, D. Fort, U. Keiderling, and G. Behr, Morphology of the Superconducting Vortex Lattice in Ultrapure Niobium, Phys. Rev. Lett. **102**, 136408 (2009).

[309] Y. Ishikawa and M. Arai, Magnetic Phase Diagram of MnSi near Critical Temperature Studied by Neutron Small Angle Scattering, J. Phys. Soc. Jpn. **53**, 2726 (1984).

[310] B. Lebech, P. Harris, J. S. Pedersen, K. Mortensen, C. I. Gregory, N. R. Bernhoeft, M. Jermy, and S. A. Brown, Magnetic phase diagram of MnSi, J. Magn. Magn. Mater. **140–144**, 119 (1995).

[311] S. V. Grigoriev, S. V. Maleyev, A. I. Okorokov, Y. O. Chetverikov, and H. Eckerlebe, Field-induced reorientation of the spin helix in MnSi near T_c, Phys. Rev. B **73**, 224440 (2006).

[312] D. Lamago, R. Georgii, C. Pfleiderer, and P. Böni, Magnetic-field induced instability surrounding the A-phase of MnSi: Bulk and SANS measurements, Physica B **385–386**, 385 (2006).

[313] A. Bauer and C. Pfleiderer, Magnetic phase diagram of MnSi inferred from magnetization and ac susceptibility, Phys. Rev. B **85**, 214418 (2012).

[314] A. Chacon, *Neutron scattering and susceptibility studies of skyrmion lattices under uniaxial pressure*, Master's thesis, Technische Unitversität München (2011).

[315] A. Chacon, A. Bauer, T. Adams, F. Rucker, G. Brandl, R. Georgii, P. Böni, and C. Pfleiderer, Uniaxial pressure studies of the helimagnetic order and the skyrmion lattice of MnSi, unpublished (2014).

[316] A. N. Bogdanov and D. A. Yablonskii, Thermodynamically stable "vortices" in magnetically ordered crystals. The mixed state of magnets, Sov. Phys. JETP **95**, 178 (1989).

[317] A. Bogdanov and A. Hubert, Thermodynamically stable magnetic vortex states in magnetic crystals, J. Magn. Magn. Mater. **138**, 255 (1994).

[318] U. K. Rößler, A. N. Bogdanov, and C. Pfleiderer, Spontaneous skyrmion ground states in magnetic metals, Nature (London) **442**, 797 (2006).

[319] A. B. Butenko, A. A. Leonov, U. K. Rößler, and A. N. Bogdanov, Stabilization of skyrmion textures by uniaxial distortions in noncentrosymmetric cubic helimagnets, Phys. Rev. B **82**, 052403 (2010).

[320] C. Pfleiderer and A. Rosch, Condensed-matter physics: Single skyrmions spotted, Nature (London) **465**, 880 (2010).

[321] A. Neubauer, C. Pfleiderer, B. Binz, A. Rosch, R. Ritz, P. G. Niklowitz, and P. Böni, Topological Hall Effect in the *A* Phase of MnSi, Phys. Rev. Lett. **102**, 186602 (2009).

[322] T. Schulz, R. Ritz, A. Bauer, M. Halder, M. Wagner, C. Franz, C. Pfleiderer, K. Everschor, M. Garst, and A. Rosch, Emergent electrodynamics of skyrmions in a chiral magnet, Nature Phys. **8**, 301 (2012).

[323] G. E. Volovik, Linear momentum in ferromagnets, J. Phys. C: Solid State **20**, L83 (1987).

[324] S. Zhang and S. S.-L. Zhang, Generalization of the Landau-Lifshitz-Gilbert Equation for Conducting Ferromagnets, Phys. Rev. Lett. **102**, 086601 (2009).

[325] J. Zang, M. Mostovoy, J. H. Han, and N. Nagaosa, Dynamics of Skyrmion Crystals in Metallic Thin Films, Phys. Rev. Lett. **107**, 136804 (2011).

[326] M. Lee, Y. Onose, Y. Tokura, and N. P. Ong, Hidden constant in the anomalous Hall effect of high-purity magnet MnSi, Phys. Rev. B **75**, 172403 (2007).

[327] A. Neubauer, C. Pfleiderer, R. Ritz, P. Niklowitz, and P. Böni, Hall effect and magnetoresistance in MnSi, Physica B **404**, 3163 (2009).

[328] N. Nagaosa, J. Sinova, S. Onoda, A. H. MacDonald, and N. P. Ong, Anomalous Hall effect, Rev. Mod. Phys. **82**, 1539 (2010).

[329] D. Xiao, J. Shi, and Q. Niu, Berry Phase Correction to Electron Density of States in Solids, Phys. Rev. Lett. **95**, 137204 (2005).

[330] R. Ritz, M. Halder, C. Franz, A. Bauer, M. Wagner, R. Bamler, A. Rosch, and C. Pfleiderer, Giant generic topological Hall resistivity of MnSi under pressure, Phys. Rev. B **87**, 134424 (2013).

[331] F. Freimuth, R. Bamler, Y. Mokrousov, and A. Rosch, Phase-space Berry phases in chiral magnets: Dzyaloshinskii-Moriya interaction and the charge of skyrmions, Phys. Rev. B **88**, 214409 (2013).

[332] F. Jonietz, S. Mühlbauer, C. Pfleiderer, A. Neubauer, W. Münzer, A. Bauer, T. Adams, R. Georgii, P. Böni, R. A. Duine, K. Everschor, M. Garst, and A. Rosch, Spin Transfer Torques in MnSi at Ultralow Current Densities, Science **330**, 1648 (2010).

[333] J. Iwasaki, M. Mochizuki, and N. Nagaosa, Universal current-velocity relation of skyrmion motion in chiral magnets, Nat. Commun. **4**, 1463 (2013).

[334] M. Tsoi, A. G. M. Jansen, J. Bass, W.-C. Chiang, M. Seck, V. Tsoi, and P. Wyder, Excitation of a Magnetic Multilayer by an Electric Current, Phys. Rev. Lett. **80**, 4281 (1998).

[335] E. B. Myers, D. C. Ralph, J. A. Katine, R. N. Louie, and R. A. Buhrman, Current-Induced Switching of Domains in Magnetic Multilayer Devices, Science **285**, 867 (1999).

[336] S. I. Kiselev, J. C. Sankey, I. N. Krivorotov, N. C. Emley, R. J. Schoelkopf, R. A. Buhrman, and D. C. Ralph, Microwave oscillations of a nanomagnet driven by a spin-polarized current, Nature (London) **425**, 380 (2003).

[337] A. Yamaguchi, T. Ono, S. Nasu, K. Miyake, K. Mibu, and T. Shinjo, Real-Space Observation of Current-Driven Domain Wall Motion in Submicron Magnetic Wires, Phys. Rev. Lett. **92**, 077205 (2004).

[338] M. Hayashi, L. Thomas, Y. B. Bazaliy, C. Rettner, R. Moriya, X. Jiang, and S. S. P. Parkin, Influence of Current on Field-Driven Domain Wall Motion in Permalloy Nanowires from Time Resolved Measurements of Anisotropic Magnetoresistance, Phys. Rev. Lett. **96**, 197207 (2006).

[339] A. A. Thiele, Steady-State Motion of Magnetic Domains, Phys. Rev. Lett. **30**, 230 (1973).

[340] K. Everschor, M. Garst, R. A. Duine, and A. Rosch, Current-induced rotational torques in the skyrmion lattice phase of chiral magnets, Phys. Rev. B **84**, 064401 (2011).

[341] K. Everschor, M. Garst, B. Binz, F. Jonietz, S. Mühlbauer, C. Pfleiderer, and A. Rosch, Rotating skyrmion lattices by spin torques and field or temperature gradients, Phys. Rev. B **86**, 054432 (2012).

[342] M. Mochizuki, X. Z. Yu, S. Seki, N. Kanazawa, W. Koshibae, J. Zang, M. Mostovoy, Y. Tokura, and N. Nagaosa, Thermally driven ratchet motion of a skyrmion microcrystal and topological magnon Hall effect, Nature Mater. **13**, 241 (2014).

[343] A. Tonomura, X. Yu, K. Yanagisawa, T. Matsuda, Y. Onose, N. Kanazawa, H. S. Park, and Y. Tokura, Real-Space Observation of Skyrmion Lattice in Helimagnet MnSi Thin Samples, Nano Lett. **12**, 1673 (2012).

[344] J. H. Han, J. Zang, Z. Yang, J.-H. Park, and N. Nagaosa, Skyrmion lattice in a two-dimensional chiral magnet, Phys. Rev. B **82**, 094429 (2010).

[345] X. Z. Yu, N. Kanazawa, W. Z. Zhang, T. Nagai, T. Hara, K. Kimoto, Y. Matsui, and Y. O. Y. Tokura, Skyrmion flow near room temperature in an ultralow current density, Nat. Commun. **3**, 988 (2012).

[346] H. S. Park, X. Yu, S. Aizawa, T. Tanigaki, T. Akashi, Y. Takahashi, T. Matsuda, N. Kanazawa, Y. Onose, D. Shindo, A. Tonomura, and Y. Tokura, Observation of the magnetic flux and three-dimensional structure of skyrmion lattices by electron holography, Nature Nano. **9**, 337 (2014).

[347] R. Takashima and S. Fujimoto, Electrodynamics in Skyrmions Merging, J. Phys. Soc. Jpn. **83**, 054717 (2014).

[348] Y. Tchoe and J. H. Han, Skyrmion generation by current, Phys. Rev. B **85**, 174416 (2012).

[349] Y. Li, N. Kanazawa, X. Z. Yu, A. Tsukazaki, M. Kawasaki, M. Ichikawa, X. F. Jin, F. Kagawa, and Y. Tokura, Robust Formation of Skyrmions and Topological Hall Effect Anomaly in Epitaxial Thin Films of MnSi, Phys. Rev. Lett. **110**, 117202 (2013).

[350] S.-Z. Lin, C. Reichhardt, C. D. Batista, and A. Saxena, Driven Skyrmions and Dynamical Transitions in Chiral Magnets, Phys. Rev. Lett. **110**, 207202 (2013).

[351] Y.-H. Liu and Y.-Q. Li, A mechanism to pin skyrmions in chiral magnets, J. Phys.: Condens. Matter **25**, 076005 (2013).

[352] S.-Z. Lin, C. Reichhardt, C. D. Batista, and A. Saxena, Particle model for skyrmions in metallic chiral magnets: Dynamics, pinning, and creep, Phys. Rev. B **87**, 214419 (2013).

[353] S.-Z. Lin and L. N. Bulaevskii, Quantum motion and level quantization of a skyrmion in a pinning potential in chiral magnets, Phys. Rev. B **88**, 060404 (2013).

[354] R. L. Silva, L. D. Secchin, W. A. Moura-Melo, A. R. Pereira, and R. L. Stamps, Emergence of skyrmion lattices and bimerons in chiral magnetic thin films with nonmagnetic impurities, Phys. Rev. B **89**, 054434 (2014).

[355] R. E. Troncoso and A. S. Núñez, Thermally assisted current-driven skyrmion motion, Phys. Rev. B **89**, 224403 (2014).

[356] X. Yu, J. P. DeGrave, Y. Hara, T. Hara, S. Jin, and Y. Tokura, Observation of the Magnetic Skyrmion Lattice in a MnSi Nanowire by Lorentz TEM, Nano Lett. **13**, 3755 (2013).

[357] H. Du, J. P. DeGrave, F. Xue, D. Liang, W. Ning, J. Yang, M. Tian, Y. Zhang, and S. Jin, Highly Stable Skyrmion State in Helimagnetic MnSi Nanowires, Nano Lett. **14**, 2026 (2014).

[358] J. Sampaio, V. Cros, S. Rohart, A. Thiaville, and A. Fert, Nucleation, stability and current-induced motion of isolated magnetic skyrmions in nanostructures, Nature Nano. **8**, 839 (2013).

[359] S.-Z. Lin, C. Reichhardt, and A. Saxena, Manipulation of skyrmions in nanodisks with a current pulse and skyrmion rectifier, Appl. Phys. Lett. **102**, 222405 (2013).

[360] L. Sun, R. X. Cao, B. F. Miao, Z. Feng, B. You, D. Wu, W. Zhang, A. Hu, and H. F. Ding, Creating an Artificial Two-Dimensional Skyrmion Crystal by Nanopatterning, Phys. Rev. Lett. **110**, 167201 (2013).

[361] H. Du, W. Ning, M. Tian, and Y. Zhang, Field-driven evolution of chiral spin textures in a thin helimagnet nanodisk, Phys. Rev. B **87**, 014401 (2013).

[362] J. Iwasaki, W. Koshibae, and N. Nagaosa, Colossal Spin Transfer Torque Effect on Skyrmion along the Edge, Nano Lett. **14**, 4432 (2014).

[363] N. Nagaosa and Y. Tokura, Topological properties and dynamics of magnetic skyrmions, Nature Nano. **8**, 899 (2013).

[364] S.-Z. Lin, C. Reichhardt, C. D. Batista, and A. Saxena, Dynamics of skyrmions in chiral magnets: Dynamic phase transitions and equation of motion, J. Appl. Phys. **115**, 17D109 (2014).

[365] J. Iwasaki, M. Mochizuki, and N. Nagaosa, Current-induced skyrmion dynamics in constricted geometries, Nature Nano. **8**, 742 (2013).

[366] A. Fert, V. Cros, and J. Sampaio, Skyrmions on the track, Nature Nano. **8**, 152 (2013).

[367] R. Duine, Skyrmions singled out, Nature Nano. **8**, 800 (2013).

[368] M. Mochizuki and S. Seki, Magnetoelectric resonances and predicted microwave diode effect of the skyrmion crystal in a multiferroic chiral-lattice magnet, Phys. Rev. B **87**, 134403 (2013).

[369] Y. Okamura, F. Kagawa, M. Mochizuki, M. Kubota, S. Seki, S. Ishiwata, M. Kawasaki, Y. Onose, and Y. Tokura, Microwave magnetoelectric effect via skyrmion resonance modes in a helimagnetic multiferroic, Nat. Commun. **4**, 2391 (2013).

[370] S. X. Huang and C. L. Chien, Extended Skyrmion Phase in Epitaxial FeGe(111) Thin Films, Phys. Rev. Lett. **108**, 267201 (2012).

[371] E. A. Karhu, U. K. Rößler, A. N. Bogdanov, S. Kahwaji, B. J. Kirby, H. Fritzsche, M. D. Robertson, C. F. Majkrzak, and T. L. Monchesky, Chiral modulations and reorientation effects in MnSi thin films, Phys. Rev. B **85**, 094429 (2012).

[372] M. N. Wilson, A. B. Butenko, A. N. Bogdanov, and T. L. Monchesky, Chiral skyrmions in cubic helimagnet films: The role of uniaxial anisotropy, Phys. Rev. B **89**, 094411 (2014).

[373] S. Polesya, S. Mankovsky, S. Bornemann, D. Ködderitzsch, J. Minár, and H. Ebert, Skyrmion magnetic structure of an ordered FePt monolayer deposited on Pt(111), Phys. Rev. B **89**, 184414 (2014).

[374] T. Ogasawara, N. Iwata, Y. Murakami, H. Okamoto, and Y. Tokura, Submicron-scale spatial feature of ultrafast photoinduced magnetization reversal in TbFeCo thin film, Appl. Phys. Lett. **94**, 162507 (2009).

[375] M. Finazzi, M. Savoini, A. R. Khorsand, A. Tsukamoto, A. Itoh, L. Duò, A. Kirilyuk, T. Rasing, and M. Ezawa, Laser-Induced Magnetic Nanostructures with Tunable Topological Properties, Phys. Rev. Lett. **110**, 177205 (2013).

[376] X. Yu, M. Mostovoy, Y. Tokunaga, W. Zhang, K. Kimoto, Y. Matsui, Y. Kaneko, N. Nagaosa, and Y. Tokura, Magnetic stripes and skyrmions with helicity reversals, P. Natl. Acad. Sci. USA **109**, 8856 (2012).

[377] M. Nagao, Y.-G. So, H. Yoshida, M. Isobe, T. Hara, K. Ishizuka, and K. Kimoto, Direct observation and dynamics of spontaneous skyrmion-like magnetic domains in a ferromagnet, Nature Nano. **8**, 325 (2013).

[378] C. Kittel, On the Theory of Ferromagnetic Resonance Absorption, Phys. Rev. **73**, 155 (1948).

[379] M. Date, K. Okuda, and K. Kadowaki, Electron-Spin Resonance in the Itinerant-Electron Helical Magnet MnSi, J. Phys. Soc. Jpn. **42**, 1555 (1977).

[380] S. Haraldson, L. Pettersson, and S. M. Bhagat, Frequency and temperature dependence of spin resonances in cubic FeGe, J. Magn. Reson. **32**, 115 (1978).

[381] M. Kataoka, Spin Waves in Systems with Long Period Helical Spin Density Waves Due to the Antisymmetric and Symmetric Exchange Interactions, J. Phys. Soc. Jpn. **56**, 3635 (1987).

[382] M. I. Kobets, K. G. Dergachev, E. N. Khatsko, A. I. Rykova, P. Lemmens, D. Wulferding, and H. Berger, Microwave absorption in the frustrated ferrimagnet Cu_2OSeO_3, Low Temp. Phys. **36**, 176 (2010).

[383] M. Mochizuki, Spin-Wave Modes and Their Intense Excitation Effects in Skyrmion Crystals, Phys. Rev. Lett. **108**, 017601 (2012).

[384] O. Petrova and O. Tchernyshyov, Spin waves in a skyrmion crystal, Phys. Rev. B **84**, 214433 (2011).

[385] Y. Onose, Y. Okamura, S. Seki, S. Ishiwata, and Y. Tokura, Observation of Magnetic Excitations of Skyrmion Crystal in a Helimagnetic Insulator Cu_2OSeO_3, Phys. Rev. Lett. **109**, 037603 (2012).

[386] S. Seki, S. Ishiwata, and Y. Tokura, Magnetoelectric nature of skyrmions in a chiral magnetic insulator Cu_2OSeO_3, Phys. Rev. B **86**, 060403 (2012).

[387] S.-Z. Lin, C. D. Batista, and A. Saxena, Internal modes of a skyrmion in the ferromagnetic state of chiral magnets, Phys. Rev. B **89**, 024415 (2014).

[388] M. Janoschek, F. Bernlochner, S. Dunsiger, C. Pfleiderer, P. Böni, B. Roessli, P. Link, and A. Rosch, Helimagnon bands as universal excitations of chiral magnets, Phys. Rev. B **81**, 214436 (2010).

[389] J. D. Koralek, D. Meier, J. P. Hinton, A. Bauer, S. A. Parameswaran, A. Vishwanath, R. Ramesh, R. W. Schoenlein, C. Pfleiderer, and J. Orenstein, Observation of Coherent Helimagnons and Gilbert Damping in an Itinerant Magnet, Phys. Rev. Lett. **109**, 247204 (2012).

[390] V. V. Kruglyak, S. O. Demokritov, and D. Grundler, Magnonics, J. Phys. D: Appl. Phys. **43**, 264001 (2010).

[391] B. Lenk, H. Ulrichs, F. Garbs, and M. Münzenberg, The building blocks of magnonic, Phys. Rep. **507**, 107 (2011).

[392] H. J. Williams, J. H. Wernick, R. C. Sherwood, and G. K. Wertheim, Magnetic Properties of the Monosilicides of Some 3d Transition Elements, J. Appl. Phys. **37**, 1256 (1966).

[393] D. Shinoda and S. Asanabe, Magnetic Properties of Silicides of Iron Group Transition Elements, J. Phys. Soc. Jpn. **21**, 555 (1966).

[394] D. Bloch, J. Voiron, V. Jaccarino, and J. H. Wernick, The high field-high pressure magnetic properties of MnSi, Phys. Lett. A **51**, 259 (1975).

[395] Y. Ishikawa, K. Tajima, D. Bloch, and M. Roth, Helical spin structure in manganese silicide MnSi, Solid State Commun. **19**, 525 (1976).

[396] K. Motoya, H. Yasuoka, Y. Nakamura, and J. Wernick, Helical spin structure in MnSi-NMR studies, Solid State Commun. **19**, 529 (1976).

[397] O. Nakanishi, A. Yanase, A. Hasegawa, and M. Kataoka, The origin of the helical spin density wave in MnSi, Solid State Commun. **35**, 995 (1980).

[398] I. E. Dzyaloshinsky, Thermodynamic theory of weak ferromagnetism in antiferromagnetic substances, Sov. Phys. JETP **5**, 1259 (1957).

[399] T. Moriya, Anisotropic Superexchange Interaction and Weak Ferromagnetism, Phys. Rev. **120**, 91 (1960).

[400] I. E. Dzyaloshinsky, Theory of helicoidal structures in antiferromagnets, Sov. Phys. JETP **19**, 960 (1964).

[401] G. Shirane, R. Cowley, C. Majkrzak, J. B. Sokoloff, B. Pagonis, C. H. Perry, and Y. Ishikawa, Spiral magnetic correlation in cubic MnSi, Phys. Rev. B **28**, 6251 (1983).

[402] M. Tanaka, H. Takayoshi, M. Ishida, and Y. Endoh, Crystal Chirality and Helicity of the Helical Spin Density Wave in MnSi. I. Convergent-Beam Electron Diffraction, J. Phys. Soc. Jpn. **54**, 2970 (1985).

[403] M. Ishida, Y. Endoh, S. Mitsuda, Y. Ishikawa, and M. Tanaka, Crystal Chirality and Helicity of the Helical Spin Density Wave in MnSi. II. Polarized Neutron Diffraction, J. Phys. Soc. Jpn. **54**, 2975 (1985).

[404] G. G. Lonzarich, The magnetic equation of state and heat capacity in weak itinerant ferromagnets, J. Magn. Magn. Mater. **54–57**, 612 (1986).

[405] Y. Ishikawa, Y. Noda, C. Fincher, and G. Shirane, Low-energy paramagnetic spin fluctuations in the weak itinerant ferromagnet MnSi, Phys. Rev. B **25**, 254 (1982).

[406] Y. Ishikawa, Y. Noda, Y. J. Uemura, C. F. Majkrzak, and G. Shirane, Paramagnetic spin fluctuations in the weak itinerant-electron ferromagnet MnSi, Phys. Rev. B **31**, 5884 (1985).

[407] T. Sakakibara, H. Mollymoto, and M. Date, Magnetization and Magnetoresistance of MnSi. II, J. Phys. Soc. Jpn. **51**, 2439 (1982).

[408] S. M. Stishov, A. E. Petrova, S. Khasanov, G. K. Panova, A. A. Shikov, J. C. Lashley, D. Wu, and T. A. Lograsso, Magnetic phase transition in the itinerant helimagnet mnsi: Thermodynamic and transport properties, Phys. Rev. B **76**, 052405 (2007).

[409] S. M. Stishov, A. E. Petrova, S. Khasanov, G. K. Panova, A. A. Shikov, J. C. Lashley, D. Wu, and T. A. Lograsso, Heat capacity and thermal expansion of the itinerant helimagnet MnSi, J. Phys.: Condens. Matter **20**, 196001 (2008).

[410] A. E. Petrova and S. M. Stishov, Ultrasonic studies of the magnetic phase transition in MnSi, J. Phys.: Condens. Matter **21**, 196001 (2009).

[411] B. Roessli, P. Böni, W. E. Fischer, and Y. Endoh, Chiral Fluctuations in MnSi above the Curie Temperature, Phys. Rev. Lett. **88**, 237204 (2002).

[412] C. Pfleiderer, D. Reznik, L. Pintschovius, H. v. Löhneysen, M. Garst, and A. Rosch, Partial order in the non-Fermi-liquid phase of MnSi, Nature (London) **427**, 227 (2004).

[413] C. Pfleiderer, G. J. McMullan, S. R. Julian, and G. G. Lonzarich, Magnetic quantum phase transition in MnSi under hydrostatic pressure, Phys. Rev. B **55**, 8330 (1997).

[414] C. Thessieu, C. Pfleiderer, A. N. Stepanov, and J. Flouquet, Field dependence of the magnetic quantum phase transition in MnSi, J. Phys.: Condens. Matter **9**, 6677 (1997).

[415] K. Koyama, T. Goto, T. Kanomata, and R. Note, Observation of an itinerant metamagnetic transition in MnSi under high pressure, Phys. Rev. B **62**, 986 (2000).

[416] C. Pfleiderer, D. Reznik, L. Pintschovius, and J. Haug, Magnetic Field and Pressure Dependence of Small Angle Neutron Scattering in MnSi, Phys. Rev. Lett. **99**, 156406 (2007).

[417] C. Pfleiderer, P. Böni, T. Keller, U. K. Rößler, and A. Rosch, Non-Fermi Liquid Metal Without Quantum Criticality, Science **316**, 1871 (2007).

[418] W. Yu, F. Zamborszky, J. D. Thompson, J. L. Sarrao, M. E. Torelli, Z. Fisk, and S. E. Brown, Phase Inhomogeneity of the Itinerant Ferromagnet MnSi at High Pressures, Phys. Rev. Lett. **92**, 086403 (2004).

[419] Y. J. Uemura, T. Goko, I. M. Gat-Malureanu, J. P. Carlo, P. L. Russo, A. T. Savici, A. Aczel, G. J. MacDougall, J. A. Rodriguez, G. M. Luke, S. R. Dunsiger, A. McCollam, J. Arai, C. Pfleiderer, P. Böni, K. Yoshimura, E. Baggio-Saitovitch, M. B. Fontes, J. Larrea, Y. V. Sushko, and J. Sereni, Phase separation and suppression of critical dynamics at quantum phase transitions of MnSi and $(\mathrm{Sr}_{1-x}\mathrm{Ca}_x)\mathrm{RuO}_3$, Nature Phys. **3**, 29 (2007).

[420] C. Thessieu, J. Flouquet, G. Lapertot, A. N. Stepanov, and D. Jaccard, Magnetism and spin fluctuations in a weak itinerant ferromagnet: MnSi, Solid State Commun. **95**, 707 (1995).

[421] A. E. Petrova, V. Krasnorussky, J. Sarrao, and S. M. Stishov, Tricritical behavior in MnSi at nearly hydrostatic pressure, Phys. Rev. B **73**, 052409 (2006).

[422] A. E. Petrova, E. D. Bauer, V. Krasnorussky, and S. M. Stishov, Behavior of the electrical resistivity of MnSi at the ferromagnetic phase transition, Phys. Rev. B **74**, 092401 (2006).

[423] A. Miyake, A. Villaume, Y. Haga, G. Knebel, B. Salce, G. Lapertot, and J. Flouquet, Pressure Collapse of the Magnetic Ordering in MnSi via Thermal Expansion, J. Phys. Soc. Jpn. **78**, 044703 (2009).

[424] J.-G. Cheng, F. Zhou, J.-S. Zhou, J. B. Goodenough, and Y. Sui, Enhanced thermoelectric power near the quantum phase transition in the itinerant-electron ferromagnet MnSi, Phys. Rev. B **82**, 214402 (2010).

[425] S. Tewari, D. Belitz, and T. R. Kirkpatrick, Blue Quantum Fog: Chiral Condensation in Quantum Helimagnets, Phys. Rev. Lett. **96**, 047207 (2006).

[426] B. Binz, A. Vishwanath, and V. Aji, Theory of the Helical Spin Crystal: A Candidate for the Partially Ordered State of MnSi, Phys. Rev. Lett. **96**, 207202 (2006).

[427] I. Fischer, N. Shah, and A. Rosch, Crystalline phases in chiral ferromagnets: Destabilization of helical order, Phys. Rev. B **77**, 024415 (2008).

[428] S. D. Yi, S. Onoda, N. Nagaosa, and J. H. Han, Skyrmions and anomalous Hall effect in a Dzyaloshinskii-Moriya spiral magnet, Phys. Rev. B **80**, 054416 (2009).

[429] F. Krüger, U. Karahasanovic, and A. G. Green, Quantum Order-by-Disorder Near Criticality and the Secret of Partial Order in MnSi, Phys. Rev. Lett. **108**, 067003 (2012).

[430] U. Karahasanovic, F. Krüger, and A. G. Green, Quantum order-by-disorder driven phase reconstruction in the vicinity of ferromagnetic quantum critical points, Phys. Rev. B **85**, 165111 (2012).

[431] C. Pfleiderer, S. R. Julian, and G. G. Lonzarich, Non-Fermi-liquid nature of the normal state of itinerant-electron ferromagnets, Nature (London) **414**, 427 (2001).

[432] N. Doiron-Leyraud, I. R. Walker, L. Taillefer, M. J. Steiner, S. R. Julian, and G. G. Lonzarich, Fermi-liquid breakdown in the paramagnetic phase of a pure metal, Nature (London) **425**, 595 (2003).

[433] P. Pedrazzini, D. Jaccard, G. Lapertot, J. Flouquet, Y. Inada, H. Kohara, and Y. Onuki, Probing the extended non-Fermi liquid regimes of MnSi and Fe, Physica B **378–380**, 165 (2006).

[434] T. R. Kirkpatrick and D. Belitz, Columnar Fluctuations as a Source of Non-Fermi-Liquid Behavior in Weak Metallic Magnets, Phys. Rev. Lett. **104**, 256404 (2010).

[435] H. Watanabe, S. A. Parameswaran, S. Raghu, and A. Vishwanath, Anomalous Fermi-liquid phase in metallic skyrmion crystals, Phys. Rev. B **90**, 045145 (2014).

[436] M. Lee, W. Kang, Y. Onose, Y. Tokura, and N. P. Ong, Unusual Hall Effect Anomaly in MnSi under Pressure, Phys. Rev. Lett. **102**, 186601 (2009).

[437] N. Manyala, Y. Sidis, J. F. DiTusa, G. Aeppli, D. P. Young, and Z. Fisk, Large anomalous Hall effect in a silicon-based magnetic semiconductor, Nature Mater. **3**, 255 (2004).

[438] K. Mittermüller, *Tieftemperatur-Röntgenpulverdiffraktometrie von komplexen metallischen Verbindungen*, Diploma thesis, Technische Unitversität München (2011).

[439] C. Thessieu, K. Kamishima, T. Goto, and G. Lapertot, Magnetization under High Pressure in MnSi, J. Phys. Soc. Jpn. **67**, 3605 (1998).

[440] J. Kindervater, T. Adams, A. Bauer, W. Häußler, R. Georgii, M. Garst, and C. Pfleiderer, Cubic anisotropies and Skyrmion lattice in $\mathrm{Mn}_{1-x}\mathrm{Fe}_x\mathrm{Si}$, unpublished (2014).

[441] K. Motoya, H. Yasuoka, Y. Nakamura, and J. H. Wernick, Magnetic Properties of MnSi-CoSi Solid Solution Alloys, J. Phys. Soc. Jpn. **44**, 1525 (1978).

[442] B. Fåk, R. A. Sadykov, J. Flouquet, and G. Lapertot, Pressure dependence of the magnetic structure of the itinerant electron magnet MnSi, J. Phys.: Condens. Matter **17**, 1635 (2005).

[443] C. Franz, F. Freimuth, A. Bauer, R. Ritz, C. Schnarr, C. Duvinage, T. Adams, S. Blügel, A. Rosch, Y. Mokrousov, and C. Pfleiderer, Real-Space and Reciprocal-Space Berry Phases in the Hall Effect of $\mathrm{Mn}_{1-x}\mathrm{Fe}_x\mathrm{Si}$, Phys. Rev. Lett. **112**, 186601 (2014).

[444] C. Schnarr, *Spin Transfer Torque Effekte in chiralen Magneten*, Diploma thesis, Technische Unitversität München (2012).

[445] C. Meingast, Q. Zhang, T. Wolf, F. Hardy, K. Grube, W. Knafo, P. Adelmann, P. Schweiss, and H. v. Löhneysen, Resistivity of $\mathrm{Mn}_{1-x}\mathrm{Fe}_x\mathrm{Si}$ Single Crystals: Evidence for Quantum Critical Behavior, in *Properties and Applications of Thermoelectric Materials*, NATO Science for Peace and Security Series B: Physics and Biophysics, edited by Z. Veljko and A. C. Hewson (Springer Netherlands, 2009) p. 261.

[446] S. V. Demishev, I. I. Lobanova, V. V. Glushkov, T. V. Ischenko, N. E. Sluchanko, V. A. Dyadkin, N. M. Potapova, and S. V. Grigoriev, Quantum Bicriticality in $\mathrm{Mn}_{1-x}\mathrm{Fe}_x\mathrm{Si}$ Solid Solutions: Exchange and Percolation Effects, JETP Lett. **98**, 829 (2013).

[447] M. N. Wilson, E. A. Karhu, A. S. Quigley, U. K. Rößler, A. B. Butenko, A. N. Bogdanov, M. D. Robertson, and T. L. Monchesky, Extended elliptic skyrmion gratings in epitaxial MnSi thin films, Phys. Rev. B **86**, 144420 (2012).

[448] K. M. Sivakumar, Y. K. Kuo, and C. S. Lue, Substitutional effect on the transport properties of MnSi, J. Magn. Magn. Mater. **304**, e315 (2002).

[449] E. Bauer, A. Galatanu, R. Hauser, C. Reichl, G. Wiesinger, G. Zaussinger, M. Galli, and F. Marabelli, Evolution of a metallic and magnetic state in (Fe,Mn)Si and Fe(Si,Ge), J. Magn. Magn. Mater. **177–181**, 1401 (1998).

[450] N. Manyala, Y. Sidis, J. F. DiTusa, G. Aeppli, D. P. Young, and Z. Fisk, Magnetoresistance from quantum interference effects in ferromagnets, Nature (London) **404**, 581 (2000).

[451] N. Manyala, J. F. DiTusa, G. Aeppli, and A. P. Ramirez, Doping a semiconductor to create an unconventional metal, Nature (London) **454**, 976 (2008).

[452] K. Ishimoto, Y. Yamaguchi, J. Suzuki, M. Arai, M. Furusaka, and Y. Endoh, Small-angle neutron diffraction from the helical magnet $Fe_{0.8}Co_{0.2}Si$, Physica B **213–214**, 381 (1995).

[453] M. A. Chernikov, L. Degiorgi, E. Felder, S. Paschen, A. D. Bianchi, H. R. Ott, J. L. Sarrao, Z. Fisk, and D. Mandrus, Low-temperature transport, optical, magnetic and thermodynamic properties of $Fe_{1-x}Co_xSi$, Phys. Rev. B **56**, 1366 (1997).

[454] S. V. Grigoriev, V. A. Dyadkin, D. Menzel, J. Schoenes, Y. O. Chetverikov, A. I. Okorokov, H. Eckerlebe, and S. V. Maleyev, Magnetic structure of $Fe_{1-x}Co_xSi$ in a magnetic field studied via small-angle polarized neutron diffraction, Phys. Rev. B **76**, 224424 (2007).

[455] M. Motokawa, S. Kawarazaki, H. Nojiri, and T. Inoue, Magnetization measurements of $Fe_{1-x}Co_xSi$, J. Magn. Magn. Mater. **70**, 245 (1987).

[456] V. Jaccarino, G. K. Wertheim, J. H. Wernick, L. R. Walker, and S. Arajs, Paramagnetic Excited State of FeSi, Phys. Rev. **160**, 476 (1967).

[457] T. Adams, S. Mühlbauer, A. Neubauer, W. Münzer, F. Jonietz, R. Georgii, B. Pedersen, P. Böni, A. Rosch, and C. Pfleiderer, Skyrmion Lattice Domains in $Fe_{1-x}Co_xSi$, J. Phys.: Conf. Ser. **200**, 032001 (2010).

[458] M. Uchida, Y. Onose, Y. Matsui, and Y. Tokura, Real-Space Observation of Helical Spin Order, Science **311**, 359 (2006).

[459] G. Meunier and M. Bertaud, Constantes cristallographiques de $CuSe_2O_5$, $CuSeO_3$ et Cu_2SeO_4, J. Appl. Cryst. **9**, 364 (1976).

[460] H. Effenberger and F. Pertlik, Die Kristallstrukturen der Kupfer(II)-oxo-selenite $Cu_2O(SeO_3)$ (kubisch und monoklin) und $Cu_4O(SeO_3)_3$ (monoklin und triklin), Monatsh. Chem. **117**, 887 (1985).

[461] A. Larrañaga, J. L. Mesa, L. Lezama, J. L. Pizarro, M. I. Arriortua, and T. Rojo, Supercritical hydrothermal synthesis of $Cu_2O(SeO_3)$: Structural characterization, thermal, spectroscopic and magnetic studies, Mater. Res. Bull. **44**, 1 (2009).

[462] K. Kohn, A New Ferrimagnet Cu_2SeO_4, J. Phys. Soc. Jpn **42**, 2065 (1977).

[463] J.-W. G. Bos, C. V. Colin, and T. T. M. Palstra, Magnetoelectric coupling in the cubic ferrimagnet Cu_2OSeO_3, Phys. Rev. B **78**, 094416 (2008).

[464] I. Živković, D. Pajić, T. Ivek, and H. Berger, Two-step transition in a magnetoelectric ferrimagnet Cu_2OSeO_3, Phys. Rev. B **85**, 224402 (2012).

[465] C. L. Huang, K. F. Tseng, C. C. Chou, S. Mukherjee, J. L. Her, Y. H. Matsuda, K. Kindo, H. Berger, and H. D. Yang, Observation of a second metastable spin-ordered state in ferrimagnet Cu_2OSeO_3, Phys. Rev. B **83**, 052402 (2011).

[466] M. C. Langner, S. Roy, S. K. Mishra, J. C. T. Lee, X. W. Shi, M. A. Hossain, Y.-D. Chuang, S. Seki, Y. Tokura, S. D. Kevan, and R. W. Schoenlein, Coupled Skyrmion Sublattices in Cu_2OSeO_3, Phys. Rev. Lett. **112**, 167202 (2014).

[467] P. Milde, E. Neuber, J. Kindervater, A. Bauer, A. Chacon, J. Waizner, M. Garst, S. Mühlbauer, H. Berger, L. M. Eng, and C. Pfleiderer, Multi-domain Skyrmion lattice in Cu_2OSeO_3, unpublished (2014).

[468] K. H. Miller, X. S. Xu., H. Berger, E. S. Knowles, D. J. Arenas, M. W. Meisel, and D. B. Tanner, Magnetodielectric coupling of infrared phonons in single-crystal Cu_2OSeO_3, Phys. Rev. B **82**, 144107 (2010).

[469] A. Maisuradze, Z. Guguchia, B. Graneli, H. M. Rønnow, H. Berger, and H. Keller, μSR investigation of magnetism and magnetoelectric coupling in Cu_2OSeO_3, Phys. Rev. B **84**, 064433 (2011).

[470] A. Maisuradze, A. Shengelaya, H. Berger, D. M. Djokić, and H. Keller, Magnetoelectric Coupling in Single Crystal Cu_2OSeO_3 Studied by a Novel Electron Spin Resonance Technique, Phys. Rev. Lett. **108**, 247211 (2012).

[471] M. Belesi, I. Rousochatzakis, M. Abid, U. K. Rößler, H. Berger, and J.-P. Ansermet, Magnetoelectric effects in single crystals of the cubic ferrimagnetic helimagnet Cu_2OSeO_3, Phys. Rev. B **85**, 224413 (2012).

[472] J. H. Yang, Z. L. Li, X. Z. Lu, M.-H. Whangbo, S.-H. Wei, X. G. Gong, and H. J. Xiang, Strong Dzyaloshinskii-Moriya Interaction and Origin of Ferroelectricity in Cu_2OSeO_3, Phys. Rev. Lett. **109**, 107203 (2012).

[473] C. Jia, S. Onoda, N. Nagaosa, and J. H. Han, Bond electronic polarization induced by spin, Phys. Rev. B **74**, 224444 (2006).

[474] C. Jia, S. Onoda, N. Nagaosa, and J. H. Han, Microscopic theory of spin-polarization coupling in multiferroic transition metal oxides, Phys. Rev. B **76**, 144424 (2007).

[475] T. Arima, Ferroelectricity Induced by Proper-Screw Type Magnetic Order, J. Phys. Soc. Jpn. **76**, 073702 (2007).

[476] H. Murakawa, Y. Onose, S. Miyahara, N. Furukawa, and Y. Tokura, Comprehensive study of the ferroelectricity induced by the spin-dependent *d*-*p* hybridization mechanism in $Ba_2XGe_2O_7$ (X = Mn, Co, and Cu), Phys. Rev. B **85**, 174106 (2012).

[477] T. Kimura, T. Goto, H. Shintani, K. Ishizaka, T. Arima, and Y. Tokura, Magnetic control of ferroelectric polarization, Nature (London) **426**, 55 (2003).

[478] M. Fiebig, Revival of the magnetoelectric effect, J. Phys. D: Appl. Phys. **38**, R123 (2005).

[479] H. Katsura, N. Nagaosa, and A. V. Balatsky, Spin Current and Magnetoelectric Effect in Noncollinear Magnets, Phys. Rev. Lett. **95**, 057205 (2005).

[480] Y. Tokura and S. Seki, Multiferroics with Spiral Spin Orders, Adv. Mater. **22**, 1554 (2010).

[481] S. Seki, Y. Yamasaki, M. Soda, M. Matsuura, K. Hirota, and Y. Tokura, Correlation between Spin Helicity and an Electric Polarization Vector in Quantum-Spin Chain Magnet $LiCu_2O_2$, Phys. Rev. Lett. **100**, 127201 (2008).

[482] Y. Tokunaga, N. Furukawa, H. Sakai, Y. Taguchi, T. Arima, and Y. Tokura, Composite domain walls in a multiferroic perovskite ferrite, Nature Mater. **8**, 558 (2009).

[483] H. Murakawa, Y. Onose, and Y. Tokura, Electric-Field Switching of a Magnetic Propagation Vector in a Helimagnet, Phys. Rev. Lett. **103**, 147201 (2009).

[484] A. A. Omrani, J. S. White, K. Prša, I. Živković, H. Berger, A. Magrez, Y.-H. Liu, J. H. Han, and H. M. Rønnow, Exploration of the helimagnetic and skyrmion lattice phase diagram in Cu_2OSeO_3 using magnetoelectric susceptibility, Phys. Rev. B **89**, 064406 (2014).

[485] Y.-H. Liu, Y.-Q. Li, and J. H. Han, Skyrmion dynamics in multiferroic insulators, Phys. Rev. B **87**, 100402 (2013).

[486] L. Kong and J. Zang, Dynamics of an Insulating Skyrmion under a Temperature Gradient, Phys. Rev. Lett. **111**, 067203 (2013).

[487] J. Iwasaki, A. J. Beekman, and N. Nagaosa, Theory of magnon-skyrmion scattering in chiral magnets, Phys. Rev. B **89**, 064412 (2014).

[488] C. Schütte and M. Garst, Magnon-skyrmion scattering in chiral magnets, arXiv:1405.1568 (2014).

[489] S.-Z. Lin, C. D. Batista, C. Reichhardt, and A. Saxena, ac Current Generation in Chiral Magnetic Insulators and Skyrmion Motion induced by the Spin Seebeck Effect, Phys. Rev. Lett. **112**, 187203 (2014).

[490] J. S. White, I. Levatić, A. A. Omrani, N. Egetenmeyer, K. Prša, I. Živković, J. L. Gavilano, J. Kohlbrecher, M. Bartkowiak, H. Berger, and H. M. Rønnow, Electric field control of the skyrmion lattice in Cu_2OSeO_3, J. Phys.: Condens. Matter **24**, 432201 (2012).

[491] A. B. Gokhale and R. Abbaschian, The Ge-Mn (Germanium-Manganese) system, Bull. Alloy Phase Diagrams **11**, 460 (1990).

[492] H. Takizawa, T. Sato, T. Endo, and M. Shimada, High-pressure synthesis and electrical and magnetic properties of MnGe and CoGe with the cubic B20 structure, J. Solid State Chem. **73**, 40 (1970).

[493] N. Kanazawa, Y. Onose, T. Arima, D. Okuyama, K. Ohoyama, S. Wakimoto, K. Kakurai, S. Ishiwata, and Y. Tokura, Large Topological Hall Effect in a Short-Period Helimagnet MnGe, Phys. Rev. Lett. **106**, 156603 (2011).

[494] O. L. Makarova, A. V. Tsvyashchenko, G. Andre, F. Porcher, L. N. Fomicheva, N. Rey, and I. Mirebeau, Neutron diffraction study of the chiral magnet MnGe, Phys. Rev. B **85**, 205205 (2012).

[495] V. I. Larchev and S. V. Popova, The polymorphism of transition metal monogermanides at high pressures and temperatures, J. Less-Common Met. **87**, 53 (1982).

[496] R. Wäppling and L. Häggström, Mössbauer study of cubic FeGe, Phys. Lett. A **28**, 173 (1968).

[497] L. Lundgren, K. A. Blom, and O. Beckman, Magnetic susceptibility measurements on cubic FeGe, Phys. Lett. A **28**, 175 (1968).

[498] L. Ludgren, O. Beckman, V. Attia, S. P. Bhattacheriee, and M. Richardson, Helical Spin Arrangement in Cubic FeGe, Phys. Scr. **1**, 69 (1970).

[499] P. Pedrazzini, H. Wilhelm, D. Jaccard, T. Jarlborg, M. Schmidt, M. Hanfland, L. Akselrud, H. Q. Yuan, U. Schwarz, Y. Grin, and F. Steglich, Metallic State in Cubic FeGe Beyond Its Quantum Phase Transition, Phys. Rev. Lett. **98**, 047204 (2007).

[500] H. Wilhelm, M. Baenitz, M. Schmidt, U. K. Rößler, A. A. Leonov, and A. N. Bogdanov, Precursor Phenomena at the Magnetic Ordering of the Cubic Helimagnet FeGe, Phys. Rev. Lett. **107**, 127203 (2011).

[501] H. Wilhelm, M. Baenitz, M. Schmidt, C. Naylor, R. Lortz, U. K. Rößler, A. A. Leonov, and A. N. Bogdanov, Confinement of chiral magnetic modulations in the precursor region of FeGe, J. Phys.: Condens. Matter **24**, 294204 (2012).

[502] L. Cevey, H. Wilhelm, M. Schmidt, and R. Lortz, Thermodynamic investigations in the precursor region of FeGe, Phys. Status Solidi B **250**, 650 (2013).

[503] U. K. Rößler, A. A. Leonov, and A. N. Bogdanov, Chiral Skyrmionic matter in non-centrosymmetric magnets, J. Phys.: Conf. Ser. **303**, 012105 (2011).

[504] M. Deutsch, O. L. Makarova, T. C. Hansen, M. T. Fernandez-Diaz, V. A. Sidorov, A. V. Tsvyashchenko, L. N. Fomicheva, F. Porcher, S. Petit, K. Koepernik, U. K. Rößler, and I. Mirebeau, Two-step pressure-induced collapse of magnetic order in the MnGe chiral magnet, Phys. Rev. B **89**, 180407 (2014).

[505] Y. Shiomi, N. Kanazawa, K. Shibata, Y. Onose, and Y. Tokura, Topological Nernst effect in a three-dimensional skyrmion-lattice phase, Phys. Rev. B **88**, 064409 (2013).

[506] S. M. Stishov and A. E. Petrova, Itinerant helimagnet MnSi, Phys.-Usp. **54**, 1117 (2011).

[507] A. Bauer, H. Berger, and C. Pfleiderer, Slow time scales at the magnetic phase transitions in Cu_2OSeO_3, unpublished (2014).

[508] I. Stasinopoulos, J. Kindervater, A. Bauer, F. Rucker, J. Waizner, A. Chacon, S. Mühlbauer, M. Garst, D. Grundler, and C. Pfleiderer, Fluctuations of Skyrmionic character in MnSi above T_c, unpublished (2014).

[509] S. S. Samatham and V. Ganesan, Precursor state of skyrmions in MnSi: a heat capacity study, Phys. Status Solidi RRL **7**, 184 (2013).

[510] S. M. Stishov, A. E. Petrova, A. A. Shikov, T. A. Lograsso, E. I. Isaev, B. Johansson, and L. L. Daemen, Lost Heat Capacity and Entropy in the Helical Magnet MnSi, Phys. Rev. Lett. **105**, 236403 (2010).

[511] A. E. Petrova, V. N. Krasnorussky, A. A. Shikov, W. M. Yuhasz, T. A. Lograsso, J. C. Lashley, and S. M. Stishov, Elastic, thermodynamic, and electronic properties of MnSi, FeSi, and CoSi, Phys. Rev. B **82**, 155124 (2010).

[512] S. M. Stishov, A. E. Petrova, S. Khasanov, G. K. Panova, A. A. Shikov, J. C. Lashley, D. Wu, and T. A. Lograsso, Experimental study of the magnetic phase transition in the MnSi itinerant helimagnet, J. Exp. Theor. Phys. **106**, 888 (2008).

[513] S. Ishiwata, M. Tokunaga, Y. Kaneko, D. Okuyama, Y. Tokunaga, S. Wakimoto, K. Kakurai, T. Arima, Y. Taguchi, and Y. Tokura, Versatile helimagnetic phases under magnetic fields in cubic perovskite $SrFeO_3$, Phys. Rev. B **84**, 054427 (2011).

[514] Y. Taguchi, Y. Oohara, H. Yoshizawa, N. Nagaosa, and Y. Tokura, Spin Chirality, Berry Phase, and Anomalous Hall Effect in a Frustrated Ferromagnet, Science **291**, 2573 (2001).

[515] M. Onoda, G. Tatara, and N. Nagaosa, Anomalous Hall Effect and Skyrmion Number in Real and Momentum Spaces, J. Phys. Soc. Jpn. **73**, 2624 (2004).

[516] P. Bruno, V. K. Dugaev, and M. Taillefumier, Topological Hall Effect and Berry Phase in Magnetic Nanostructures, Phys. Rev. Lett. **93**, 096806 (2004).

[517] Y. Shiomi, S. Iguchi, and Y. Tokura, Emergence of topological Hall effect from fanlike spin structure as modified by Dzyaloshinsky-Moriya interaction in MnP, Phys. Rev. B **86**, 180404 (2012).